LASER CALIBRATION AND EVENT RECONSTRUCTION IN DOUBLE CHOOZ EXPERIMENT

by

YUJING SUN

ION STANCU, COMMITTEE CHAIR
JEROME K. BUSENITZ
ALLEN B. STERN
DAWN R. WILLIAMS
WEI ZHU

A DISSERTATION

Submitted in partial fullfillment of the requirements
for the degree of Doctor of Philosophy
in the Department of Physics and Astronomy
in the Graduate School of
The University of Alabama

TUSCALOOSA, ALABAMA

2013

Copyright Yujing Sun 2013
ALL RIGHTS RESERVED

ABSTRACT

The neutrino oscillation mixing angle θ_{13} was the last mixing angle that had not been determined precisely in 2006 when I started my Ph.D studies. It is exciting to witness how θ_{13} has evolved from a limit to a precisely measured mixing angle in a short period. The Double Chooz reactor neutrino experiment was the first to report strong evidence for a non-vanishing value of θ_{13} at the beginning of 2012. The latest analysis, which includes a combined "rate+shape" analysis of hydrogen and gadolinium capture inverse β-decay events, has yielded $\sin^2 2\theta_{13} = 0.109 \pm 0.035$ with only one detector running. This value is consistent with the current numbers from the Daya Bay and Reno experiments.

In such a high-precision experiment, precise calibrations are crucial in reaching the ultimate sensitivity. The laser calibration system was developed by the University of Alabama group to calibrate PMT constants such as gains and time offsets, as well as measure the charge likelihoods which are used in the event energy reconstruction and supplement the time likelihoods in improving the position reconstruction accuracy. The second part of this thesis is devoted to the hardware and software development of the laser calibration system, as well as MC studies and data analyses for extracting the PMT gains, time offsets and charge likelihoods.

The event reconstruction utilizes the PMT time and charge information to determine the event location and energy, which are essential parameters for all physics analyses. A good understanding of the detector response significantly reduces the detector related systematic errors and improves the sensitivity, especially in the two detector phase, where the dominant uncertainties from the reactor flux mostly cancel out. The third part of this thesis is dedicated to the reconstruction algorithm developed by our group, position accuracy studies and energy reconstruction studies, which aims towards fully understanding the detector response.

LIST OF ABBREVIATIONS

ADC	Analog-to-digital converter
ANL	Argonne National Laboratory
ASIC	Application-specific integrated circuit
ATLAS	A Toroidal LHC Apparatus
Bis-MSB	4-bis-(2-methylstyryl)benzene
CERN	European Organization for Nuclear Research
CHORUS	CERN Hybrid Oscillation Research Apparatus
CKM	Cabibbo-Kobayashi-Maskawa
CMS	Compact Muon Solenoid
DAQ	Data acquisition
DCGLG4sim	Double Chooz generic LAND Geant4 simulation
DCRecoPulse	Double Chooz PMT pulse reconstruction and pedestal analysis package
DCRoSS	Double Chooz readout simulation software
DONUT	Direct Observation of NU Tau
DUQ	Digit unit of charge
EDF	Électricité de France
Fermilab	Fermi National Accelerator Laboratory
FIFO	First in first out
FPGA	Field-programmable gate array
FWHM	Full width at half maximum
GALLEX	Gallium Experiment
H/NH	Hit/no-hit
HPW	Harvard-Purdue-Wisconsin
IDLI	Inner detector light injection

ILL	Institut Laue-Langevin
IMB	Irvine-Michigan-Brookhaven
K2K	KEK to Kamioka
Kamiokande	Kamioka Nucleon Decay Experiment
KamLAND	Kamioka Liquid Scintillator Antineutrino Detector
KATRIN	Karlsruhe Tritium Neutrino Experiment
KEK	The High Energy Accelerator Research Organization
LEP	Large Electron-Positron Collider
LHC	Large Hadron Collider
LI	Light injection
LSND	Liquid Scintillator Neutrino Detector
MAMBO-II	Mampe Bottle-II
MARE	Microcalorimeter Arrays for a Rhenium Experiment
MAROC2	Multi anode read out chip
MC	Monte Carlo (computer simulated data)
MiniBooNE	Mini Booster Neutrino Experiment
MINOS	Main Injector Neutrino Oscillation Search
MINUIT	CERN function minimization and error analysis package
MSW	Mikheyev-Smirnov-Wolfenstein
MURE	Monte Carlo N-Particle Utility for Reactor Evolution
NDF	Neutral density filter
NOνA	Neutrinos at the Main Injector Off-Axis ν_e Appearance
NOMAD	Neutrino Oscillation Magnetic Detector
NUSEX	Nucleon Stability Experiment
PE	Photoelectron
PMNS	Pontecorvo-Maki-Nakagawa-Sakata
PMT	Photomultiplier tube
PPO	2,5-diphenyloxazole
O-PXE	Ortho-Phenylxylylethane
QCD	Quantum chromodynamics

QLLK	Charge negative log-likelihood
RecoBAMA	Reconstruction package developed by the University of Alabama group
SAGE	Soviet-American Gallium Experiment
SLAC	Stanford Linear Accelerator Center
SNO	Sudbury Neutrino Observatory
T2K	Tokai to Kamioka
TLLK	Time negative log-likelihood
TR	Transmission rate
UA1	Underground Area 1
WMAP	Wilkinson Microwave Anisotropy Probe

ACKNOWLEDGMENTS

First of all, I want to express the deepest appreciation to the most important person, Ion Stancu, who has helped me with all my achievements. It is my great honor and pleasure to have you as my advisor. I would not have been able to get here without your help which is not only in academic research but also in every aspect of my life. I appreciate very much your patience in correcting my mistakes and my writings every time. I especially thank you for listening to my heart voice and helping me through all those tough times in my life when I was almost knocked down. You possess so many merits and set such a model that I wish to emulate. Please accept my deepest gratitude again for all your patient guidance, enthusiastic encouragement and useful critiques in my research work.

I want to thank my dissertation committee members: Jerry Busenitz, Allen Stern, Dawn Williams, and Wei Zhu for their dedication and commitment for making the corrections and the questions.

My grateful thanks are to Wusheng Dai and Yong Liu. Wusheng Dai enlightened me in many courses during my undergraduate and graduate studies in Tianjin University, which made my graduate life in Tuscaloosa much easier. Wusheng is one of the most knowledgeable people I have ever seen in my life. It really opened my mind when talking to him. Yong is a diligent, humble, obliging person who gave me a lot of useful advice and assistance on starting my present project.

I would like to thank the entire Double Chooz collaboration, especially people from the calibration group, Masaki Ishitsuka, Zelimir Djurcic, as well as Bernd Reinhold from the energy reconstruction group. I want to thank Jason Goon who helped me on laser hardware knowledge and Juergen Reichenbacher for radioactive sources information. I would like to thank Lindley Winslow and Kazuhiro Terao. Kazu took his time explaining how to run Common Trunk and check in code to me. I would like to thank Glenn Horton Smith who patiently gave me a lot of explanations and advice on MC simulation. Thanks to Novella Pau for explaining the pulse reconstruction to me. Thanks also to Camillo Marinai for arranging my trip to Columbia University (Nevis).

I would also like to thank Denis Perevalov and Ranjan Dharmapalan who helped me settled down when I arrived at UA. Your friendship over the past years means a lot to me. I would like to thank Christopher Grant and Greg Keefer for the help on programming problems. A thank you to Shak Fernandes who helped read and correct this dissertation. Another thank to Nathan Papapietro who helped explain some theory questions for me.

I would also like to extend my thanks to the entire physics department of UA. Technicians Danny Whitcomb and Jason Kuykendall in the physics department offered me great help. The credits of hardware part of laser calibration system have to be given to the professional work from machinists: David Key, Joe Howell and Mike Perrigin.

I wish to thank my family for their support and encouragement throughout my study.

Finally, I want to extend my grateful thanks to all those who helped me but whose names are not mentioned above. I wish I could write another dissertation to express my gratitude to all of you. Every favor I have received from you encouraged me to move forward.

CONTENTS

LIST OF TABLES

LIST OF FIGURES

Chapter 1

Neutrino Experiment History

In this chapter neutrino history is discussed chronologically, highlighting both significant theoretical postulations and experimental discoveries.

The birth of neutrinos can be traced back from the late 19th century to the early 20th century, when alpha, beta and gamma radioaction was gradually discovered.

In 1896, Henri Becquerel discovered radiation from uranium salts [1] and Pierre and Marie Curie isolated radium [2], which turns out to be a much more radioactive source than uranium. In 1899, two categories of radiation, named alpha and beta, were discovered by Ernest Rutherford [3]. In 1900, Paul Ulrich Villard found evidence for a third type of radiation coming from radium, which he called gamma radiation [4]–[7]. Two years later, Pierre and Marie Curie pointed out that the particles produced by beta radiation were only electrons. Meanwhile, Frederick Soddy and Ernest Rutherford hypothesized that the three existing kinds of radioactivity are of different types [8]. Around 1904, Rutherford postulated that helium atoms make up alpha radiation. Later, beta and gamma particles were identified as electrons and high energy photons, respectively, emitted by radioactive nuclei. The basic knowledge about the three different types of radiation had been established.

What followed was the problem with the energy of the outgoing electron in β-decays, which was expected to be monoenergetic (as in standard two-body decays). Independent studies by Lise Meitner, Otto Hahn, William Wilson and Von Baeyer, and James Chadwick in 1914 indicated that the electron – energy spectrum is continuous, in direct contradiction with the energy conservation law which had been verified by experiments again and again in history. However, the spectrum was shown very clearly to be continous by Charles Drummond Ellis along with colleagues between 1920 and 1927 [9]–[14]. Some famous scientists like Niels Bohr found it hard to believe. It was Wolfgang Pauli who, in 1930, proposed a hypothetical particle, the neutrino [15], which was first named the "neutron". This name was soon taken by James Chadwick in the discovery of the neutron in February 1932 [16]. Obviously, neutrons are too heavy to be the particle suggested by Pauli. In October 1933, Pauli stated at the Solvay conference in Bruxelles:

> *"... their mass can not be very much more than the electron mass. In order to distinguish them from heavy neutrons, Mister Fermi has proposed to name them 'neutrinos'. It is possible that the proper mass of neutrinos be zero... It seems to me plausible that neutrinos have a spin 1/2... We know nothing about the interaction of neutrinos with the other particles of matter and with photons: the hypothesis that they have a magnetic moment seems to me not funded at all."*

In the same year, Francis Perrin showed that the neutrino mass had to be much lower than the electron mass [17]. The first antiparticle, the positron, was discovered by Carl David Anderson [18], which verified Paul Adrien Maurice Dirac's theory and confirmed Pauli and Enrico Fermi's neutrino idea. By the end of the year, Frederic Joliot-Curie found the beta plus decay while Fermi took the neutrino hypothesis and built his theory of beta decay [19]. The next year, in 1934, Hans Bethe and Rudolf Peierls found that the cross section of neutrinos interacting with matter was extraordinarily small, billions of times smaller than that of the electron [20]. Thus it was doubted at that time if the neutrinos could in fact be detected. In order to detect neutrinos, one can imagine that not only an abundant neutrino source is needed, but a large detector is also necessary.

The first neutrino detection experiment was carried out by Frederick Reines and Clyde Cowan at the nuclear power plant of Hanford, Washington, in 1953. No persuasive indication of a positive detection signal (only about 2σ significance) emerged from the analysis performed during the summer of the same year [21] since the background was too large (with a signal-to-noise ratio of about 1:20). Three years later, they built a second detector composed of 400 liters of water and a cadmium chloride mixture at a different nuclear power plant, in Savannah River, South Carolina. The neutrino interaction in the detector is the inverse β-decay,

$$\bar{\nu}_e + p \to e^+ + n,$$

which is still being used today to detect electron antineutrinos. The prompt annihilation between the positron and electrons in the surrounding material, emitting two back-to-back gammas, along with the 15 μs delayed neutron capture by cadmium nuclei, makes a unique signature for neutrino events detection [22]. This time, Reines and Cowan also managed to reduce the background and made improvements in other aspects of the experiment, which lead to a signal-to-reactor associated accidental background in excess of 20:1 and the signal-to-reactor independent background ratio of 3:1. Finally in 1959, their result convincingly showed the existence of neutrinos [23, 24] at a significance level of approximately five sigmas. Frederick Reines was awarded the Nobel Prize for the detection of the neutrino in 1995.

In 1957, the neutrino oscillations theory was developed by the Italian physicist Bruno Pontecorvo [25, 26], who later settled in the Soviet Union. The theory states that if there are more than one species of neutrino, oscillations between different species may occur. In 1958, Maurice Goldhaber, Lee Grodzins, and Andrew Sunyar from the Brookhaven National Laboratory proved that the helicity of neutrinos is left-handed [27]. This means that only neutrinos with their spins along the opposite direction of their motion exist.

The next quest for neutrino flavors began with the question of whether the neutrino that comes along with an electron is the same as that associated with a muon. In 1959, after a discussion between Tsung-Dao Lee and Melvin Schwartz, the latter found a way to expose a neutrino detector to a pion decay beam, which is abundant in muon neutrinos. The pions are produced by a high energy proton beam reacting with matter. Tsung-Dao Lee and Chen Ning Yang were enthusiastic about the idea and began to calculate the expected cross sections, while Schwartz together with Leon Lederman and Jack Steinberger found the ideal detector for their experiment when looking at the spark chamber constructed by James

Cronin and his team at Princeton. At the beginning of 1962, the spark chamber was ready to detect the neutrinos coming out of the Brookhaven accelerator, with a flux of hundreds of millions of neutrinos per hour. There were about 40 interactions per hour clearly observed in the detector, 6 of which were identified as background of electron type; the remaining 34 were identified as a muon type, which concluded the existence of the second kind of neutrino, namely the ν_μ [28]. Steinberger, Lederman, and Schwartz won the Nobel Prize for this achievement in 1988.

The discoveries and studies of quarks also imply their inevitable relation to leptons and neutrinos in particular, which opens a door for further development of weak theories. In 1962, Ziro Maki, Masami Nakagawa and Shoichi Sakata introduced the concepts of neutrino flavor mixing and flavor oscillations [29].

In 1964, the feasability of detecting neutrinos from the sun was proposed by John Bahcall [30] and Raymond Davis [31]. In the late 1960s, Davis built a 600 tons chlorine-based detector in the Homestake mine 3000 meters underground. The resulting analysis showed that only 1/3 of neutrinos predicted by the standard solar model were detected in the chlorine detector, which was only sensitive to electron neutrinos [32]. This is the origin of the famous and long-standing "solar neutrino problem", which was resolved in 2002. The solar neutrino anomaly led to a lot of experiments looking to confirm the unexpected deficit, such as GALLEX (Gallium Experiment) [33], SAGE (Soviet-American Gallium Experiment) [34], Kamiokande (Kamioka Nucleon Decay Experiment) [35] and SNO (Sudbury Neutrino Observatory) [36]. Eventually, the idea of neutrino oscillation solved the problem.

In 1964, the quark model was independently proposed by physicists Murray Gell-Mann [37] and George Zweig [38, 39]. In 1968, deep inelastic scattering experiments at the Stanford Linear Accelerator Center (SLAC) [40, 41] showed that the protons are not point-like elementary particles. The particles inside protons were later identified as up and down quarks. In 1970, Sheldon Glashow, John Illiopoulos and Luciano Maiani predicted the second quark family [42], which was confirmed later in 1974 [43]. In 1973, Makoto Kobayashi and Toshihide Maskawa noted that the experimental observation of CP violation could be explained if there were a third pair of quarks [44]. Also in 1973, a new type of interaction, named neutral current interaction, was discovered [45]. Shortly afterward, the discovery was confirmed by scientists at Fermilab (Fermi National Accelerator Laboratory). This new type of interaction strongly supported Sheldon Glashow [46], Abdus Salam [47], and Steven Weinberg's [48] unification theory of weak and electromagnetic interactions, which was proposed a few years earlier.

In 1975, Martin Perl discovered the third generation of leptons, namely the τ [49]. Joined by Reines' detection of the neutrino, Perl won the 1995 Nobel Prize for the discovery of the tau lepton. With the discovery of the τ lepton, scientists knew that ν_τ must be there, but it took a long time until ν_τ was discovered.

In 1976, the Hawaii workshop made a design of a new generation neutrino detectors which subsequently led to the IMB (Irvine-Michigan-Brookhaven), HPW (Harvard-Purdue-Wisconsin) and Kamiokande detectors. In 1977, Leon Lederman and his team found the third generation of quarks, the bottom quark, at the Stanford accelerator [50].

In the 1980s, the IMB experiment, the first massive underground neutrino detector for nucleon decay search was built in the 2000-foot-deep Morton Salt mine near Cleveland, Ohio. Meanwhile in Japan, the Kamiokande experiment was constructed in the Kamioka zinc mine. In 1983, the UA1 (Underground Area 1) experiment discovered the W boson by its decay into electron and antineutrino [51] and later they also discovered the Z boson [52]. The discovery of weak gauge bosons and neutrinos was a milestone in physics history.

The recognition of non-zero mass of neutrinos was gradually established in the 1980s. In 1979, Reines undertook the measurement of the ratio of antineutrinos on deuterium between neutral current and charged current reactions. Although there was no conclusion, this motivated the Institute Laue Langevin (ILL) team in Grenoble to look for evidence of neutrino oscillation near the nuclear reactor, which led to a trend of searching for neutrino oscillations near nuclear power plants all over the world. The other contribution of the ILL team was that it gave birth to other experiments, such as Goesgen (in Switzerland) and Bugey (in France). In 1984, Bugey claimed to have seen oscillations, but Goesgen had not. However, by improving the experiment, Bugey later claimed no oscillations. In 1985, IMB [53] and Kamiokande [54] observed the "atmospheric neutrino anomaly", which referred to the fact that the muon neutrino flux of atmospheric neutrinos is substantially lower than the expected value.

In 1985, Stanislav Mikheyev and Alexei Smirnov [55] developed Lincoln Wolfenstein's theory [56, 57] about the phenomenon of neutrino oscillations enhanced by matter, which became to be known as the MSW (Mikheyev-Smirnov-Wolfenstein) effect (after the main three authors). Part of the solar neutrino deficit could have come from this effect. Before neutrinos come out of the sun, they travel a long path inside the sun where the matter is dense enough to induce a flavor change. The IMB experiment that was designed for detecting proton decay was also able to detect neutrinos and saw a shortage of atmospheric muon neutrinos, which was initially believed to be a detection inefficiency. In the same year, a Russian team announced the very small but non-zero neutrino mass by investigating the tritium β-decay:

$$^3H \rightarrow {}^3He + e^- + \nu_e.$$

In 1987, Kamiokande [58] along with IMB [59] observed a simultaneous burst of neutrinos from Supernova 1987A. This remains the only neutrino observation of a supernova burst to date.

In 1988, Kamiokande reported a 40% deficit of expected ν_μ from the atmospheric neutrino flux [60]. Kamiokande is not only able to detect neutrinos over a wide range of energies, but is also able to distinguish the reactions of ν_μ and ν_e. However, the Frejus [61] and NUSEX (Nucleon Stability Experiment) [62] experiments reported no deficit of ν_μ interactions. In 1989, Kamiokande became the second experiment observing a significant deficit (2/3) in the solar neutrino flux, which confirmed the "solar neutrino anomaly" [63].

In 1989, CERN (European Organization for Nuclear Research) announced by studying the Z boson lifetime that only three light neutrino families are allowed [64]–[67]. This result was based on the first month of data at LEP (Large Electron-Positron Collider). The Z boson, whose lifetime is about 10^{-23} s, can decay into a particle and antiparticle pair like neutrino and antineutrino. The combined result from the four LEP experiments, ALEPH (Apparatus for LEP Physics at CERN), DELPHI (Detector with Lepton, Photon and Hadron Identification), L3, and OPAL (Omni-Purpose Apparatus for LEP), gave $N_\nu = 2.9840 \pm 0.0082$ [68] as obtained from the width of the invariant mass distribution.

In 1990, IMB confirmed the deficit of atmospheric ν_μ interactions reported by Kamiokande after improving the ability in identifying ν_μ interactions [69]. From 1991 to 1992, the SAGE [70] experiment in Russia and GALLEX [71] in Italy confirmed the solar neutrino deficit in radiochemical experiments. In 1992, NOMAD (Neutrino Oscillation Magnetic Detector) and CHORUS (CERN Hybrid Oscillation Research Apparatus) were built at CERN to detect neutrino oscillations by searching for ν_τ appearance in a ν_μ beam. In 1994, the Kamiokande and IMB experiments used a beam from the KEK accelerator laboratory to test their detectors' ability in distinguishing ν_μ and ν_e. The test confirmed their early results and promoted these two groups to form the nucleus of the Super-Kamiokande project, which started its operation two years later in 1996.

In 1995, GALLEX [72] observed a 40% deficit of solar neutrinos over the entire energy spectrum. SAGE [73] confirmed this number and Kamiokande [74] reported a 50% deficit of the neutrinos with energy between 7 to 20 MeV. The Homestake [75] experiment witnessed a 70% deficit of ^{7}Be and ^{8}B neutrinos. These experiments could also be explained by the MSW effect.

In 1997, the atmospheric ν_μ disappearance rate at the Soudan-II experiment [76] confirmed the observation made by Kamiokande and IMB. The Soudan-II experiment also became the first experiment using an iron detector to detect ν_μ disappearance. In 1998 Super-Kamiokande, with the analysis of more than 500 days of data, reported anomalies both in the atmospheric and solar neutrino sectors. The atmospheric ν_μ result showed that the deficit varies depending on the distance the neutrinos travel, which points directly to neutrino oscillations, and implicitly a non-zero neutrino mass [77, 78]. In 1999, Fermilab started its main injector which is a proton accelerator that can also produce and accelerate antiprotons and inject them into the Tevatron. The main injector provides MINOS (Main

Injector Neutrino Oscillation Search, started in 2005) with an intense beam of muon flavored neutrinos at energies of a few GeV. In 2000, the direct detection of ν_τ was reported by the DONUT (Direct Observation of NU Tau) [79] experiment at Fermilab. In the same year, Super-Kamiokande found out that the atmospheric ν_μ do not oscillate into sterile neutrinos but rather into ν_τ [80].

The neutrino oscillations model can explain most of the experiment results, but there are still some anomalies, such as the LSND (Liquid Scintillator Neutrino Detector) result of oscillations between $\bar{\nu}_\mu$ and $\bar{\nu}_e$ [81]. The LSND experiment in Los Alamos used a $\bar{\nu}_\mu$ beam of up to 52.8 MeV from μ^+ decay at rest, looking for the $\bar{\nu}_e$ appearance in a detector with a baseline of 30 m. An excess of 87.9 ± 22.4 (stat.) ± 6.0 (syst.) $\bar{\nu}_e$ events can be interpreted as neutrino oscillations with a Δm^2 ranging from 0.2 eV^2 to 2 eV^2. This is incompatible with the widely accepted neutrino oscillations model, where $\Delta m^2_{21} = 7.53^{+0.18}_{-0.18} \times 10^{-5}$ eV^2 and $|\Delta \mathrm{m}^2_{32}| = 2.473^{+0.070}_{-0.067} \times 10^{-3}$ eV^2 for the normal hierarchy ($|\Delta \mathrm{m}^2_{32}| = 2.427^{+0.042}_{-0.065} \times 10^{-3}$ eV^2 for the inverted hierarchy), as required by the solar and atmospheric anomalies, respectively. A remedy would require the existence of at least one light "sterile" neutrino.

In 2001 to 2002, the SNO collaboration detected the neutral currents from solar neutrinos, along with charged currents and elastic scatters, giving the persuasive statement that the solar neutrino problem is caused by neutrino oscillations [82]. In 2002, Masatoshi Koshiba and Raymond Davis were awarded the Nobel Prize for detecting solar neutrinos as well as supernova neutrinos. Also in 2002, KamLAND (Kamioka Liquid Scintillator Antineutrino Detector) began its operation in January and announces the result of reactors $\bar{\nu}_e$ deficit in November [83]. Combined with the earlier solar neutrino result, it gave the correct parameters for the solar neutrino deficit. In 2003, the K2K (KEK to Kamioka) long-baseline neutrino oscillation experiment used an accelerator-produced neutrino beam to probe the atmospheric neutrino oscillation parameter Δm^2_{23} [84]. In 2004, Super-Kamiokande [85] and KamLAND [86] ruled out non-oscillations neutrino models by showing evidence for both neutrino reappearance and disappearance. In 2006, the MINOS experiment published their results on the atmospheric oscillation parameters measurement using an accelerator-based neutrino beam at Fermilab. It observed consistent results on Δm^2_{23} with the K2K and Super-Kamiokande experiments.

By 2006, the neutrino oscillations model had been well established based on the observation of numerous experiments. The neutrino mixing angle $\sin^2 2\theta_{12} = 0.86^{+0.05}_{-0.06}$ and the neutrino squared-mass splitting $\Delta m^2_{21} = 8.0^{+0.6}_{-0.4} \times 10^{-5}$ eV^2 are measured by solar and KamLAND data, while the neutrino mixing angle $\sin^2 2\theta_{23} > 0.92$ and the neutrino squared-mass splitting $\Delta m^2_{32} = 2.4^{+0.6}_{-0.5} \times 10^{-3}$ eV^2 are measured by Super-Kamiokande. The upper limit of θ_{13} ($\sin^2 2\theta_{13} \leq 0.19$ at 90% confidence level) is given at the $\Delta m^2_{31} = 1.9 \times 10^{-3}$ eV^2 value by the analysis of the CHOOZ data.

Chapter 2

Neutrino Oscillations

Neutrinos are elementary particles which rarely interact with matter, and are therefore very difficult to detect. According to the Standard Model, neutrinos are supposed to be massless. However, experimental evidence accumulated over the past decades indicates that neutrinos must have a small, but non-zero mass. There are three generations (or flavors) of neutrinos: the electron neutrino, ν_e, the muon neutrino, ν_μ, and the tau neutrino, ν_τ, which are created with the corresponding lepton flavors (e, μ, or τ, respectively). The quantum mechanical phenomenon through which the neutrino flavor changes during propagation is called *neutrino oscillations*, as first suggested by Bruno Pontecorvo [25, 26].

2.1 Standard Model

The Standard Model [87]–[90] is the most widely accepted theory that describes the elementary particles and their fundamental interactions, namely the electromagnetic, weak, and strong interactions. The theory is based on relativistic quantum field theory and local gauge groups. The internal symmetries of the Lagrangian density of the Standard Model are given by:

$$SU(3)_C \times SU(2)_W \times U(1)_Y. \tag{2.1}$$

The strong force in quantum chromodynamics is described by $SU(3)_C$. The electromagnetic and weak processes can be unified, manifesting as a single force known as the electroweak force. The electroweak theory is described by $SU(2)_W \times U(1)_Y$. The unification is through spontaneous symmetry breaking, where a scalar field, the Higgs, acquires a non-zero vacuum expectation value. It explains why there is only one massless mediating boson (photon) and how the $W^{\pm}$ and Z^0 bosons acquire masses via the Higgs mechanism. The number of generators (gauge bosons) is $n^2 - 1$ in an $SU(n)$ group, and only one in the $U(1)$ group. Therefore, there are 8 gluons in QCD (quantum chromodynamics) and 4 bosons ($W^{\pm}$, Z^0 and the photons) in the electroweak theory.

The Standard Model includes 12 fermions and 4 gauge bosons, as illustrated in from Fig.2.1. Each particle also has a corresponding antiparticle.

The fermions, having spin 1/2, abide by the Pauli exclusion principle and spin-statistics. The fermions are further categorized by the interactions they experience. There are six quarks undergoing all four basic forces and six leptons interact via three of the forces, i.e., all except the strong interaction. There are three generations in each group of quarks (u, d), (c, s), (t, b) and leptons (e, ν_e), (μ, ν_μ), (τ, ν_τ). Each generation exhibits similar physical behavior, but the masses between generations increase dramatically. The particles in the first generation are stable while the particles in the second and third generations decay very quickly and can only be detected through high energy experiments; none of the neutrinos is known to decay.

The quarks interact predominantly via the strong interaction because they carry color charge. They also carry electric charge and weak isospin which allow them to interact electromagnetically and weakly. Quarks are never observed free, only in bound states, forming color-neutral composite particles. This phenomenon is called color confinement. The color-neutral composites may be achieved in two ways: a quark and an antiquark of opposite color form a meson, or three quarks with a colorless composition form a baryon. The protons and neutrons are well known baryons with the smallest mass.

The six leptons do not carry color charge so that they do not interact via the strong

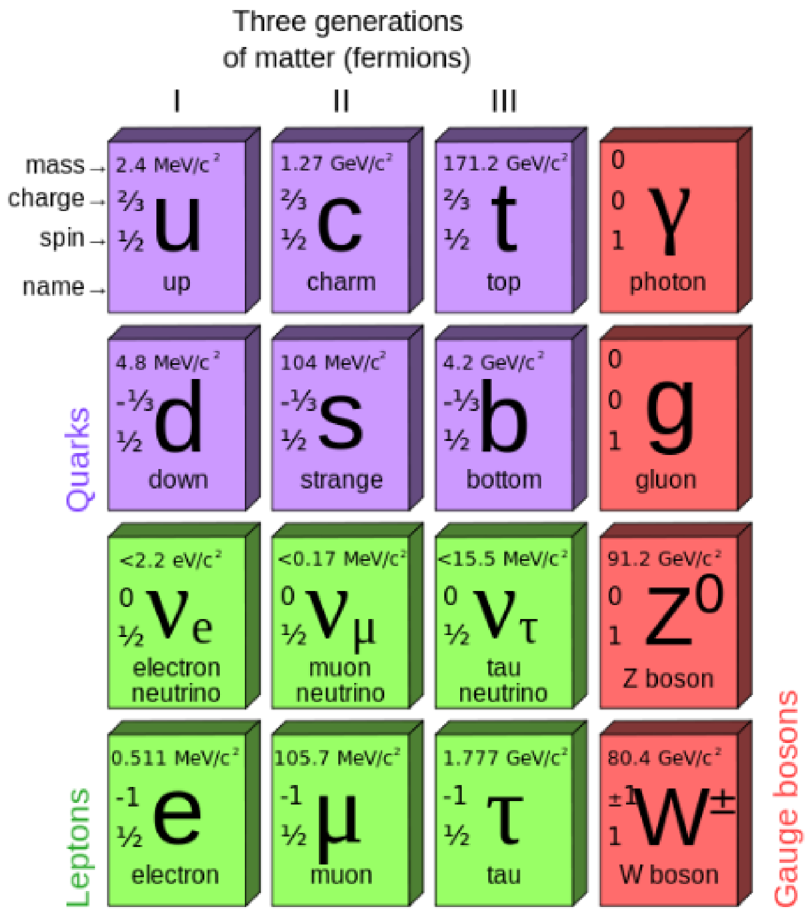

Figure 2.1: The Standard Model of elementary particles, with gauge bosons in the rightmost column [91].

force, and the three neutrinos do not have electric charge, so that they only interact via the weak and gravitational forces.

The gauge bosons are listed in the right column of Fig.2.1. Photons are the mediators of the electromagnetic force and are massless. $W^{\pm}$ and Z^0 are massive bosons mediating the weak force. Photons, $W^{\pm}$ and Z^0 bosons together mediate the electroweak interaction. The eight gluons are massless and mediate the strong interactions. They are labeled by a combination of color and anticolor charge, and therefore can also interact mutually. All four gauge bosons have spin 1. All the interactions between the Standard Model particles are illustrated in Fig.2.2. The basic interactions from which Feynman diagrams in the Standard Model are built are illustrated in Fig.2.3.

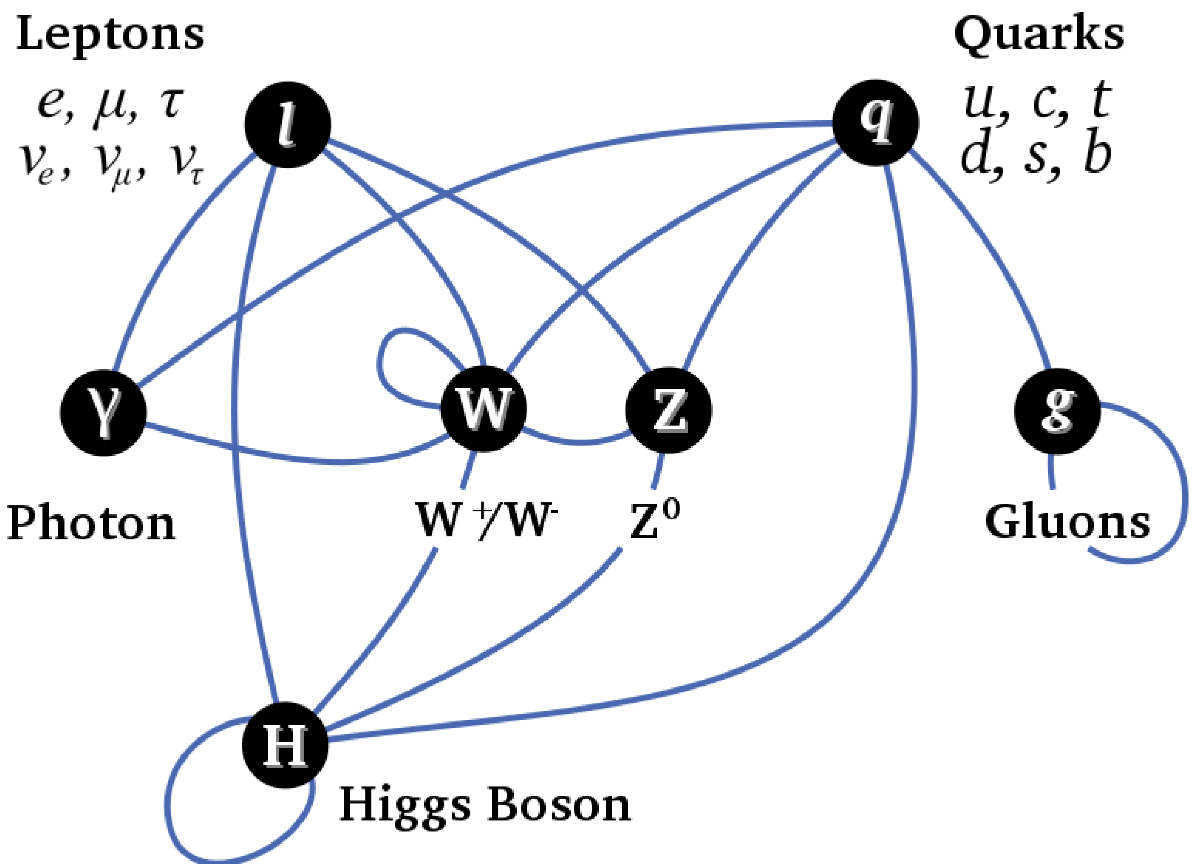

Figure 2.2: Summary of interactions between particles described by the Standard Model.

According to the Standard Model, neutrinos are massless and interact only weakly by neutral currents (by exchanging a Z^0 boson) and charged currents (by exchanging a $W^\pm$ boson). The reason why they were suggested to be massless is because helicity experiments have only observed left-handed neutrinos and right-handed antineutrinos [27]. If neutrinos have non-zero mass, one can always boost into a reference frame that flips their helicity. The consequence would require $\nu_R = \bar{\nu}_L$, which implies that the lepton number is not a conserved quantity, and thus lepton symmetry would be broken. In the Standard Model, there is no requirement that the lepton number has to be a conserved quantity. In this case, neutrinos are described by Majorana spinors, where two components ν_R and $\bar{\nu}_L$ do not change under charge conjugation.

For a Dirac particle, both the right-handed and left-handed helicity states exist. Maybe all fermions are Dirac spinors and are described by the Dirac equation. Neutrinos are charge

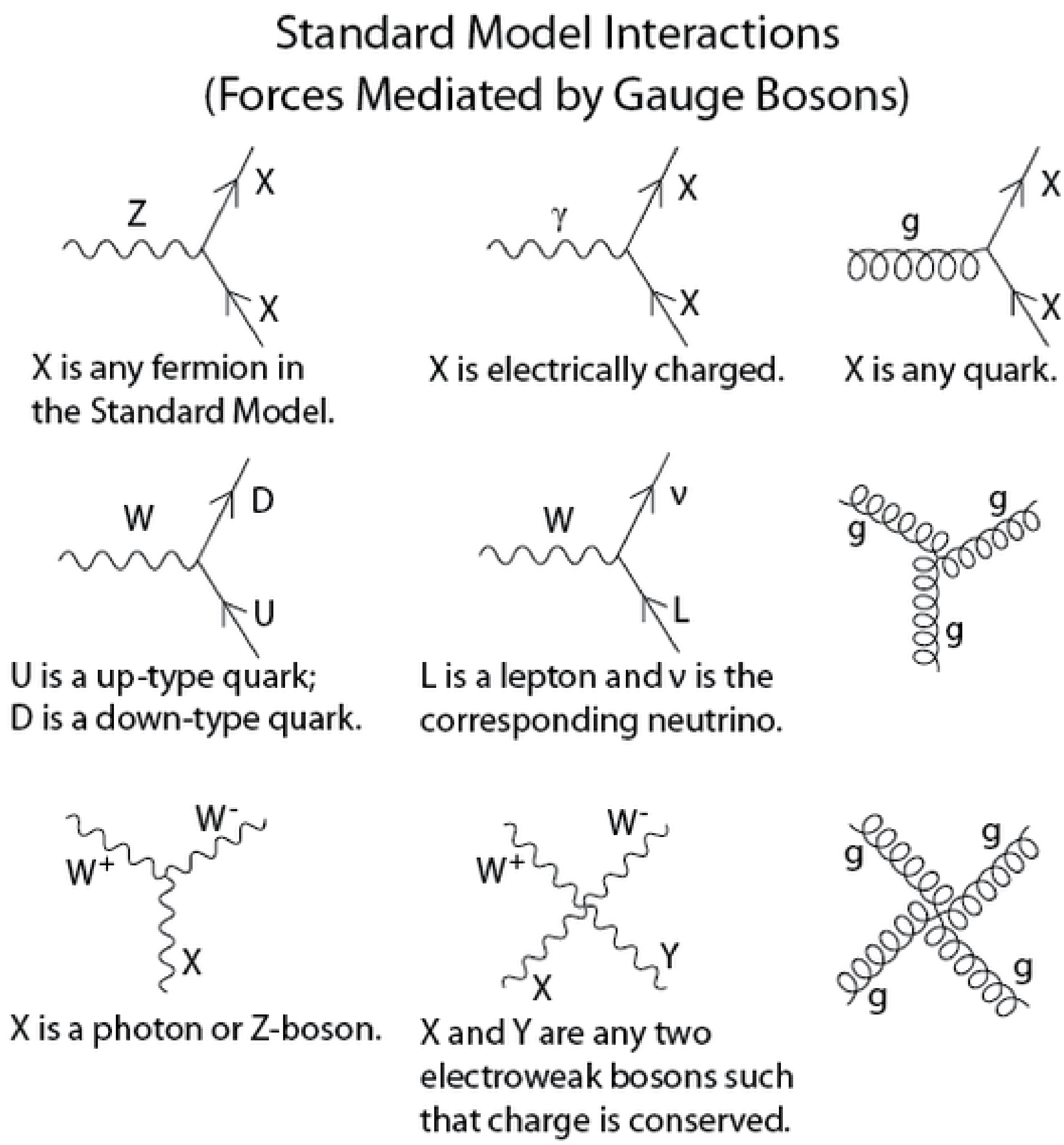

Figure 2.3: The above interactions form the basis of the Standard Model. Feynman diagrams in the Standard Model are built from these vertices. Modifications involving Higgs boson interactions and neutrino oscillations are omitted. The charge of the $W^{\pm}$ bosons are dictated by the fermions they interact with; the conjugate of each listed vertex (i.e. reversing the direction of arrows) is also allowed.

neutral and could be described by either Dirac or Majorana spinors. The discovery of neutrinoless double β-decay would determine whether neutrinos are Dirac or Majorana. In these experiments, one of the two emitted antineutrinos works as a neutrino annihilating with another, showing that neutrinos are their own antiparticles, i.e., they must be Majorana spinors. Otherwise, they are Dirac spinors and satisfy the Dirac equation.

The Higgs boson was first theorized by Robert Brout, Franois Englert, Peter Higgs, Gerald Guralnik, Carl Richard Hagen, and Tom Kibble in 1964 [92]–[95]. The Higgs is a massive scalar elementary particle with no intrinsic spin, which is a key building block in the Standard Model. Other elementary particles such as quarks and leptons gain their masses through Yukawa couplings to the scalar Higgs field. Photons do not interact with the Higgs field and therefore have no mass, while the $W^{\pm}$ and Z^0 bosons are massive through coupling to the Higgs field. Because of the heavy masses of $W^{\pm}$ and Z^0, they interact with themselves and decay in a short time. Searching for Higgs bosons began at LHC (Large Hadron Collider) at CERN in early 2010 and Fermilab's Tevatron in late 2011. On 4 July 2012, ATLAS (A Toroidal LHC Apparatus) and CMS (Compact Muon Solenoid), the two main experiments at the LHC, reported independently that they found a new particle with a mass of about 125 GeV/c^2, which is consistent with predictions [96, 97]. Although the observed particle is similar to the Standard Model predicted Higgs in several respects, further study is ongoing to confirm whether it is the Higgs boson.

The Standard Model has been tested by many experiments and its predictions of new particles have been experimentally confirmed. The Standard Model was built up during the mid- to late- 20th century through a collaborative effort, based on the experimental discoveries and theoretical advances. The current formulation was finalized in the mid-1970s upon the experimental discovery of quarks. Later discoveries of the bottom quark (1977), the top quark (1995), and the τ neutrino (2000) have strongly supported the Standard Model. The most recent discovery of the Higgs boson completed the set of predicted particles and almost finalized the Standard Model framework, since the Higgs mechanism gives birth to the masses of all elementary particles in the Standard Model, including the quarks, leptons and $W^{\pm}$ and Z^0 bosons. Only minor amendments and 19 experimental constants need to be achieved. It is considered a *theory of almost everything* because of its ability in explaining numerous experimental results. However, the Standard Model does not incorporate the full theory of gravitation – described by general relativity, which in turn falls short of describing dark matter or dark energy, which only experience gravity out of the four basic forces (dark matter may also interact weakly). Although the Standard Model is considered to be a theoretically self-consistent theory, it has difficulties in explaining the origin of its parameters and some features are incorporated in a rather ad hoc way. Listed below are unsolved problems in the Standard Model:

1. Number and origin of the parameters: The Standard Model relies on 19 parameters that can only be derived from experiment. The 19 parameters are the masses of the six quarks (u, d, c, s, b, t) and the three leptons (e, μ, τ), the Higgs mass and vacuum expectation value v, which couples the Yukawa coefficients to determine the fermion masses, three angles and one phase of the Cabibbo-Kobayashi-Maskawa (CKM) matrix; a QCD vacuum phase; and three coupling constants $g1$, $g2$, $g3$ of the gauge groups in Eq. (2.1). There are seven more parameters for neutrinos which are not included in the original 19 parameters: they are three masses and four Pontecorvo-Maki-Nakagawa-Sakata (PMNS) matrix elements. There could be 2 more (namely α_1 and α_2, as discussed in Section 2.2.2) if neutrinos are Majorana particles.

2. Hierarchy problem: When fundamental parameters, such as Higgs mass calculated from tree level, are different from the measured values as related by renormalization, the hierarchy problem occurs. Typically, the fundamental parameters and renormalization parameters are closely related. However, in some cases, there are delicate cancellations between the fundamental quantities and the quantum corrections. For instance, the Higgs mass that is calculated from the tree level needs to be corrected because of the presence of virtual particles. The quantum corrections are power-law divergent, but they may be cut off at Planck scale where the Standard Model description breaks down and quantum gravity plays a significant role. Even though the corrections are much higher than the Higgs mass, which means that the bare Higgs mass has to be fine-tuned to cancel the quantum corrections. The fine-tuning is thought to be unnatural.

3. Strong CP problem: Charge conjugation (C) transforms a particle into its antiparticle, while parity (P) transforms the current physics system to its mirror image. The CP symmetry states that the laws of physics should be the same if a particle undergoes both C and P transformations. CP violation in weak interactions, discovered in 1964, shows that the probabilities for the neutral kaon, K_L^0, transforming into $\pi^+ + e^- + \bar{\nu}_e$ and the reverse processes $\pi^- + e^+ + \nu_e$ are not exactly the same [98]. CP violation might explain the excess of matter over antimatter in our present universe. However, there is no such experimental result in regards to the strong interaction in QCD. The CP symmetry in QCD seems to be conserved for no apparent reason, and this fine-tuning is deemed unnatural.

4. Gravity: The incompatibility of the Standard Model and the most successful theory of gravity, general relativity, leaves a significant gap in the unification of all four basic forces. The Standard Model can only explain 4% of the energy present in the universe. It is now known that 24% out of the missing 96% should be dark matter that interacts through gravity and possibly the weak force, while the rest of which should be dark energy interacting only through gravity. Attempts to explain dark energy as vacuum energy in the Standard Model would result in a mismatch of 120 orders of magnitude.

5. Neutrino masses: The neutrino masses are zero in the Standard Model, but measured to be small but non-zero from atmospheric [99], solar [100], reactor [101, 102, 103, 104] and accelerator [84, 105] neutrino oscillation experiments. Mass terms can be added by hand, but this introduces new theoretical problems, such as the origin of the neutrino masses and the type of their masses.

These difficulties bring chances for further developments. Theoretical developments in physics beyond the Standard Model will seek a way to explain all the deficiencies of the Standard Model. Various extensions of the Standard Model through supersymmetry, string theory, M-theory, extra dimensions, etc., may answer some or all the questions, but they have to be tested by experiments.

2.2 Neutrino Oscillations

2.2.1 Neutrino Mass

The reason why neutrinos were originally suggested to be massless has been discussed in Section 2.1. However, recent experiments [106] beginning from Super-Kamiokande in 1998 have collected irrefutable evidence for neutrino oscillations, which have been postulated for more than 40 years [107]. The direct consequence of the discovery of neutrino oscillations leads to non-zero neutrino masses.

The absolute neutrino masses have not been measured as of 2013. The Troitsk experiment [108] in Russia and the Mainz experiment [109] in Germany have set the best direct limits on the ν_e mass by measuring the end point energy of the tritium β-decay. A neutron in the tritium nucleus decays by the process:

$$^3H \rightarrow {}^3He + e + \bar{\nu}_e.$$

The released energy is split between the outgoing electron and the antineutrino. If the neutrino has a non-zero mass, the continuous energy spectrum of the electron should be smaller than the total energy released by the β-decay (approximately 18.57 keV), as illustrated in Fig. 2.4. The current upper limit for electron neutrinos is $m_{\nu_e} < 2.2$ eV [110]. The other two types of direct neutrino limits are $m_{\nu_\mu} < 0.17$ MeV from momentum analysis of a surface muon beam [111] and $m_{\nu_\tau} < 15.5$ MeV from tau decay [112].

The ultimate goal is to address the topic of neutrino masses and their small values compared to the corresponding leptons in the same generation. The cosmological hot dark matter constraint gives the limit of neutrino masses to be $\sum m_\nu < 0.41$ eV [113]. Direct laboratory experiment measurements KATRIN (Karlsruhe Tritium Neutrino Experiment) [114] will

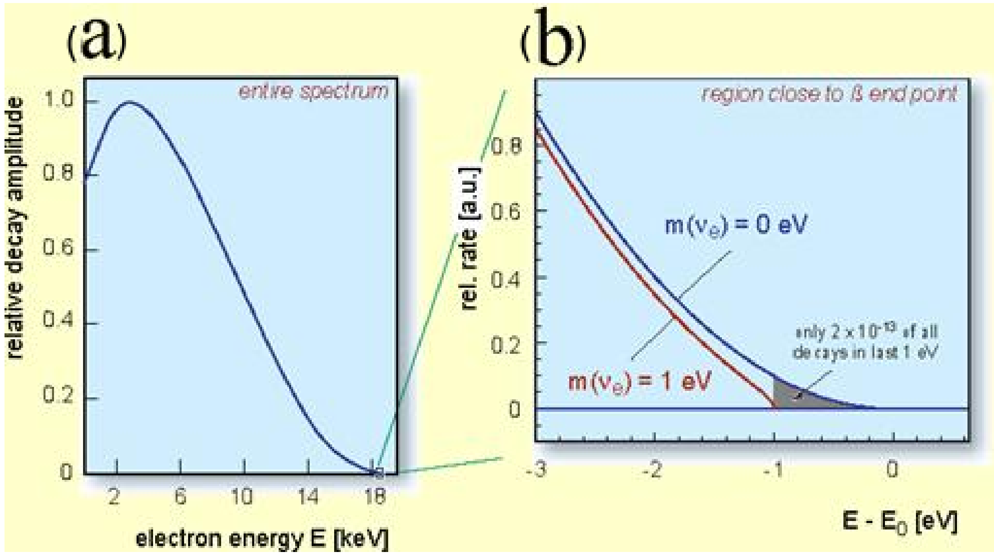

Figure 2.4: The full electron kinetic energy spectrum in tritium β-decay is shown in (a). The end point is shown enlarged in (b) where a hypothetical red curve for $m_{\nu_e} = 1$ eV is superimposed.

have a sub-eV precision by measuring the spectrum of electrons emitted from the β-decay of tritium. The MARE (Microcalorimeter Arrays for a Rhenium Experiment) [115] uses arrays of low temperature calorimeters measuring the β-decay of ^{187}Re ($Q = 2.47$ keV, the lowest known in nature), with a final sensitivity down to 0.2 eV. Neutrino oscillations experiments are sensitive to the Δm^2 for each combination of two masses, as discussed in Section 2.2.2. The mass hierarchy of neutrinos has not been determined, but this can be measured with the help of matter effects and oscillation parameters, especially for large enough values of the θ_{13} mixing angle. Illustration of this problem as well as other open questions will be discussed in Section 2.4.

Incorporating the neutrino mass into the Standard Model can be realized through Dirac mass or Majorana mass. In the Dirac mass case, the right-handed neutrinos are assumed to exist and they are sterile as opposed to active, which means that they do not participate in weak interactions. Neutrinos acquire mass in a similar way as the other fermions do, by coupling with the Higgs field, but with relatively smaller coupling constants. The origin of the Dirac mass can be explained by the Higgs mechanism; however, there is no explanation for the smallness of the mass in the framework. In the Majorana case, neutrinos are their own antiparticles, where the lepton number conservation is violated. The seesaw mechanism [116]–[119] might explain the smallness of neutrino masses, which is out of scope of the Standard Model.

2.2.2 Neutrino Oscillations Formalism

Neutrino oscillations are the quantum mechanical phenomenon in which a neutrino created with a specific lepton flavor can later be measured to have a different flavor. Neutrinos are created and interact as flavor eigenstates $|\nu_\alpha\rangle$, where $\alpha = e, \mu, \tau$, while they propagate as mass eigenstates $|\nu_i\rangle$, where $i = 1, 2, 3$, which may be different than the flavor eigenstates. The relationships between these eigenstates are given by:

$$|\nu_\alpha\rangle = \sum_i U_{\alpha i} |\nu_i\rangle \qquad \text{and} \qquad |\nu_i\rangle = \sum_\alpha U^*_{\alpha i} |\nu_\alpha\rangle .$$

For the standard three generations theory, the 3×3 unitary mixing matrix U is the so-called PMNS matrix [25, 26, 120],

$$U = \begin{pmatrix} U_{e1} & U_{e2} & U_{e3} \\ U_{\mu 1} & U_{\mu 2} & U_{\mu 3} \\ U_{\tau 1} & U_{\tau 2} & U_{\tau 3} \end{pmatrix},$$

which is typically parameterized as:

$$\begin{aligned} U &= \begin{pmatrix} 1 & 0 & 0 \\ 0 & c_{23} & s_{23} \\ 0 & -s_{23} & c_{23} \end{pmatrix} \begin{pmatrix} c_{13} & 0 & s_{13}e^{-i\delta} \\ 0 & 1 & 0 \\ -s_{13}e^{i\delta} & 0 & c_{13} \end{pmatrix} \begin{pmatrix} c_{12} & s_{12} & 0 \\ -s_{12} & c_{12} & 0 \\ 0 & 0 & 1 \end{pmatrix} \begin{pmatrix} e^{i\alpha_1/2} & 0 & 0 \\ 0 & e^{i\alpha_2/2} & 0 \\ 0 & 0 & 1 \end{pmatrix} \\ &= \begin{pmatrix} c_{12}c_{13} & s_{12}c_{13} & s_{13}e^{-i\delta} \\ -s_{12}c_{23} - c_{12}s_{23}s_{13}\, e^{i\delta} & c_{12}c_{23} - s_{12}s_{23}s_{13}\, e^{i\delta} & s_{23}c_{13} \\ s_{12}s_{23} - c_{12}c_{23}s_{13}\, e^{i\delta} & -c_{12}s_{23} - s_{12}c_{23}s_{13}\, e^{i\delta} & c_{23}c_{13} \end{pmatrix} \begin{pmatrix} e^{i\alpha_1/2} & 0 & 0 \\ 0 & e^{i\alpha_2/2} & 0 \\ 0 & 0 & 1 \end{pmatrix}, \end{aligned}$$

in terms of the mixing angles θ_{12}, θ_{13}, and θ_{23}, and the phase factors δ, α_1, and α_2. The abbreviations c_{ij} and s_{ij} stand for $c_{ij} = \cos\theta_{ij}$ and $s_{ij} = \sin\theta_{ij}$, respectively. The phase factors α_1 and α_2 are non-zero only if neutrinos are Majorana particles, and do not enter the oscillations phenomena. The phase factor δ is non-zero only if neutrino oscillations violate CP symmetry, and is therefore referred to as the CP violating phase.

The propagation of the neutrinos can be described by plane wave solutions in *natural units* ($c = \hbar = 1$):

$$|\nu_i(t)\rangle = e^{-i\,(E_i t - \mathbf{p}_i\cdot\mathbf{x})}|\nu_i(0)\rangle,$$

where, E_i is the energy of the mass eigenstate i, t is the time from the start of the propagation, $\mathbf{p}_i$ is the momentum vector, and $\mathbf{x}$ is the position of the particle relative to its starting position. In the ultrarelativistic limit $p_i = |\mathbf{p}_i| \gg m_i$, and therefore:

$$E_i = \sqrt{p_i^2 + m_i^2} \simeq p_i + \frac{m_i^2}{2p_i} \approx E + \frac{m_i^2}{2E}.$$

Using also $t \approx L$, where L is the distance traveled from the creation point to the detection point, the wave function becomes:

$$|\nu_i(L)\rangle = e^{-i\,m_i^2 L/2E}|\nu_i(0)\rangle.$$

Therefore, the probability that a neutrino created originally as flavor α will be observed as possessing flavor β at a distance L is simply:

$$\begin{aligned} P_{\alpha\to\beta} &= |\langle\nu_\beta|\nu_\alpha(t)\rangle|^2 = \left|\sum_i U^*_{\alpha i}U_{\beta i}e^{-i\,m_i^2 L/2E}\right|^2 \\ &= \delta_{\alpha\beta} - 4\sum_{i>j} Re(U^*_{\alpha i}U_{\beta i}U_{\alpha j}U^*_{\beta j})\,\sin^2\left(\frac{\Delta m^2_{ij}L}{4E}\right) + 2\sum_{i>j} Im(U^*_{\alpha i}U_{\beta i}U_{\alpha j}U^*_{\beta j})\,\sin\left(\frac{\Delta m^2_{ij}L}{2E}\right), \end{aligned}$$

where $\Delta m^2_{ij} \equiv m_i^2 - m_j^2$. In case of the antineutrinos, all the U (U^*) matrix elements must be replaced by their complex conjugate, which does not affect the first sum but change the sign of the second one. In case of no CP violation, the second sum vanishes identically since all of the elements of the U matrix become real. By restoring c and $\hbar$, the oscillation term, $\Delta m_{ij}^2 L/4E$ can be written as:

$$\frac{\Delta m^2\, c^3\, L}{4\hbar E} = \frac{[\mathrm{GeV}]\,[\mathrm{fm}]}{4\hbar c} \times \frac{\Delta m^2}{[\mathrm{eV}]^2} \frac{L}{[\mathrm{km}]} \frac{[\mathrm{GeV}]}{E} \approx 1.267 \times \frac{\Delta m^2}{[\mathrm{eV}]^2} \frac{L}{[\mathrm{km}]} \frac{[\mathrm{GeV}]}{E}.$$

The above formula for three neutrino oscillations is general but rather complicated. Fortunately, in most cases, one of the mass eigenstates effectively decouples, such that only the mixing between two neutrinos plays an important role. In such cases it is sufficient to consider only a two neutrino mixing matrix,

$$U = \begin{pmatrix} \cos\theta & \sin\theta \\ -\sin\theta & \cos\theta \end{pmatrix},$$

where the probability for neutrino oscillations is reduced to

$$P_{\alpha\to\beta} = \sin^2 2\theta \sin^2\left(\frac{\Delta m^2 L}{4E}\right) \quad \text{for} \quad \alpha \neq \beta.$$

Equivalently

$$P_{\alpha\to\beta} = \sin^2 2\theta \sin^2\left(1.267\, \frac{\Delta m^2 L}{E}\right),$$

with Δm^2 expressed in eV^2, L is expressed in km and E is in GeV, or alternatively L is expressed in m and E is in MeV.

2.3 Current Knowledge

Over the past four decades, neutrino oscillations have been observed by a relatively large set of experiments using neutrinos from different sources. The current values and constraints of the neutrino oscillation parameters are given by the combined analyses of several experiments in Table 2.1:

Parameter	Value
Δm^2_{21}	$(7.53^{+0.18}_{-0.18}) \times 10^{-5}$ eV^2
$\lvert\Delta m^2_{32}\rvert$	$(2.473^{+0.070}_{-0.067}) \times 10^{-3}$ eV^2 (normal hierarchy)
	$(2.427^{+0.042}_{-0.065}) \times 10^{-3}$ eV^2 (inverted hierarchy)
$\tan^2\theta_{12}$	$0.436^{+0.029}_{-0.025}$
$\sin^2\theta_{23}$	$0.413^{+0.037}_{-0.025}$ (normal hierarchy)
	$0.594^{+0.021}_{-0.022}$ (inverted hierarchy)
$\sin^2 2\theta_{13}$	0.089 ± 0.011

Table 2.1: Current values for the neutrino oscillation mixing parameters.

2.4 Open Questions

Through many decades, remarkable progress has been made in the studies of neutrino oscillations, including the measurements of oscillation angles and mass square differences. Recently, $\sin^2 2\theta_{13}$ has been measured to be $\sin^2 2\theta_{13} = 0.109 \pm 0.030\,(\text{stat.}) \pm 0.025\,(\text{syst.})$ by Double Chooz [102], $\sin^2 2\theta_{13} = 0.089 \pm 0.010\,(\text{stat.}) \pm 0.005\,(\text{syst.})$ by Daya Bay [103], and $\sin^2 2\theta_{13} = 0.113 \pm 0.013\,(\text{stat.}) \pm 0.019\,(\text{syst.})$ by Reno [104], which is large enough to allow experimental determination of CP violation phase and mass hierarchy in the near future. There are currently some ongoing experiments aimed to address these unsolved issues. This section provides an overview of outstanding problems, some of which are expected to be solved in a decade or so.

1. Do neutrino interactions violate CP?

The strong and electromagnetic interactions seem to be invariant under the CP transformation by current knowledge; however, CP invariance is slightly violated for certain types of weak decays. The CP violation plays an important role in explaining the existence of our present matter-dominated universe. The universe consists mainly of matter instead of an equal amount of matter and antimatter as it is expected. It is plausible to assume that an equal amount of matter and antimatter was created at the beginning of the Big Bang, while CP violation in the extreme conditions of the first seconds after the Big Bang created the imbalance. If CP symmetry is preserved, there should have been total cancellation of particles and antiparticles, which in turn would have resulted in a sea of radiation without matter, which is not the case.

The determination of the CP violation phase in neutrino oscillations can be realized by examining the difference between a certain type of neutrino oscillations and its CP conjugation, e.g.,

$$\begin{aligned}&P(\nu_\mu \to \nu_e) - P(\bar{\nu}_\mu \to \bar{\nu}_e)\\ =&\frac{1}{2}\sin 2\theta_{13}\sin 2\theta_{12}\sin 2\theta_{23}\cos\theta_{13}\sin\delta\left(\sin\frac{\Delta m_{12}^2 L}{2E} + \sin\frac{\Delta m_{23}^2 L}{2E} + \sin\frac{\Delta m_{31}^2 L}{2E}\right).\end{aligned}$$

The $\sin 2\theta_{13}$ appears as a multiplication factor (along with the sine of the CP violation phase), whose size decides the ability to measure CP violation. It has been measured to be large enough to allow practical experiments involving accelerator and reactor experiments, ν_μ and $\bar{\nu}_\mu$ oscillation experiments, and experiments with different baselines to figure out the CP violation phase. The near term experiments T2K (Tokai to Kamioka) [121] and NOνA (Neutrinos at the Main Injector Off-Axis ν_e Appearance) [122] are sensitive to CP violation, mass hierarchy, and θ_{13}. With a more precise determination of the θ_{13} mixing angle, these two experiments may be able to shed light on the CP violation phase and the mass hierarchy problem.

2. What are the absolute masses of the neutrino mass eigenstates?

   What is the hierarchy of the neutrino mass spectrum, normal or inverted?

The absolute neutrino mass scale raises the question of why the mass range of elementary particles is so large. The neutrino mass hierarchy is a fundamental issue in neutrino oscillations, which is entangled with the mixing angles and the CP phase. From solar neutrino data, Δm_{21}^2 has been determined to be positive, which leaves us with two possible scenarios, the normal or inverted hierarchy, as shown in Fig. 2.5. The understanding of the mass

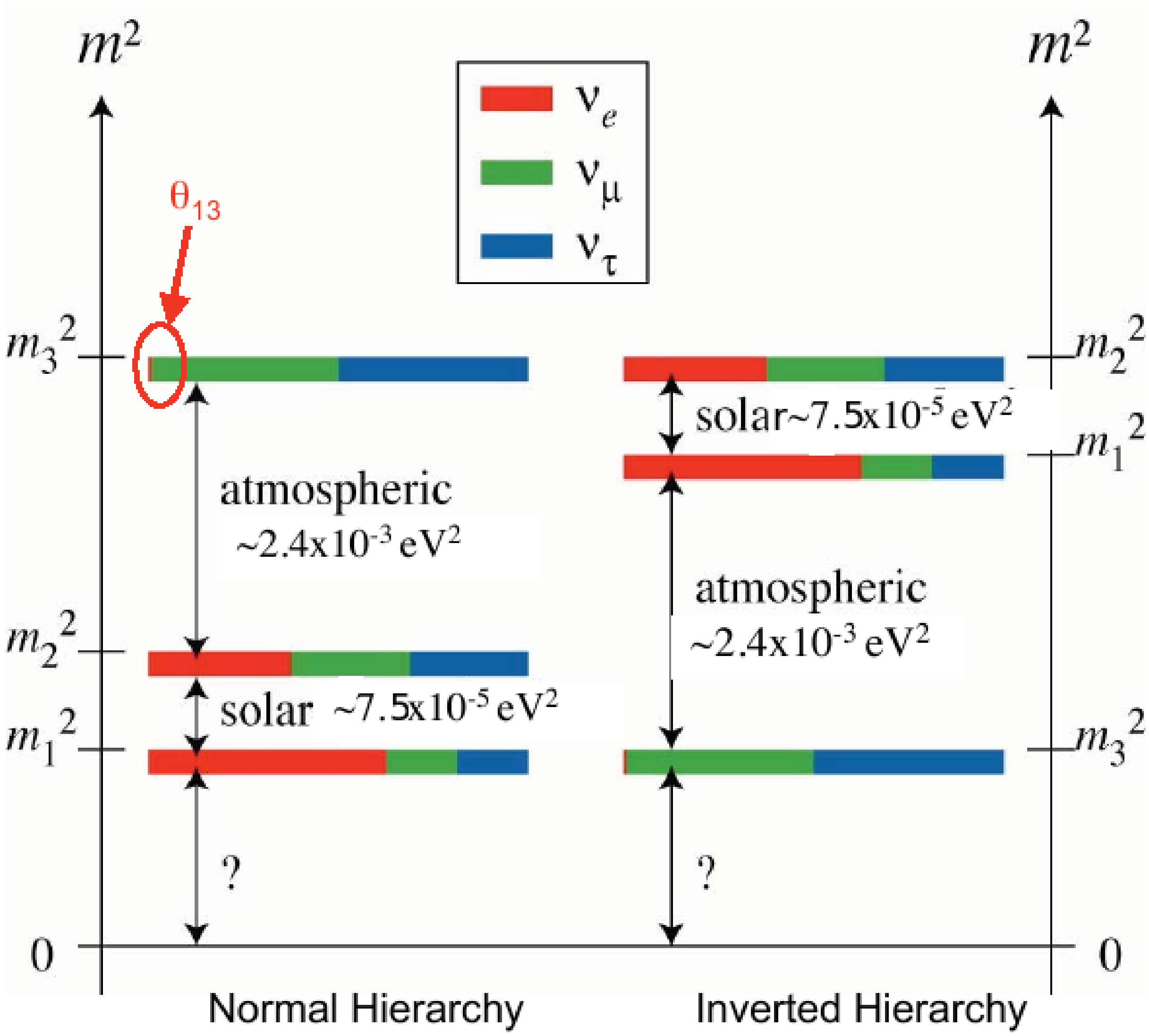

Figure 2.5: The flavor content of neutrino mass eigenstates for the two hierarchies, normal or inverted, as labeled.

hierarchy problem breaks the degeneracies of neutrino oscillation parameters. The current value of θ_{13} also gives us opportunity to measure it with the help of matter effects. In the two neutrino oscillations model with only electron and muon neutrinos, the Hamiltonian of the neutrino system in the vacuum is:

$$H_{vac} = \frac{\Delta m^2}{4E} \begin{pmatrix} -\cos 2\theta & \sin 2\theta \\ \sin 2\theta & \cos 2\theta \end{pmatrix}.$$

With the presence of matter effects (with constant matter density), the electron neutrinos interact with matter through the W and Z channels, while the muon neutrinos only interact through the Z channel. Therefore, the Hamiltonian of the neutrino system in matter yields,

$$H_M = H_{vac} + V_W \begin{pmatrix} 1 & 0 \\ 0 & 0 \end{pmatrix} + V_Z \begin{pmatrix} 1 & 0 \\ 0 & 1 \end{pmatrix}.$$

The last term can be dropped since it is proportional to the unitary matrix. The Hamiltonian can be rewritten as,

$$H_M = H_{vac} + \frac{V_W}{2} \begin{pmatrix} 1 & 0 \\ 0 & -1 \end{pmatrix} + \frac{V_W}{2} \begin{pmatrix} 1 & 0 \\ 0 & 1 \end{pmatrix}.$$

Again, the last term can be dropped. Therefore, we have,

$$H_M = \frac{\Delta m^2}{4E} \begin{pmatrix} -(\cos 2\theta - x) & \sin 2\theta \\ \sin 2\theta & \cos 2\theta - x \end{pmatrix},$$

with $x = 4EV_W/2\Delta m^2 = \pm 2\sqrt{2} G_F N_e E/\Delta m^2$, where $V_W = \pm\sqrt{2} G_F N_e$ is the matter potential. The sign is positive for neutrinos and negative for antineutrinos. If we define,

$$\Delta m_M^2 = \Delta m^2 \sqrt{\sin^2 2\theta + (\cos 2\theta - x)^2}, \tag{2.2}$$

and

$$\sin^2 2\theta_M = \frac{\sin^2 2\theta}{\sin^2 2\theta + (\cos 2\theta - x)^2}, \tag{2.3}$$

then

$$H_M = \frac{\Delta m_M^2}{4E} \begin{pmatrix} -\cos 2\theta_M & \sin 2\theta_M \\ \sin 2\theta_M & \cos 2\theta_M \end{pmatrix}.$$

We know that in the vacuum,

$$P_{\mu e} = \sin^2\theta_{23}\sin^2 2\theta_{13}\sin^2\left(\frac{\Delta m^2_{31}L}{4E}\right) + \text{“subleading”}.$$

The magnitude of the probability depends on the value of θ_{13}, but is insensitive to the sign of Δm^2_{31}. If we compare the Hamiltonians in vaccum and in matter, we know that $P_{\mu e}$ can be expressed as the same form with substituting $\sin^2 2\theta_{13}$ and Δm^2_{31} to the effective forms in Eqs. (2.2) and (2.3), respectively,

$$P_{\mu e} \approx \sin^2\theta_{23}\sin^2 2\theta_{13M}\sin^2\left(\frac{\Delta m^2_{31M}L}{4E}\right).$$

The transition probability $P_{\mu e}$ depends on the sign of x through the $\sin^2 2\theta_{13M}$ term, which in turn depends on the sign of Δm^2_{31}. Thus, $P_{\mu e}$ is different for two different mass hierarchies and also different for neutrinos and antineutrinos.

3. Are neutrinos their own antiparticles?

The physics described by the Dirac equation can be expressed in several representations. The Dirac-Pauli representation is the most general one, while the Weyl representation is the one which deals with helicity eigenstates. For a massless fermion, the Dirac equation simplifies into two independent equations using the Weyl representation. In the Standard Model, the chargeless and massless neutrinos only differ from their antiparticles by their chirality. However, since neutrino oscillation experiments have shown that neutrinos must have mass, it opens the door for two different possibilities of neutrino mass: Dirac or Majorana.

In the Standard Model, assuming right-handed neutrinos exist, a Dirac neutrino mass can be incorporated by coupling to the Higgs field as other fermions do. The corresponding mass term is called a Dirac mass, m_D, and the Dirac Lagrangian is written as:

$$L_D = -m_D\bar{\phi}\phi = -m_D\left(\bar{\phi}_L\phi_R + \bar{\phi}_R\phi_L\right).$$

The explanation for a Dirac mass term is still a puzzle since it is many orders of magnitude smaller than other fermion masses, as Fig. 2.6 indicates.

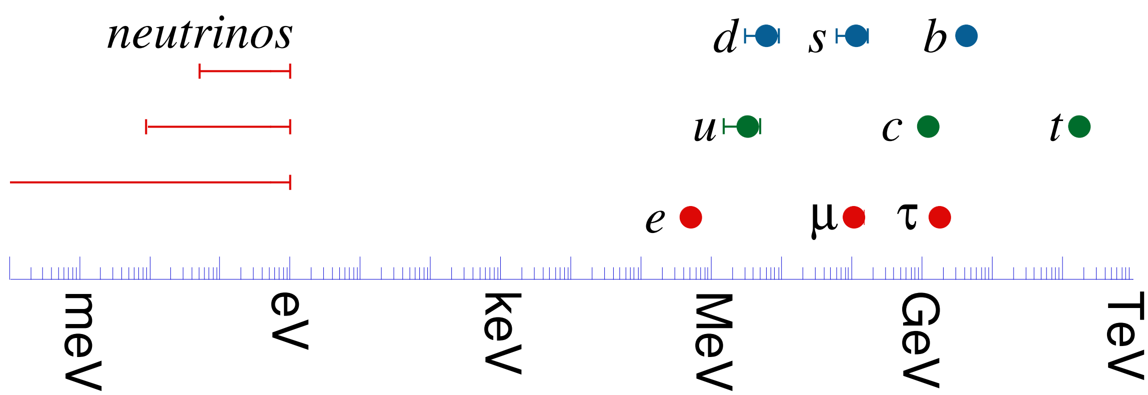

Figure 2.6: Neutrino and other fermion masses spectrum illustrations.

The Majorana mass was first proposed by Ettore Majorana [123] to treat the electrically neutral particle as its own antiparticle. The Dirac equation is relativistically invariant when substituting the Dirac spinor with its charge conjugate for a massive fermion field. The charge conjugate operator transforms a particle spinor into the equivalent antiparticle spinor ($\phi^C = C\bar{\phi}^T$). The Lagrangian mass term has both chirality states; however, Majorana neutrinos are their own antiparticles so that the right-handed Majorana neutrino is not necessary:

$$L_M = -\frac{m_M}{2}\bar{\phi}\phi = -\frac{m_M}{2}\left(\bar{\phi}_L^C\phi_L + \bar{\phi}_L\phi_L^C\right).$$

The Majorana spinor does not conserve the lepton number since it is not invariant under U(1) transformations as a Dirac spinor is ($\phi \rightarrow e^{i\alpha}\phi$).

Some experiments searching for the nature of the neutrino mass type are underway [124, 125], primarily searching for neutrino-less double β-decays [126]–[133]. The process of double β-decay as Fig. 2.7 shows, consists of two neutrons decaying into a proton and an electron each through a regular β-decay. If neutrinos have Majorana mass, the neutrino-less decay mode can be observed as a second order weak process. Figure. 2.8 gives the spectrum of two emitted electrons together with an example of neutrino-less double β-decay signature with perfect energy resolution.

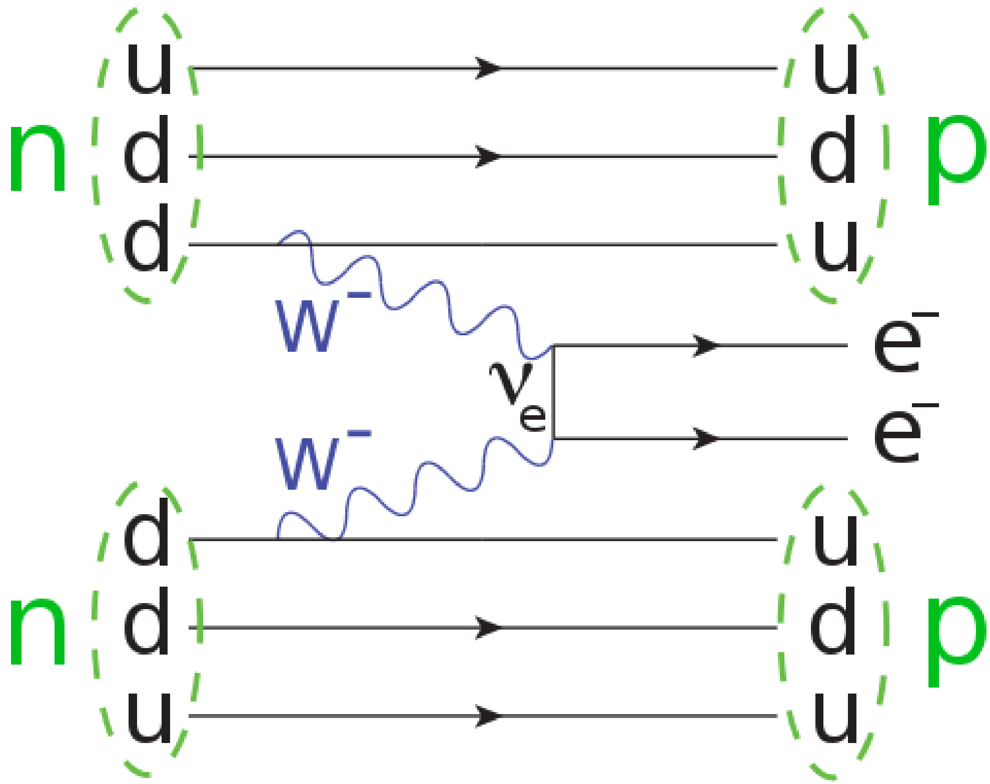

Figure 2.7: The process of neutrino-less double β-decay: two neutrons converted into two protons and two electrons.

If neutrinos are Dirac particles, there is no reason the neutrino masses are so small. However, if both of the Dirac and Majorana mass terms are present, the explanation becomes natural with the see-saw mechanism. Suppose that there are two Majorana neutrinos, one of which is almost massless and the other one is very heavy. The Lagrangian mass term can be written in definite mass states:

$$L_{mass} = \begin{pmatrix} \bar{\nu} & \bar{N} \end{pmatrix} \begin{pmatrix} m & 0 \\ 0 & M \end{pmatrix} \begin{pmatrix} \nu \\ N \end{pmatrix}.$$

Suppose the light neutrino is mostly composed of left-handed helicity state ν_L and the heavy state is mostly composed of right-handed helicity state N_R. The relationship between the

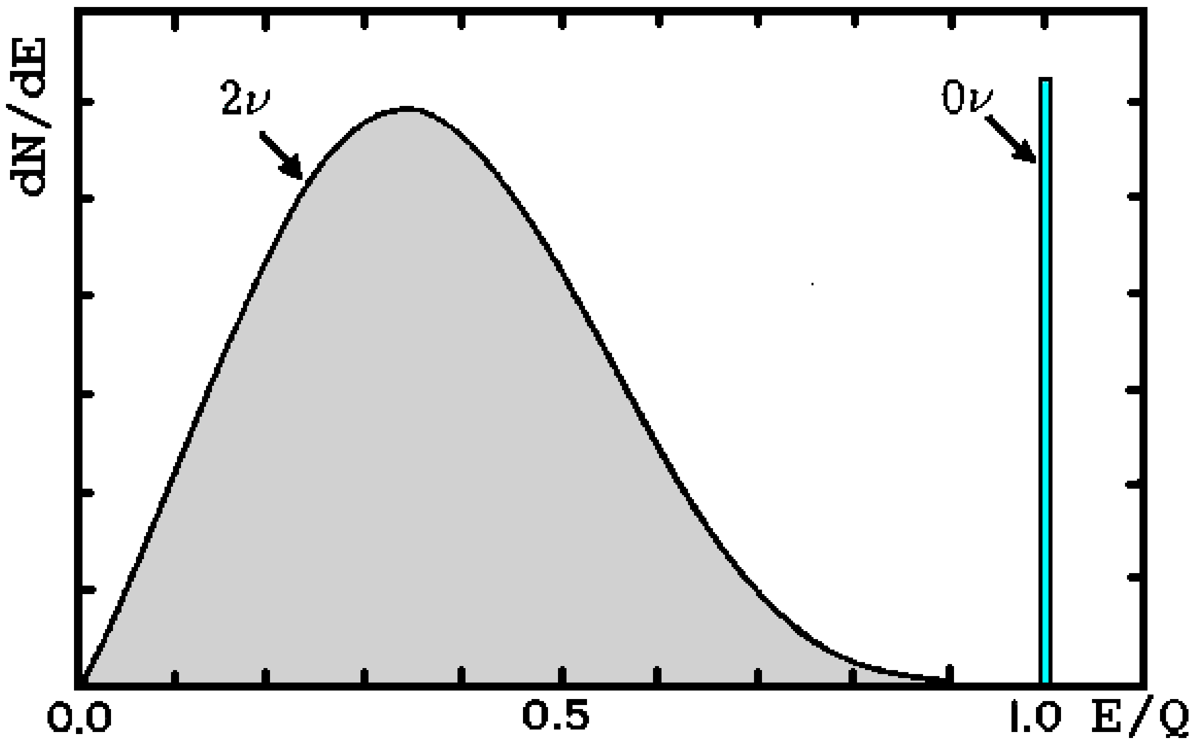

Figure 2.8: An example of two electrons energy spectrum with the signature of $0\nu\beta\beta$-decay.

mass eigenstates and the helicity eigenstates is:

$$\begin{pmatrix} \nu & N \end{pmatrix} = \begin{pmatrix} \cos\theta & -\sin\theta \\ \sin\theta & \cos\theta \end{pmatrix} \begin{pmatrix} \nu_L \\ N_R \end{pmatrix},$$

and the Lagrangian can be written as:

$$\begin{aligned} L_{mass} &= \begin{pmatrix} \bar{\nu_L} & \bar{N_R} \end{pmatrix} \begin{pmatrix} c & -s \\ s & c \end{pmatrix}^{-1} \begin{pmatrix} m & 0 \\ 0 & M \end{pmatrix} \begin{pmatrix} c & -s \\ s & c \end{pmatrix} \begin{pmatrix} \nu_L \\ N_R \end{pmatrix} \\ &= \begin{pmatrix} \bar{\nu_L} & \bar{N_R} \end{pmatrix} \begin{pmatrix} mc^2 + Ms^2 & sc(M-m) \\ sc(M-m) & ms^2 + Mc^2 \end{pmatrix} \begin{pmatrix} \nu_L \\ N_R \end{pmatrix}, \end{aligned}$$

where c represents $\cos\theta$ and s represents $\sin\theta$. If one defines $m_L = mc^2 + Ms^2$, $m_D =$

$sc(M-m)$ and $m_R = ms^2 + Mc^2$, the M matrix can be written as:

$$M = \begin{pmatrix} m_L & m_D \\ m_D & m_R \end{pmatrix}. \tag{2.4}$$

The physical masses m_1 and m_2 are the eigenvalues of the matrix in Eq. (2.4):

$$m_{1,2} = \frac{1}{2}\left[(m_L + m_R) \pm \sqrt{(m_L - m_R)^2 + 4m_D^2}\right].$$

Since we know the solutions should be m and M and from the assumption that $m \ll M$, the approximate solutions of the Eq. (2.4) are:

$$m_1 \approx m_D^2/m_R = m,$$
$$m_2 \approx m_R = M.$$

The Dirac mass m_D is approximately on the order of MeV (which is the mass scale of leptons), while the Majorana mass is on the order of GUT scale, which is about 10^{16} GeV. By assuming a large mass right-handed Majorana neutrino, the lightness of the left-handed neutrino mass is naturally explained.

4. How many neutrino species are there? Are there sterile neutrinos?

There are three kinds of neutrinos that have been discovered corresponding to three charged leptons. The LEP experiments yield the allowed number of active light neutrinos $N_\nu = 2.9840 \pm 0.0082$ [68]. Indirect evidence could be detected from cosmological measurements such as the temperature fluctuations in the cosmic microwave background. The astrophysical observations from the WMAP (Wilkinson Microwave Anisotropy Probe) experiment gives $N_\nu = 3.046$ [134] in terms of the effective number of neutrinos. Recently, some experimental evidences have been shown for the existence of sterile neutrinos, such as LSND [81], which allows $\Delta m^2 \sim O(1)$ eV^2. It is incompatible with current values given in

Table 2.1, which suggests sterile neutrinos as solutions. As the name indicates, the sterile neutrinos do not interact via the weak force but only via gravity, which is too weak on the subatomic scale to be observed. The MiniBooNE (Mini Booster Neutrino Experiment) [135] experiment was intented to confirm or deny the LSND anomaly, but its results are inconclusive. The Gallium [136] and reactor anomaly [137], which appeared later, also support a similar Δm^2 scale as LSND anomaly. The existence of sterile neutrinos may bring the total number of neutrinos up to four or five (or even six).

Chapter 3

The Double Chooz Experiment

3.1 Overview

The Double Chooz experiment has been designed to measure the neutrino mixing angle θ_{13} – without the ambiguity of matter effects and/or CP violation [138]. A multi-detector setup can extend the reach in sensitivity for θ_{13} with reduced systematic error. The experimental setup consists of two functionally identical detectors, the far and the near, at 1050 m and 400 m respectively from the Chooz nuclear cores. The existing original Chooz laboratory has been reused for the far detector hall. The experiment has two phases as proposed: the first one with the far detector only, in which $\sin^2 2\theta_{13}$ was designed to reach a sensitivity of 0.06 after 1.5 years of data taking. The second phase, where both the near and far detectors are running simultaneously, should reach a sensitivity of 0.03 or better after an additional 3 years of operation, as shown in Fig. 3.1. The combined "rate+shape" analysis of hydrogen and gadolinium capture inverse β-decay events has measured the current value to $\sin^2 2\theta_{13} = 0.109 \pm 0.035$ with only one detector running.

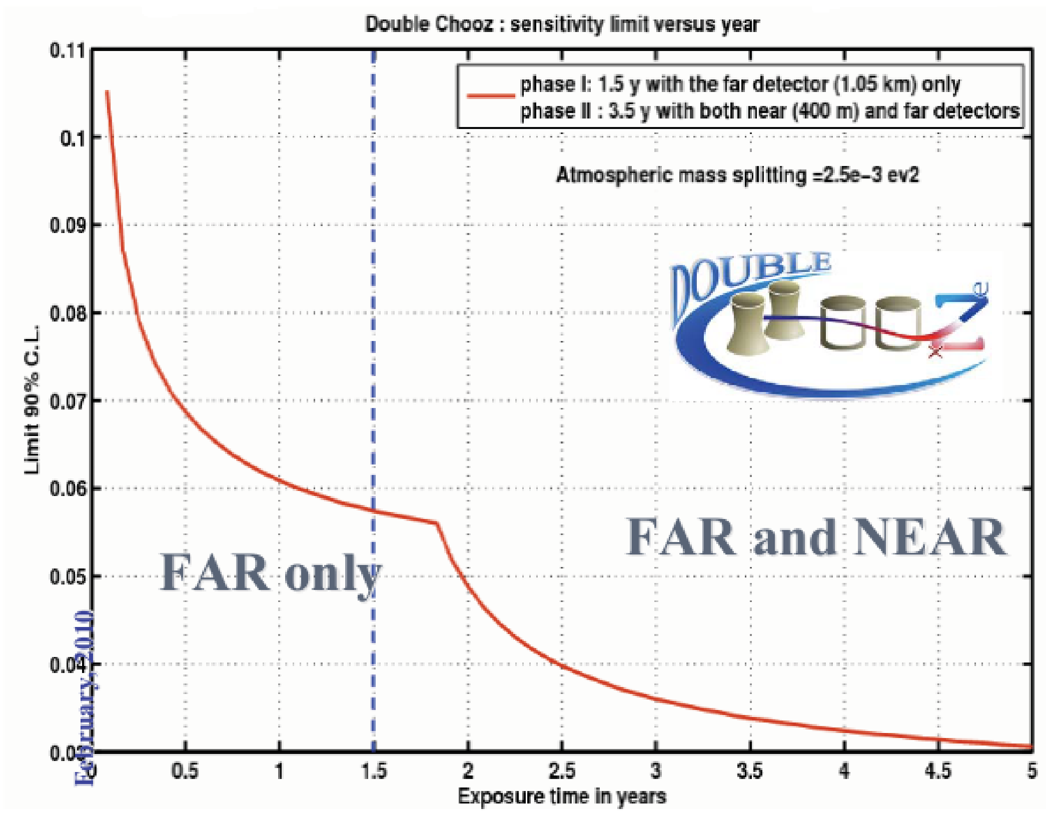

Figure 3.1: Expected Double Chooz sensitivity to $\sin^2 2\theta_{13}$ as a function of time.

3.2 Reactor

3.2.1 Neutrino Production

The pair of reactors producing the antineutrinos used in the experiment is located at the Chooz-B nuclear power station in the Ardennes region, operated by Électricité de France (EDF), as shown in Fig. 3.2. Antineutrinos are produced in the B1 and B2 cores from β-decays of the fission products. Over 99.7% of the fissions come from four main isotopes: ^{235}U, ^{239}Pu, ^{241}Pu and ^{238}U. Both reactors are pressurized water reactors of the N4 type (4 steam generators), which is the most powerful reactor type in operation in the world, with the characteristic of being able to vary their output from 30% to 95% of full power in less than 30 minutes. The thermal power of each reactor is evaluated with a step of 1 minute through the temperature of the water in the primary loop. The detailed study on

Figure 3.2: The Double Chooz experimental site.

the uncertainty of the thermal power measurement is performed by EDF and documented in Refs. [139]–[141]. Both reactors started in 1997, with a maximum thermal power of 4.25 GW_{th} each, and an electric power of 1.5 GW_e. At the nominal full thermal power of 4.25 GW_{th}, the final thermal power uncertainty is 0.5% at 1 σ confidence level. There are 205 fuel assemblies in the Chooz cores which are constructed from 264 fuel rods. The fuel cycle is about one year, when one third of the assemblies are replaced by fresh fuel assemblies. The rest of the assemblies are redistributed to give a homogeneous flux across the core. There are four assembly types which are differentiated by their initial ^{235}U enrichment of 1.8%, 3.4% and 4%; there are two types of 4% enrichment assemblies: the stardard one, with UO_2 fuel rods, and the one with enhanced neutron absorption with 12 fuel rods containing Gd_2O_3.

The reactions taking place in the nuclear cores at the Chooz power plant are fission reactions of the four main isotopes. The fission rates for the isotopes are shown in Fig. 3.3 for a particular fuel cycle. Since no experimental data on ^{238}U are available at the present time, a calculation of the spectrum for ^{238}U [142] based on the contributions from all fission products is used. This requires a huge amount of information on all possible β-branches involved and the weighting factors of all the fission products. The β-spectra for the other three isotopes measured at ILL [143]–[145] have been used. The antineutrino spectrum for each fission isotope is the result of the β-decays of many different fission products. The conversion of the β spectra to antineutrino spectra has been improved recently by using more data on the many β transitions and higher order energy corrections [142, 146]. We use the conversion from [146], including the corrections for off-equilibrium effects [147]. The uncertainty on these spectra is energy-dependent; over the entire neutrino spectrum it is estimated to be approximately 3%.

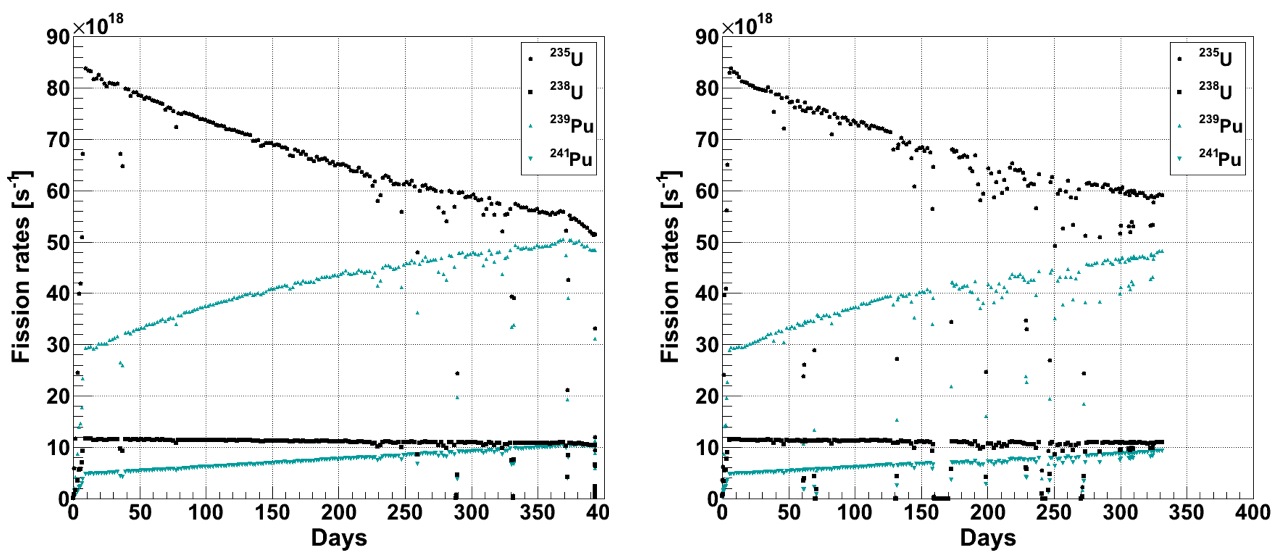

Figure 3.3: Fission rates of various isotopes for the Chooz B_1 and B_2 cores, starting from fuel cycle 12 (B_1 08/26/2010 and B_2 11/15/2010). More than 99.7% of the neutrinos are emitted by ^{235}U, ^{238}U, ^{239}Pu, and ^{241}Pu [148].

3.2.2 Cross Section

The mean cross section per fission is taken as the effective spectrum averaged cross section:

$$\langle \sigma_f \rangle = \sum_k \alpha_k \langle \sigma_f \rangle_k = \sum_k \alpha_k \int_0^\infty S_k(E_\nu) \sigma_{IBD}(E_\nu) \, \mathrm{d}E_\nu,$$

where the integration variable E_ν is the energy of the antineutrino and α_k is the fractional fission rate. The fractional fission rates are normalized such that $\sum_k \alpha_k = 1$, where the sum goes over the k^{th} isotope (k = ^{235}U, ^{239}Pu, ^{238}U, ^{241}Pu) and $S_k(E_\nu)$ is the reference spectrum of the k^{th} isotope. The fuel composition of the core determines the fraction rate, α_k, which in turn requires a full simulation of the reactors.

The inverse β-decay cross section is from the simplified form of Vogel and Beacom [149]:

$$\sigma_{IBD}(E_\nu) = E_{e^+} K \sqrt{E_{e^+}^2 - m_e^2},$$

where

$$E_{e^+} = \frac{1}{2} \left[\sqrt{m_n^2 - 4m_p \left(-E_\nu + \Delta + \frac{\Delta^2 - m_e^2}{2m_p} \right)} - m_n \right],$$

and m_e and E_{e^+} are the positron mass and energy, respectively. The variables m_n and m_p are the masses of the neutron and proton, respectively, and $\Delta = m_n - m_p$. The constant K = 0.961 $\times$ 10^{43} cm^2 is inversely proportional to the neutron lifetime – from the MAMBO-II (Mampe Bottle-II) measurement [150]. A picture of the reactor antineutrino energy spectrum, the inverse β-decay cross section and the expected observed positron spectrum is shown in Fig. 3.4.

The mean energy released per fission can be expressed as follows,

$$\langle E_f \rangle_R = \sum_k \alpha_k \langle E_f \rangle_k, \tag{3.1}$$

where $\langle E_f \rangle_k$ is the mean energy released per fission per isotope, as summarized in Table 3.1.

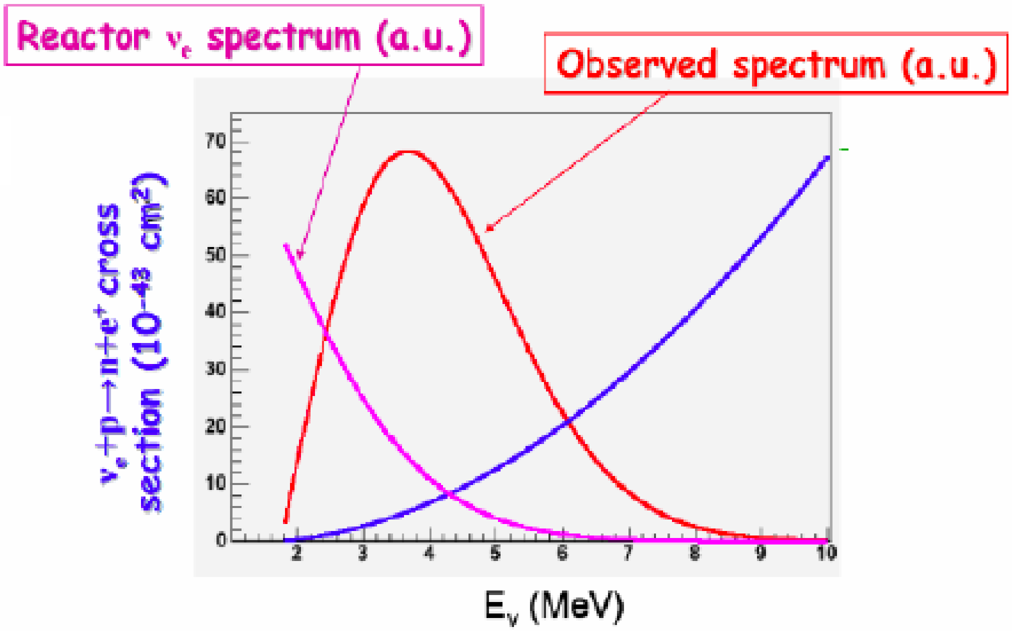

Figure 3.4: Reactor antineutrino spectrum (pink), inverse β-decay cross section (blue) and expected observed spectrum (red). Arbitrary units are used for the antineutrino spectrum and the observed positron spectrum.

The variations of the different isotopes are smaller than 6%; therefore, to first order approximation, the thermal power is relatively insensitive to the fuel composition. However, different isotopes have different antineutrino spectra $S_k(E_\nu)$, which couple to the cross section generating different observed spectrum. The observed antineutrino spectrum affects both the rate and shape analyses. This is why an accurate description of the reactor model, especially the evolution of α_k, is particularly important and requires a significant amount of effort.

Isotope	$\langle E_f \rangle_k$ (MeV)	$\langle \alpha_k \rangle$
^{235}U	201.92 ± 0.46	0.496 ± 0.016
^{239}Pu	209.99 ± 0.60	0.351 ± 0.013
^{238}U	205.52 ± 0.96	0.087 ± 0.006
^{241}Pu	213.60 ± 0.65	0.066 ± 0.007

Table 3.1: Average energy released per fission per isotope – from Ref. [151].

3.2.3 Reactor Simulation

MURE (Monte Carlo N-particle utility for reactor evolution) and DRAGON [152]–[155] are both open source codes that have been chosen to work complementarily for modeling the Double Chooz reactor cores. MURE is a 3D full core simulation with Monte Carlo (MC) techniques to simulate the neutron transport in the core. DRAGON can model individual fuel assemblies, and is a 2D simulation code that uses approximations to deterministically solve the neutron transport equation in the core. EDF provides detailed information for the locations and initial burnup (the fraction of fuel atoms that underwent fission) of each assembly, with which a full core simulation was carried out using MURE for each cycle, with time steps of 6 to 48 hours, depending on the operating conditions. In addition, the composition at the beginning of each fuel cycle needs to be determined according to the burnup of each assembly. To achieve this, MURE and DRAGON are both used in simulating the assembly level for all four fuel assembly types. The results are compared with EDF's own simulation and the uncertainty due to the simulation technique is evaluated, leading to a 0.2% systematic uncertainty in the fractional fission rate α_k. The result of each time step from the MURE full core simulation is written into the (MySQL) database, so that the α_k and the antineutrino flux can be calculated over any arbitrary time period. The systematic uncertainties on the α_k are determined by changing the input conditions (such as thermal power, boron concentration, moderator temperature and density, initial burnup error, control rod positions, choice of nuclear databases, choice of energies released per fission, and statistical error of the MURE MC) and observing the effect on the fission rate relative to the nominal simulation. The overall uncertainty is the quadrature sum of the individual errors, where the errors are considered to be independent. The moderator density and control rod positions contribute mostly to the overall uncertainties. The covariance matrix used in the final χ^2 (as shown in Eq. (3.5)) fit is constructed with the above contributions, as well as the correlations between the isotopes fission rates due to the thermal power constraint.

3.2.4 Inverse Beta Decay Rate

In the current one-detector phase, the sensitivity to θ_{13} is limited by large uncertainties in the reference spectra. To minimize this effect, the normalization of the cross section per fission for each reactor is anchored to the Bugey4 rate measurement at 15 m [156] (the very close distance of 15 m guarantees high statistics and that no neutrino oscillations effects are introduced):

$$\langle\sigma_f\rangle_R = \langle\sigma_f\rangle^{Bugey} + \sum_k \left(\alpha_k^R - \alpha_k^{Bugey}\right)\langle\sigma_f\rangle_k, \tag{3.2}$$

where R represents each of the two reactor cores. The second term corrects for the difference in fuel composition between Bugey4 and each of the Chooz cores.

The expected number of antineutrinos assuming no oscillations in the i^{th} energy bin with the Bugey4 anchor point yields:

$$N_i^{exp,R} = \frac{\epsilon N_p}{4\pi}\frac{1}{L_R^2}\frac{P_{th}^R}{\langle E_f\rangle_R}\left(\frac{\langle\sigma_f\rangle_R}{\sum_k \alpha_k^R\langle\sigma_f\rangle_k}\sum_k \alpha_k^R\langle\sigma_f\rangle_k^i\right),$$

where ϵ is the detection efficiency, N_p is the number of protons in the target, L_R is the distance from the center of the detector to the center of each reactor, and P_{th}^R is the thermal power. $\langle E_f\rangle_R$ is the mean energy released per fission defined in Eq. (3.1), and $\langle\sigma_f\rangle_R$ is the mean cross section per fission defined in Eq. (3.2). P_{th}^R, $\langle E_f\rangle_R$ and $\langle\sigma_f\rangle_R$ are time-dependent variables. $\langle E_f\rangle_R$ and $\langle\sigma_f\rangle_R$ depend on the reactor fuel composition evolution and P_{th}^R depends on the operation of the reactor.

3.3 Neutrino Detection

The neutrino signal detection is through the interaction between the electron antineutrinos and the protons in the neutrino target, $\bar{\nu}_e + p \rightarrow e^+ + n$. This process is referred to as inverse β-decay, and is illustrated in Fig. 3.5. The signature of the inverse β-decay events is a prompt positron-electron annihilation signal, followed by the neutron capture on gadolinium with a capture time of approximately 30 μs. The prompt energy can be directly related

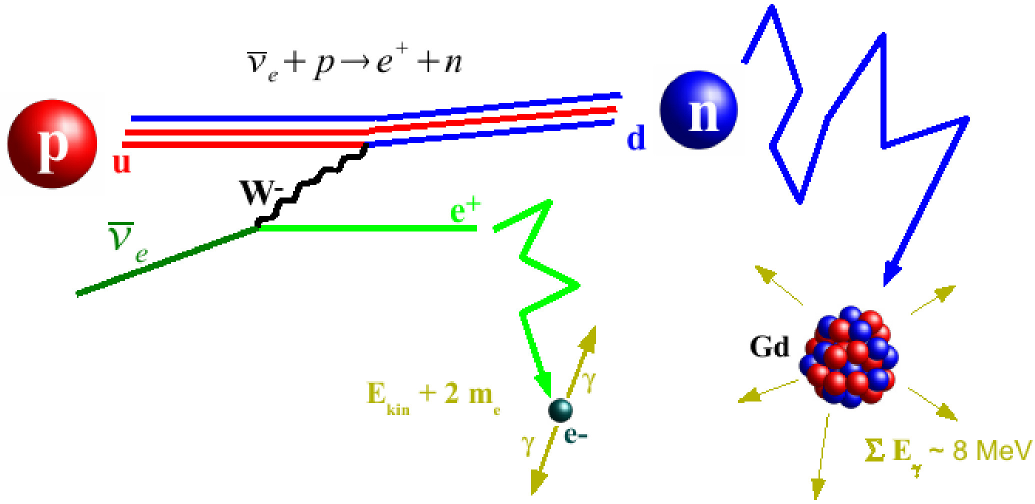

Figure 3.5: Illustration of the inverse β-decay process.

to the energy of the incoming antineutrino as in Eq. (3.3) at the end of this section, while the gadolinium-captured neutrons have a signature of about 8 MeV energy (shared among 3–4 gammas). Alternatively, the neutron can be also captured on hydrogen to yield a 2.2 MeV γ. This can work as a complementary signature because of its longer capture time (approximately 200 μs) and lower capture energy, but allows for more backgrounds. The relationship between the positron energy and the incoming neutrino energy can be calculated using the basic energy and momentum conservation laws. Although the neutrino has a small but non-zero mass, its contribution to the total energy is negligible. Since the proton energy is mainly contributed by its mass, we assume the protons to be initially at rest. Thus, the four-momentum vectors of the $\bar{\nu}_e$ and of the proton are $(0, \vec{p}_{\bar{\nu}_e})$ and $(m_p, 0)$, respectively, and the four-momentum vectors of the e^+ and neutron in the final state are $(m_{e^+}, \vec{p}_{e^+})$ and $(m_n, \vec{p}_n)$, respectively. Therefore, we must have:

$$\begin{cases} \vec{p}_{\bar{\nu}_e} = \vec{p}_{e^+} + \vec{p}_n, \\ E_{\bar{\nu}_e} + E_p = E_{e^+} + E_n. \end{cases}$$

Denoting the angle between the outgoing positron and the incident $\bar{\nu}_e$ to be θ and the angle between the outgoing neutron and incident $\bar{\nu}_e$ is ϕ. Here we use natural units in which $c = 1$ and $\hbar = 1$, and the relativistic energy momentum relationship of $E^2 = p^2 + m^2$:

$$\begin{cases} E_{\bar{\nu}_e} = \sqrt{E_{e^+}^2 - m_{e^+}^2}\cos\theta + \sqrt{E_n^2 - m_n^2}\cos\phi & \text{momentum conservation in the z direction,} \\ \sqrt{E_{e^+}^2 - m_{e^+}^2}\sin\theta = \sqrt{E_n^2 - m_n^2}\sin\phi & \text{momentum conservation in the transverse direction,} \\ E_{\bar{\nu}_e} + E_p = E_{e^+} + E_n & \text{energy conservation.} \end{cases}$$

The three independent equations can be combined into a single one by eliminating two unknowns, namely ϕ and E_n, and thus the relationship between the positron energy and the incoming neutrino energy yields:

$$E_{\bar{\nu}_e} = \frac{1}{2}\frac{2m_p E_{e^+} + m_n^2 + m_p^2 - m_e^2}{m_p - E_{e^+} + \sqrt{E_{e^+}^2 - m_{e^+}^2}\cos\theta}.$$

The visible energy in the detector is the total energy deposited by the inverse β-decay as seen by the inner detector PMTs. For the prompt event of the inverse β-decay, it consists of the total energy of the detected positron plus the energy of its annihilation on an electron, i.e.,

$$E_{vis} = E_{e^+} + m_e.$$

The neutron recoil energy is of the order of 10 keV, which is negligible. Furthermore, if we assume the final neutron state is also stationary, then the angle θ between the outgoing e^+ and the incident $\bar{\nu}_e$ can be set to zero. Herewith we have:

$$E_{\bar{\nu}_e} = E_{e^+} + (m_n - m_p).$$

With $m_n - m_p = 1.293$ MeV and $m_e = 0.511$ MeV, the threshold energy for an antineutrino to trigger the inner detector yields simply 1.804 MeV. The relation between the visible energy

E_{vis} and the antineutrino energy $E_{\bar{\nu}_e}$ can be expressed as:

$$E_{vis} = E_{\bar{\nu}_e} - (m_n - m_p) + m_e = E_{\bar{\nu}_e} - 0.782\,\mathrm{MeV}. \tag{3.3}$$

The visible energy spectrum without oscillations can be predicted with the reactor model. Neutrino oscillations introduce energy spectrum distortions, which may be used as an additional signature of neutrino oscillations, along with the overall reduction in data.

3.4 Detector

The Double Chooz detector system consists of four concentric cylinders, namely the neutrino target, the gamma catcher, the buffer and the inner veto. There are in total 390 Hamamatsu R7081 10-inch PMTs [157]–[159] forming 18 rings installed on the stainless steel buffer inner wall to detect light from the inner volumes. The PMTs have been chosen with low background glass which contributes only a few Hz to the singles rate. They are oriented to be pointing mainly towards the center of the detector to maximize the amount of light collected for events distributed uniformly throughout the neutrino target. The neutrino target, gamma catcher and buffer together compose the inner detector. Outside the optical separation of the buffer stainless steel vessel is a 50-cm-thick inner veto region which has 78 8-inch PMTs installed for tagging spallation neutrons produced near the outside of the detector and vetoing the cosmic muon. The detector is surrounded by demagnetized steel shielding to suppress external γ-rays. The main detector is covered by the outer veto system. The anatomy of the Double Chooz far detector is shown in Fig. 3.6.

The design goal of radiopurity concerning accidental coincidences is less than about 0.8 events/day. Before installation, all parts of the Double Chooz detector were screened for their content of radioactive isotopes. This was done by direct γ spectroscopy with different germanium detectors in underground laboratories. In addition, neutron activation analyses have been performed for the neutrino target and gamma catcher acrylic vessels as well as the wavelength shifter PPO (2,5-diphenyloxazole) [160]. Analysis of BiPo-coincidences from U

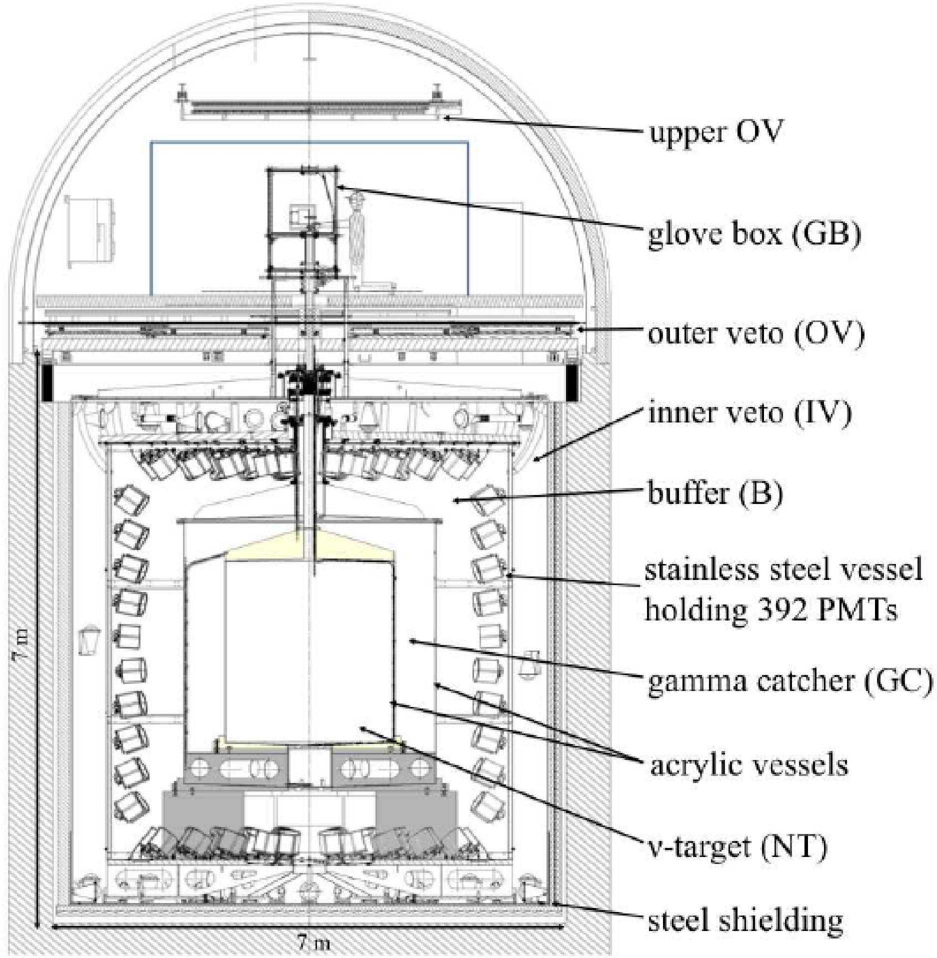

Figure 3.6: A cross-sectional view of the Double Chooz detector system.

and Th decay has shown their concentrations in the neutrino target and gamma catcher to be below the design goal of 10^{-13} g/g. The accidentals rate is also below the goal of 0.33 ± 0.03 events/day. The correlated backgrounds of (α, n)-process with ^{210}Po reacting on ^{13}C can be estimated to be less than 1.5×10^{-2} events/day (scaled from the result of KamLAND [161]), which is much smaller than the neutrino signal of approximately 37 events/day at the far detector.

3.4.1 Neutrino Target

The neutrino target is a cast acrylic cylinder of 115 cm radius, 245.8 cm height, and 8 mm thickness, containing 10.3 m^3 of liquid scintillator. A chimney on the center top of the neutrino target allows calibration sources to be deployed. The liquid scintillator is a mixture of 80% n-dodecane as the main solvent, 20% aromatic solvent ortho-phenylxylylethane (o-PXE), 0.007 g/cm^3 of fluor PPO, 20×10^{-6} g/cm^3 of wavelength-shifter bis-MSB (4-bis-(2-methylstyryl)benzene) and 1 g/l (or 0.123% by weight) gadolinium as a β-diketonate complex. The optical stability of the gadolinium-loaded scintillator, which limited the sensitivity of the CHOOZ experiment, has been improved. The scintillator design has to take into consideration the basic requirements of gadolinium solubility, optical transparency, radiopurity and chemical stability. The compatibility of the organic liquid to the contacted material, especially the acrylics, is very important. A metalorganic complex of metal-β-diketone, Gd(III)-tris-(2,2,6,6-tetramethyl-heptane-3,5-dionate), has been chosen to provide a higher solubility of the gadolinium, which does not dissolve enough in the organic solvents used for liquid scintillators. The stability and its high vapor pressure make it work properly. The radioactive contaminations, such as U, Th and K, can be sublimed out. The gadolinium peak of neutron capture has been measured in situ as a function of elapsed time to evaluate the optical stability of the scintillator, as shown in Fig. 3.7. In a one-year data-taking period, the energy response variation is within 1%, which is very stable. The slight increasing peak energy response in time is probably caused by PMT gain drifts and readout effects.

The primary wavelength shifter PPO and secondary wavelength shifter bis-MSB are added to shift the scintillation light into a more transparent region. Double Chooz upgraded the light yield model designed for general metal loaded scintillators, according to which the neutrino target light yield was tuned. The absolute number of protons is crucial in the Double Chooz experiment. With the precise knowledge of the weight of each chemical in the scintillator, the error on the proton number has been minimized. The neutrino target scintillator weight was determined with a precision of 0.04% after thermalization. The hydrogen fraction is known within 0.3%, including both the uncertainties from scintillator ingredients weights and the knowledge on not fully defined impure chemicals which introduce hydrogen content errors. These errors are of per mil level for the main components [160].

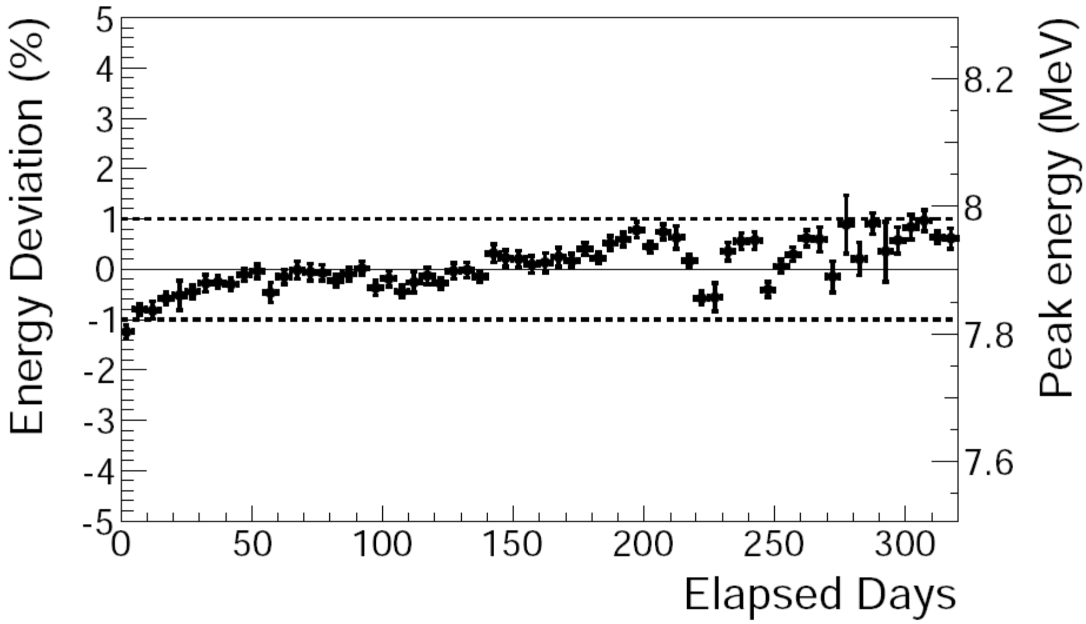

Figure 3.7: Average target detector response evolution in time, as measured by the mean energy of the gadolinium capture peak arising from interaction of spallation neutrons in the neutrino target [162].

3.4.2 Gamma Catcher

The gamma catcher region is 55 cm thick and made of the same acrylic as the neutrino target, loaded with gadolinium-free liquid scintillator. The gamma catcher liquid scintillator is composed of 30% n-dodecane, 66% Ondina 909 oil, 4% o-PXE, 0.002 g/cm^3 PPO, and 20×10^{-6} g/cm^3 bis-MSB. It was tuned to match the light yield and density of the target volume scintillator in order to increase the uniformity of the detector response and ensure the safety of the fragile acrylic modules. The vessel itself is 12 mm thick and is designed to measure the γs from neutron capture on gadolinium and from positron annihilation escaping the neutrino target, as well as to reject the background from fast neutrons (as discussed in Section 3.7.2.2). All liquid densities in the four volumes (neutrino target, gamma catcher, buffer, inner veto) were matched to be 0.804 ± 0.001 g/cm^3 at 15°C to avoid mechanical stress on the detector vessels. For the wavelength of light above 430 nm where the bis-MSB absorption effect is negligible, the attenuation lengths were measured in the laboratory before detector filling. The values turn out to be more than 7 m for the neutrino target and

10 m for the gamma catcher, which are both above the corresponding vessel dimensions. The attenuation length in the buffer is about 30 m, which is much more than those in the neutrino target and gamma catcher.

3.4.3 Buffer

The buffer vessel is made of 3-mm-thick stainless steel, where 390 PMTs are mounted on the interior surface with the base circuit enclosed by a transparent epoxy resin. The PMTs are equipped with angle-adjustable mounting jigs and shielded by mu-metal cylinders to prevent interference from the earth's magnetic field. The buffer region is 105 cm thick and contains 114.2 m^3 of non-scintillating mineral oil to decrease the accidental background from the PMTs radioactivity and surrounding rock. It serves to lower the singles rate by two orders of magnitude compared to that in the CHOOZ experiment [163], such that the final singles rate in the neutrino target and gamma catcher should be below 10 Hz. A total number of 800 PMTs were carefully characterized for both detectors (the near and the far) with many crucial characteristics [157, 158, 164]. The single photoelectron (PE) peak to valley ratio was 4 with a threshold of 0.25 PE; the quantum efficiency times collection efficiency was 23%; the transit time spread was 3 ns FWHM (full width at half maximum); the afterpulse probability was 2.7% in average; the charge output was linear up to 300 PEs per PMT; the dark rate was approximately 2 kHz with 20-hours measurement after the high voltage was turned on. After installation and commissioning, it has been observed that some PMTs sporadically and spontaneously emit light from their base circuit through the epoxy resin. However, since these non-physical events have different signal patterns from those generated by neutrino events, they can be safely removed by imposing $Q_{max}/Q_{tot} < 0.09$ (where Q_{max} is the maximum charge recorded by a single PMT and Q_{tot} is the total charge collected in that event) and $t_{RMS} < 40$ ns (where t_{RMS} is the RMS value of all times at the PMTs). The characteristics of these light noise events are typically that one PMT was favored in charge, while the PMT times were spread out. The light spread homogeneity is the main discrimination between physics events and light noise events. Additional studies have shown that the charge and time components of the RecoBAMA (reconstruction package developed by the University of Alabama group) functional value can also remove these light noise events with high efficiency. A detailed discussion of RecoBAMA is presented in Section 8.1.

3.4.4 Inner Veto

Outside the buffer is a 50-cm-thick layer surrounded by a cylindrical stainless steel vessel filled with liquid scintillator, shielding the inner detector against cosmic muon-induced spallation neutrons and external radioactivity sources. The inner veto region with 6.8 m height and 3.3 m radius is optically separated from the inner detector. The 90 m^3 liquid scintillator in the inner veto is a mixture of linear alkyl benzene and n-alkanes, with 0.002 g/cm^3 PPO as fluor and 20×10^{-6} g/cm^3 bis-MSB as a secondary wavelength shifter. The inner veto efficiency in identifying cosmic muons was optimized by MC simulations [165], where the focus was on maximizing the charge collection per unit energy and the muon and muon-correlated background events rejection efficiency. After the optimization, the inner veto consists of 78 Hamamatsu R1408 8-inch PMTs with 24 on top, 12 at the midway point of the side walls, and the remaining 42 at the bottom. The outer side walls of the buffer vessel are covered with reflective VM2000 sheets, while the inner veto inner surfaces are painted with highly reflective white paint (AR100/CLX coating from MaxPerles). All the inner veto PMTs and their bases were placed into stainless steel encapsulations with a transparent PET (polyethylene terephthalate) window at the front end. To match the optical properties of the inner veto scintillator, the capsules are filled with mineral oil. Evaluated in conjuction with the outer veto, the inner veto muon rejection efficiency was found to be larger than 99.99% for muons crossing the inner veto volume.

3.4.5 Outer Veto

The outer veto consists of a muon tracking system 15 cm above the shielding steel, providing a coordinate system to locate the through-going muons. It consists of two separate parts: the lower outer veto and the upper outer veto. The lower outer veto is installed right above the

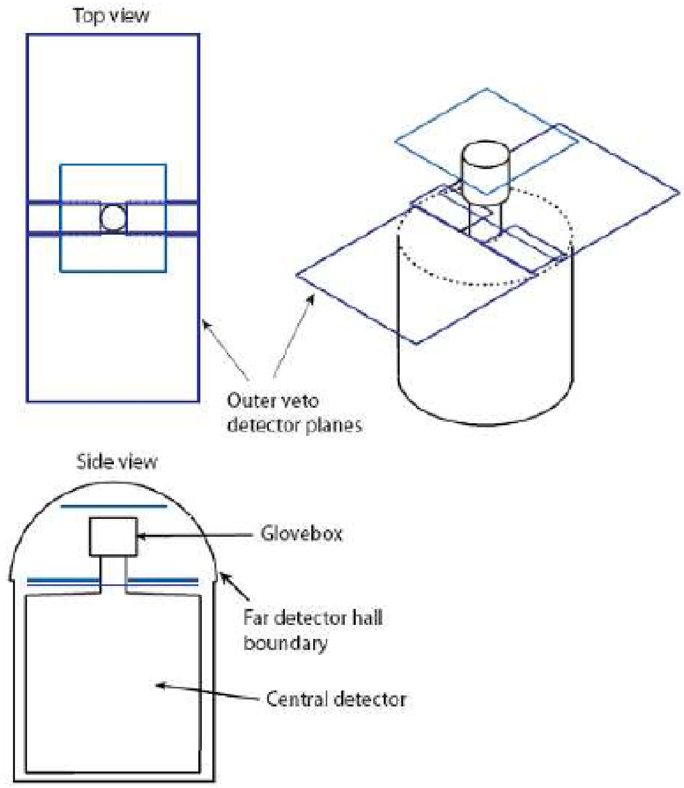

Figure 3.8: Outer veto layout in the far detector hall [166].

inner veto shielding, while the upper outer veto is installed on top of the detector hall, above the chimney and glove box. The center of the outer veto is at the chimney, and was designed with an area of 13 m $\times$ 11 m with a 1.1 m $\times$ 0.3 m opening for the chimney. Because of the limitation of the far detector hall, the actual size for the far detector was limited to 13 m $\times$ 7 m. The distance between the two layers is about 5 m which optimizes the tracking capability. Both layers have (x,y) coordinates to measure the through-going muons. There are 44 plastic scintillator modules assembled in two layers: 36 of them are mounted on the lower outer veto and the rest are installed on the upper outer veto. The modules are placed in two layers with orthogonal orientations in x and y directions. Each module consists of 64 (5 cm $\times$ 1 cm $\times$ 320 cm or 360 cm) scintillator strips. Wavelength-shifting fibers are threaded into the hole running through the strip length where the strips are extruded. All 64 fibers are connected at one end to a Hamamatsu H8804 multi-anode PMT (M64) while the other ends are mirrored. Each M64 is connected to a custom front-end board with an FPGA (field-programmable gate array) and a MAROC2 (multi anode read out chip) ASIC (application-specific integrated circuit) [167], which can adjust the electronic gain of each of the 64 channels. The charge information of the strip is seen on a multiplexed 12-bit ADC (analog-to-digital converter) when the outer veto receives a signal over the threshold.

3.5 Data Acquisition

The diagram of the full readout and data acquisition (DAQ) system of the inner detector and inner veto is shown in Fig. 3.9. The signal goes through the electronics elements including the high voltage splitter and supply, the front-end electronics, the trigger system [168] and the flash-ADC digitizing electronics [169, 170]. The PMT signal (5 mV per PE) and the high voltage (about 1.3 kV) share the same cable connected to a single PMT which will be decoupled by the high voltage splitter. The high voltage is provided by CAEN-A1535P [171] power supplies.

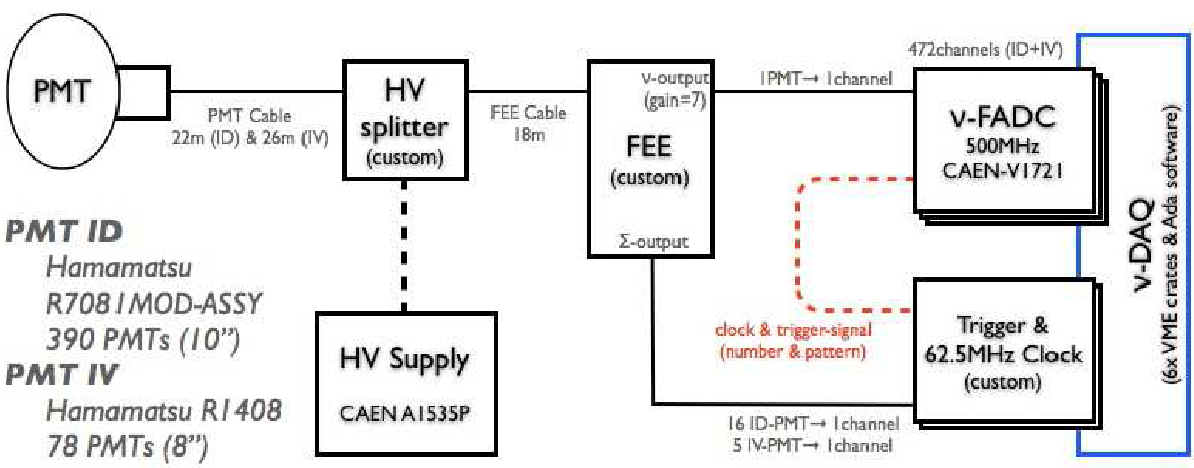

Figure 3.9: Diagram of the Double Chooz readout and DAQ systems [162].

3.5.1 Front-End Electronics

The signals in the front-end electronics are optimized with amplification, large signal clipping, baseline stability and coherent noise filtering. The front-end electronics stretch the summed signals which are proportional to charge and delivers them to the trigger system. To filter the events and minimize overshooting that can cause trigger dead time, the sum-signal undergoes a subtraction of the input amplitude after about 100 ns. The low energy neutrino-like signals are amplified by a factor of 7.8 [172], while the high energy muon-like signals are attenuated by a factor of 0.55 to match the dynamic range of the ν-FADC and μ-FADC respectively. In the inner detector, each front-end electronics module contains 8 channels, while 2 modules make a sub-group which is the basic unit for the sum-signal to be constructed. For the inner veto, the total number of PMTs in a sub-group is 6.

3.5.2 Flash-ADC

There are two kinds of FADCs, namely ν-FADCs and μ-FADCs, which are responsible for the digitization of the PMT signals. The ν-FADCs record events below 15 MeV which have been amplified previously by the front-end electronics, while the μ-FADCs record the higher energy signals by attenuating them from the front-end electronics. Since the μ-FADCs have not been in use, the discussion below focuses on the ν-FADCs only. The ν-FADC system relies on 64 CAEN-Vx1721 [171] waveform digitizers developed by CAEN with Double Chooz collaborators from the Astroparticule et Cosmologie group (Université Paris Diderot) and customized to allow the DAQ to better handle a coincidence driven experiment. The waveform digitizer consists of 8 channels with a 500 MHz sampling rate (which leads to 2 ns digitization in the timing resolution) and 8 bit resolution. Each of the channels contains 2 MB memory split into 1024 memory buffers which can hold up to 4 μs worth of data. The digitization process is illustrated in Fig. 3.10, where the ν-FADC continuously writes data in the current page up to the 2048^{th} sample until the trigger is inserted. If no trigger signal is received, the 2049^{th} sample will overwrite the first sample

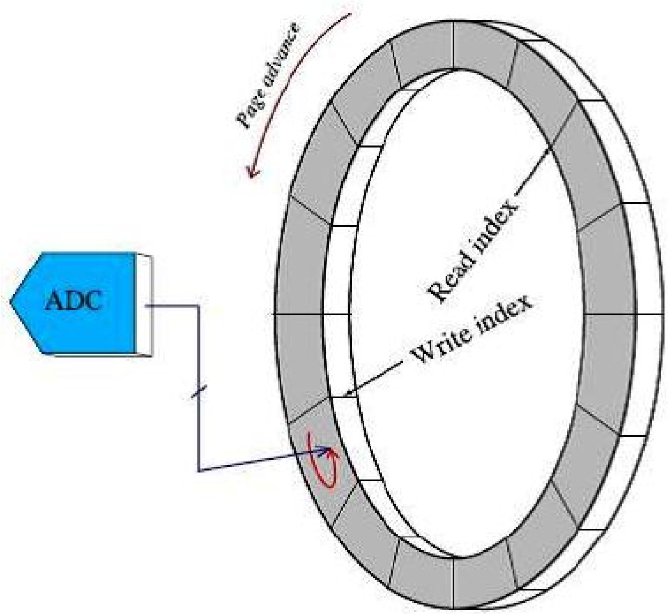

Figure 3.10: Operation of the digitizer as a FIFO (first in first out) [173].

and so forth. After a trigger signal, the *Read index* will mark the page with an event to be read out and the *Write index* will increase by 1 according to the current page, so that the next event will be written on the next page. Several events can be stored at the same time until they are ready to be read out. There will be a dead time [173] when the *Write index* catches up with the *Read index* in the previous cycle. When triggered, only a 256 ns waveform is recorded, which is a compromise between data volume and the ability to collect all light produced in an event. The 256 ns digitized waveform in each trigger has over 90% of the scintillation light. The charge deposited in each channel is at the single PE level when the total energy is smaller than about 3 MeV. The single PE level charge has an amplitude of 40 mV and generates about 10 samples. The single PE fluctuations are relatively much larger than the uncertainty caused by digitization, which is negligible in comparison. High energy muon events with total energy above 100 MeV may lead to an amplitude saturation resulting in some degree of non-linearity of energy resolution. It has no effect on the neutrino events since their maximum energy scale is an order of magnitude smaller. Although a few ADCs baseline swinging has been detected within 100 μs window after a muon, the overall variation of the baseline and its width is below one ADC count. There are several front-end electronics power cyclings each year which also induce a baseline bias of the order of sub-1 mV which, although tiny, can cause an unmeasurable bias in the zero charge definition due to the limited sampling. Therefore, a non-linearity effect in the signal around a single PE charge is introduced. A stronger signal has more charge and the bias becomes more and more negligible. This single PE non-linearity has been thoroughly studied, measured and calibrated.

3.5.3 Trigger

The trigger system is implemented in two stages: the hardware trigger, which determines whether or not an event has occurred based on the analog sums of the PMT signals, and the software trigger, which further reduces the data volume. A diagram of the Double Chooz trigger system is shown in Fig. 3.11. There are 3 trigger boards and 1 trigger master board. Trigger boards A and B are used for the inner detector PMTs, and the veto trigger board is for the inner veto PMTs. At the hardware trigger level, half of the inner detector PMT sub-groups make up a super-group; two separate super-groups A and B can cause an inner detector trigger. The PMTs in sub-groups are uniformly distributed in the volume, so that one of them can be used to monitor the performance and efficiency of the other.

At the software trigger level, the trigger types are defined based on the integral of the signal. There are 4 types of signal: prescaled, neutrino-like, neutron-like and muon-like. The threshold values for the different signals are described in Table 3.2. The scaling factor of prescaled trigger events is 1,000, which means that the system triggers once every 1,000 such events. This is an effective way to study the trigger efficiency and low energy background, while limiting the amount of low energy triggers below the rate that the system can handle. The threshold for neutrino-like signals is set below the minimum positron signal of 1.022 MeV. The neutron-like signal threshold is set below the 8 MeV neutron capture energy on gadolinium. The muon-like threshold allows only high energy cosmic muons. Other than those, each input channel having 16 PMTs is divided into two lines, namely, high and low

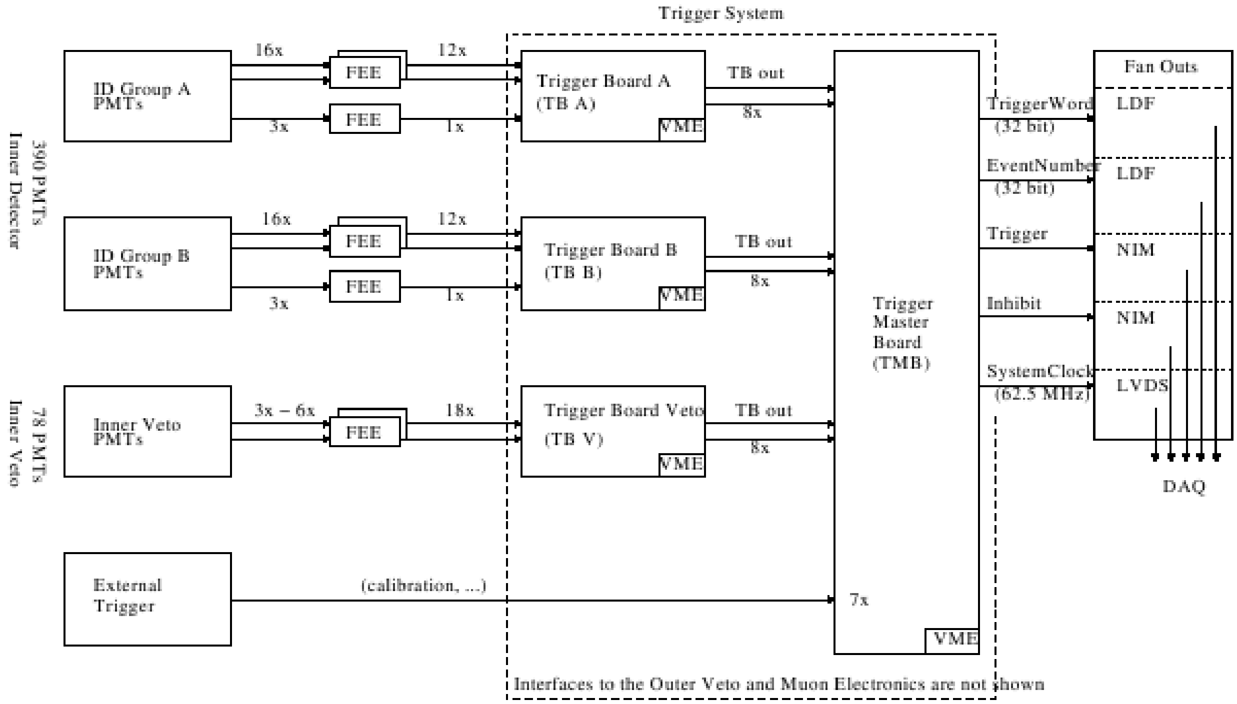

Figure 3.11: Schematic overview of the trigger system – from Ref. [174].

group thresholds, allowing a trigger based on the multiplicity (Fig. 3.12). The separation also helps reduce the impact of noisy PMTs. The reason why the high group threshold is the same as the low group threshold is only because it has not been used. It can help in monitoring the stability of the threshold by comparing the two.

Trigger type	Threshold energy (MeV)
prescaled	0.2
neutrino-like	0.35
neutron-like	5
muon-like	50
group threshold low	0.25 (70% of neutrino-like)
group threshold high	0.25 (70% of neutrino-like

Table 3.2: Inner detector trigger thresholds.

In order to synchronize, the trigger system has a 62.5 MHz clock distributed to the FADCs. The trigger boards have a 16 ns resolution which means that they measure and store the time in steps of 16 ns. The trigger boards pass an 8-bit word to the trigger master

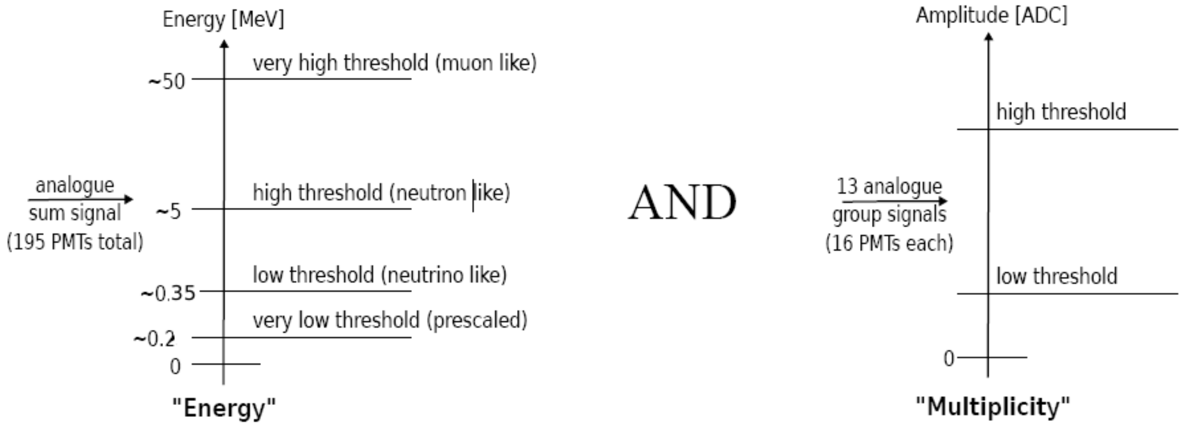

Figure 3.12: Schematic principle of the trigger decision of the Double Chooz experiment. The detector is triggered by a logical AND of the deposited energy inside the detector and a multiplicity condition representing the number of active groups of PMTs. The analogue sum signal is the summation of all group signals and its pulse height corresponds to the energy deposited in the detector [168].

board which makes the decision and passes a 32-bit word to the FADCs including 3 × 8-bits from 3 trigger boards and 8 reserved bits for external triggers (including inner detector LEDs, inner veto LEDs, tagged calibration sources, a 470 nm laser, a 375 nm laser, a dead-time monitor and outer veto triggers). Although the sub-group multiplicity information is available, the inner detector triggers use the trigger of overall energy at about 0.35 MeV. The trigger has an efficiency of 100% at the analysis threshold of 0.7 MeV as shown in Fig. 3.13, which is demonstrated by two monitors running at 2 Hz. These monitors can also provide the extra baseline monitoring, background and dark current information by randomly sampling the detector.

The situation for the inner veto trigger is a little bit different, where both the energy and sub-group multiplicity information may cause the trigger. The inner veto triggers if the energy is above 10 MeV, which corresponds to 8 cm of a minimum ionizing muon track when 2 or more sub-groups are hit. The inner detector and the inner veto are both read out by the same DAQ upon any trigger of either the inner detector or inner veto. The DAQ can sustain up to 200 triggers/second.

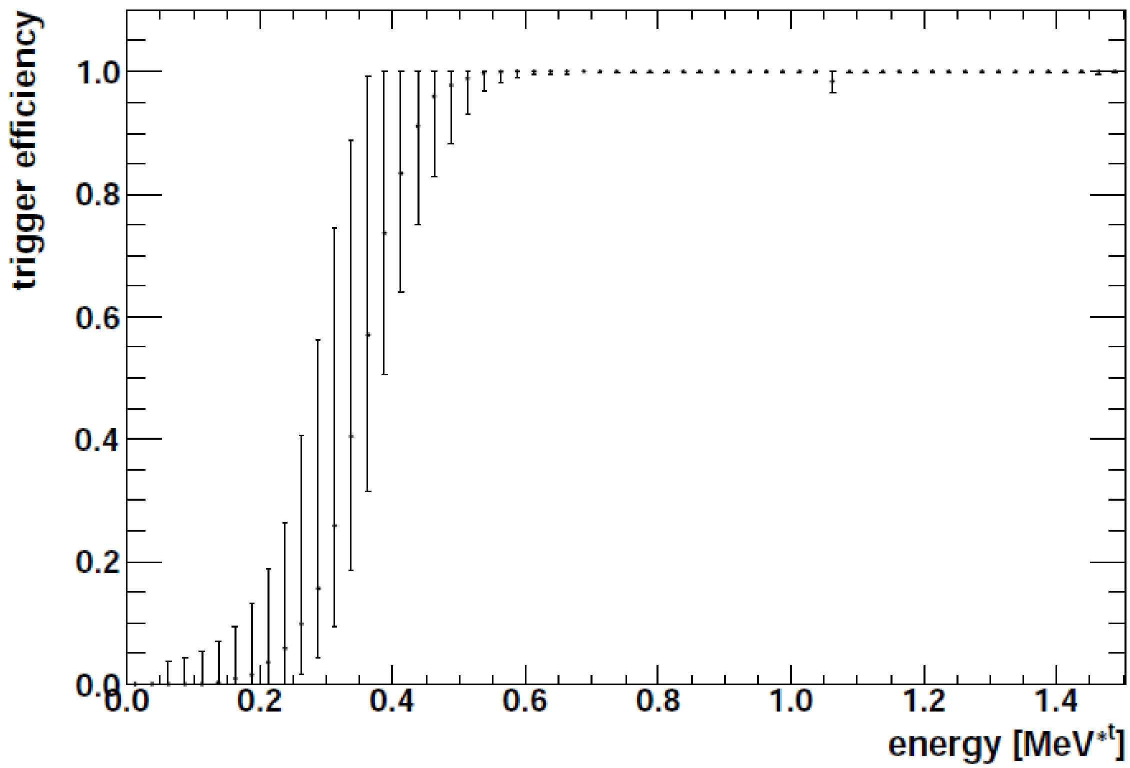

Figure 3.13: Trigger efficiency as a function of visible charge in MeV obtained by stretcher signal analysis using events taken with prescaled threshold. The trigger efficiency is 100% and systematic uncertainties on the trigger efficiency above 0.7 MeV is within 0.4%.

3.6 Calibration

3.6.1 Calibration Overview

The calibration is critical to a high precision experiment such as Double Chooz. Frequent calibration is necessary for all of the calibration constants, as well as for detector monitoring purposes. The relative detection efficiency between the two detectors should be known with an uncertainty of no more than 0.5%, while the uncertainty on the absolute energy scales for e^+ and γ are supposed to be within 1%. To achieve this goal, Double Chooz uses several dedicated calibration systems (the light injection system, radioactive sources, laser system), as well as natural means including cosmic rays and natural radioactivity. The light injection (LI) system described in Section 3.6.2.3 periodically injects light of different wavelengths into the inner detector and the inner veto, which is working as the primary method for the PMT constants calibration, such as gains and time offsets. The radioactive sources discussed in Section 3.6.3.2 are deployed along the z axis and through the guide tube (as discussed in Sections 3.6.2.1 and 3.6.2.2, respectively) during special calibration campaigns to check the reconstruction precision, monitor the detector stability, and calibrate the energy response of the detector. The laser calibration system will be discussed in Chapter 4, and focuses primarily on the PMT gains and time offsets. It is also used in the charge likelihoods extraction and systematic studies of the position reconstruction accuracy. The cosmic rays studies include stopping muons, spallation neutrons and cosmogenic radioactive isotopes, aiming to monitor the detector energy response and stability, which in turn affects the fitting of the prompt neutrino energy spectrum shape in measuring the θ_{13} mixing angle. In the absence of the articulated arm designed to measure the detector response away from the z axis, the off-zaxis spallation neutron capture events (several thousand per day) on hydrogen and gadolinium are very useful in studying the detector energy response. The articulated arm will be described in Section 3.6.2.4.

3.6.2 Calibration Systems

3.6.2.1 Z-axis System

The z-axis system is designed for deploying the laser diffusers, LED-flasher and radioactive sources through the vertical central axis into the target region through the chimney. The system is mounted inside a sealed glovebox and the radioactive sources or laser diffusers are made to be easily interchangeable. The z-axis deployment systems are designed to be identical for both the near and far detectors. The z-axis system is an automated fish-line scheme consisting of a microstepper motor with an interchangeable driving spool, a guide pulley where a teflon-coated wire runs over and down into the neutrino target through the chimney, and a weight interface with a calibration source attached at the deployment end. A mockup of the z-axis system is shown in Fig. 3.14. There is also a shaft encoder on the

Figure 3.14: Mockup of z-axis system at Argonne National Laboratory (ANL) [175].

guide pulley to cross check the source position in addition to that of the motor. The control is via a graphical user interface on a connected laptop. The material meets compatibility requirements for the Double Chooz experiment, which allows only acrylics and teflon-coated surfaces in contact with the neutrino target scintillator. The deployments via z axis can reach all the positions along the longitudinal axis of the detector in the neutrino target (Fig. 3.15). Its accuracy is estimated to be within 1 cm.

3.6.2.2 Guide Tube

The guide tube system is installed in the gamma catcher for radioactive sources deployments. The design, development and tests were performed at the University of Alabama and the illustration of the path and full scale prototype are shown in Fig. 3.16. When deployed via

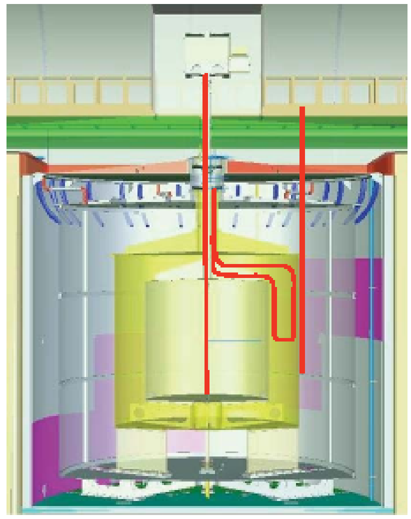

Figure 3.15: Sketch of z-axis, guide tube and buffer tube routes.

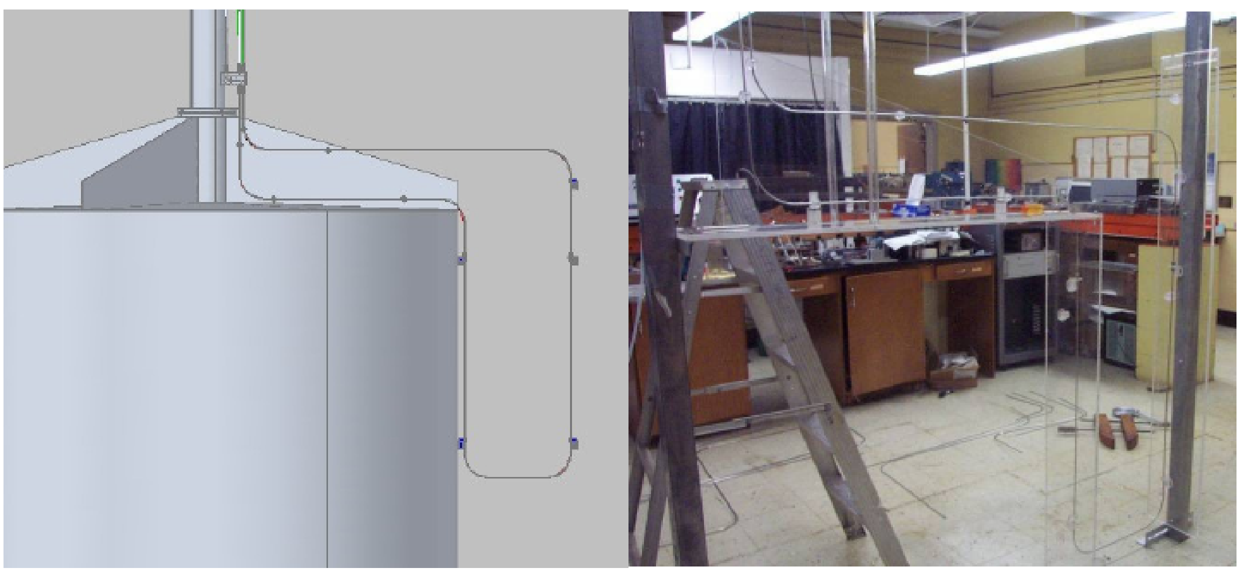

Figure 3.16: Guide tube layout in the gamma catcher and full scale phototype in the University of Alabama lab [176].

the guide tube, the source is attached to a motor-driven wire and guided through a closed-loop tube. The perpendicular distance between the deployed source and the neutrino target wall could be within 2 mm at some places. The deployment accuracy is estimated to be approximately 1 cm along the tube.

3.6.2.3 Light Injection

The light injection system is a multi-wavelength LED-fiber system (385, 425 and 470 nm for the inner detector, and 365 and 475 nm for the inner veto) for measuring PMTs and readout electronics gains and time offsets, regularly providing PMT constant tables for well-defined time periods. It injects light into the inner detector (Fig. 3.17) and the inner veto from fixed points to illuminate all the PMTs. The optical fibers are routed inside the detector with one end of the fibers connected to the PMT acrylic support structure and the other end of the fibers attached to the LEDs. The LI calibration runs are taken regularly between a set of physics runs for monitoring the stability of the PMT gains and time offsets. The LED frequency, light intensity and pulse width can be selected by remote shifters via graphical user interface. The PMT gains change with different power cycles, while the time offsets are almost invariant in time. Therefore, regular calibration for gains and time offsets monitoring is necessary. The LI data also helps in correcting the PMT charge non-linearity effects which arise from readout electronics and charge reconstruction.

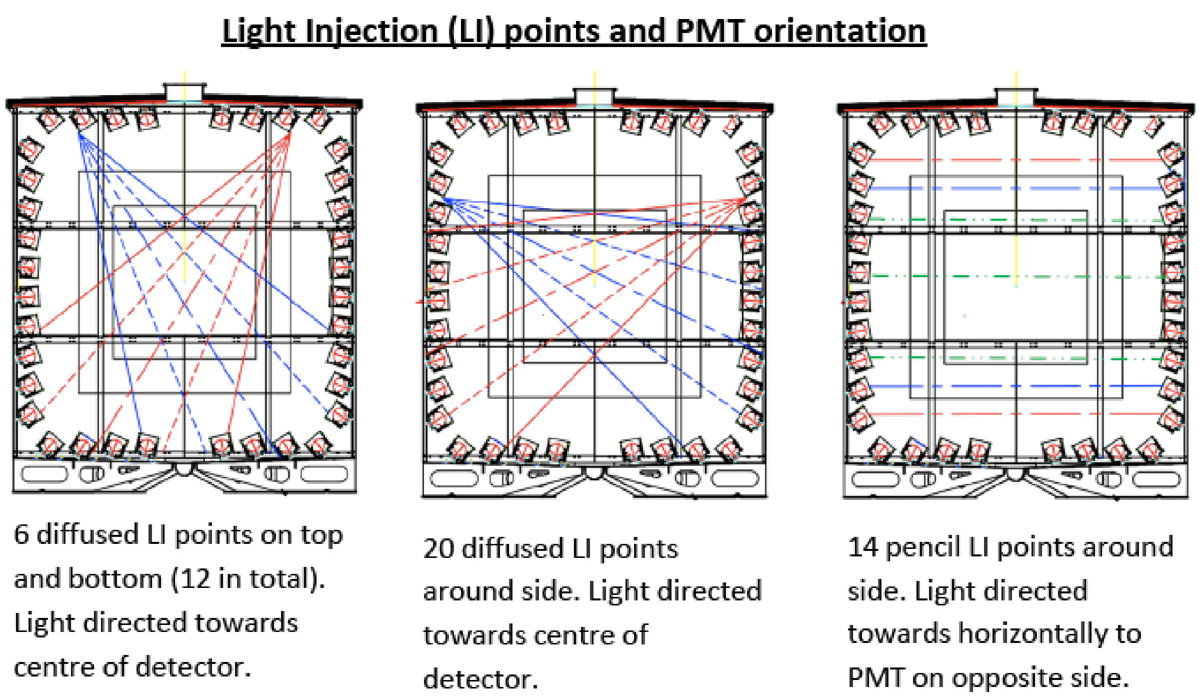

Figure 3.17: The illustration of IDLI (inner detector light injection) [177].

3.6.2.4 Articulated Arm

The articulated arm system consists of a telescoping support rod, pivot and segmented arm [178]. The z-axis system can only deploy sources along the central z axis and cannot reach the other regions of the neutrino target, which is of essence for energy scale studies. This full target volume deployment system will be connected to the glovebox via a dedicated flange on the top and deployed into the neutrino target region through the chimney. After reaching the planned z position in the neutrino target, it will flex to a horizontal position and extend the attached radioactive sources to purposed ρ and ϕ as shown in Fig 3.18. The source will be mounted on the last segment of the arm and the optical finder is mounted to the segment close to the source rod. The articulated arm calibration is tentatively scheduled to be deployed for the first time at the end of 2013.

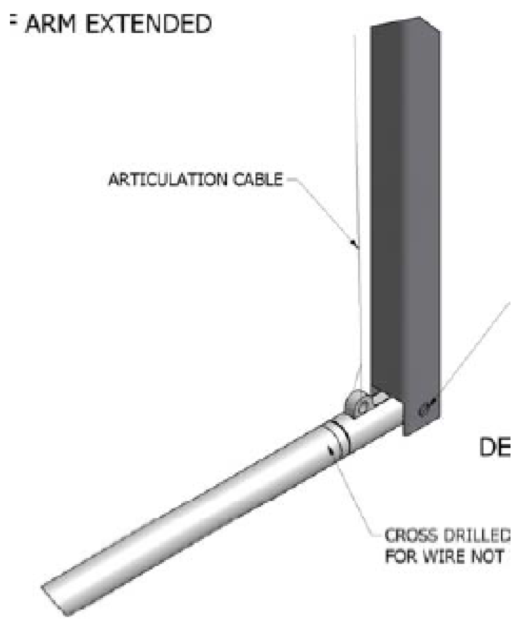

Figure 3.18: Schematic view of the articulated arm – from Ref. [178].

3.6.3 Calibration Sources

3.6.3.1 Laser

The development and detailed studies of the laser calibration system will be discussed in Chapter 4.

3.6.3.2 Radioactive Sources

The radioactive sources that have been deployed in Double Chooz experiment consist of the following four radio-isotopes: ^{137}Cs, ^{68}Ge, ^{60}Co, and ^{252}Cf.

- ^{137}Cs

  The ^{137}Cs decays by β emission to ^{137}Ba (95%) and the other 5% are going to the ground state of ^{137}Ba with a half-life of about 30.17 years [179]. The ^{137}Ba later emits a mono-energetic 0.662 MeV γ with a half-life of about 153 seconds, which can be used in the scintillator energy scale study.

- ^{68}Ge

  The ^{68}Ge captures an electron and decays into the positron-emitting isotope ^{68}Ga with a half-life of 270.95 days. The annihilation of the positron and electron emits a 1.022 MeV γ (2$\times$0.511 MeV), which is close to the threshold energy of the prompt inverse β-decay events. Through it, the trigger efficiency can be measured.

- ^{60}Co

  ^{60}Co has a half-life of 5.27 years and is a synthetic radioactive isotope of cobalt. It decays into ^{60}Ni by beta emission. Two γs are emitted through the activated ^{60}Ni nucleus with energies of 1.17 and 1.33 MeV.

- ^{252}Cf

  96.9% ^{252}Cf decays into ^{248}Cm by α decay (emitting two protons and two neutrons). The other 3.1% undergoes spontaneous fission. With a half-life of about 2.64 years,

^{252}Cf is a very strong neutron emitter with an average multiplicity of 3.76; it is used in neutron efficiency and energy scale studies.

The deployments of radioactive sources can occur in both z-axis and guide tube with sources sealed in miniature capsules. During the first calibration campaign of September 2011, the rates of the untagged radioactive sources ^{137}Cs, ^{68}Ge and ^{60}Co were about 30 Bq, and the neutron emission rate for ^{252}Cf was approximately 20 Hz [180]. In the second calibration campaign of June 2012, the same sources as in the first calibration campaign were used. Due to the long half-life of ^{137}Cs and ^{60}Co, their rates were still at the same level as in the first campaign, while the rate of ^{68}Ge dropped to approximately 15 Bq and the neutron rate of ^{252}Cf became 15 Hz. In the third calibration campaign of June 2013, the same ^{137}Cs and ^{60}Co were still being used, while the other two sources were too weak and needed to be replaced. The new ^{68}Ge had a rate of about 20 Bq and the new ^{252}Cf had a neutron rate of 27 Hz [181].

3.6.3.3 LED Flasher

The LED flasher is a battery-powered light emitter that is hermetically sealed in a container made of teflon and plexiglas with each joint double-sealed by teflon O-rings (Fig. 3.19). The teflon diffuser sphere has a 5 cm diameter and emits light in eight intensity levels with 128 pulses at each level before moving to the next one. The central LED flasher was deployed before the filling of the far detector and the PMT time offsets were obtained with a precision of approximately 0.5 ns [182]. Unfortunately, during the reboot of the read-out processors, a problem was found that made the time offsets fluctuate significantly. Before the official physics run was started, the problem was resolved, but the original time offsets determined with the LED flasher in the empty detector were never used in any analysis.

Figure 3.19: Prototype of LED flasher. The diameter of the diffuser ball is 2 inches [183].

3.7 Backgrounds

Double Chooz is a high precision experiment requiring great control and knowledge of the backgrounds. Background events can mimic the inverse β-decay events induced by the $\bar{\nu}_e$ flux by a prompt positron-like event followed by a neutron-like delayed event which may or may not be correlated with the primary. The following selection criteria are used to select the inverse β-decay candidate events and eliminate as many background events as possible. The inverse β-decay event selections in the first analysis paper [102] include the first four criteria listed below, while the second analysis paper [162] includes all of the following criteria:

1. $0.7 < \mathrm{E}_{prompt} < 12.2$ MeV.
2. $6.0 < \mathrm{E}_{delayed} < 12.0$ MeV.
3. $2 < \Delta t_{prompt/delayed} < 100$ μs (about 3 times of the neutron capture time on gadolinium).
4. Multiplicity: no additional valid triggers from 100 μs preceding the prompt signal to 400 μs after it.

5. Showering-μ veto for β-n background reduction: candidates within a 0.5 s window after a muon depositing more than 600 MeV crosses the inner detector.

6. Cosmogenic β-n background reduction: candidates whose prompt signal is coincident with an outer veto signal.

The backgrounds can be categorized into two main groups: accidental and correlated backgrounds. Two random and unassociated events with energies in the prompt and delayed energy ranges respectively, which happen coincidentally within a time window consistent with that of an inverse β-decay event could make an accidental background event. Two associated events from a single source mimicing the inverse β-decay event would be treated as a correlated background event. The primary sources of accidental backgrounds are the prompt events from natural radioactivity of the materials constructing the detectors followed by a neutron-like candidate. The correlated backgrounds are from the products of cosmic ray interactions. By learning from the experience of the Chooz experiment, the design of the Double Chooz detector was improved by introducing a gamma catcher volume and an outer veto resulting in a further reduction of entering backgrounds. The construction materials were carefully selected to limit radioactivities. A 300 m.w.e. (meter water equivalent) of overburden shields the far detector from cosmic rays, which reduces the muon flux inside the lab by more than two orders of magnitude, from about 100 μ/s/m^2 (above ground, at sea level [184]) to approximately 0.43 ± 0.02 μ/s/m^2.

3.7.1 Accidental Backgrounds

The main source of the accidental backgrounds is the random association of the natural radioactivity of the materials constructing the detectors, liquids and the surrounding rock of the cavern with a neutron-like event or photons from bremsstrahlung radiation caused by muons traversing the surrounding rock. This background mimics the inverse β-decay signal which needs to be understood and characterized. Since most of the singles are in the low energy region ($<$ approximately 3 MeV), a very high singles rate may prevent the detector from setting the trigger threshold at a low enough level to accept all prompt positrons of the inverse β-decay reaction.

The accidental background rate depends on the singles rate such as gammas, betas or neutrons, which can be estimated by applying the neutrino selection cuts with coincidence windows shifted by 1 s, which removes correlations on the time scale of the neutron capture on hydrogen and gadolinium. This is called the "offtime" window method. Since it is a random association, the statistics can be also increased by using 198 windows, each shifted by 500 μs with respect to the previous one.

The radioactivity rate was measured to be 8.2 events/second in the prompt energy range from 0.7 to 12.2 MeV, while the neutron-like rate was found to be 18 events/hour. The total accidental background rate is determined to be 0.261 $\pm$ 0.002 events/day at analysis level. Both rates are quite stable and reproducible, which is proved by repeating the procedure 30 times. The variations turn out to be consistent with statistical error, with no systematic deviation. Figure 3.20 shows the agreement between the accidental prompt spectrum and the properly scaled natural radioactivity energy distribution. The light noise by individual PMTs mentioned in Section 3.4.3 is well controlled by imposing the $Q_{max}/Q_{tot} < 0.09$ and $t_{RMS} < 40$ ns cuts. It only contributes less than 1% to the overall accidental background. Study of isotopes such as U, Th and K in the surrounding rock and materials also help estimate the single rate. Moreover, the isotopes have well known energy spectra which could be used as a free source of natural calibration.

3.7.2 Correlated Backgrounds

Correlated backgrounds are created by sources which induce both prompt and delayed signals. Cosmic muons are the sources for most of these backgrounds. Although the overburden rock provides a natural shield, some of the cosmic rays will still penetrate into the detector and create backgrounds. Cosmogenic isotopes are generated by passing muons interacting with carbon atoms in the scintillator. Some of them contribute to accidental backgrounds

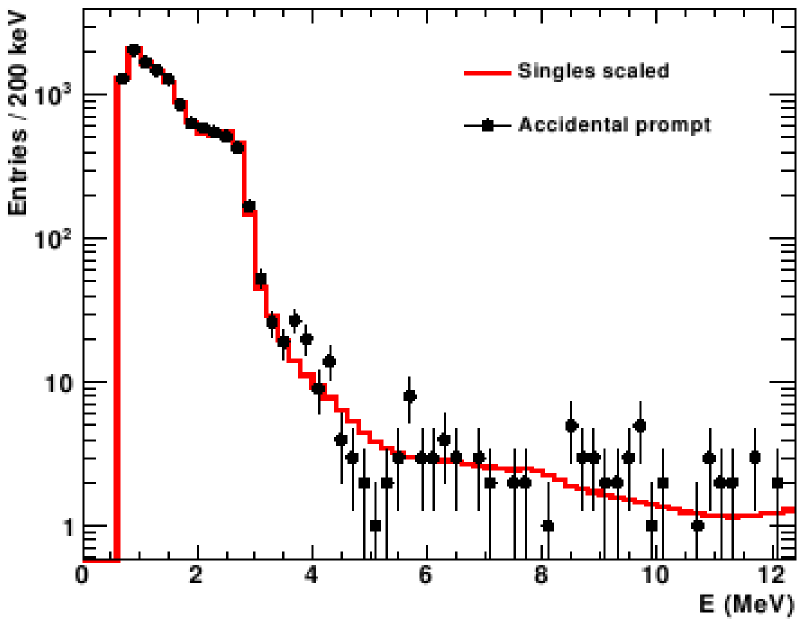

Figure 3.20: The accidental prompt spectrum (black markers with error bars) superimposed to the radioactivity energy distribution measured in Double Chooz scaled to the same number of entries (red line) [162].

with only β-decay, while β-n emitters such as ^{8}He and ^{9}Li contribute to the correlated background. Fast neutrons are also produced by muons interacting with the material surrounding the detector. In addition, some low energy muons may enter through the chimney without being tagged by the inner or the outer veto and stop and decay at the top of the inner detector. The short muon track mimics the prompt signal while low-energy Michel electrons from the subsequent decay mimic the delayed signal.

3.7.2.1 Cosmogenic Isotopes

Cosmic muon induced radioisotopes ^{8}He and ^{9}Li are the main sources of cosmogenics background. They create a pair of correlated events by β-n decay which can be identified from the time and space correlation to their parent muon. A decay scheme diagram for ^{9}Li is shown in Fig. 3.21. The ^{9}Li has a lifetime of 178 ms and the ^{8}He has a lifetime of 119 ms. Such long lifetimes make them unable to be discriminated on an event-by-event basis, nor vetoed for several isotope lifetimes because of the significant loss of exposure time. The analysis of

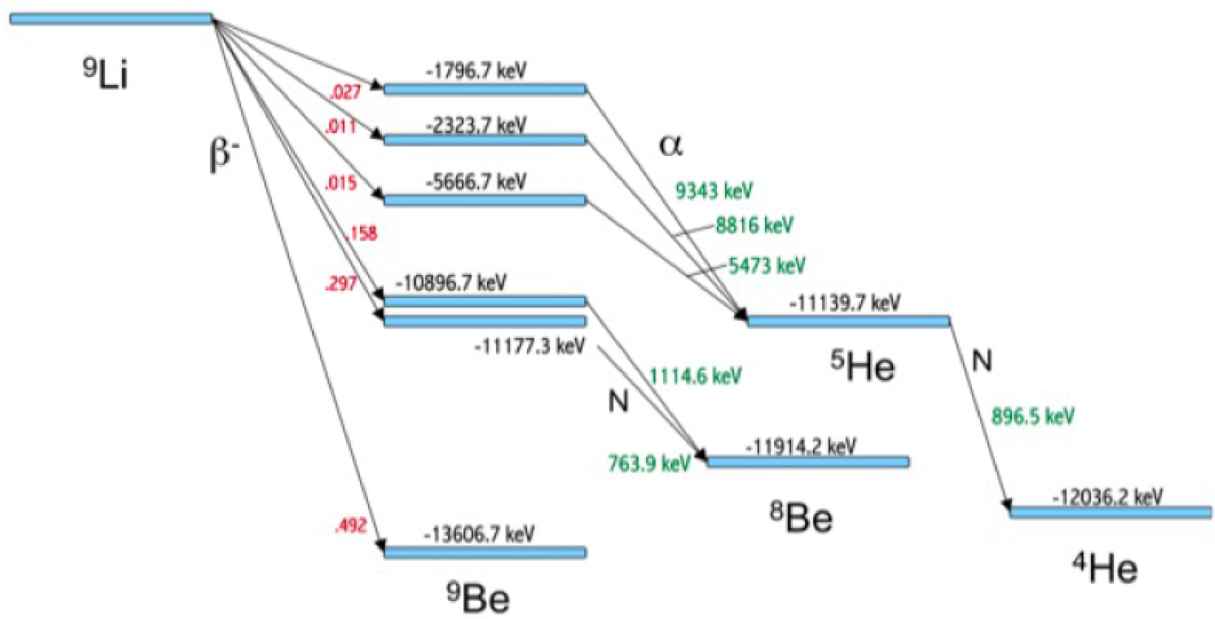

Figure 3.21: Decay scheme for ^{9}Li. The largest decay mode goes to the ground state of ^{9}Be, however the other decay modes go first to excited states of ^{9}Be, which then break up further, producing a ^{8}Be and a neutron or else isotopes of helium and a neutron [185].

the time difference $\Delta t_{\mu\nu} = t_\mu - t_\nu$ (where t_μ is the muon time and t_ν is the inverse β-decay like candidate-pairs) in terms of an exponential shape is performed on three muon energy regions (no correction for energy non-linearities has been applied in the inner detector):

1. $E_\mu^{vis} > 600$ MeV. Showering muons crossing the neutrino target have a high probability in producing cosmogenic isotopes. The fit on $\Delta t_{\mu\nu}$ returns the value of the β-n rate to be 0.95 ± 0.11 events/day.

2. $275 < E_\mu^{vis} < 600$ MeV. Lower energy muons can still cross the gamma catcher and neutrino target and will contribute to cosmogenic isotopes with a rate of 1.08 ± 0.44 events/day for a distance cut of $d_{\mu\nu} < 80$ cm. This distance cut can remove the majority of uncorrelated pairs. The corresponding cut efficiency is determined from the lateral distance profile obtained for $E_\mu^{vis} > 600$ MeV. The approach is validated by a comparative study of cosmic neutrons that show an almost congruent profile with very little dependence on E_μ^{vis} above 275 MeV.

3. $E_\mu^{vis} < 275$ MeV. Low energy muons can only cross the buffer volume and reach the rim of the gamma catcher. No β-n emitters inside neutrino target are found. The fit on $\Delta t_{\mu\nu}$ gives an upper limit of 0.3 events/day with a distance cut of $d_{\mu\nu} < 80$ cm.

The overall rate of correlated backgrounds from β-n emitters is determined to be $2.05^{+0.62}_{-0.52}$ events/day. The result from inner veto muon tracking is consistent within the uncertainty.

Cosmogenic ^{12}B events have a lifetime of 29 ms. The primary decay mode (97%) where a 13.4 MeV β^- is released, overlaps the energy ranges of both prompt and delayed events [186]. Therefore, it may be coincidentally correlated with its parent muon, a neutron, or another ^{12}B as a prompt or delayed event. A decay scheme diagram for ^{12}B is shown in Fig. 3.22. The background associated with ^{12}B is relatively small and can be efficiently removed from the data set used for ^{9}Li analysis by imposing a maximum distance cut of 90 cm between the prompt and delayed events, only introducing a 1% inefficiency. The production rate of ^{12}B from muon capture on ^{12}C and the β-decay spectrum is well known so that ^{12}B can be used as a gauge for studying the ^{9}Li rate.

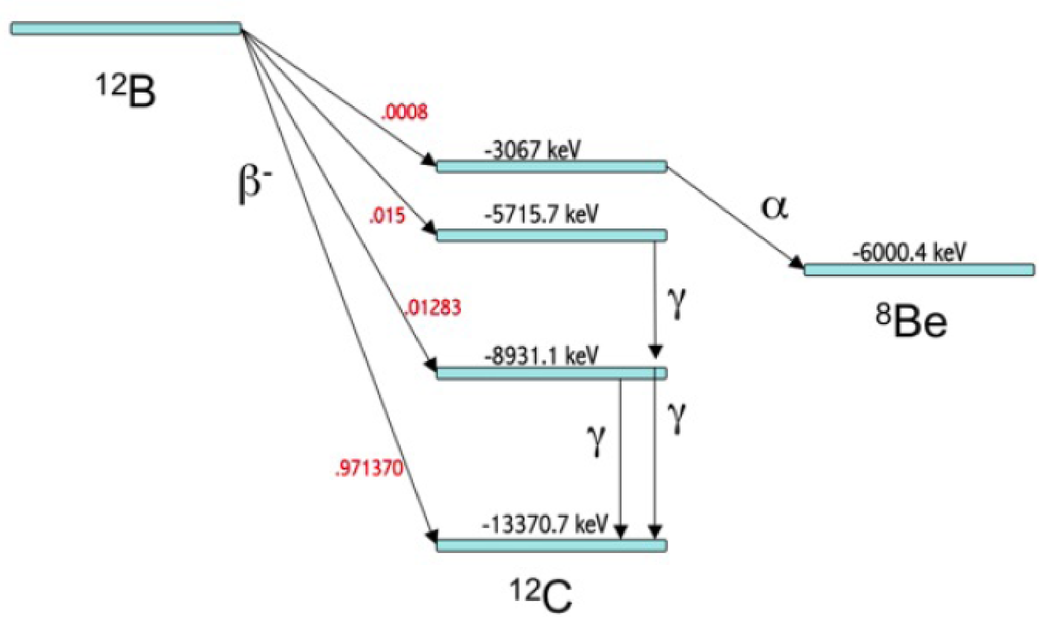

Figure 3.22: β-decay scheme for ^{12}B. Over 97% of the time, ^{12}B goes to the ground state of ^{12}C by emitting a β^- with a Q value of 13.4 MeV [187].

A vetoing time of 0.5 s has been applied to the data after a showering muon over 600 MeV to partially reduce the correlation between the cosmogenic isotopes and their parent muons. The overall exposure time is therefore reduced by approximately 5%. However, it also results in 0.89 ± 0.10 events/day reduction in the β-n background. The residual cosmogenic isotope background rate is 1.25 ± 0.54 events/day. The prompt β spectrum of correlations between β-n emitters and their parent muons in the data is shown in Fig. 3.23. Random coincidental backgrounds have been statistically taken out. The selections have been applied for $E_\mu > 620$ MeV; the distance between prompt and delayed events is $\Delta r_{\mu\nu} < 0.7$ m and the time difference is $\Delta t_{\mu\nu} < 600$ ms.

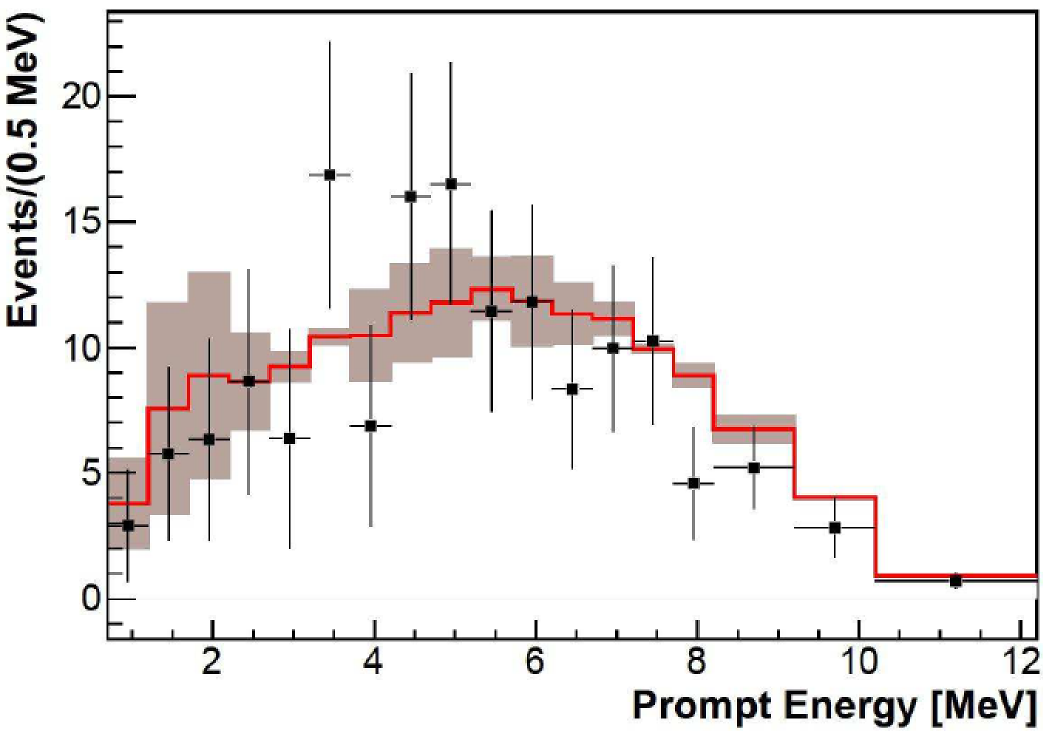

Figure 3.23: The prompt β spectrum of the β-n emitters ^{8}He and ^{9}Li from data (black squares) and MC (red line), assuming ^{9}Li is the dominant contribution [162].

3.7.2.2 Fast Neutrons and Stopping Muons

The cosmogenic muon-induced events can be reduced by the 1 ms veto time after each tagged muon. However, the muons missing the detector or the low energy muons escaping the muon tagging may also contribute to the backgrounds. Two such contributors have been found to be fast neutrons and stopping muons.

Fast neutrons are created when cosmogenic muons interact with the materials inside or surrounding the detector. Since the 1 ms veto time effectively vetos the fast neutrons created inside the detector, the primary background source is the fast neutrons coming from outside the detector. The long interaction length allows fast neutrons to enter all the way into the inner detector, with recoil protons as prompt signals, and are captured right after by gadolinium as delayed signals. There is no way to distinguish fast neutron background from the neutrino signal since the time and spatial correlation is similar to the inverse β-decay events. A flat prompt energy distribution is expected; however, a small slope could be seen due to non-linearity effects from the scintillator.

Stopping muons events mostly concentrate at the top of the inner detector around the chimney. The energy released from the short travelling path mimics the prompt event and the Michel electron mimics the delayed event. The Michel electrons with an energy range of 0.511 to 52.8 MeV overlap with both the prompt and delayed energy regions. The time differences from prompt to delayed events have a 2.2 μs muon lifetime.

Two backgrounds can be distinguished by their correlated times. By studying the energy region from 12 MeV to 30 MeV for the reason of eliminating the inverse β-decay events, two backgrounds can be obtained with high purity. With $\Delta t > 10$ μs, a $97^{+3}_{-8}\%$ pure sample of fast neutrons can be obtained, while by requiring $\Delta t < 10$ μs, a $88 \pm 7\%$ pure sample of stopping muons can be obtained. A flat continuum has been observed for fast neutrons and stopping muons backgrounds in the energy region of 12 to 30 MeV which verified our expectation and can be directly extrapolated to the inverse β-decay region. The estimate of the background rate from fast neutrons and stopping muons is approximately 0.75 events/day.

The inner veto and outer veto can provide an independent cross check on the extrapolated result. The inner veto trigger readout with any inner detector trigger and its low threshold of about 1 MeV give it the ability to detect recoiled protons and H-captured neutrons. The inner veto tagging efficiency is $33 \pm 5\%$ with low accidental tagging. The inner veto can effectively tag on fast neutrons, while the outer veto muon tracking system is more sensitive to stopping muons. $41 \pm 23\%$ of the fast neutrons and stopping muons candidates in the energy region of 12 to 30 MeV are tagged by the outer veto, of which $74 \pm 12\%$ are stopping muons. The accidental rate of outer veto tagging is 0.06%.

The analyses of fast neutrons and stopping muons have been performed using different combinations of inner veto and outer veto tagging. Fast neutrons inner veto-tagging of prompt events and outer veto-vetoing were applied for the inverse β-decay selection. Two sources of background on the tagged fast neutrons have been identified and the associated backgrounds were rejected.

1. Natural radioactivity in the inner veto accidentally coincides with a genuine inverse β-decay event. By imposing a time correlation of energy depositions in the inner detector and inner veto, it was reduced to 12%.

2. Compton scattering in the inner detector and inner veto accidentally coincides with a gadolinium capture. By imposing a spatial cut of prompt and delayed events in the inner detector, it was reduced to 2%.

The background of the inner veto-tagged fast neutrons sample was measured in an off-time window to be 14% and can be directly subtracted. The remaining 86% are pure fast neutrons with a spectrum which is in agreement with the linear expectation with a small positive slope. The total fast neutrons rate was measured to be 0.30 ± 0.14 events/day. A pure sample of stopping muons can be obtained from analyzing their delayed events, Michel electrons, in the energy window from 20 MeV to 60 MeV because no correlation exists between the stopping muons prompt energy and the delayed energy. The stopping muons prompt energy spectrum also agrees with the linear expectation, but with a small negative slope. The total stopping muons rate was measured to be 0.34 ± 0.18 events/day. Since both fast neutrons and stopping muons have linear spectral shapes, the combined analysis was performed to obtain the total rate of 0.67 ± 0.20 events/day, which is shown in Fig. 3.24. Different analysis techniques gave consistent results, including inner veto and outer veto

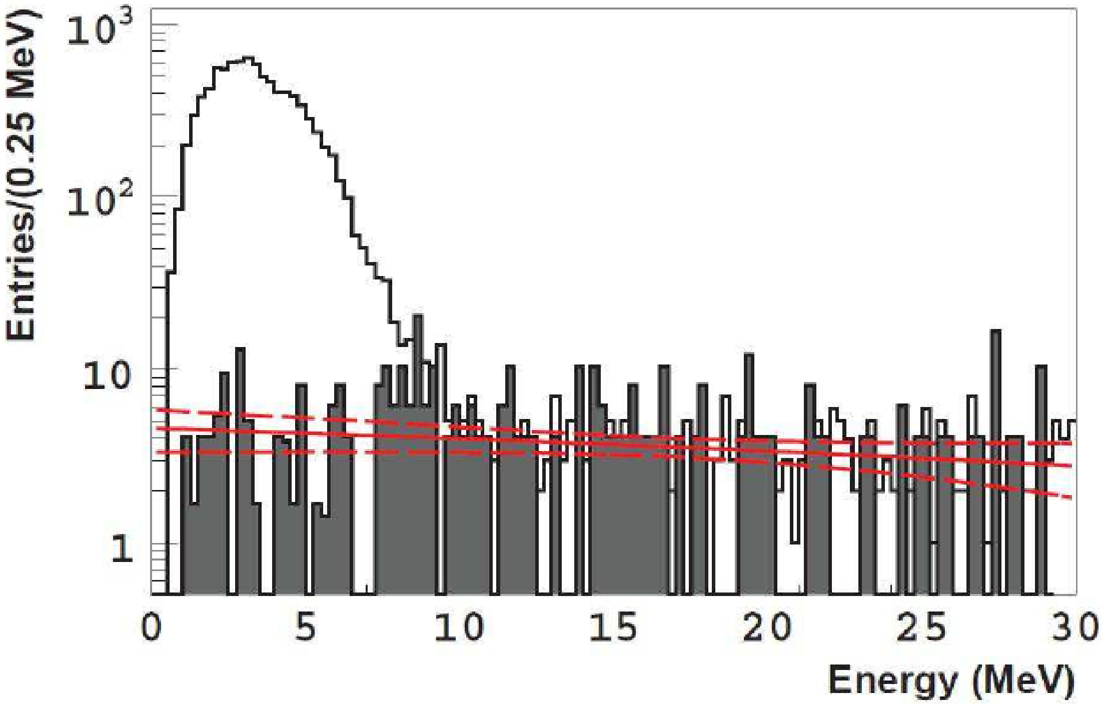

Figure 3.24: Fast neutrons and stopping muons combined spectral model best fit (solid red) with $\pm 1\sigma$ (dashed red), energy distribution of tagged fast neutrons and stopping muons population (gray histogram) and inverse β-decay spectrum [162].

tagging without outer veto-vetoing. It turned out that the outer veto vetoing reduces the correlated backgrounds by 30%.

3.8 Double Chooz Analysis Result

The analysis in the Double Chooz second publication is based on the 227.93 live days data taken between April 13th, 2011 and March 15, 2012, with the far detector only. In order to achieve the best sensitivity, both rate and shape analysis are combined for fitting the oscillation parameter θ_{13}. The event selection criteria were discussed in Section 3.7. High statistics MC samples were generated with necessary corrections, such as detector energy response, to match the detector performance and were compared with the data. The energy spectrum was binned with 18 variably-sized bins between 0.7 and 12.2 MeV. The data was separated into two periods according to the thermal power of the reactors for separating background and signal flux. The signal/background ratio varies as reactor power since the $\bar{\nu}$ flux depends on the thermal power, while the backgrounds are constant in time. The first integration period contains the data with only 20% or less of the nominal thermal power, and the second one has all the other data included. The observed number of signal and background events are predicted for each energy bin following the same integration period division as the data:

$$N_i^{pred} = \sum_{R=1,2}^{Reactors} N_i^{\nu,R} + \sum_{b}^{Bkgd} N_i^b,$$

where the index i runs over the 2×18 bins for two integration periods. The index b runs over three backgrounds of accidental, cosmogenic isotopes (mainly ^{9}Li) and correlated (fast neutrons and stopping muons). The index R denotes the two detectors of Chooz, namely B_1 and B_2. Backgrounds were calculated by the measured rates and the live time in each integration period.

	Reactors both on	One reactor $P_{th} < 20\%$	Total
Livetime (days)	139.27	88.66	227.93
Inverse β-decay candidates (data)	6088	2161	8249
$\bar{\nu}_e$ event from reactor B1	2910.9	774.6	3685.5
$\bar{\nu}_e$ event from reactor B2	3422.4	1331.7	4754.1
Accidentals	36.4	23.1	59.5
Cosmogenic isotope	174.1	110.8	284.9
Correlated fast neutron & stopping muon	93.3	59.4	152.7
Total prediction	6637.1	2299.7	8936.8

Table 3.3: Summary of observed inverse β-decay candidates, with corresponding signal and background predictions for each integration period assuming no oscillation [162].

Table 3.3 lists the predicted inverse β-decay and background events number for the null-oscillation hypothesis. The correlations between energy bins used the technique of error propagation where the systematic and statistical uncertainties are propagated through a covariance matrix M_{ij},

$$M_{ij} = M_{ij}^{sig} + M_{ij}^{det} + M_{ij}^{stat} + M_{ij}^{eff} + \sum_{b}^{Bkgd} M_{ij}^b. \tag{3.4}$$

In each term on the right hand side of Eq. (3.4), the matrix $M^A_{ij} = cov(N_i^{pred}, N_j^{pred})_A$ is the covariance of N_i^{pred} and N_j^{pred} due to uncertainty A. Table 3.4 shows all the uncertainties associated with each source. Some of the uncertainties only float entries from one energy bin to others without overall normalization correction. The M_{ij}^{sig} is predicted by the knowledge of the energy spectrum of the inverse β-decay prompt events. For the accidental backgrounds, the uncertainties are precisely measureed so that a diagonal covariance matrix is given. The fast neutrons/stopping muons spectrum is allowed to float with a small slope. The energy spectrum for ^{9}Li was obtained from MC simulation. The elements in the covariance matrix contributions vary according to the oscillation and other fit parameters in each step of the χ^2 minimization. The χ^2 function for the two-neutrino oscillation hypothesis is given by:

$$\begin{aligned}\chi^2 &= \sum_{i,j}^{36} \left(N_i - N_i^{pred}\right) \times (M_{ij})^{-1} \left(N_j - N_j^{pred}\right)^T \\ &+ \frac{\left(\epsilon_{FN/SM} - 1\right)^2}{\sigma^2_{FN/SM}} + \frac{\left(\epsilon_{Li\text{-}9} - 1\right)^2}{\sigma^2_{Li\text{-}9}} + \frac{\left(\alpha_E - 1\right)^2}{\sigma^2_{\alpha_E}} + \frac{\left(\Delta m^2_{31} - \Delta m^2_{31,MINOS}\right)^2}{\sigma^2_{MINOS}}. \qquad (3.5)\end{aligned}$$

Source	Uncertainty [%]
Reactor flux	1.67%
Detector response	0.32%
Statistics	1.06%
Efficiency	0.95%
Cosmogenic isotope background	1.38%
Fast neutron/Stopping muon	0.51%
Accidental background	0.01%
Total	2.66%

Table 3.4: Summary of signal and background normalization uncertainties in the analysis relative to the total prediction [162].

The scales of the two backgrounds (^{9}Li, fast neutron and stopping muon) are allowed to vary, as seen in Eq. (3.5). The quantity $\sigma_{\alpha_E} = 1.13\%$ denotes the uncertainty in allowing the energy scale for the predicted signal and ^{9}Li events to vary. Since the uncertainty of the accidental rate is precisely measured, it is fixed during the minimization. The advantage of this technique for using energy information is that one can get some background knowledge from the fit, especially in the bins between 8 and 12 MeV containing only a few inverse β-decay events. The constraints of the mass splitting term Δm^2_{31} use the MINOS result [105] where the error has been symmetrized.

Using the MINOS Δm^2_{31} value as a contraint for θ_{13}, the best-fit gives $\sin^2 2\theta_{13} = 0.109 \pm 0.030$ (stat.) $\pm\, 0.025$ (syst.) at $\Delta m^2_{31} = 2.32 \times 10^{-3}$ eV^2, with a $\chi^2/NDF = 42.1/35$. The fit using both Δm^2_{31} and θ_{13} as free parameters with Δm^2_{31} constrained to be < 0.01 gives the result of $\Delta m^2_{31} = 2.7 \pm 1.9 \times 10^{-3}$ eV^2 and $\sin^2 2\theta_{13} = 0.093 \pm 0.078$ which are both consistent with Δm^2_{31} from MINOS and our best-fit θ_{13} with Δm^2_{31} constrained by the MINOS result.

Table 3.5 summarizes the starting values and best-fit results of the fit parameters and their uncertainties. The measured energy spectrum and the best-fit spectrum are shown in Fig. 3.25. The rate-only analysis generates a best-fit value of $\sin^2 2\theta_{13} = 0.170 \pm 0.052$ with the $\chi^2/NDF = 0.50$. The compatibility probability is 30% for the rate-only and rate+shape analyses, which depends on the way the correlated errors are handled. The analysis result for using only data in the first Double Chooz publication [102] (April 13, 2011 to September 18, 2011) and data taken since (September 18, 2011 to March 15, 2012) are compared. Using only one integration period technique, the best-fit value for the data in the first publication is $\sin^2 2\theta_{13} = 0.0744 \pm 0.046$ with $\chi^2/NDF = 18.3/17$, while the best-fit value for the data taken since the first publication is $\sin^2 2\theta_{13} = 0.143 \pm 0.043$ with $\chi^2/NDF = 9.54/17$.

Fit parameter	Initial value	Best-fit value
^{9}Li background $\epsilon_{Li\text{-}9}$	(1.25 ± 0.54) d^{-1}	(1.00 ± 0.29) d^{-1}
FN/SM background $\epsilon_{FN/SM}$	(0.67 ± 0.20) d^{-1}	(0.64 ± 0.13) d^{-1}
Energy scale α_E	1.000 ± 0.011	0.986 ± 0.007
$\Delta m^2_{31}(10^{-3}$ eV$^2)$	2.32 ± 0.12	2.32 ± 0.12

Table 3.5: Parameters in the oscillation fit. The initial values are determined by measurements of background rates or detector calibration data. The best-fit values are outputs of the minimization procedure [162].

The total number of antineutrino events collected is 7751.9 (excluding all the backgrounds), which is 91.85% of the total expected rate in the absence of oscillations. A

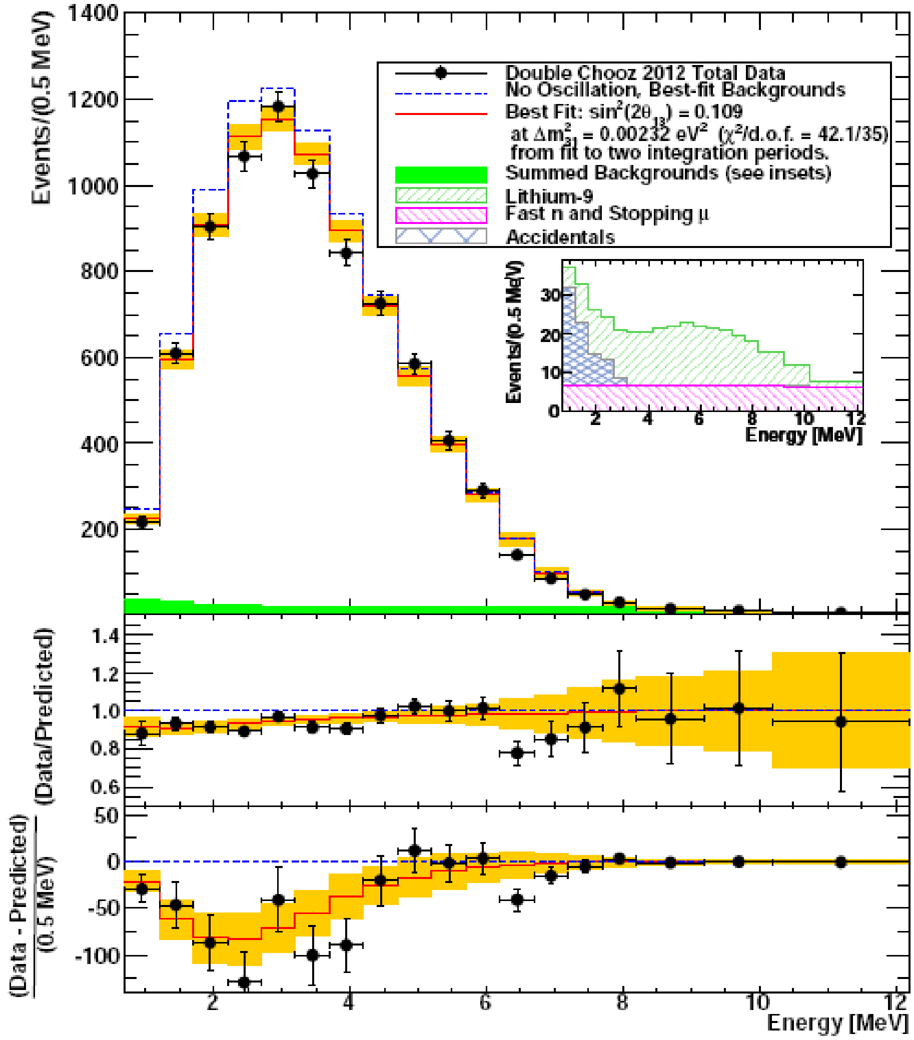

Figure 3.25: Measured prompt energy spectrum for both integration periods (data points) superimposed on the expected prompt energy spectrum, including backgrounds (green region), for the no-oscillation (blue dotted curve) and best-fit (red solid curve) at $\sin^2 2\theta_{13} = 0.109$ and $\Delta m^2_{31} = 2.32 \times 10^{-3}$ eV^2. Inset: stacked spectra of backgrounds. Bottom: differences between data and no-oscillation prediction (data points), and differences between best fit prediction and no-oscillation prediction (red curve). The orange band represents the systematic uncertainties on the best-fit prediction [162].

further-reduced background/signal rate sample was prepared at the sacrifice of the total livetime, in order to cross-check our analysis result. The best-fit of this sample gives $\sin^2 2\theta_{13} = 0.109 \pm 0.044$ and $\Delta m^2_{31} = 2.32 \times 10^{-3}$ eV^2, which is in good agreement with the standard analysis.

The Feldman and Cousins frequentist method has been adopted to evaluate the confidence

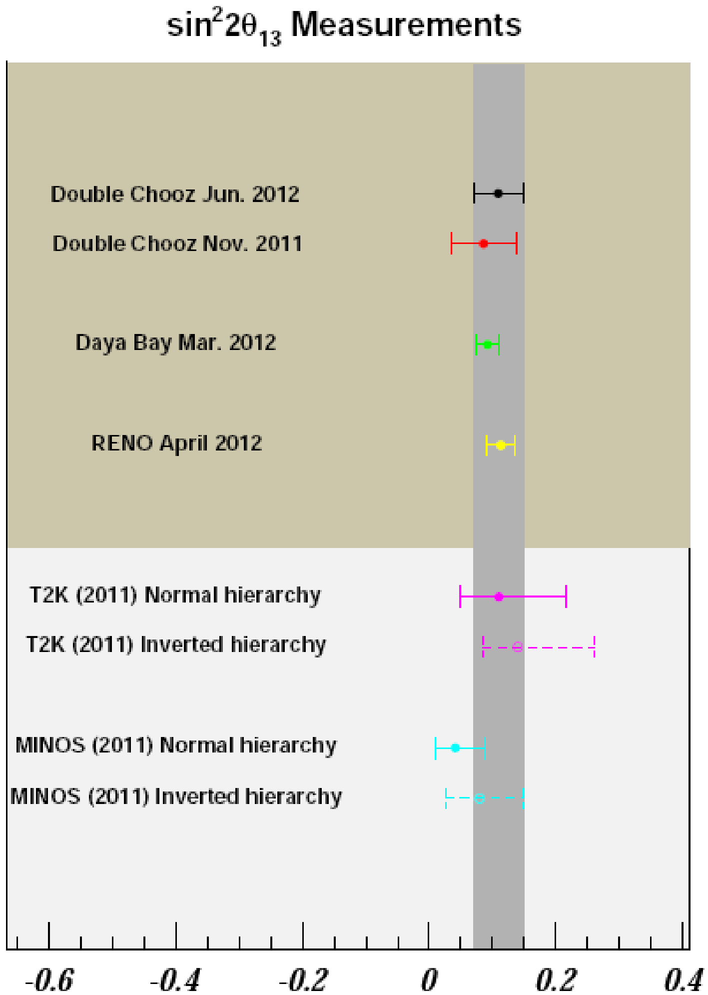

Figure 3.26: Comparison of recent reactor- and accelerator-based measurements of $\sin^2 2\theta_{13}$ from the first and second Double Chooz publication [102] [162], Daya Bay [103], RENO [104], T2K [121], and MINOS [188]. The error bars correspond to 1σ. For T2K and MINOS the CP phase δ has been fixed to $\delta = 0$.

intervals for the θ_{13} mixing angle [189]. 10,000 simulated experiments were generated at 21 test points in the range $0 \leq \sin^2 2\theta_{13} \leq 0.25$. The $\Delta\chi^2$ gives the 68% (90%) confidence level of 0.067 (0.043) $< \sin^2 2\theta_{13} <$ 0.15 (0.18). The no-oscillation hypothesis is excluded at 99.8% (2.9σ).

Chapter 4

Laser Calibration System

4.1 Introduction

Calibrations play a key role in attaining the designed θ_{13} sensitivity in the Double Chooz experiment by making the two detectors as identical as possible. Even for the current phase when only one detector is running, the PMT charges and times need to be precisely calibrated in order to reach a high precision result. The University of Alabama group is responsible for the development of the laser calibration system, operation and data analysis. The laser system consists of the laser light source, the laser-spool, the weight interface and the diffuser. Two types of lasers are used: a UV laser with a wavelength of 375 nm is mainly responsible for the PMT gains and charge likelihoods calibrations, while a blue laser of 470 nm wavelength is used in calibrating the PMT time offsets.

This chapter describes the laser system in some detail. The data analysis, including extracting calibration constants of the inner detector PMT gains, time offsets, and charge likelihoods, will be discussed in Chapters 5, 6, and 7, respectively.

4.2 Hardware Overview

4.2.1 Laser Heads

The two PicoQuant lasers LDH-P-C 470 and LDH-P-C 375 (Fig. 4.1) are picosecond pulsed diode laser heads which deliver 0.3 mW at low power level (narrow pulse) and 1 mW at high power level (wide pulse) of average output power. The 470 and 375 nm laser heads can emit light pulses as short as 70 and 50 ps FWHM respectively, at repetition rates ranging from single shot up to 40 MHz. The $\lambda = 470$ nm laser does not excite the Double Chooz scintillator as indicated by Fig. 4.2, and therefore the short pulse capability is ideal for PMT timing measurements. On the other hand, the $\lambda = 375$ nm laser does excite the scintillator and therefore the resulting light patterns should look like regular events in the detector, which makes this laser ideal for studying both charge and time distributions at the PMTs.

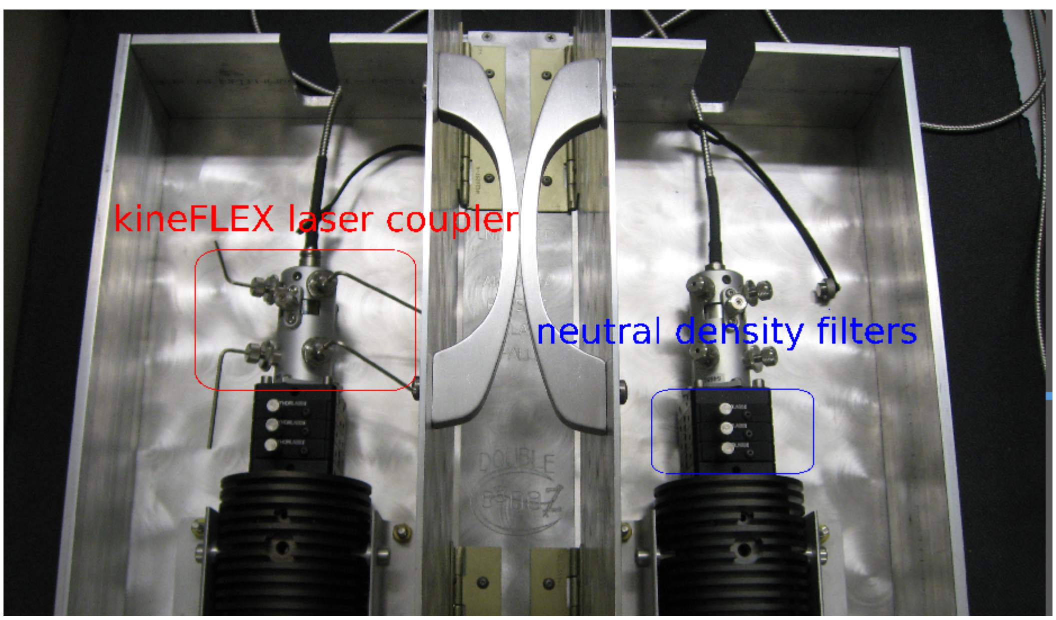

Figure 4.1: The two Double Chooz laser heads in their aluminum enclosure. The alignment screws and neutral density filters holders are shown as marked.

The kineFLEX laser couplers mounted on the laser heads as shown in Fig. 4.1 are high-precision, ultra-stable manipulators for coupling the optical fibers to the laser heads. The $\lambda = 470$ nm laser head is coupled to an SM450 single-mode fiber, while the $\lambda = 375$ nm

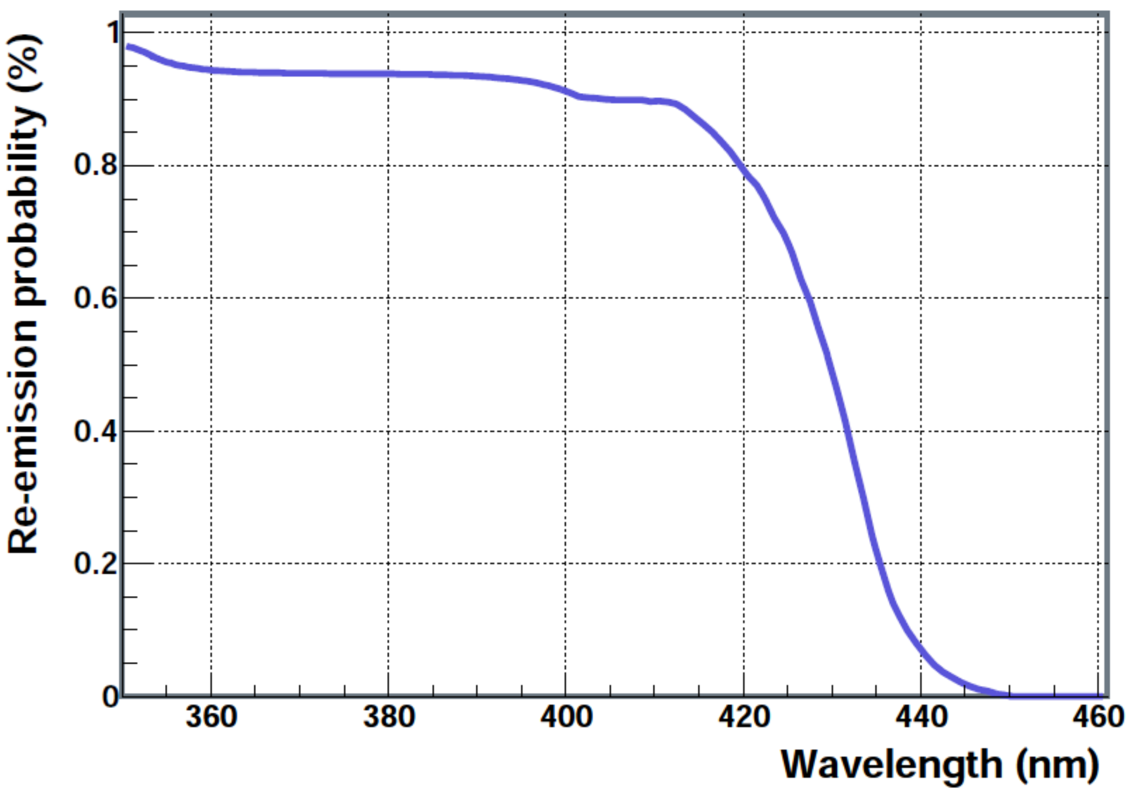

Figure 4.2: Reemission probability for the Double Chooz neutrino target scintillator as a function of the incident wavelength [173].

laser head is coupled to a 200/220/245 HOH (high hydroxyl groups) multi-mode fiber. The alignment of the laser coupler and the fiber affects the maximum light output, which is significant in the charge likelihoods calibration. Alignment was made by tuning the four screws (as labeled in Fig. 4.1) to optimize the light output for each of the two lasers. The light output measurement was performed using a Thorlabs PM100D power meter and the results for different laser driver intensities are shown in Fig. 4.3. Once the light output is optimized, the locking mechanisms on the adjustment screws ensure long-term stability.

Neutral density filters (NDF) can be inserted between the laser head and the couplers to reduce the light yield from the lasers and adjust the light level in the detector to the desired intensity. Because the laser intensity affects the width of the laser pulse proportionally, coarse adjustments are performed with combinations of up to three filters from two identical sets, while fine adjustments are achieved using the intensity setting on the laser driver around the

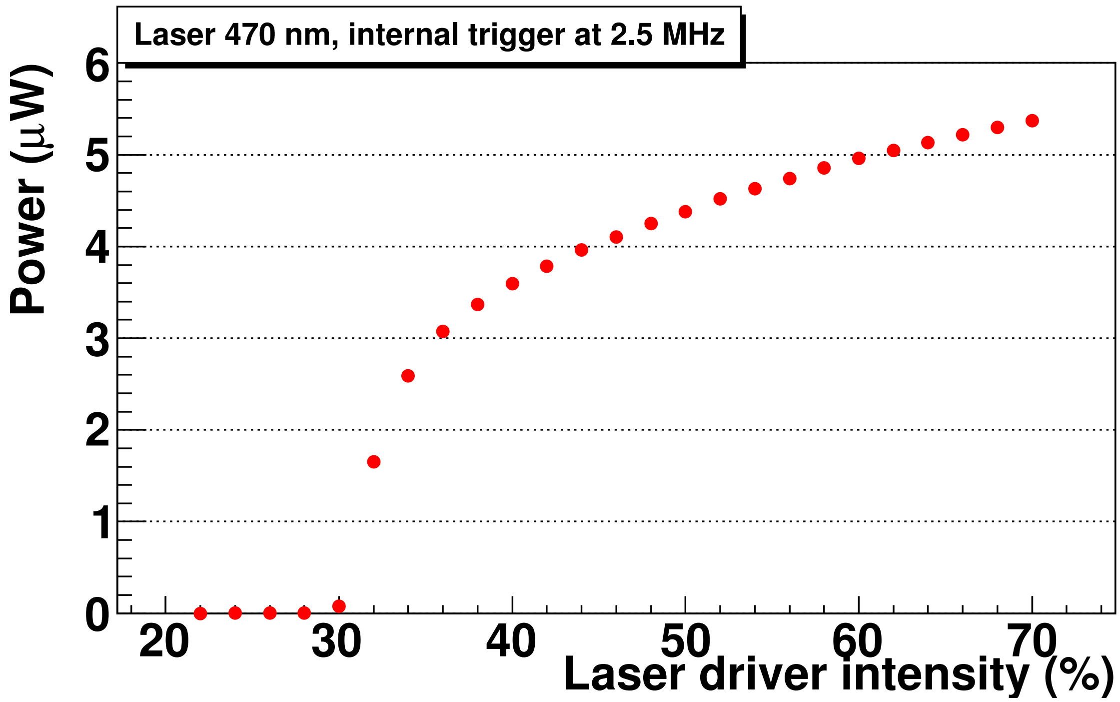

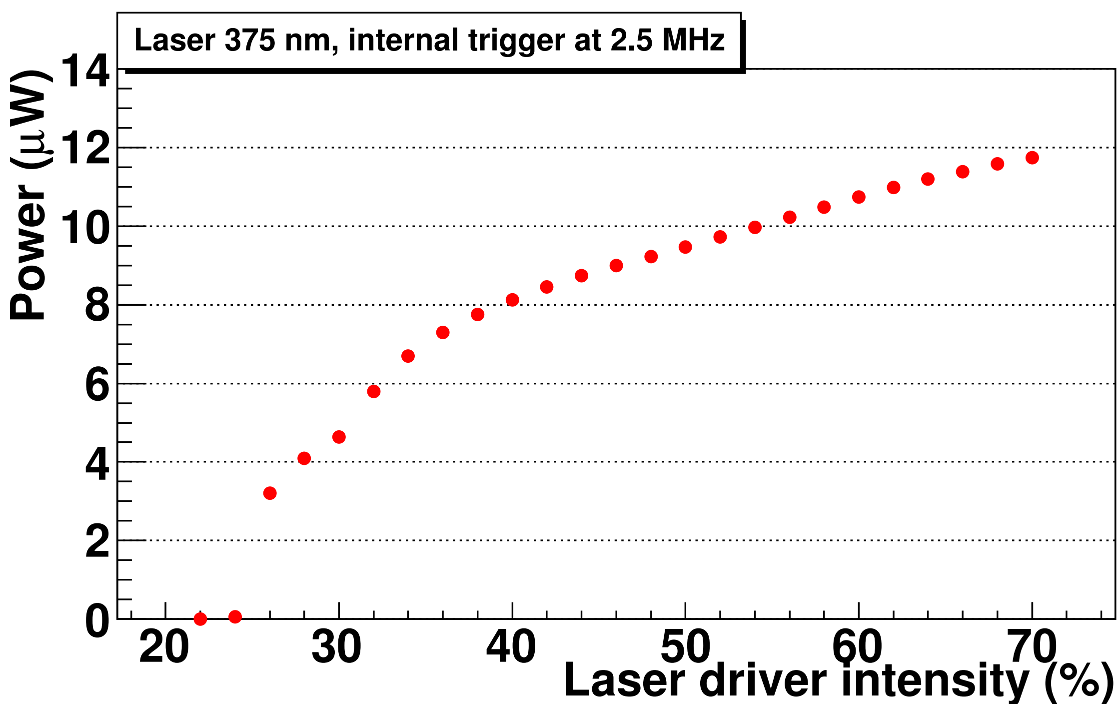

Figure 4.3: Power output of the 470 and 375 nm laser systems as a function of the laser driver intensity after optimal coupler adjustments.

nominal intensity of 40%. The transmission rate (TR) has been measured for both lasers, as shown in Table 4.1. The measurements were obtained by averaging the results from UA's 2-inch R2154 PMT (as described in Section 4.2.3) placed at a distance of 36 cm and the Thorlabs PM100D power meter.

NDF optical density	Theoretical TR %	470 nm TR %	375 nm TR %
0	100.00	100.00	100.00
0.1	79.43	78.34	66.76
0.2	63.10	65.82	48.11
0.3	50.12	52.15	31.81
0.4	39.81	37.51	20.72
0.5	31.62	28.91	13.93
0.6	25.12	23.81	9.68
1	10.00	9.48	1.23
1.3	5.01	5.32	0.80
2	1.00	0.87	0.03
3	0.10	0.06	0.00
4	0.01	0.01	0.00

Table 4.1: Transmission rates for the neutral density filters. The theoretical values are calculated at $\lambda = 470$ nm using the optical density equation: $A_\lambda = -\log_{10}(I_1/I_0)$, where A_λ is the absorbance at a certain wavelength λ, I_0 and I_1 are the laser intensities before and after passing through the neutral density filter. The discrepancy between the measured UV transmission rate and the calculated numbers is due to the fact that the transmission rate is wavelength sensitive.

4.2.2 Laser Driver

The PicoQuant PDL 800-B (Fig. 4.4) is a stand-alone driver for the picosecond pulsed diode lasers with wavelengths ranging from 375 to 1990 nm and dedicated for single wavelength laser heads of the LDH-P/FA Series. The driver allows users to vary the output power of the connected laser head and provides a synchronization signal with each laser pulse. Five discrete frequencies can be selected at 40, 20, 10, 5 and 2.5 MHz from an internal trigger, while an external trigger can provide any rate over the laser frequency range, i.e., up to 40 MHz.

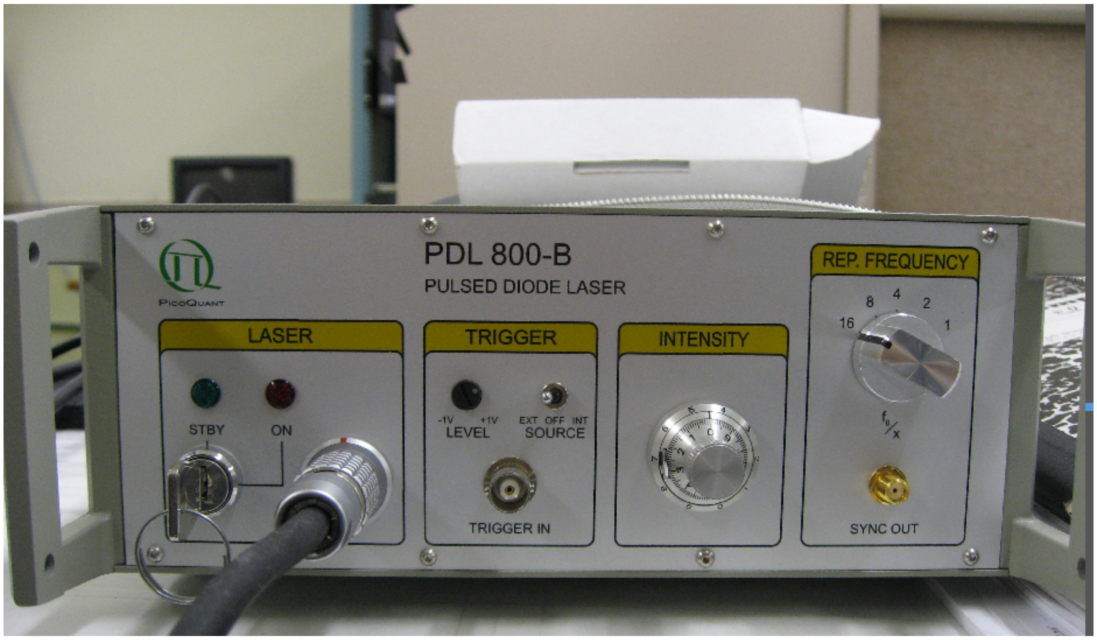

Figure 4.4: The PicoQuant PDL 800-B laser driver.

Our external trigger is supplied by a stand alone digital pulse generator of type USBpulse100, as shown in Fig. 4.5. The USBpulse100 pulse generator is connected to a computer through the USB port and is manipulated by its controlling program. Its output through the BNC connector yields up to 100 MHz and 10 ns resolution pulse generation. A double pulse trigger system can be realized by utilizing a double stack USBpulse100 system connected to an externally powered USB hub.

4.2.3 Dark Box for Isotropy Measurements

A 1.2 m cubic dark box provides a light tight environment for isotropy measurements of the laser diffusers. The dark box contains a 2-inch R2154 PMT [191] and its corresponding data acquisition system [192, 193] from Bridgeport-Instruments [192]. The PMT is attached to a multichannel analyzer system that can control the PMT high-voltage and measure the pulse energy, arrival time, triggering, and perform pulse shape analysis. The multichannel analyzer system is connected to a control computer through a USB cable. A Bridgeport-Instruments modified IGOR-PRO user-interface system [192, 193] takes charge of data readout. The

Figure 4.5: The USBpulse 100 module [190].

PMT and multichannel analyzer system are mounted on a slider piece to a semi-circular track of 49 cm inner radius inside the dark box (Fig. 4.6). The PMT can slide along the track and can be fixed at 5° intervals, while the track can rotate from the outside of the dark box and can be fixed at 5° intervals.

4.2.4 Laser Diffusers

Two issues are essential in the development of the Double Chooz laser calibration system, namely the light output level and the isotropy. For the gains and charge likelihoods calibration, the light output level must range from single PE levels up to about 40 PEs at the PMTs. Highly isotropic light distribution is required for both charge- and time-related calibrations.

The laser diffusers were designed and tested with appropriate materials in order to meet the light intensity and isotropy requirements. The laser diffuser diagram is shown in Fig. 4.7 for the λ=470 nm diffuser. Both the 470 and 375 nm laser diffusers consist of an 80-mm-diameter hollow acrylic sphere and a 53-mm-long neck. The 470 nm laser diffusers have a 4

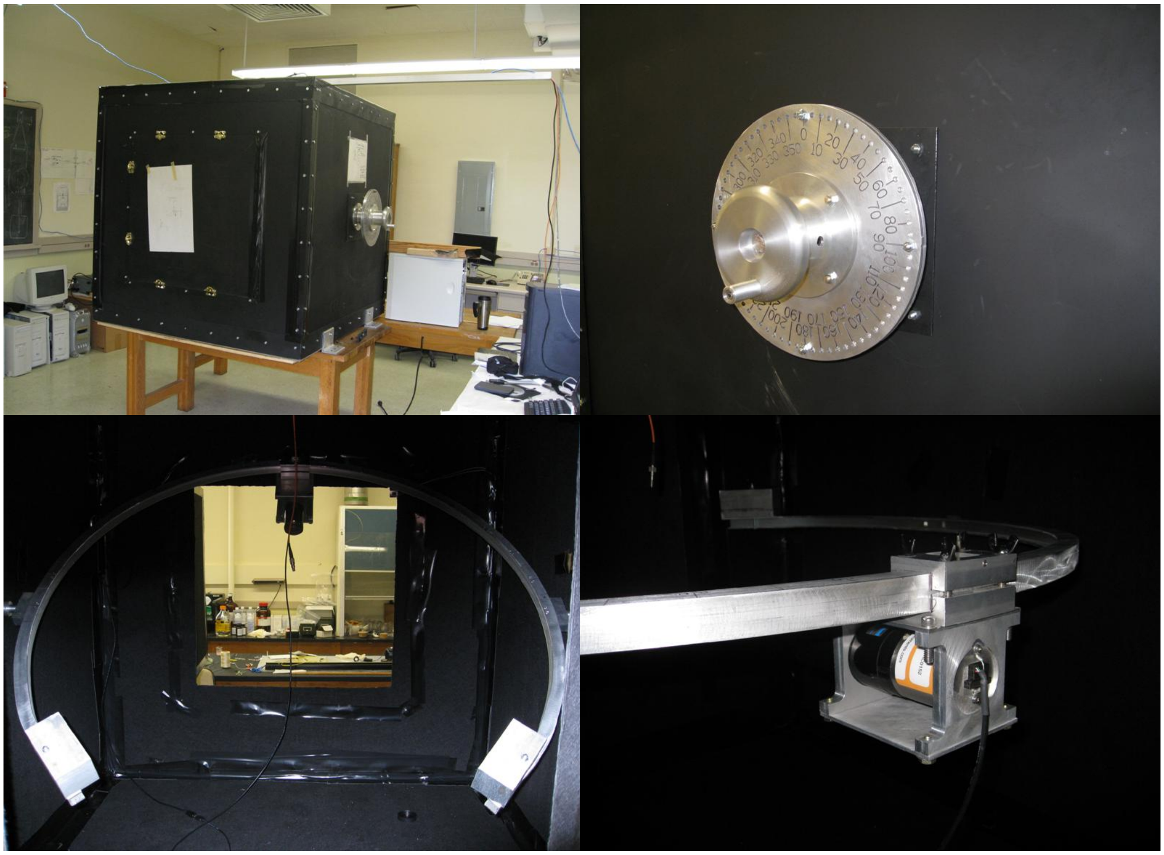

Figure 4.6: The PMT dark box (top left) and its rotation wheel (top right). The rotational track (bottom left) and PMT mount inside the PMT dark box (bottom right).

mm wall thickness, while the 375 nm laser diffusers have a 6 mm wall thickness. The spheres are made up of two threaded hemispheres. Acrifix 2R0190 acrylic cement was applied to the joints before the hemispheres were assembled; this is the same glue which was used in the assembly of all acrylic components in Double Chooz (the neutrino target vessel, gamma catcher vessel and their support structures). The fact that the hemispheres are threaded and glued (as opposed to glued only) lowers the risk of the diffusers coming apart. The top of the laser diffuser has a threaded structure so that the neck can be screwed into the laser sphere. The final 470 nm acrylic diffusers are filled with GE silicone sealant (GE5000) and tipped with optical cement and TiO_2 at ratio of 800:1. The 375 nm acrylic diffusers are filled with Double Chooz target scintillator liquid without the gadolinium loading.

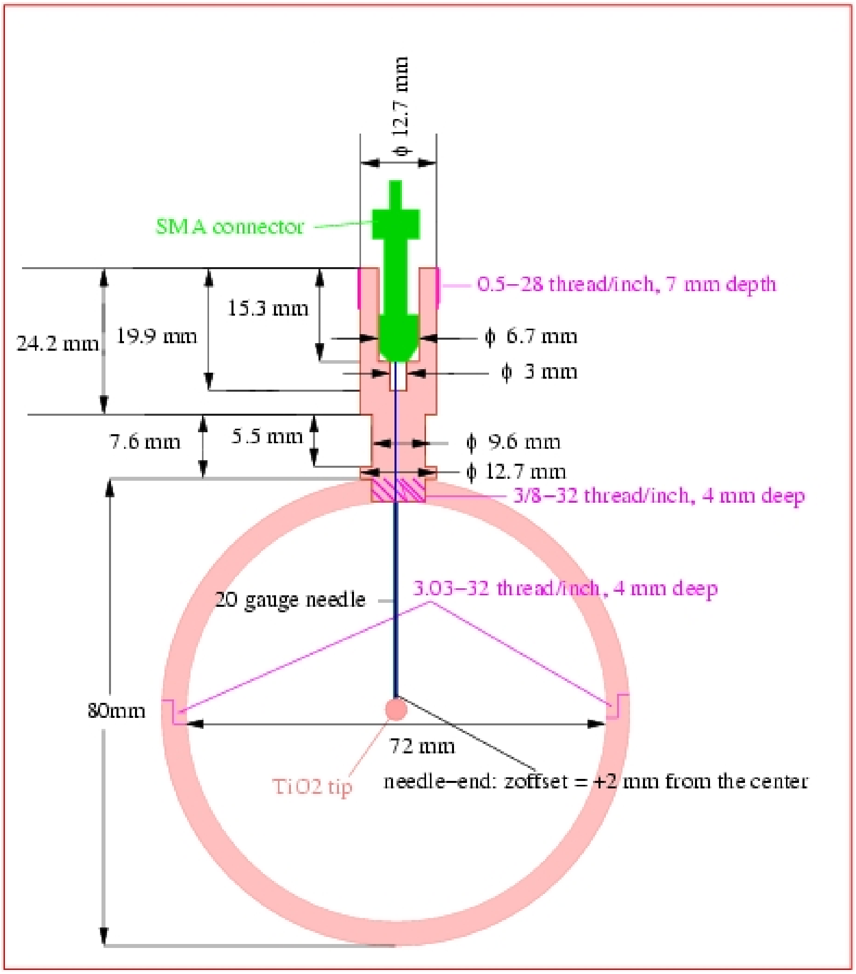

Figure 4.7: The final 470 nm laser diffuser design and cut-out from Ref. [194].

4.2.5 Laboratory Setup

The isotropy test setup includes the laser, the laser coupler, a single mode fiber, two FC-FC adapters, one SMA-SMA adapter, a multimode fiber of 50 microns and the laser diffuser, as illustrated in Fig. 4.8(a). A single mode fiber connects to a FC-FC adapter on top of the dark box. On the other side of the FC-FC adapter inside the dark box, a 0.6 m multimode patch cord fiber is attached. The other end of the fiber has an SMA connector which is connected to the diffuser via an SMA-SMA adapter. The laser diffuser is hung to hooks attached at the top of the dark box via two strings for stable suspension.

The isotropy test data of both the 470 and 375 nm lasers in the so-called standard scan

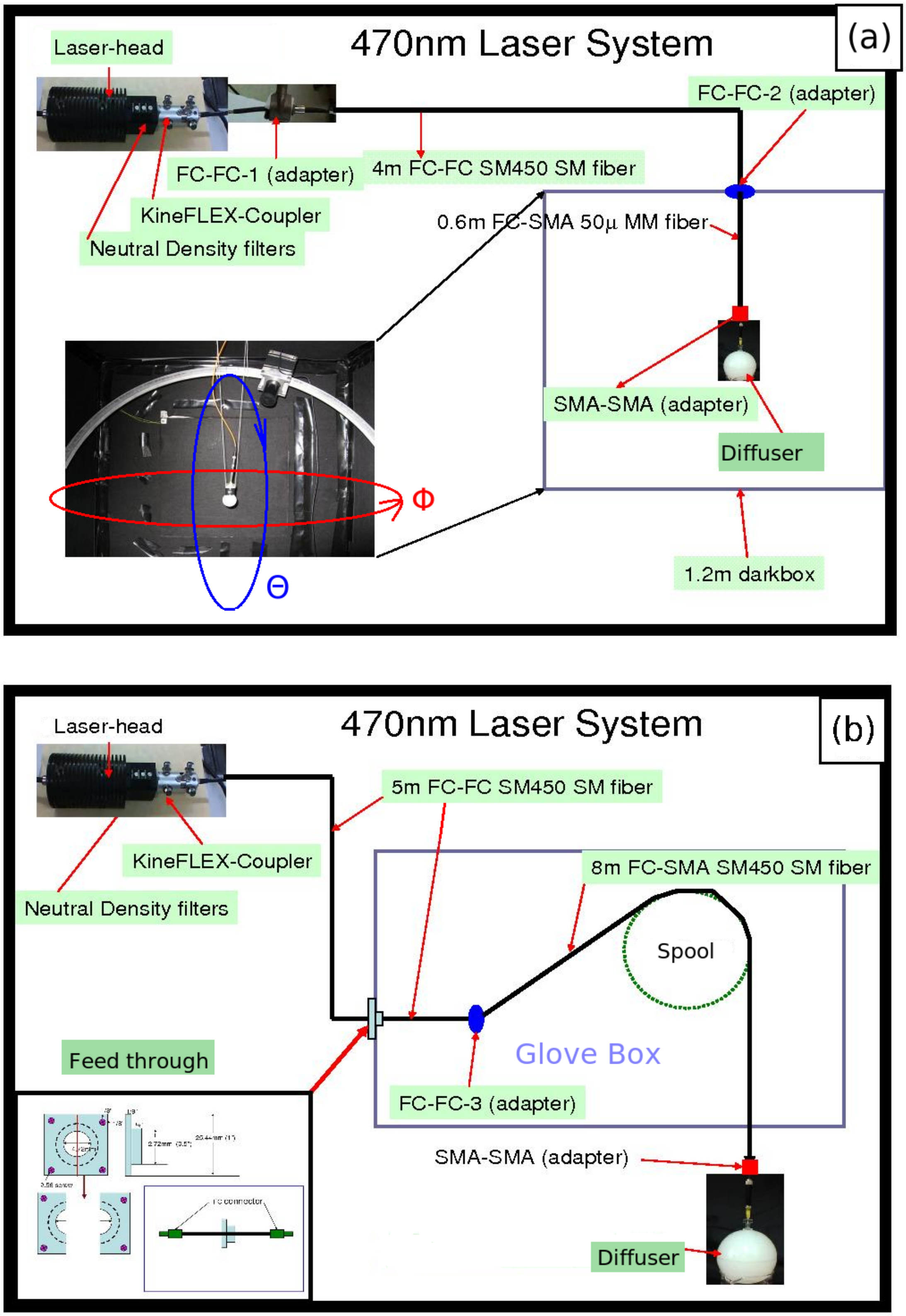

Figure 4.8: The laser system setup for (a) the isotropy test and (b) on-site data taking.

were taken at an interval of 20° on both the horizontal and rotational track. The positions were properly translated into ordinary spherical coordinates, as illustrated in the top panel of Fig. 4.9. By taking out some redundant points and incorporating some extra points, the positions in the full scan distribute more uniformly in the 2-dimensional space, as illustrated in the bottom panel of Fig. 4.9. The standard scan is easy to achieve experimentally, but does not offer a uniform coverage of the phase space. In order to do that, the full scan was carried out each period of time.

The setup for the Double Chooz calibration data-taking is shown Fig. 4.8(b). The major difference to that of the laboratory setup in Fig. 4.8(a) exists inside the glove box where the PMT system is replaced by the laser spool, which helps extend the 5 m FC-FC patch cord with another FC-FC patch cord connected via an FC-FC adapter. In addition, an acrylic weight interface which encloses a 194 g, stainless steel piece (3.81 cm long and 2.54 cm square SS-304) was designed to overcome the buoyancy and keep the optical fibre taut when the entire assembly is submersed in the neutrino target liquid. It also minimizes the neck shadowing and lensing effect of the laser diffuser, which was designed to avoid shadowing of the PMTs on the top of the cylinder while the diffuser is deployed at its lowest position. To avoid any possible contamination, all the materials that will be exposed to the gadolinium-loaded scintillator have been manufactured only of materials approved for compatibility, i.e., acrylic and teflon (which encloses the umbilical cord and optical fiber).

4.3 Blue Laser Diffuser

The blue laser diffusers are filled with GE silicone sealant. The fiber is plugged into the diffuser through the diffuser neck inside a blunt needle. The fiber end is tipped with a mixture of optical cement and TiO_2 with a ratio of 800:1. The threaded-groove hemisphere joints seal the internal materials hermetically. The isotropy study indicated that the effects from the threaded-groove structure were negligible.

Systematic studies about how the diffuser diameter sizes (46, 65 and 80 mm) affect

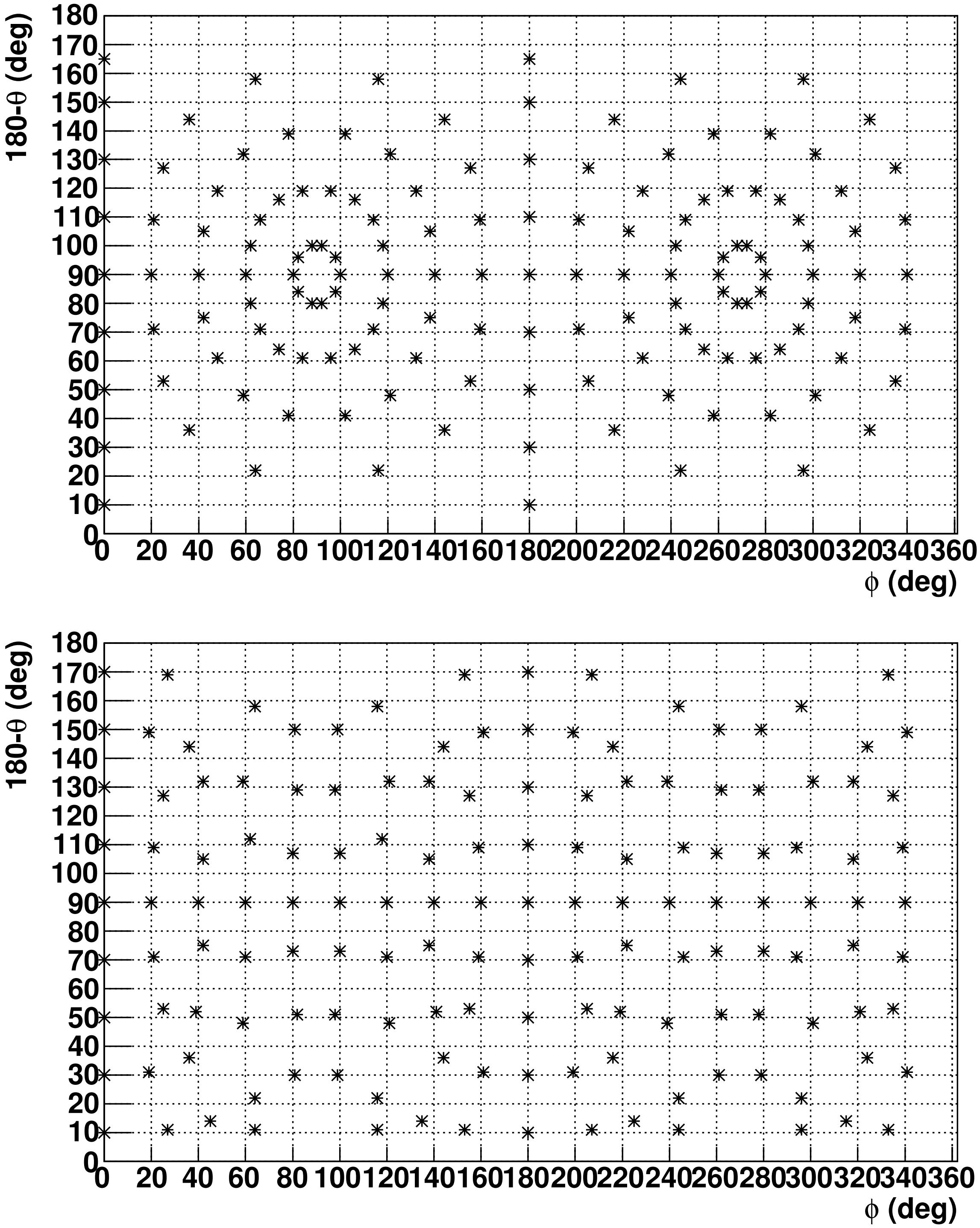

Figure 4.9: Standard PMT scan coordinates system (top) and full PMT scan coordinates system (bottom).

the light isotropy have shown that the isotropy improves with increasing diffuser size, as illustrated in Fig. 4.10. All of the anisotropy measurements were taken using the standard

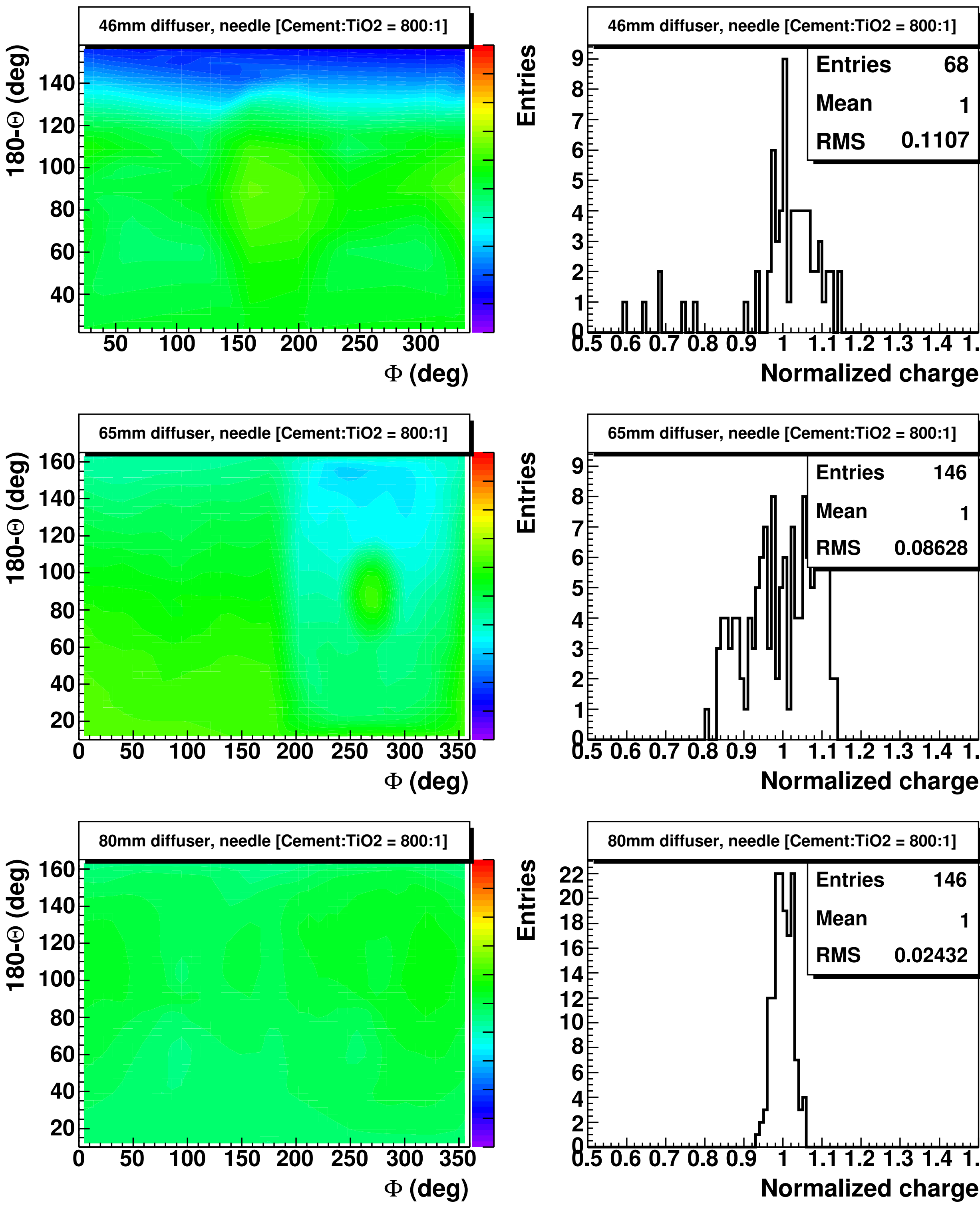

Figure 4.10: Light yield distributions (θ, ϕ) for the corresponding diameter size of 46 (top left), 65 (center left) and 80 (bottom left) mm spheres filled with GE silicone sealant and the fiber end tipped with optical cement and TiO_2 mixture at 800:1 ratio.

scan locations displayed in the top panel of Fig. 4.9, where the PMT locations are not as isotropic as in full scan (shown in the bottom panel of Fig. 4.9). After the test, the result from the standard scan locations is approximately 17% underestimated compared to that from the full scan PMT locations. It does not affect the final result much. The laser diffuser is to be deployed through the chimney which has an inner diameter of 97 mm at the smallest part. As a precaution, any contact between the diffuser and the chimney should be avoided; therefore, the design of the diffusers was finalized with a diameter of 80 mm. The anisotropy of the final design is less than 3%.

Performance stability is significantly important because there was a long time delay from when the diffusers were made to their deployment. The time evolution of a particular diffuser's anisotropy is shown in Fig. 4.11. From this plot we conclude that the anisotropy of this sphere remains approximately constant at an RMS of 2.5%. The variations can be attributed to small variations in the position where the laser diffuser was attached in the dark box. The average light yield measured by the 2-inch PMT is also illustrated in Fig. 4.11. A variation RMS of 8.7% from the light yield was due to the external contaminant of the connectors (dirt on the fiber core open surface). The data indicate that the laser diffuser isotropy does not change with respect to time.

4.4 UV Laser Diffuser

The UV laser diffusers are filled with the Double Chooz scintillator without gadolinium loading. For the test performed at the University of Alabama, the scintillator was manufactured following the same chemical compositions that was used in the Double Chooz experiment as obtained from the MPIK Heidelberg (which developed the original scintillator) [195]. The ingredients, PXE, dodecane and fluor mixture, were obtained from the Dixie Corporation of Texas, the UA KamLAND group, and the RPI Corporation, respectively. They were mixed in a 1000 ml beaker with an electric mixing propeller stirring for 12 hours. The liquid mixture consists of dodecane and PXE in the ratio of 80:20. The n-dodecane reduces the

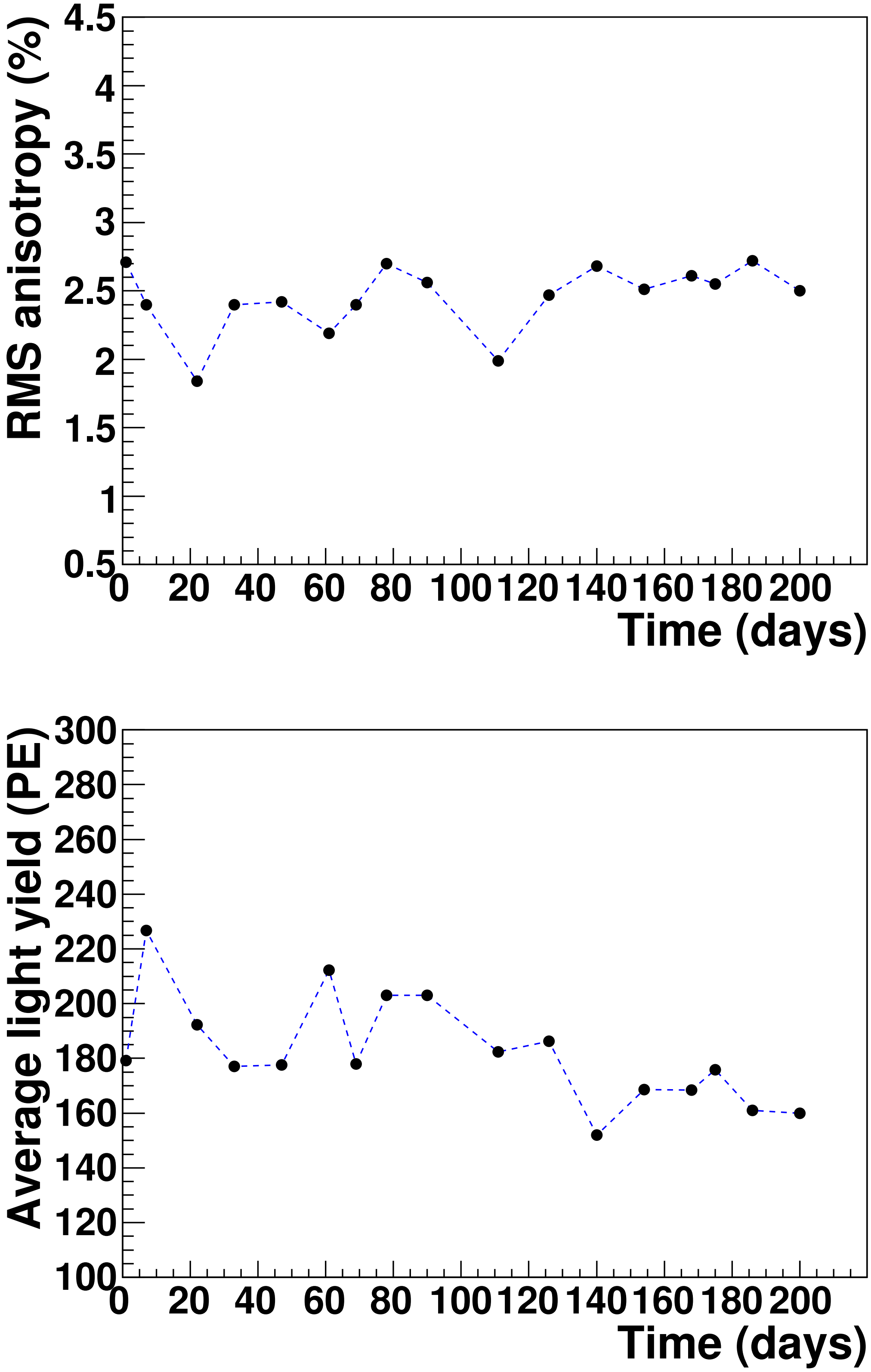

Figure 4.11: The RMS anisotropy (top) and measured light yield (bottom) for the 80 mm acrylic 470 nm laser diffuser as a function of time.

light yield but has better material compatibility with acrylics. The fluor in the mixture is composed of PPO (0.007 g/cm^3) and bis-MSB (20×10^{-6} g/cm^3). The liquid mixture was sealed into the UV laser diffusers and ready for the isotropy test. The UV diffusers used for the actual deployment in Double Chooz were assembled on site, using target scintillator provided by the MPIK Heidelberg group identical to that used in Double Chooz (except for the gadolinium loading). The setup of the UV test is the same as that for the $\lambda = 470$ nm laser diffuser as shown in Fig. 4.8 (a) but only with the 470 nm laser head, coupler and blue laser diffuser replaced by the 375 nm laser head, its corresponding coupler, and the UV laser diffuser.

4.4.1 Isotropy

Our initial isotropy test started using our own liquid scintillator mixture. In order to verify the photons conversion position, we used the following configurations where the connector neck fiber-end was offset by 10, 6, 4, and 1.4 mm from the center of the sphere. We also prepared a connector neck fiber-end tipped with the mixture of optical cement and TiO_2 at the ratio of 800:1 with a z offset of 4 mm for this test. The tests were done for all the configurations with and without the weight interface in order to demonstrate that the weight interface does not generate any unexpected shadowing, as shown in Fig. 4.12.

The results from these configurations are shown in Figs. 4.13 and 4.14. The plot in Fig. 4.15 summarizes the tests, showing that the isotropy improves with smaller value for the z offset. At z offset of 10, 6, and 4 mm, there are four data points that were taken at different times, which shows that these distributions are consistent with respect to time.

4.4.2 Screw-In/Threaded Sphere

With all above results, we turned to our final Double Chooz laser diffuser design with threaded hemispheres joints (Fig. 4.16). We decided to use a threaded design in order to make sure that the hemisphere joints are hermetically sealed. This laser diffuser was filled with the Double Chooz liquid scintillator obtained from C. Buck (MPIK) [195]. The

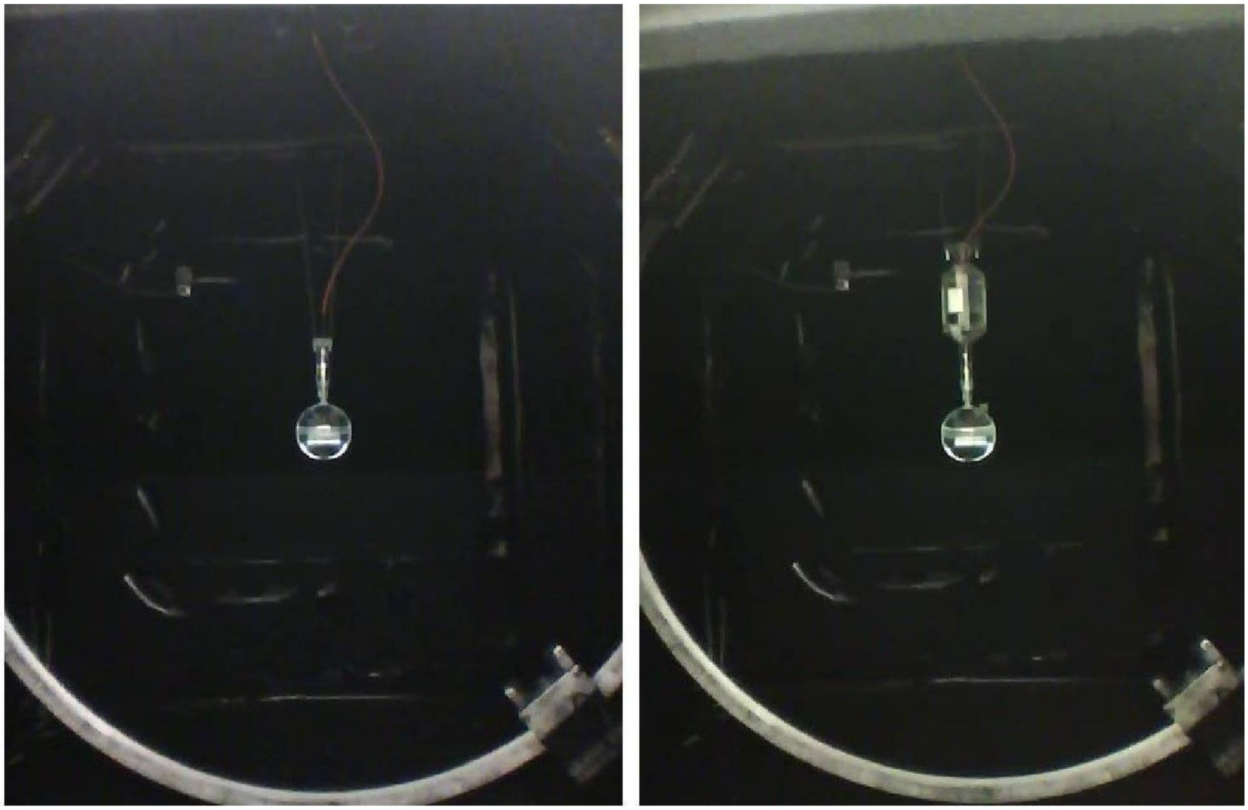

Figure 4.12: The UV isotropy configuration with (right) and without (left) the weight interface. The weight interface consists of a 6.35 cm diameter and 11.43 cm long tapered cylinder with an embedded SS-304 stainless steel piece and a 6.99 cm neck.

configurations of z offset at 5.8, 4.0, 3.0, 1.6, 1.0, 0.6 and 0.0 mm were tested. The results showed that there is no significant difference in the anisotropy RMS values and distribution structures between the screw-in and the glue-on sphere. The lowest anisotropy RMS value of 7.9% was also obtained when there was no z offset. In order to get a better isotropy, we also tested configurations with a tip of optical cement and TiO_2 at ratio of 880:1 and 750:1 with z offset at 2.3 and 1.6 mm. The results indicated that TiO_2 decreased the anisotropy from an RMS of 7.9 % (no tip) to about 6.6 %. We repeated the configuration of z offset at 0.0 mm and the tip at ratio of 750:1 with two different neck connectors and also with a new threaded sphere. The new threaded sphere had more glue in the joint region which increased the transmission of light from the liquid scintillator. The results are summarized in Fig. 4.17.

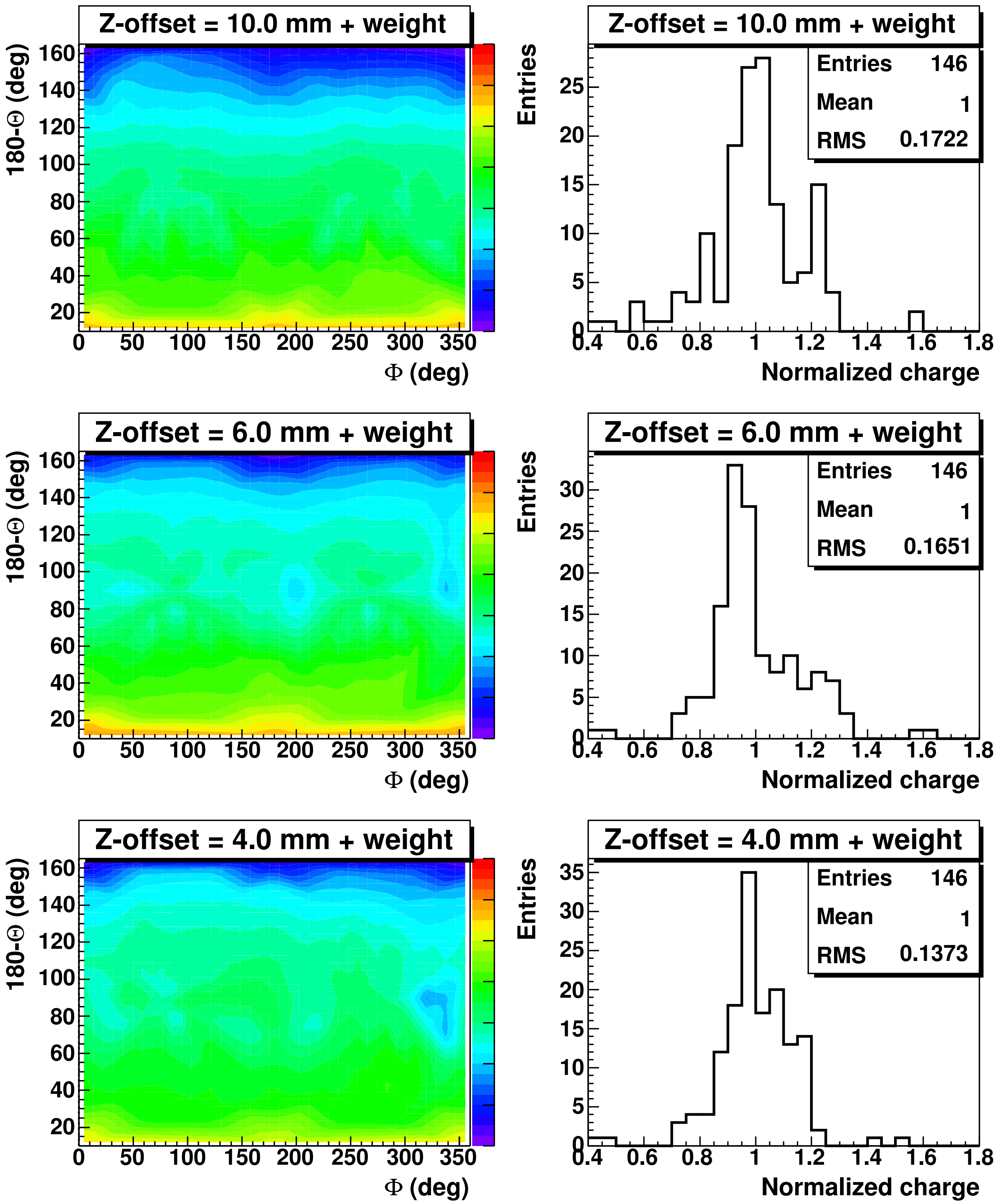

Figure 4.13: Left: light distributions in (θ, ϕ) associated with the 80 mm glue-on spheres (attached to a weight interface) that were z offset from the center of the sphere at 10, 6, and 4 mm, respectively. Right: corresponding RMS (anisotropy) values. The data was taken by Yujing Sun.

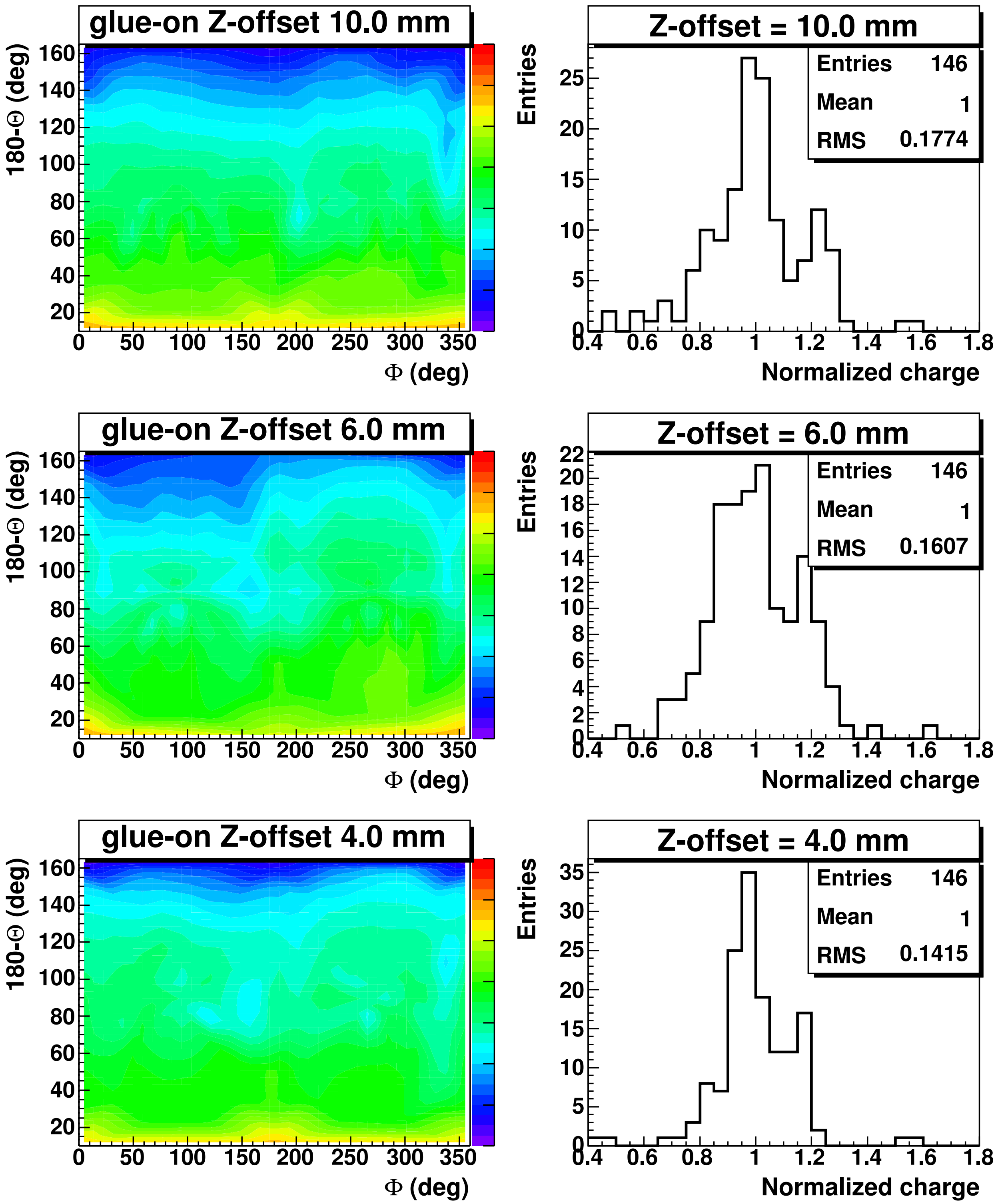

Figure 4.14: Left: light distributions in (θ, ϕ) associated with the 80 mm glue-on spheres (without a weight interface) that were z offset from the center of the sphere at 10, 6, and 4 mm, respectively. Right: corresponding RMS (anisotropy) values. The data was taken by Yujing Sun.

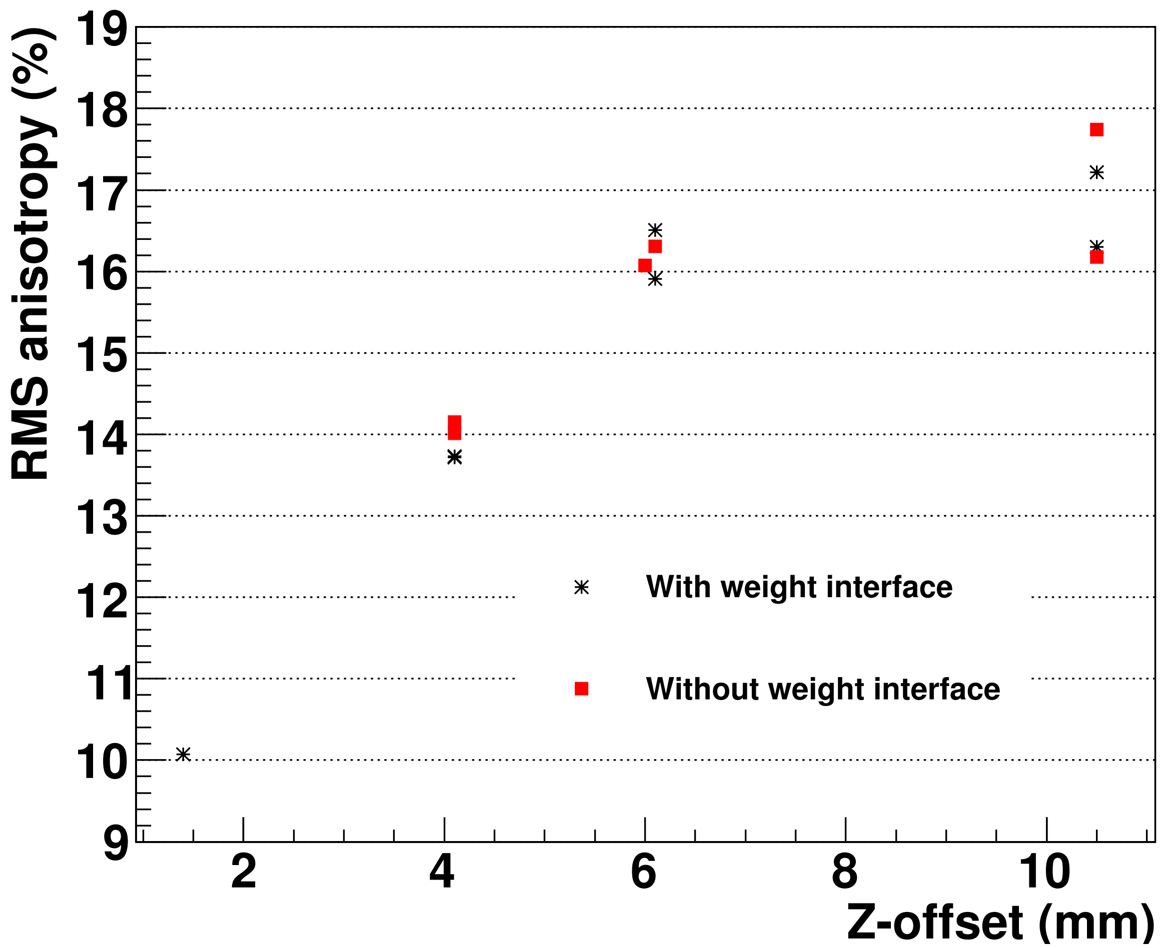

Figure 4.15: Summary of the anisotropy measurements for different configurations (as labeled) as a functionn of the z offset.

The conclusion can be drawn that the best isotropy was obtained when there was no z offset to the fiber guide tube. The TiO_2 tip helped the isotropy slightly but decreased the overall light output. Since the total light output is significant in the UV laser deployment, the TiO_2 tip was not implemented in the UV diffuser in order to maximize the light output. Thus, the final configuration has no z offset and no TiO_2 tip.

4.4.3 The Double Chooz Acrylic (GS0Z18)

For compatibility reasons, we intended to manufacture the final sphere from the same acrylic used in forming the Double Chooz neutrino target and gamma catcher, namely GS0Z18.

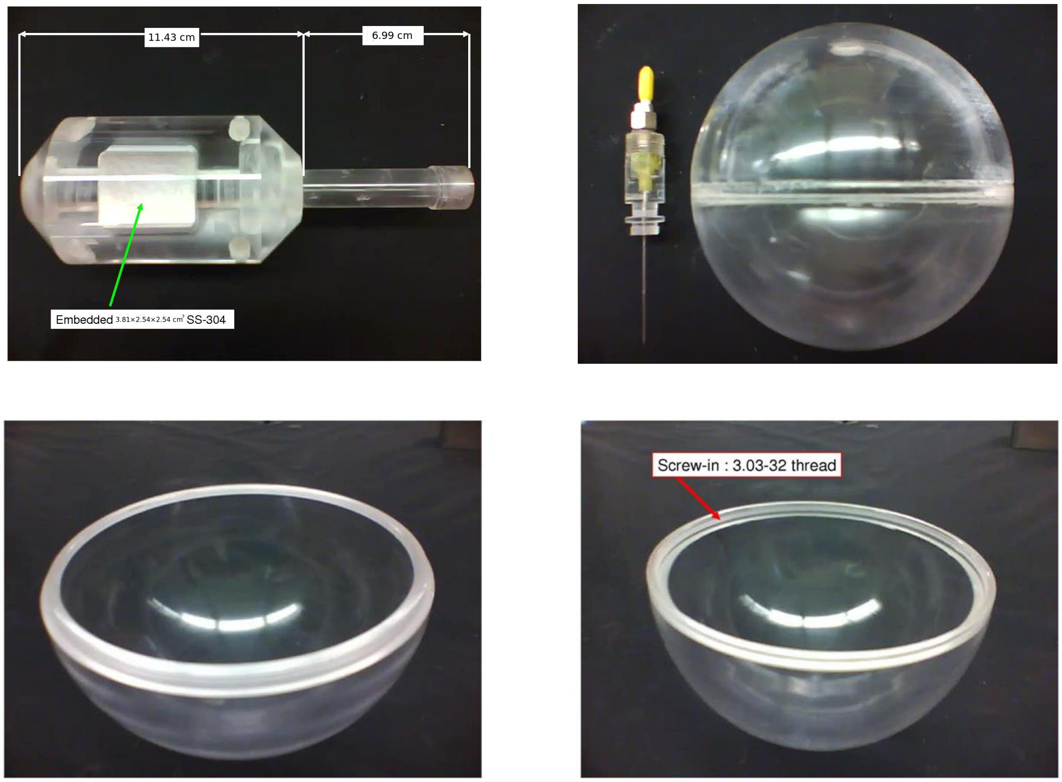

Figure 4.16: The Double Chooz laser diffuser (top right) and weight interface (top left) system. The acrylic sphere is built from threaded bottom (bottom left) and top (bottom right) hemispheres.

Three new spheres as well as their corresponding connector necks were manufactured. Figure 4.18 shows the isotropy test result from these three Double Chooz acrylic spheres which became the best result we had seen until then. The average anisotropy RMS is smaller than 5%. However, after final filling with the Double Chooz gadolinium-free scintillator, cracks were observed when the connector neck was screwed and glued to the GS0Z18 acrylic sphere. This behavior was not observed in the acrylic purchased from McMaster-Carr [196]. We had no alternative but to switch back to the acrylics from McMaster-Carr and redo the isotropy tests. In addition to the cracks around the connector neck, a crack around the equator of the screw-in joints was also observed if the temperature of the sphere was greater than 15°C. For an extra precaution, the final UV laser diffusers were reinforced by thickening the acrylic shell from 4 mm to 6 mm.

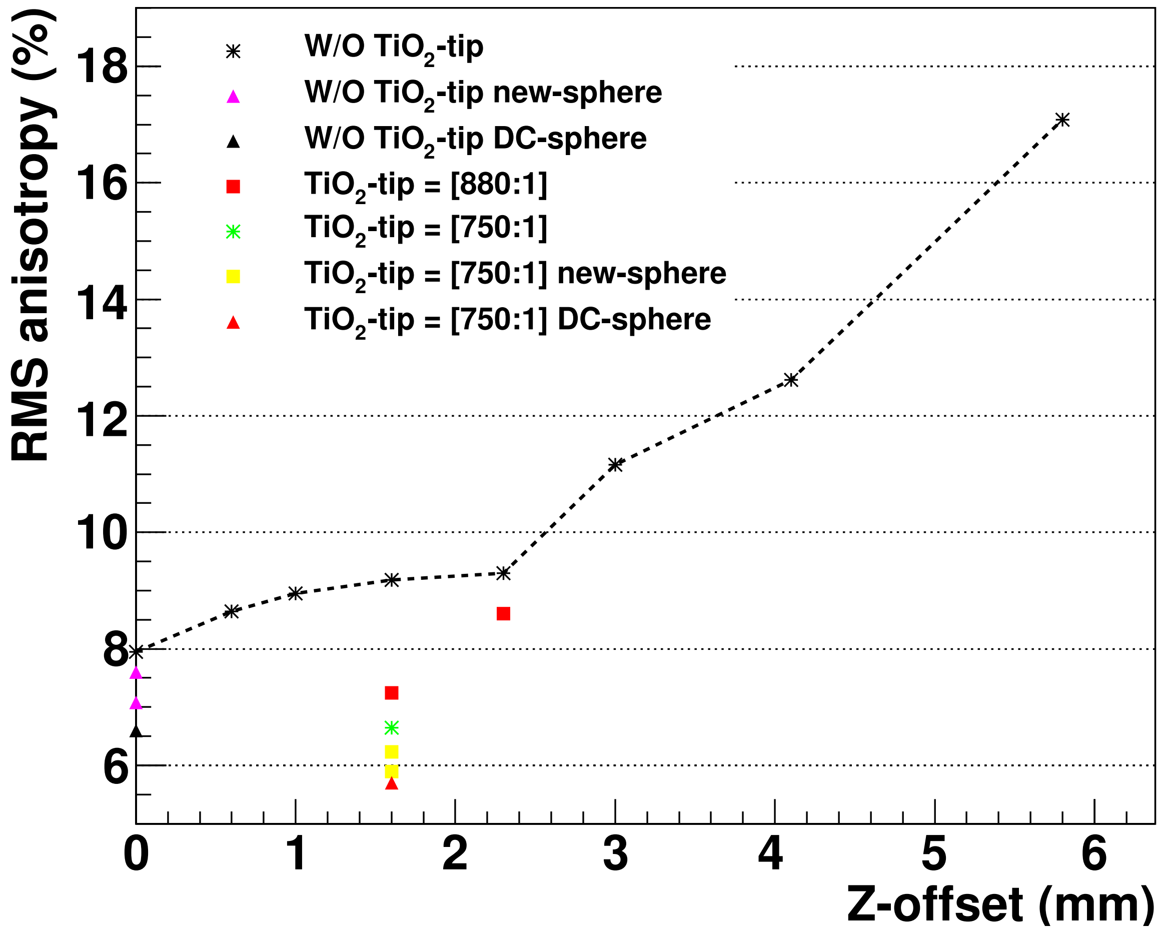

Figure 4.17: The systematic results including the tests of TiO_2 tip, another new sphere and a sphere made of the Double Chooz acrylic.

4.4.4 The Final UV Laser Diffuser Design

The anisotropy results of the final UV laser diffuser design are shown in Fig. 4.19. An average anisotropy of approximately 5% was achieved and the best isotropic sphere shown in Fig. 4.19 was picked as the main deployment sphere. The light yield detected by the 2-inch PMT in the dark box at 36 cm from these final laser diffusers is approximately 600 PEs at a 21% laser intensity, or approximately 1,583 PEs at 35% laser intensity. This would correspond to 887 PEs in the nearest Double Chooz PMTs when the diffuser is deployed at the center, running at 35% laser intensity.

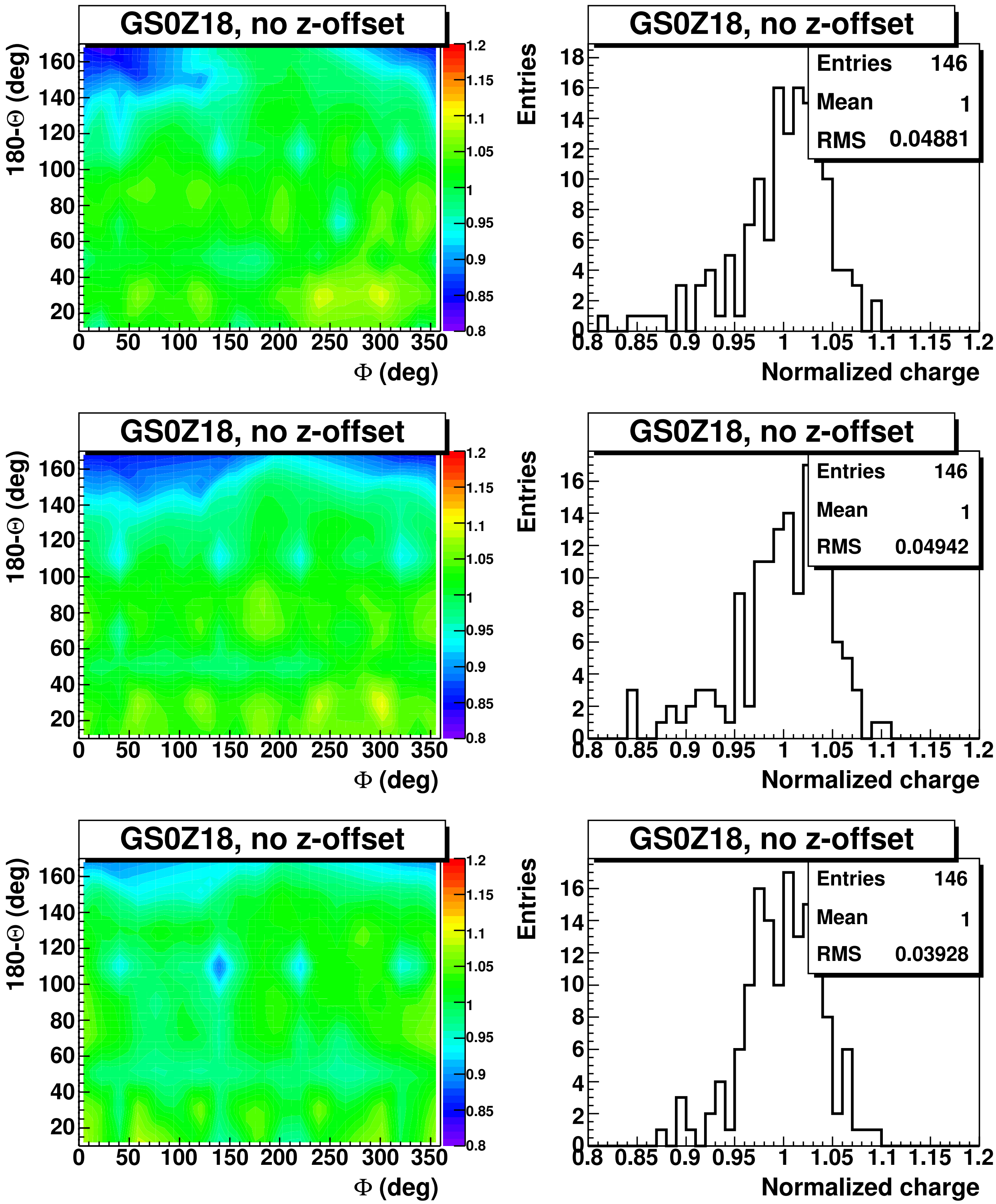

Figure 4.18: Left: light distributions in (θ, ϕ) associated with the 80 mm threaded GS0Z18 acrylic spheres with no z offset. Right: corresponding RMS (anisotropy) values.

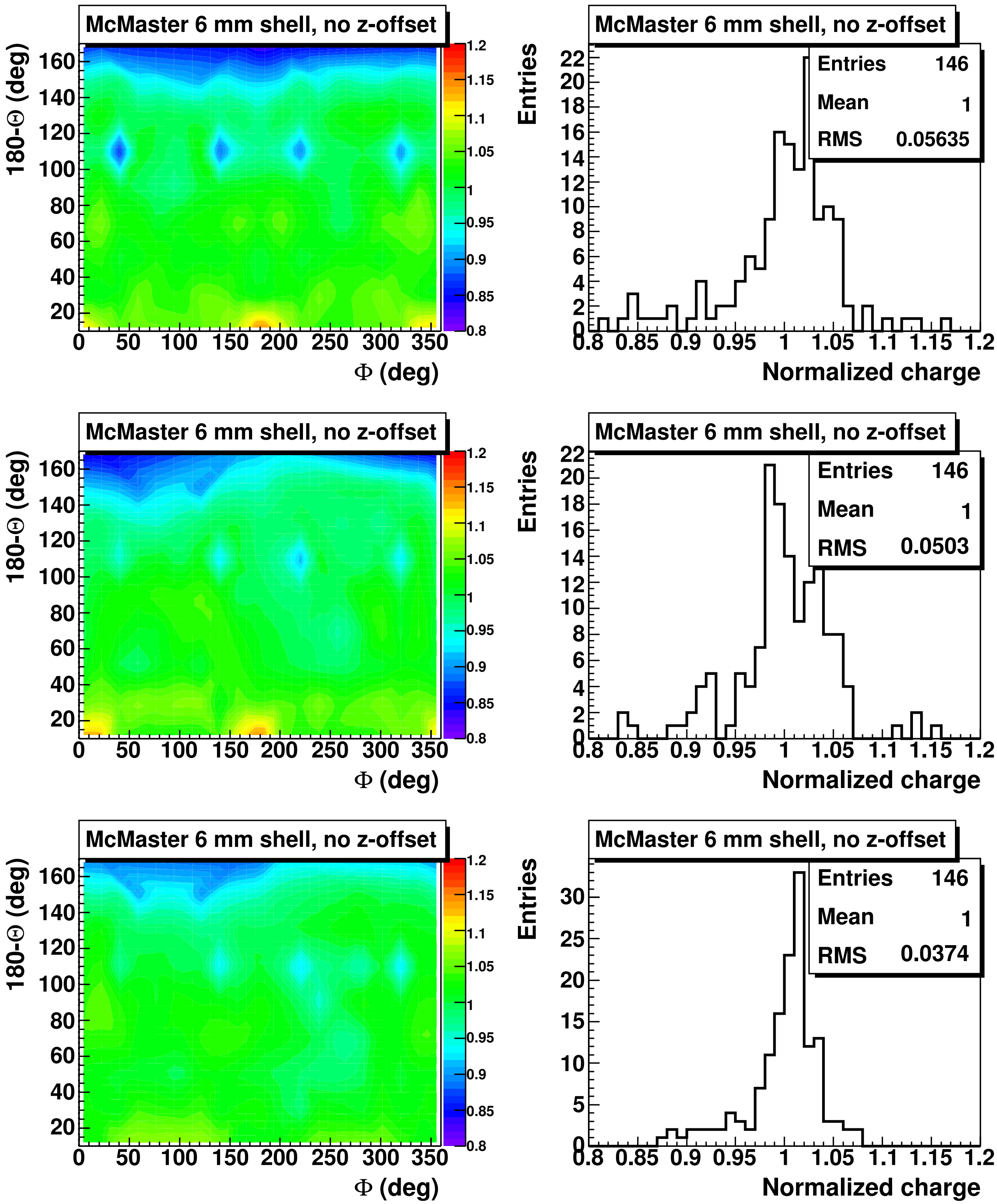

Figure 4.19: Left: light distributions in (θ, ϕ) associated with the 80 mm threaded McMaster-Carr's acrylic spheres with no z offset. The shell of these spheres is 6 mm thick. Right: corresponding RMS (anisotropy) values.

4.5 Spool and Weight Interface Deployment Test

Before deployment, the reliability and stability of the laser spool from which the fiber and support wire hang, must be tested. The fiber and support wire is contained inside an umbilical cord that has a teflon tubing with 2.8 mm outer diameter and 2.14 mm inner diameter. The spool was taken to the roof of the Department of Physics and Astronomy. The cord on the spool was unravelled and fully extended, and taken back. The process was repeated 200 times with the weight interface attached to the end of the teflon tubing. The spool was taken back to the laboratory for light yield measurements every 25 deployments. Connecting and disconnecting the connector about 100 times to the center of the spool was performed in order to take into account misalignment to the single mode core which is only 7 microns thick. Figure 4.20 indicates that we can repeatedly deploy the system with comparable light throughout.

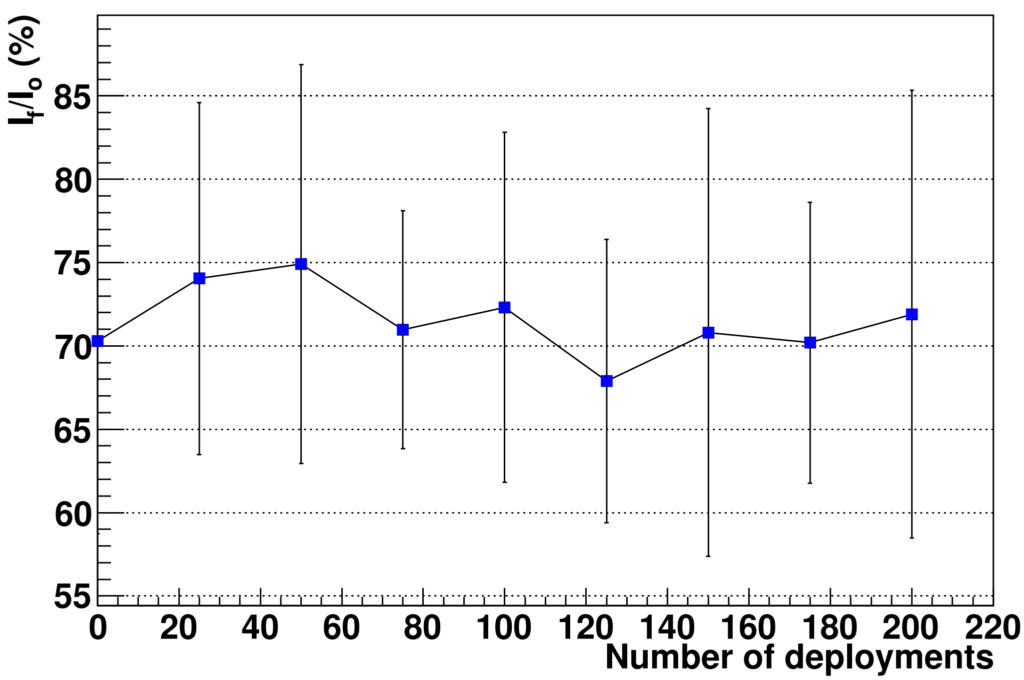

Figure 4.20: The results from the spool deployment test. The light output is measured with the power meter after every 25 deployments for about 100 times connecting and disconnecting to take into account alignment effect. I_f and I_o denote the intensity measured before and after putting on the spool. The error bars come from the light output variations from the about 100 times repeat.

Chapter 5

Gains Calibration

5.1 Introduction

The PMT gain is the conversion factor which translates the PMT charge from the raw units, specific to a particular experiment, to photoelectrons (PE):

$$q_{PE} = \frac{q_{DUQ}}{gain},$$

where q_{PE} is the PMT charge in units of PE, while q_{DUQ} is the PMT raw charge. In the Double Chooz experiment, the raw charge units are called DUQ (digital units of charge). Our strategy to obtain the PMT gains is to lower the laser intensity level so that almost every PMT hit is at the single PE level. In this case, according to the definition above, the gain is simply the mean of the charge distribution at the PMT. If the PMT charge response is a Gaussian distribution, the PMT gain can be taken as the fitted mean value of the Gaussian function. Otherwise, we use the mean of the charge distribution as the PMT gain. The advantage of the latter method is that it does not depend on the shape of the PMT charge response.

In Section 5.2, I will introduce the features of our analysis software and our test run results. A MC blind test, referred to as the *data challenge*, is also discussed in this section.

In Section 5.3, the calibration data analysis will be discussed. I will also describe the problem that we have encountered during the analysis, and systematic checks of the PMT gains derived from different methods using neutron capture events on hydrogen and gadolinium from the ^{252}Cf calibration source taken on May 15, 2012.

5.2 Monte Carlo Simulations

5.2.1 Software Development

The single PE rate can be approximately calculated from the total event hit multiplicity, N_{hit}, as follows. Assuming that the PMT hits are governed by Poisson statistics,

$$P(n;\mu) = \frac{\mu^n e^{-\mu}}{n!}, \tag{5.1}$$

where μ is the predicted charge on the PMT, the number of hit PMTs and no-hit PMTs can be calculated from:

$$N_0 = N_{tot}P_0 = N_{tot}e^{-\mu}, \tag{5.2}$$

and

$$N_{hit} = N_{tot}(1 - P_0) = N_{tot}(1 - e^{-\mu}),$$

respectively, where N_{tot} represents the total number of PMTs. Equation (5.2) directly yields

$$e^{-\mu} = \frac{N_0}{N_{tot}},$$

and thus the predicted charge μ is simply given by:

$$\mu = -\ln\left(\frac{N_0}{N_{tot}}\right). \tag{5.3}$$

Assuming a low level light intensity where only 15 PMTs get hit and all PMTs have the same predicted charge μ, which is $\mu = -\ln[(390 - 15)/390] \approx 0.03922$, the fraction of single

PE hits (relative to all hits) yields:

$$\frac{P_1}{P_{hit}} = \frac{\mu e^{-\mu}}{1 - e^{-\mu}} = \frac{\mu}{e^{\mu} - 1} = 1 - \frac{\mu}{2} + O(\mu^2) = 98.05\%. \tag{5.4}$$

Therefore, if we can lower the number of PMT hits to 15, approximately 98% hits are at the single PE level. A multiplicity below 15 hits would increase the single PE rate, but on the other hand it would also increase the data-taking time to collect enough statistics. To balance them, we take 15 hits as our initial requirement for the light level.

For simulating the UV laser calibration, MC events of 375 nm photon bombs (isotropically emitted photons) with 500 photons/event were generated at three positions along the z axis with $z = 0$ and ± 90 cm. These two off-center positions are picked based on the consideration that they are right in the middle of two PMT rings, as well as far enough from the center but not too close to the neutrino target boundary. 60,000 events were generated at the center, while 20,000 were simulated at $z = \pm 90$ cm. The average numbers of hits per event are 14.9, 14.5 and 15.0 for $z = +90$ cm, $z = 0$ and $z = -90$ cm respectively. The corresponding number of hits and the occupancies of each PMT for the three different positions are shown in Fig. 5.1. The occupancy is the fraction of a number of hits in a total number of events, $f = N_{hit}/N_{tot}$, and relates to the single PE fraction as:

$$\frac{P_1}{P_{hit}} = \frac{[-\ln(1-f)]\,(1-f)}{f}. \tag{5.5}$$

The average single PE fraction is approximately 98% based on the calculation from Eq.(5.4), where we assume all the PMTs have the same predicted charge μ. For the source at the center, for the nearest 2 rings to the light source located symmetrically between them (where the single PE rate should be the lowest) we still have an occupancy of 0.052 as shown in the middle panel of Fig. 5.1, which makes $P_1/P_{hit} = 97.3\%$. As shown in the top and bottom panels of Fig. 5.1, the occupancy for the source at the top and bottom vertices has an upper limit of 0.1, which can be translated into the lower limit of single PE rate of 94.8% according

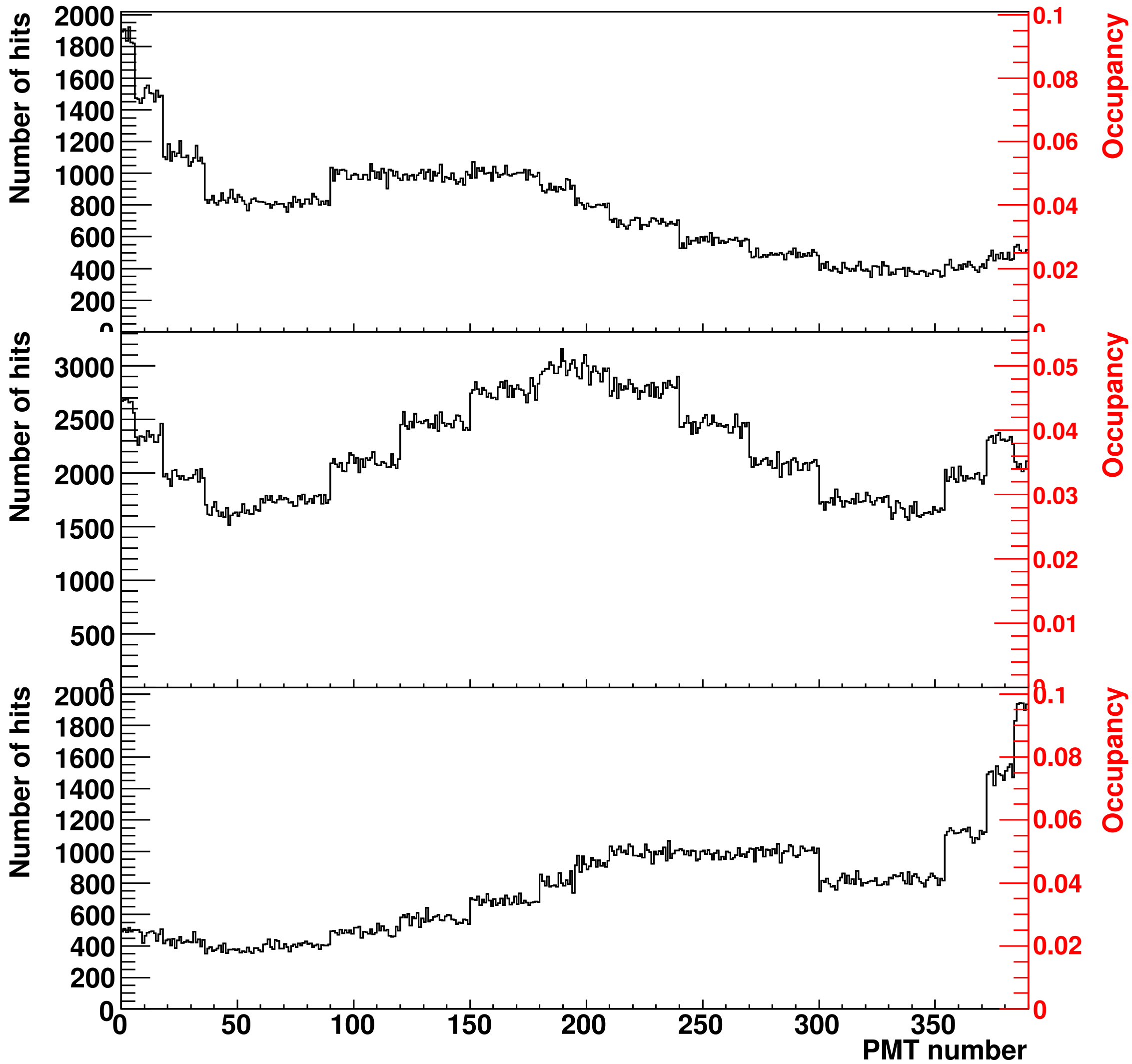

Figure 5.1: Total number of hits and occupancy versus PMT number for simulated MC UV laser events generated at $z = +90$ cm (top), $z = 0$ (center) and $z = -90$ cm (bottom).

to Eq. (5.5). In summary, the single PE rate for the source at the center has a lower limit of 97.3% while when source is at the top or bottom, the lowest single PE rate cannot be smaller than 94.8%.

The MC data from the hit-level simulations DCGLG4sim (Double Chooz generic LAND Geant4 simulation) is processed through DCRoSS (Double Chooz readout simulation software) and then DCRecoPulse (Double Chooz PMT pulse reconstruction and pedestal analysis package). The physics processes of MC events are simulated at the Geant4-based

DCGLG4sim level, which does not account fully for the detector acceptance and efficiencies, such as trigger, time-window, digitisation, thresholds, pileup, etc. The events are further processed by the readout system simulation, DCRoSS, which smears the charge and generates the corresponding data-like digitized waveforms, and switches its unit from PE to DUQ. At this level, the charge information both in PE and DUQ is kept. The effects such as non-linearities, finite PMT time and charge resolution, etc, are introduced at this level. The DCRecoPulse package will subtract the baselines and calculate the PMT charges and times from the waveforms, in data or as generated by DCRoSS in MC. In this particular exercise, the MC events were only processed through DCRoSS and the charge information in PE was analyzed.

The analysis software has two control parameters and runs without any additional operator input, with all analysis results being generated automatically. The control parameters are:

1. *Statistics*: the lowest number of effective entries for each PMT; default = 1,000.

2. *Occupancy*: the highest hit rate for each PMT to be analyzed; default = 0.05.

Failure to meet the first requirement would result in no analysis for that particular PMT. For a certain vertex, if the occupancy of one PMT is higher than the user's input, all entries from this vertex to that PMT will not be used.

In this particular test, the *Statistics* and the *Occupancy* control parameters were set to 2,000 and 0.06 respectively. One may also set the limit for the overflow of the raw charge histogram and the χ^2 value of the Gaussian fit. These two parameters would not affect the analysis but will show up in the "status" column of the text summary if the corresponding parameters exceed the limit. Figure 5.2 is the output text summary of this particular exercise in which all relevant information is included. It starts with the run time of the analysis, followed by the control parameters for this particular run with *Statistics* (L), *Occupancy* (H), *Bad channel* (B), *Too many overflows* (O) and *Bad fitting* χ^2 (C). The number of PMTs with high occupancy appears in the summary part. The main part of

```
PMT Gain Calibration
run taken on 2009-09-15 21:07:56
L->Statistics lower than 2000 (default 1000)
H->Occupancy higher than 0.06 (default 0.05)
B->Bad Channel
O->Overflow more than 5%
C->Bad fitting Chi-sqr
##################  summary  #################
There are 390 PMTs in total // unusable PMTs summary is in the end of the file
Top vertex: # of high occupancy PMTs 19
Ctr vertex: # of high occupancy PMTs 0
Btm vertex: # of high occupancy PMTs 18
##################    end    #################
PMT  Top(occu/entry)  Ctr(occu/entry)  Btm(occu/entry)  Usable_entry  Gain    Gainspread  Status  Overflow  Chisqr
0    H  0.095/1893       0.045/2674       0.025/492        3166          1.0003  0.2818              0         190
1    H  0.095/1908       0.045/2683       0.025/509        3192          1.0117  0.2891              0         109
2    H  0.092/1836       0.045/2693       0.024/486        3179          0.9793  0.2934              0         94
3    H  0.096/1922       0.044/2660       0.026/515        3175          0.9911  0.2926              0         86
4    H  0.091/1825       0.044/2666       0.024/489        3155          1.0057  0.2921              0         102
5    H  0.091/1817       0.043/2565       0.025/505        3070          1.0030  0.2827              0         138
6    H  0.074/1474       0.039/2337       0.025/499        2836          1.0047  0.2928              0         93
7    H  0.073/1468       0.038/2264       0.025/502        2766          1.0035  0.2847              0         121
8    H  0.072/1442       0.039/2343       0.024/488        2831          0.9991  0.2893              0         118
9    H  0.074/1474       0.039/2341       0.021/419        2760          0.9918  0.2804              0         132
10   H  0.077/1540       0.038/2301       0.023/465        2766          0.9977  0.2966              0         100
11   H  0.078/1555       0.040/2391       0.024/483        2874          1.0212  0.2899              0         120
12   H  0.075/1507       0.039/2338       0.024/490        2828          1.0004  0.2930              0         109
13   H  0.075/1503       0.039/2361       0.025/493        2854          0.9967  0.2840              0         129
14   H  0.073/1453       0.038/2290       0.024/480        2770          0.9883  0.2934              0         107
15   H  0.076/1521       0.038/2286       0.022/432        2718          0.9831  0.2933              0         99
16   H  0.074/1481       0.039/2353       0.024/474        2827          1.0128  0.2910              0         104
17   H  0.075/1490       0.041/2463       0.025/507        2970          0.9902  0.2784              0         136
18      0.055/1104       0.033/1969       0.021/415        3488          1.0300  0.2838              0         177
19      0.054/1087       0.033/1996       0.022/435        3518          0.9976  0.2722              0         206
20      0.059/1185       0.032/1945       0.022/441        3571          1.0040  0.2832              0         127
21      0.054/1079       0.031/1876       0.020/403        3358          1.0041  0.3003              0         93
22      0.057/1135       0.034/2024       0.022/445        3604          0.9844  0.2769              0         165
23      0.055/1107       0.034/2029       0.019/386        3522          1.0110  0.2871              0         142
                                                   ......
371     0.020/401        0.033/1978       0.056/1123       3502          1.0124  0.2777              0         208
372     0.023/452        0.038/2304    H  0.075/1490       2756          1.0192  0.2816              0         127
373     0.024/480        0.039/2334    H  0.075/1505       2814          1.0066  0.2986              0         111
374     0.026/513        0.039/2350    H  0.075/1510       2863          1.0095  0.2979              0         73
375     0.022/449        0.038/2279    H  0.071/1418       2728          0.9892  0.2905              0         90
376     0.024/489        0.039/2355    H  0.077/1541       2844          0.9912  0.2786              0         128
377     0.023/464        0.040/2378    H  0.075/1492       2842          0.9904  0.2757              0         112
378     0.025/499        0.039/2313    H  0.074/1482       2812          0.9976  0.2902              0         106
379     0.023/460        0.039/2314    H  0.073/1455       2774          0.9789  0.2918              0         131
380     0.023/460        0.038/2296    H  0.076/1513       2756          0.9990  0.2961              0         89
381     0.025/501        0.038/2307    H  0.077/1535       2808          1.0108  0.2877              0         114
382     0.023/454        0.039/2338    H  0.078/1554       2792          0.9954  0.3133              0         72
383     0.023/459        0.038/2267    H  0.073/1469       2726          1.0042  0.2888              0         129
384     0.027/538        0.035/2107    H  0.091/1830       2645          1.0018  0.2995              0         101
385     0.027/549        0.034/2058    H  0.097/1938       2607          0.9886  0.2911              0         67
386     0.026/516        0.035/2085    H  0.097/1943       2601          0.9977  0.2989              0         108
387     0.025/497        0.034/2014    H  0.097/1939       2511          0.9996  0.2795              0         97
388     0.025/503        0.034/2042    H  0.095/1898       2545          1.0036  0.2857              0         111
389     0.026/518        0.035/2112    H  0.097/1934       2630          1.0113  0.2990              0         81
************************  Unusable PMTs Summary  ************************
0 Bad PMTs
0 PMTs lack of statistics
9 PMTs' overflow more than 5%
1 PMTs have Bad fitting Chi-sqr
************************  Unusable PMTs  ************************
PMT     reason
97      Overflow more than 5%
180     Overflow more than 5%
184     Bad fitting Chi-sqr
200     Overflow more than 5%
219     Overflow more than 5%
222     Overflow more than 5%
253     Overflow more than 5%
279     Overflow more than 5%
301     Overflow more than 5%
342     Overflow more than 5%
```

Figure 5.2: Output text summary generated by the analysis software.

this text file covers all the information for each PMT, including the occupancies and entries for three vertices (H appearing in the front indicates that it has a high occupancy), usable entries, calibrated gain, single PE distribution width, status (could be one or many of “L”, “H”, “B”, “O”, “C”), number of overflows, and χ^2. The summary of problematic PMTs, as well as their channel numbers and reasons are shown in the end.

It is obvious from Fig. 5.1 that some PMTs have a high occupancy, for instance, the top PMTs for the light source at $z = +90$ cm, and the bottom PMTs for the light source at $z = -90$ cm. These data will be omitted for failing to pass the second selection criterion.

As an example, the charge distribution for PMT 0 is shown in Fig. 5.3; it is fitted well by a Gaussian distribution. The input gains were drawn from a Gaussian distribution of mean 1.0 PE and width 0.02 PE (i.e., practically identical for all 390 PMTs). The width of the single PE charge distributions were from a Gaussian distribution of mean 0.3 PE and width 0.01 PE. The result of the fitted mean values for all 390 PMTs are shown in the top panel of

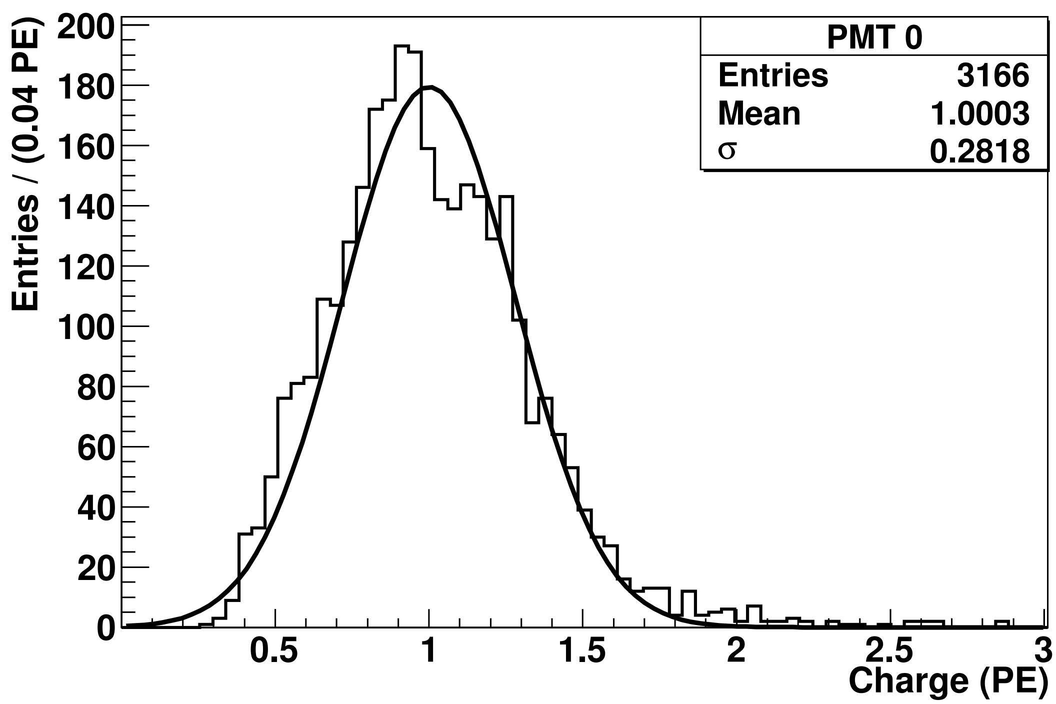

Figure 5.3: The charge distribution and Gaussian fit for the calibrated charge of PMT 0 (MC simulation).

Fig. 5.4, which yields an almost uniform distribution with a small variation. We can recover the input gains with a precision of 2%, as shown in the middle panel of Fig. 5.4. We can also recover the widths (0.29 versus 0.30 PE generated), as shown in the bottom panel of Fig. 5.4.

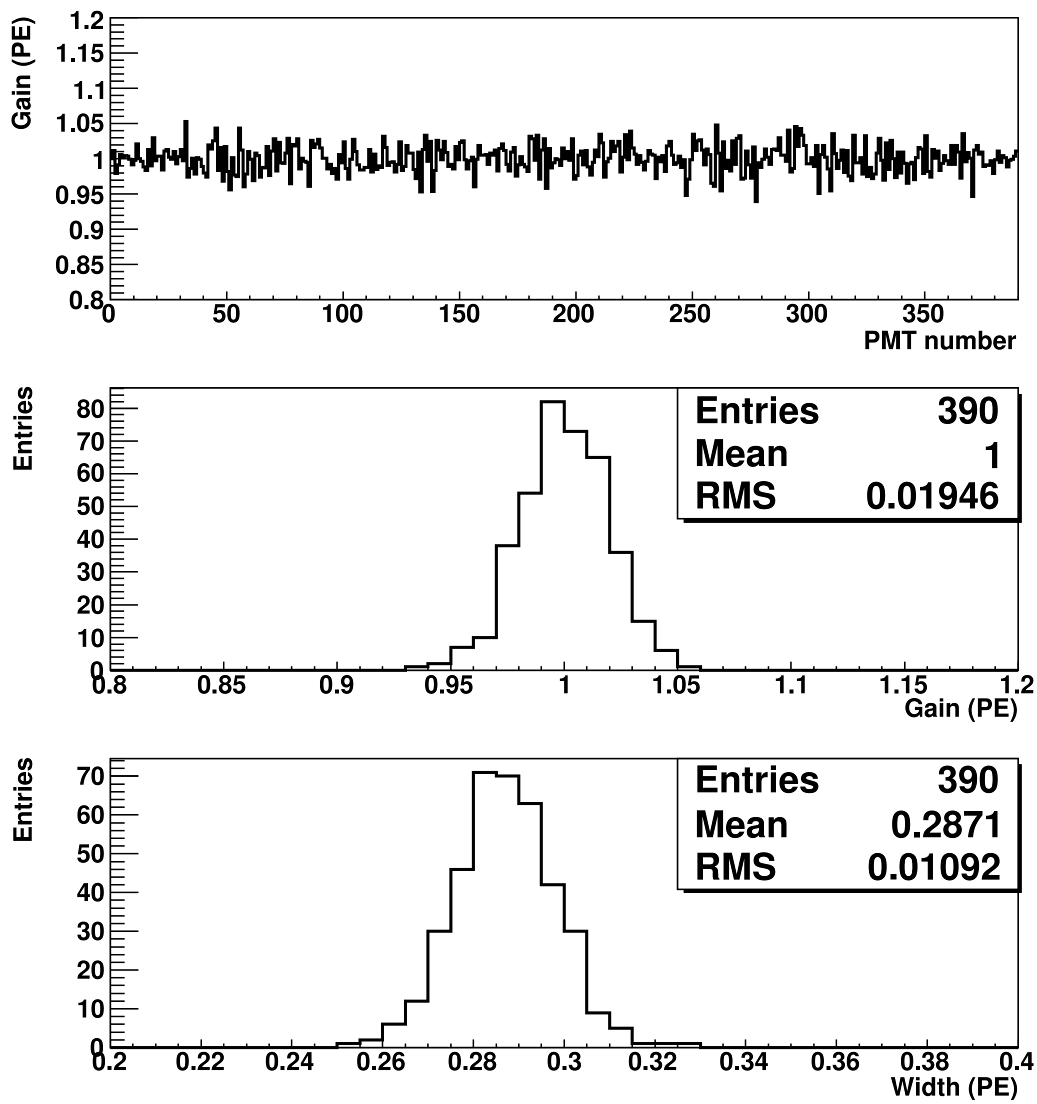

Figure 5.4: The result of fitted PMT gains for 390 PMTs (top), their projections (middle) and the fitted widths projections (bottom).

Figure 5.5 displays the mean values and widths of the charge distribution for all 390 PMTs. The average value of the charge histogram means is slightly higher than that of the fitted values only because of the small fraction of multiple hits. The user can decide to

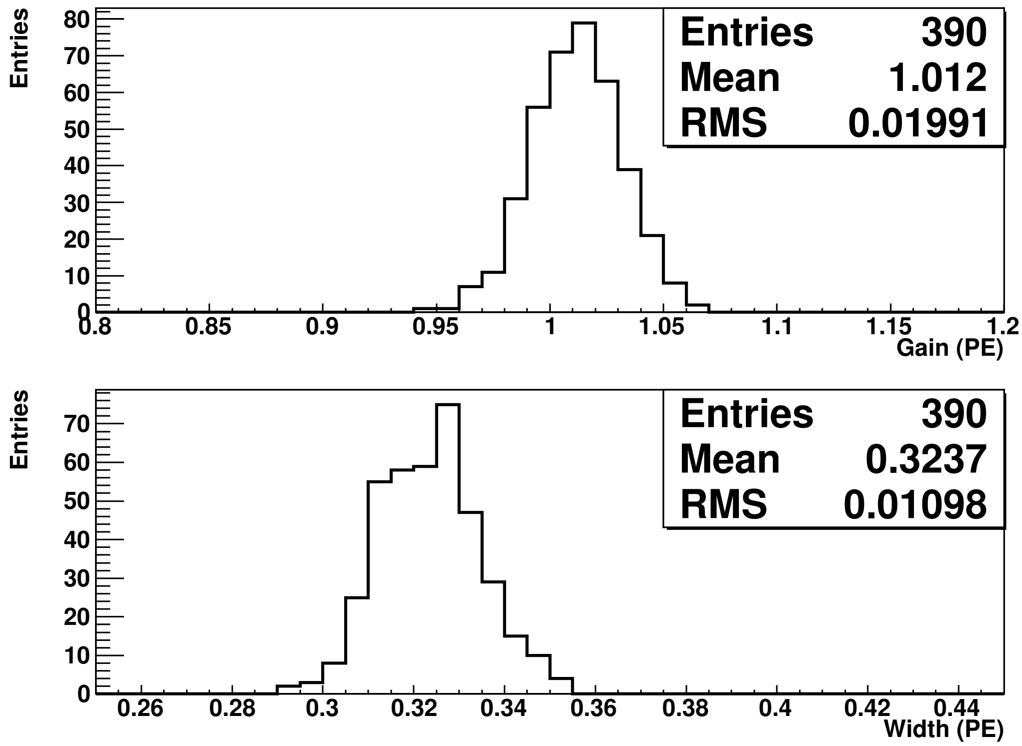

Figure 5.5: The result of PMT gains from the mean values of the charge distributions (top) and their widths (bottom).

use the mean values as the PMT gains calibration result if the charge distributions are not Gaussians.

5.2.2 Data Challenge

Before the Double Chooz experiment started taking data, a *data challenge* was undertaken in the summer of 2010 in order to simulate the real data analysis. Monte Carlo calibration data were generated by our collaboration with some input gain values that were randomly assigned to the PMTs, to which I had no access beforehand. This MC has the full simulation, i.e., processed through DCRecoPulse. The input gains have a Gaussian distribution of mean 50 DUQ and width 7 DUQ. The calibration results were compared to the true values after the analysis.

In the *data challenge*, the power of the laser was simulated at the twice of the intensity (about 30 hits/event) of that in the previous exercise because we wanted to test the software with possible scenarios which could happen during the deployment. The reason for this particular test is that it is very difficult to precisely control the light levels within the detector during actual deployments since the alignment of the fibers causes variations in coupling efficiency each time the connection is reestablished. In each deployment at a new position, the diffuser connected to the fiber on the spool only when the target position was reached. A short test run was taken with a standard neutral density filter which was immediately processed and analyzed. According to the total raw charge yielded from the test data, we calculated how many and which neutral density filters to be used for our desired light levels based on the transmission rates given by Table 4.1. Since the calibration constants have not been applied, the total raw charge has some non-linearity effect. The translation from the total charge to total number of PMT hits is not simply linear. And also the transmission rates for the neutral density filters are discrete numbers which can only yield the a close light level to the purposed one sometimes. Therefore, we consider the worst case scenario in which the laser delivers twice the intensity we desired. More statistics were generated this time with 100,000 events at each position, which turns out to be very close to the actual statistics of the real calibration data. The total number of hits and the occupancies for each PMT at three different positions are plotted in Fig. 5.6. As clearly seen in this figure, the occupancies are about twice of those in the last exercise in Fig. 5.1, as expected.

The charge distribution and the corresponding fit of PMT 0 is shown in Fig. 5.7. As the light intensity became twice of that in the last exercise, the multiple PE contamination, in particular contributions from the double PE hits cannot be ignored anymore. The fitting function becomes now the sum of two Gaussians with a total of six parameters – which are not fully independent. Assuming charge linearity, the mean value at the second PE peak must be twice the value at single PE peak, and the second PE width is $\sqrt{2}$ times of the single PE width. If the PMT hits are governed by a perfect Poisson distribution, the fitting function would yield:

$$N\left\{\frac{e^{-\mu}\mu}{\sqrt{2\pi}\sigma}\exp\left[-\frac{1}{2}\left(\frac{x-G}{\sigma}\right)^2\right]+\frac{e^{-\mu}\mu^2}{2\sqrt{2\pi}\sigma}\exp\left[-\frac{1}{2}\left(\frac{x-2G}{\sqrt{2}\sigma}\right)^2\right]\right\},$$

Figure 5.6: Total number of hits and occupancy versus PMT number for simulated MC UV laser events generated at $z = +90$ cm (top), $z = 0$ (center) and $z = -90$ cm (bottom) for the *data challenge*.

where N is the total magnitude, G and σ denote the single PE gain value and the corresponding distribution width. However, in the case in which the single PE inefficiency is non-negligible, we let the magnitudes of these two Gaussians vary freely, namely,

$$\frac{N_1}{\sqrt{2\pi}\sigma} \exp\left[-\frac{1}{2}\left(\frac{x-G}{\sigma}\right)^2\right] + \frac{N_2}{\sqrt{2\pi}\sigma} \exp\left[-\frac{1}{2}\left(\frac{x-2G}{\sqrt{2}\sigma}\right)^2\right]. \tag{5.6}$$

There are now 4 independent parameters in this fitting function: the magnitude of the single

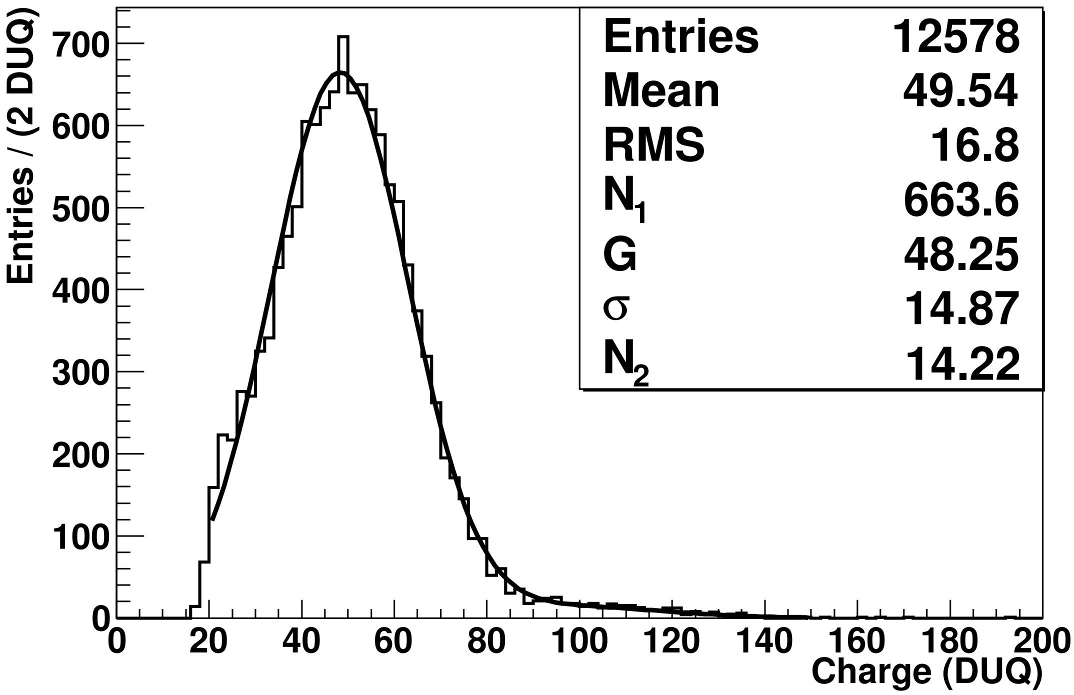

Figure 5.7: Raw charge distribution for PMT 0 in the *data challenge*, fitted to a sum of two Gaussians as given by Eq. (5.6).

PE peak N_1, the magnitude of the second PE peak N_2, the single PE gain G and width σ. This function gives a good fit with an average χ^2/NDF of 1.58, which in turn implies that the single PE charge distribution is well approximated by a Gaussian.

The result of the fitted gains is shown in Fig. 5.8, while the comparison to the generated values is shown in Fig. 5.9. As from the top panel of Fig. 5.9 which shows the difference between the fitted and the generated gains, the calibrated values do not agree well with the generated ones: they are on average 15% smaller than the generated values. When the difference is plotted versus the generated values, as shown in the bottom panel of Fig. 5.9, one can see that the difference increases as the generated values increase. But in general it appears that there is less charge as expected. Further investigations revealed that the charge loss happens at the pulse reconstruction level in the DCRecoPulse algorithm. The pulse reconstruction algorithm was eventually corrected but the gain calibration in *data challenge* was not repeated.

Besides fitting the single PE histograms and taking the mean values as PMT gains, we

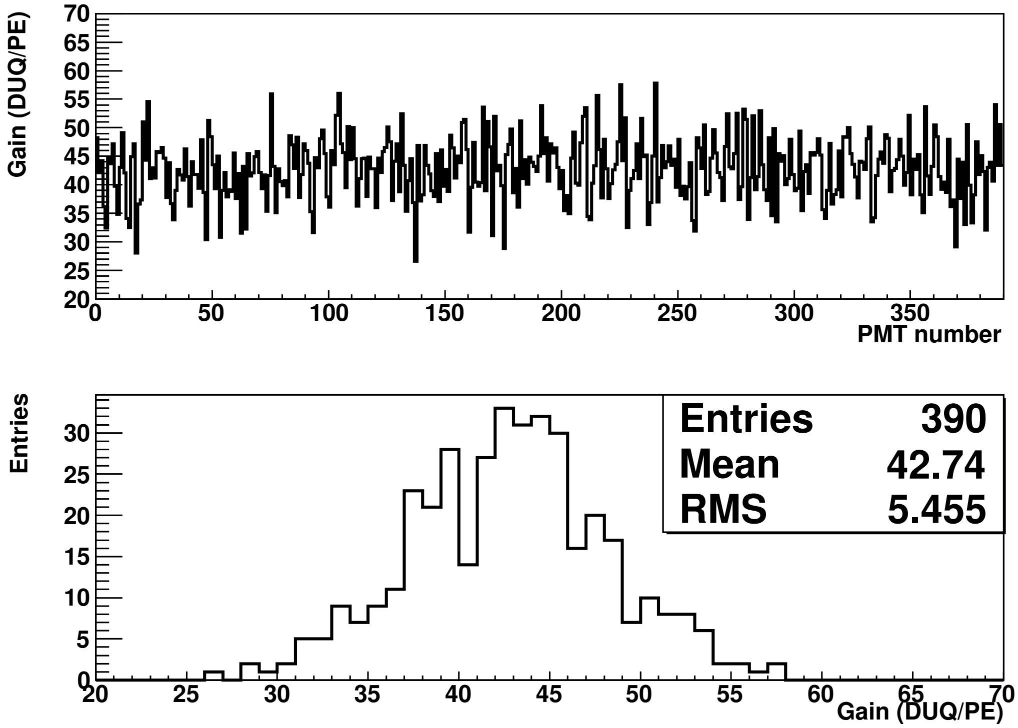

Figure 5.8: The result of fitted PMT gains versus PMT number (top) and their projection (bottom) for the *data challenge*.

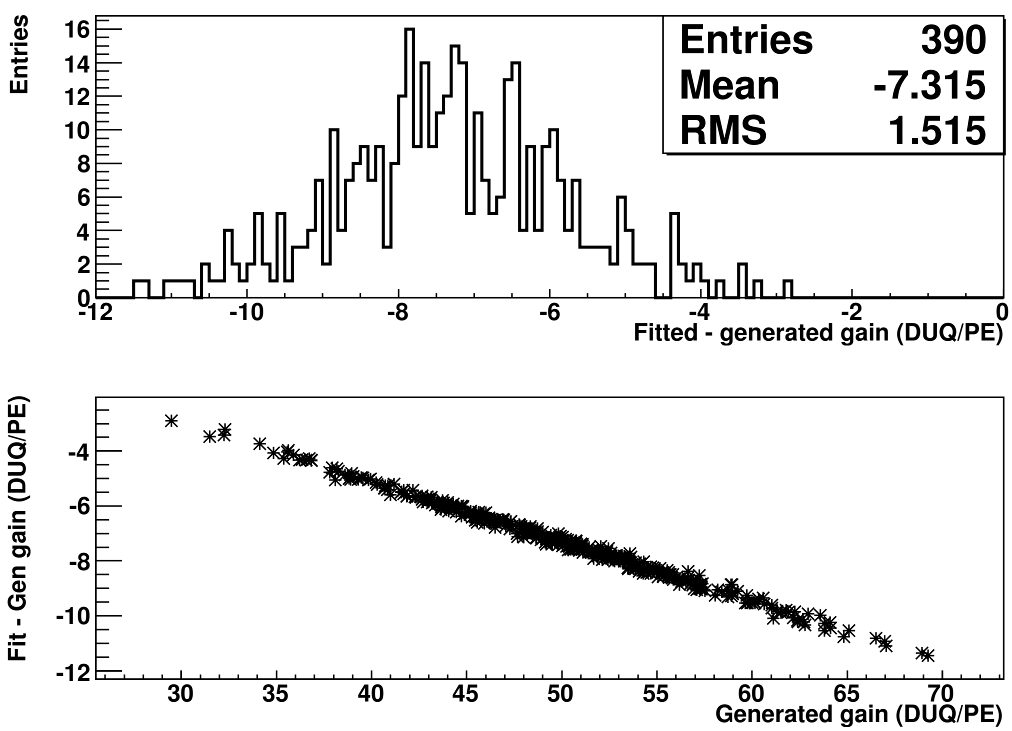

Figure 5.9: Comparison of the fitted gains to the generated values (top) and the comparison versus generated values (bottom) for the *data challenge*.

have considered an alternative scenario in case the single PE distribution is too far away from a Gaussian and the laser intensity is higher than expected. In such case, only using the mean values would result in the overestimation of the gains. Taking the same example in which the predicted charge is $\mu = 0.04$ PE (as in the example in Section 5.2.1), we know that the single PE fraction is described by Eq. (5.4). The fractions of 2 and 3 PEs are:

$$\frac{P_2}{P_{hit}} = \frac{\mu^2 e^{-\mu}}{(1-e^{-\mu})2!} = 1.96\%, \tag{5.7}$$

$$\frac{P_3}{P_{hit}} = \frac{\mu^3 e^{-\mu}}{(1-e^{-\mu})3!} = 0.026\%, \tag{5.8}$$

etc. Taking into account these contributions and assuming that for some $n > N$ they become negligible, the gains have to be corrected by a factor of:

$$Correction_N = \sum_{n=1}^{N-1} nP_n + N(1 - \sum_{n=1}^{N-1} P_n). \tag{5.9}$$

Therefore the corrected mean value becomes:

$$Mean_{corr} = \frac{Mean_{histo}}{Correction_N}.$$

Putting the numbers from Eqs. (5.4), (5.7), (5.8) into Eq. (5.9), the correction to $N = 4$ PE for $\mu = 0.04$ is calculated to be 1.02 which means that taking the mean values as gains would overestimate the gains by 2%.

The correction can be made to any given order, but from Fig. 5.10, we know that even with an occupancy of up to 0.5, the correction to $N = 4$ PE is as accurate as higher order corrections. Therefore, we decided to use correction to $N = 4$ PE. The results of taking means and corrected means as gains are shown in Fig. 5.11. Comparing the corrected means in the bottom panel of Fig. 5.11 to those in Fig. 5.8, the difference is only 0.3%, which verifies the charge distributions are perfect Gaussians. If it is compared to the histogram

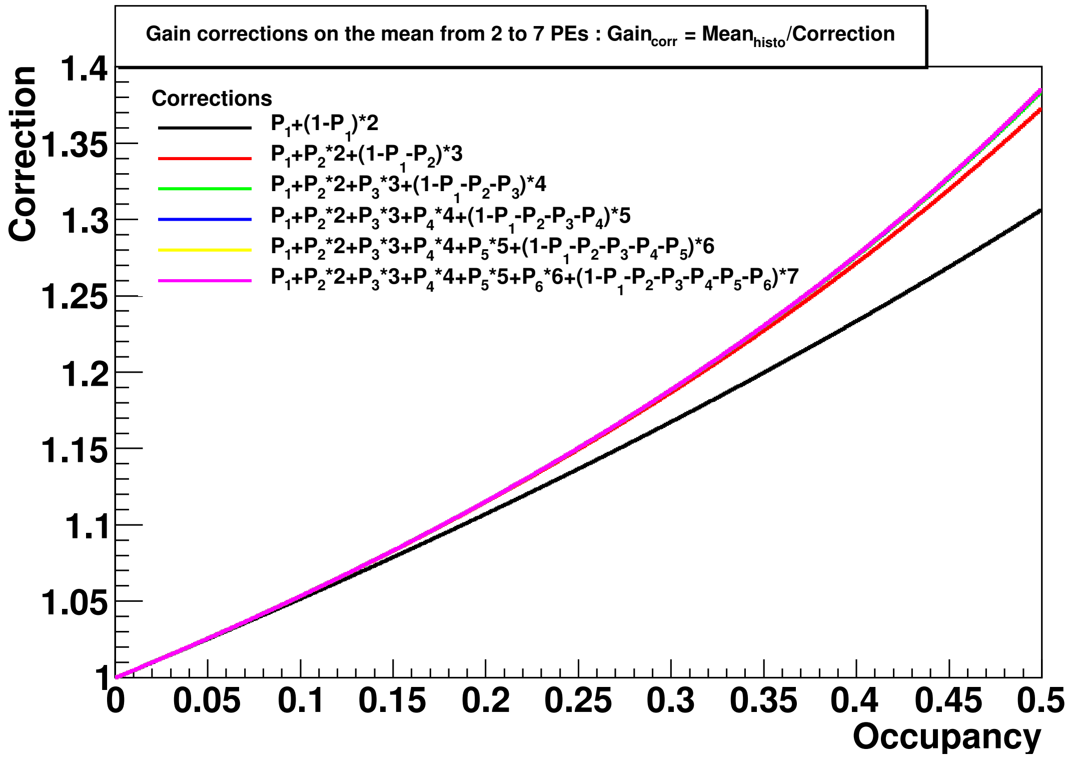

Figure 5.10: Corrections on the mean from 2 to 7 PEs with respect to occupancy.

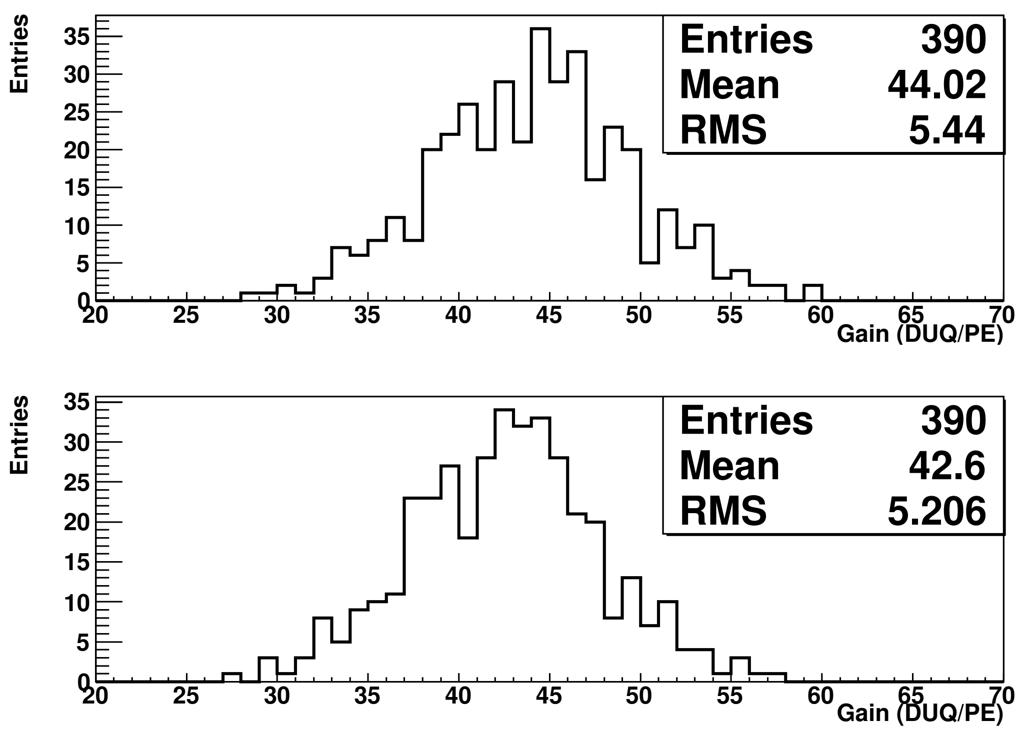

Figure 5.11: The result of PMT gains from the charge distribution means for 390 PMTs (top) and the corrected means (bottom) as obtained for the *data challenge*.

mean values in the top panel of Fig. 5.11, the average corrected gain is 3.2% less, which approximates the level of double PE contamination as postulated.

5.3 Data Analysis

5.3.1 Analysis

The laser calibration runs were taken with the external trigger generated by the laser system. The event selection, which includes the requirement for the extenal trigger to be set, also includes a light noise cut and a charge cut. A light noise cut of $Q_{max}/Q_{tot} < 0.4$ was applied (as opposed to 0.09 in the neutrino prompt events), as shown in the top panel of Fig. 5.12. A charge cut of $250 < Q_{tot} < 4,000$ DUQ was applied for preventing missing light noise events by previous cut or high energy background events coincident with the laser trigger, as shown in the bottom panel of Fig. 5.12. The combination of these two cuts eliminates about

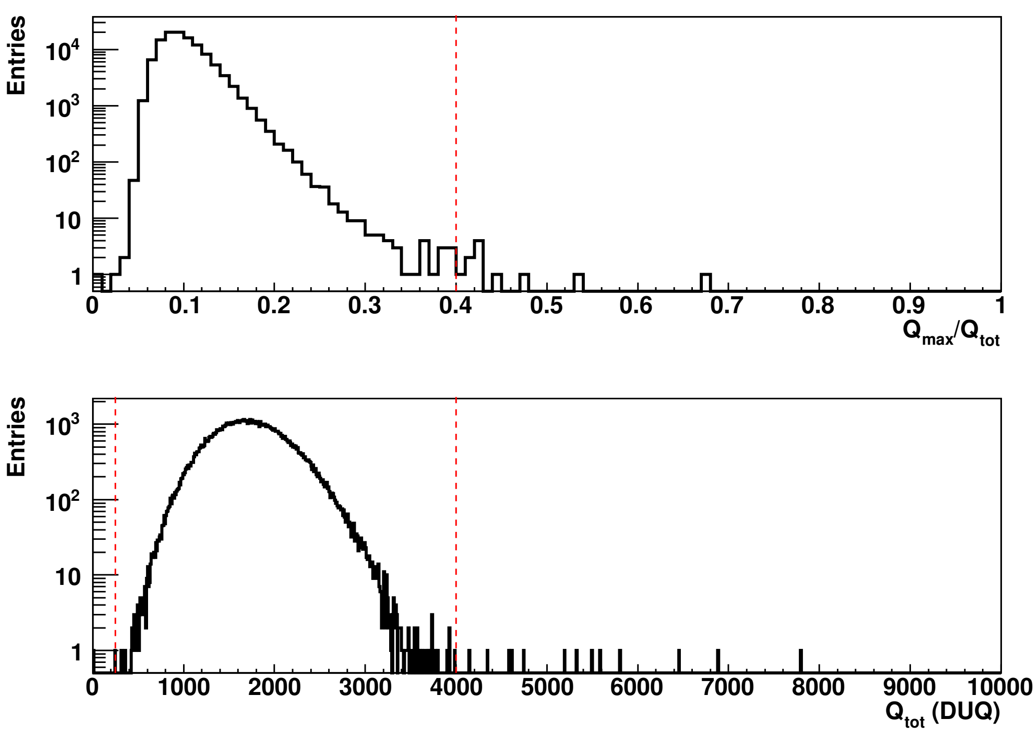

Figure 5.12: Illustration of the two analysis cuts: $Q_{max}/Q_{tot} < 0.4$ and $250 < Q_{tot} < 4{,}000$ DUQ for the central $\lambda = 375$ nm laser run 43798.

0.03% events. The laser was run at intensities that gave 18–21 hits/event, which is roughly between the two MC exercises discussed in Section 5.2. The laser diffuser was deployed at three positions, namely $z = 0$ and $z = \pm 92$ cm which are slight different than $z = \pm 90$ in MC. All the relevant information is summarized in Table 5.1. The total number of hits and occupancies for each PMT at 3 positions are shown in Fig. 5.13.

Run #	z (cm)	Average Nhits	Q_{max}/Q_{tot}	Q_{tot} (DUQ)	Total events	Trigger events	Selected events
43798	0	21.1	< 0.4	(250, 4k)	114,854	113,358	113,325
43808	-92	17.8	< 0.4	(250, 4k)	114,708	113,214	113,179
43852	92	19.1	< 0.4	(250, 4k)	114,566	112,906	112,880

Table 5.1: Run numbers, positions, average multiplicities and selection criteria as well as total number of events, laser triggered events and selected events after the light noise cut and total charge cut discussed above for the $\lambda = 375$ nm laser data for PMT gains calibration.

The analysis was very similar to the one for *data challenge*. Based on the PMT charge distribution, the same fitting function as in Eq.(5.6) was used for the raw charge distribution. With the exception of several PMTs, almost all PMTs have an excellent fit quality. The raw charge distributions for PMTs 0–14 are shown in Fig. 5.14.

There are in total 15 inactive PMTs which were directly read in from the database. From the concept of software development, the PMT occupancies at each diffuser position decide whether we will use the entries or not. Since our fitting function includes the double PE effect, the criterion does not need to be very stringent. A value of 0.12 was given as an upper limit for the occupancy to accept all the PMTs (as can be seen from Fig. 5.13) and no PMTs lacked sufficient statistics. As we can read from the middle panel of Fig. 5.15 the fitted result of gains has shown the average value of 73.1 DUQ/PE which confirms the number 71.2 DUQ/PE used in the Double Chooz first publication [102] as obtained from the IDLI system. The result of the fitted widths are given in the bottom panel of Fig. 5.15. If we only look at the central source data, the variations of occupancy are within a relatively small region from 0.04 to 0.08. Comparing the gains from 3 positions to those from the central data only, the result in Fig. 5.16 indicates that the RMS of the differences is only 1.8%.

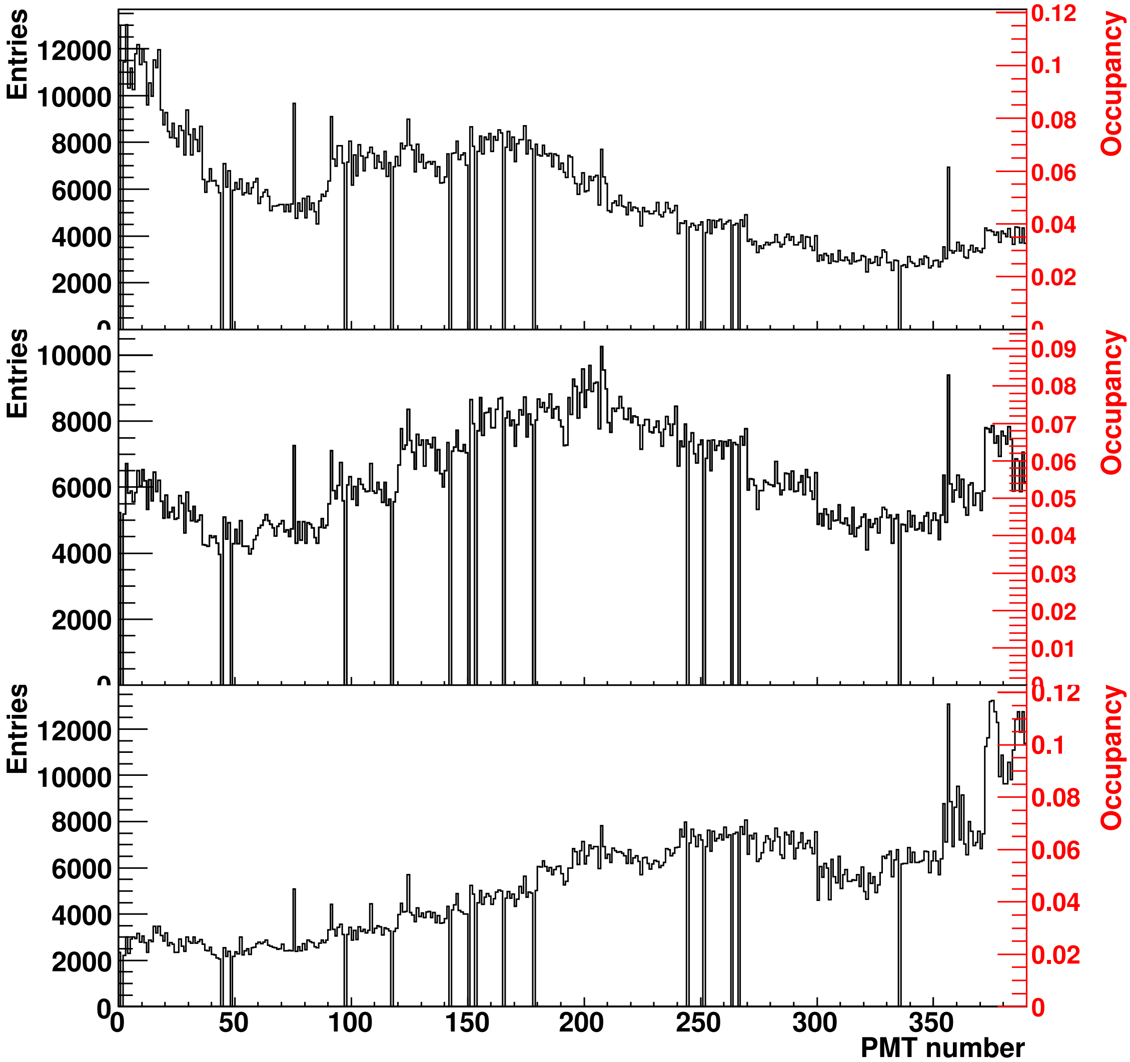

Figure 5.13: Total number of hits and occupancy versus PMT number for the UV laser calibration events deployed at $z = +92$ cm (top: run 43852), $z = 0$ (center: run 43798) and $z = -92$ cm (bottom: run 43808).

From the top panel of Fig. 5.17, the average value of 82.12 DUQ/PE for the distribution of histogram means is 12% higher than that from the fitted means as shown in the middle panel of Fig. 5.15, which might be an indication that some of the PMTs might have a non-Gaussian charge response. This average value of histogram means is only about 2.5% more than that of 79.99 DUQ/PE for that of the corrected means as shown in the bottom panel of Fig. 5.17, which in another way verifies that the laser data has a very high percentage of single PE hits.

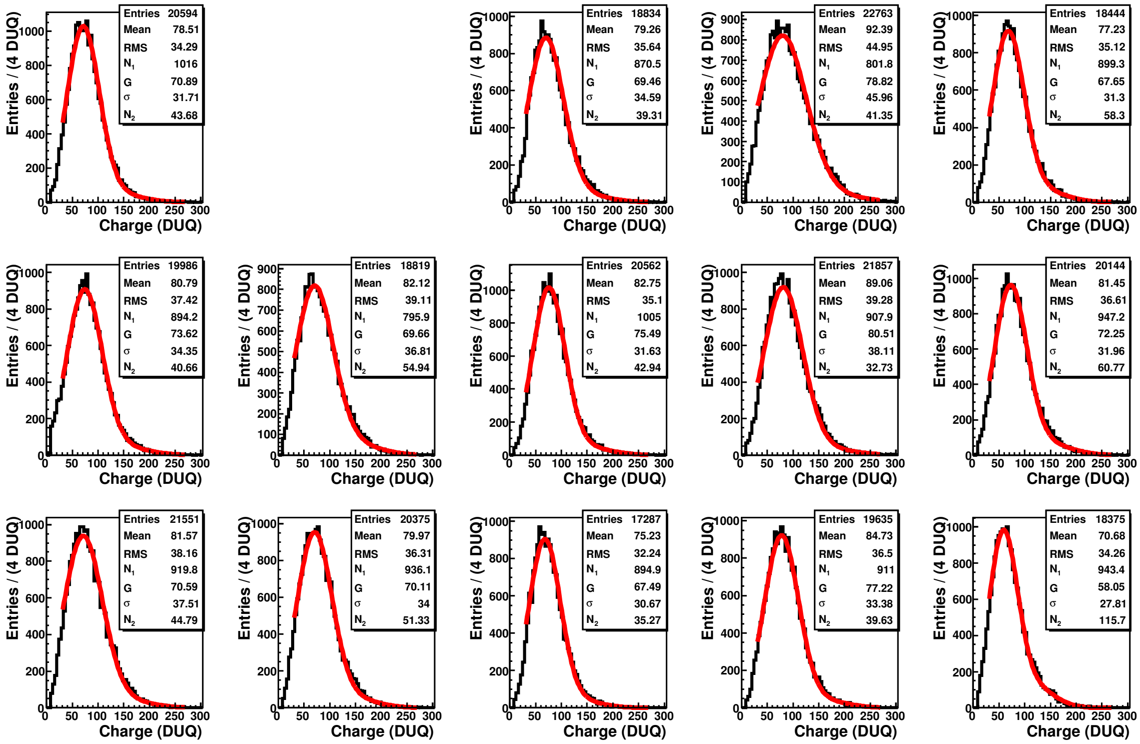

Figure 5.14: PMT 0–14 raw charge histograms fitted by the sum of two Gaussians. PMT number 1 is not active and thus the corresponding charge distribution is missing.

5.3.2 Further Investigation of the N_2/N_1 Ratio

We expected the ratios of the second PE contribution N_2 to the single PE contribution N_1 to be consistent with the theoretical values under the assumption of Possion distribution having 10% single PE inefficiency, $\epsilon_1 = 0.1$, as discussed later in the charge likelihoods analysis of Chapter 7. With the existence of a non-negligible single PE inefficiency, the predicted charge μ in Eq.(5.1) is no longer calculated as $-\ln(P_{nh})$ but as derived in Ref. [197] instead:

$$\mu = -\ln P_{nh}[1 + \epsilon_1 + \epsilon_1^2(1 + 0.5 \ln P_{nh}) + O(\epsilon_1^3)].$$

According to Poisson statistics,

$$\frac{N_2}{N_1} = \frac{\mu^2 e^{-\mu}}{2!} \frac{1}{\mu e^{-\mu}} = \frac{\mu}{2},$$

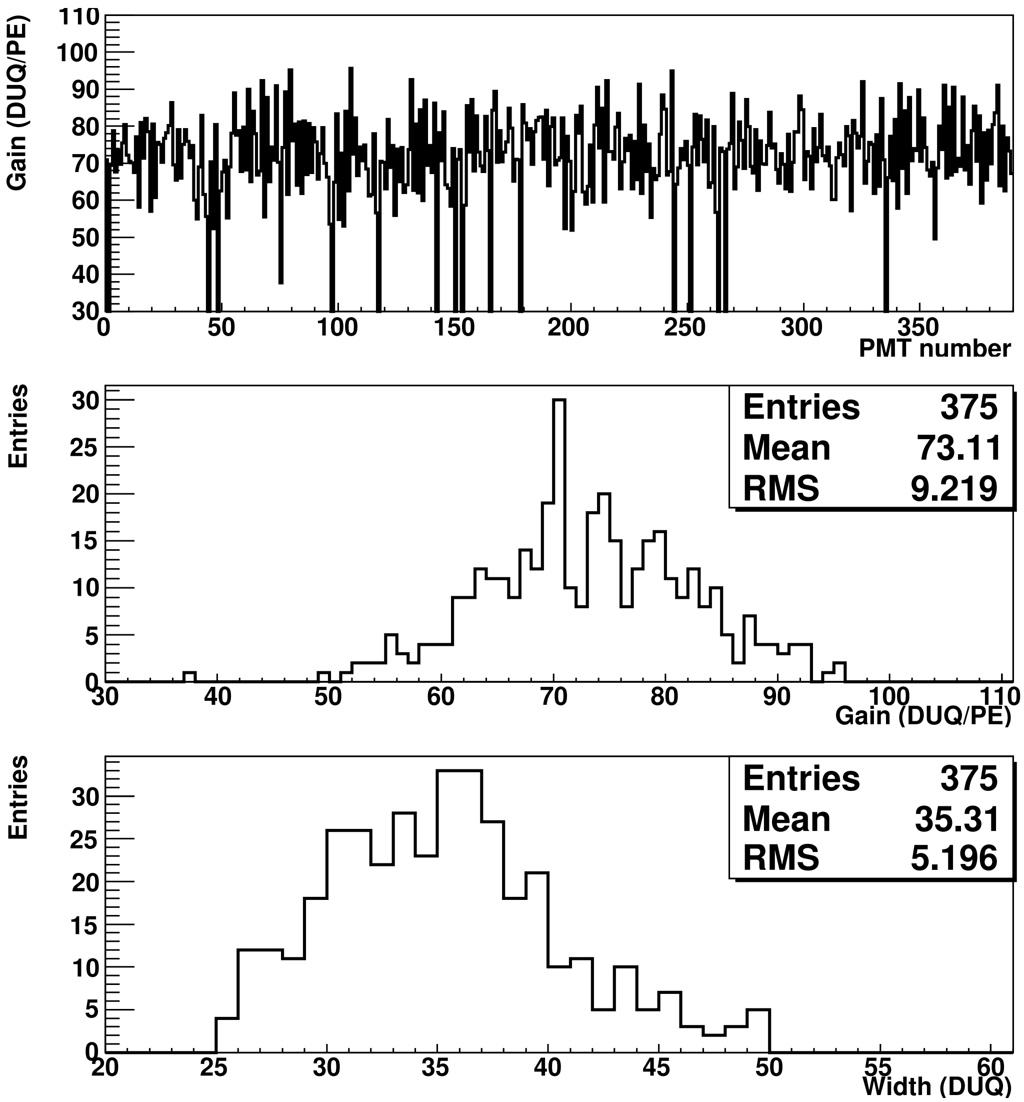

Figure 5.15: The fitted PMT gains for 390 PMTs (top), their projections (middle) and the fitted widths (bottom).

and with the $\epsilon_1 = 0.1$, N_1 becomes $N_1(1-10\%) = 9N_1/10$. The predicted N_2/N_1 becomes,

$$\frac{N_2}{N_1} = \frac{\mu}{2}\frac{10}{9} = \frac{5\mu}{9}.$$

Based on the above calculation, with an average $\mu = 0.065$ (calculated from the occupancies of 390 PMTs when the source is deployed at the center, using Eq.(5.3)), the average N_2/N_1 should now be approximately 0.036. By comparing the fitted N_2/N_1 ratios with the calculated ones, we found that most PMTs have consistent results; however, some PMTs

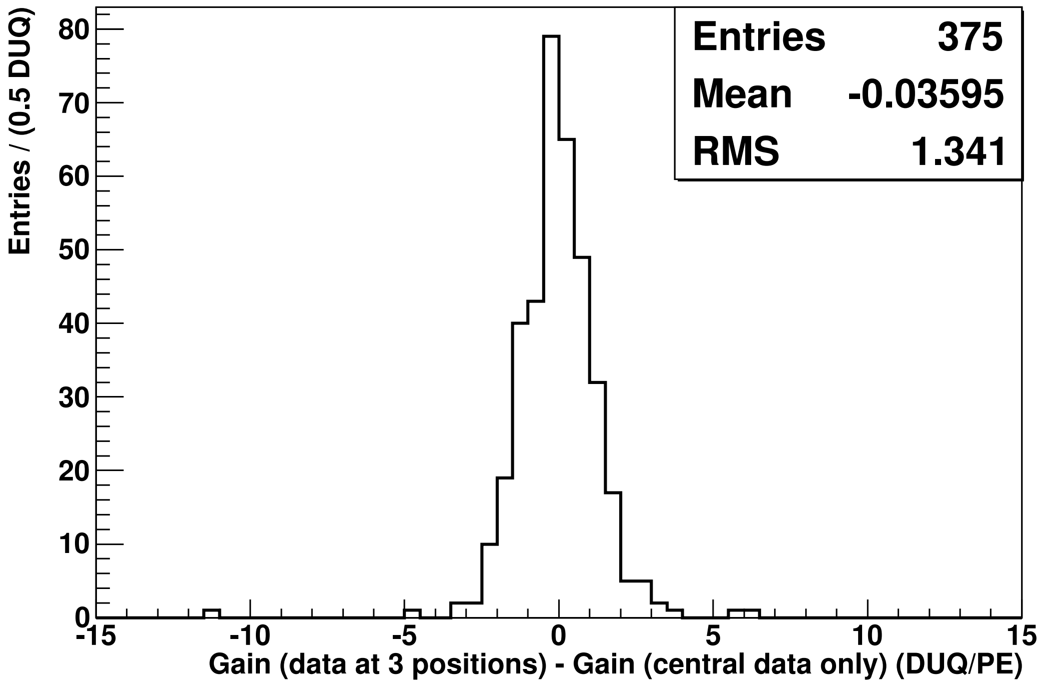

Figure 5.16: Comparison of gains derived by using data from all 3 positions to those from the central data only. The differences have a spread of $1.341/73.12 \approx 1.8\%$.

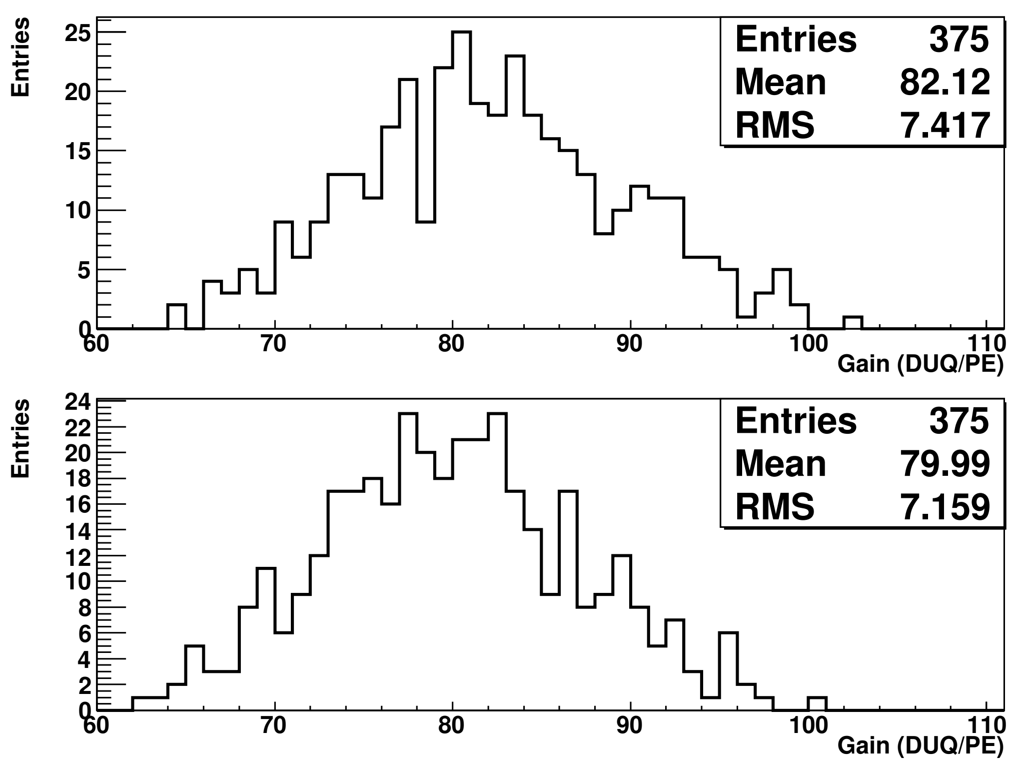

Figure 5.17: PMT gains obtained from the uncorrected charge distribution means (top) and corrected means (bottom) of the raw charge distribution.

have relatively large deviations. We grouped them into 3 categories as shown in Fig. 5.18, namely $N_2/N_1 < 2.5$, $2.5 \leq N_2/N_1 < 6$ (i.e., a high N_2/N_1 ratio), and $N_2/N_1 \geq 6$ (i.e., a very high N_2/N_1 ratio). One PMT from each group is shown in Fig. 5.19 to illustrate how the charge distributions and the corresponding fits look like. None of the fits appears to be particularly bad. In Fig. 5.20, the no-hit probability for these 3 groups of PMTs are shown versus the predicted charge, as obtained from the negative logarithm of the no-hit probability. Normally, this is expected to be a straight line with a unit slope. Deviations from unity typically give a measure of the single PE inefficiency. For the PMTs in the $0 < N_2/N_1 < 2.5$ region, their no-hit probability is similar to that of all PMTs, while the other 2 groups have a relatively higher non-hit probability. Nonetheless, the fitted no-hit probability values confirmed the single PE inefficiency to be consistent with approximately 10%, as observed in the charge likelihoods study in Chapter 7.

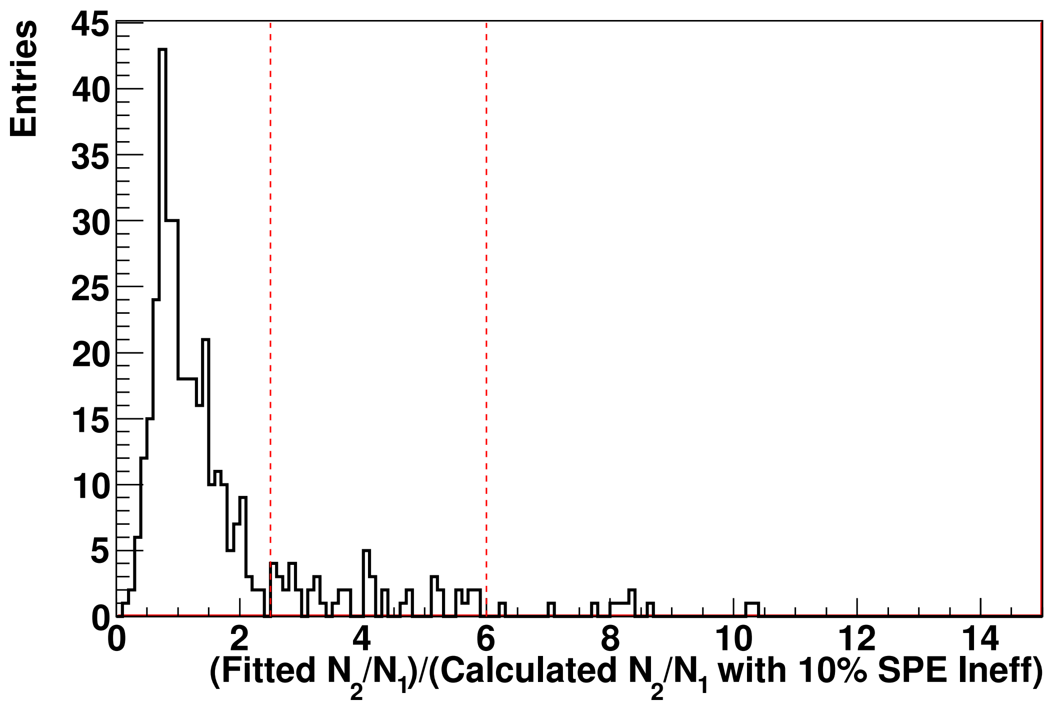

Figure 5.18: The ratios of fitted N_2/N_1 to calculated N_2/N_1 with 10% single PE inefficiency are categorized into 3 groups, as labeled by the vertical dashed lines.

If a PMT charge distribution is purely Gaussian-like, one would see a normal N_2/N_1 ratio,

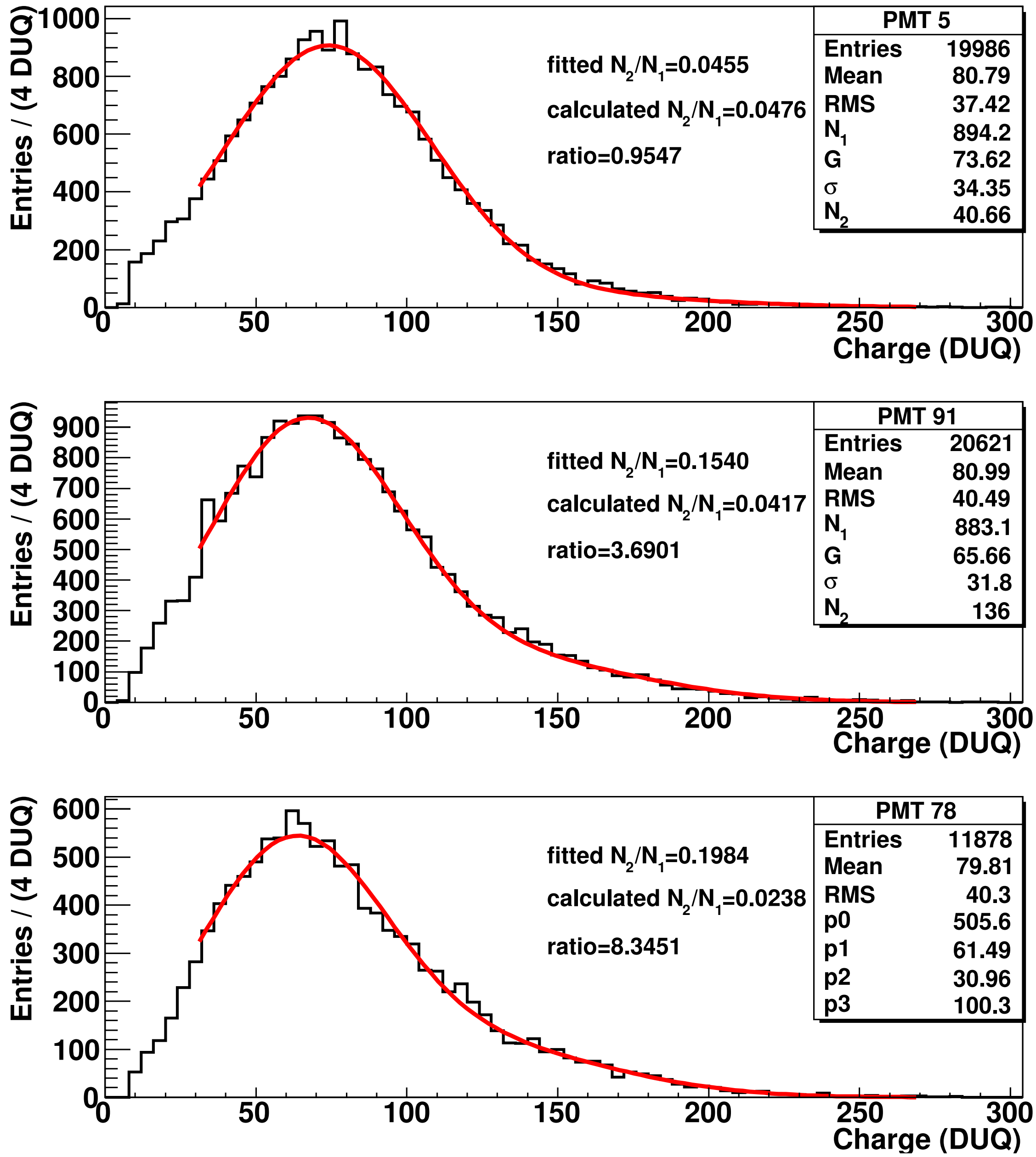

Figure 5.19: Three fitting examples of PMTs from 3 groups categorized in Fig. 5.18.

and one would take the fitted mean as the gain. The abnormal N_2/N_1 ratio indicates that the charge distributions of those PMTs may substantially deviate from a Gaussian. In such cases, the fitted means might no longer be a good representation of the gains. If so, we should take the means of the histograms as gains. To decide which set of gains works better, we compared the energy resolutions for ^{252}Cf neutron capture peak on hydrogen and gadolinium by using

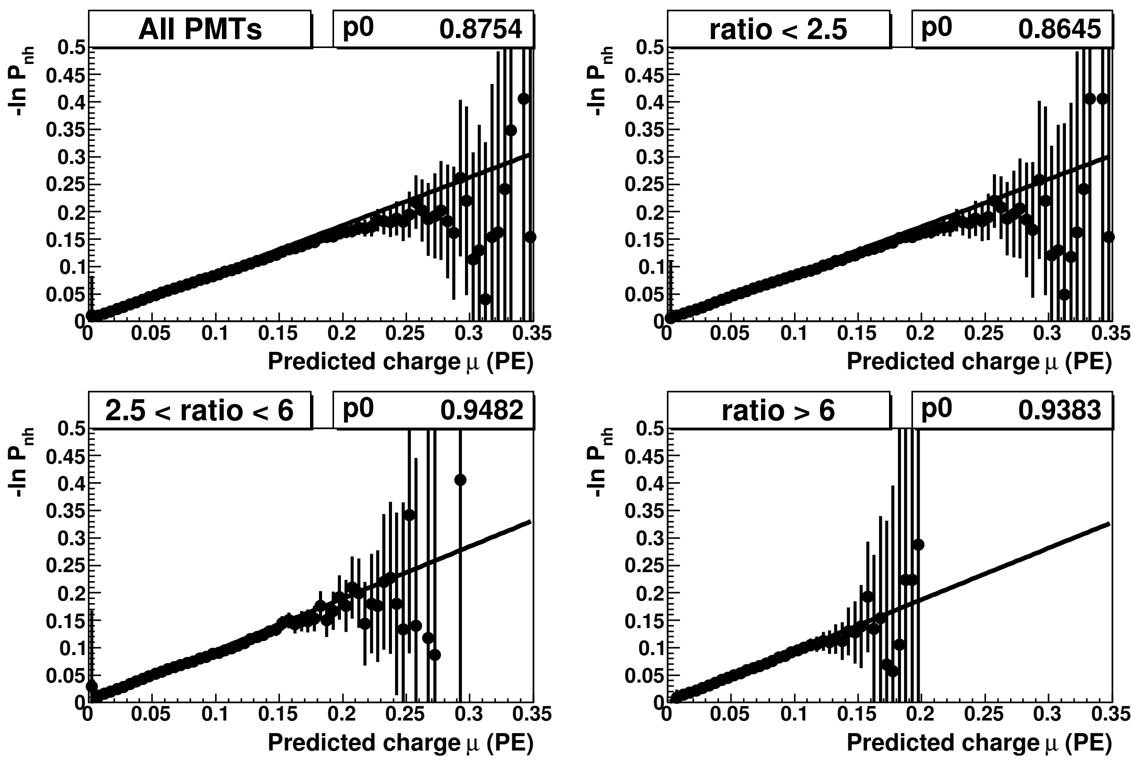

Figure 5.20: No-hit probability for all PMTs (top left) and for the PMTs in the groups as categorized graphically by the N_2/N_1 ratio in Fig. 5.18.

different sets of gains including fitted gains, histogram mean gains, and linearized PE gains. The linearized gains are calibrated from the IDLI calibration data. They are introduced to deal with the non-linear charge responses in the electronics, which appear when the PMT charges are below about 3 PEs. A linearized gain is composed of a constant gain (for high value of charge), and a linearly-varying gain below 200 DUQ (approximately 3 PEs, some PMTs have positive slopes while some have negative ones). The energy spectra for ^{252}Cf neutron capture peak on hydrogen and gadolinium are in Figs. 5.21 and 5.22 respectively, showing that the energy resolutions at these energies are largely insensitive to which set of gains is used.

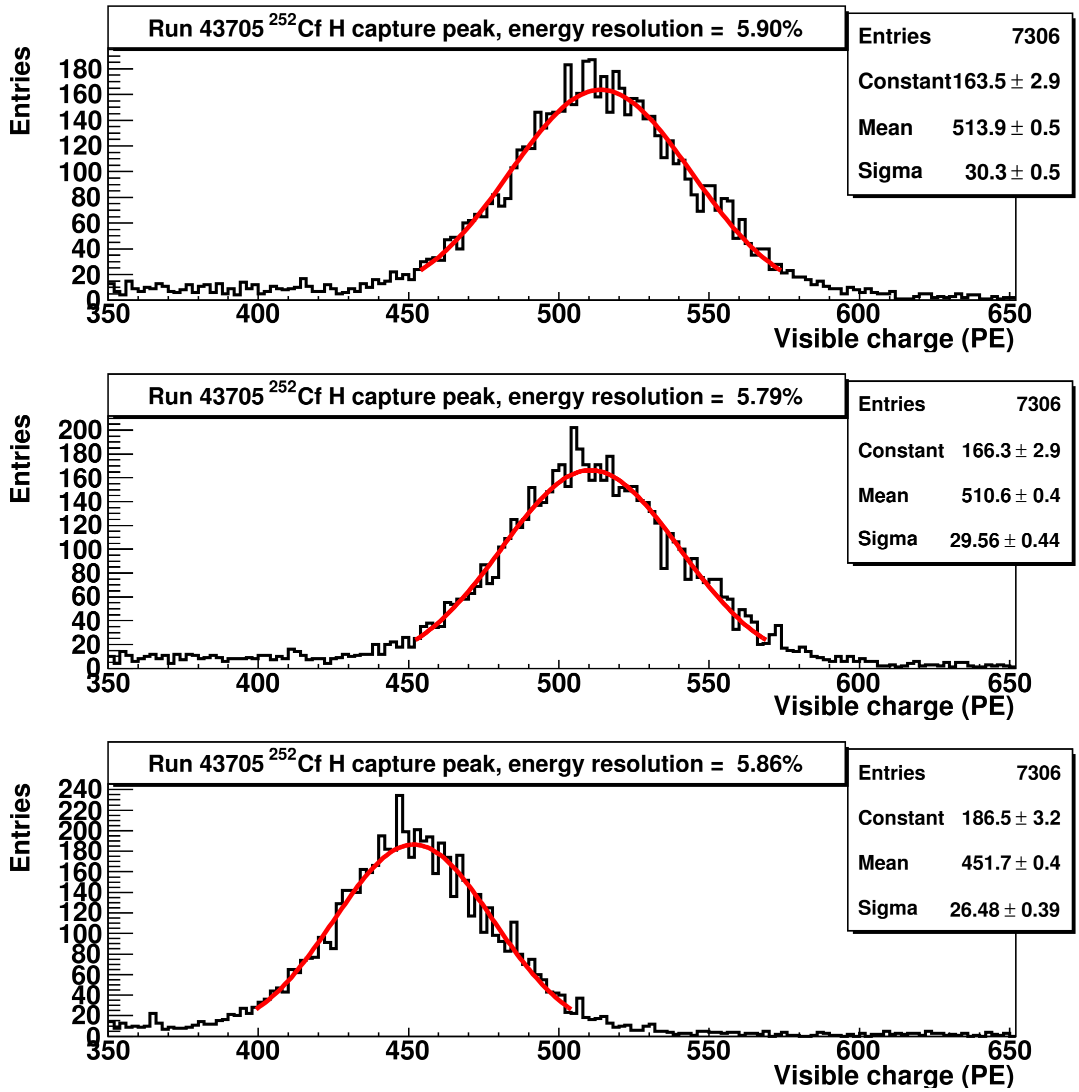

Figure 5.21: Energy resolution obtained from the visible charge distribution for the 2.2 MeV γ from the neutron capture peak on hydrogen of a ^{252}Cf source deployed at $z = 0$ using the stardard IDLI linearized PE gains (top), fitted gains (middle), and histogram mean gains (bottom).

5.4 Conclusion

The UV Laser PMT gains calibration is expected to be the most precise gains calibration for its capability to produce high percentage of single PE level hits at the PMTs. However, the instability of PMT gains over time (caused by power cycles) makes it practically unusable, as deployment operations are typically performed only once a year. The laser calibrated fitted

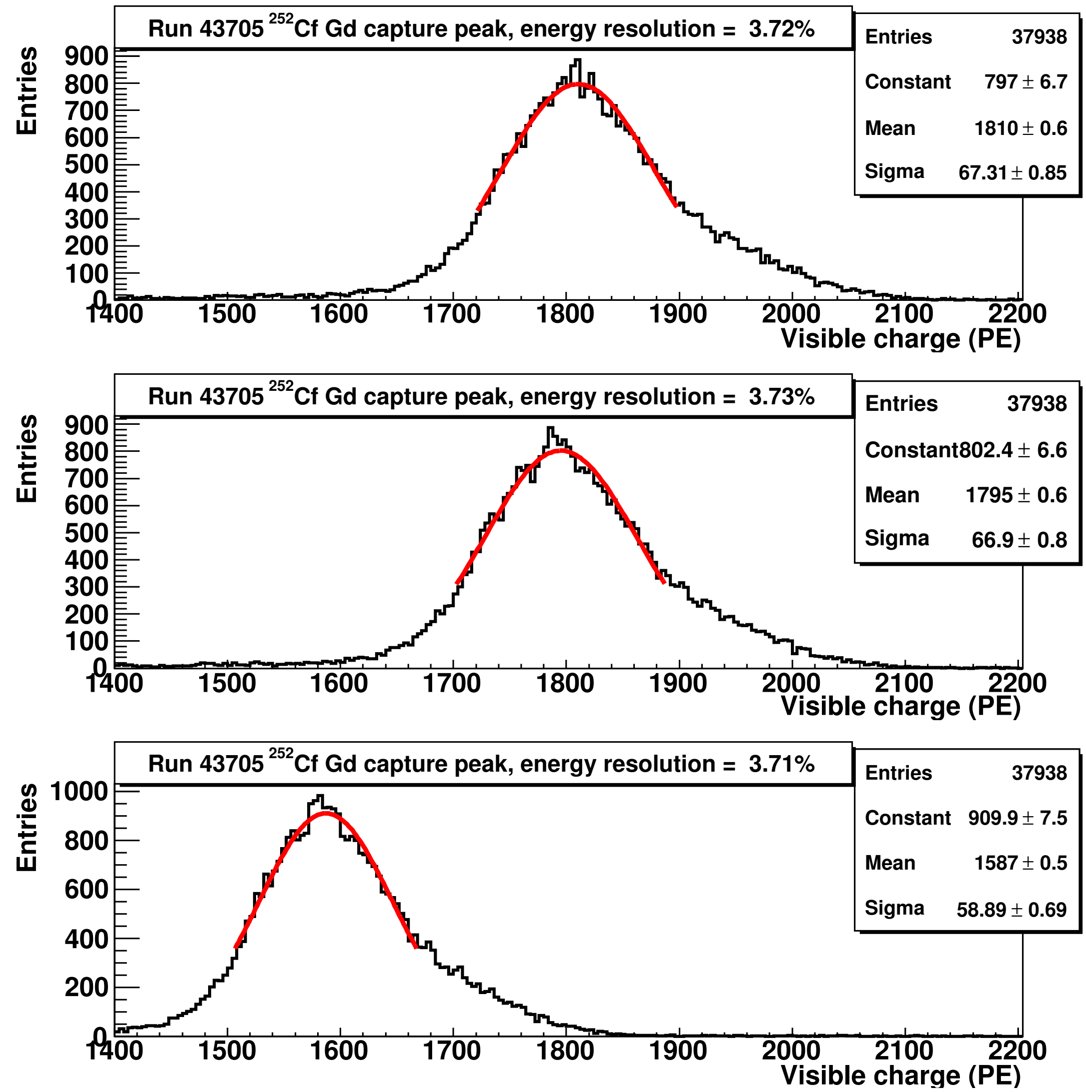

Figure 5.22: Energy resolution obtained from the visible charge distribution for the 8 MeV neutron capture peak on gadolinium of a ^{252}Cf source deployed at $z = 0$ using the stardard IDLI linearized PE gains (top), fitted gains (middle), and histogram mean gains (bottom).

gains confirmed the values which had been used in the Double Chooz first publication [102] as obtained from the IDLI system. Most of the PMTs have a Gaussian-like charge response, while a small fraction (approximately 16%) do not. After tests of the energy resolution for the ^{252}Cf neutron capture peaks on hydrogen and gadolinium, the performance of laser calibrated gains (fitted and mean) and linearized gains from the IDLI calibration show similar results.

Chapter 6

Time Offsets Calibration

6.1 Introduction

The PMT time offset is defined by the time elapsed between the incidence of a photon on the photocathode of the PMT and the time stamp of the associated signal. This delay depends on the PMT signal transit time, the length of the cable, the front-end electronics response time, and the pulse threshold. The relevant time constants are initially determined prior to installation; however, slight changes are possible after installation due to temperature changes, stressing of cables during transport/deployment, etc. The PMT time offsets play an essential role in the position reconstruction accuracy. The calibrated PMT time offsets are normalized such that $\sum t_i^{off} = 0$, where the index i goes over all the inner detector PMTs. Any overall shift would be irrelevant as it can be absorbed into a corresponding shift in the event time.

The blue (λ = 470 nm) laser is used for this calibration because this wavelength does not excite the scintillator. Therefore, the short pulses of light (of about 50–70 ps) generated by the laser maintain their width as they propagate through the optical media. If a PMT is hit by more than one PE, typically the earliest arrival time will be recorded as the PMT time, which introduces a so-called time slewing effect. The magnitude of the time slewing depends not only on the magnitude of the charge, but also on the width of PMT time distribution. Therefore, even if one goes to high levels of light, where time slewing effects become independent of the PMT charge, one may still have small variations on a PMT-by-PMT basis. The alternative is to choose a low intensity that leads to a high percentage of single PE hits, which minimizes the time slewing effect to a negligible level. However, if the intensity is too low, there will not be enough hits in the events, which in turn decreases the accuracy of the reconstructed event time in the absence of a reference timing signal. To balance them, we chose an intensity that gives approximately 30 hits/event. Normally, the procedure for determining the time offsets needs a reference time; our approach obtains the event time self-consistently, and demonstrates the feasibility of such an approach.

The PMT time offsets analysis procedure developed here needs data from 2 positions: a central one ($z = 0$) and an off-center position, as described in more detail in Section 6.2. The central data is used to determine the time offsets for a given value of the speed of light, c_n, while the off-center data is used for the c_n determination. In Section 6.3, I will introduce the features of the analysis software, the test run, and *data challenge* results all based on MC simulations. The calibration data analysis will be discussed in Section 6.4. I will refer to the analysis using the combination of central ($z = 0$) and top ($z = +92$ cm) data as CTR+TOP while the combination of central and bottom ($z = -92$ cm) data as CTR+BTM in the following discussion. Considering that the central and top data were taken during the same deployment, where the relative distance should be more reliable than CTR+BTM, the result from the CTR+TOP analysis is taken to be the standard. The CTR+BTM result is used for consistency checks. Additional cross checks from higher intensity blue laser runs are also discussed in Section 6.4. A summary of the PMT time offsets calibration results is given in Section 6.5.

6.2 Procedure

The procedure to extract the PMT time offsets also provides an in-situ measurement of the speed of light at this wavelength ($\lambda = 470$ nm). We initially have no knowledge about the

PMT time offsets which are accordingly initialized to 0, and the speed of light c_n is given a reasonable starting value of $c_n = 20$ cm/ns. The PMT corrected time at the i^{th} PMT is defined as the measured PMT time, t_i, minus the (unknown) event time, t_0, and the photon propagation time, r_i/c_n,

$$t_{corr,i} = t_i - t_0 - \frac{r_i}{c_n}, \tag{6.1}$$

where r_i is the distance from the vertex to the PMT, and c_n is the effective speed of light in the medium. We call c_n the effective speed of light because the Double Chooz inner detector does not consist of a homogeneous medium for light propagation. The reason why we can use an effective speed of light is because the refraction indexes among the three media, the neutrino target, gamma catcher and buffer, as well as the acrylic vessels are supposed to be closely matched with small differences.

The algorithm is based on a time-likelihood only determination of the event time for a fixed vertex position (i.e., the depolyment position). We first start with the events at the detector center and use the negative logarithm of the corrected time distributions as time likelihood lookup tables to determine the event time in the next iteration. Meanwhile, the new event times will build up new corrected time distributions. In each iteration, the fitted peak of the corrected time on each PMT becomes the time offset for the next iteration. The procedure repeats until all the time offsets converge.

Next, we are going to use the obtained time offsets, time likelihood lookup tables with the data from the off-center position to determine c_n. We fill the corrected time histograms for each ring without subtracting the propagation time. We fit the distributions and plot the fitted peaks versus distances from the vertex to the corresponding rings. The inverse slope becomes the speed of light for the next iteration. The entire procedure is repeated until both the time offsets and c_n converge.

There are four control parameters in the analysis software:

1. *PMT statistics*: total number of hits in a PMT; failing to meet this requirement, the PMT will not be analyzed or used for determining the c_n; default = 1,000.

2. *Ring statistics*: total number of average hits in a ring of PMT; decides whether or not we will use the ring in determining c_n; default = 1,000.

3. *Occupancy*: hit rate (ratio of the number of hit events to the number of total events); high occupancy will make the PMT or the ring unusable during different processes; default = 0.15.

4. c_n: initial value for the effective speed of light; default = 20 cm/ns.

6.3 Monte Carlo Simulation

To test our software, laser MC events at $\lambda = 470$ nm with 1,000 photons/event were simulated at three positions of $z = 0$ and ± 90 cm. The events average 31.8 hits for $z = +90$ cm (20,000 events), 31.1 hits for $z = 0$ (30,000 events), and 30.8 hits for $z = -90$ cm (20,000 events).

The main peak of the PMT corrected time distributions can be well fitted by a Gaussian, as shown in Fig. 6.1 for a particular PMT. The second peak caused by light reflections on the buffer wall, could only produce a negligible small effect, and is therefore ignored in generating the time likelihoods. As a general starting point for 390 PMTs, we used the negative logarithm of a Gaussian with a mean value at 0 (i.e., all initial time offsets are zero) and a width of 1 ns. The procedure for deciding when the PMT time offsets iteration terminates is when the RMS of those time offsets differ between the current and the previous iterations by less than 0.015 ns. The entire procedure stops when the change in c_n is smaller than 0.01 cm/ns. In this test, the PMT and ring statistics were set to 1,100 and 1,200 respectively. The occupancy was kept at the default value and the c_n started at 19.81 cm/ns instead of the default value for a test only.

The result of PMT time offsets using the combination of CTR+BTM is shown in the top panel of Fig. 6.2. Since the truth values of the PMT time offsets are identically 0, the projection of calibrated PMT time offsets is also the comparison. This yields an error of 0.214 ns. The overall performance is more or less limited by the 2 ns time digitization, which in turn is determined by the 500 MHz sampling rate of the readout electronics. This is why

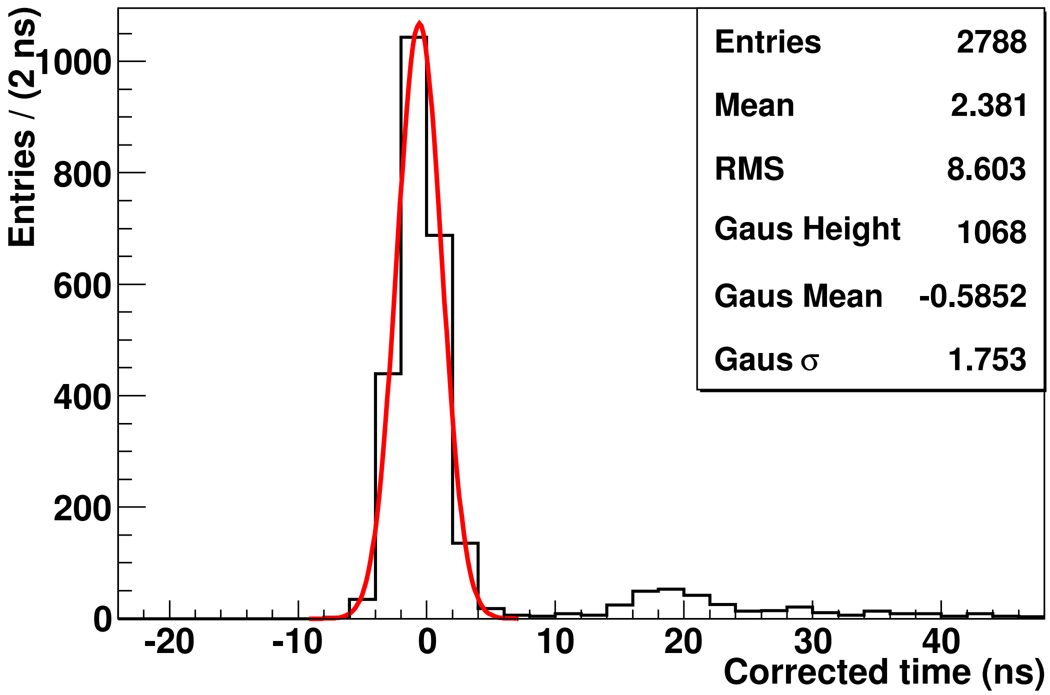

Figure 6.1: MC corrected time distribution of PMT 0 fitted to a Gaussian (source at $z = 0$, all input time offsets are 0). The second peak is casued by light reflection off the buffer wall.

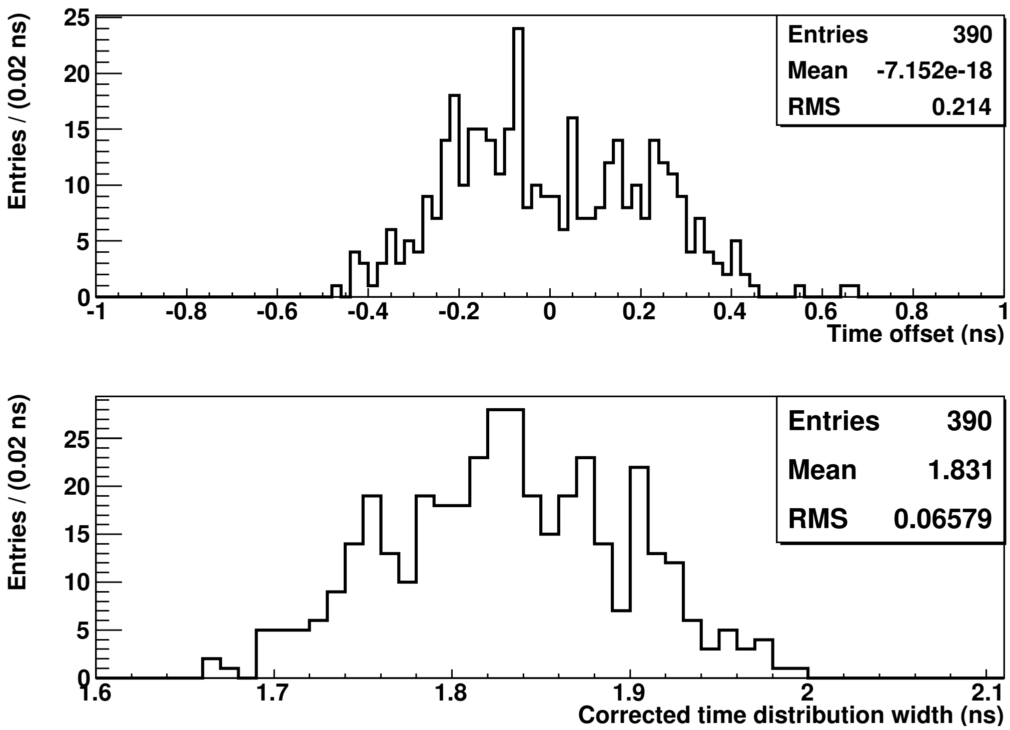

Figure 6.2: The resulting time offsets (top) for identically vanishing input time offsets and the corrected time widths (bottom) for all 390 PMTs which determined the final set of time likelihood lookup tables (MC data).

the corrected time distribution in Fig. 6.1 has a bin size of 2 ns. A finer bin size would result in a discrete distribution. The result of the PMT corrected time distribution width is shown in the bottom panel of Fig. 6.2, which is in good agreement with all PMTs being identical. The final value of the speed of light c_n at $\lambda = 470$ nm can be read from Fig. 6.3 to yield $c_n = 19.54$ cm/ns. Another two test runs with c_n starting from extreme values (10 cm/ns or 30 cm/ns) converge to the same result for both the PMT time offsets and c_n within 7 overall iterations. This demonstrates that our approach does not depend on the input starting values.

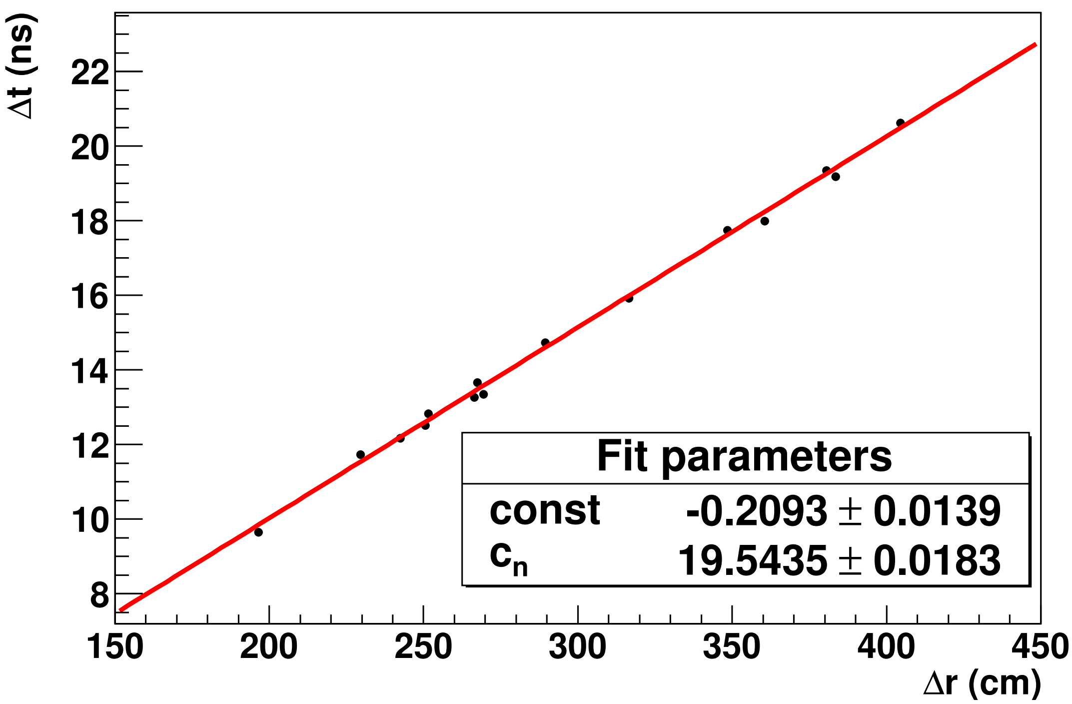

Figure 6.3: The speed of light c_n from the linear fit on Δr and Δt using the CTR+BTM combination. The error bars are too small to be seen as they are masked by the markers themselves.

6.3.1 Data Challenge

The MC calibration data for the *data challenge* was generated with random input PMT time offsets (according to the spread in the distribution of the actual time offsets in the MiniBooNE experiment) with an average of 10 ns and a width of 2.75 ns. The overall shift of 10 ns was introduced on purpose in this exercise. A total of 30,000 events were simulated at each of the three positions of $z = 0$ and ± 90 cm. In this exercise, all the parameters in the software were set to the default values. The comparison between the calculated and generated time offsets is shown in Fig. 6.4. Here we have shifted the distribution by 10 ns since the time offsets result is normalized such that $\sum t_i^{off} = 0$ and the overall shift is irrelevant (as discussed in Section 6.1). The time offsets are determined here with an error of 0.15 ns.

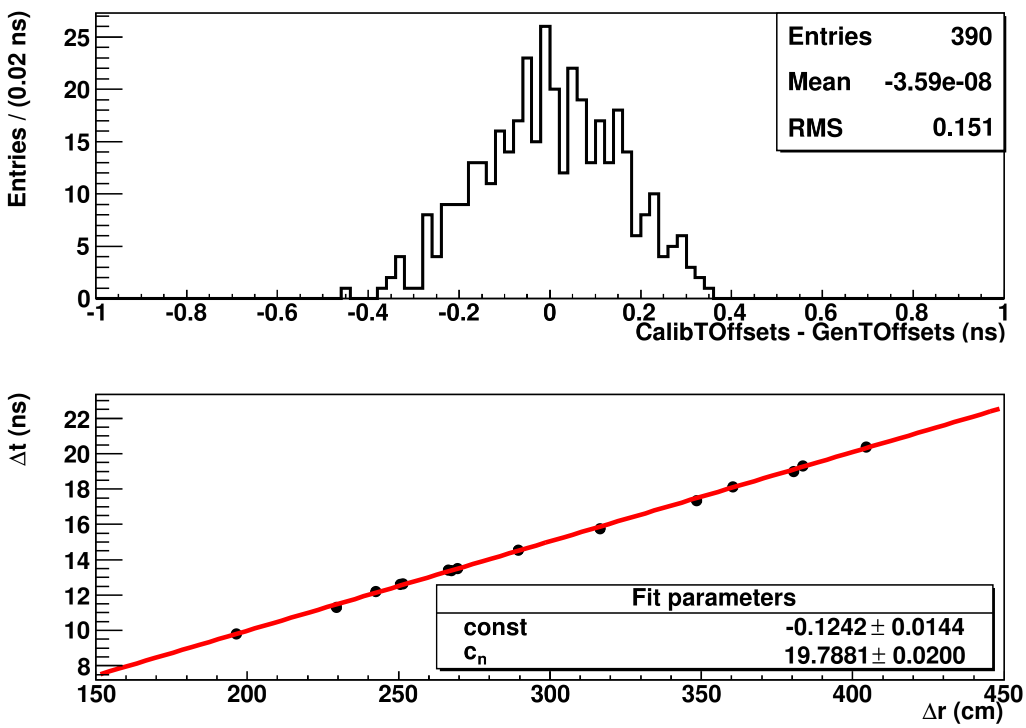

Figure 6.4: Difference between calibrated and generated time offsets (top) and the final iteration speed of light from the linear fit by using the CTR+TOP combination (bottom) in the *data challenge*. The error bars in the bottom plot are masked by the markers.

6.4 Data Analysis

6.4.1 Analysis

The $\lambda = 470$ nm laser data for PMT time offsets calibration were taken on June 13–14, 2012 during the same calibration deployments used for the gains and the charge likelihoods. Similarly to the UV laser diffuser, the blue laser diffuser was deployed at 3 positions, namely $z = -92$ cm (run number 45609), $z = 0$ cm (45634), and $z = +92$ cm (45636). Each run was taken for 750 s at a frequency of 150 Hz and thus should contain about 112,500 events. The run information and the corresponding selection criteria applied for the time offset analysis are shown in Table 6.1. Figure 6.5 shows the two analysis cuts on run 45634. Figure 6.6 shows the single PE hit probability for each PMT calculated based on Possion statistics.

Run #	z (cm)	Average Nhits	Q_{max}/Q_{tot}	Q_{tot} (DUQ)	Total events	Trigger events	Selected events
45609	−92	30.6	< 0.2	(1k, 5k)	114,697	113,205	112,379
45634	0	31.6	< 0.2	(1k, 5k)	114,700	113,208	112,785
45636	92	33.7	< 0.2	(1k, 5.5k)	114,541	113,051	112,446

Table 6.1: Run numbers, positions, average multiplicities and selection criteria as well as total number of events, laser triggered events and selected events after the light noise cut and total charge cut for the $\lambda = 470$ nm laser data for PMT time offsets calibration. All 3 runs are very close to the target multiplicity which is 30 hits/event.

The total statistics for all three positions are about 4 times more than those in MC, which accordingly fulfill the requirement of 1,000 lowest number of entries. The speed of light, c_n, was initialized to 20 cm/ns. Because of the variation of PMT quantum efficiencies, it is relatively difficult to draw a rigid line for the occupancy limit. A value of 0.22 was given so that all the entries are usable. The red dashed lines label the lower limit of the P_1/P_{hit} as shown in Fig. 6.6, which is translated from the occupancy upper limit of 0.22,

$$\frac{P_1}{P_{hit}} = \frac{\mu e^{-\mu}}{1 - e^{-\mu}} = \frac{-\ln(1 - 0.22) \times (1 - 0.22)}{0.22} \approx 0.88.$$

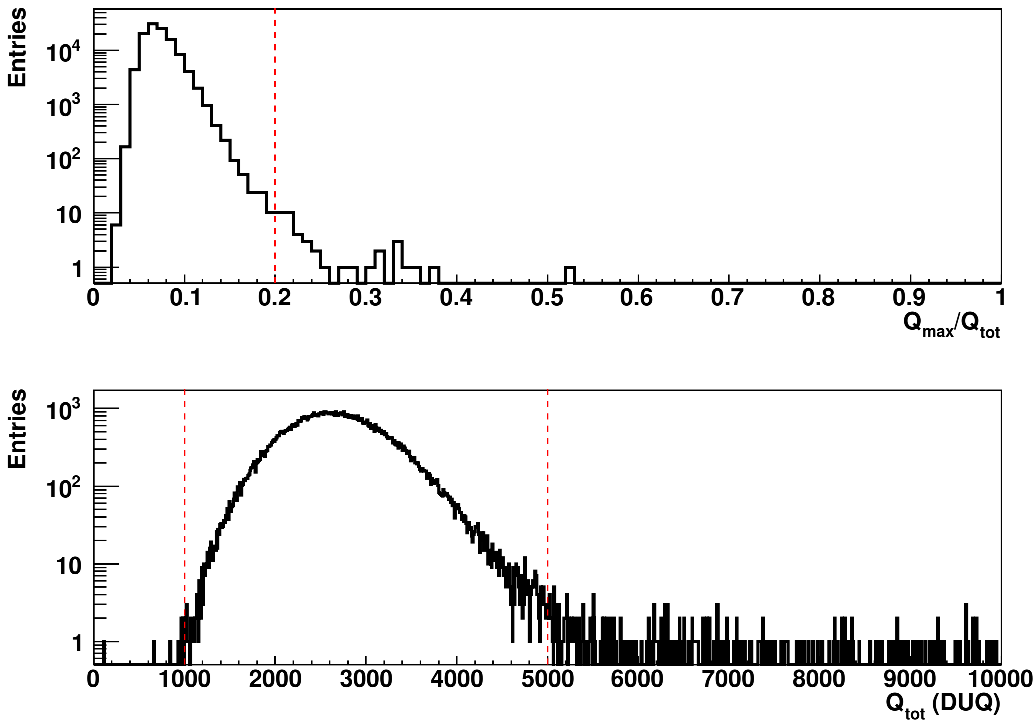

Figure 6.5: Illustration of the two analysis cuts: $Q_{max}/Q_{tot} < 0.2$ and $1{,}000 < Q_{tot} < 5{,}000$ DUQ for the central $\lambda = 470$ nm laser run 45634.

We first fitted the corrected time distribution to the functional form below:

$$f(x) = P_1 \exp\left[P_3 (P_0 - x) + P_3^2 P_2^2/2\right] \left[1 - \mathrm{Erf}\left(\frac{P_2 P_3}{\sqrt{2}} + \frac{P_0 - x}{\sqrt{2} P_2}\right)\right]$$
$$+ P_4 + P_5 \exp\left\{-0.5 \left[(x - P_0 - P_6)/P_7\right]^2\right\} + P_8 \exp\left\{-0.5 \left[(x - P_0 - P_9)/P_{10}\right]^2\right\},$$

which consists of one exponentially-modified Gaussian (i.e., a Gaussian convoluted with an exponential), a constant and another two Gaussians. The quality of the fit was not satisfactory, especially on the second peak, as one example of PMT 0 is shown in the top panel of Fig. 6.7. After carefully examining the shape of the PMT corrected time distributions, it turned out that the buffer reflections contributes much more than that in the MC studies. The corrected time distributions also suggest that the $\lambda = 470$ nm light may excite the scintillator to some extent. This effect cannot be ignored in the data. Consequently, we changed the fitting function to the one in Eq. (6.2) with 15 parameters, which is now composed of two exponentially-modified Gaussians, a constant and another two Gaussians.

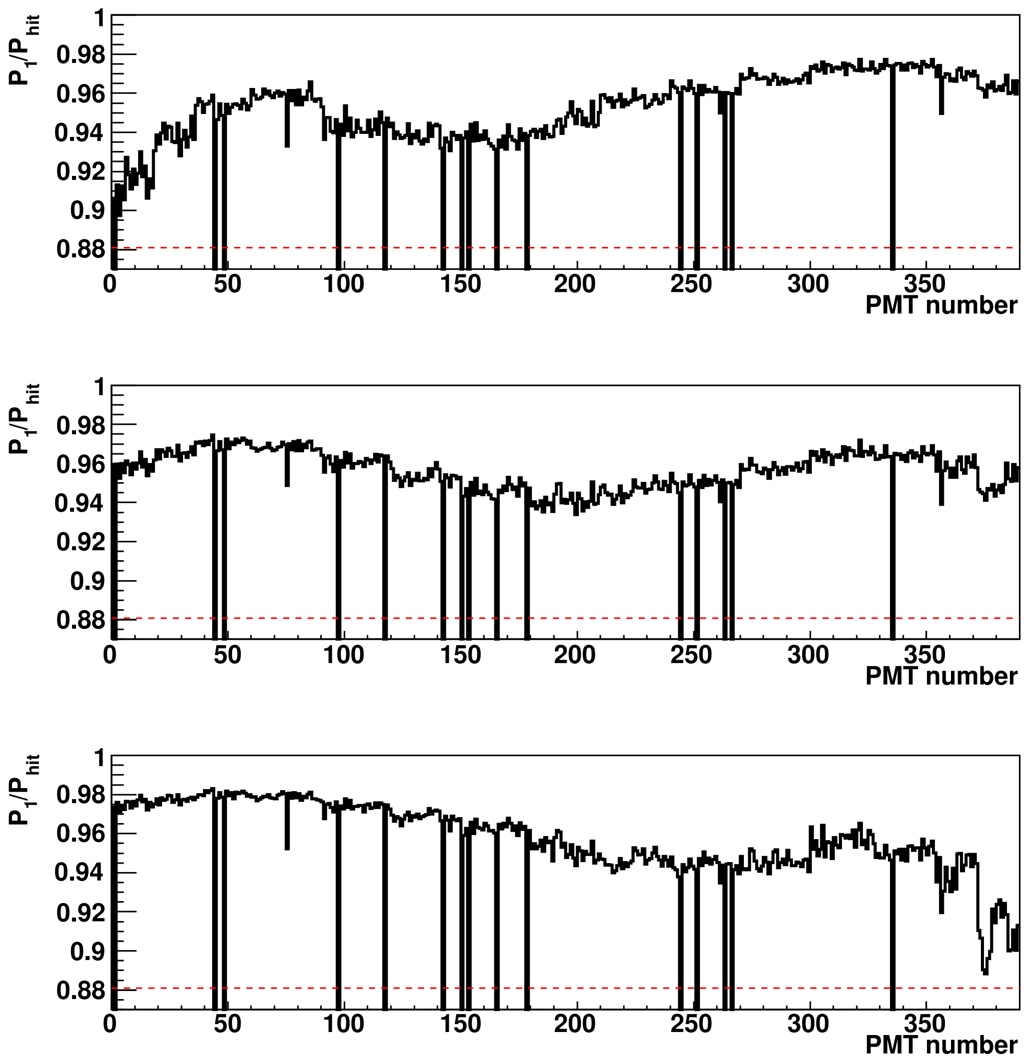

Figure 6.6: PMTs' single PE hit probabilities for blue laser calibration events deployed at $z = +92$ cm (top), $z = 0$ (center) and $z = -92$ cm (bottom). The red dashed lines label the lower limit of P_1/P_{hit} rate, translated from the occupancy upper limit of 0.22.

The two exponentially-modified Gaussians mainly take care of the main peak and second peak. The other two Gaussians cover the third peak and give a complementary fit to the second peak, whose shape is rather complicated in some cases. The constant represents the noise. This functional form gives a good quality of the fit to PMT 0 (as well as the rest of PMTs), as the same example of PMT 0 is shown in the bottom panel of Fig. 6.7. The

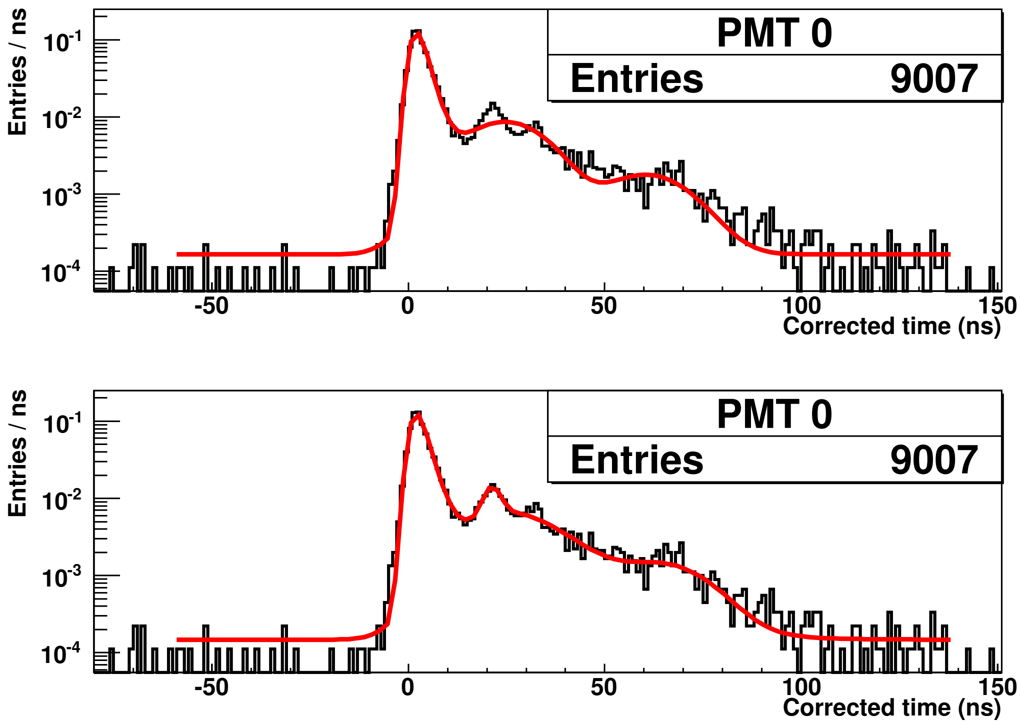

Figure 6.7: Corrected time distributions for PMT 0 is fitted to the trial functional form (top) and the form in Eq. (6.2) (bottom) using data from run 45634 with the diffuser deployed at the center.

explicit functional form is given below:

$$
\begin{aligned}
f(x) = P_5 \Bigg\{ & P_6 \exp\left[P_3 \left(P_0 - x\right) + P_3^2 P_2^2/2\right] \left[1 - \mathrm{Erf}\left(\frac{P_2 P_3}{\sqrt{2}} + \frac{P_0 - x}{\sqrt{2} P_2}\right)\right] \\
& + \left(1 - P_6\right) \exp\left[P_4 \left(P_1 + P_0 - x\right) + P_4^2 P_8^2/2\right] \left[1 - \mathrm{Erf}\left(\frac{P_8 P_4}{\sqrt{2}} + \frac{P_1 + P_0 - x}{\sqrt{2} P_8}\right)\right]\Bigg\} \\
& + P_7 + P_9 \exp\left\{-0.5 \left[\left(x - P_0 - P_{10}\right)/P_{11}\right]^2\right\} + P_{12} \exp\left\{-0.5 \left[\left(x - P_0 - P_{13}\right)/P_{14}\right]^2\right\},
\end{aligned}
\tag{6.2}
$$

where x represents the corrected time. The meaning of the parameters P_0–P_{14} in Eq.(6.2) above are listed in Table 6.2.

The PMT time offsets started from the IDLI calibrated time offsets and the corrected time lookup tables started with a general set of parameters, giving the best fit to corrected times of all 375 active PMTs. The corrected time distributions were fitted over a finite range (16 ns after the earliest time and 16 ns before the latest time) and the parameter P_0 became

P_0	1st exponentially-modified Gaussian's position
P_1	2nd exponentially-modified Gaussian's position (relative to P_0)
P_2	1st exponentially-modified Gaussian's σ_1
P_3	1st exponentially-modified Gaussian's τ_1
P_4	2nd exponentially-modified Gaussian's τ_2
P_5	Magnitude of the two exponentially-modified Gaussians
P_6	Relative magnitude of 1st exponentially-modified Gaussian
P_7	Noise
P_8	2nd exponentially-modified Gaussian's σ_2
P_9	1st Gaussian's magnitude
P_{10}	1st Gaussian's position (relative to P_0)
P_{11}	1st Gaussian's σ
P_{12}	2nd Gaussian's magnitude
P_{13}	2nd Gaussian's position (relative to P_0)
P_{14}	2nd Gaussian's σ

Table 6.2: Description of parameters in the fitting function in Eq.(6.2).

the time offset for the next iteration. The procedure was repeated until the parameters P_0 and P_2 converged. For the stopping criteria, we require the spread in the changes of time offsets (the parameter P_0) and their widths (the parameter P_2), be both smaller than 0.05 ns.

Next, we were going to obtain the event time, t_0, and thereby the PMT corrected time distributions for top vertex. Due to the existence of reflection, the time likelihood lookup tables for central data were no longer valid. A new set of lookup tables and corrected time distributions can be self-consistently obtained for the top vertex. The rest of the procedure was the same as in MC. The inverse slope of the (Δt, Δr) plot gave the speed of light for the next iteration until its change was smaller than 0.1% of the current speed of light. Here a slight modification was made. The old stopping criterion was 0.01 cm/ns. The new one roughly corresponded to 0.02 cm/ns (assuming the speed of light is around 20 cm/ns) only because getting lookup tables for the top vertex prolonged the procedure. The new criterion could reduce 1 or 2 iterations with satisfactory precision. Since the top and central data were taken in the same deployment and the bottom data was taken in a separate deployment (the day before), the center-top distance is more reliable compared to the distance between the center and bottom. Therefore, CTR+TOP is treated as the standard calibration result, while CTR+BTM works as a consistency check. It took two iterations for the time offsets to converge and another three routine iterations (two iterations for getting a set of stable time lookup tables for the top vertex, and another 1 iteration for calculating the event times of the top vertex) in getting the speed of light, c_n. There were two such overall iterations of the above procedure for c_n to converge. The entire running time of the program took approximately one full day.

The result of CTR+TOP (standard) laser calibrated PMT time offsets are compared with those obtained from the IDLI data, as shown in Fig. 6.8. As demonstrated in MC studies, the IDLI calibrated time offsets have an error of one half nanosecond [198], which agrees with the distribution width in Fig. 6.8. The speed of light c_n is determined to be 20.095 ± 0.017 cm/ns, as shown in Fig. 6.9. The error is only from the fit function, which in turn reflects the errors in the individual corrected times in each ring.

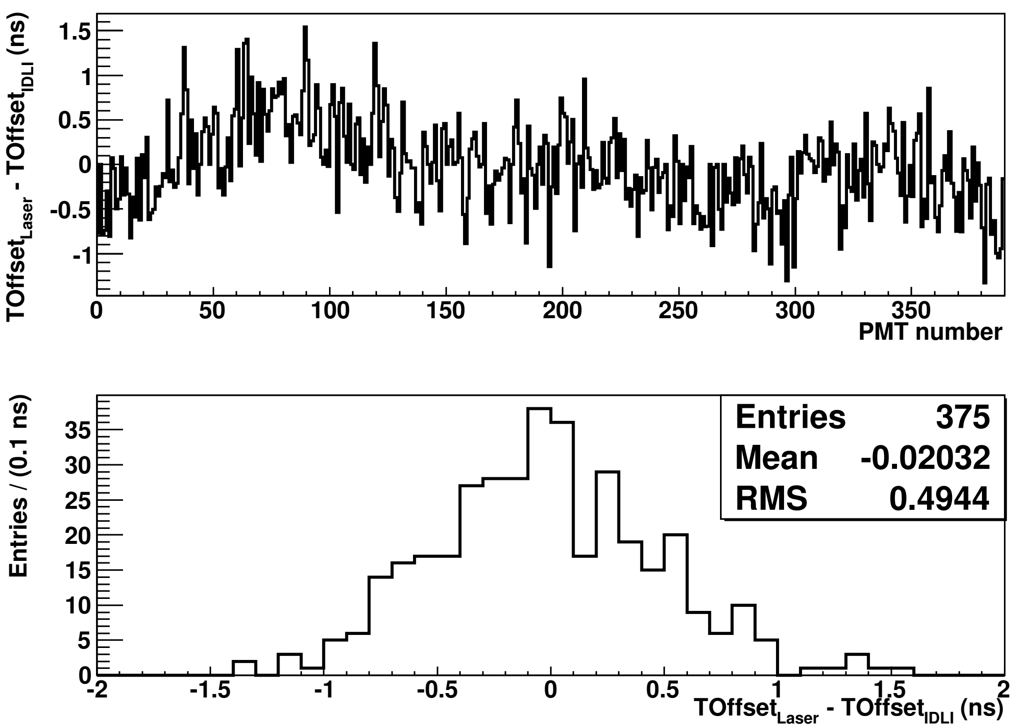

Figure 6.8: Laser calibrated PMT time offsets using the CTR+TOP data set are compared to those obtained from the IDLI data.

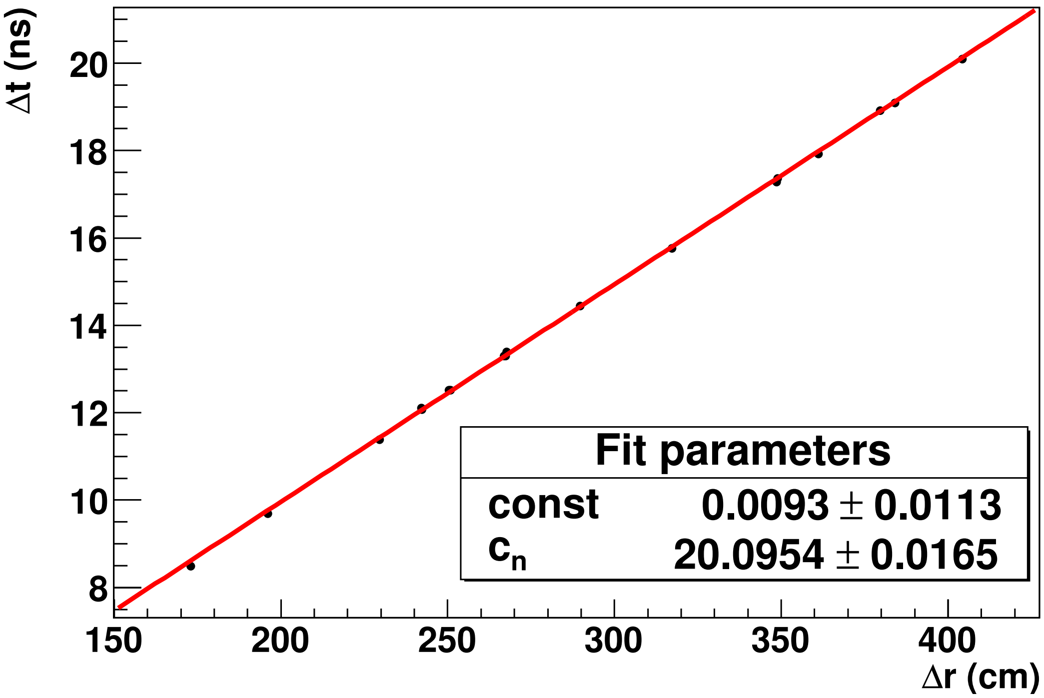

Figure 6.9: Laser calibrated effective speed of light c_n from the linear fit using CTR+TOP data. The error bars are too small to be seen.

6.4.2 Systematic Error Estimation

The deployment position accuracy of the z-axis system is expected to be within 1 cm. The errors on the time offsets and the speed of light c_n could be calculated based on the assumption of a maximum deviation of ± 1 cm from the nominal position. We derived another 2 sets of time offsets and c_n values by shifting the central vertex to 0 ± 1 cm and the top vertex to 92 ± 1 cm. In Fig. 6.10, we compare these 2 sets of time offsets to the standard ones. The widths of the differences are both about 0.035 ns which corresponds to an error of 16% with respect to the estimated error of 0.2 ns (as described in Section 6.3). The speed of light for both of the shifted vertices are plotted in Fig. 6.11. Taking the square root of the quadratic sum of the fitting errors and the differences (between the standard one and the ± 1 cm shifted ones) as errors on the speed of light, the result yields $c_n = 20.095^{+0.017}_{-0.026}$ cm/ns.

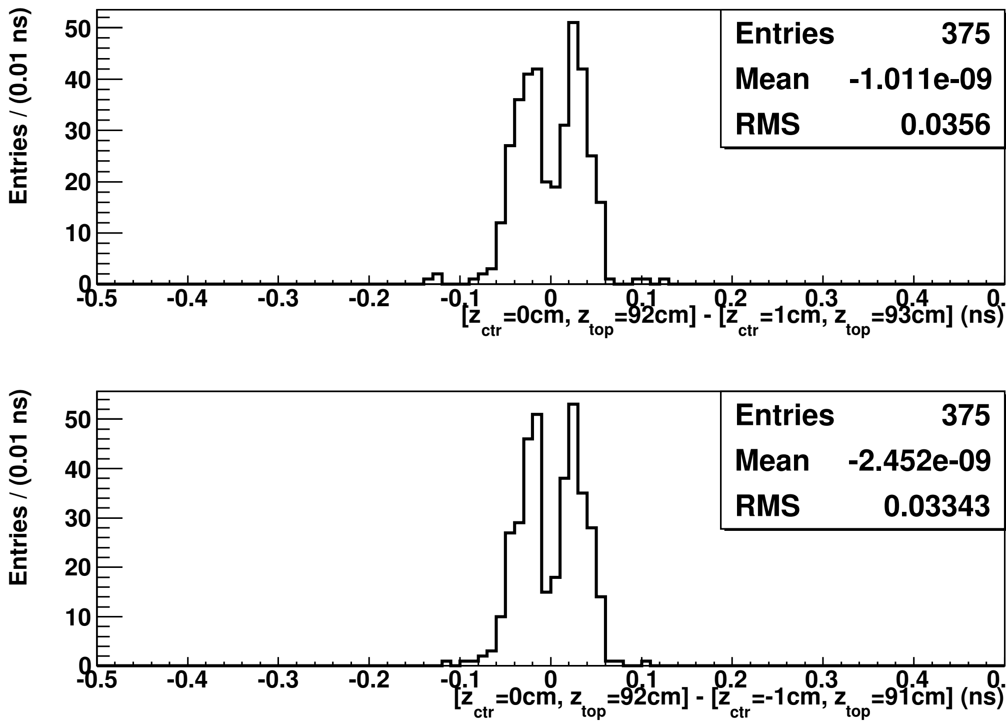

Figure 6.10: Difference in the time offsets when assuming the center and top positions are both shifted by +1 cm (top), or −1 cm (bottom).

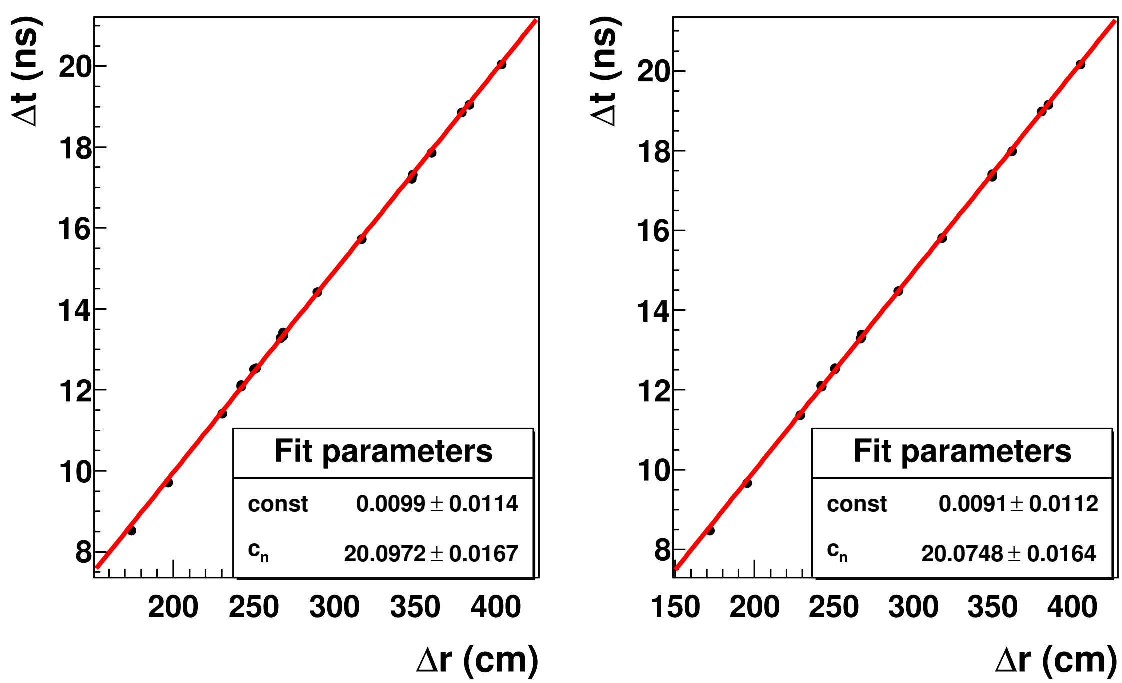

Figure 6.11: Effective speed of light from the linear fit when assuming the center and top positions are off by −1 cm (left), or +1 cm (right). The error bars are too small to be seen.

6.4.3 Consistency Checks

The calibration analysis results discussed above were obtained by starting with the time offsets obtained from the IDLI data. To prove that the results are independent of the starting values for the PMT time offsets, the program was run again starting with the raw PMT times, i.e., no initial time offsets. The result is compared with the standard result in Fig. 6.12, which yields a small error of 0.021 ns. In Fig. 6.13, the two speeds of light are shown to differ by only 0.006%. All evidence strongly suggests that our analysis does not depend on the initial values used in the iterative procedure.

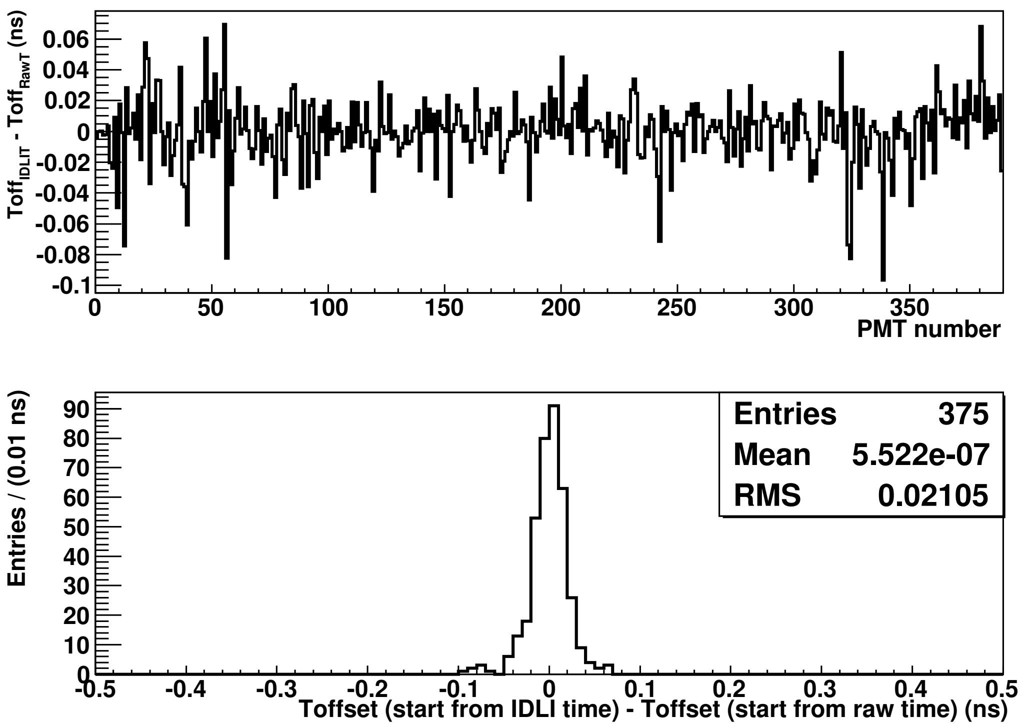

Figure 6.12: Consistency check for PMT time offsets derived by starting from the calibrated times as obtained from the IDLI and the uncalibrated times.

The standard analysis used only top and central data. To check the consistency of the performance, we used the combination of the central and bottom data to derive another set of results. Not only can we compare the results, but also use them to reconstruct the position of the data not used in the corresponding analysis and compare it to the known deployed position. Figure 6.14 shows the comparison of the time offsets obtained from the

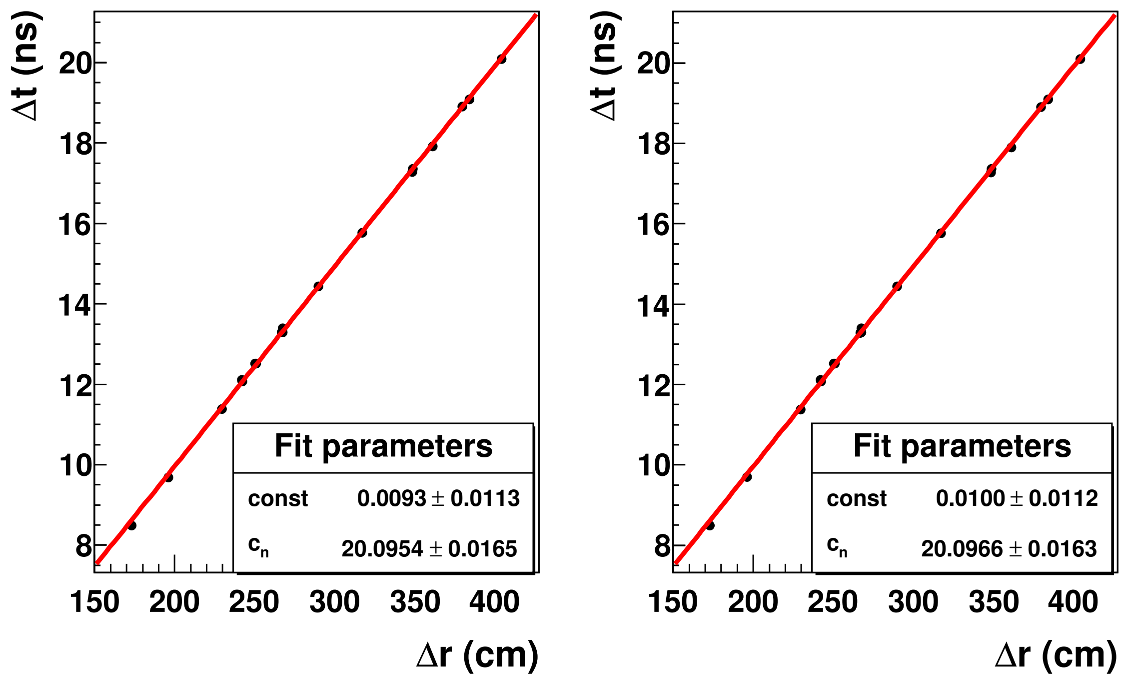

Figure 6.13: Comparison of the effective speed of light results from the linear fit starting with the calibrated times as obtained from the IDLI (left) and uncalibrated times (right). The error bars are too small to be seen.

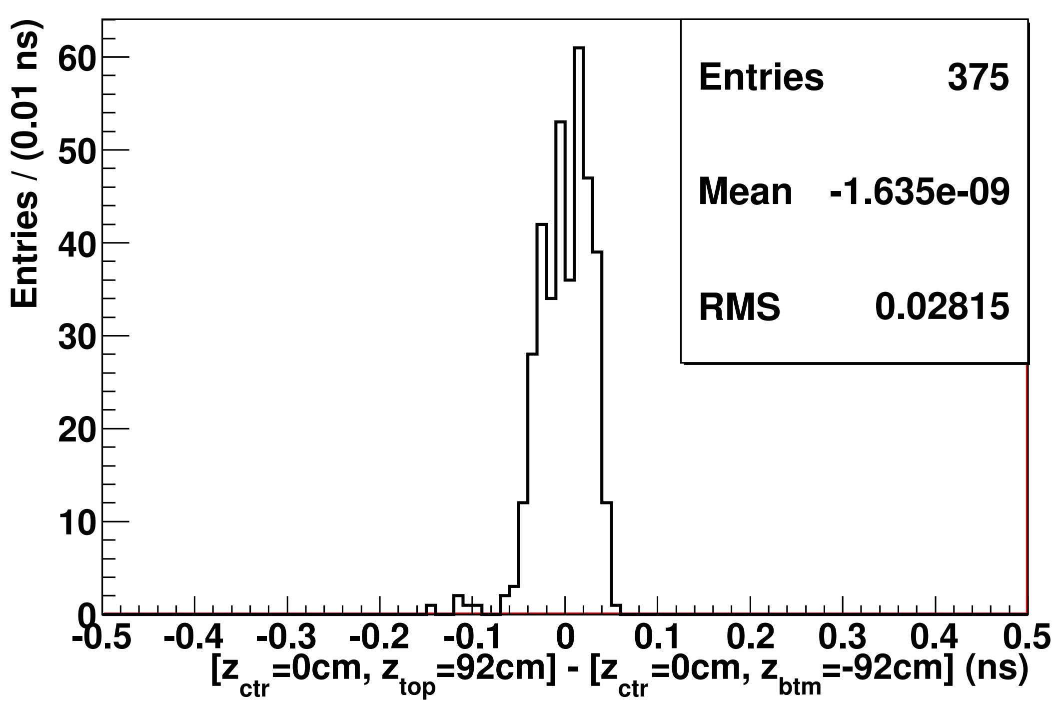

Figure 6.14: Time offsets difference as obtained from the CTR+TOP and CTR+BTM data sets.

combination of the CTR+TOP data to those obtained from the CTR+BTM data. The RMS of the differences 0.028 ns is even smaller than those in the error estimation. The speed of light from the CTR+BTM analysis is plotted in Fig. 6.15. Comparing this to the result from the CTR+TOP data in Fig. 6.9, we can see a discrepancy of approximately 1.7%.

The reconstruction of the bottom vertex by using the time offsets and c_n derived from the CTR+TOP analysis is shown in Fig. 6.16. The result tells us that the x and y vertex coordinates are in excellent agreement with the deployed position, while the z component is shifted by 3 cm downward. Figure 6.17 is the reconstruction result of the top vertex by using the time offsets and c_n from the CTR+BTM data. A systematic shift of 3 cm downward is also obtained.

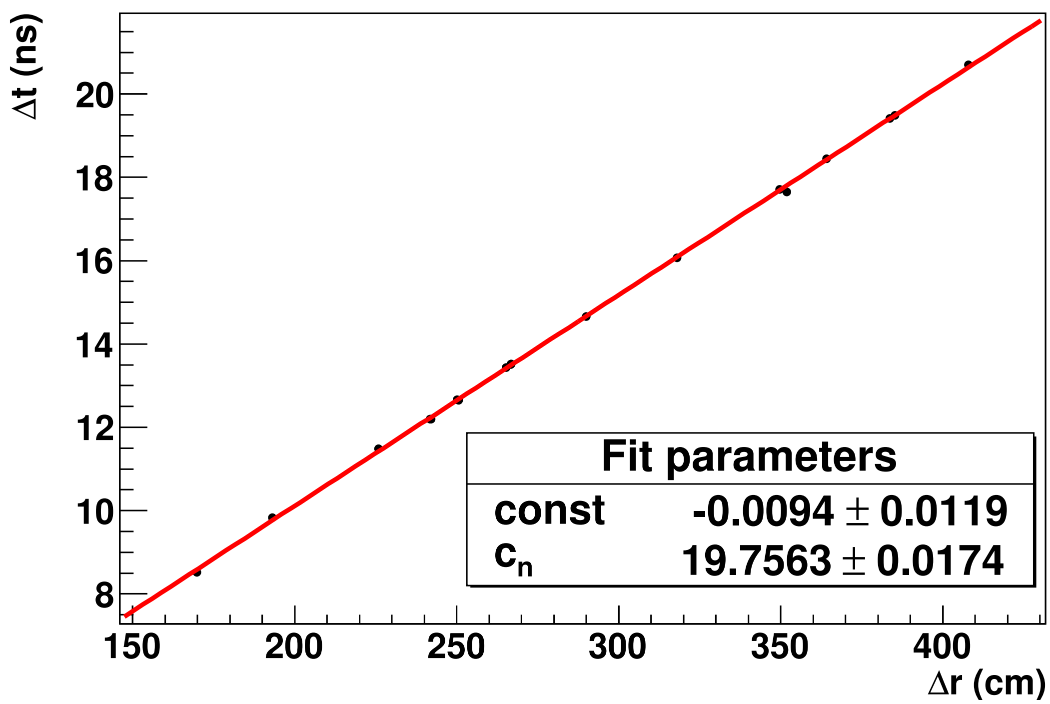

Figure 6.15: Effective speed of light from the linear fit using the CTR+BTM data. The error bars are too small to be seen.

Although the z-axis system deployment error is within 1 cm for all three vertices, we also investigated whether there is a systematic shift of the detector center, or if the top or bottom vertex is individually off by more than 1 cm as the reconstruction indicated. Since the systematic shift observed from the vertex reconstruction is 3 cm downward for both top

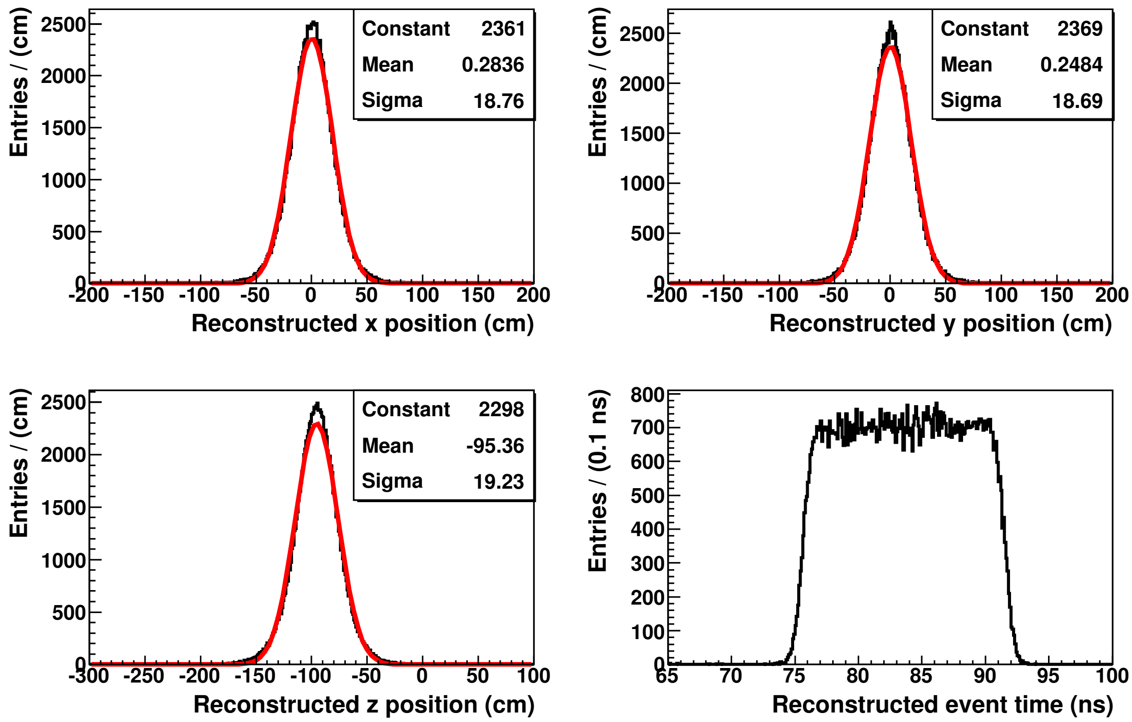

Figure 6.16: Bottom vertex reconstruction ($z = -92$ cm) using time offsets and c_n result from the CTR+TOP data and the reversed top lookup tables. The positions were fitted to a Gaussian. The reconstructed event times verified the 16 ns spread window and the edge effect came from the finite resolution of the event time reconstruction.

and bottom vertices, we first shifted all vertices down by 3 cm and repeated everything from scratch. The new reconstruction result showed another 3 cm shift in the same direction. The overall shift did not explain the behavior.

We then kept the top and central vertices fixed and shifted only the bottom vertex up and down to find the position that yielded the exact same results for the time offsets and c_n to those derived from the CTR+TOP data at the nominal position. In Fig. 6.18, the time offsets from the CTR+BTM data (with $z_{ctr} = 0$ and $z_{btm} = -91, -93, -94, -95$ cm) are compared with those from the CTR+TOP data at the nominal position. The closest result is obtained when placing the bottom vertex at $z = -94$ cm (2 cm lower than the nominal position). The most consistent c_n is about 0.32% higher than that from the CTR+TOP data, which is also derived from the same position as shown in Fig. 6.19. In Fig. 6.20, the time offsets from the CTR+TOP data (with $z_{ctr} = 0$ and $z_{top} = +89, +90, +91, +93$) are

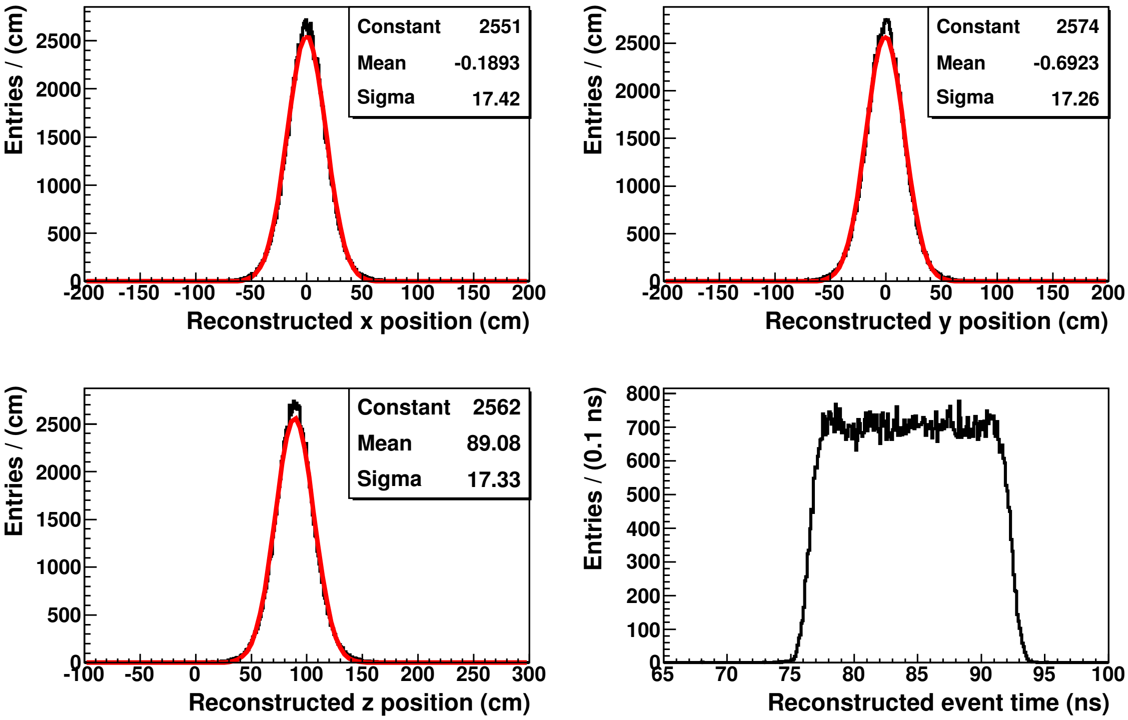

Figure 6.17: Top vertex reconstruction ($z = +92$ cm) using time offsets and c_n result from the CTR+BTM and reversed bottom lookup tables. The positions were fitted to a Gaussian. The event times verified the 16 ns spread window and the edge effect came from the finite resolution of the event time reconstruction.

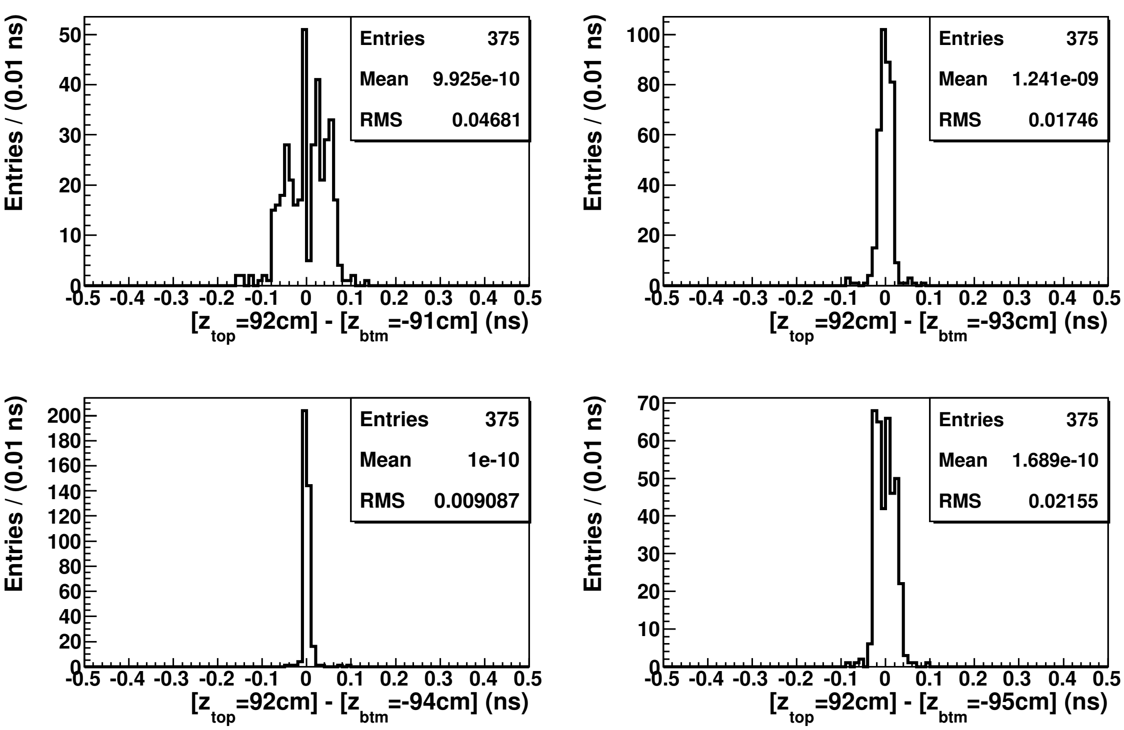

Figure 6.18: Time offsets comparison for the CTR+BTM data (with $z_{ctr} = 0$ and $z_{btm} = -91$, -93, -94, -95 cm) to the CTR+TOP data at nominal position.

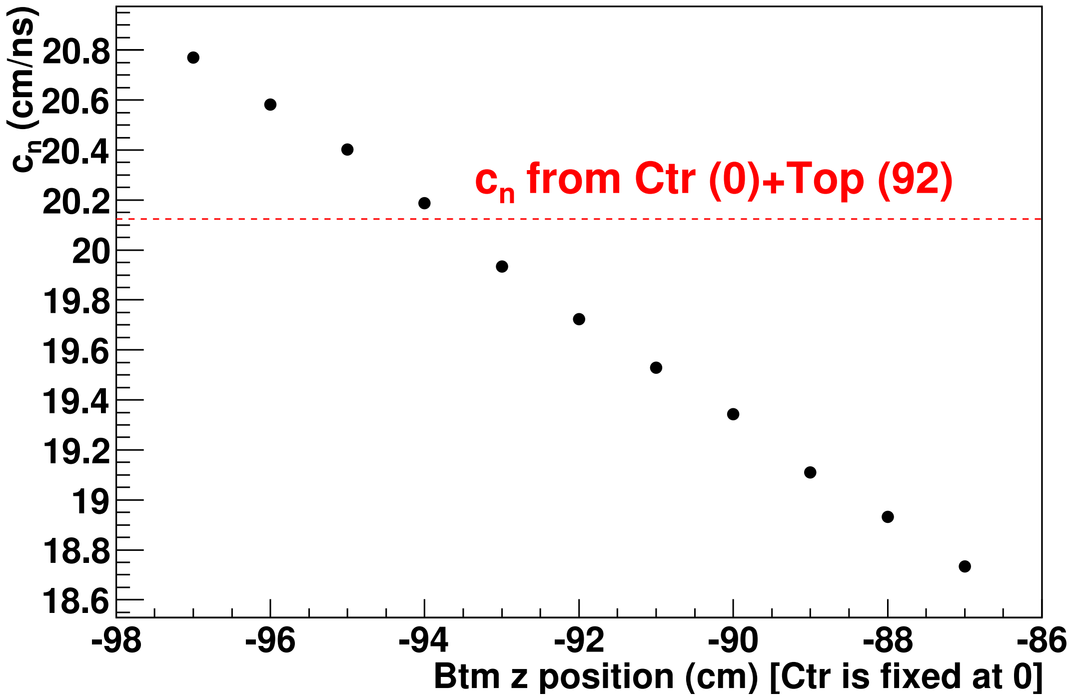

Figure 6.19: Effective speed of light results from the CTR+BTM data (with $z_{ctr} = 0$ and $z_{btm} = -97, ..., -87$ cm) and the CTR+TOP data at nominal position (red dashed line).

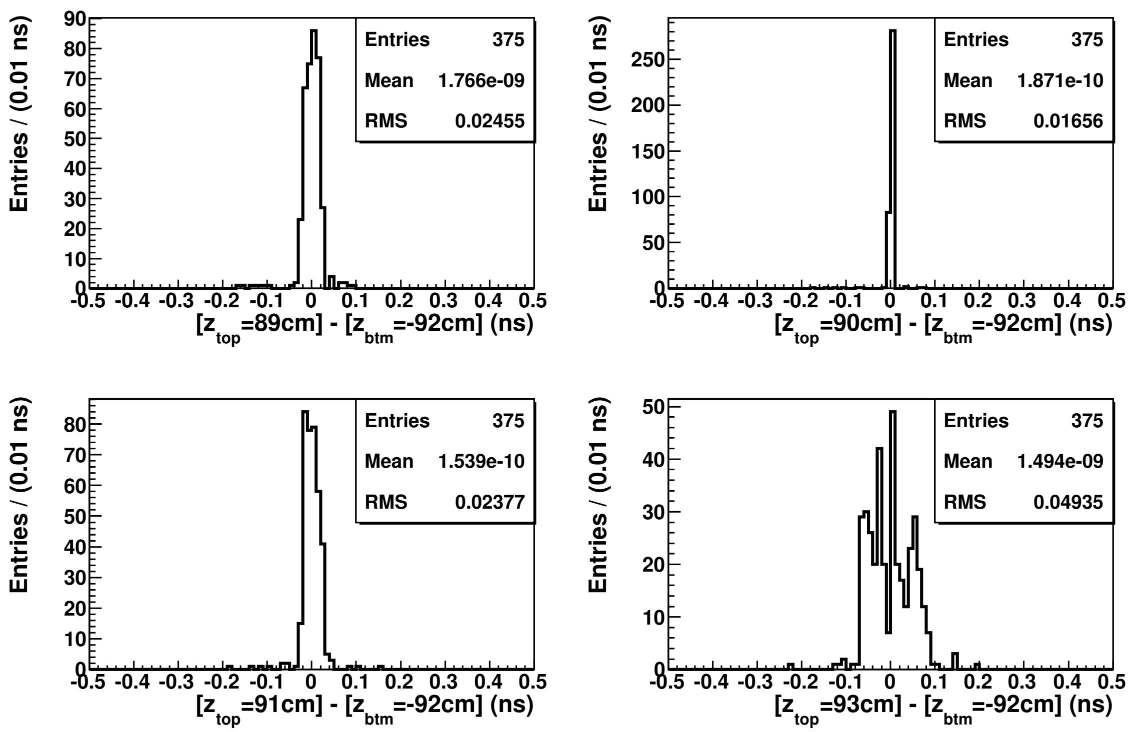

Figure 6.20: Time offsets comparison for the CTR+TOP data (with $z_{ctr} = 0$ and $z_{top} = 89$, 90, 91, 93 cm) to the CTR+BTM data at nominal position.

compared with those from the CTR+BTM data at the nominal position. In Fig. 6.21, the c_n from the CTR+TOP (with $z_{ctr} = 0$ and $z_{top} = +89$, $+90$, $+91$, $+92$, $+93$, $+94$) data is compared with that from the CTR+BTM data at nominal position. The closest time offsets and c_n results come from the top vertex at $z = 90$ cm which is also 2 cm lower than the nominal position.

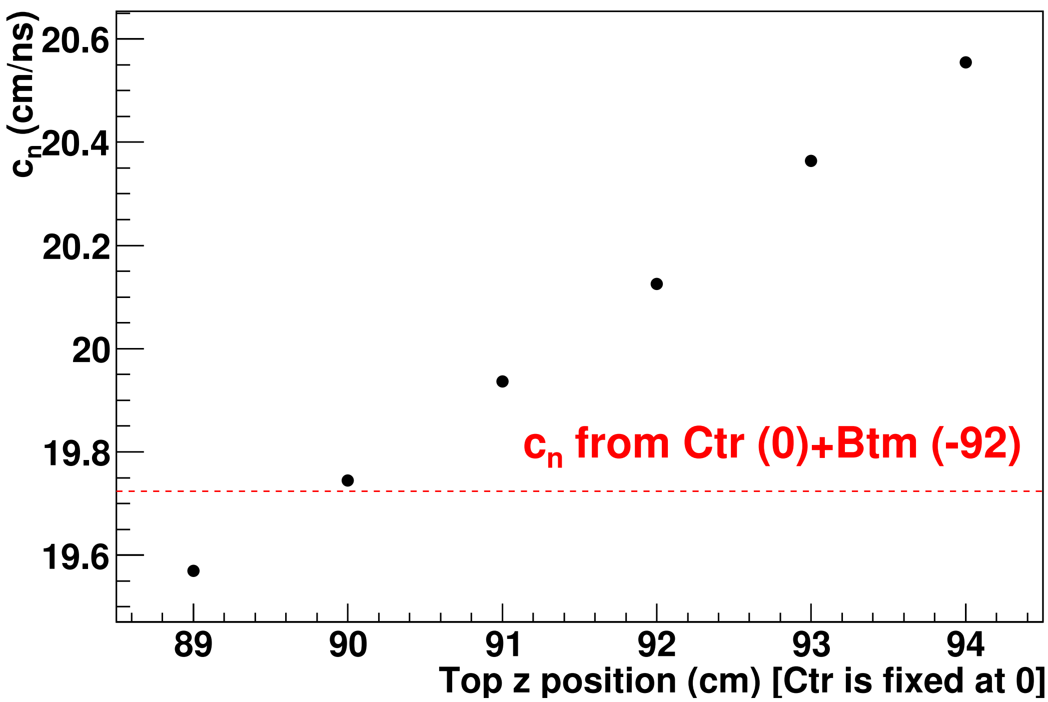

Figure 6.21: Effective speed of light results from the CTR+TOP data (with $z_{ctr} = 0$ and $z_{top} = 89, ..., 94$ cm) and the CTR+BTM data at nominal position (red dashed line).

Next, we used all the results obtained above to reconstruct the opposite vertex, i.e., using the data from the other off-center deployment. The reconstructed z positions are plotted in Figs. 6.22 and 6.23. The time offsets and c_n obtained from the CTR+BTM ($z = -94$ cm) analysis reconstructed the top vertex at 91 cm, while the time offsets and c_n from CTR+TOP ($z = 90$ cm) reconstructed the bottom vertex at -93.5 cm. The reconstructed positions were 1 and 1.5 cm off the targets when using almost the same time offsets and c_n as derived from those vertices.

During the reconstruction, because of the existence of reflections, we cannot simply utilize

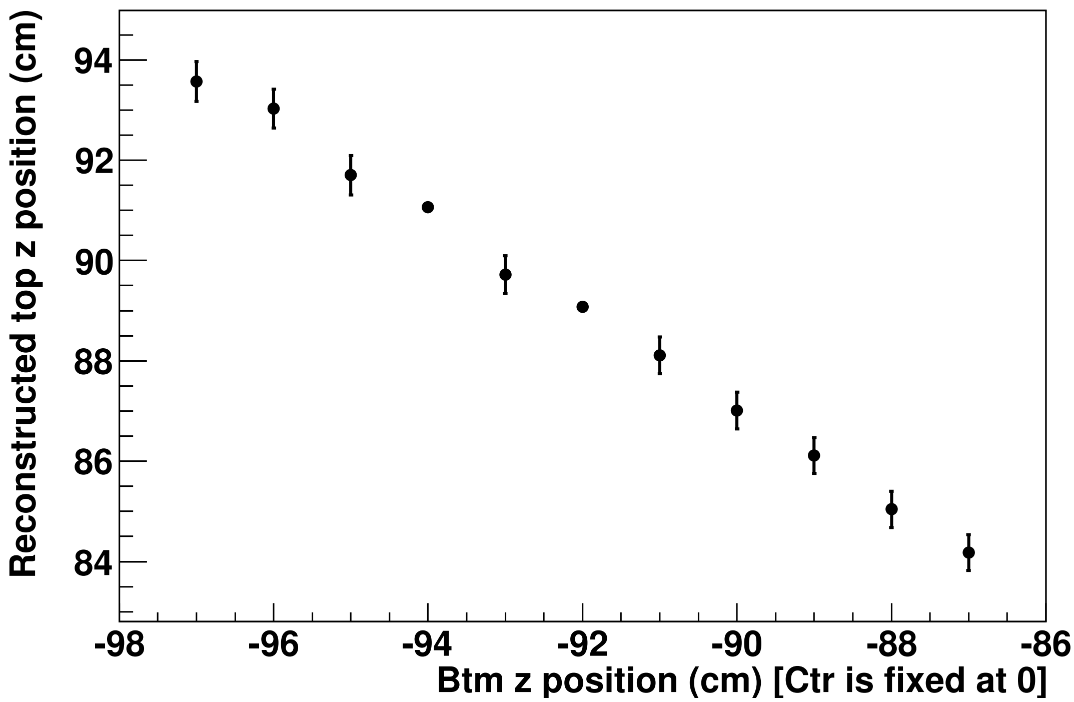

Figure 6.22: Top vertex reconstruction using time offsets and c_n from the CTR+BTM data (with $z_{ctr} = 0$ and $z_{btm} = -97, ..., -87$ cm).

the time likelihood lookup tables derived from the central data (as the secondary peaks associated with reflections depend on the location of the source). We cannot extract them from the data to be reconstructed either, since in that case the reconstruction would not be totally independent. What we did was reverse the top (bottom) vertex's ring lookup tables to work on the bottom (top) vertex reconstruction. The assumption has been made that the vertex to be reconstructed is around the opposite position of the one used in the analysis. However, there is no way to completely avoid any knowledge of the reconstructed vertex because the position and magnitude of the second reflection peak in the corrected time distribution is position-dependent. Taking the reversed time lookup tables is the best way to limit our knowledge of the reconstructed vertex to a minimum level, but it might have an impact on the reconstruction. Comparing the corrected time distributions in all 18 rings to the corresponding reversed ones of the opposite vertex, the rings 0–8 for the top vertex are showing good agreement with the reversed rings 9–17 for the bottom vertex; however,

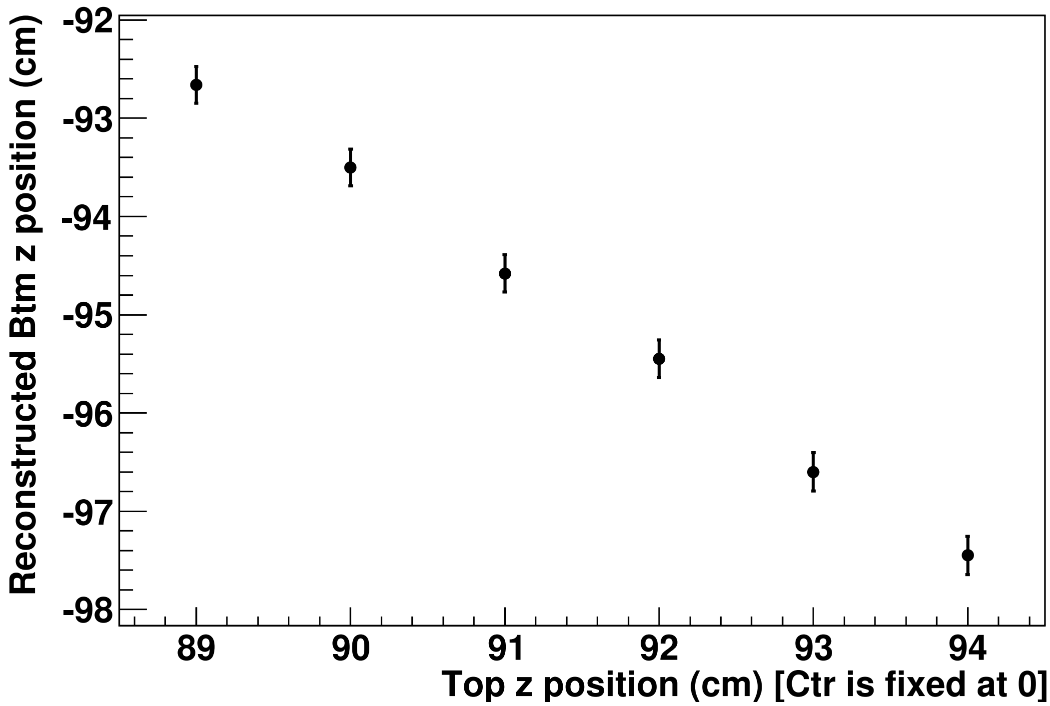

Figure 6.23: Btm vertex reconstruction using time offsets and c_n from the CTR+TOP data (with $z_{ctr} = 0$ and $z_{top} = 89, ..., 94$ cm).

the rest are not. The comparison of the last 4 rings (ring 14, 15, 16, 17) when the vertex is at the top to the reversed first 4 rings (ring 0, 1, 2, 3) when the vertex is at the bottom is plotted in Fig. 6.24. Not only are the second peaks off, but also the magnitudes do not match. The discrepancy is getting more pronounced as more of the inner most rings are considered.

To understand how the time offsets, c_n and the reversed time lookup tables affect the reconstruction result, a reconstruction study of the $z = -92$ cm laser data by using different combinations of those variables was carried out. The results are listed in Table 6.3.

It can be concluded from comparing the odd and even lines that using the time offsets from the CTR+TOP data or from the CTR+BTM data does not affect the reconstruction much. However, if we choose c_n as obtained from the CTR+TOP data instead of c_n from the CTR+BTM data with bottom time likelihood lookup tables, the vertex is about 1.5 cm lower. If we compare the same time offsets and c_n but different time likelihood lookup

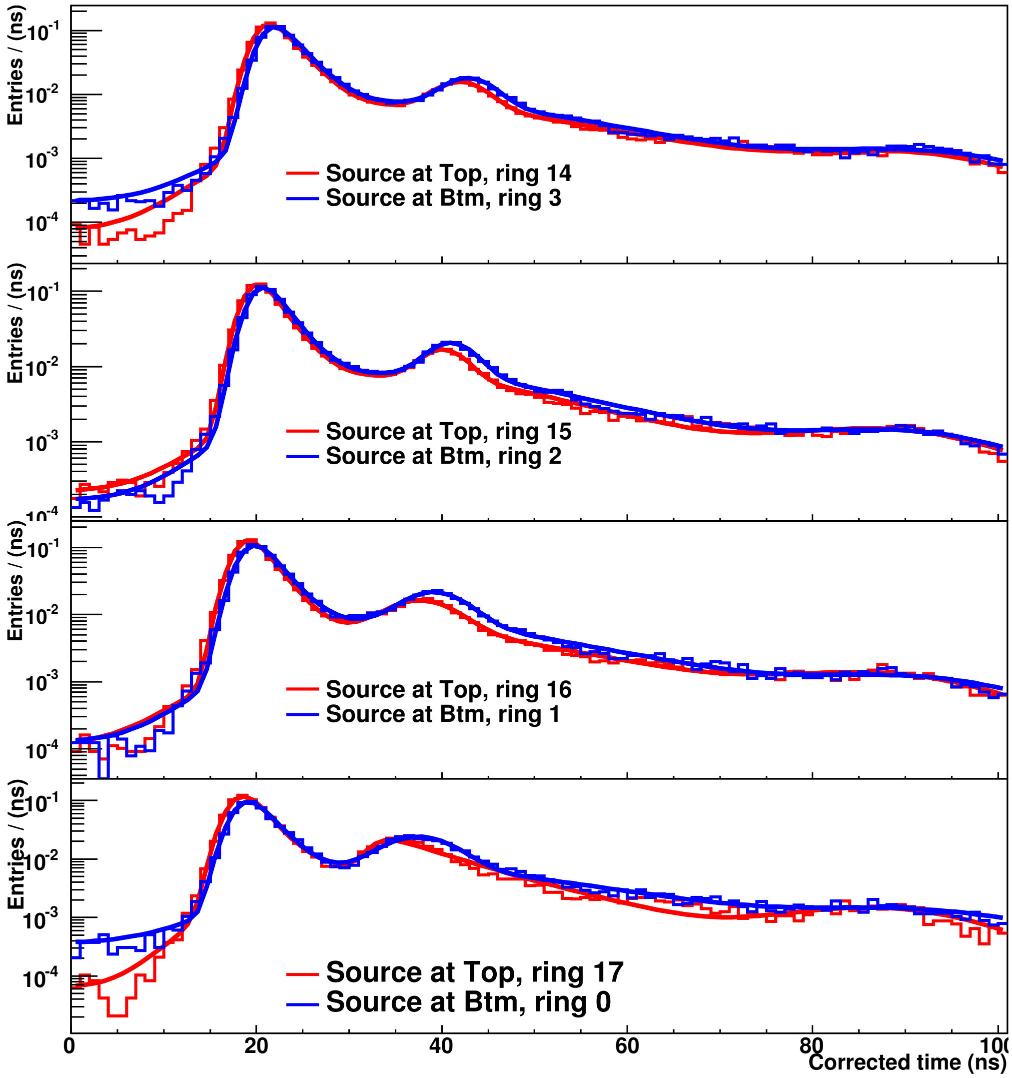

Figure 6.24: Corrected time comparison of rings 14–17 with laser deployed at the top vertex ($z = +92$ cm) to rings 0–3 with laser deployed at the bottom vertex ($z = -92$ cm).

tables, the reconstructed position is also about 1.1–1.5 cm lower as we have seen when using reversed top time likelihood lookup tables. Moreover, by using c_n obtained from the CTR+TOP data and reversed top time likelihood lookup tables, we observed an overall 3 cm downward movement. The conclusion can be drawn that using reversed time likelihood lookup tables can result in a maximum 1.5 cm bias on the reconstructed z position.

Similar studies need to be performed when data at the 3 positions can be taken within the same deployment, since in that case, we minimize the uncertainty of the relative distances between the top and central and the central and bottom deployed positions.

Lookup tables	Time offsets	c_n	Reconstructed z coordinate (cm)
Bottom	CTR+BTM	CTR+BTM	-92.31 ± 0.19
Bottom	CTR+TOP	CTR+BTM	-92.55 ± 0.19
Bottom	CTR+BTM	CTR+TOP	-93.91 ± 0.19
Bottom	CTR+TOP	CTR+TOP	-94.06 ± 0.19
Reversed Top	CTR+BTM	CTR+BTM	-93.47 ± 0.19
Reversed Top	CTR+TOP	CTR+BTM	-93.80 ± 0.19
Reversed Top	CTR+BTM	CTR+TOP	-95.34 ± 0.19
Reversed Top	CTR+TOP	CTR+TOP	-95.38 ± 0.19

Table 6.3: Bottom ($z = -92$ cm) vertex reconstruction with different combinations of the PMT time offsets, c_n and time lookup tables. 10,000 events at each position are used.

6.4.4 PMT Time Offsets Cross Checks

This study was performed to check the relative PMT time offsets using the geometrical symmetries of the detector. For this purpose we use a short central $\lambda = 470$ nm laser run of higher intensity, which was only used to establish the light level in the detector. Despite the fact that almost every other PMT fires, the higher light levels are irrelevant for this study. The information of this run is shown in Table 6.4.

Run #	z (cm)	Average Nhits	Total charge (PE)	Length (s)	Total events	Laser events	Selected events
45633	0	189.2	300.3	30	5067	5001	4989

Table 6.4: Run number, position, average multiplicity, total charge, run length as well as total number of events, laser triggered events and selected events after the light noise cut and total charge cut for the $\lambda = 470$ nm laser calibration test run used in this study.

The raw time on a PMT, t_i, can be expressed as below:

$$t_i = \frac{r_i}{c_n} + t_i^{off} + t_0,$$

where the t_0 is the event time, t_i^{off} is the time offset for the i^{th} PMT, and r_i/c_n is the light propagation time from the vertex to the i^{th} PMT. Since the z-axis deployment has an azimuthal symmetry, the PMTs in any given ring always have a common distance to the vertex. We took advantage of this feature and randomly assigned each ring a reference PMT (in this study, the first active PMT in each ring is taken as references) and subtracted the reference PMT time from the other PMT times. Since both PMTs are in the same ring and therefore have the same propagation time, the corresponding terms cancel out, except for the time offsets:

$$t_i - t_{ref} = \left(\frac{r_i}{c_n} + t_i^{off} + t_0\right) - \left(\frac{r_{ref}}{c_n} + t_{ref}^{off} + t_0\right) = t_i^{off} - t_{ref}^{off}.$$

Note that any additional time slewing corrections should also cancel, as the average charges at the two PMTs are roughly equal. The subtractions of the raw PMT times become the differences between the time offsets of the i^{th} PMT and the reference PMT. In this way, we have an independent check of the PMT offsets derived in the standard analysis. Strictly speaking, the checks are on the time offsets differences between two PMTs in one ring. Figure 6.25 shows the time differences between PMTs 181–189 to reference PMT 180. The binning is limited by the 2 ns timing resolution from the 500 MHz electronics sampling rate, as already mentioned before. The fit function is a Gaussian plus a constant; the fit errors on the mean value are plotted in Fig. 6.26. The total number of entries is 357 instead of 390 is because the 15 inactive PMTs and the 18 reference PMTs are taken out. Figure 6.27 shows the comparison of the PMT time offsets differences between the laser calibration and this study. The spread in the difference is 0.23 ns, which is contributed to by the fit errors on the PMT time differences and the error from the standard time offsets calibration. Since we know that the fit error is on average 0.13 ns, the error on the laser calibrated time offsets can be calculated as:

$$\sigma = \sqrt{0.23^2 - 0.13^2} \approx 0.19 \text{ ns}.$$

This number is close to the estimate of 0.15 ns obtained in the MC studies described in Section 6.3.1. The slight difference can be explained by the relatively more complex corrected time distributions that change our fit function from a pure Gaussian (as assumed in the MC studies) to the one in Eq. (6.2).

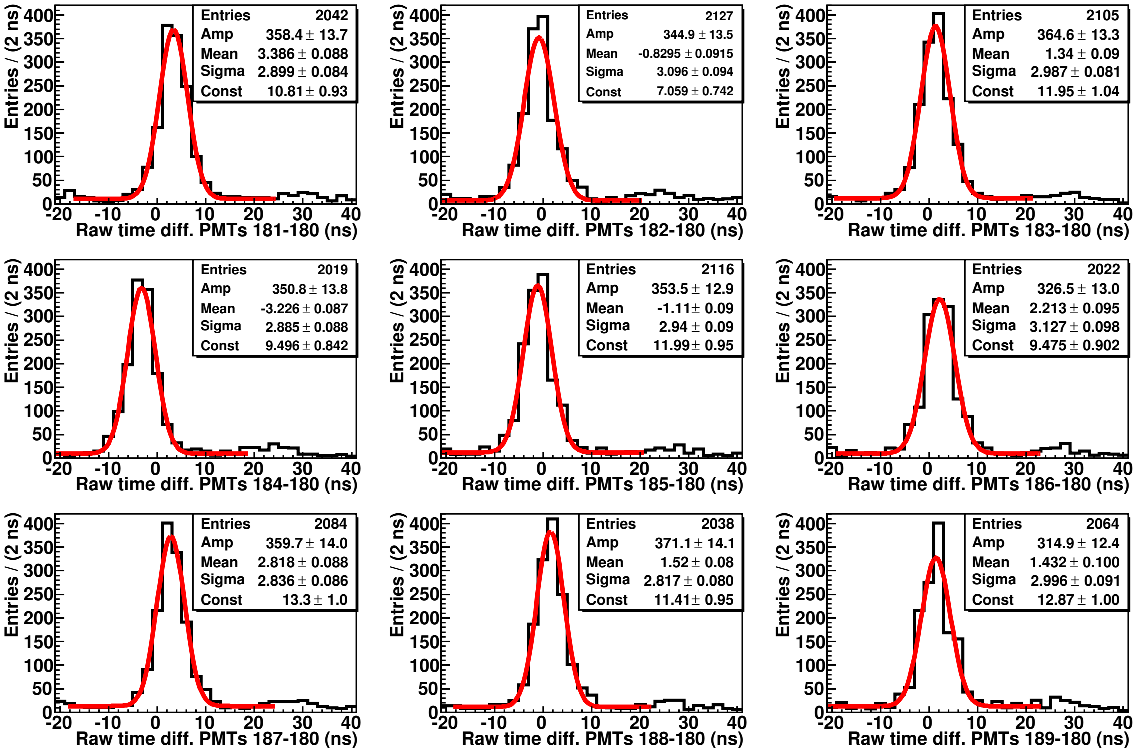

Figure 6.25: Raw time difference for PMTs 181–189 with respect to PMT 180 taken as reference. The distributions are fitted to a Gaussian plus a constant.

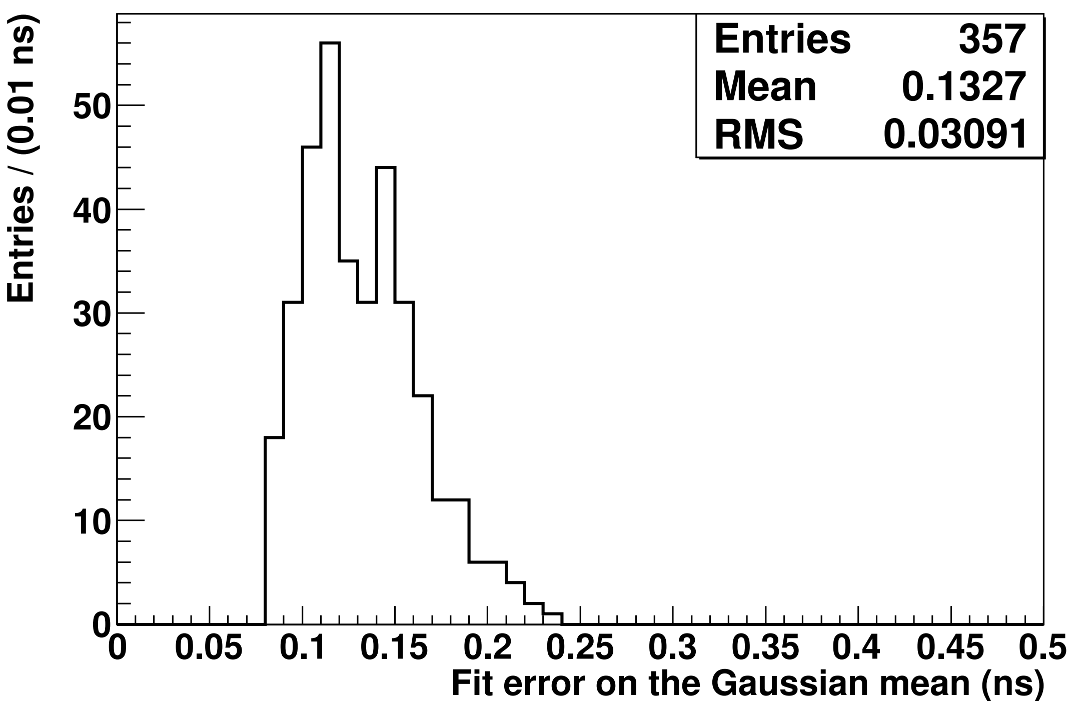

Figure 6.26: Distribution of the fit errors on the Gaussian means for the raw time (relative time offsets) differences.

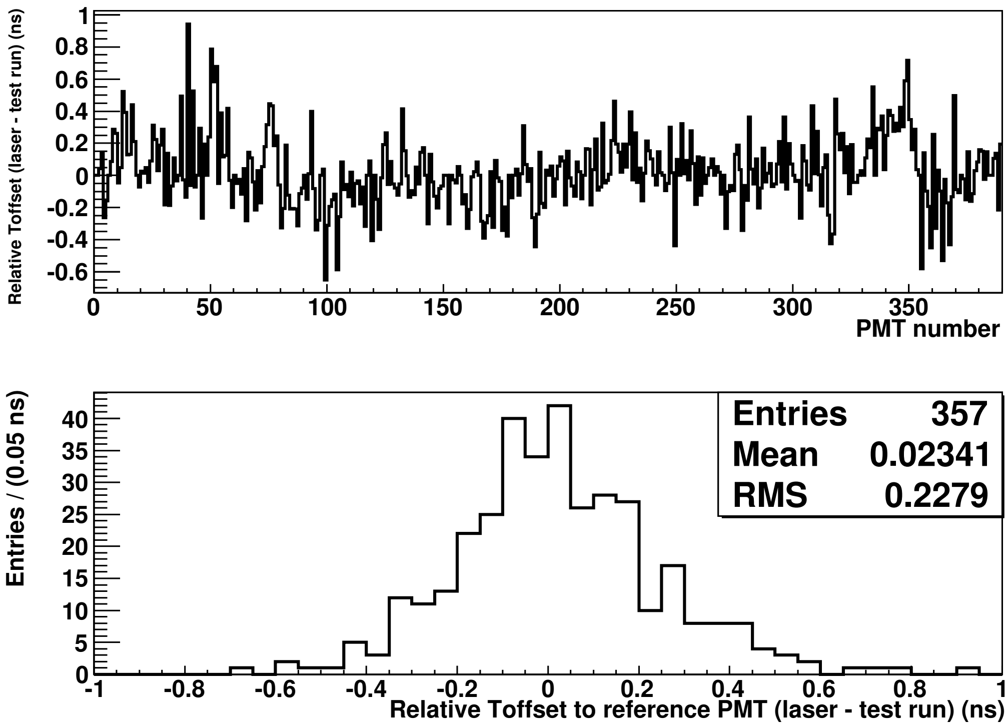

Figure 6.27: Relative PMT time offsets differences between: 1, the calibration data analysis. 2, the test run used in this study.

6.4.5 Different c_n Values in the Different Optical Media

The study in Ref. [199] extracts c_n without the dependence of PMT time offsets. However, when it is restricted to only one effective c_n, it confirms the value of c_n obtained in this analysis. When it uses different values in the three different optical media (the neutrino target, the gamma catcher, and the buffer), it has shown evidence of big differences among them, especially in the buffer:

- neutrino target: $c_n^{NT} = 19.954 \pm 0.107$ cm/ns,
- gamma catcher: $c_n^{GC} = 20.309 \pm 0.647$ cm/ns,
- buffer: $c_n^{BF} = 22.836 \pm 0.550$ cm/ns.

To check this result, I modified my code by changing from a single effective c_n value to three different values in the three volumes; the time offsets calibration part stays the same. In Fig. 6.28, the c_ns starting with a common value of 20 cm/ns ended with $c_n^{NT} = 20.092$

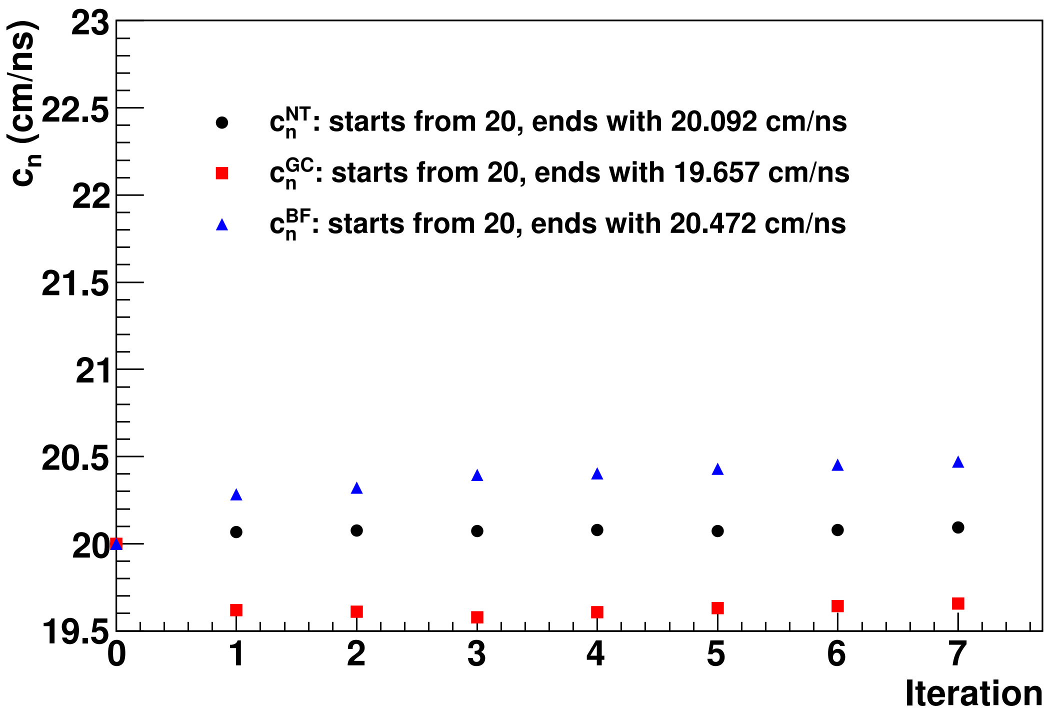

Figure 6.28: Evolution of the three values of the effective speed of light in the different volumes as labeled, starting from 20 cm/ns.

cm/ns, $c_n^{GC} = 19.657$ cm/ns and $c_n^{BF} = 20.472$ cm/ns, respectively. However, when starting with the values obtained in Ref. [199], the results ended at different values of $c_n^{NT} = 20.310$ cm/ns, $c_n^{GC} = 20.835$ cm/ns and $c_n^{BF} = 21.738$ cm/ns, as shown in Fig. 6.29. Currently, we do not understand why they do not converge to a unique set of results.

6.5 Conclusion

The PMT time offsets calibration as obtained using the blue laser data is the most precise calibration, as demonstrated by MC studies, with an estimated error on the time offsets of about 0.15 ns. Our error estimation is based on a ± 1 cm overall shift from the nominal deployment position, which yields $c_n = 20.095^{+0.017}_{-0.026}$ cm/ns and a spread of only 0.35 ns in the distribution of the time offsets differences. By starting from uncalibrated PMT times, the results are almost the same as those starting with the PMT times obtained from the IDLI calibration, which proves that our analysis does not depend on the starting values. The

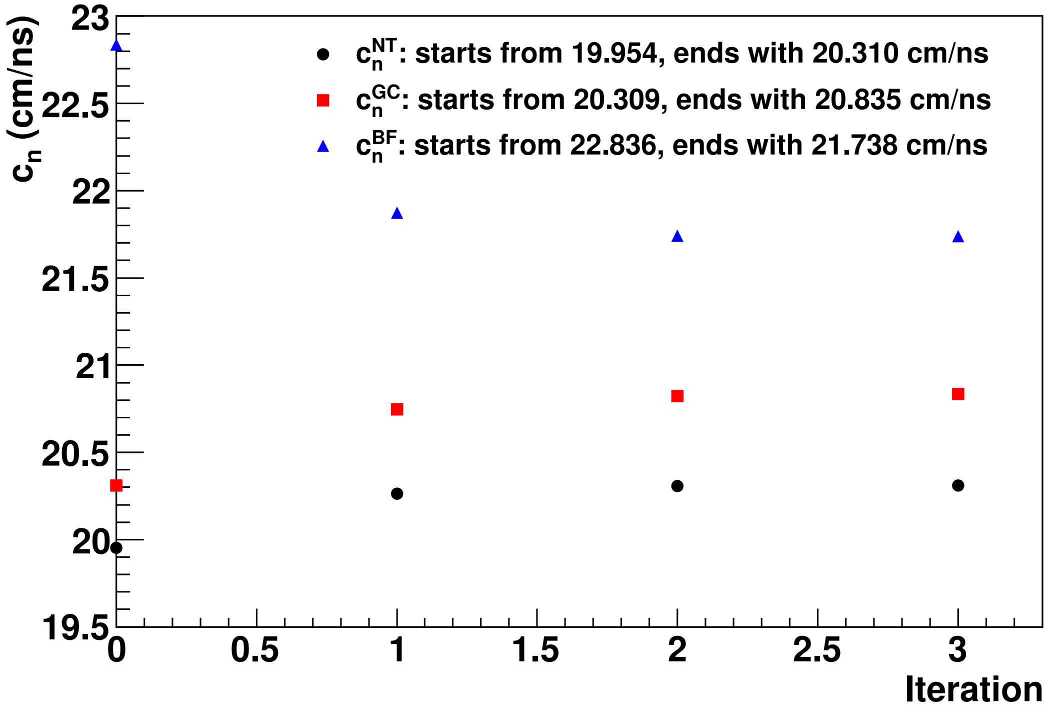

Figure 6.29: Evolution of the three values of the effective speed of light in the different volumes as labeled, starting from the values obtained in Ref. [199].

consistency check between using the CTR+BTM data and the CTR+TOP data shows a 1.7% discrepancy in c_n. The reconstruction for both top and bottom vertices using the PMT time offsets and c_n derived by the other two vertices indicates a 3 cm systematic downward shift. We understand it comes from the 1.7% discrepancy of c_n and using the reversed time likelihood lookup tables. The study of PMT time offsets differences from the higher intensity laser test run shows good consistency with the standard time offsets. In the last study of 3 different values for the speed of light in different volumes, the results depend on the starting points, which still needs to be understood. The PMT time offsets from the laser calibration have been in use in all Double Chooz physics analyses since March 2013.

Chapter 7

Charge Likelihoods

7.1 Introduction

The charge likelihood (QLLK) $P_q(q;\mu)$ is the probability of measuring a charge q when a predicted charge μ is expected at a given PMT. Charge likelihoods are used to determine the total light flux generated in an event, which in turn is proportional to the event energy. The proportionality constant is determined from calibration sources of well-defined energy, e.g., radioactive sources. In addition, the QLLKs work to supplement the time likelihoods in increasing the position reconstruction accuracy.

The requirement and procedure for extracting the QLLKs are discussed in Section 7.2. The extractions of MC and data QLLKs are discussed in Sections 7.3 and 7.4, respectively.

7.2 Charge Likelihoods Analysis

To determine the QLLKs one needs a high statistics sample of events covering all possible predicted charge values that could occur in the prompt event of an $\bar{\nu}_e$ signal. The highest energy that the prompt event of an $\bar{\nu}_e$ signal can reach in the Double Chooz neutrino target is about 8 MeV. By generating 8 MeV positrons at the neutrino target corner, where some PMTs have the closest path to the vertex, we determined that a maximum charge of 30

PEs can be reached for a single PMT. The charge likelihoods have to be able to cover the predicted charge at 30 PE, which means that the highest predicted charge has to be a somewhat larger than 30 PE. Six different intensities of photon bombs with $\lambda = 375$ nm were simulated at positions $z = 0$ and ± 90 cm with 1.111, 3.333, 10, 30, 90, 270 kphotons/event, which correspond approximately to 0.139, 0.417, 1.25, 3.75, 11.25, 33.75 MeV in positron-equivalent energy. The predicted charge coverage of the top vertex at $z = +90$ cm is shown in Fig. 7.1. The intensities increase by a factor of 3, which leaves no gap and provides enough statistics in the entire range of predicted charge from 0 to 30 PE and some statistics in the range greater than 30 PE. The reason why the maximum intensity for the laser events is about 4 times higher than the maximum positron events energy at the corner of the target volume is because the distance from the corner to the nearest PMTs (60 PMTs in the rings

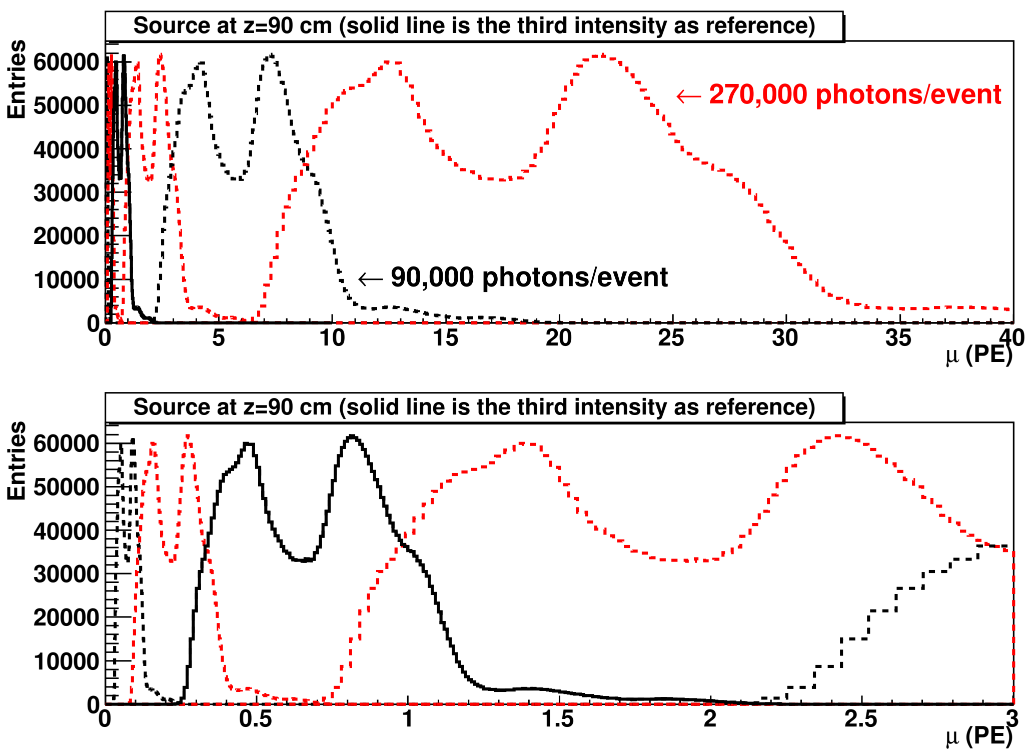

Figure 7.1: Coverage of predicted charge μ with six different intensities of photon bombs simulated at $z = 90$ cm with 1.111, 3.333, 10, 30, 90, 270 kphotons/event which correspond approximately to 0.139, 0.417, 1.25, 3.75, 11.25, 33.75 MeV. 10,000 events at each intensity were generated.

6 and 7) is about half of that from the top vertex to the same PMTs, and the solid angles scale primarily as the inverse of the distance squared. The distance from the 6 PMTs in the ring 0, 12 PMTs in the ring 1 and 18 PMTs in the ring 2 are closer to the top vertex than the 60 PMTs in the rings 6 and 7 by factors of 0.72, 0.81 and 0.95. They provide less statistics and can be used to cover the predicted charge range above 30 PE at the highest laser intensity.

The light emitted by the neutrino-induced events in the Double Chooz experiment is dominated by scintillation light, thus isotropic. For an ideal detector, where light propagation can be described by only attenuation (extinction) and the PMTs acceptance is only affected by the incident angle with respect to the PMT normal, the amount of light at any PMT i with quantum efficiency ε_i can be calculated as:

$$\mu_i = \Phi' \varepsilon_i \frac{A_{PMT}}{r_i^2} e^{-r_i/\lambda} g(\cos \eta_i), \tag{7.1}$$

where Φ' is the event flux, ε_i is the quantum efficiency of the PMT, A_{PMT} is the surface area of the PMT, λ is the effective attenuation length, r_i is the distance from the vertex to the PMT and η_i is the corresponding incident angle, as illustrated in Fig. 7.2.

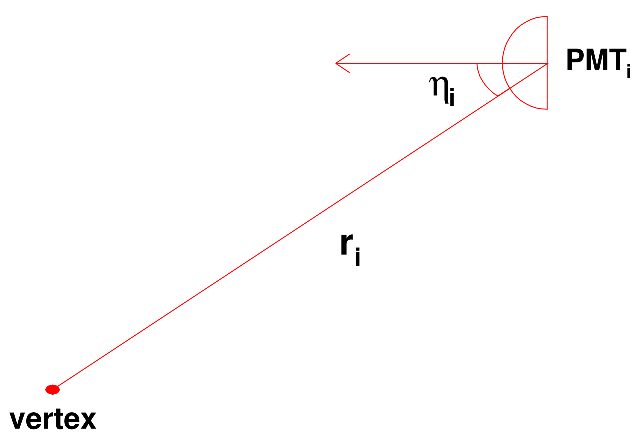

Figure 7.2: The definitions of r_i, the distance from the vertex to the hit PMT i, and η_i, the corresponding incident angle.

The overall absolute quantum efficiency can be absorbed into the definition of the flux Φ', and thus the ε_i in the expression above can be replaced by the relative quantum efficiency with the normalization below:

$$\frac{1}{N}\sum_{i=1}^{N}\epsilon_i = 1.$$

The constant A_{PMT} in Eq. (7.1) comes from an approximation under the long distance assumption, $r_i \gg R_{PMT}$, where R_{PMT} is the PMT radius as shown in Fig. 7.3. Under this assumption, we have,

$$\theta_i \approx \frac{R_{PMT}}{r_i},$$

and

$$\cos\theta_i = 1 - \frac{\theta_i^2}{2!} + O(\theta_i^4).$$

The solid angle that a PMT occupies in Fig. 7.3 is therefore,

$$\Omega = 2\pi(1-\cos\theta_i) = \pi\frac{R_{PMT}^2}{r_i^2} + O(\frac{R_{PMT}^4}{r_i^4}) \approx \frac{A_{PMT}}{r_i^2}.$$

Since all the inner detector PMTs have the same size, A_{PMT} can be treated as a constant and absorbed into the flux Φ'. Therefore, with the redefinition of the flux,

$$\Phi = \Phi' A_{PMT}\sum_{i=1}^{N}\varepsilon_i,$$

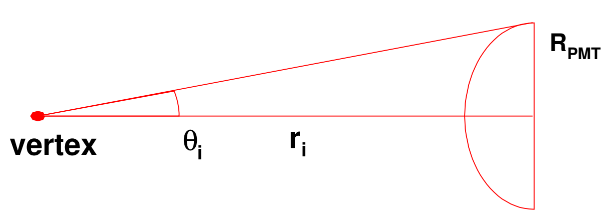

Figure 7.3: The definitions of r_i, the distance from the vertex to the hit PMT, θ_i, the opening angle covering the entire hit PMT surface, and R_{PMT}, the hit PMT radius.

the predicted amount of light becomes:

$$\mu_i = \Phi \epsilon_i \frac{e^{-r_i/\lambda}}{r_i^2} g(\cos\eta_i) \equiv \Phi \omega_i. \tag{7.2}$$

Here, the definition of the solid angle,

$$\omega_i = \epsilon_i \frac{e^{-r_i/\lambda}}{r_i^2} g(\cos\eta_i),$$

is extended to not only includes merely the inverse distance squared, but also the attenuation length effect. Because of the existence of three volumes, scattering, reflection, absorption and reemission, a simple exponential decay cannot fully describe the light propagation. The details of the extension of the optical model and the studies will be described in Section 8.3.

However, in the QLLKs extraction one does not have to explicitly calculate the predicted charge μ using Eq. (7.2), because there are only three deployed positions. For a fixed point vertex, μ_i can be expressed as the multiplication of the flux Φ and the effective solid angle ω_i of the i^{th} PMT as shown in Eq. (7.2), which does not change for different events. In such case, there are two ways to derive the set of effective solid angle $(\omega_i)_{i=1,390}$, as we discuss in the following.

1. The solid angles from the total visible charge

Assuming that the hit statistics are governed by a Poisson distribution, the total probability of detecting a set of number of photons, (n_i); for a set of predicted charges μ_i with the PMTs is:

$$\mathcal{L} = \prod_{i=1}^{390} P(n_i, \mu_i) = \prod_{i=1}^{390} \frac{e^{-\mu_i} \mu_i^{n_i}}{n_i!}.$$

The flux Φ is related to μ_i by Eq. (7.2). The most likely flux Φ can be found by maximizing the event likelihood, $\mathcal{L}$, or minimizing the negative logarithm:

$$-\ln\mathcal{L} = -\ln\left(\prod_{i=1}^{390}\frac{e^{-\mu_i}\mu_i^{n_i}}{n_i!}\right) = \sum_{i=1}^{390}\left(\mu_i - n_i\ln\mu_i + \ln n_i!\right).$$

Therefore,

$$0 = \frac{d\left(-\ln\mathcal{L}\right)}{d\Phi} = \frac{d\left[\sum_{i=1}^{390}\left(\mu_i - n_i\ln\mu_i + \ln n_i!\right)\right]}{d\Phi} = \sum_{i=1}^{390}\left(\omega_i - \frac{n_i}{\Phi}\right) \Rightarrow \sum_{i=1}^{390}\omega_i = \frac{1}{\Phi}\sum_{i=1}^{390}n_i, \tag{7.3}$$

and the second derivative is positive:

$$\sum_i\left(\frac{n_i}{\Phi^2}\right) > 0. \tag{7.4}$$

Obviously, since the n_i and flux Φ are always positive, Eq. (7.4) holds for any value of Φ. And Eq. (7.3) gives the most likely flux Φ:

$$\Phi = \frac{\sum_{i=1}^{390}n_i}{\sum_{i=1}^{390}\omega_i}. \tag{7.5}$$

However, realistic PMTs record a continuous charge q_i as opposed to discrete number of PEs, n_i. If the PMT gains are calibrated and the PMT responses are linear, ignoring PMT threshold effects, in average, $Q = \sum_{i=1}^{390} q_i = \sum_{i=1}^{390} n_i$ and therefore,

$$\Phi = \frac{\sum_{i=1}^{390}qi}{\sum_{i=1}^{390}\omega_i} = \frac{Q}{\Omega}. \tag{7.6}$$

The variations of Φ due to the change of event positions are automatically introduced through

Ω. For a fixed light source, the solid angles do not change from event to event. In the limit of large statistics, the total measured charge at PMT i should be equal to the total predicted charge, namely $\langle q_i \rangle = \langle \mu_i \rangle$:

$$Q_i = \sum_{j=1}^{N} q_{ij} = \sum_{j=1}^{N} \mu_{ij} = \sum_{j=1}^{N} \Phi_j \omega_i = \omega_i \sum_{j=1}^{N} \Phi_j,$$

where j runs over all the event numbers, i.e., from 1 to N. Thus, Q_i and ω_i only differ by a factor of $\sum_{j=1}^{N} \Phi_j$, which should be the same for all of the 390 PMTs. Therefore, the PMT total charge is proportional to its solid angle, ω, in the limit of large statistics.

2. The solid angles from the hit/no-hit probability

The advantage of this method is that the event flux probability is determined from the PMTs hit/no-hit information and no longer as $\Phi = Q/\Omega$, which minimizes the effect from potential problems related to the PMT charge, e.g., threshold, electronics response, charge calculation, etc. The PMTs charges only come in when correcting individual PMT solid angles in each iteration. The procedure starts with the hit and no-hit probability from Possion statistics, $P_{hit} = 1 - e^{-\mu}$ and $P_{nh} = e^{-\mu}$, respectively, and any set of solid angles (the solid angles obtained from method 1 can be used as a good starting point). The hit/no-hit probability is used to determine the event fluxes, which in turn will change the PMTs predicted charges. The PMT solid angles will be corrected by the measured-to-predicted charge ratio, q/μ. The hit/no-hit probability as a function of the predicted charge is therefore changed as well. The entire procedure is repeated until the hit/no-hit probability and the solid angles converge.

In this procedure, only low intensity data are used since they introduce relatively small error: if the number of hit PMTs is close to the total number of PMTs, the error on the reconstructed flux would be large. Moreover, above a certain intensity, all PMTs are hit and thus this method would not converge.

With the hit/no-hit probability and solid angles from either method 1 or 2, we extended our procedure to higher intensity runs to obtain a starting set of QLLKs. The final QLLKs can be self-consistently determined using the full charge minimization, in which the flux is determined by the full QLLKs and the no-hit likelihood. The procedure of obtaining QLLKs is simple: a 2-dimensional histogram $H(q, \mu)$ is filled with measured and predicted charges for all PMTs. $H(q, \mu)$ needs to be normalized such that for each bin of μ_j, we have:

$$\int H(q, \mu_j) dq = 1, \qquad \forall j = 1, ..., N_\mu,$$

where N_μ represents total number of bins in μ. The first bin for each μ is filled by the number of no-hits (which includes all the zero hits and those below the threshold). For each 1-dimensional histogram of certain μ value, the bins on charge q can be written as:

$$h_{ij} = H(q_i, \mu_j),$$

and the normalization is:

$$h_{1j} + \Delta q \sum_{i=2}^{N_q} h_{ij} = 1, \qquad \forall j = 1, ..., N_\mu,$$

where N_q represents the total number of bins in charge q, and Δq is the bin size on q. With the proper normalization, the 2-dimensional histogram $H(q, \mu)$ directly yields the charge likelihoods.

7.3 Monte Carlo Simulations

In this MC exercise, solid angles from method 2 were adopted. After 2 iterations of the hit/no-hit probability minimization, both the hit/no-hit probability and the solid angles were stable and the corresponding results are shown in Figs. 7.4 and 7.5, respectively. From

Fig. 7.4, we learn that the PMT responses in MC are in very good agreement with a Poisson-like distribution (i.e., the slope in the no-hit probability is close to unity). The slight difference between the parameter P_0 in the top and bottom panels of Fig. 7.4 is caused by the PMT response variations.

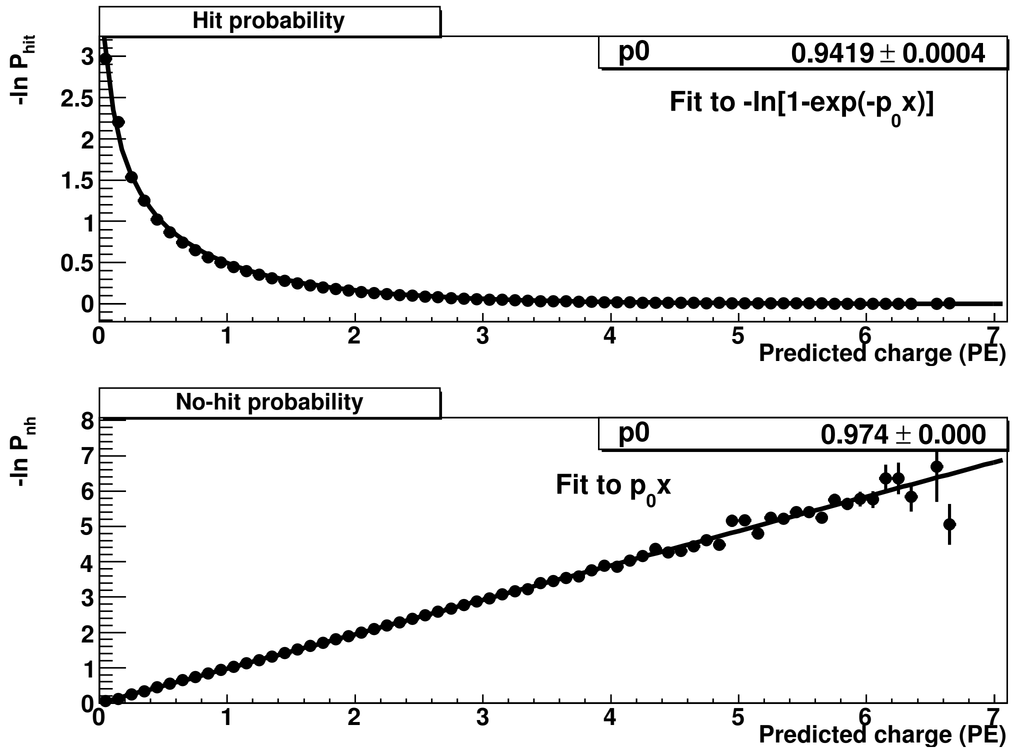

Figure 7.4: Hit/no-hit probability results as obtained from the MC data.

After full charge minimization, the no-hit probability and QLLKs for $1 < q < 1.1$ PE, $2 < q < 2.1$ PE, $5 < q < 5.1$ PE and $10 < q < 10.1$ PE are shown in Figs. 7.6 and 7.7, respectively. In the same figures, the results from first principles calculations are also shown. Here the charge likelihoods are calculated as:

$$P_q(q, \mu) = \sum_{n=0}^{\infty} P_q(q, n) P(n, \mu) = \mu e^{-\mu} \left[P_q(q, 1) + P_q(q, 2) \frac{\mu}{2!} + P_q(q, 3) \frac{\mu^2}{3!} + ... \right],$$

where the $P(n, \mu)$ is assumed to be a Poisson function, and the $P_q(q, n)$ are PMT n-PE charge response normalized to unity, as shown in Fig. 7.8. The single PE response, $P_q(q, 1)$, was derived by simulating 2 MeV electrons and recording the charge of PMTs that received only

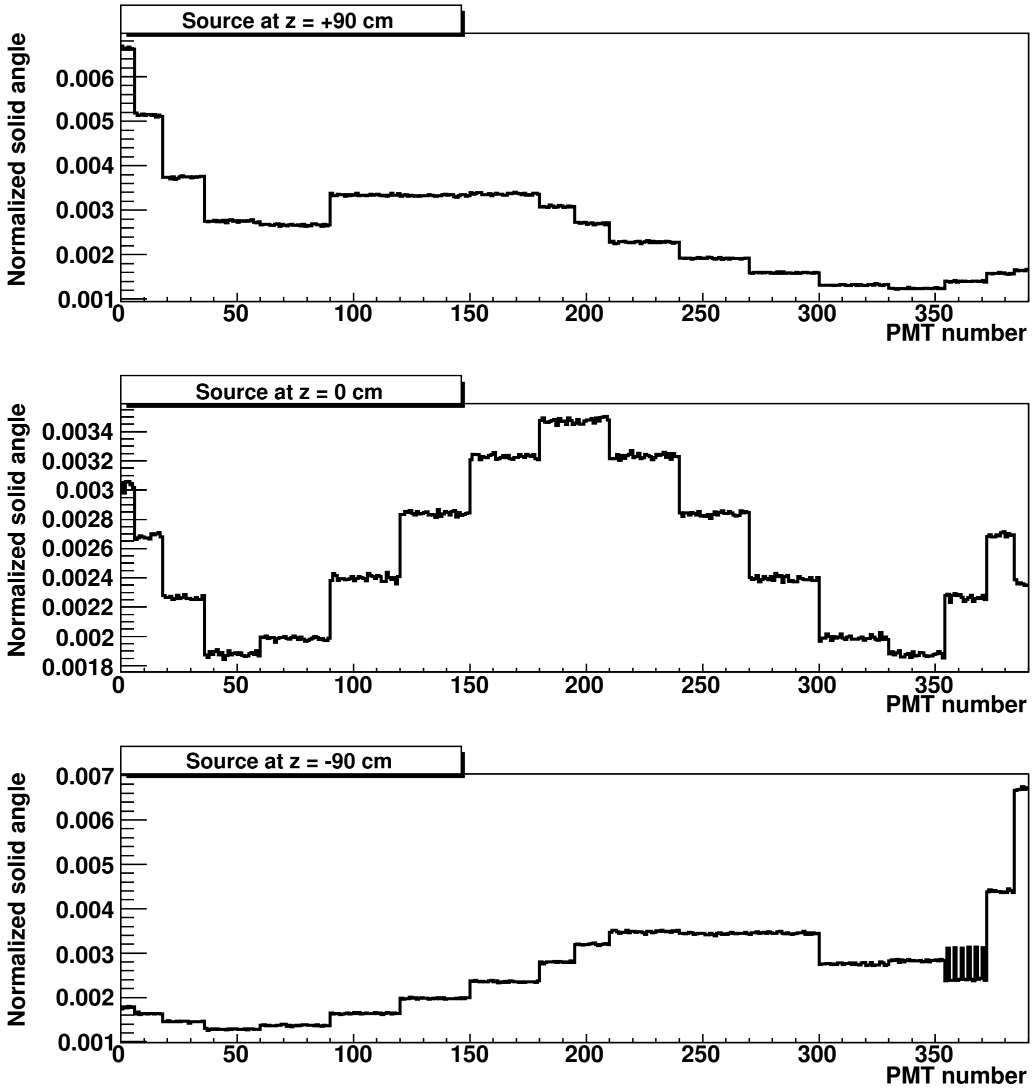

Figure 7.5: Normalized solid angles ($\sum \omega_i = 1$) for 390 PMTs after the hit/no-hit minimization with MC generated vertices at $z = 0$ and ± 90 cm.

a single PE hit. The higher response functions, $P_q(q, n \geq 2)$, were obtained by randomly sampling $P_q(q, 1)$ n times. In calculating $P_q(q, \mu)$, the infinite sum starts at $n = 1$ since $P_q(q, 0) = 0$ and terminates at some finite value of n when the contributions from the following terms become negligible.

Next we examine the minimum of the QLLKs for different values of the predicted charge, which should be a measure for the linearity of the charge response. From Fig. 7.7, we see that the minimum of the QLLKs happens around $\mu = q$ for q above 1 PE, while for q below or at

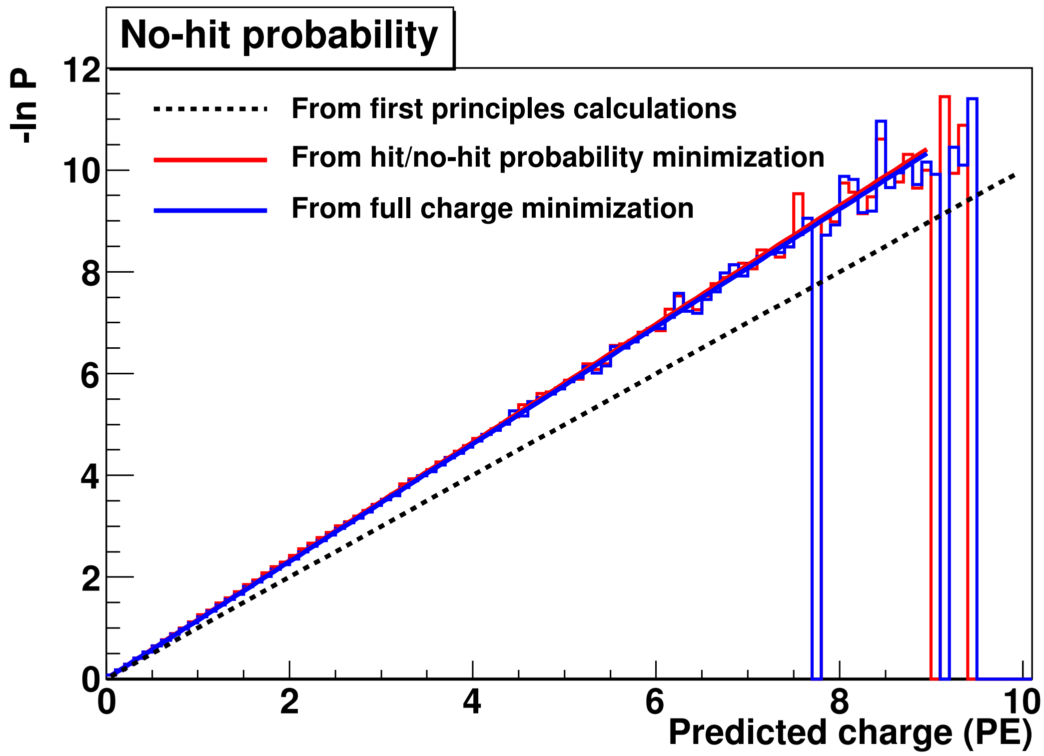

Figure 7.6: The no-hit probability as obtained from the hit/no-hit probability minimization, full charge minimization, and first principles calculations (as labeled).

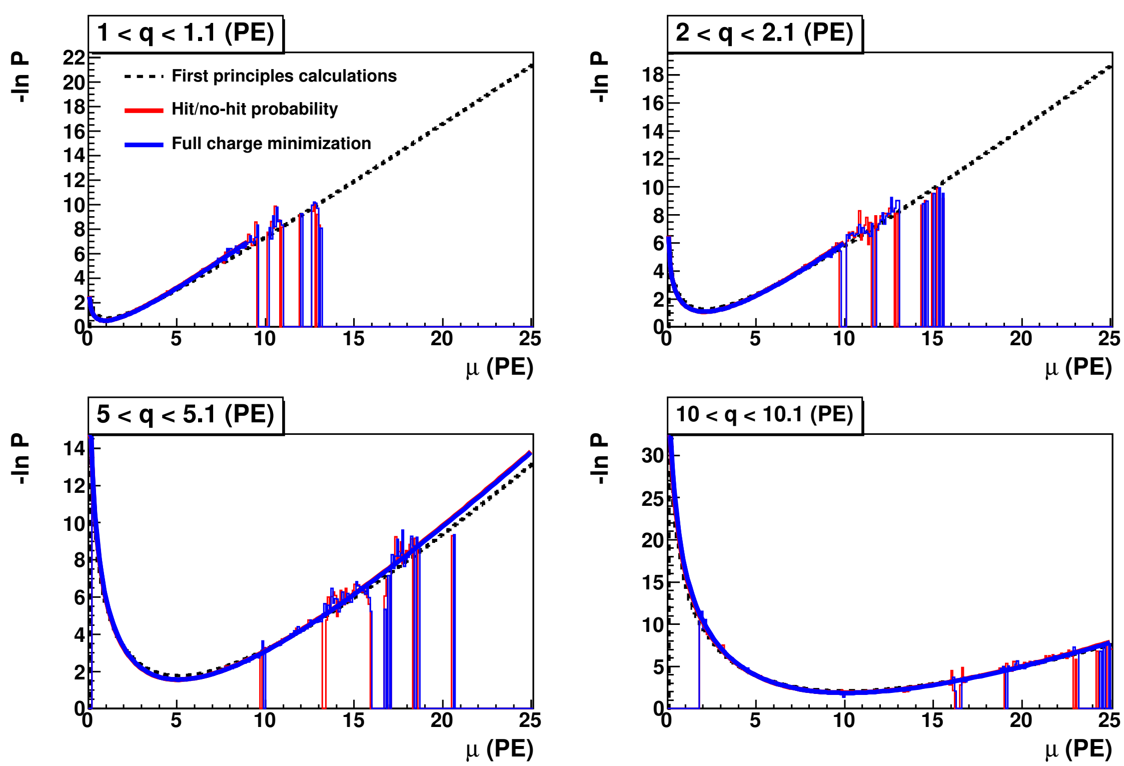

Figure 7.7: QLLKs for four different measured charge bins as obtained from the hit/no-hit minimization, full charge minimization, and first principles calculations (as labeled).

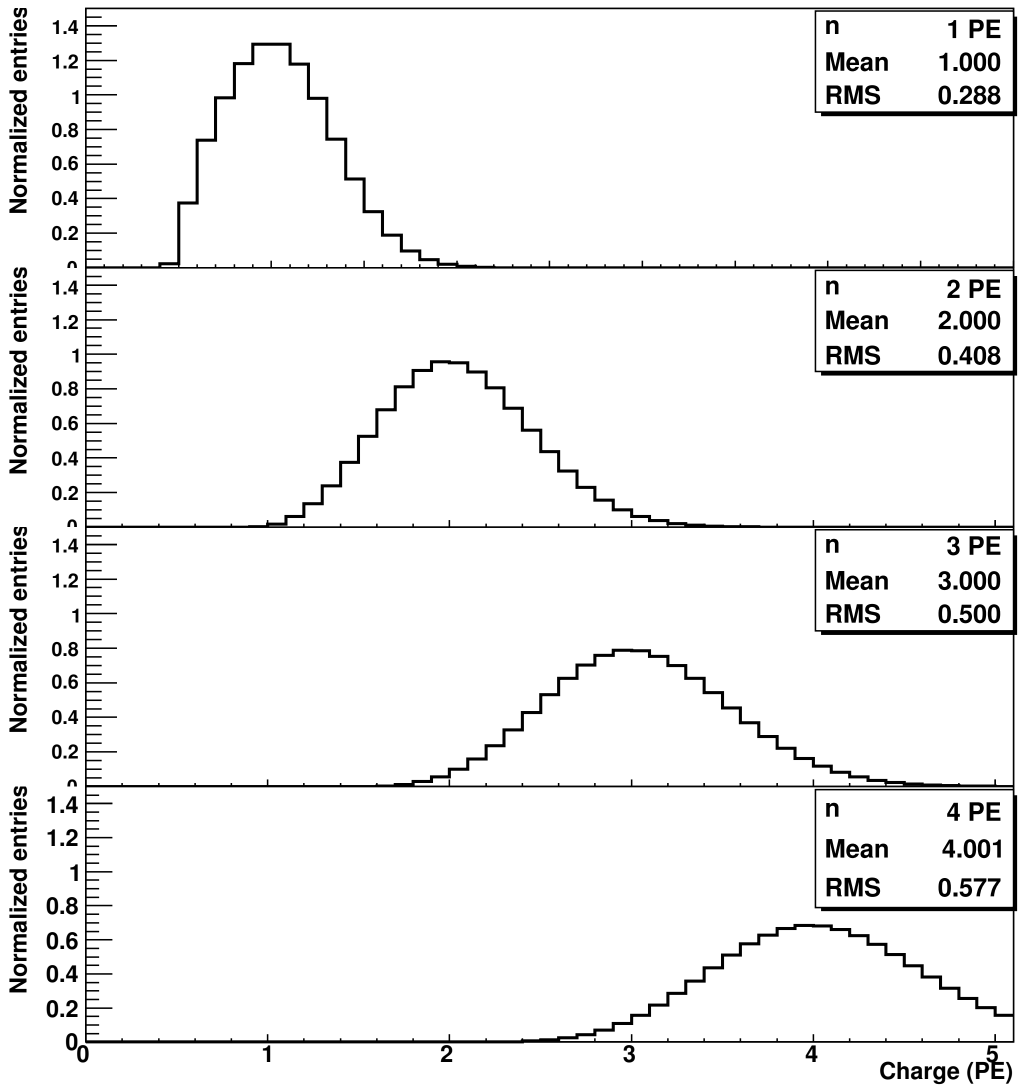

Figure 7.8: PMT charge response functions $P_q(q, n)$ for $n = 1$–4 PE. The single PE response function, $P_q(q, 1)$, is obtained from MC simulation, while the higher response functions are obtained from randomly sampling $P_q(q, 1)$ n times.

1 PE, the minimum of the QLLKs always appears to occur at $\mu = 1$ regardless of the actual value, as we show in Fig. 7.9. Additionally, as can be seen from Fig. 7.9, all functions are similar except for the vertical displacement. The calculated minima of the charge likelihoods as a function of the measured charge q are illustrated in Fig. 7.10. Indeed, the minima for $q \leq 1$ PE are around 1 PE, while those for $q > 1$ PE are around $\mu_{min} = q$, with very small variations. As μ_{min} represents the most likely value of μ with a given charge q, it is easy to understand why they have such behavior. Moreover, the plot also shows that the charge

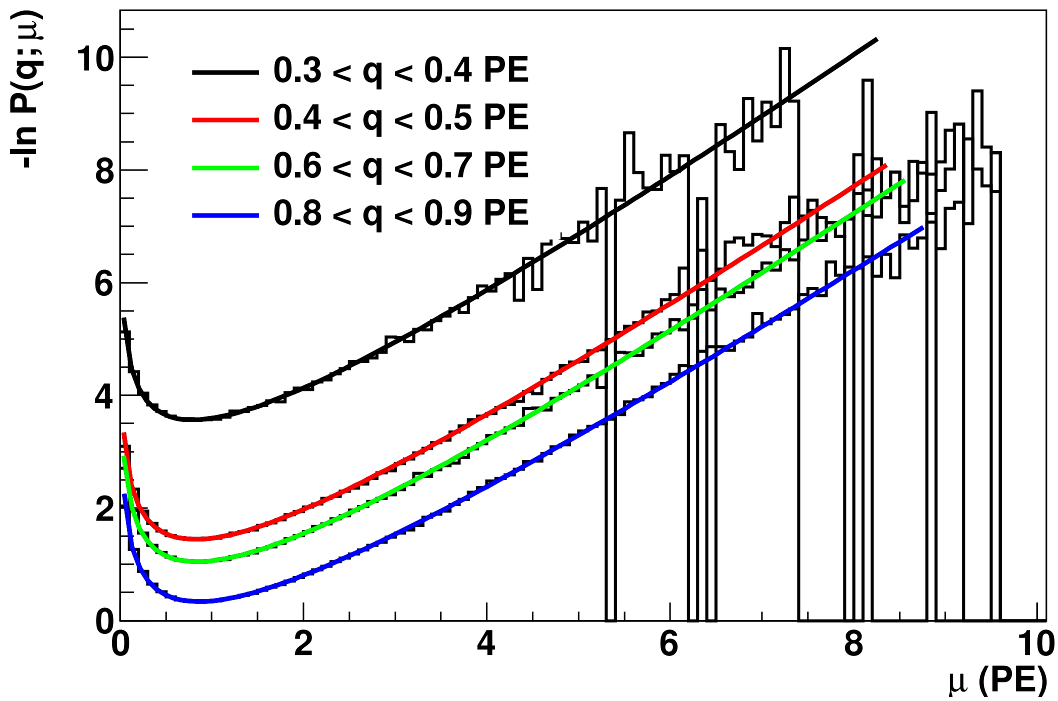

Figure 7.9: QLLKs for several charges below the single PE level as obtained from the full charge minimization. (MC simulations)

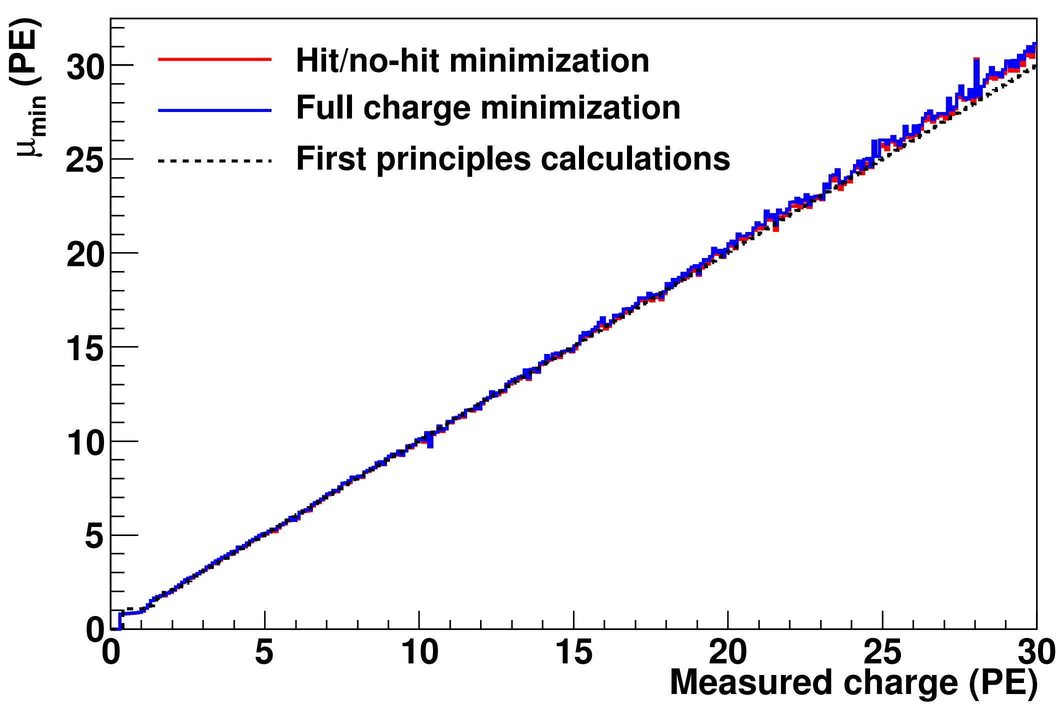

Figure 7.10: The minimums of the QLLKs as a function of q for the hit/no-hit minimization, the full charge minimization, and the first principles calculations. (MC simulations)

response of the PMTs is very close to linear over the measured charge range considered in this study.

If the QLLKs can be well-fitted by a certain function, we can store it more easily by saving only the parameters of the function and load them quickly. We find that the following parametrization:

$$f(x) = p_0 x - p_1 \ln(x) + p_2 + p_3 x^{0.3} + p_4 x^{0.7} \tag{7.7}$$

gives a good fitting quality over a wide range of charge, as indicated in Fig. 7.11.

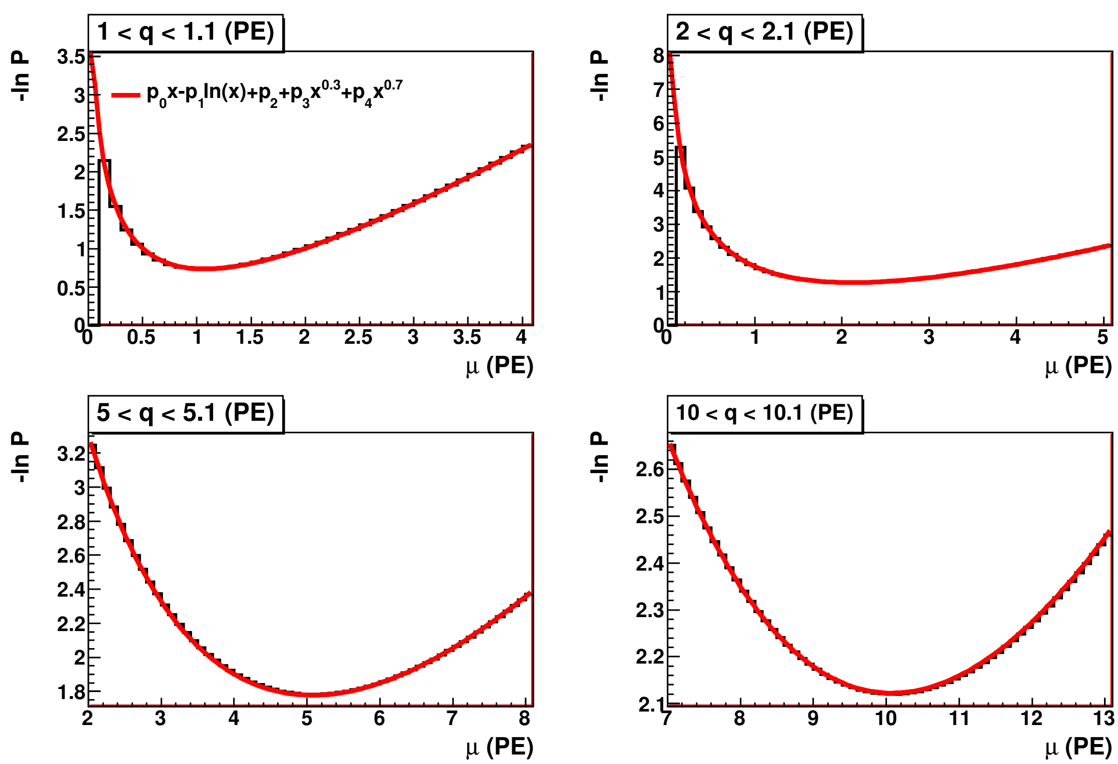

Figure 7.11: Charge likelihoods fitting examples by the function in Eq. (7.7).

7.4 Data Analysis

The laser runs used in extracting the QLLKs and the corresponding selection criteria are shown in Table 7.1. Most of the charge likelihoods calibration data were taken on May 17–18, 2012 during the same deployments used for the gain calibrations. Eight different

Run #	z (cm)	Average Nhits	Q_{max}/Q_{tot}	Q_{tot} (DUQ)	Total charge (PE)	intensity
43799	0	59.6	< 0.15	(0, 8k)	71.6	1
43800	0	115.6	< 0.07	(7k, 16k)	153.6	2
43801	0	195.7	< 0.07	(17k, 30k)	311.1	3
43802	0	340.8	< 0.05	(65k, 95k)	1088.0	4
43803	0	365.6	< 0.05	(125k, 160k)	1958.0	5
43804	0	369.2	< 0.05	(175k, 220k)	2745.0	6
43805	0	369.9	< 0.04	(220k, 280k)	3459.8	7
43806	0	370.0	< 0.04	(240k, 310k)	3749.7	8
43809	-92	50.1	< 0.15	(1.8k, 8k)	59.9	1
43810	-92	112.4	< 0.07	(7k, 16k)	152.6	2
43811	-92	189.6	< 0.07	(17k, 30k)	313.1	3
43812	-92	328.8	< 0.05	(65k, 95k)	1108.3	4
43813	-92	360.3	< 0.05	(130k, 175k)	2096.6	5
43814	-92	365.2	< 0.05	(170k, 215k)	2626.7	6
43815	-92	368.3	< 0.04	(220k, 280k)	3443.1	7
43816	-92	368.8	< 0.04	(240k, 300k)	3712.5	8
43853	92	56.2	< 0.15	(2k, 8k)	71.5	1
43854	92	100.2	< 0.07	(6k, 15k)	131.7	2
43855	92	173.9	< 0.07	(15k, 26k)	271.3	3
43856	92	329.9	< 0.05	(65k, 90k)	1062.2	4
43857	92	362.6	< 0.05	(130k, 170k)	2073.5	5
43858	92	367.0	< 0.05	(170k, 220k)	2670.0	6
43859	92	368.9	< 0.04	(215k, 270k)	3336.7	7
43860	92	369.3	< 0.04	(230k, 290k)	3586.9	8
45689	0	370.1	< 0.02	(470k, 560k)	7052.6	9
45690	0	370.1	< 0.02	(520k, 600k)	7699.8	10
45692	-92	370.1	< 0.02	(450k, 530k)	6642.1	9
45693	-92	370.1	< 0.02	(490k, 580k)	7307.8	10

Table 7.1: The UV ($\lambda = 375$ nm) laser runs' information for the purpose of charge likelihoods calibration including run number, laser deployed position, number of hitted PMT, maximum charge to total charge ratio Q_{max}/Q_{tot} (light noise cut), total visible charge cut and average number of PEs. After cuts, all the runs have number of entries between 23,000 and 24,000.

intensities data were obtained at 3 positions of $z = 0$ and $z = \pm 92$ cm. Adjustments had been made for better alignment which increased the UV laser maximum intensity output. Another four runs (45689, 45690, 45692 and 45693) with higher intensities were also taken at $z = 0$ and $z = -92$ cm on June 15, 2012 following the laser coupler realignment. This operation increased the intensity output and enlarged the effective range of both q and μ. All runs are 150 s long and were taken at a rate of 150 Hz.

We started with the same procedure as in the MC. The three lowest intensity data at each position were used in the hit/no-hit probability minimization. After four iterations, the minimized parameter in hit/no-hit probability (the slope in $-\ln P_{nh}$) became stable at about 0.91, as shown in the top left and bottom left panels of Fig. 7.12. The no-hit slope indicates a single PE inefficiency of about 9%, which might be caused by a combination of threshold effects, detection inefficiency in the electronics, and charge reconstruction inefficiency. In this case, the fitting function has to be extended accordingly from the assumption of pure Poisson statistics to include a single PE inefficiency. The coresponding result from the hit/no-hit probability minimization indicates a 17% single PE inefficiency, as shown in the top middle and bottom middle panels of Fig. 7.12. Since the single PE inefficiency is large, we may also

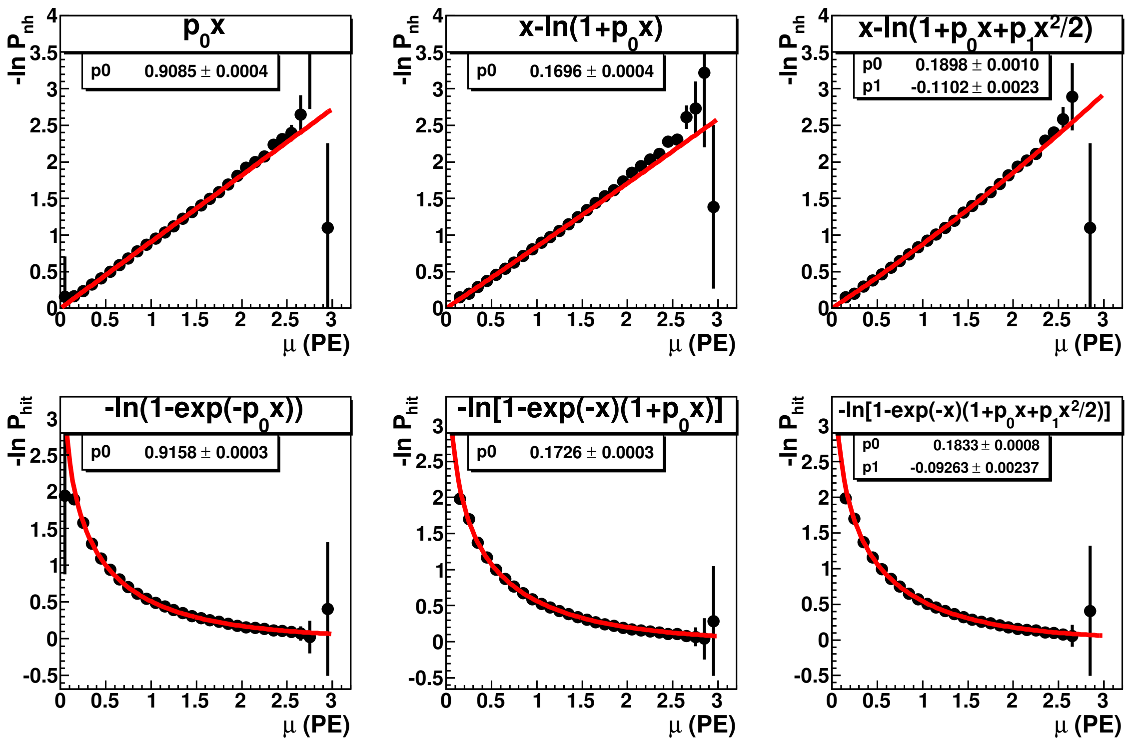

Figure 7.12: Hit/no-hit probability minimization fitted by functions corresponding to Poisson statistics (top left and bottom left), Poisson statistics with single PE inefficiency (top middle and bottom middle), and Poisson statistics with single PE and double PE inefficiencies (top right and bottom right). The slight difference between the parameters P_0 and P_1 in the top and bottom plots is caused by PMT response variations.

consider the double PE inefficiency to be included in our model as well in order to be able to allow for such effects. We assume that the efficiencies for $n \geq 3$ PE are at the 100% level.

Therefore, assuming Poisson statistics with only single PE inefficiency ϵ_1 and double PE inefficiency ϵ_2, the no-hit probability of any PMT can be written as:

$$P_{nh} = P_0 + \epsilon_1 P_1 + \epsilon_2 P_2 + ... = e^{-\mu}\left(1 + \epsilon_1\mu + \epsilon_2\frac{\mu^2}{2} + ...\right).$$

Herewith, the negative logarithm of the no-hit probability is:

$$-\ln P_{nh} = \mu - \ln\left(1 + \epsilon_1\mu + \epsilon_2\frac{\mu^2}{2} + ...\right),$$

and the corresponding negative logarithm of the hit probability yields:

$$-\ln P_{hit} = -\ln\left[1 - e^{-\mu}\left(1 + \epsilon_1\mu + \epsilon_2\frac{\mu^2}{2} + ...\right)\right].$$

As shown in the right panels of Fig. 7.12, the double PE inefficiency tends to become negative after several iterations, which cannot be physical. Although this appears to indicate that the double PE inefficiency should be zero, we still tried the hit/no-hit minimization to the single PE + double PE inefficiencies again by confining the parameter ϵ_2 to be positive, and obtained a set of solid angles and starting fluxes for the full charge minimization. In the full charge minimization, ϵ_1 and ϵ_2 are fitted from the no-hit probability and the evolutions of ϵ_1 and ϵ_2 in the full charge minimization are displayed in Fig. 7.13 where ϵ_1, after an initial increase, tends to be vanishing as the iteration increases, while ϵ_2 increases monotonically. Such a behavior is unphysical and therefore, we abandoned the double PE inefficiency. The following study only includes a non-vanishing single PE inefficiency.

After running the full charge minimization, we checked the ratios of total measured charge q to total predicted charge μ for all PMTs. The q/μ as a function of the PMT number for all intensities is shown in the left column of Fig. 7.14. From it, we can observe not only a ~10% variation, but also a slightly tilted structure.

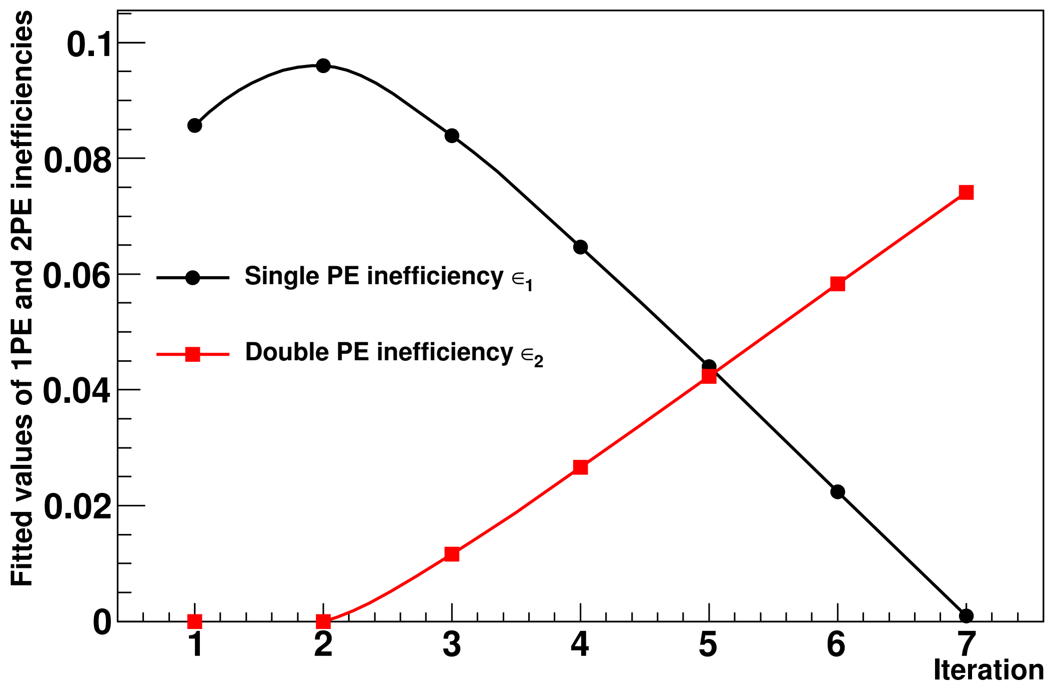

Figure 7.13: Evolutions of the single and double PE inefficiencies in the no-hit function in the full charge minimization.

Then we recalculated the charge likelihoods using the full charge minimization by taking the solid angles from the normalized charge q of intensities 7 and 8 (runs 43859 and 43860 for the top, 43805 and 43806 for the center, 43815 and 43816 for the bottom). The q/μ ratios for the 3 vertices had shown a very good uniformity in right column of Fig. 7.14. The variations shown when the source is at center and bottom are caused by the second deployment runs (45689, 45690, 45692 and 45693) in which the positions were slight different for the sake of deployment uncertainty. Had these runs been taken out, the q/μ ratio would have been as good as the source at the top.

Finally, two sets of solid angles for center and bottom source positions were used. For intensities 1 to 8, all three vertices used the corresponding normalized charge q from intensities 7 and 8, while for intensities 9 to 10 at the center and bottom, the corresponding normalized charge q from these two intensities were used. Since the solid angles were directly taken from the normalized charge and because the starting fluxes of high intensities (5 to

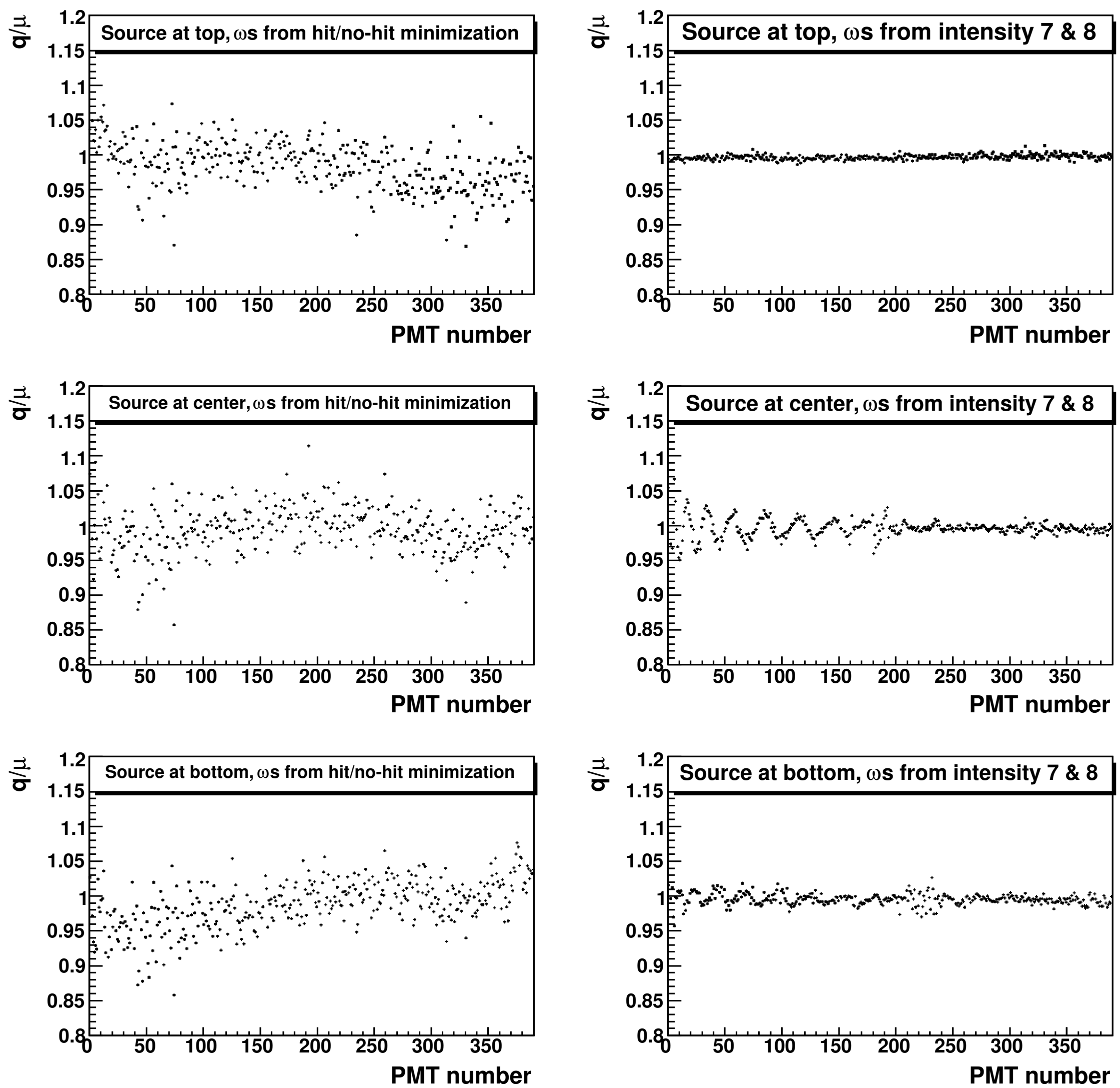

Figure 7.14: The q/μ as a function of PMT number at three deployed positions for solid angles from hit/no-hit minimization (left column) and the normalized charge q of intensities 7 and 8 (right column) at corresponding positions.

10) cannot be derived from hit/no-hit minimization (since almost all the PMTs are hit), the procedure of hit/no-hit minimization could be automatically skipped. All one needed to do was to directly run the full charege minimization with the flux starting from $\sum q_i / \sum \omega_i$ and to be minimized for each iteration.

Next, we looked at the q/μ ratio as a function of PMT number for different intensities when the source is deployed at the top position as shown, in Fig. 7.15. The center and bottom vertices have similar behavior. The q/μ ratios for the lowest and the second lowest

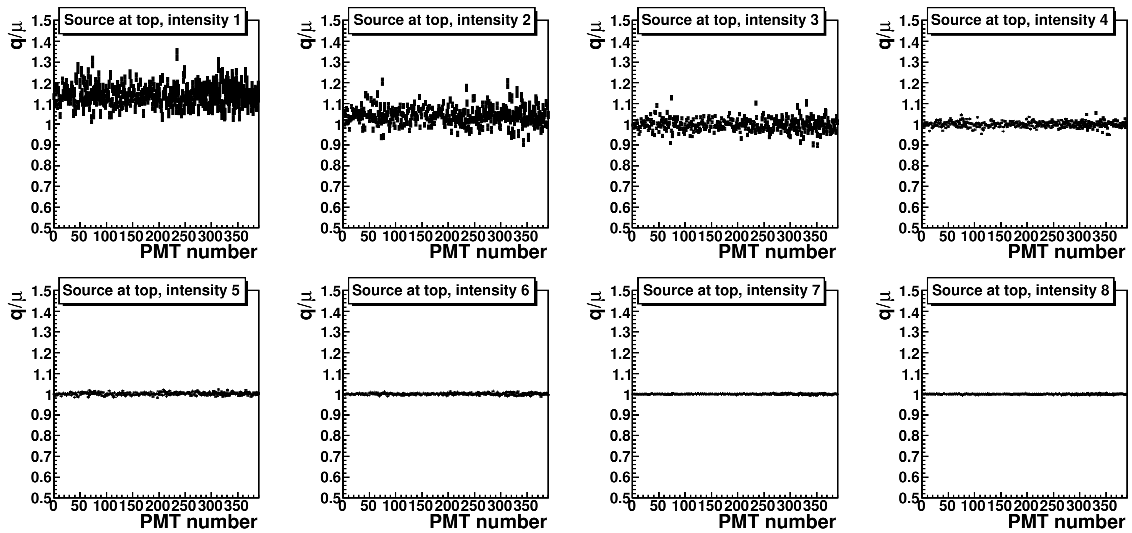

Figure 7.15: q/μ ratio as a function of PMT number for different intensities when the source is deployed at the top position ($z = +92$ cm).

intensities are averaged at about 1.14 and 1.04 respectively, which are higher than they are supposed to be. The q/μ ratios for the rest of the intensities are centered properly at unity. The variation goes down as the intensity rises because higher intensity always has higher statistics with the same number of events and the PMT charge non-linearity disappears when the charge is higher than about 3 PE.

The reason why low intensities had such behavior was found to be related to the bin size in μ in the 2-dimensional histogram $H(q, \mu)$. Changing the bin size from 0.1 to 0.01 PE in the μ dimension can keep high intensities q/μ ratios the same but have low intensities q/μ ratios back to normal. However, the bin size of 0.01 PE would increase the amount of calculation and therefore slow down the overall procedure, while changing nothing in the high μ part. A combined bin size (0.01 PE when $\mu \leq$1 PE and 0.1 PE when $\mu >$1 PE) was a perfect solution and the QLLKs from the old binning and combined binning are compared in Fig. 7.16. From a far perspective, they look the same. Zooming into the range of $0 < \mu < 1$ PE, the discrepancy appears at the very end of the low μ part which makes the q/μ ratio back to normal as shown in Fig. 7.17. Applying the combined binning, the second lowest intensity average q/μ ratio deviates from unity by only 0.7%, and the lowest intensity average

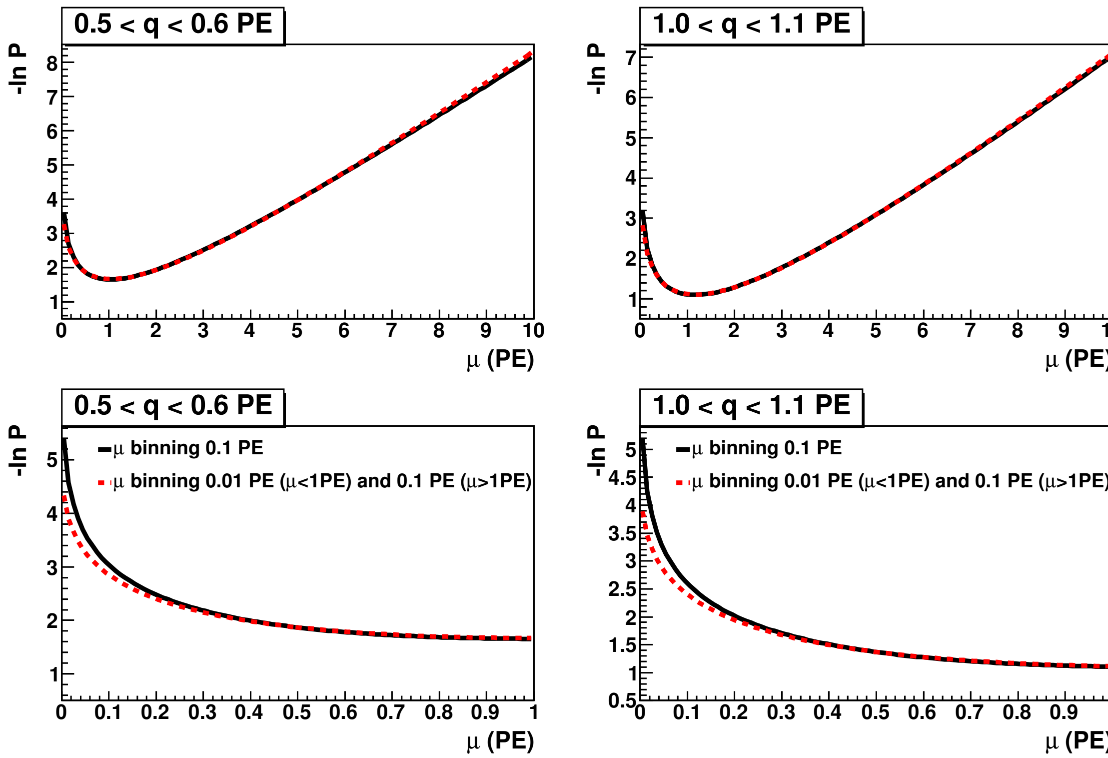

Figure 7.16: Comparison of QLLKs for 0.1 PE bin size and combined bin size on μ when charge is between 0.5 and 0.6 PE as well as 1.0 and 1.1 PE.

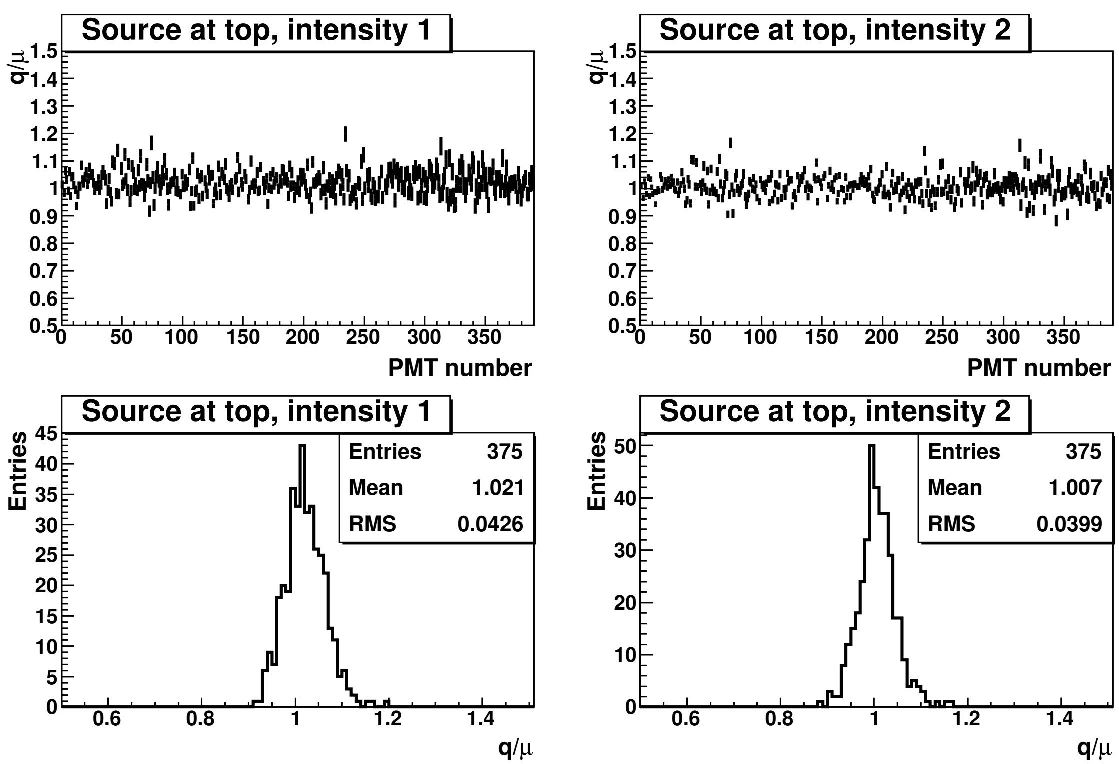

Figure 7.17: q/μ ratio and its projection for lowest two intensities using combined binning.

value is 2.1% higher than unity. In order to understand what caused the 2.1% deviation, the low μ part of no-hit probability and q/μ ratio was examined in Fig. 7.18. As one can notice in the left panel of Fig. 7.18, there is a small deviation from the no-hit probability fitting function at the tail of μ, and the q/μ ratio has a rising trend for very low μ values, as seen in the right panel of Fig. 7.18.

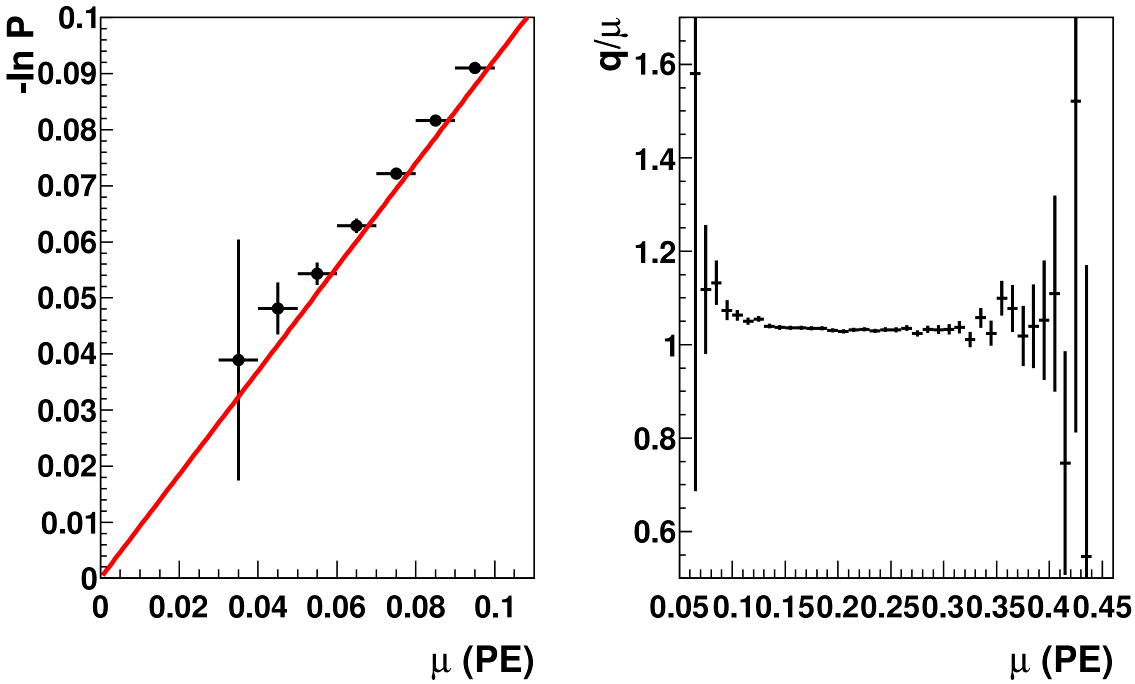

Figure 7.18: No-hit probability in the range of $0 < \mu < 0.1$ PE (left) and q/μ as a function of μ for the lowest intensity (right).

If all PMTs are identical, the contribution of low μ values will come from a ring or certain rings of PMTs with the lowest flux. However, in reality PMTs have variations in every aspect, which means this effect may only be contributed to by certain PMTs which have relatively low responses (i.e., quantum efficiencies). As an illustration, the PMTs, which have low μ values, are shown in Fig. 7.19. It is obvious that the most frequent contributor to all of the 4 ranges of μ is from the PMT 43. Around PMT 43, PMT 46 and 52 have the second-highest entries. At the other end, namely the bottom PMTs, PMT 321 is the most active at the low μ region. Figure 7.20 explicitly shows that if PMT 43, 46, 52 and 321 were taken out, the

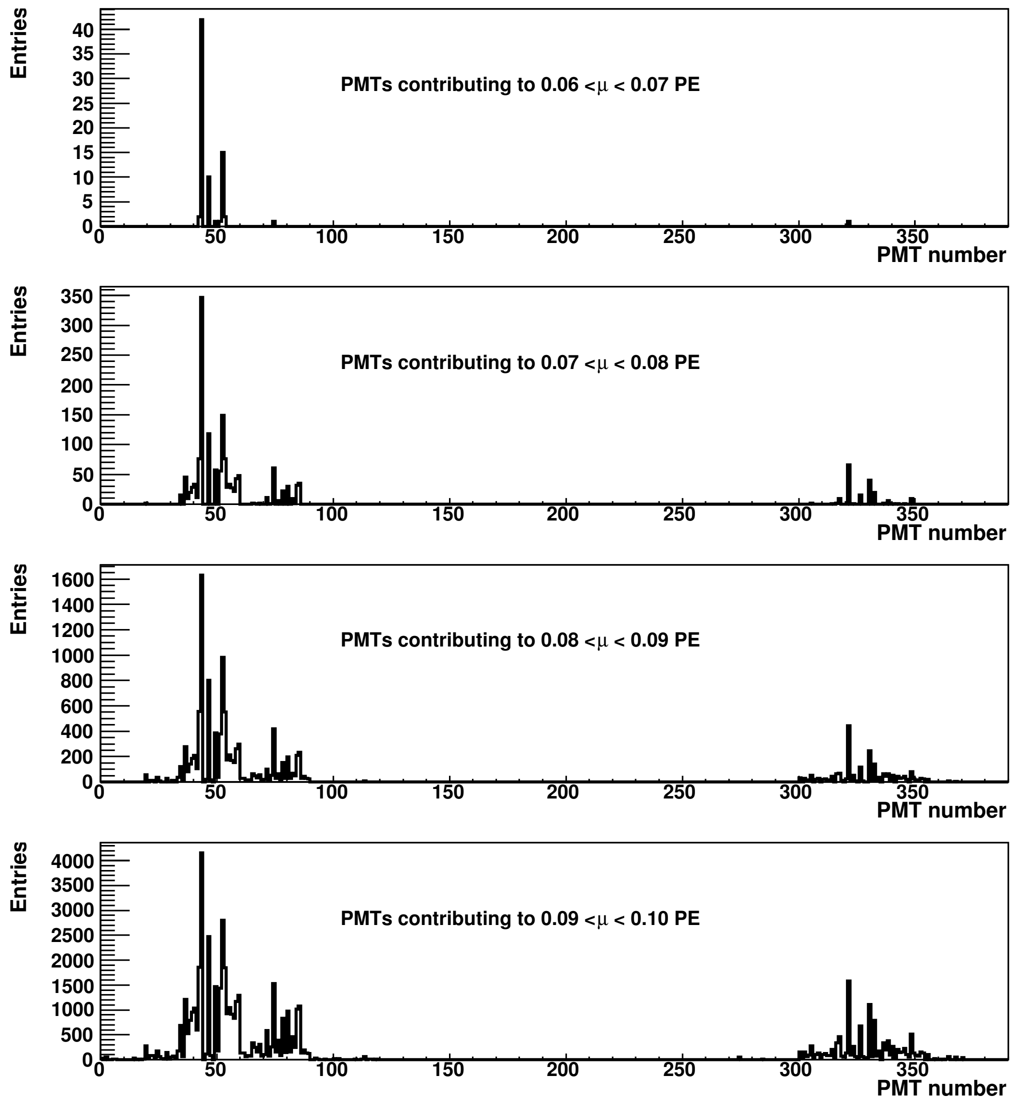

Figure 7.19: The contribution of certain μ value ranges as a function of PMT number.

q/μ ratio as a function of μ looks much more uniform than it used to be. It can be concluded that some PMTs having relatively low responses are really the main contributors of the low μ anomaly. Since these PMTs do not have a significant impact on the result of QLLKs, we will keep using all the active PMTs.

The last thing left was the convincing criterion with which the full charge minimization stopped. Although the QLLKs went stable after several iterations, a clear definition would make the procedure much more persuasive. The plots of the evolution of the single PE inefficiency, ϵ_1, and its change as a function of iteration number are shown in Fig. 7.21. The

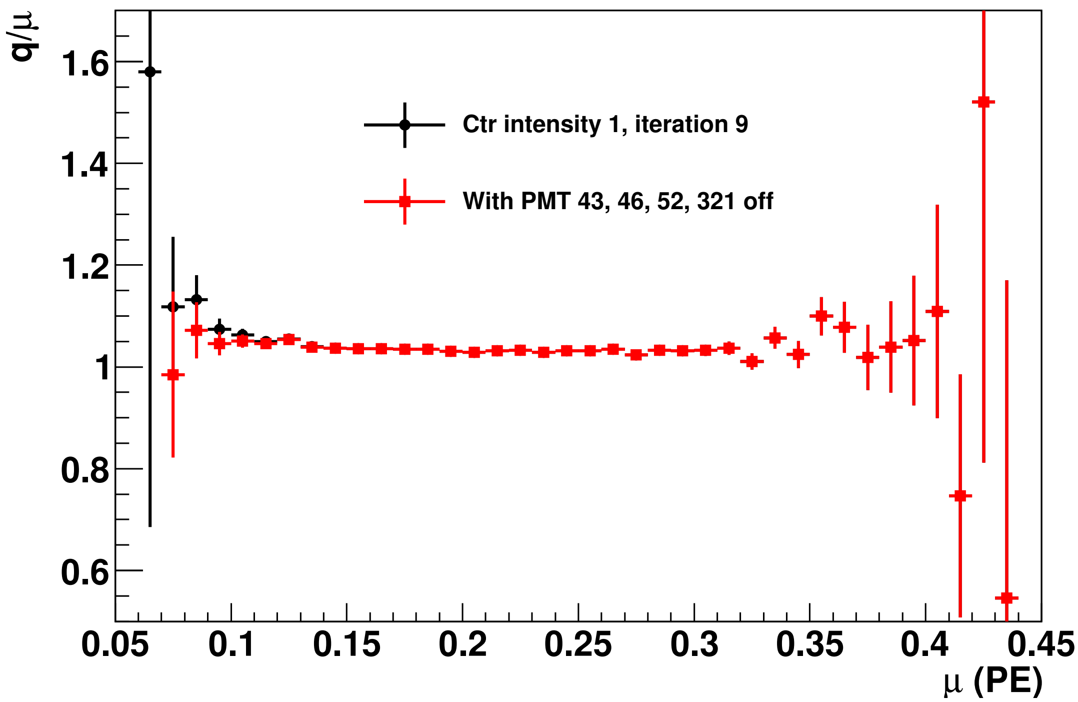

Figure 7.20: q/μ ratio as a function of μ for center intensity 1 laser data (run 43799) with and without PMTs 43, 46, 52 and 321.

parameter ϵ_1 goes to the minimum at iteration 9 and the changes for ϵ_1 above iteration 9 are always smaller or about 0.5%. One may notice that in Fig. 7.21 ϵ_1 is about 8%, while in Fig. 7.13 it is about 17%. The result in the full charge minimization is more accurate than that in the hit/no-hit probability minimization because it takes advantage of the PMT charge information. Looking at the evolutions of the q/μ ratios in Fig. 7.22, we learned that the differences between q/μ ratios for various intensities expanded first and then stayed constant at around iteration 9. All the evidences indicated that iteration 9 was the best stopping point and the QLLKs were extracted from it.

Finally, Figs. 7.23 and 7.24 display the results of QLLKs for some q values compared with those derived from the first principles calculations in MC. The minima of the QLLKs as a function of the measured charge q are plotted in Fig. 7.25. Superimposed are the minima of the QLLKs from MC (first principles calculations) for comparison, from which the linear charge response in both data and MC is concluded.

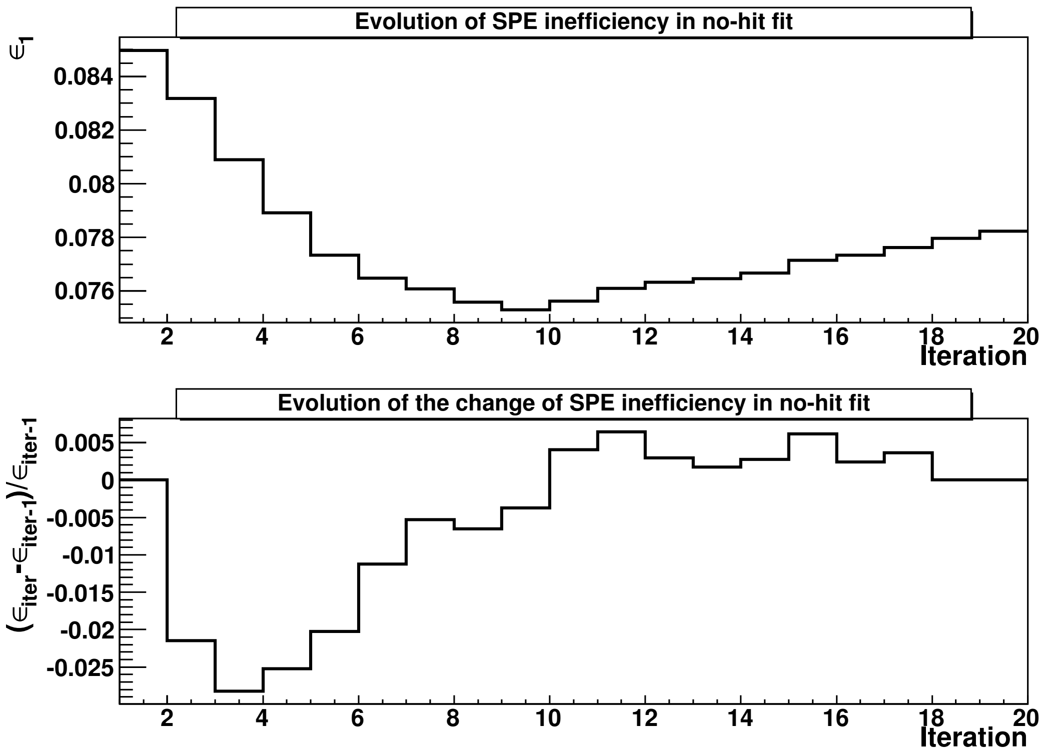

Figure 7.21: Evolutions of single PE inefficiency and its change in no-hit probability fit.

The QLLKs obtained from MC (first principles calculations) which have been used in all Double Chooz analyses to date have been updated to the laser calibrated QLLKs since March 2013.

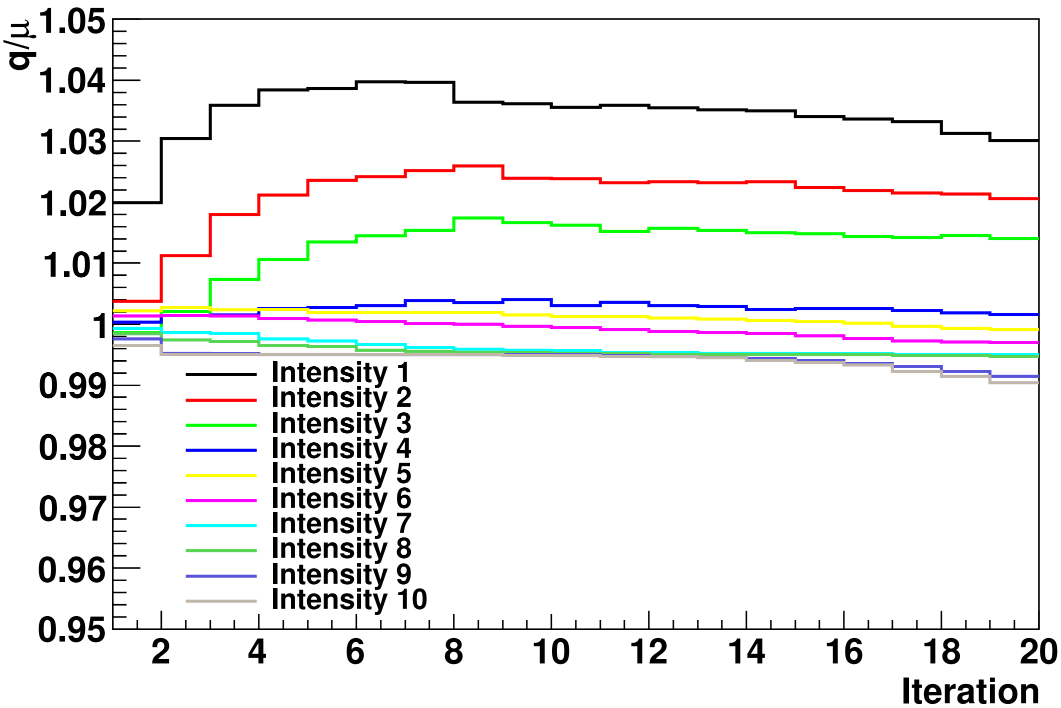

Figure 7.22: Evolutions of the q/μ ratios for different laser intensities deployed at the center.

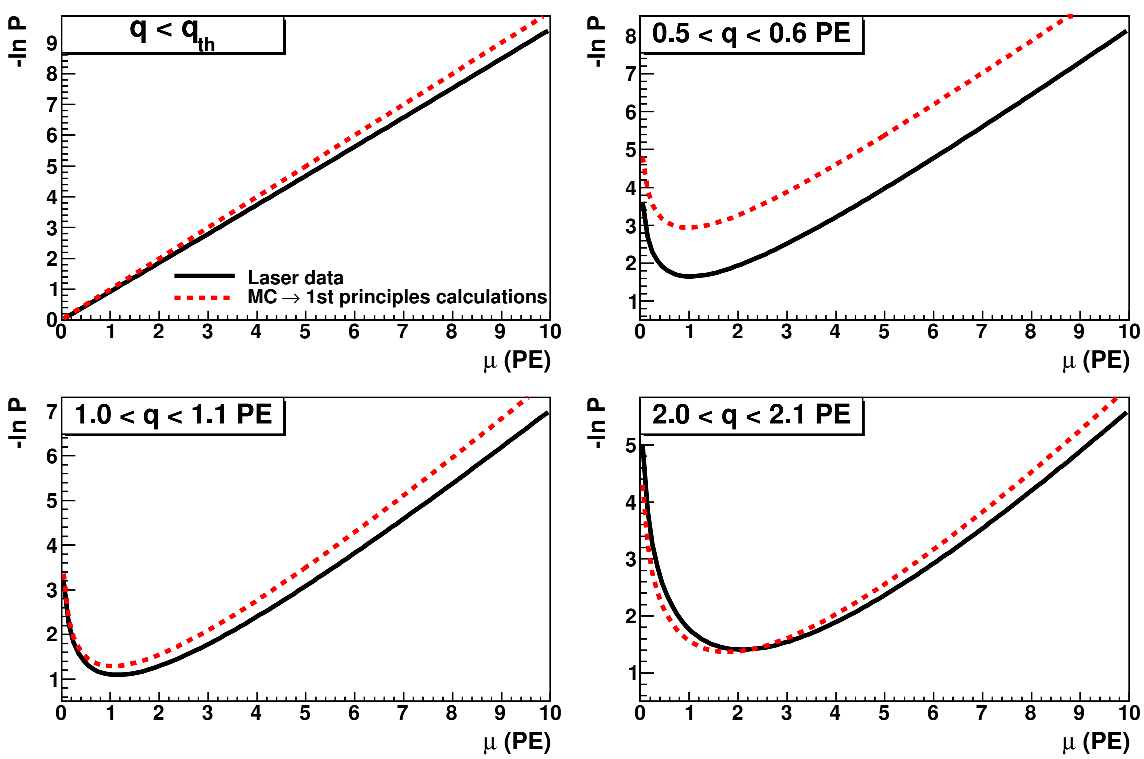

Figure 7.23: QLLKs from the laser calibration data superimposed with the MC QLLKs (from first principles calculations) for no-hit, $0.5 < q < 0.6$ PE, $1.0 < q < 1.1$ PE and $2.0 < q < 2.1$ PE.

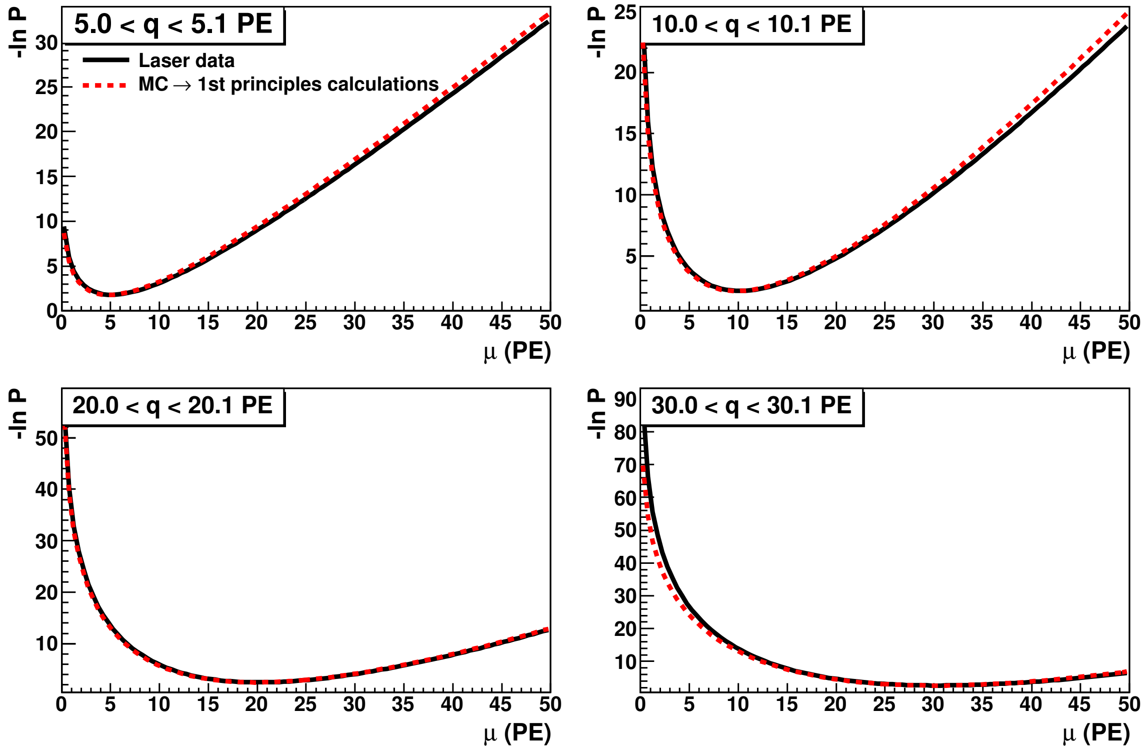

Figure 7.24: QLLKs from the laser calibration data superimposed with the MC QLLKs (from first principles calculations) for $5.0 < q < 5.1$ PE, $10.0 < q < 10.1$ PE, $20.0 < q < 20.1$ PE and $30.0 < q < 30.1$ PE.

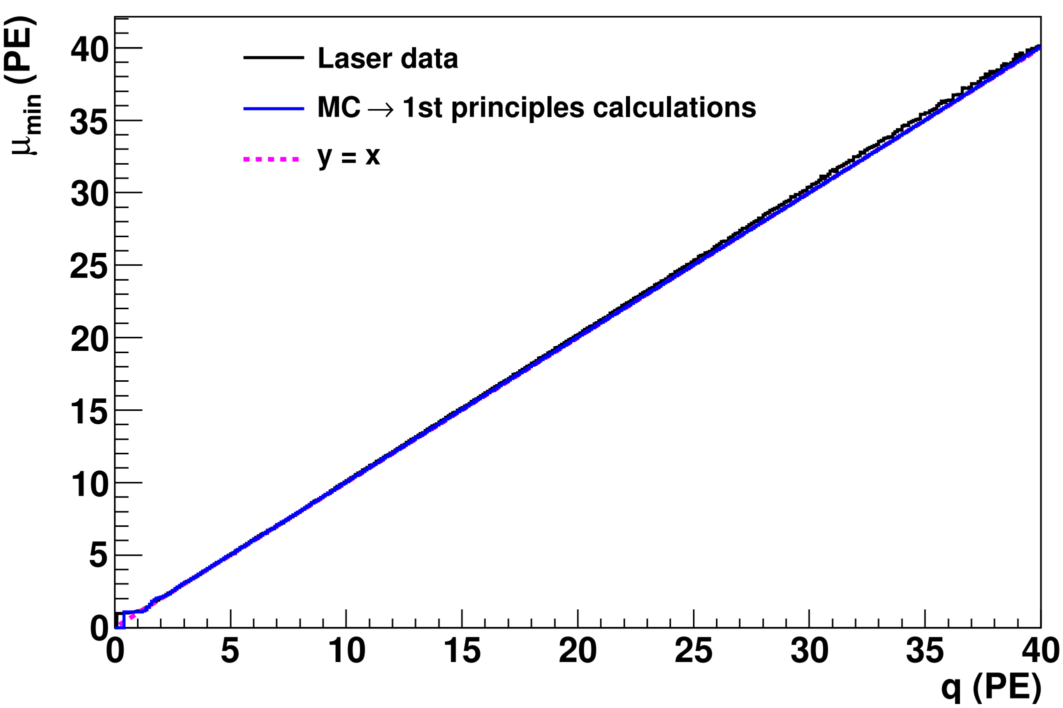

Figure 7.25: The minima of the QLLKs from the laser data and MC (first principles calculations) as a function of the measured charge.

Chapter 8

Event Reconstruction

8.1 Overview

The event reconstruction algorithm used in the Double Chooz analyses has been developed by the University of Alabama group, and is called internally RecoBAMA. In order to achieve the most powerful event reconstruction one has to take advantage of all available information, i.e., all PMT recorded charge and time (including the zero hits). RecoBAMA is based on both charge and time likelihoods (TLLKs). Each of the two likelihoods can be used for event reconstruction by itself, where using only the PMT time information (T-only) performs better than that using only the PMT charge information (Q-only). RecoBAMA underwent several algorithm changes: first using T-only, then using time and hit/no-hit probability (T+H/NH), finally using both charge and time (QT) information in March 2011, which corresponds to the current version. However, the different versions, including Q-only, T-only and T+H/NH, have been used by the University of Alabama group for position accuracy and resolution studies. The advantage of the different reconstruction algorithms, such as Q-only and T-only, is that they require a restricted and complementary set of input parameters. For instance, the Q-only algorithm needs the PMT gains, optical model and the QLLKs, while the T-only algorithm needs the PMT time offsets, optical model and the TLLKs. Before the PMT gains or PMT time offsets were available with sufficient precision, the comparisons between individual algorithms were significant in estimating the quality of the reconstruction. The full set of input parameters needed for the full QT algorithm can be determined by dedicated calibrations or from data themselves; they are as follows:

- PMT gains;
- PMT time offsets;
- effective speed of light in the medium;
- charge likelihoods;
- time likelihoods;
- optical model.

We have already discussed the first four sets of input parameters using the laser calibration data in Chapters 5, 6 and 7. In Section 8.2 and Section 8.3, the extraction of the TLLKs and the optical model will be discussed, respectively. In Section 8.4, the concept of the reconstruction algorithm and the corresponding MC studies are discussed. The event energy reconstruction will be described in Section 8.5, which strongly depends on the optical model. In RecoBAMA, the flux Φ (light intensity per unit solid angle) is calculated by using the approximate solution in Eq. (7.5) of Section 7.2, which turns out to be as good as the minimized one using charge likelihoods. Both the calculated and minimized fluxes rely on the proper optical model. Therefore, the correct optical model is crucial and a careful study becomes significant. Section 8.6 contains a summary and concluding remarks.

8.2 Time Likelihoods

The current time likelihood lookup tables have been extracted from MC events. The time likelihood function is defined as the probability of detecting a photon hit at time t_{corr} when a predicted charge μ is expected at the PMT,

$$P_t(t_{corr};\mu) = \sum_{n=1}^{\infty} P_t(t_{corr};n)P(n;\mu),$$

where the summation index n is the number of PEs hitting the PMT. $P_t(t_{corr};n)$ is the probability of measuring a time t_{corr} at a PMT which has a number n of photon hits; $P(n;\mu)$ is the probability of detecting a number of photon hit n with a predicted charge μ, which is assumed to be given by the Poisson distribution. The corrected time is defined in Eq. (6.1).

In order to obtain the corrected time distributions samples of $P_t(t_{corr};n)$, MC electron events with energies between 1 to 6 MeV were generated uniformly in the neutrino target. The $P_t(t_{corr};n)$ functions were derived by fitting the n-PE corrected time distributions as shown in Fig. 8.1 for $P_t(t_{corr};1)$ to $P_t(t_{corr};4)$. The abrupt end in the corrected time distributions at about 200 ns is due to the fact that the MC uses the same event time window as

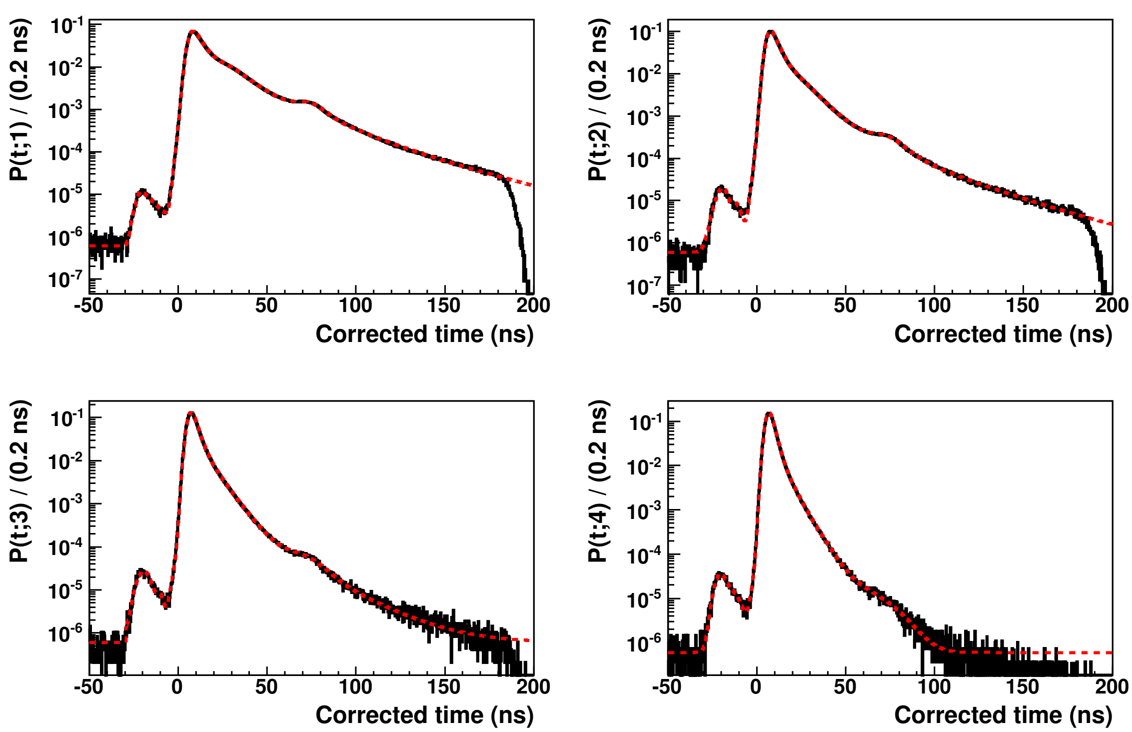

Figure 8.1: $P(t;1)$ to $P(t;4)$ derived by 1–6 MeV electron events uniformly generated in the neutrino target (MC simulations).

the data, which is 256 ns. In the MC, the default event time starts at 50 ns; by subtracting the event time and the photon propagation time, the corrected times therefore terminate at less than 200 ns as shown in Fig. 8.1. The peak at about −20 ns is caused by PMT prepulses, as explained below.

A diagram of how a PMT detects photons is illustrated in Fig. 8.2. An incident photon strikes the photocathode and produces an electron via the photoelectric effect. The electron is accelerated and directed by the focusing electrode towards the first dynode. Each dynode has a more positive electrical potential than its predecessor, where each of the accelerated electrons will produce several low energy electrons, which are then accelerated to the next dynode. With an ever-increasing number of electrons being produced at each stage, the final electrons cascade with an accumulation of charge reaches the anode creating a sharp current pulse, which indicates the arrival of the incident photon at the photocathode. Two out-of-time pulses are possible, as follows:

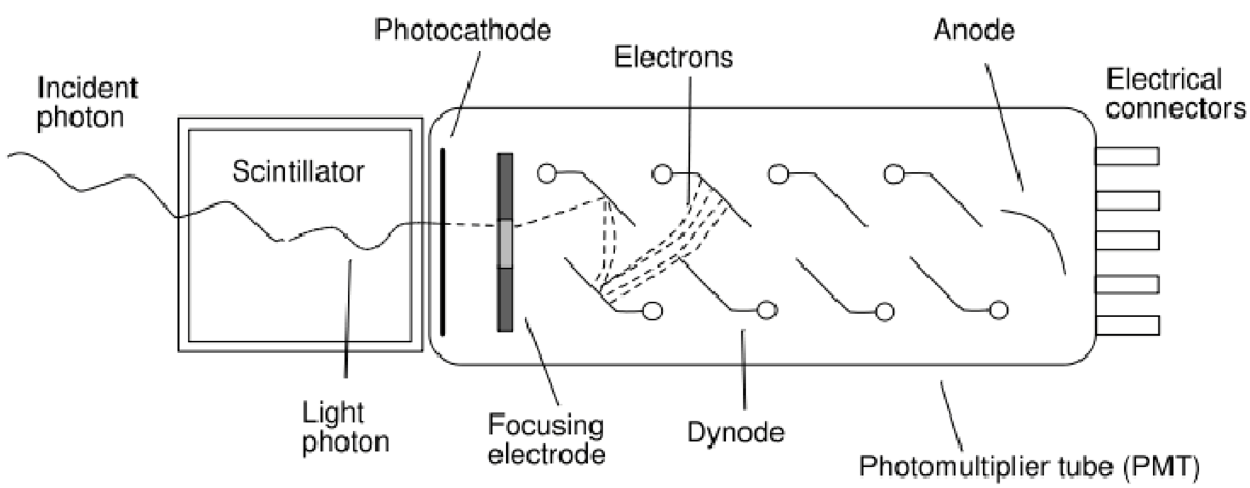

Figure 8.2: Schematic of a PMT coupled to a scintillator.

- Prepulse: photon penetrates the photocathode and directly strikes the dynode, which emits one or more secondary electrons.

- Afterpulse: there are two types of afterpulses:

1. Short delay afterpulse – usually caused by the elastic scattering of electrons on the first dynode, which usually takes about several nanoseconds to several tens of nanoseconds after the signal pulse.

2. Longer delay afterpulse – caused by the positive ions generated by the residual gases in the PMT. The positive ions drift back to the photocathode and produce electrons which result in the afterpulse. The delay time ranges up to several microseconds.

The range of the TLLKs extends from −50 ns to 450 ns as extrapolated from the functional form of the fit. If the corrected time goes outside these bounds, the value at the corresponding boundary is imposed. The predicted charge μ ranges from 0 to 10 PEs with a bin size of 0.1 PE. The TLLK for any μ value can be linearly interpolated from the lookup tables. The reconstructed position resolution using the full QT algorithm for 1–6 MeV electrons is shown in Fig. 8.3.

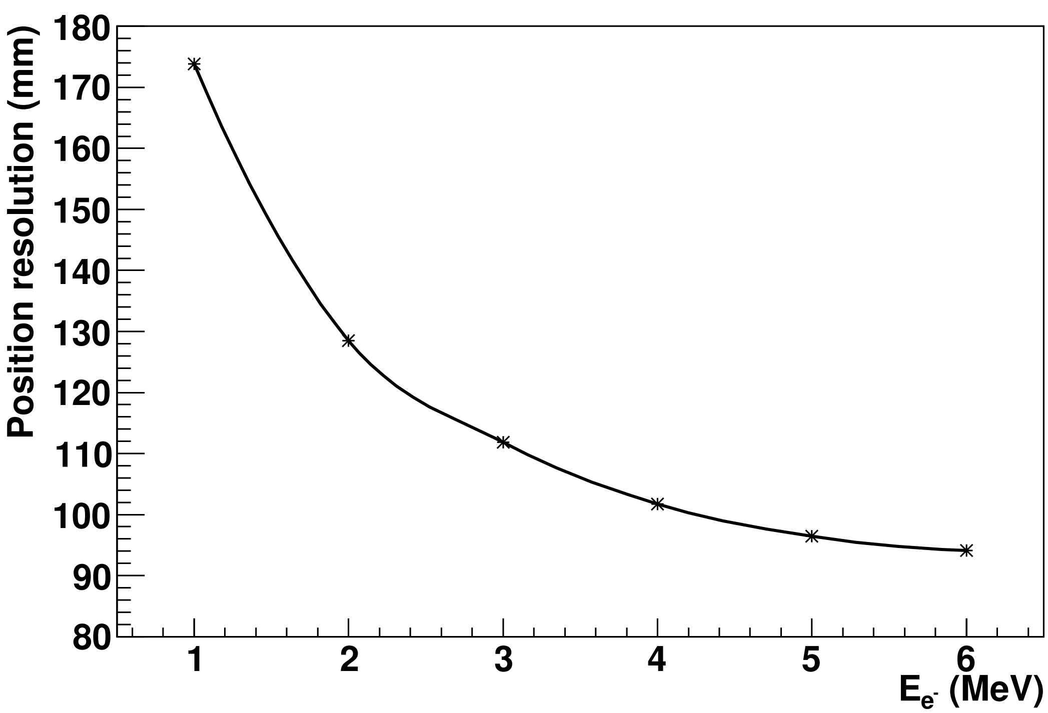

Figure 8.3: Reconstruction position resolutions for 1–6 MeV electron events using the full QT algorithm.

The $P_t(t_{corr}; n)$ distributions had been obtained using the MC generated vertex. One could also use the reconstructed vertex instead. It turned out that there was no obvious difference between them, as can be seen from Fig. 8.4, which means the reconstructed vertex is accurate enough for deriving the TLLKs. If the corrected time distributions for Double Chooz data are significantly different from those obtained from the MC, the TLLKs can be updated self-consistently by using Double Chooz physics data, either source calibration data or cosmic-ray data (e.g., 2.2 MeV γ from hydrogen capture neutron events induced by cosmic muons).

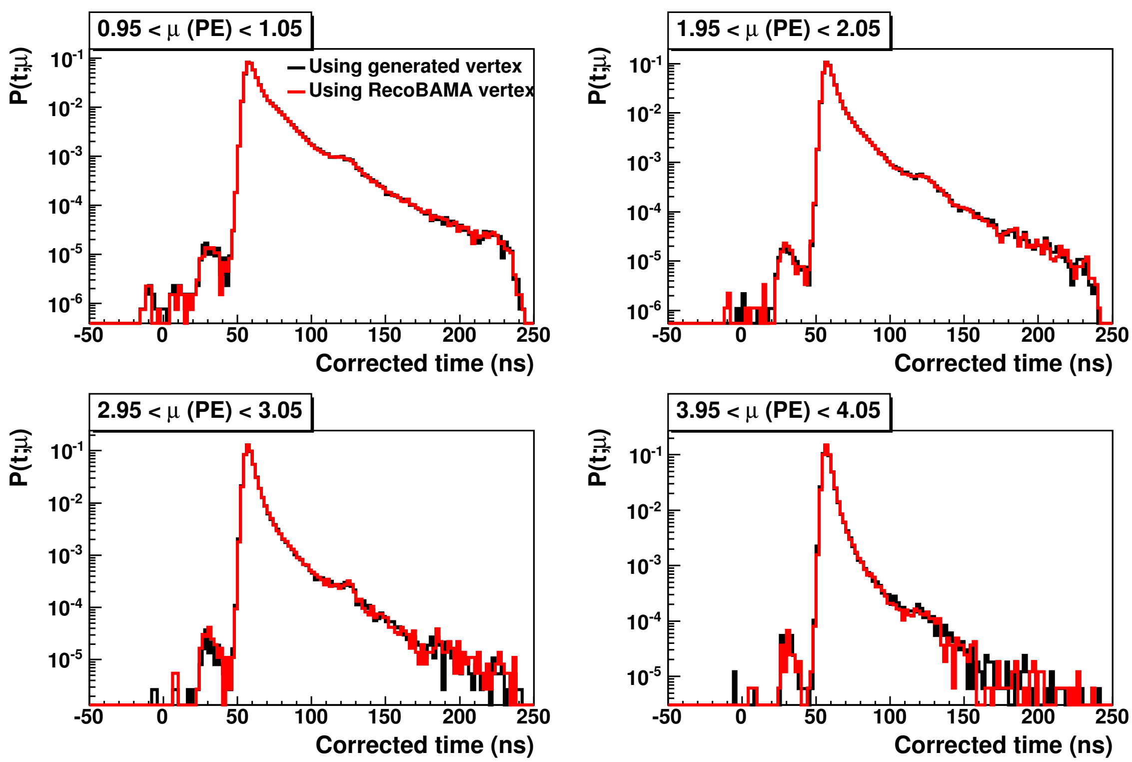

Figure 8.4: Corrected time distributions as obtained using the generated and reconstructed vertex for different μ.

The corrected time distributions obtained from MC were compared to those obtained from 2.2 MeV hydrogen capture neutron events. This study is based on 3,428 2.2 MeV γs from data collected over a period of 9 hours. The spallation neutrons should be coincident with a primary muon event defined as inner veto charge > 10,000 DUQ with a coincidence window $10 < \Delta t < 400$ μs, as labeled in the top panel of Fig. 8.5. The hydrogen capture neutron events should have a total charge between 480 PE and 720 PE; this corresponds to 1.76 to 2.64 MeV, which symmetrically covers the peak, as shown in the bottom panel of Fig. 8.5. Noise and inner veto events are eliminated by requiring $Q_{max}/Q_{tot} < 0.07$ and inner veto charge $<$ 1,000 DUQ, respectively.

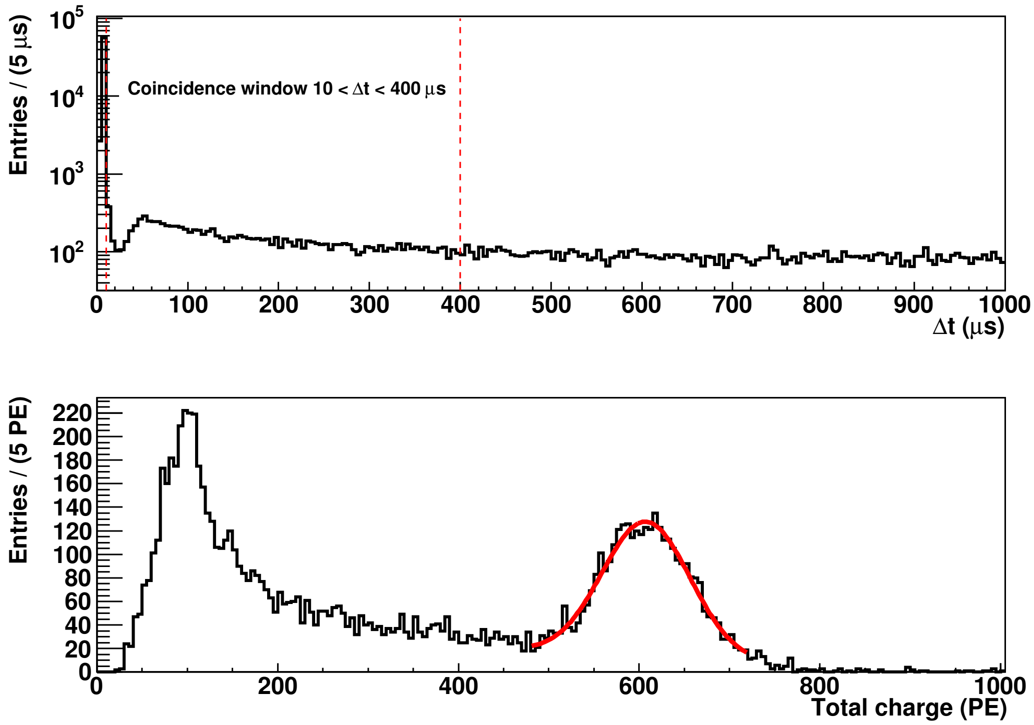

Figure 8.5: The coincidence events with previous muon as a function of time difference (top), and the 2.2 MeV n-H peak cut (bottom).

The comparison of the corrected times from MC and data is shown in Fig. 8.6, which demonstrates that the agreement is relatively good, except for the noise level and the pre-pulse. However, the main features, i.e., the corrected time distribution width, the peak locations, decay time constants are fine. Therefore, the TLLKs from the MC have been kept in use.

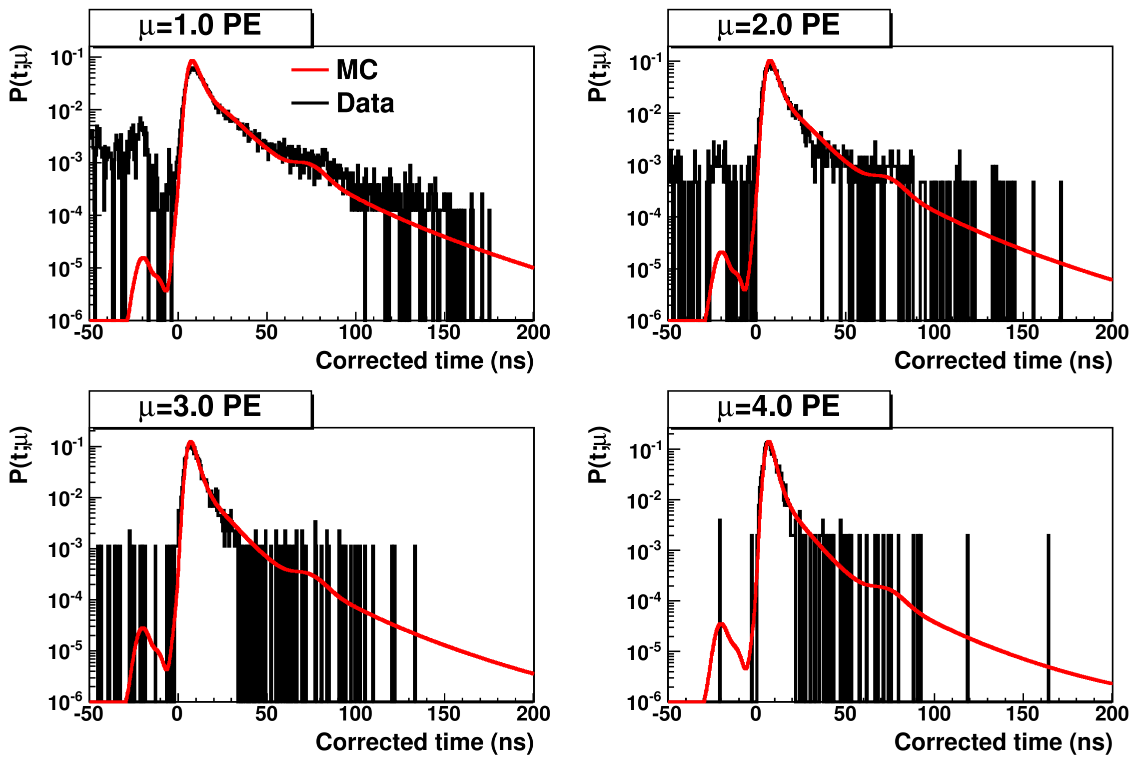

Figure 8.6: Comparison of corrected time distributions from MC to those from n-H data for different predicted charge values, as labeled.

8.3 Optical Model

As discussed in Section 7.2, the predicted charge in the simplest optical model is expressed in Eq. (7.2). Because of the existence of three volumes, scattering, reflection, absorption and reemission, a simple exponential decay could not fully describe the light propagation, which can be generalized as $f(r)$:

$$\mu_i = \Phi\epsilon_i \frac{f(r_i)g(\cos\eta_i)}{r_i^2}. \tag{8.1}$$

The $f(r_i)$ was simply extended by adding a constant to it which turned out to work relatively well for both MC and data; therefore, we always call $f(r_i)$ *effective attenuation*. The effective area $g(\cos\eta_i)$ is normalized to unity at $\cos\eta_i = 1$. Two extreme cases help us understand it better: if the PMTs are spherical, then $g(\cos\eta) = 1$, whereas for a flat disc, $g(\cos\eta) = \cos\eta$. The true $g(\cos\eta)$ must lie between these two functional forms.

The parameterization of $f(r)$ and $g(\cos\eta)$ can be realized iteratively by using events uniformly generated in neutrino target or including a wider range of gamma catcher. It is called *standard iteration method* in the following context. In each iteration, we corrected the q/μ ratios which have to be 1, independent of r or $\cos\eta$. If $q/\mu \neq 1$, corrections are applied to the $f(r)$ and $g(\cos\eta)$ functions until they finally managed to be stable at 1. The flux Φ in Eq. (8.1) can be either calculated by Eq. (7.6) for simplicity, or minimized by using the charge likelihoods. It turned out that the two fluxes work equally well (this is only true in this particular case when the electronics responses are ideal and the PMT hits are governed by Poisson statistics), and we always use the former one, i.e., total charge divided by total solid angle (unless otherwise stated).

8.3.1 Monte Carlo Parameterization

The MC parameterization based on a sample of 500,000 1 MeV electrons uniformly distributed in the neutrino target has been used from 2009 to January 2013. The large number of events guarantees sufficient statistics in each grid of r and $\cos\eta$. We find that the effective attenuation function $f(r)$ takes the functional form of,

$$f(r) = (1 - 0.3876)\exp\left(-r/0.5245\right) + 0.3876,$$

where r is expressed in meters, and the effective area function $g(\cos\eta)$ has a form of,

$$g(\cos\eta) = \begin{cases} 8.8133 - 32.847\cos\eta + 42.580\cos^2\eta - 17.546\cos^3\eta & (\cos\eta > 0.72), \\ 0.4 + 0.4\cos\eta & (\cos\eta < 0.72). \end{cases}$$

In the effective area function, the value 0.72 comes from the fact that only the entries of $\cos\eta > 0.72$ are available for events in the neutrino target. The analytical continuation is based on the consideraion of the unphysical regions behind the PMTs where $f(-1) = 0$. The function was normalized such that $f(1) = 1$. In the vertex minimization, if the trial vertex is behind PMT or out of the buffer, a punishing term would be added to the final functional value.

8.3.2 Data Parameterization

As Double Chooz data became available in large statistics, the parameterization was updated by using n-H data taken from April 13, 2011 to September 18, 2011. These events include both neutrino target and gamma catcher. The corresponding selection criteria are documented in Ref. [200]. The PMT charges have been calibrated by the linearised gains as explained in Section 5.3. We assume that all relative quantum efficiencies are unity. After several iterations, the fitting functions and the corresponding q/μ ratios with respect to r and $\cos\eta$ are shown in Figs. 8.7 and 8.8, respectively. Most of the part of the q/μ ratios, as shown in Figs. 8.7 and 8.8 with high statistics, is well within 2% of unity. Looking at the q/μ ratio as a function of the PMT number in Fig. 8.9, we see variations as large as 10%. These variations could be attributed to variations in the PMT quantum efficiencies. This parameterization replaces the previous one in Section 8.3.1 and became effective from January 2013.

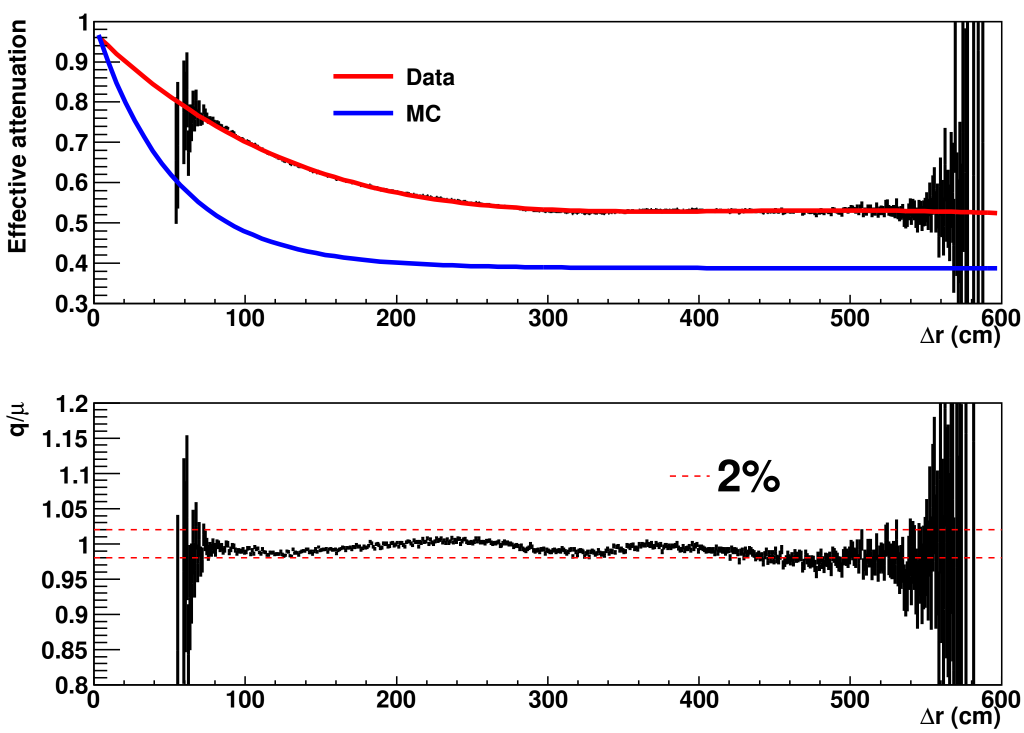

Figure 8.7: Effective attenuation $f(r)$ superimposed with that from MC parameterization and the corresponding q/μ ratio using n-H data.

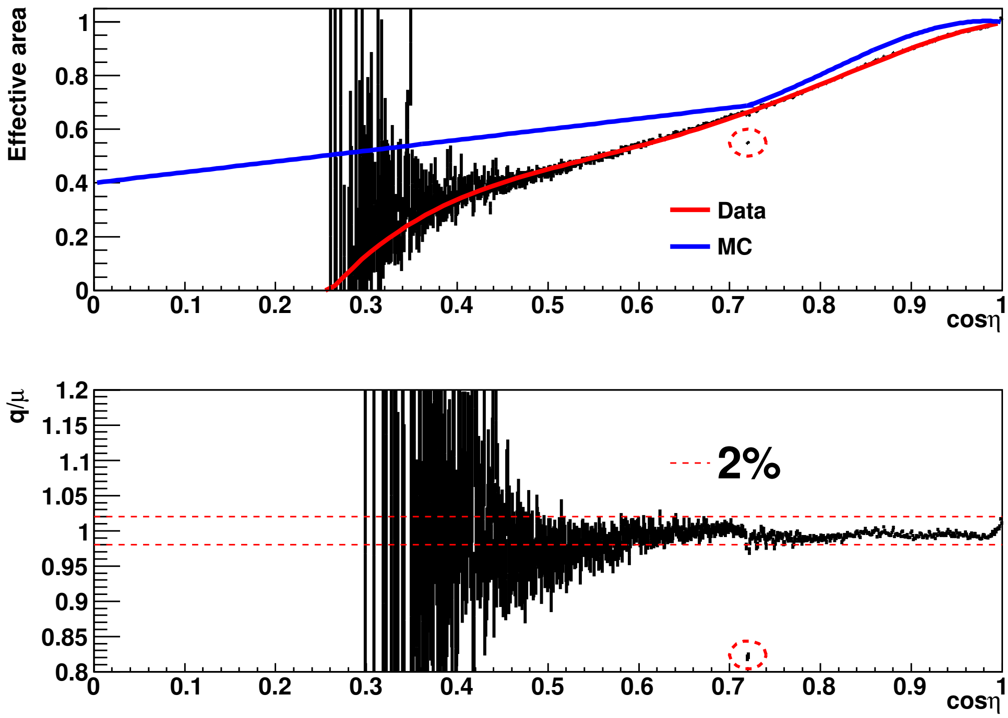

Figure 8.8: Effective area $g(\cos\eta)$ superimposed with that from MC parameterization and the corresponding q/μ ratio using n-H data.

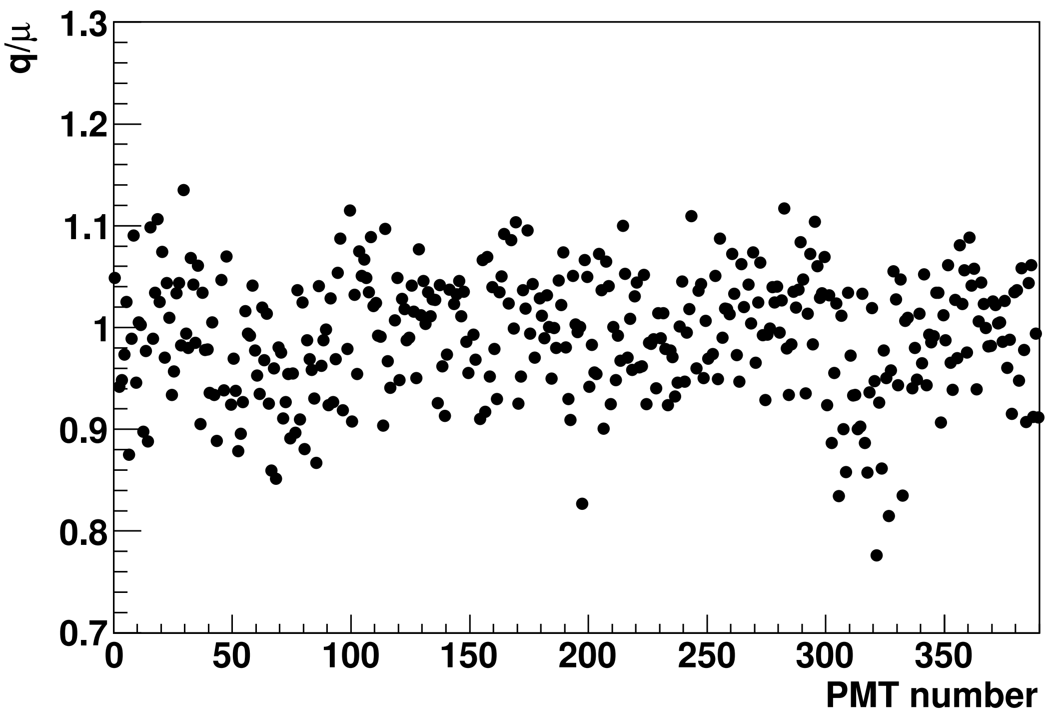

Figure 8.9: q/μ ratios as a function of PMT number which yield a measure of the spread in the relative quantum efficiencies.

One notices in Fig. 8.8 that there is a point with $\cos\eta = 0.72$ which has a very low q/μ ratio as shown. Figures 8.10 and 8.11 are showing the PMTs which receive such events and where these events happen. We have seen that the value $\cos\eta = 0.72$ is the lower limit of events distributed in neutrino target. This anomaly might be caused mostly by the events at the boundary of the neutrino target and gamma catcher, where complicated processes might take place at the border of different optical properties.

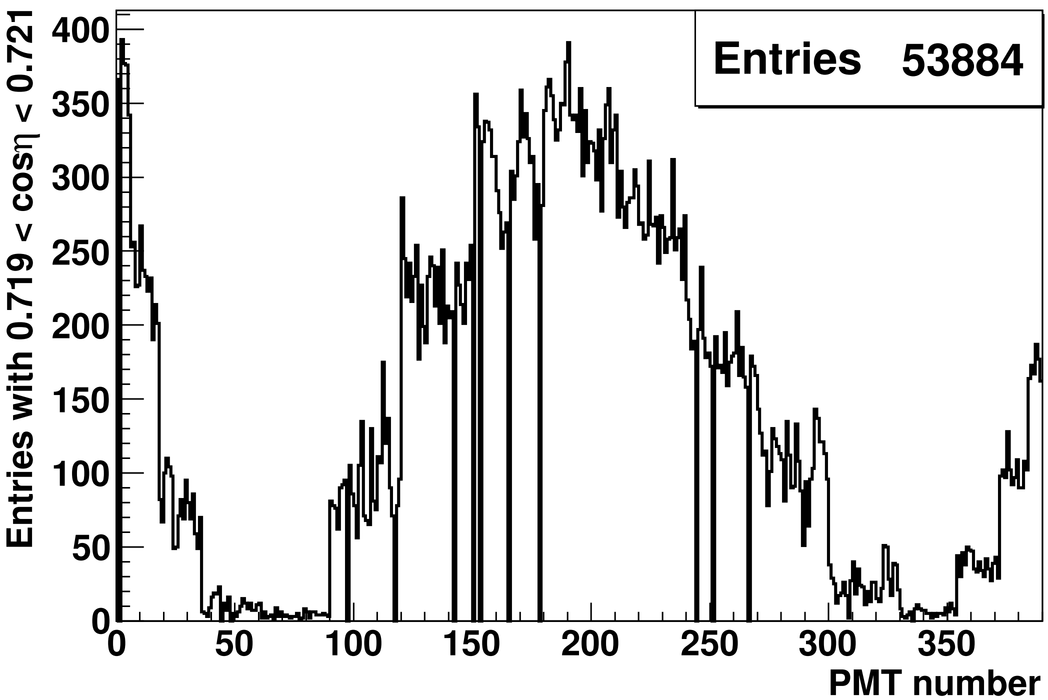

Figure 8.10: The number of PMT hits when $0.719 < \cos\eta < 0.721$.

8.4 Position Reconstruction

In this section, the basic concept of the reconstruction algorithm is introduced and the performance of the four algorithms, namely Q-only, T-only, T+H/NH and QT is examined.

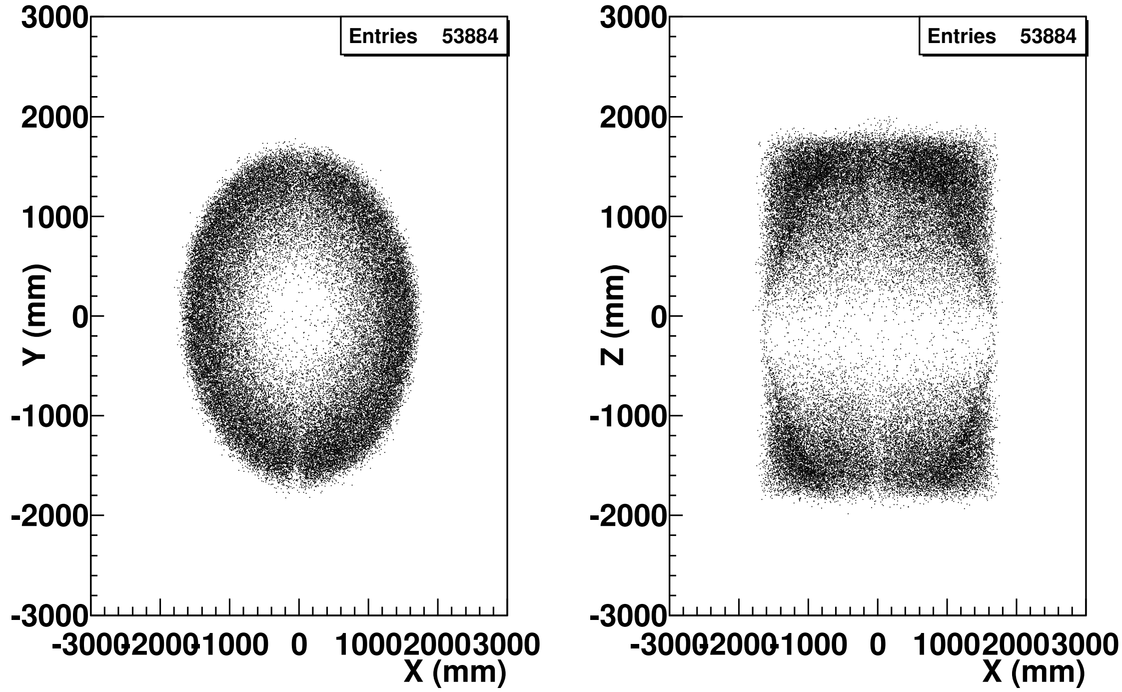

Figure 8.11: Vertices distribution when any PMT in those events has $0.719 < \cos\eta < 0.721$.

8.4.1 Event Reconstruction Concept

The charge at any given PMT is determined by the total event energy, the event topology, the solid angle it subtends, and the optical properties of the medium. The time at the PMT depends particularly on its distance to the vertex, but also on the total energy. Although light propagation in the detector is characterized by the effective speed of light in the medium, multiple PE hits introduce time-slewing effects. If a PMT is struck by more than one photon, the earliest arriving photon time will be recorded as the PMT time in Double Chooz. A study of how the mean arrival time and width of the distribution evolve as a function of the number of PE is shown in Fig. 8.12, assuming for simplicity a single PE signal with a Gaussian width of 1 ns. Multiple PE time distributions were obtained by taking the earliest time among the n hits. As the number of PEs increases, the arrival time becomes earlier, while the distribution becomes narrower. Other effects, such as reflections, scattering, absorption and reemission, as well as PMT quantum efficiencies also influence the charge and time information at the PMTs.

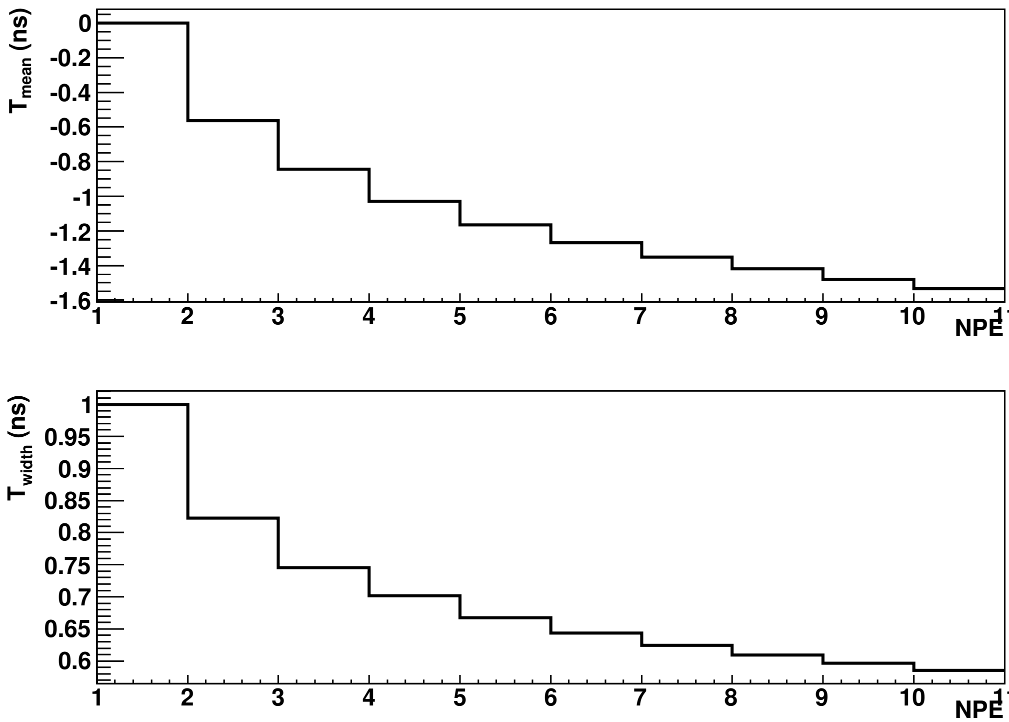

Figure 8.12: Evolution of mean time and distribution σ as a function of the number of hits.

The event reconstruction uses the charge and time information from all PMTs in the detector to determine the event time, t_0, position, x_0, y_0, z_0, and light flux Φ. All the reconstructed parameters form a complete set $X = (x_0, y_0, z_0, t_0, \Phi)$, which fully describes an event.

For a given set of event parameters, the likelihood to record a set of charges (q_i) and corrected times $(t_{corr,i})$ is given by:

$$\mathcal{L}(X) \quad = \quad \prod_{q_i=0} P_q(0;\mu_i) \prod_{q_i>0} P_q(q_i;\mu_i)\, P_t(t_{corr,i};\mu_i) \ ,$$

where the first product goes over the PMTs which are not hit, while the second one goes over the PMTs which are hit, with a charge q_i registered at time t_i. The $P_q(q_i;\mu_i)$ and $P_t(t_{corr,i};\mu_i)$ have been defined in Section 7.1 and Section 8.2, respectively. Both P_q and P_t are functions of the predicted charge μ_i for each PMT, which in turn depends on the event energy, event position, etc., as predicted by the optical model. Inversely, the best possible set of event parameters for a given set of charges (q_i) and corrected times ($t_{corr,i}$) is obtained by maximizing the event likelihood $\mathcal{L}(X)$, or equivalently, minimizing the negative log-likelihood function:

$$F(X) = -\ln \mathcal{L}(X) = -\sum_{i} \ln P_q(q_i; X) - \sum_{q_i>0} \ln P_t(t_{corr,i}; X) = F_q(X) + F_t(X).$$

The standard minimization package MINUIT (CERN function minimization and error analysis package) [201] is used to find the minimum of $F(X)$ among all possible values of X.

8.4.2 Position Reconstruction Performance

In the Double Chooz experiment, the reconstructed position is used mainly for event energy correction by the energy map, which is a function of ρ and z as a result of the azimuthal symmetry of the detector. The reconstructed position can also be used in the selection of the radioactive source calibration data and the cosmic muon induced backgrounds. The position resolution from all of these four algorithms (Q-only, T-only, T+H/NH, and QT) needs to be well understood. Since the maximum energy that the prompt event of the inverse β-decay may generate is around 8 MeV, MC positron events with energies of 0.5, 1, 2, ..., 8 MeV were uniformly generated in the neutrino target. This study aims to not only characterize the performance, but also study the effect of time offset uncertainties. The time offsets uncertainties are chosen from 0.0 to 4.0 ns with an interval of 0.5 ns based on the fact that the time offsets uncertainty is approximately 3.5–4.0 ns (based on the spread of the time offsets derived from the IDLI) for the PMT raw time, while the IDLI calibrated time offsets uncertainty is about 0.5 ns. Ten different sets of events were simulated at $\sigma_{toff} = 0.5$ ns and $\sigma_{toff} = 4.0$ ns in order to estimate the spread in the reconstruction errors from these two particular data points.

The comparison of the reconstructed (using QT algorithm) to the generated positions of 1 and 8 MeV positron events in each dimension with precisely known time offsets are shown in Figs. 8.13 and 8.14. The uncertainty in each direction is approximately 8.0 cm and 5.3

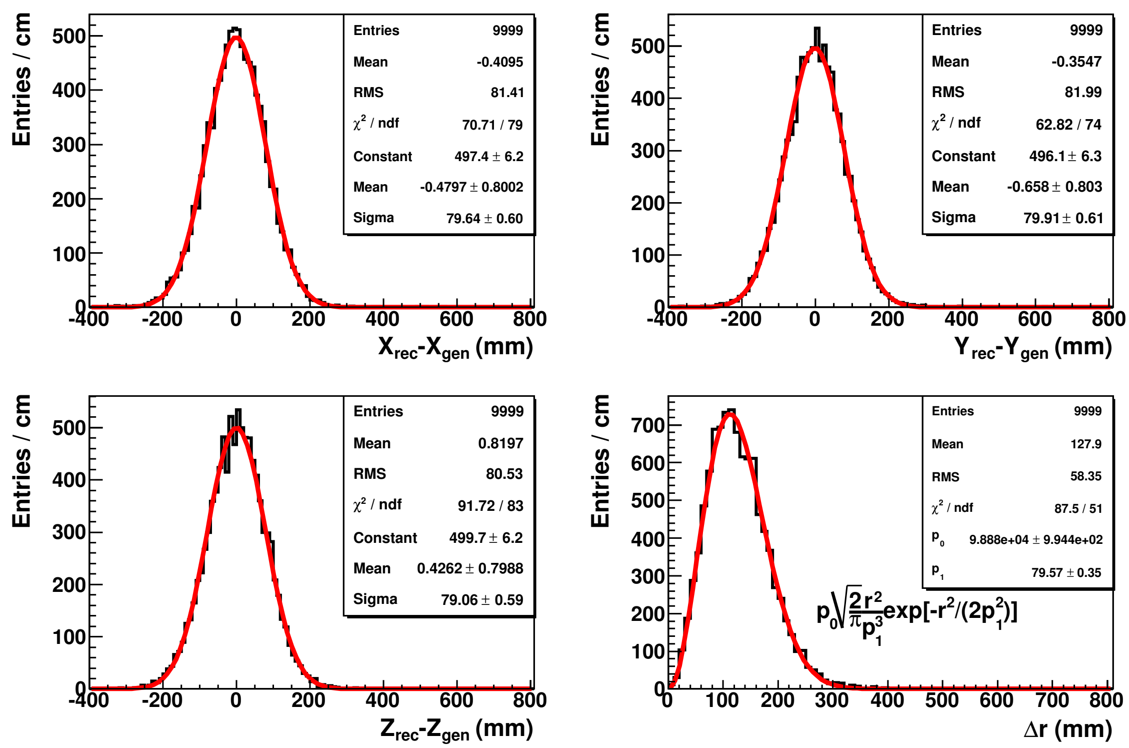

Figure 8.13: Comparison of reconstructed (using QT algorithm) x, y, z and Δr to the generated values for 1 MeV positrons. The x, y and z components are fitted to a simple Gaussian while the Δr is fitted to the Rayleigh distribution as shown in the plot. The PMT time offsets uncertainty $\sigma_{toff} = 0.0$ ns.

cm for 1 and 8 MeV positrons, respectively. The Δr is fitted by the Rayleigh distribution, in which the parameter p_1 confirms the distribution widths of x, y and z components. There is no systematic shift in any coordinate for these two energies, and this is true for any of the intermediate energy values.

The position resolution as a function of the time offsets uncertainty reconstructed by the T-only algorithm is summarized in Fig. 8.15. The position resolution degrades as the uncertainty in the time offsets increases, as expected. The uncertainty in the position reconstruction decreases as the energy increases, because more energetic events emit more light, which help locate the position more precisely. The corresponding estimated errors at $\sigma_{toff} = 0.5$ ns and $\sigma_{toff} = 4.0$ ns are generated by repeating the reconstruction 10 times at respective values, where at $\sigma_{toff} = 0.5$ ns, the error is too small to be seen.

Figures 8.16 and 8.17 are the same plots but reconstructed by the T+H/NH and QT

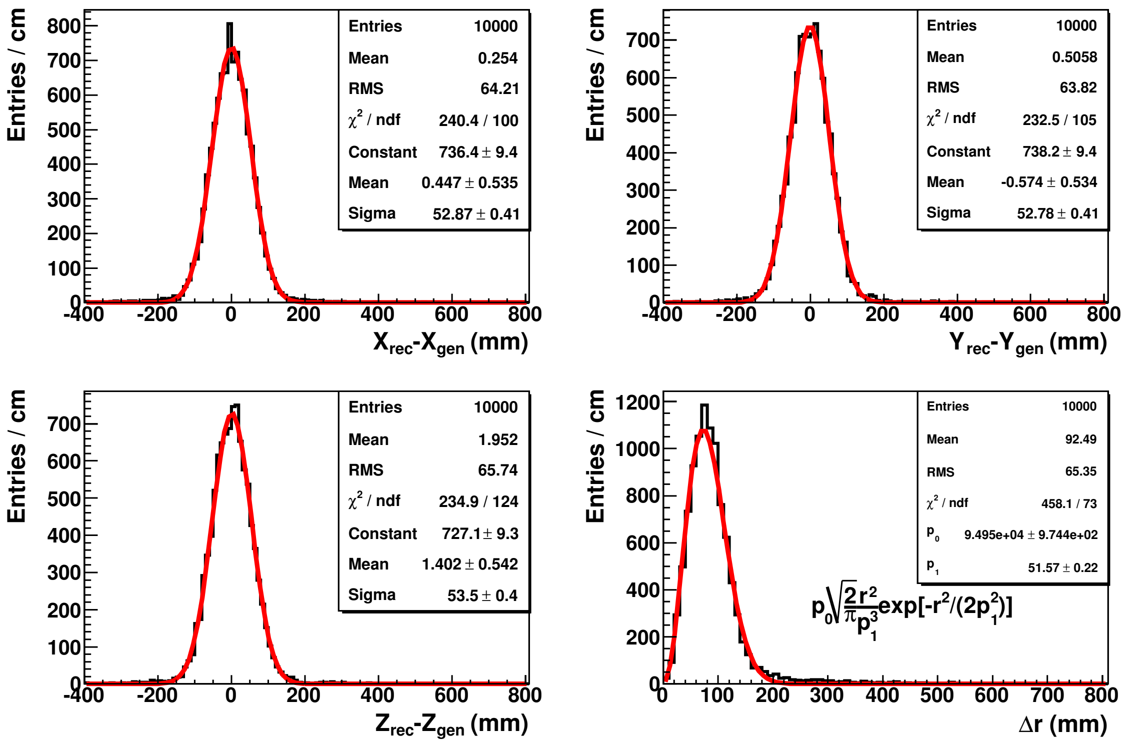

Figure 8.14: Comparison of reconstructed (using QT algorithm) x, y, z and Δr to the generated values for 8 MeV positrons. The x, y and z components are fitted to a simple Gaussian while the Δr is fitted to the Rayleigh distribution as shown in the plot. The PMT time offsets uncertainty $\sigma_{toff} = 0.0$ ns.

algorithms, respectively. The trends with respect to the time offsets uncertainty and energy are similar. Comparing all of these three plots, the reconstruction position resolution is obviously improving as one uses more information in charge in addition to the timing information.

The direct comparisons of the four algorithms as a function of the time offsets uncertainty for each individual energy are plotted in Fig. 8.18. Obviously, the result from using the Q-only algorithm is not influenced by the time offsets uncertainty. Somewhere between 2 and 3 ns in the PMT time offsets uncertainty, the Q-only algorithm becomes better than the T-only algorithm. The Q-only algorithm can be even better than T+H/NH at large values in the time offset uncertainty as the event energy increases. It can be concluded that with large uncertainty in the time offsets, the reconstruction quality of high energy events becomes more and more dominated by the charge component information.

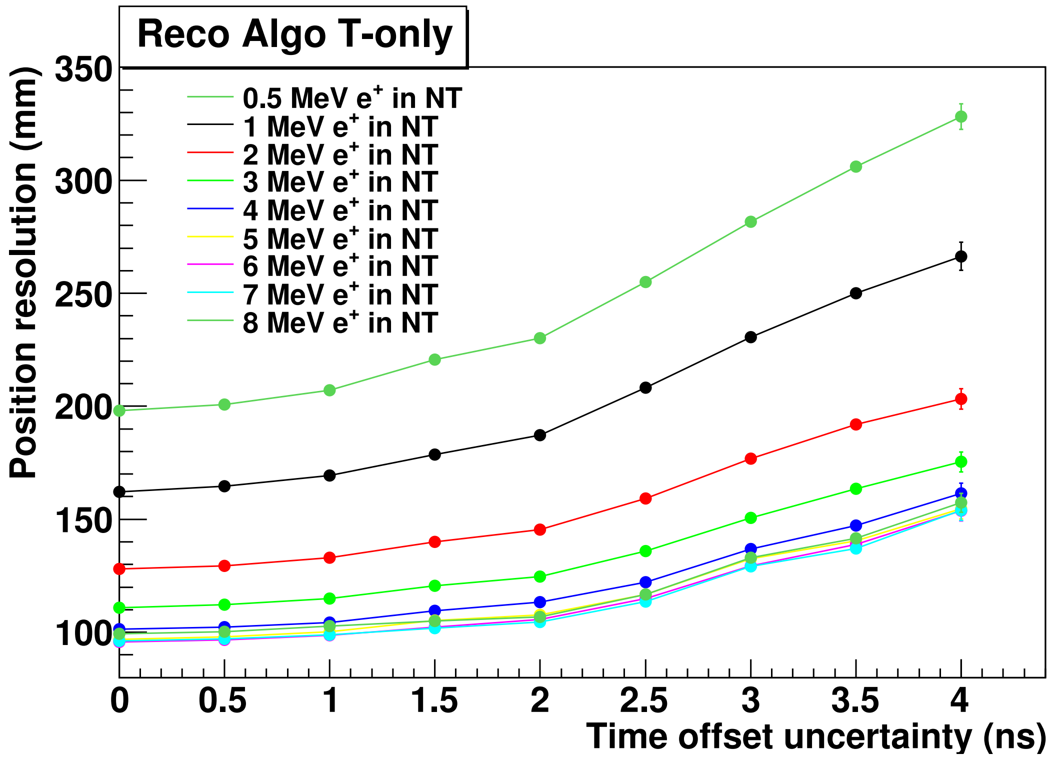

Figure 8.15: T-only algorithm reconstruction spatial position resolution for 0.5 to 8 MeV positrons as a function of time offsets uncertainty.

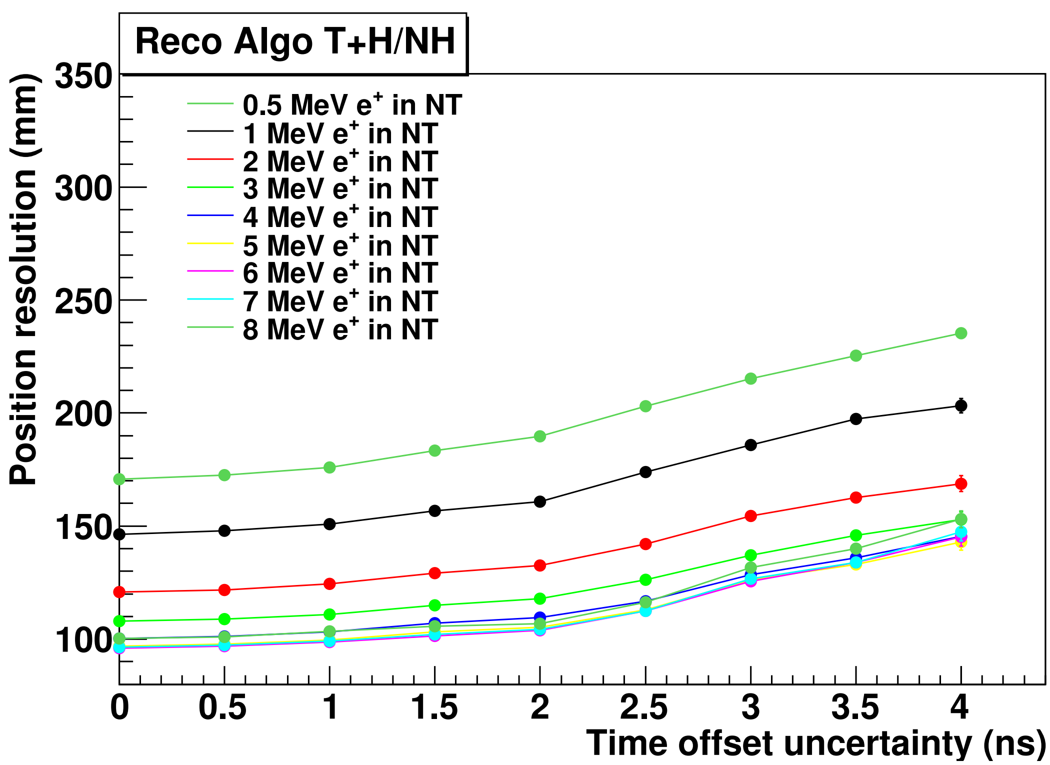

Figure 8.16: T+H/NH algorithm reconstruction spatial position resolution for 0.5 to 8 MeV positrons as a function of PMT time offsets uncertainty.

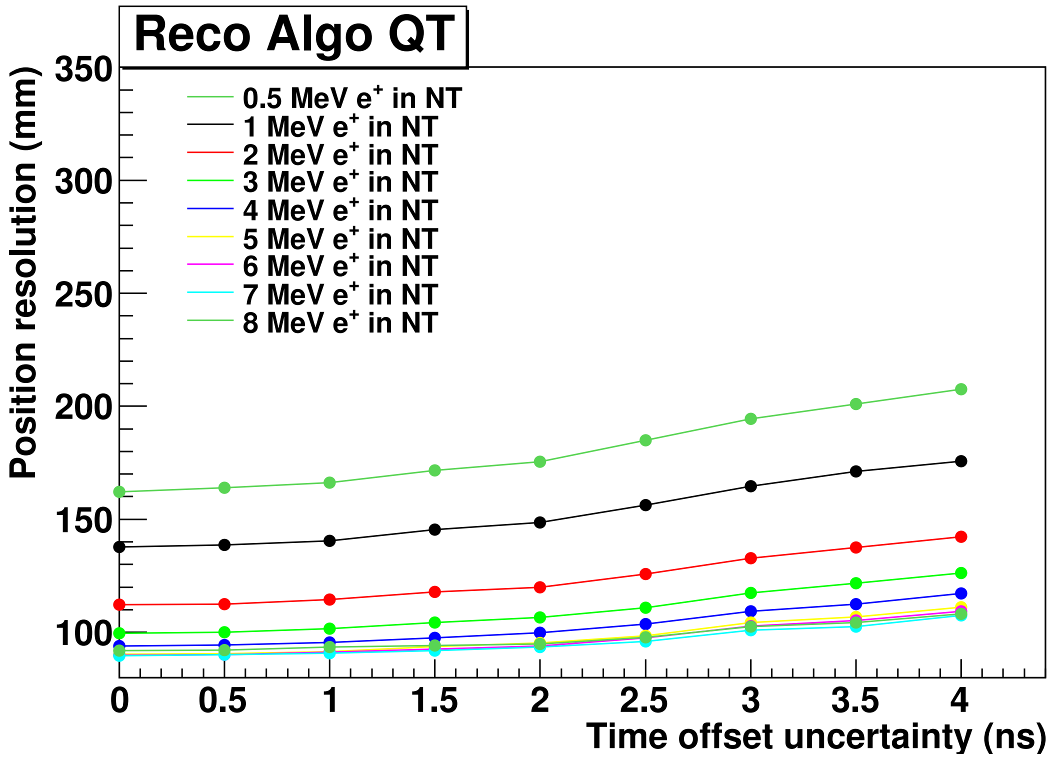

Figure 8.17: QT algorithm reconstruction spatial position resolution for 0.5 to 8 MeV positrons as a function of time offsets uncertainty.

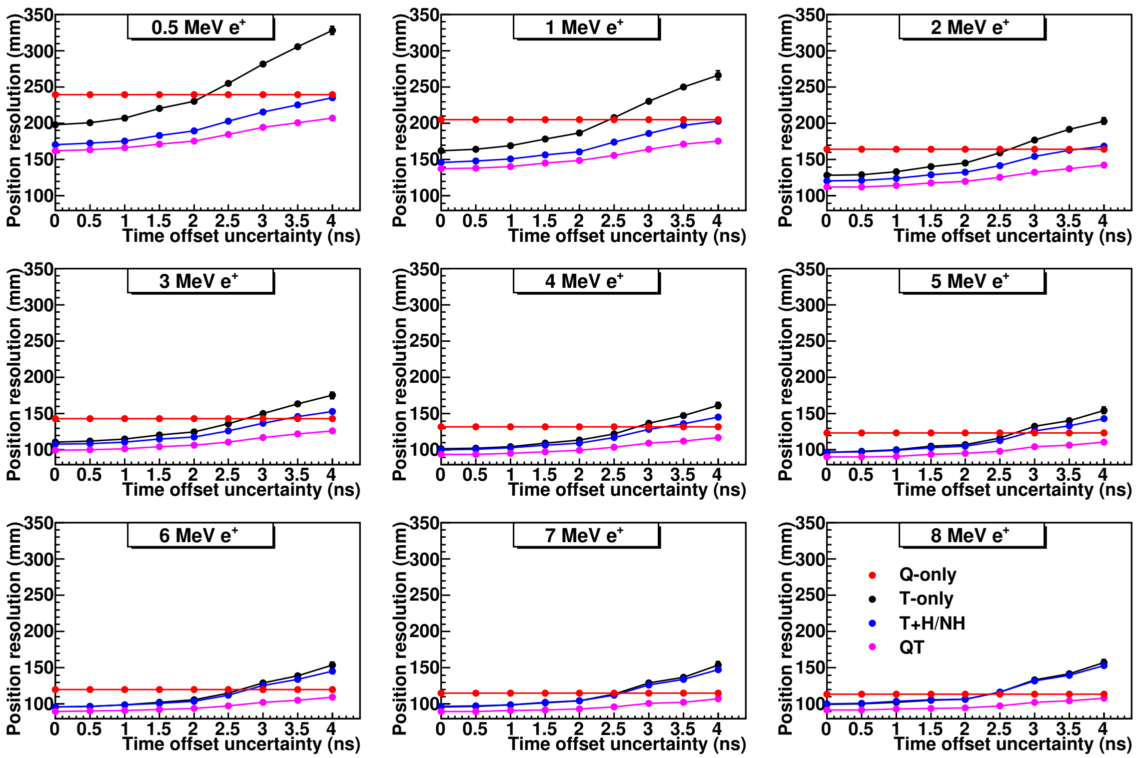

Figure 8.18: Comparison of the reconstruction position resolution for four algorithms as a function of PMT time offsets uncertainty for each individual energy from 0.5 to 8 MeV.

8.4.3 Position Reconstruction Performance in Data

During the commissioning phase, when no calibration source data were available to test the position reconstruction accuracy and the time offsets were not known, taking advantage of the charge likelihoods became more significant in the event reconstruction. Looking at the differences between different reconstruction algorithms for 2.2 MeV n-H events gives us some idea about the reconstruction quality. The comparison of Q-only with T-only algorithms for the n-H data is shown in Fig. 8.19 with and without the time offsets. Our rough estimate of the time offset uncertainty before and after the IDLI time offsets are applied is 3.5 ns and 0.5 ns, respectively (the 3.5 ns comes from the fact that the IDLI time offsets have a spread of 3.5 ns). The reconstructed vertex differences between the different algorithms for the same energy of gamma events in MC were examined as well. As we have seen in Fig. 8.18, there is not much difference between the position resolutions of $\sigma_{toff} = 0$ and 0.5 ns. Thus, in MC simulation, the comparison plots were made with $\sigma_{toff} = 0.0$ ns and $\sigma_{toff} = 3.5$ ns as

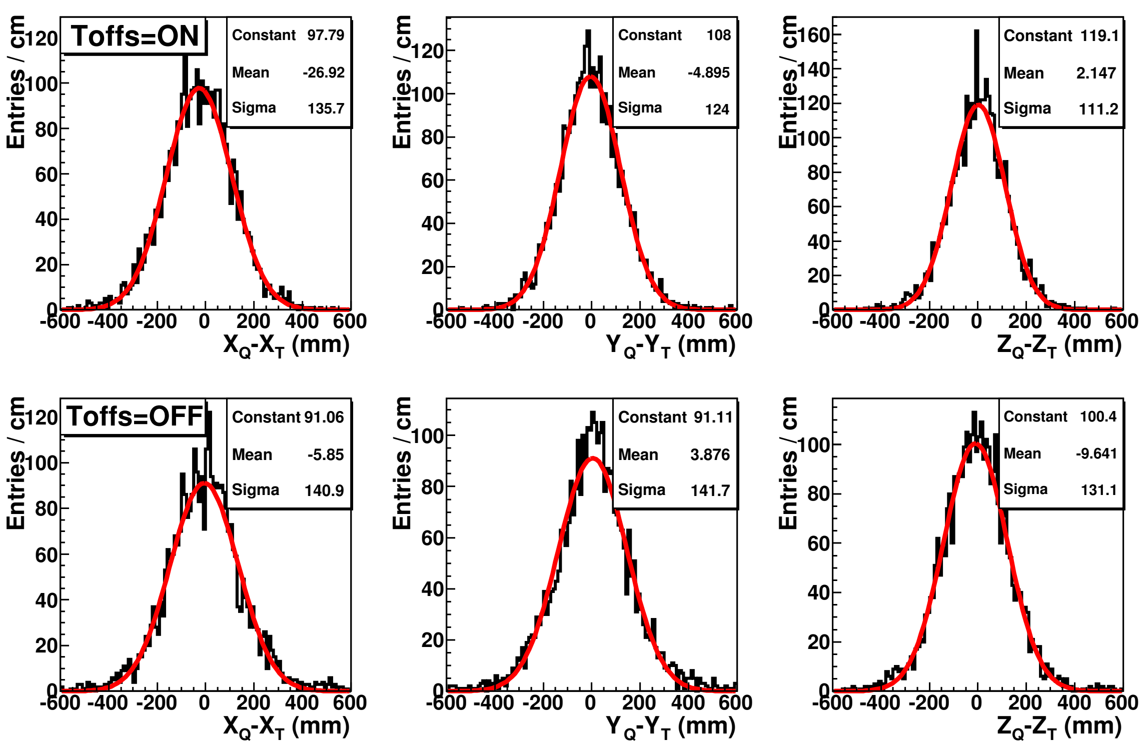

Figure 8.19: Difference between the reconstruction result of Q-only and T-only algorithms in x, y and z for the Double Chooz 2.2 MeV γ data with and without PMT time offsets.

displayed in Fig. 8.20. The data and MC comparison plots for Q-only with T+H/NH and QT algorithms are shown in Figs. 8.21, 8.22, 8.23 and 8.24. Because the neutron capture in the neutrino target is dominated by gadolinium capture, the amounts of H capture events in the neutrino target and gamma catcher are not proportional to their volumes. Therefore, in MC, the amount of events in the neutrino target and gamma catcher were mixed at the ratio obtained from the data. Comparing the results with and without time offsets, one finds that the one with time offsets always has smaller distribution width in the data, while the situation is reversed in the MC. However, the rough magnitude in the data and MC were consistent to some extent.

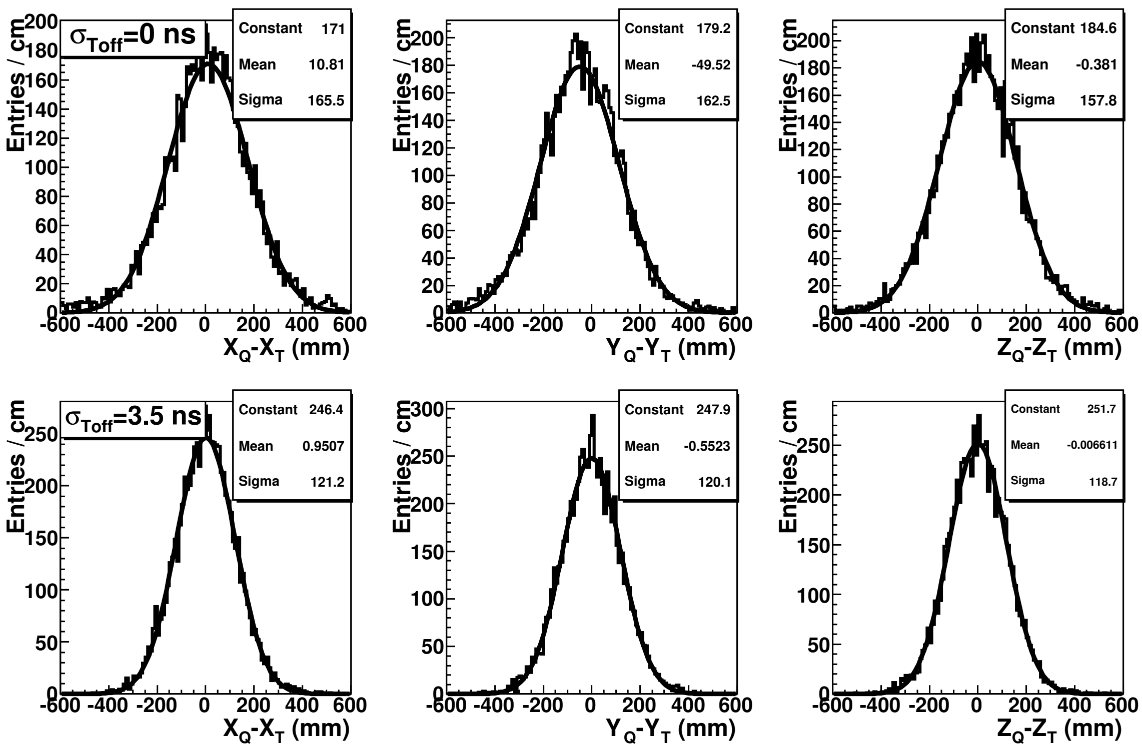

Figure 8.20: Difference between the reconstruction result of Q-only and T-only algorithms in x, y and z for MC 2.2 MeV γ events with $\sigma_{toff} = 0.0$ ns and $\sigma_{toff} = 3.5$ ns.

In the MC, the position resolutions of the differences between the Q-only and T+H/NH algorithms for $\sigma_{toff} = 0.0$ ns and $\sigma_{toff} = 3.5$ ns as a function of positron energy are plotted in Fig. 8.25 for contrast. From this plot, one can clearly see that for all positron energies the position resolution becomes larger when the uncertainty in the PMT time offsets is bigger.

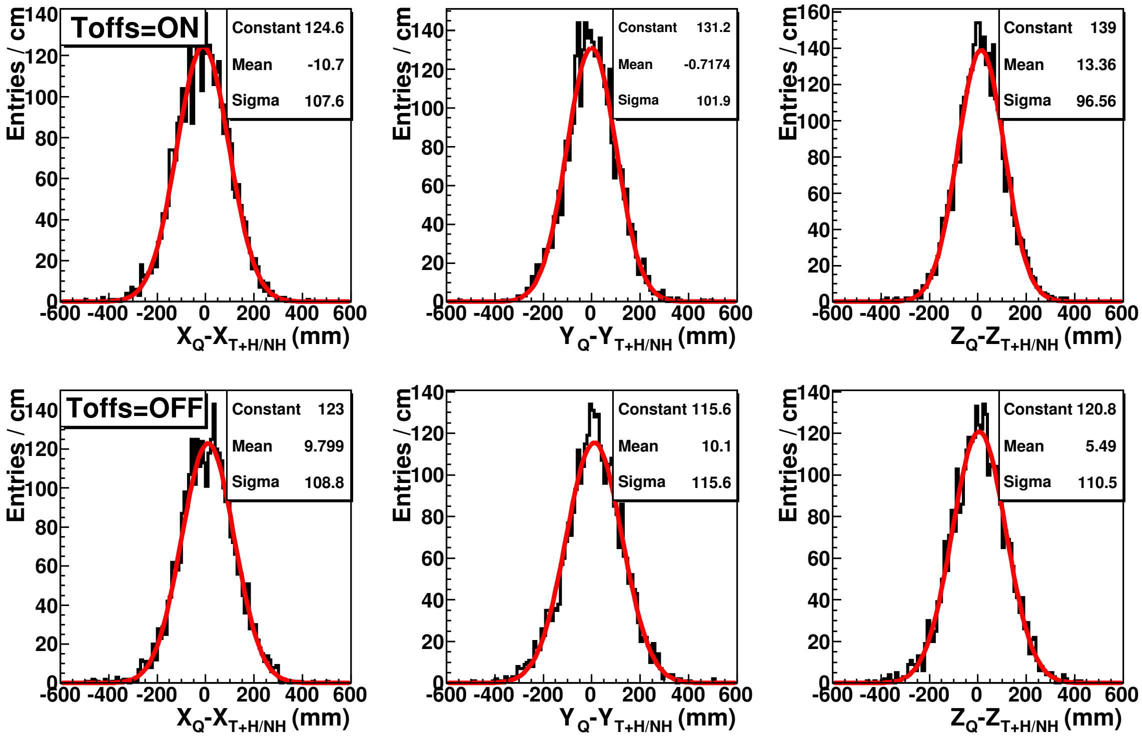

Figure 8.21: Difference between the reconstruction result of Q-only and T+H/NH algorithms in x, y and z for the Double Chooz 2.2 MeV γ data with and without PMT time offsets.

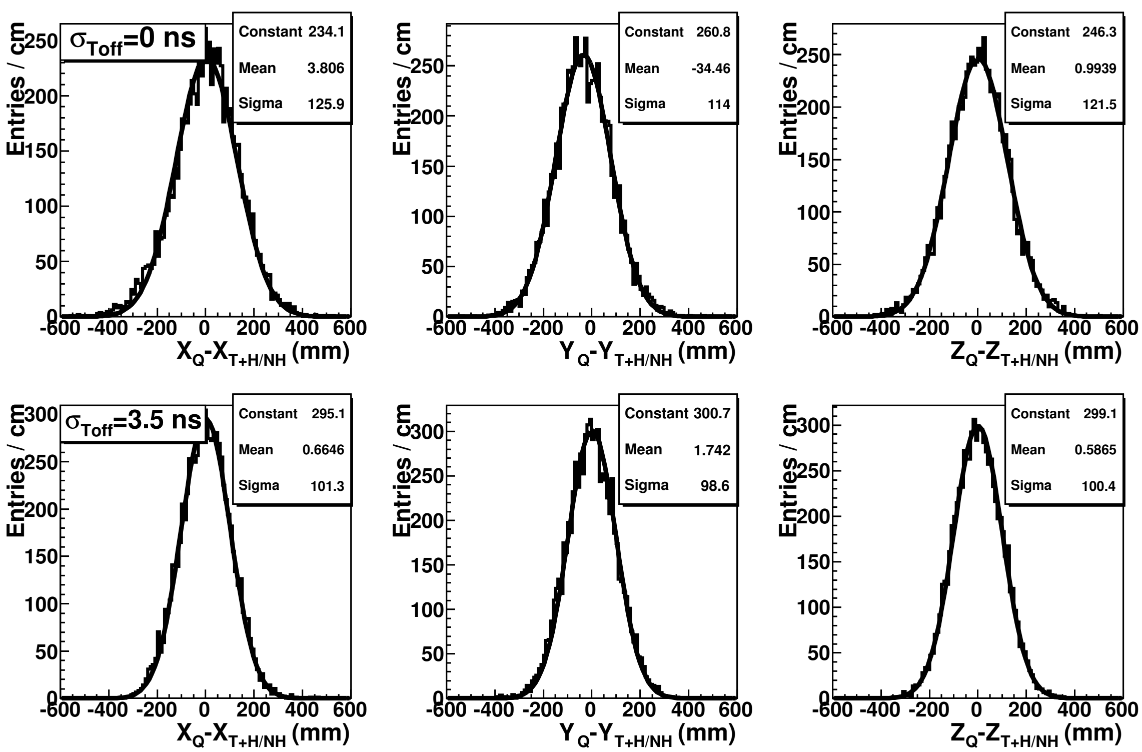

Figure 8.22: Difference between the reconstruction result of Q-only and T+H/NH algorithms in x, y and z for MC 2.2 MeV γ events with $\sigma_{toff} = 0.0$ ns and $\sigma_{toff} = 3.5$ ns.

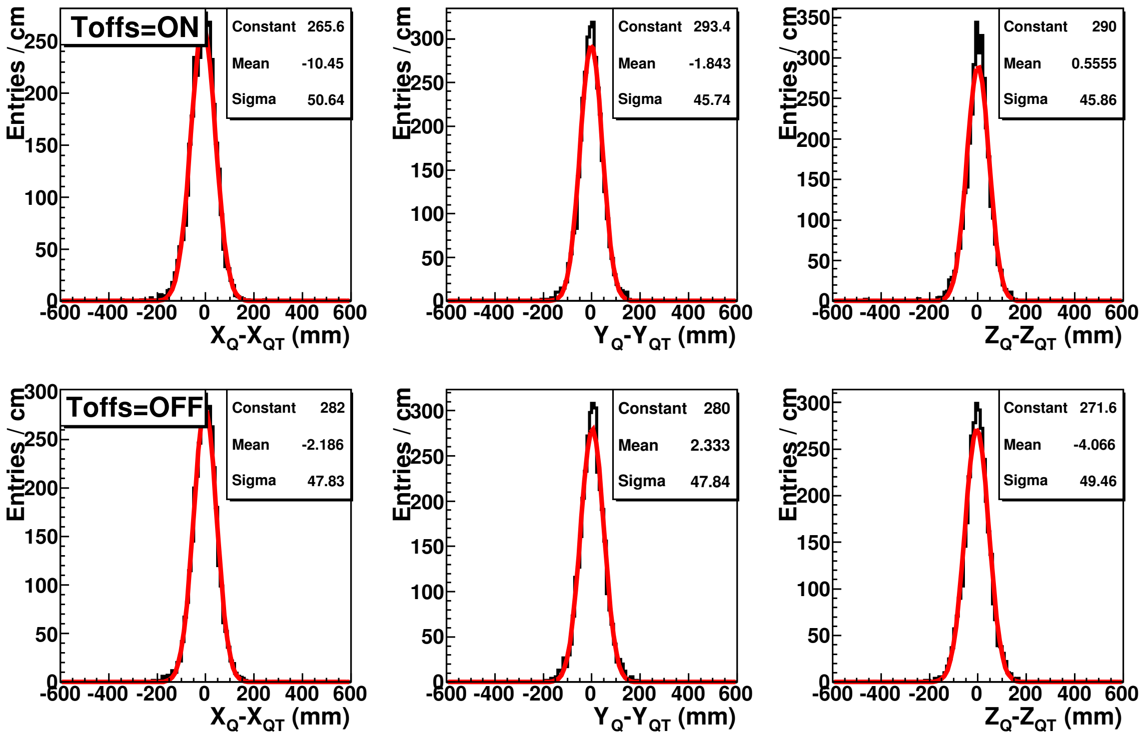

Figure 8.23: Difference between the reconstruction result of Q-only and QT algorithms in x, y and z for the Double Chooz 2.2 MeV γ data with and without PMT time offsets.

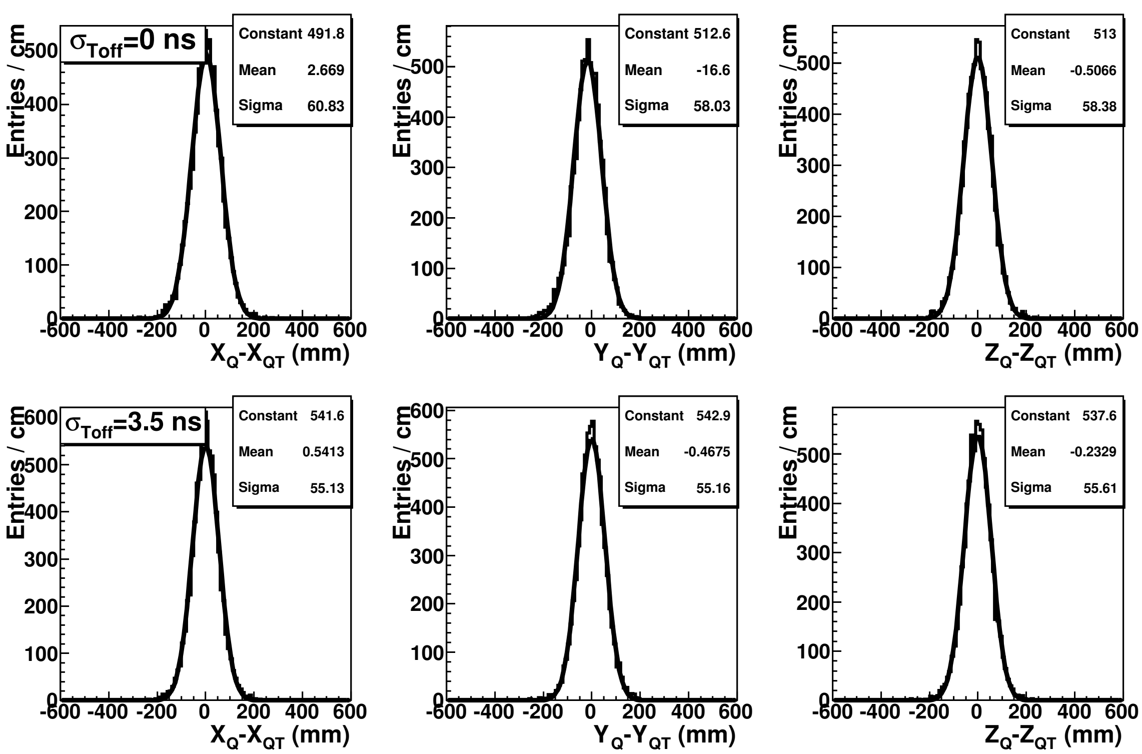

Figure 8.24: Difference between the reconstruction result of Q-only and QT algorithms in x, y and z for MC 2.2 MeV γ events with $\sigma_{toff} = 0.0$ ns and $\sigma_{toff} = 3.5$ ns.

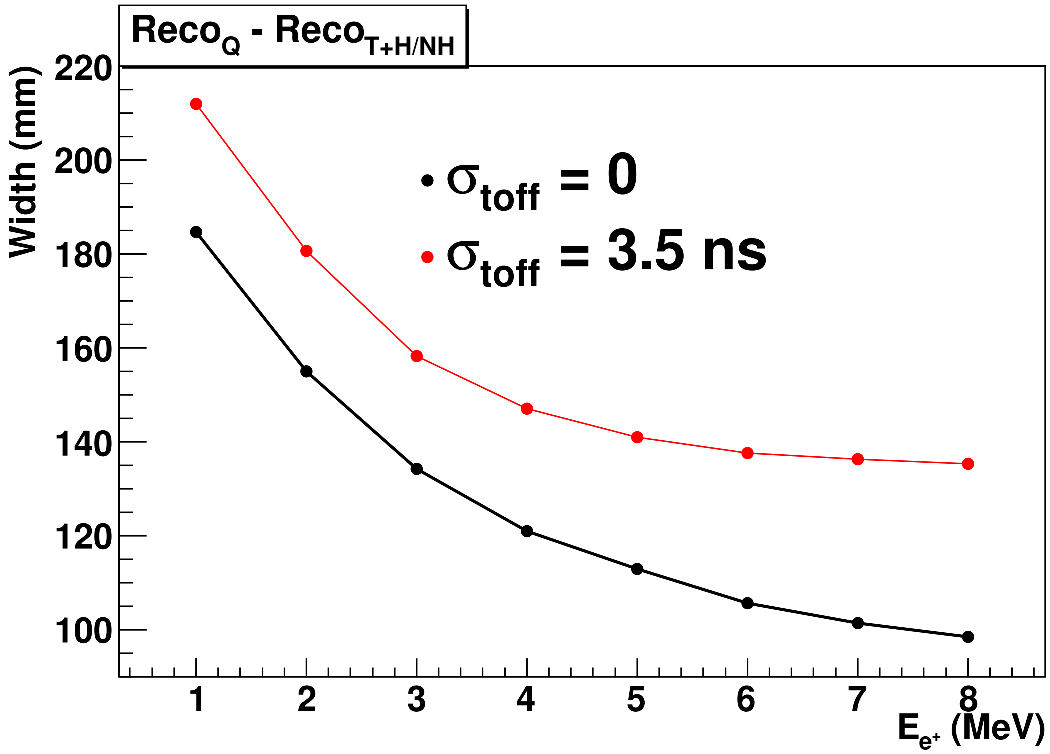

Figure 8.25: Width of the difference between the Q-only and T+H/NH reconstructions as a function of positron energy for $\sigma_{toff} = 0.0$ ns and $\sigma_{toff} = 3.5$ ns in MC.

After obtaining our first calibration data, the performance of the reconstruction has been evaluated by using radioactive sources deployed along the z-axis in the neutrino target and guide tube in the gamma catcher. Figure 8.26 illustrates the systematic shift between the reconstructed position and the real deployed vertex for all of the four algorithms. The lowest systematic shift comes from the T+H/NH algorithm which could be attributed to a combination of several reasons, such as the average gain used for all PMTs, uncertainty in the time offsets, the error on the effective speed of light, the reflection on the buffer inner walls, and the reflection and refraction on the neutrino target and gamma catcher support structures, which is discussed in Section 8.5.1.

Looking at the spatial resolution on ^{137}Cs, ^{60}Co and ^{68}Ge deployed at the neutrino target center as shown in Fig. 8.27, accuracies of 30.6 cm for ^{137}Cs, 22.4 cm for ^{60}Co, and 21.1 cm for ^{68}Ge have been achieved.

RecoBAMA is doing a good job in reconstruction. However, there are still problems

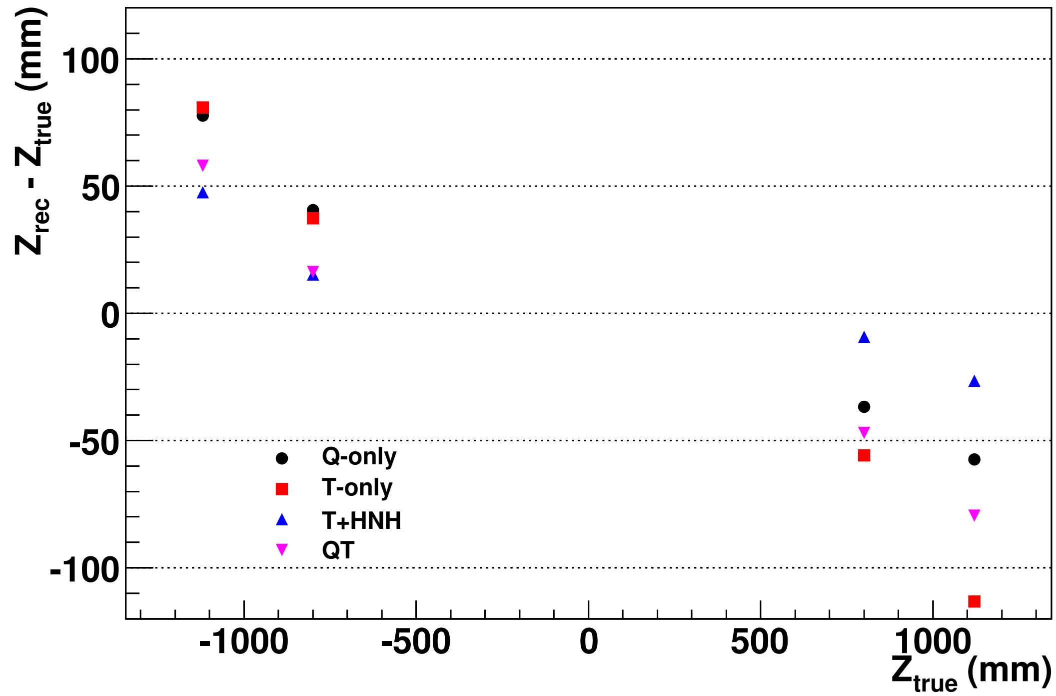

Figure 8.26: Systematic shift in the z direction for the first radioactive source calibration using ^{60}Co deployed at $z = -1120, -800, 800$ and 1120 mm along the z-axis.

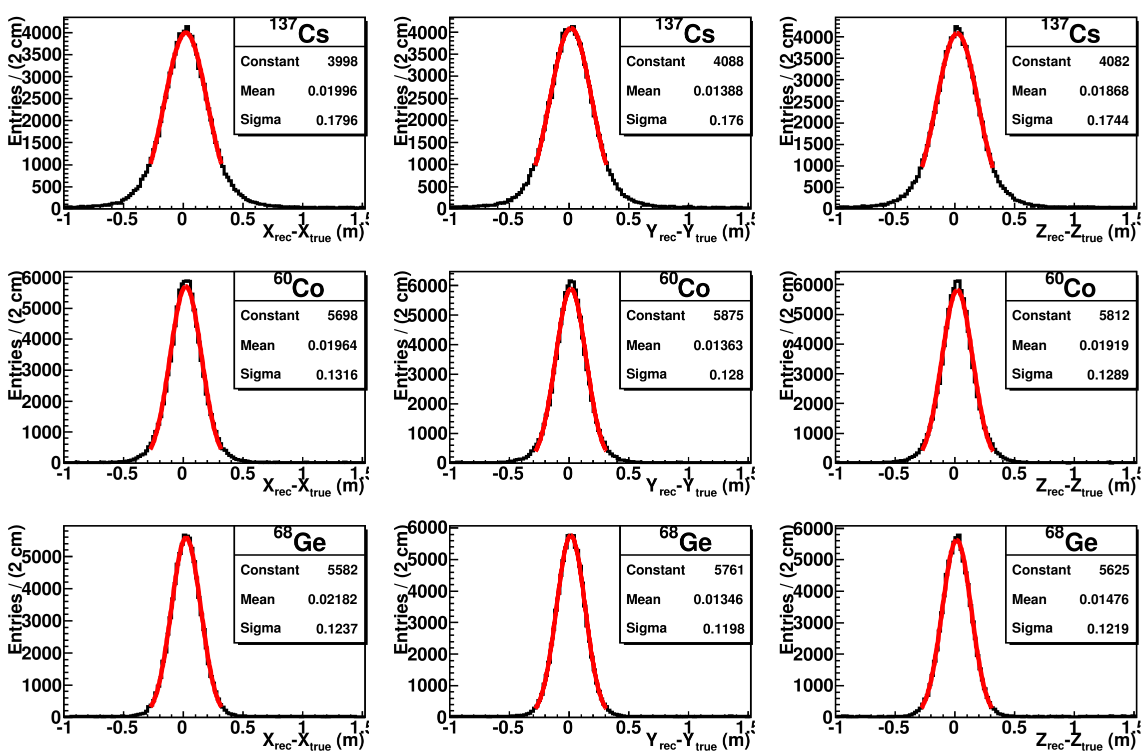

Figure 8.27: Reconstruction position resolution of ^{137}Cs, ^{60}Co and ^{68}Ge at the center.

which need to be addressed. More work has to be done to understand the systematic shift, as shown in Fig. 8.28, which is the difference of the reconstructed and deployed position as a function of the deployed position for three gamma sources ^{137}Cs, ^{68}Ge and ^{60}Co. The biases increase as the sources depart from the center. We believe that specular reflections off the buffer walls may play a role in the systematic shifts. However, due to disagreement between the data and the MC in terms of reflections, these effect cannot be properly included in the TLLKs.

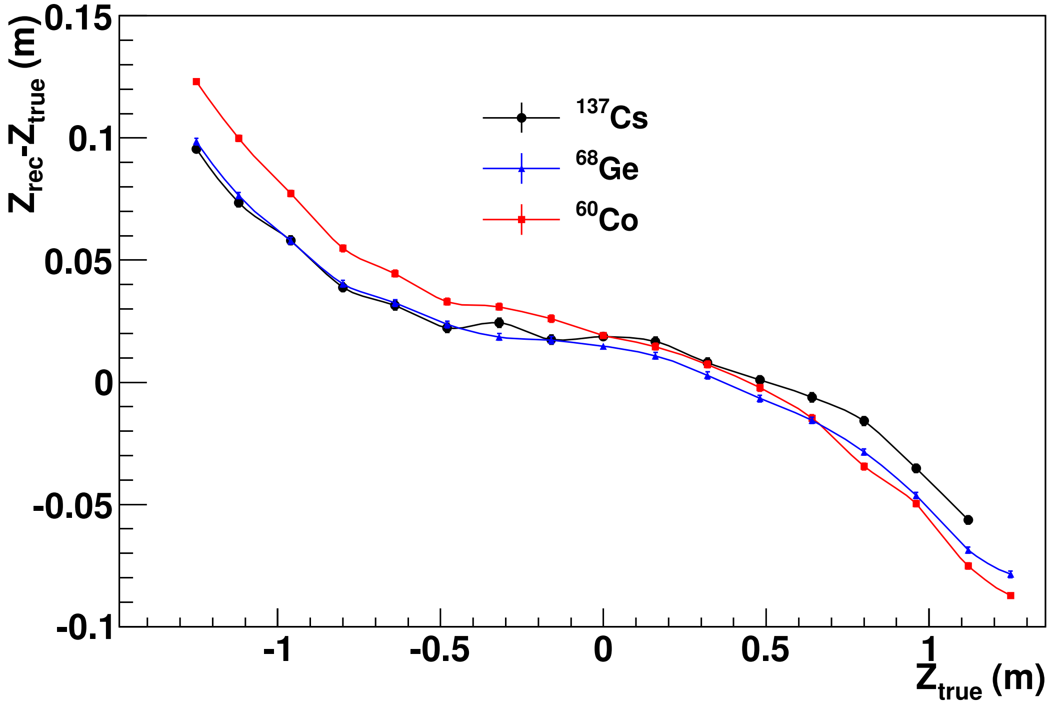

Figure 8.28: Systematic shift in the z direction for radioactive source calibrations, ^{137}Cs, ^{68}Ge, ^{60}Co, deployed along the z-axis.

8.5 Energy Reconstruction

We have talked about the calibration and position reconstruction. All of them play an important role in the energy reconstruction, which is the key parameter in the shape analysis of the mixing angle θ_{13}.

As discussed in Section 8.3, the event energy is related to the flux Φ by an overall constant (to first order). The most likely flux Φ can be either determined by using the charge likelihoods or calculated approximately as given by Eq. (7.6), under the premise of the correct optical model. In the event reconstruction, for each vertex, we calculate the flux using Eq. (7.6) and then in the last step one can either fit for all parameters, or keep the vertex fixed and minimize only for Φ. A proper optical model would take care of the energy response without the need of position corrections. Therefore, the quality of the energy reconstruction is determined by the validity of the optical model, which in turn depends on the effective attenuation and effective area functions, $f(r_i)$ and $g(\cos\eta_i)$ in Eq. (8.1), assuming that the optical model is this simple.

Alternatively, one can measure the energy by correcting the total charge by position. This procedure needs a mapping of the total charge response, which could be done by using well known energy calibration sources covering not only z axis but also points with a variety of ρ and ϕ in the neutrino target. Before the articulated arm is ready, the calibration sources can only be deployed through z-axis and guide tube. The cosmic muon induced n-H data can be used for this purpose instead. However, since we do not know where these events really happen, they have to rely on the reconstructed positions, which accordingly depend on the position reconstruction prerequisites – which include the optical model.

8.5.1 Reflections off the Support Structure

In this section, the parameterizations of the effective attenuation and effective area functions in MC are discussed. The measured-to-predicted charge ratio as a function of distance and $\cos\eta$ has a variation within 1%. We required that the variation of the reconstructed flux in the neutrino target should be within ±1%. However, the flux close to the boundary of the neutrino target is about 3% higher than that at the center. Further investigations show that the measured-to-predicted charge ratios for the top and bottom PMTs have a variation up to 30% for discrete vertices. The abnormal q/μ ratios are found to be caused by the reflections on the support structures.

A thorough understanding of the optical model in MC helps improve the detector response correspondence of MC to data. The effective attenuation and effective area functions, $f(r)$ and $g(\cos\eta)$, were extracted from the MC data as shown in Fig. 8.29 and 8.30. Since there are some changes in MC, the $f(r)$ and $g(\cos\eta)$ have to be obtained from the current version. These two figures illustrate the functional forms of $f(r)$ and $g(\cos\eta)$ superimposed with those in RecoBAMA obtained from MC and data as discussed in Sections 8.3.1 and 8.3.2, and the corresponding q/μ ratios. The $f(r)$ function has a slight rise at the region of $\Delta r > 440$, which looks not physical. We did not understand it initially but attributed to reflections following later studies. Except for a bump at $\cos\eta = 0.93$ and a dip at $\cos\eta = 0.99$ as shown in Fig. 8.30, the PMT angular response function looks relatively smooth. The q/μ ratios are within 0.5–1% in both Δr and $\cos\eta$ compared to 2% in the data (as illustrated in Figs. 8.7 and 8.8). The 2-dimensional plot of q/μ versus Δr and $\cos\eta$, as shown in Fig. 8.31 also indicates that except the boundary, where the statistics are low, all

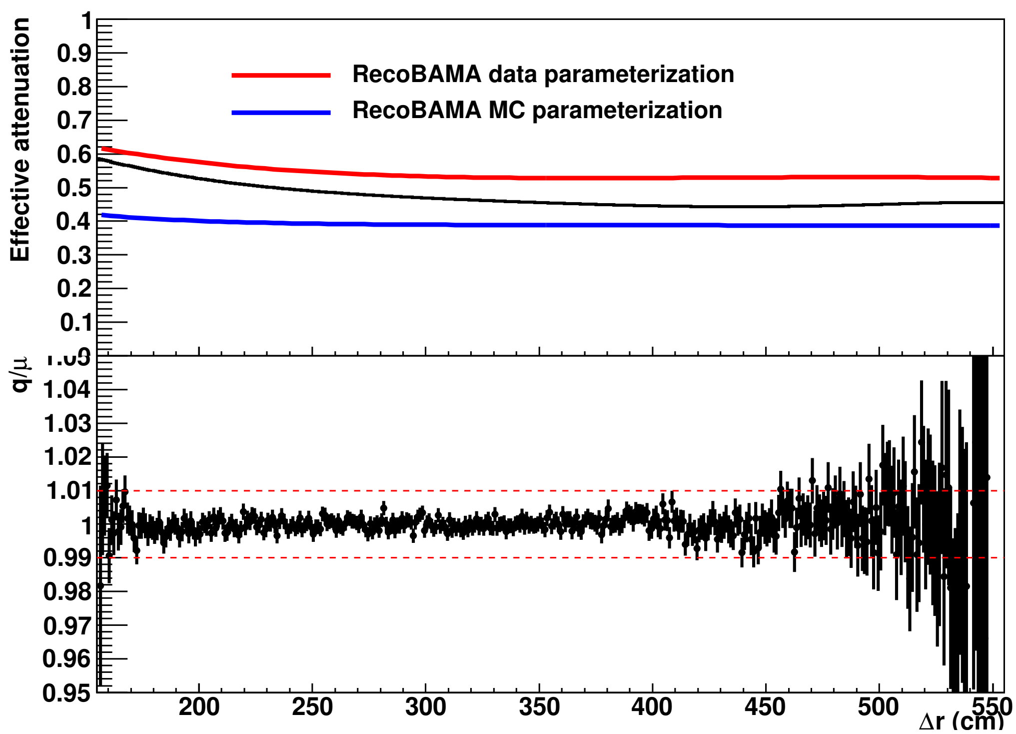

Figure 8.29: Effective attenuation $f(r)$ and the corresponding q/μ ratio using 1 MeV MC electron events uniformly distributed in the neutrino target.

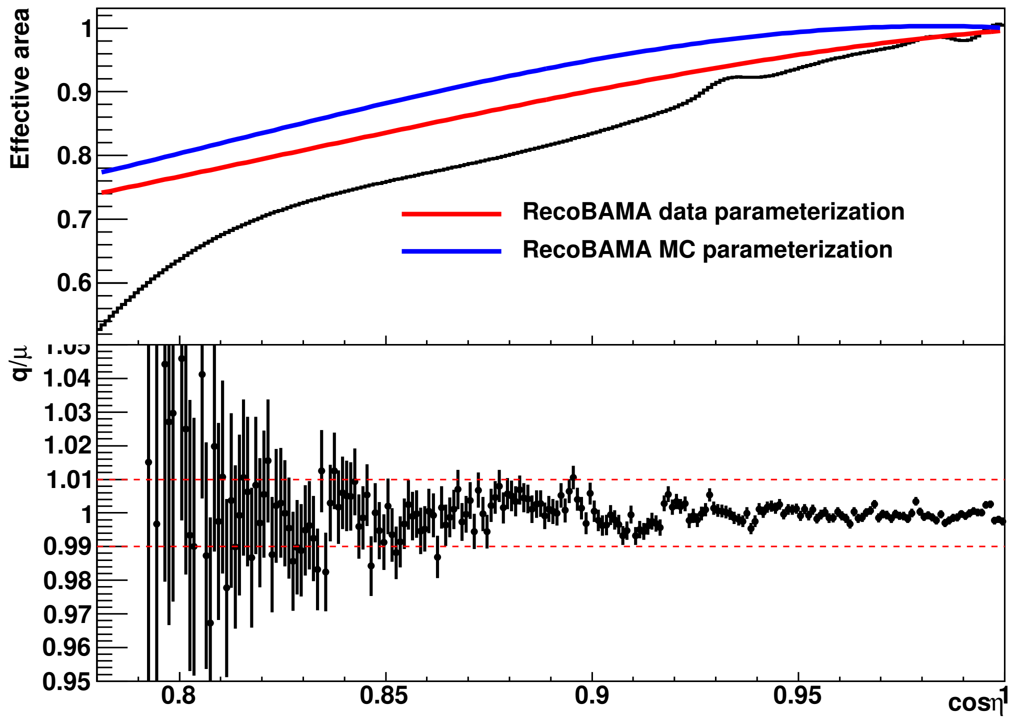

Figure 8.30: Effective area $g(\cos\eta)$ and the corresponding q/μ ratio using the same MC data set as in Fig. 8.29.

of the region has a variation of at most 2%. The important conclusion is that no obvious correlation exists between the effective attenuation and the effective area. Looking at the q/μ ratio as a function of PMT number, as shown in Fig. 8.32, there are some relatively large variations grouped by PMT rings, which might indicate some issues which we have not fully understood. Considering that one ring has more than 3% deviation, and 2 rings have more than 2% deviation, this effect is acceptable as long as the variation of the reconstructed energy all over the neutrino target is at the sub-percent level, which is our primary goal. To test the reconstructed energy variations, we need large statistics at every point inside the neutrino target. Such a huge project cannot be achieved by limited computational power. The azimuthal symmetry of the detector helped us reduce a lot of test points. The test points at the combinations of the following coordinates are picked for this study:

- $z = 0$, ± 30 and ± 90 cm
- $\rho = 0$, 50 and 100 cm

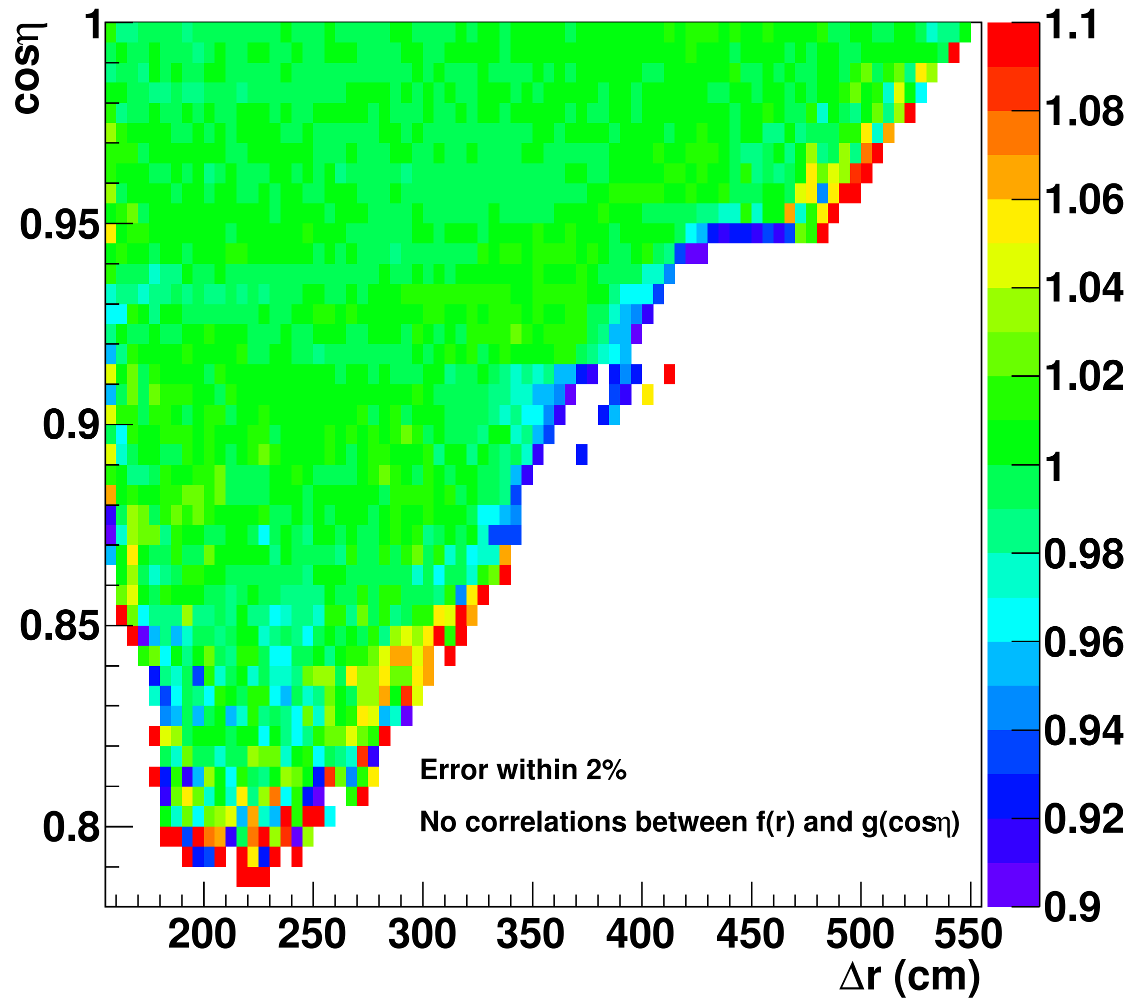

Figure 8.31: Two-dimensional q/μ ratio as a function of Δr and $\cos\eta$.

- $\phi = 0$, 6, 12 and 18°.

The z coordinates of the test points were simulated at the center and the same height as the PMTs in the middle rings. The ρ values were picked so that the distributions are along the center of neutrino target ($\rho = 0$), about half way to the boundary ($\rho = 50$ cm), and close to the boundary ($\rho = 100$ cm) with the gamma catcher being at 115 cm. Except for two PMT rings closest to the center, all the rings on the side wall have 30 PMTs uniformly distributed in ϕ which means a 12° interval between two consecutive PMTs. Therefore the test points are selected with two angles directly facing a column of PMTs and the other two residing right between two columns of PMTs. There are in total five such planes which makes the

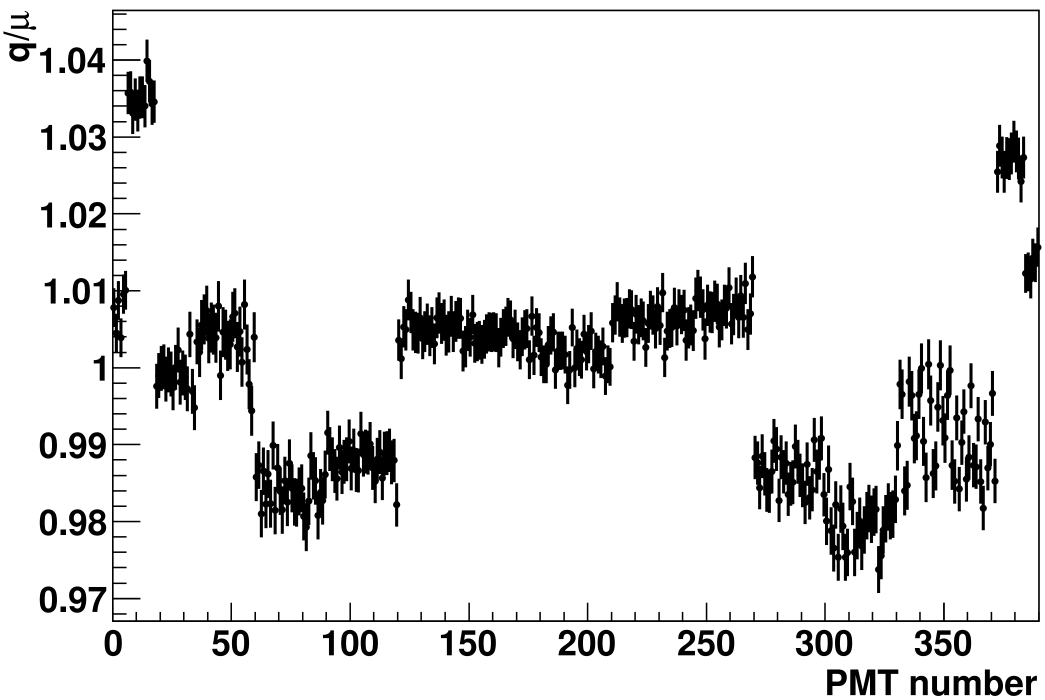

Figure 8.32: q/μ ratio as a function of PMT number using the same MC data as in Fig. 8.29.

total number of 45 points. Using the $f(r)$ and $g(\cos\eta)$ derived above, the normalized flux Φ and total charge Q with respect to center for points with $\phi = 0$ are listed in Table 8.1. The reason why only points with $\phi = 0$ are shown is that only obvious variations in z and ρ were observed. The differences between points having the same z and ρ but different ϕ are very small.

In general, there is some improvement by using the flux Φ instead of total charge Q, but the magnitude is not as much as expected. It also can be seen that the points close to the center (i.e., $z \leq 30$ cm and $\rho \leq 50$ cm) have variations within 1%, but when they get close to the boundary of either side or top and bottom, the deviations are larger and larger. The most deviation among those 15 points takes place at the position at $z = -90$ cm and $\rho = 100$ cm highlighted in red in Table 8.1; 3.7% is beyond our goal of $\pm 1\%$.

To figure out what happened, we first examined the charge prediction on individual PMTs for those test points. Four points with $z = 30$ and $\rho = 100$ cm are plotted in Fig. 8.33. From the plot, the q/μ ratios for the side PMTs (numbers 90 through 299) have small variations,

z (cm)	ρ (cm)	Φ/Φ_0	Q/Q_0
0	0	1	1
	50	0.9963±0.0008	0.9959±0.0008
	100	1.0257±0.0008	1.0365±0.0008
30	0	1.0010±0.0008	1.0062±0.0008
	50	1.0050±0.0008	1.0088±0.0008
	100	1.0285±0.0008	1.0395±0.0008
−30	0	0.9909±0.0008	0.9964±0.0007
	50	1.0056±0.0008	1.0098±0.0008
	100	1.0337±0.0008	1.0457±0.0008
90	0	1.0136±0.0008	1.0273±0.0008
	50	1.0190±0.0008	1.0327±0.0008
	100	1.0287±0.0008	1.0307±0.0008
−90	0	0.9997±0.0008	1.0138±0.0008
	50	1.0124±0.0008	1.0268±0.0008
	100	1.0370±0.0008	1.0405±0.0008

Table 8.1: Normalized flux and total charge with respect to the detector center for test points with $\phi = 0$.

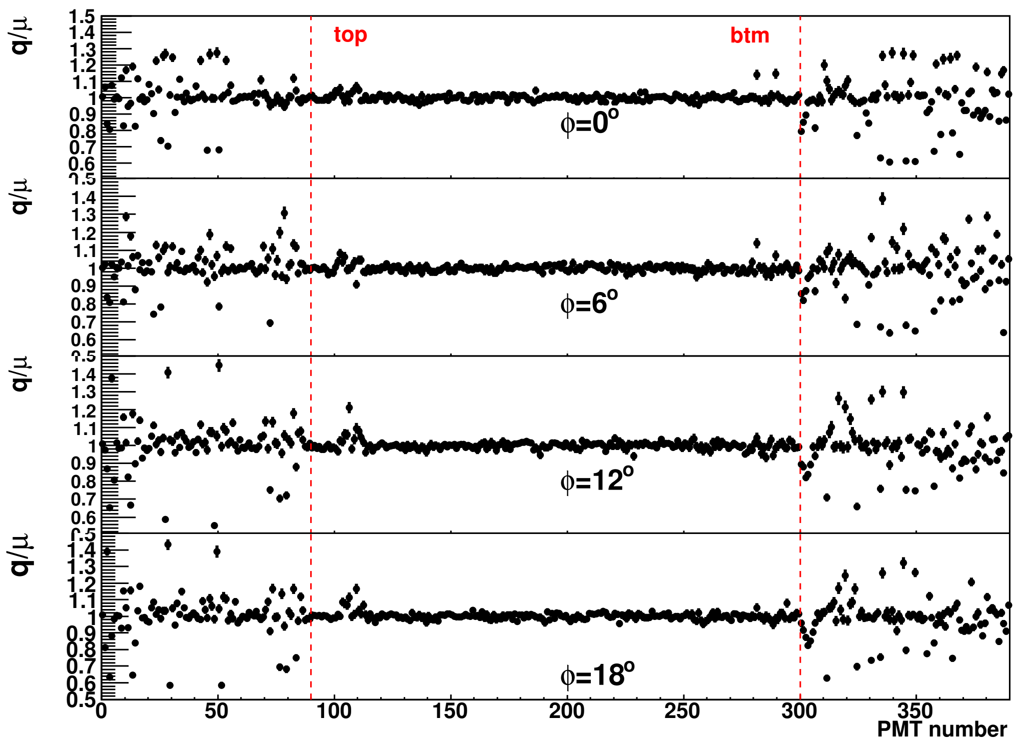

Figure 8.33: q/μ ratio as a function of PMT number for four test points with $z = 30$ cm and $\rho = 100$ cm.

but large variations appear for the top and bottom PMTs, where the departure from unity can reach up to 30%. This must be due to the interference during light propagation (e.g. reflection, refraction, or obstruction).

In order to verify the validity of our procedure, we repeated the same process by using only the side PMTs (numbers 90–299). The same normalized flux and total charge results are shown in Table 8.2, which clearly fulfilled our requirement. All the flux variations are well within 1%, except the one at $z = 0$ and $\rho = 100$ cm is labeled with red color and approximately equals 1%. On the other hand, the total visible charge shows variations of up to 15.5%, which are much higher than those using all PMTs.

z (cm)	ρ (cm)	Φ/Φ_0	Q/Q_0
0	0	1	1
	50	0.9993±0.0011	1.0350±0.0014
	100	1.0102±0.0011	1.1552±0.0015
30	0	0.9985±0.0011	0.9866±0.0014
	50	1.0013±0.0011	1.0222±0.0014
	100	1.0086±0.0010	1.1333±0.0015
−30	0	0.9967±0.0011	0.9851±0.0014
	50	0.9989±0.0011	1.0230±0.0014
	100	1.0073±0.0011	1.1348±0.0015
90	0	0.9907±0.0012	0.8813±0.0013
	50	0.9926±0.0012	0.9002±0.0013
	100	0.9983±0.0012	0.9491±0.0013
−90	0	0.9900±0.0012	0.8829±0.0013
	50	0.9948±0.0012	0.9040±0.0013
	100	1.0031±0.0012	0.9574±0.0013

Table 8.2: Normalized flux and total charge with respect to the detector center for test points with $\phi = 0$ using only side PMTs (numbers 90–299).

By looking at the geometry of Double Chooz acrylic vessels in Fig. 8.34, the abnormal q/μ ratios for the top and bottom PMTs might come from reflections and/or refractions from the support structures, namely the girders and stiffeners.

The advantage of MC simulation is that we can change the detector as we wish. By simulating the detector geometry with the neutrino target and gamma catcher support structures on and off, we generated events at 13 places along the connection path of PMT 0 and 387

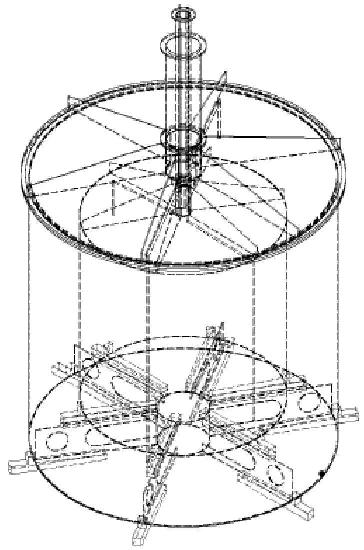

Figure 8.34: Three-dimensional view of Double Chooz acrylic vessels.

in the neutrino target with an interval of 20 cm and the middle point right at the center, as shown in Fig. 8.35. The reasons why we picked these two PMTs and the 13 vertices are because these two PMTs are facing each other and the light received by the PMTs is practically of normal incidence. Figure 8.36 shows the total charge collected by PMT 0 and PMT 387 for each vertex with and without the neutrino target and gamma catcher support structures. The plot indicates that the support structures really have an impact on the PMTs total charge. The gamma catcher support has a relatively small impact, while the neutrino target support affects all the vertices for PMT 387 and a couple of positions for PMT 0.

If the abnormal q/μ ratio is indeed caused by the neutrino target support structure, the PMTs receiving a higher or a lower amount of light than predicted must have their light propagation path across the acrylic. Figure 8.37 shows the q/μ ratio with respect to the pathlength inside the neutrino target acrylic stiffener. The negative numbers represent the closest approaches to the acrylic when the trajectory does not intersect the support structures. From the plot, one can see that the variations in the q/μ ratio are increasing when the light paths are getting closer and closer to the acrylic. It becomes extremely large

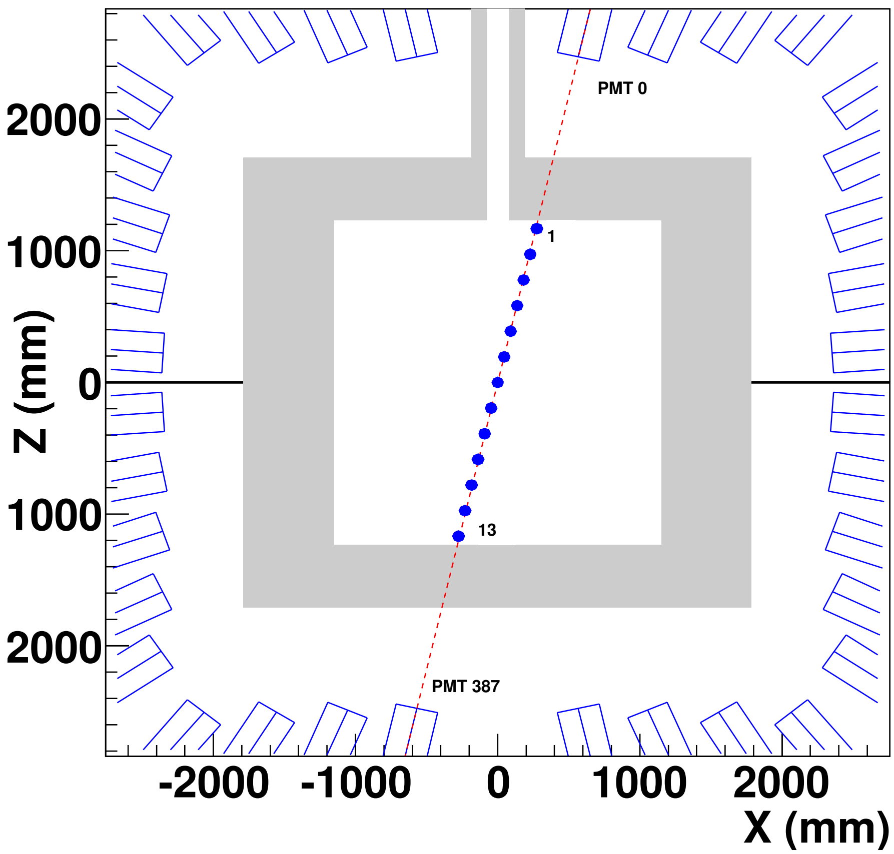

Figure 8.35: Illustration of 13 vertices along the connection path of PMT 0 and 387 in the neutrino target.

when the paths intersected the acrylic, which indicates that there are definite effects from the support structures.

Next we investigate what exactly happens when light crosses the stiffener. To accomplish that, each photon information at every step is recorded in detail, which prevents us from gaining large statistics. According to Fig. 8.36, the largest difference in the amount of light that PMT 0 receives occurs at the second point with coordinates of (x = 223.5 mm, $y = 0$, z = 974.7 mm). This time, only one hundred 1 MeV electron events were simulated at that vertex. A total of 152 photons directly hit PMT 0 while 19 photons were reflected by the neutrino target support structure, which results in a $19/152 \approx 12.5\%$ reflection light by the neutrino target support structure reflection, as shown in Fig. 8.38. This process is called *Fresnel reflection*: when light moves from a medium of a given refractive index n_1

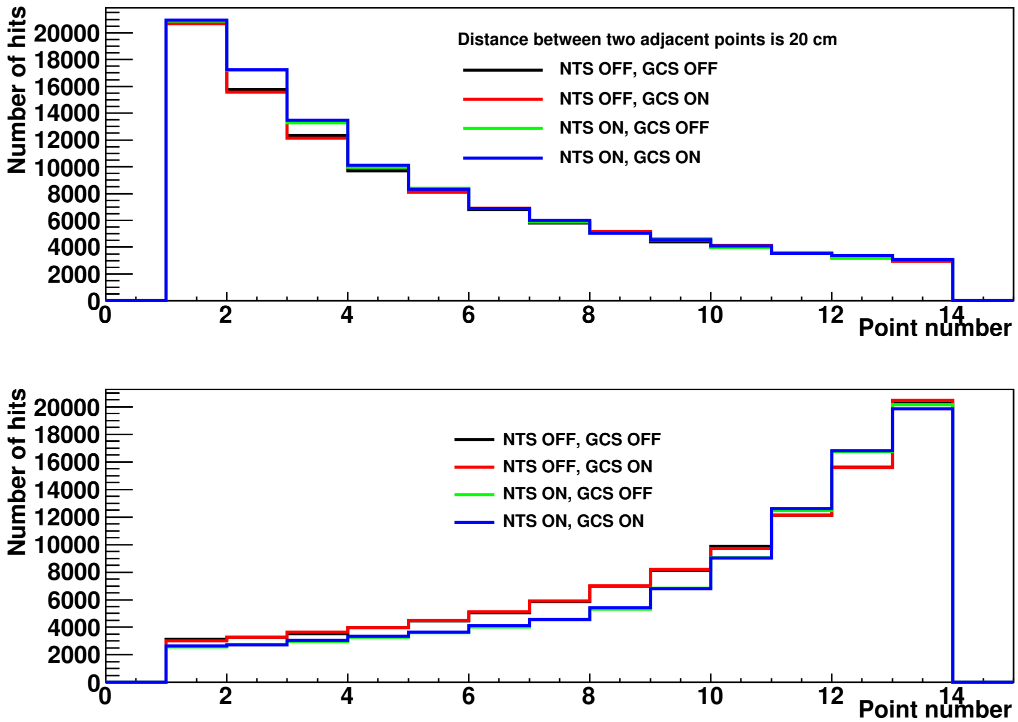

Figure 8.36: Total charges at vertices generated at the connection path of PMT 0 and 387 in the neutrino target with and without the neutrino target and gamma catcher supports.

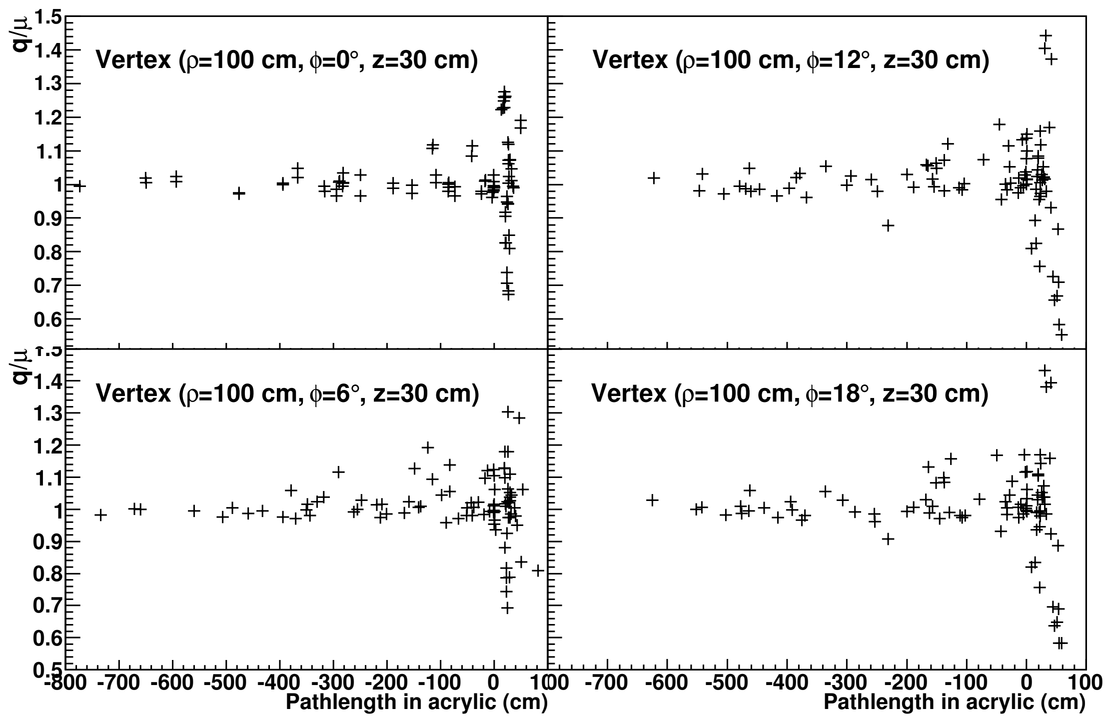

Figure 8.37: q/μ as a function of the closest approach from the light path to the neutrino target stiffener.

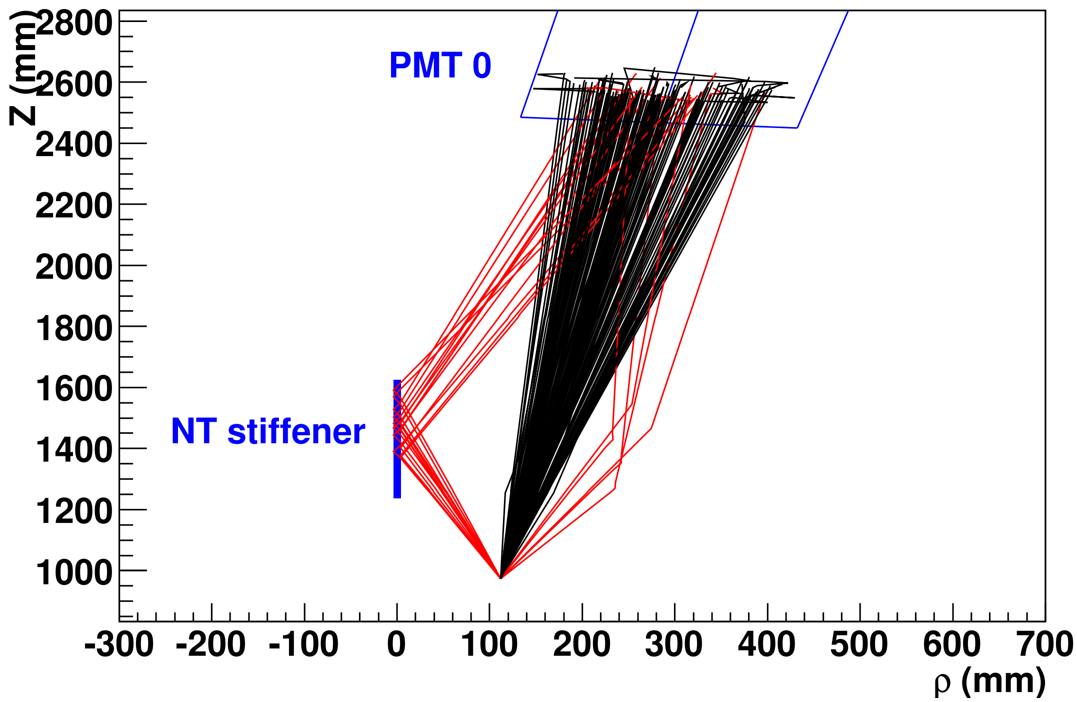

Figure 8.38: Illustration of the light paths hitting PMT 0 in a hundred 1 MeV electron events. There are 152 (black) photons strike PMT 0 directly, while 19 (red) reach there by reflection via neutrino target support structure. Fourteen out of those 19 photons concentrate on one piece of neutrino target stiffener as shown in the plot.

into a second medium with refractive index n_2, both reflection and refraction may occur. The reflection coefficient for s-polarized light (its electric field is perpendicular to the plane containing the incident, reflected, and refracted lights) is given by:

$$R_s = \left| \frac{n_1 \cos\theta_i - n_2 \cos\theta_t}{n_1 \cos\theta_i + n_2 \cos\theta_t} \right|,$$

while for p-polarized (its electric field is parallel to the plane described above) light is given by:

$$R_p = \left| \frac{n_1 \cos\theta_t - n_2 \cos\theta_i}{n_1 \cos\theta_t + n_2 \cos\theta_i} \right|,$$

where θ_i is the incident angle, θ_t is the refraction angle, and their relation is given by Snell's law:

$$\frac{\sin\theta_i}{\sin\theta_t} = \frac{n_2}{n_1}.$$

This also explains why some PMTs receive less light than predicted; it is caused by the acrylic support in the way of the direct light propagation which reflects the light to somewhere else other than the aimed PMT.

The reflection on the support structures is very sensitive to the event position. A couple of centimeters (our reconstruction error is in the order of 10 cm) off the target may shift the focus to another PMT or somewhere else, which increases the difficulty of accurate charge prediction at the PMTs. Therefore, this effect is difficult to implement in RecoBAMA.

8.5.2 The Double Chooz Attenuation Lengths and Reflections off the Buffer Inner Surface

In this section extensions of our optical model are discussed. The incorporation of three attenuations in different volumes does not improve the charge prediction on PMTs nor the reconstructed flux. This idea was therefore abandoned. We also found that the buffer inner surface reflections contribute to the PMT charge. The calculation of the reflection light based on the assumption of specular reflections were performed. The incorporation of the reflection improved the reconstructed flux, however, due to the large amount of calculation and the fact that no data were available at that time, there is no urgent need to incorporate the reflection model into RecoBAMA.

The Double Chooz inner detector contains three different volumes: neutrino target, gamma catcher and buffer, each of them having a different liquid and therefore a different attenuation length, as shown in Fig. 8.39.

Besides the support structure reflections and different optical properties in three volumes, we also found that the buffer inner surface reflection has an impact on the PMT predicted charge by examining the photon tracks. Detailed studies were performed towards understanding these effects. Combinations of various configurations were simulated in the MC, aiming to show the magnitude of the impact introduced by the three attenuation lengths and reflections. The simulated configurations include:

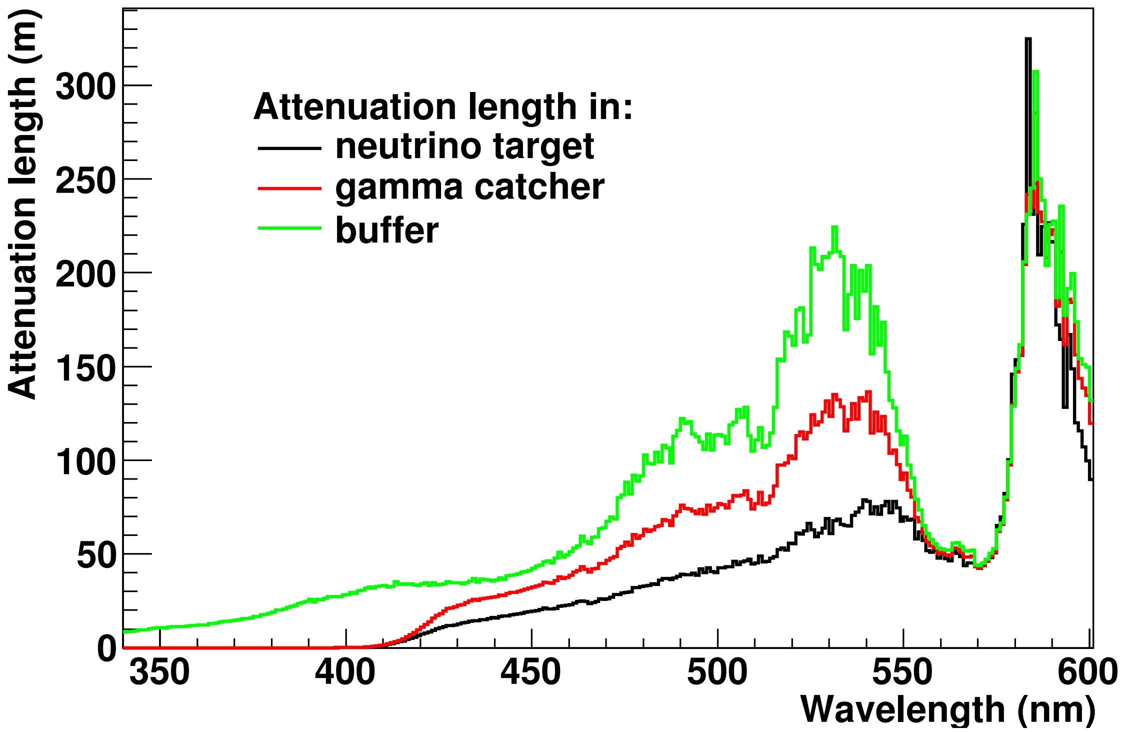

Figure 8.39: Attenuation lengths in neutrino target, gamma catcher and buffer from MC input table.

1. Same liquid in all volumes, no reflections, no support structures:
   - neutrino target scintillator (extract single attenuation length λ_{tv})
   - gamma catcher scintillator (extract single attenuation length λ_{gc})
2. Default liquids, no reflections, no support structures:
   - compare the simplest model (with a single, effective attenuation length λ_{eff}) with λ_{tv}, λ_{gc}, λ_{bf}
3. Same liquid in all volumes, with reflections and support structures:
   - neutrino target scintillator (extract single attenuation length λ_{tv}^{refl})
   - gamma catcher scintillator (extract single attenuation length λ_{gc}^{refl})
4. Default liquids, with reflections and support structures:

- Scenario A: simplest model with a single, effective attenuation length, λ_{eff}
- Scenario B: using λ_{tv}, λ_{gc}, and λ_{bf}

Figure 8.40 shows the effective attenuation and effective area from the standard iteration method applied to each configuration. The effective area for all configurations are almost the same, as expected, since this is primarily a PMT property, while the effective attenuation length can be grouped by two categories with respect to the existence of reflections and support structures. Without reflections and supports, the effective attenuation lengths can be well characterized by a sum of an exponential and a constant, while for the case with reflections and supports, they can only be fitted well by a polynomial. The changes with respect to different liquids are very small.

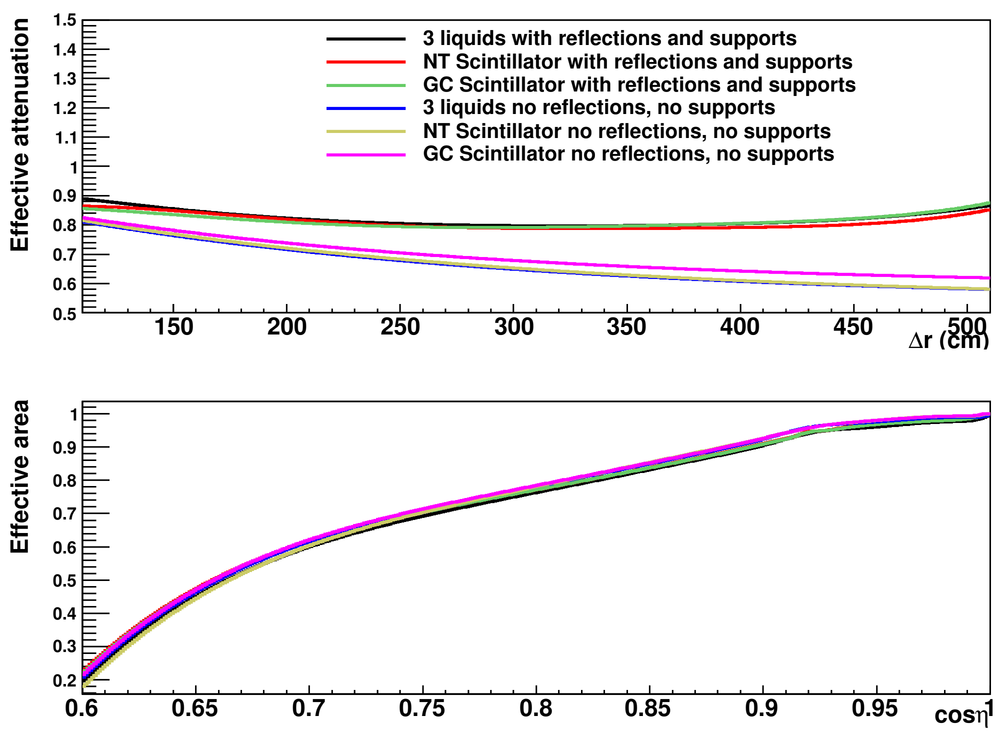

Figure 8.40: Effective attenuation and effective area for all the MC simulated configurations.

The three different attenuation lengths can be extracted by calculating the pathlengths in each volume and correcting by the corresponding q/μ ratios, which is similar as that for only one effective attenuation length. Figure 8.41 shows the three effective attenuation functions and the corresponding q/μ ratios as a function of pathlength in each volume.

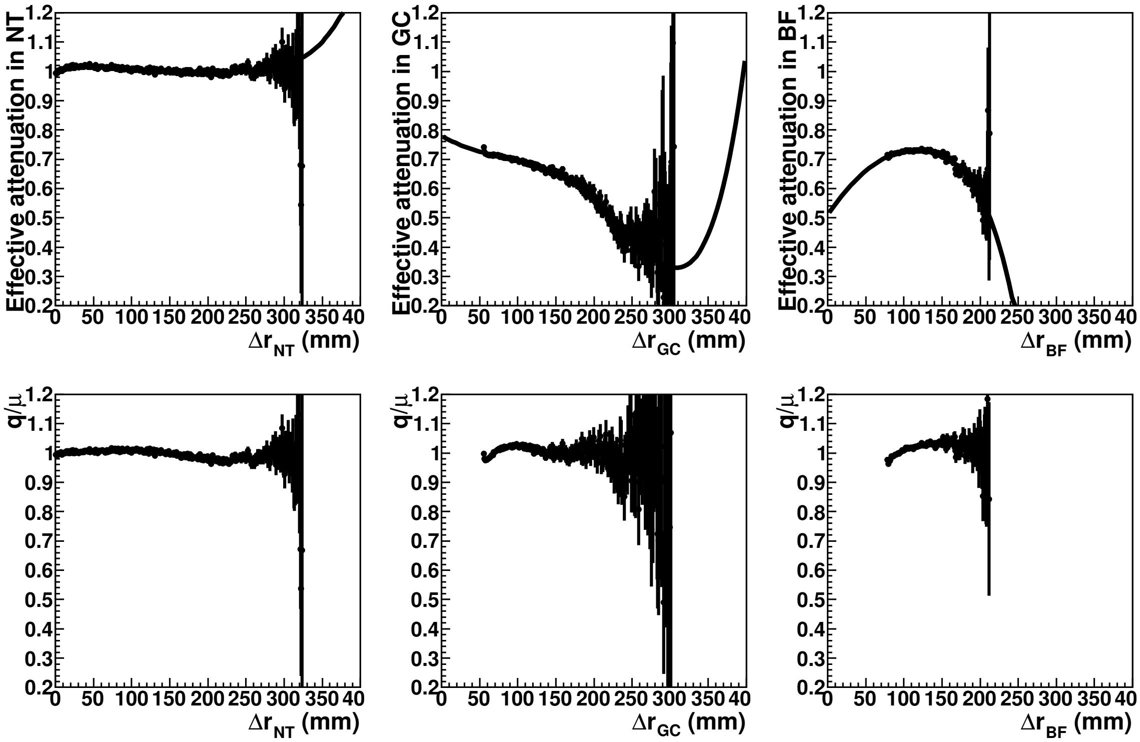

Figure 8.41: Effective attenuation functions and the corresponding q/μ ratios in the neutrino target, gamma catcher and buffer.

They cannot be fitted well by an exponential or a sum of an exponential and a constant. Therefore, they are fitted to polynomials. The q/μ ratios are not as good as that for only one effective attenuation length. The flux reconstruction also indicates that using three attenuation lengths in the optical model does not help, but enlarges the deviation from approx 2% (as shown in Fig. 8.42) to 5%. The idea of correcting for three attenuation lengths was therefore abandoned.

As in Section 8.5.1, test events at 45 points were simulated for each configuration meant to check how well the effective attenuation and effective area work in the flux reconstruction. This time, the coordinates of these 45 points were a little different from those used in the previous studies because of the PMTs position changed in the MC. Similar as in Section 8.5.1, the test points coordinates were simulated at the center and the same height as the PMTs in the middle rings, which were changed to $z = \pm 25$ cm and $z = \pm 75$ cm. All the ρ and ϕ coordinates were kept the same.

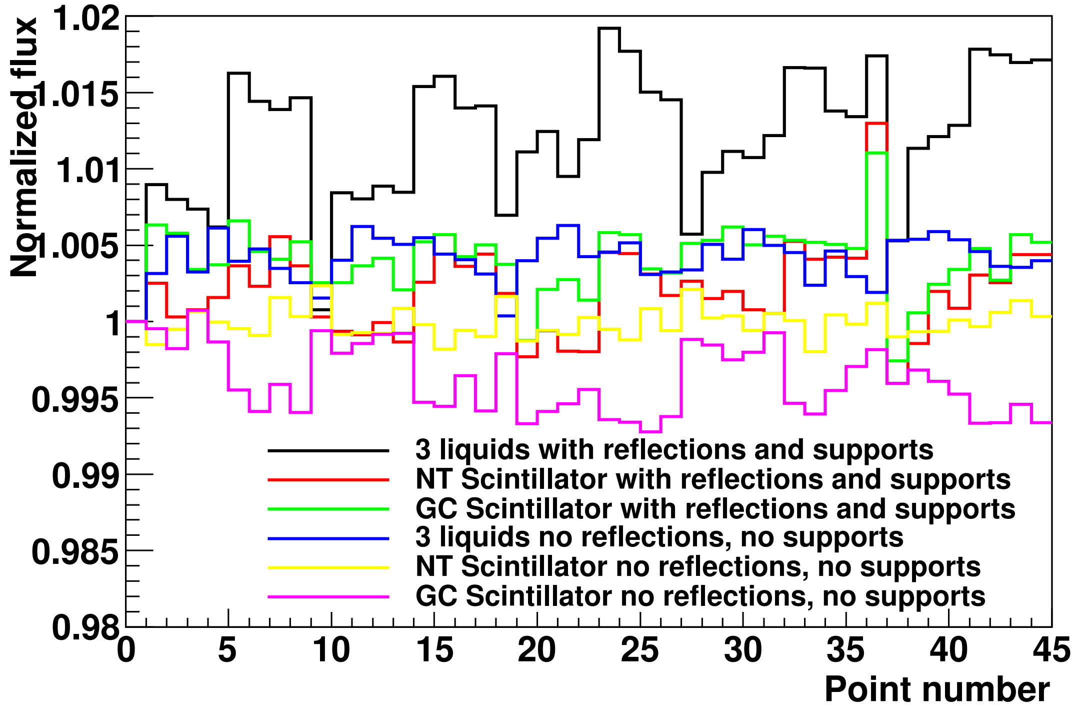

Figure 8.42: Normalized reconstructed flux at 45 points. Points 0–8 are at $z = 0$. Points 9–17 are at $z = 25$ cm. Points 18–26 are at $z = 75$ cm. Points 27–35 are at $z = -25$ cm. Points 36–44 are at $z = -75$ cm. In each group of 9 points in the same z plane, the first one represent $\rho = 0$, the second to the fifth represent $\rho = 50$ cm and $\phi = 0$, 6, 12 and 18°, respectively, and the sixth to the ninth represent $\rho = 100$ cm and $\phi = 0$, 6, 12 and 18°, respectively.

The flux at these 45 test points were obtained using the effective attenuation and effective area from each individual configuration, as shown in Fig. 8.42. Without the buffer reflections and support structures, the variations of the reconstructed fluxes are well within 1% or even smaller for the neutrion target scintillator, gamma catcher scintillator and default liquids in three volumes. With the buffer reflections and support structures, if all three volumes are filled with the same liquid (neutrino target or gamma catcher scintillator), only one point at $z = -75$ cm and $\rho = 0$ has a deviation of more than 1%. The default configuration, which has three liquids, buffer reflections and support structures, has relatively larger variations when either ρ or z goes towards the neutrino target boundary. The conclusion can be drawn that the effects from both the different liquids in the three volumes and buffer reflections are entangled in creating significant variations in the flux.

If we can understand the buffer reflection, we may be able to lower the flux variations to the level of 1%. The reflections on the buffer have both specular and diffuse components. Later studies in MC in Section 8.5.3 indicate that the diffuse reflection is more dominant than the specular reflection. However when we first saw this effect, we straightforwardly thought all the reflections are specular reflections. If only specular reflections exist, the characterization of the reflection on the top and bottom of the detector is a simple flat mirror reflection, while on the side, it is a little tricky but not hard to calculate.

In most cases there are two points on the side which reflect the light to a certain PMT. However, in most of such cases, there is always one point which resides behind the PMT which does not contribute at all, which leaves only one point that can reflect the light to the PMT, as shown in the top left panel of Fig. 8.43. In the special cases when the projections of the vertex and the PMT on the (x, y) plane are on the same diameter of the detector, there could be four solutions (again, one hits the PMT from behind and therefore is ignored) as shown in the top right panel of Fig. 8.43. The fractions of total predicted reflection lights including those from the top, bottom and side with respect to the total light for each PMT are plotted in the top panel of Fig. 8.44, superimposed with the actual fractions of reflected light simulated by the MC. The PMTs in the special cases are those having more fraction of reflected light which reside at the peaks in the top panel of Fig. 8.44. The calculations of such cases only considered one solution on the diameter. If three solutions had been all considered, the calculated amount of reflected light would have been over-predicted. In general, the calculation fits the simulation very well.

If one considers the PMTs finite size, there should always be two regions on the side wall, which could contribute to the total reflection. The bottom left and bottom right panels of Fig. 8.43 display only one area labeled by the green curve since the other one does not contributed (as it strikes the PMT from the back). One may have noticed that the reflection areas for the special cases are extremely large. If using those effective areas, the amount of reflected light were also much over-predicted, as indicated in the middle panel of Fig. 8.44. If the reflection areas were limited to a maximum of PMT area for all the cases, the prediction

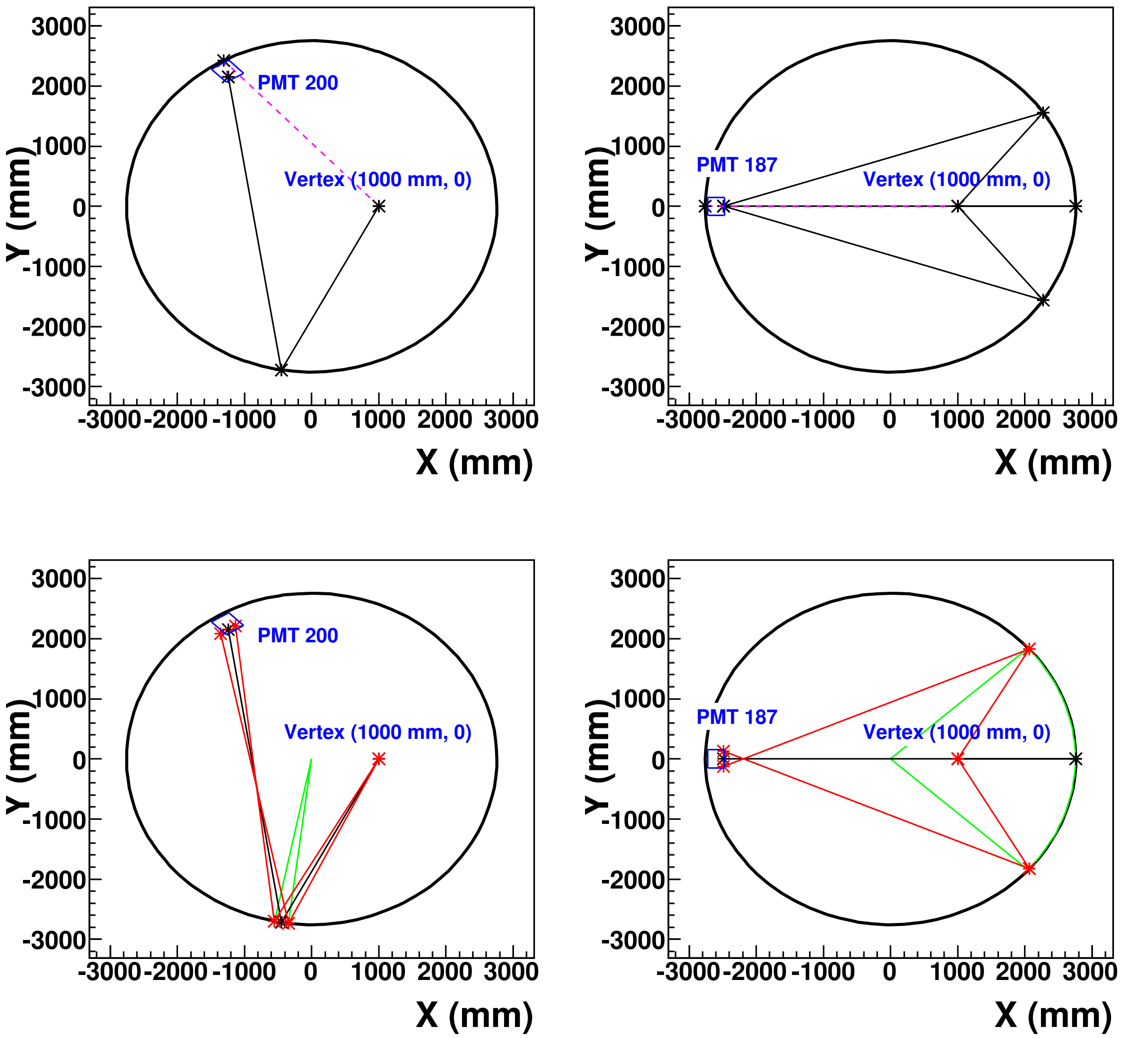

Figure 8.43: The two reflection solutions on the side of the detector for PMT 200 (top left) when the vertex is at $x = 1000$ mm and $y = 0$. The one in dashed pink strikes the PMT from behind which does not contribute. The reflection solutions on the side of the detector for PMT 187 (top right) for the same vertex. The one in dashed pink strikes the PMT from behind which does not contribute. The range of the reflection solution on the side of the detector when condisering the PMTs' finite size for PMT 200 (bottom left) and PMT 187 (bottom right) for the same vertex. The green area on the side wall indicates the effective reflection area.

looks perfect as shown in the bottom panel of Fig. 8.44. But there is no physical reason that we can perform such limit. Even though, the solution without considering the finite PMT area is good enough for making the variations of reconstructed fluxes at 45 test points within 1% as can be seen in Fig. 8.45. The black curve in Fig. 8.45 is the one using the attenuation length and effective area extracted from the default configuration to reconstruct the flux for

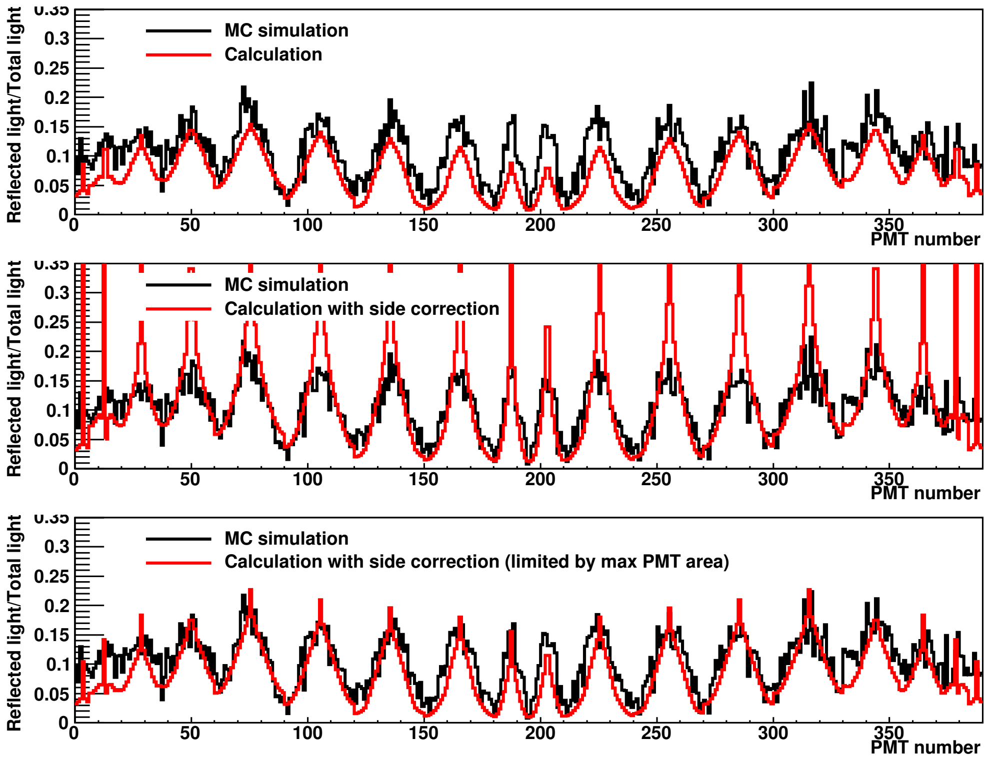

Figure 8.44: The fractions of total predicted reflection lights with respect to the total lights for each PMT superimposed with the actual fractions of reflection light simulated by MC.

this configuration. The red curve uses the attenuation length and effective area from the case with 3 liquids but no reflection to reconstruct the flux for the default configuration. Having the reflection effect incorporated, we reconstructed the flux within 1%.

Incorporating reflections is complicated and will slow down the speed of RecoBAMA. We first wanted to examine how the current optical model and parameterizations of effective attenuation and effective area in RecoBAMA worked on energy reconstruction and then decide whether to change or keep it. We extended our samples to the entire (x, z) plane in which 10,000 1 MeV electron events were simulated every 10 cm in each direction to cover the entire neutrino target. Looking at the normalized fluxes all over the place inside the neutrino target in the left panel of Fig. 8.46, the RecoBAMA optical model works well for the entire volume in which the reconstructed energy variation in most of the neutrino target region is within 1% and a maximum of 2% in the other areas except for the region near the center bottom of the neutrino target, which is very close to the neutrino target support structure

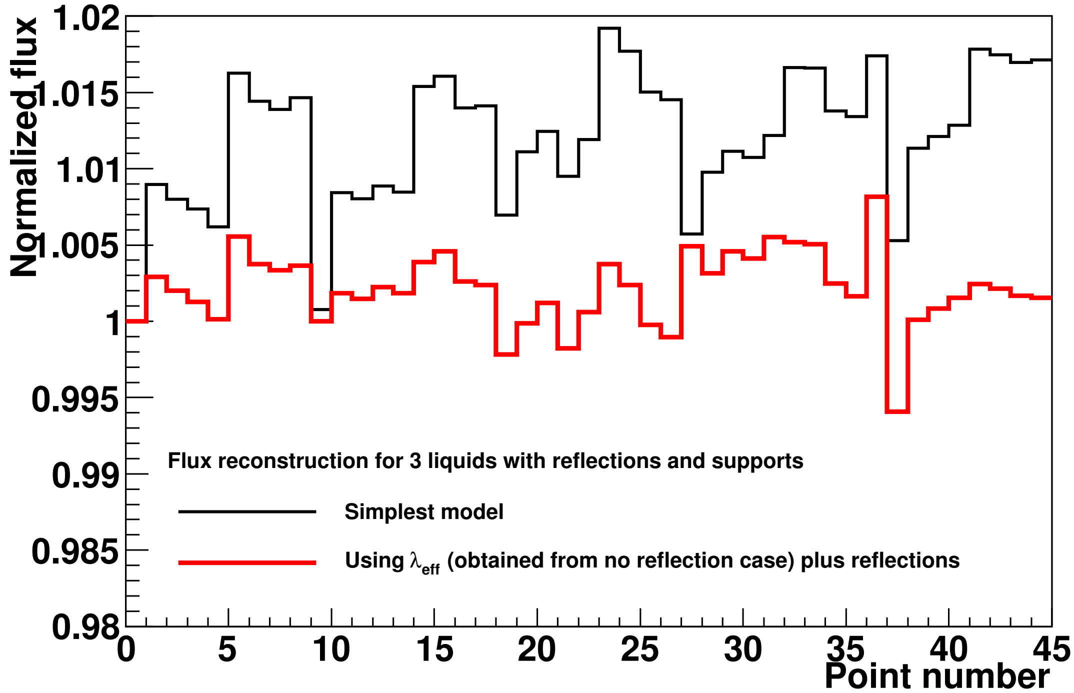

Figure 8.45: Comparison of reconstructed fluxes with or without considering reflection.

at the bottom. Large deviations were found there which are caused by the reflection on the support. The reconstructed flux has an obvious improvement compared to the normalized total charge in the right panel of Fig. 8.46 which has a maximum 7% deviation, excluding the area near the center bottom of the neutrino target.

Our optical model agrees well with the MC and there was no urgent need to extend or modify it before the Double Chooz data were available. Extension or modification might be required if large variations were observed in the energy reconstruction for the Double Chooz data.

8.5.3 Energy Reconstruction in the Data

In this section, the reflections on the buffer wall in data are discussed. We identified the second peak structure in the PMTs corrected time distribution as the reflection light for the calibration data. MC simulations were performed to reproduce the same corrected time distribution as in the calibration data. We found that the default MC parameters yield the

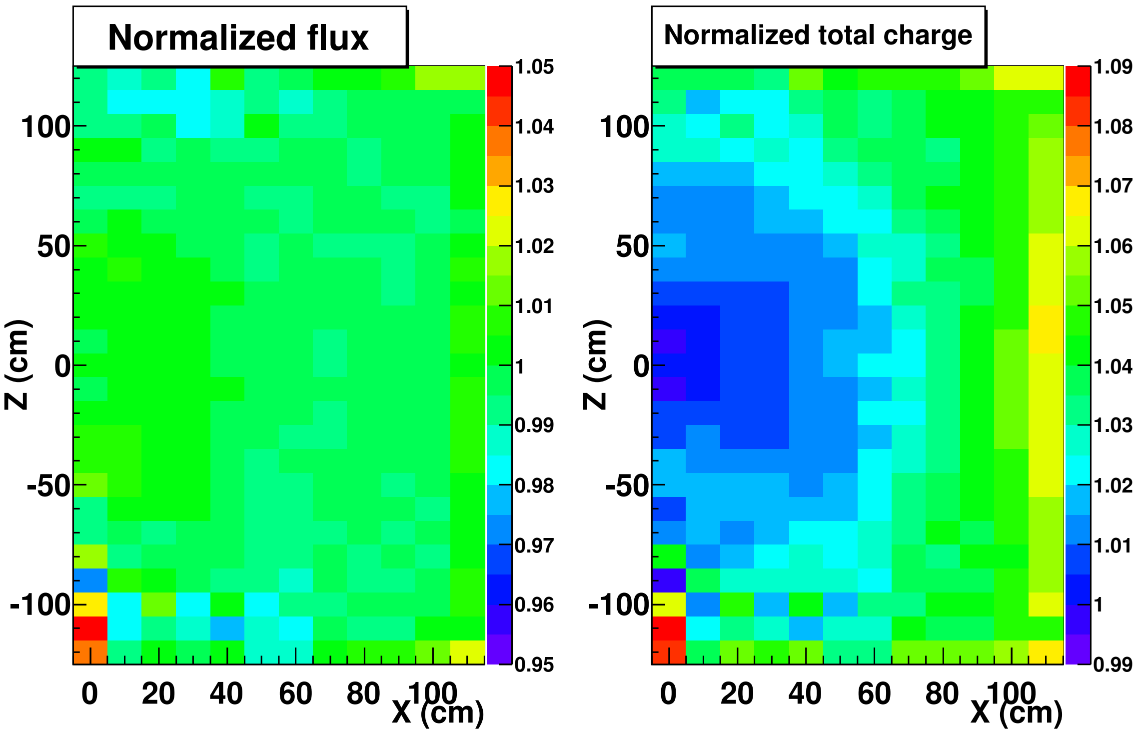

Figure 8.46: Normalized fluxes using optical model without reflection and normalized total charge in the (x, z) plane (MC simulation, neutrino target only).

closest corrected time distribution as in the calibration data. The default MC parameters suggests diffuse reflections are dominant in MC. Our modelling of diffuse reflections predicts the reflected charge on PMTs very well in MC. However, we still need more calibration data to understand what type of reflections happen in the data. The parameterizations of the effective attenuation and effective area in current optical model cannot give the same energy response as obtained from the calibration data and n-H data. I examined that with the current optical model in so far as what parameterizations can mostly recover the energy response in the calibration data and n-H data. However, the parameterizations that generates the best energy response cannot correctly predict the charge on PMTs. Unfortunately, we were unable to recover the n-H map with the current optical model. However, the feasibility of our procedure has been proved by MC at the end of this section.

As the calibration data became available, we checked the total charge and flux of all the calibration sources deployed at various positions along the z axis. We found that the total charge at the vertex close to the boundary of the neutrino target is 7% less than that in the center, as shown in Fig. 8.47. The current solution to this problem is to impose a correction for each vertex. As argued before, if the optical model is understood correctly, the flux will be proportional to the energy without the need of any position correction. However, if we calculate the flux based on the current optical model, the result is even worse than the total visible charge as Fig. 8.48 indicates.

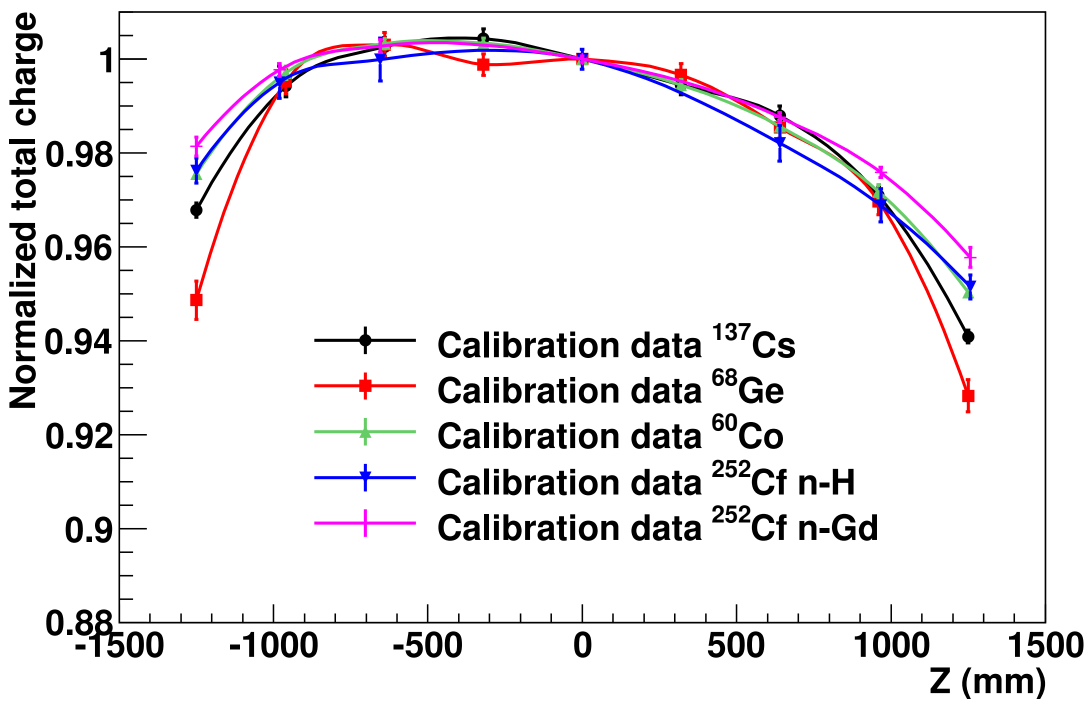

Figure 8.47: Normalized total charge of all the calibration sources at different positions along the z axis.

In order to understand this problem, we need to make sure that our optical model and the parameters are appropriate. The q/μ ratio of each ring for the z axis vertices has shown that our optical model is sufficiently accurate, but if we look at the charge on the two inner-most rings as a function of distance for the ^{137}Cs, ^{68}Ge and ^{60}Co sources in Fig. 8.49 by correcting only the solid angle effect, the further PMTs receive more charge than the near PMTs, which means there is no room for the attenuation length. If we take a detailed look at each ring's corrected time for vertex at $z = \pm 1120$ mm and $z = \pm 1250$ mm [202], we can clearly see a

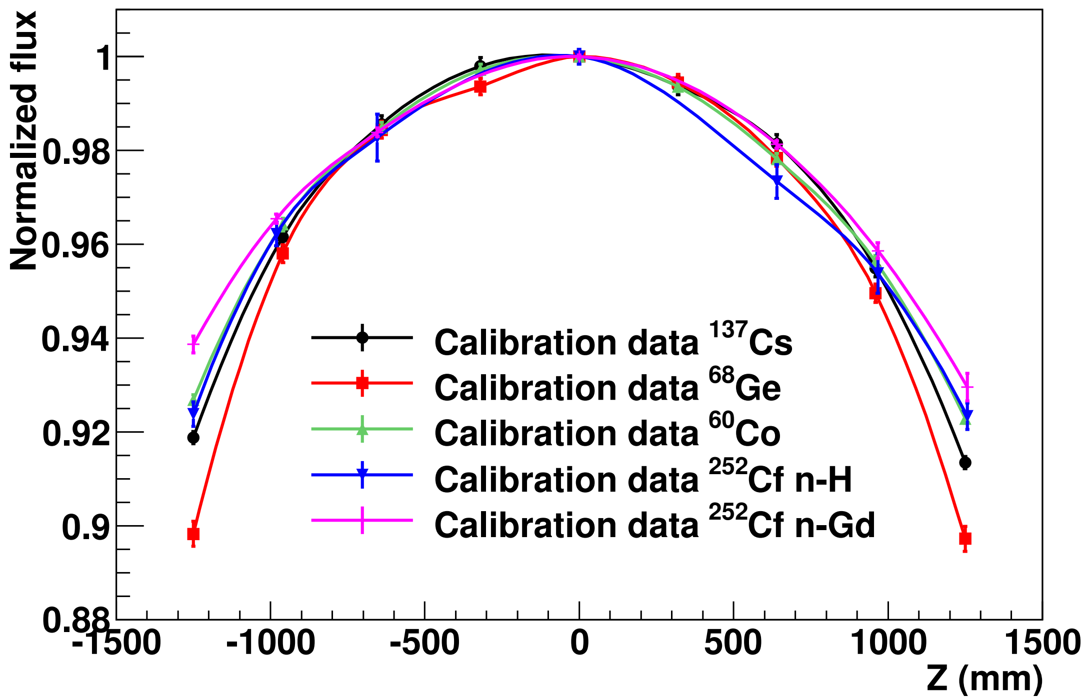

Figure 8.48: Normalized flux of all the calibration sources at different positions along the z axis.

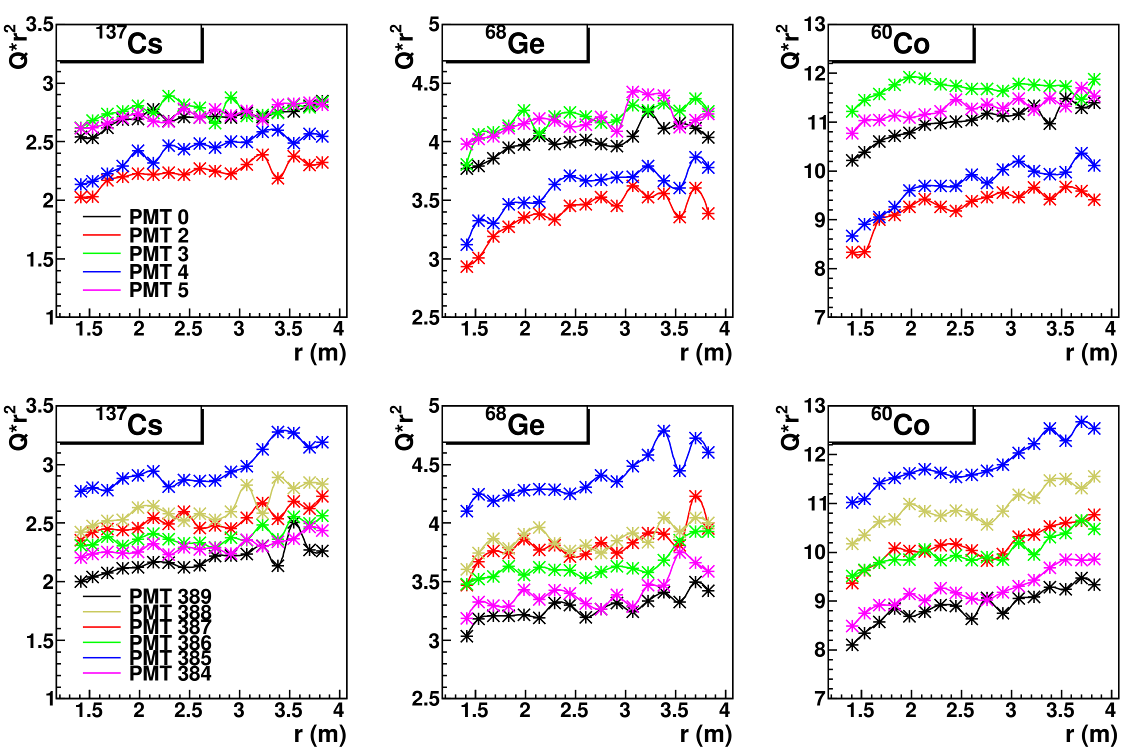

Figure 8.49: Qr^2 of inner most rings at the top and bottom for the ^{137}Cs, ^{68}Ge and ^{60}Co sources.

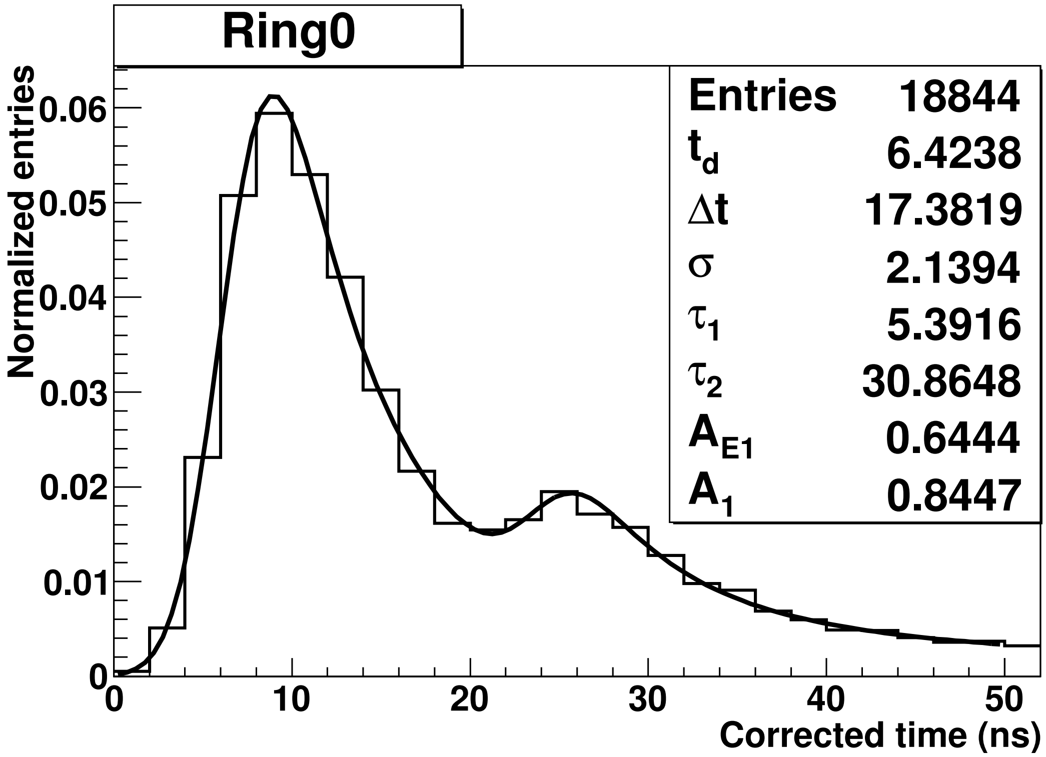

Figure 8.50: Corrected time distribution for all PMT in ring 0 fitted to Eq. (8.2) for the ^{60}Co source deployed at (0, 0, −1120 mm).

second peak structure at the PMTs on the opposite side of the vertex. Figure 8.50 shows the corrected time distribution of ring 0 when the ^{60}Co is deployed at $z = -1120$ mm. The first peak and second peak were fitted to a Gaussian with distribution σ modified by two Exponentials with constants τ_1 and τ_2. The only differences between the first and second peak are the Gaussian's position and the relative magnitude. The fitting function is given below:

$$
\begin{aligned}
f(x) = A_1 \Bigg\{ & \frac{A_{E1}}{2\tau_1} \exp\left(\frac{t_d - x}{\tau_1} + \frac{\sigma^2}{2\tau_1^2}\right) \left[1 - \mathrm{Erf}\left(\frac{\sigma}{\sqrt{2}\tau_1} + \frac{t_d - x}{\sqrt{2}\sigma}\right)\right] \\
& + \frac{1 - A_{E1}}{2\tau_2} \exp\left(\frac{t_d - x}{\tau_2} + \frac{\sigma^2}{2\tau_2^2}\right) \left[1 - \mathrm{Erf}\left(\frac{\sigma}{\sqrt{2}\tau_2} + \frac{t_d - x}{\sqrt{2}\sigma}\right)\right] \Bigg\} \\
& + (1 - A_1) \Bigg\{ \frac{A_{E1}}{2\tau_1} \exp\left(\frac{t_d + \Delta t - x}{\tau_1} + \frac{\sigma^2}{2\tau_1^2}\right) \left[1 - \mathrm{Erf}\left(\frac{\sigma}{\sqrt{2}\tau_1} + \frac{t_d + \Delta t - x}{\sqrt{2}\sigma}\right)\right] \\
& + \frac{1 - A_{E1}}{2\tau_2} \exp\left(\frac{t_d + \Delta t - x}{\tau_2} + \frac{\sigma^2}{2\tau_2^2}\right) \left[1 - \mathrm{Erf}\left(\frac{\sigma}{\sqrt{2}\tau_2} + \frac{t_d + \Delta t - x}{\sqrt{2}\sigma}\right)\right] \Bigg\},
\end{aligned}
\tag{8.2}
$$

where the first peak position t_d represents the arrival time of direct light, the time difference between the first and second peak Δt represents the time difference between the direct light and the reflected light, A_{E1} is the relative magnitude of the first exponential and A_1 is the relative magnitude of the first peak. It has also been confirmed that similar effects happened for events in the guide tube. Figure 8.51 displays the layout of the guide tube vertex positions. In Fig. 8.52, the corrected time distributions for 15 PMTs from the vertex circled in Fig. 8.51 are plotted. These distributions shown in red (bottom row, left) are PMTs which have an obvious second peak; they are all on the opposite side of the buffer wall, while the others do not exhibit a second peak structure. We were further convinced that the source of the extra light is from buffer wall reflections.

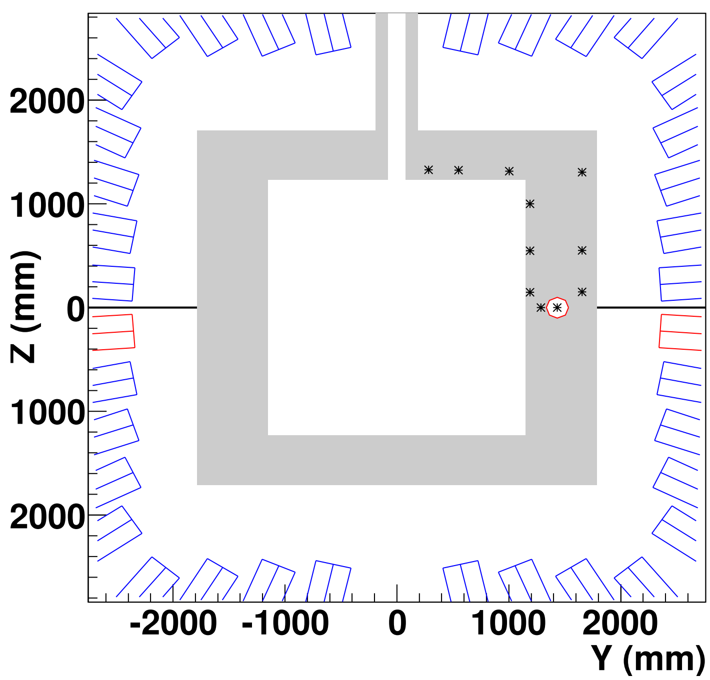

Figure 8.51: Deployment positions through the guide tube.

8.5.3.1 Type of Reflection

With the obvious second peak structure in the corrected time distribution, we postulated that it was specular reflection whose arrival time is dominated by the time at the second

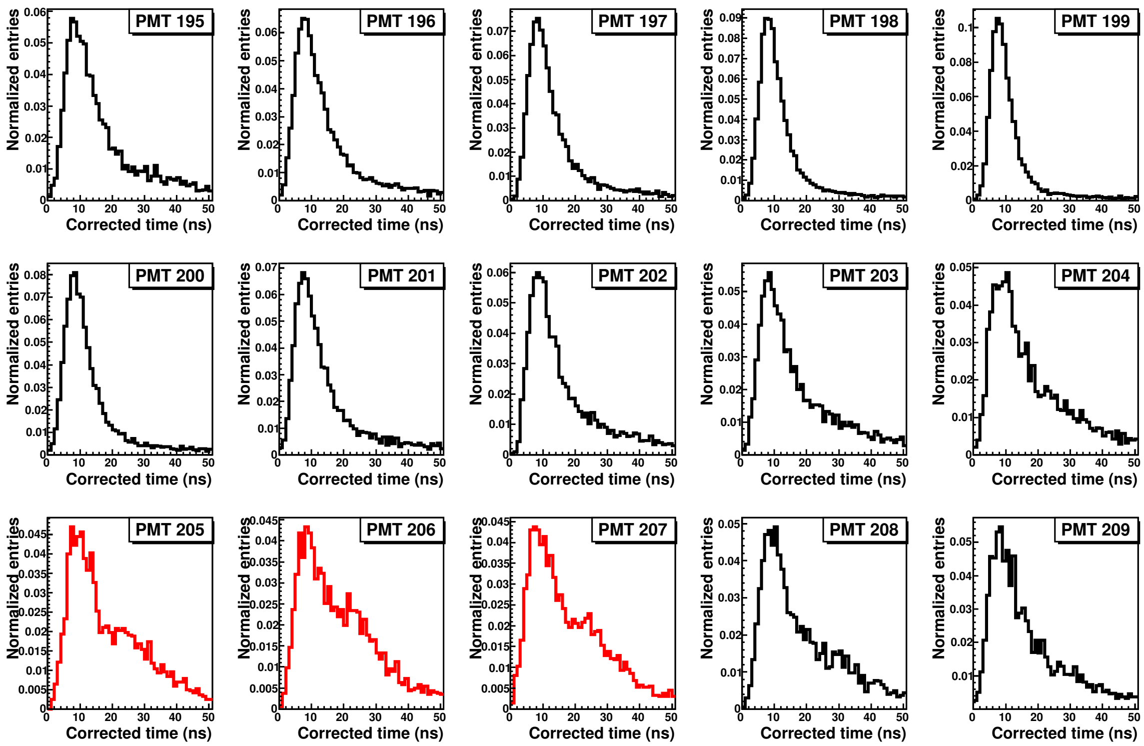

Figure 8.52: Corrected time distributions of PMT 195 to 209 at the ring labeled in red in Fig. 8.51 when source is deployed in the guide tube circled vertex in Fig. 8.51. The PMTs 205, 206, 207 show evidence of reflections.

peak characterized by $t_0 + t_d + \Delta t$. The next question is where does this reflection happen: top, bottom or side wall. All possible pathlengths for each z axis vertex were calculated. Figure 8.53 is an illustration of how light travels from the vertex at (0, 0, -1120 mm) to PMT 0 assuming all possible reflections off the buffer walls.

Our current knowledge of the speed of light in the detector is accurate enough to calculate the time difference of the direct and reflected light. The comparison of the time difference between the fitted second peak and first peak in the corrected time distribution to that calculated from the pathlengths is shown in Fig. 8.54, where the opposite side reflections seem to match the data to a relatively good degree.

Next, we turned to the MC simulation. We first checked if different sources (electrons, positrons, photons) with the same amount of visible charge makes any difference in the

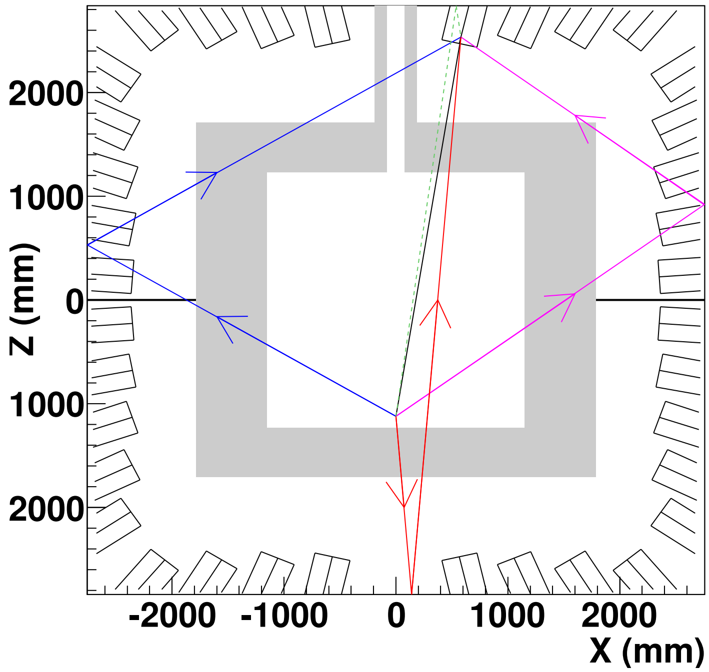

Figure 8.53: All possible reflection paths (assuming specular reflection) from a light source at (0, 0, −1120 mm) to PMT 0.

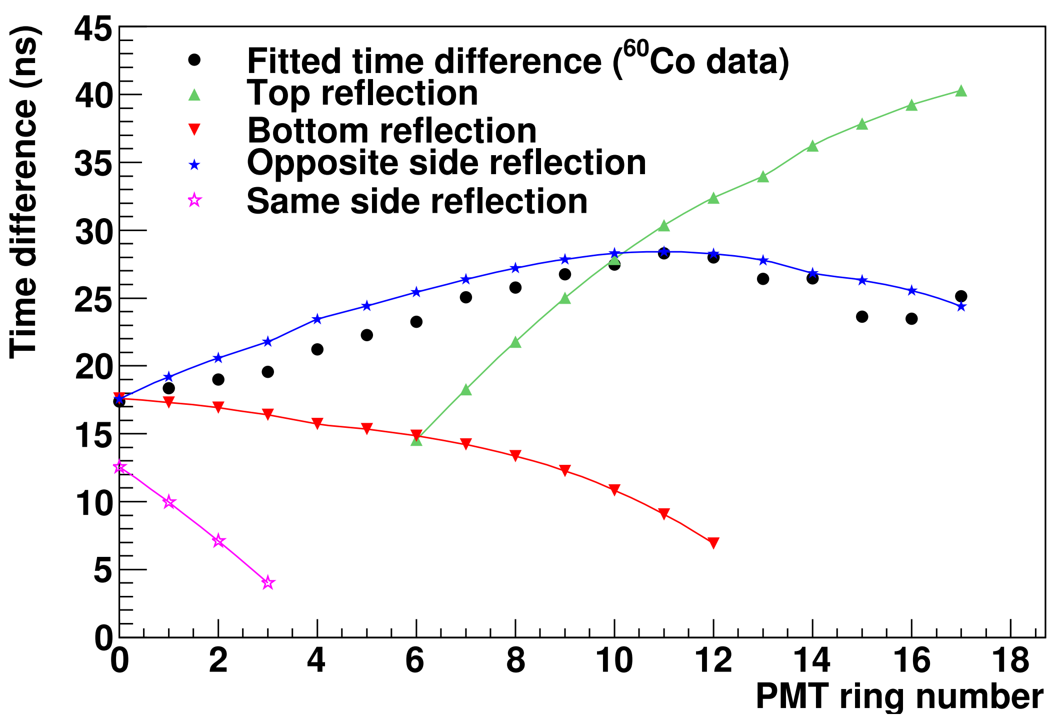

Figure 8.54: Comparison of the corrected time Δt (2nd peak - 1st peak) with specular reflection model when the source is deployed at (0, 0, −1120 mm).

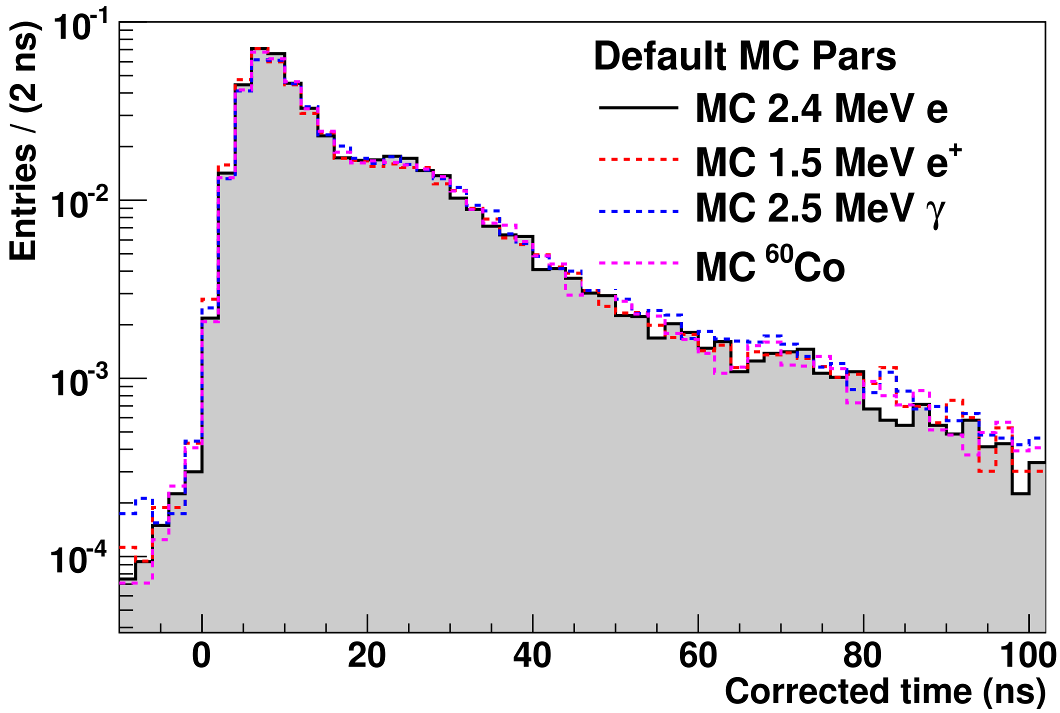

Figure 8.55: Comparison of the corrected time of ring 0 for 4 sources with the same visible energy scale in MC when the events were generated at (0, 0, −1120 mm).

corrected time distribution in Fig. 8.55. The different sources generate almost identical corrected time distributions. In the MC the buffer reflection is controlled by two parameters: reflectivity and polish. The reflectivity describes how much portion of light is reflected, and the polish represents the allocation of diffuse and specular reflections (e.g., polish = 0 means pure diffuse reflection and polish = 1 means pure specular reflection). We tested combinations of 9 different configurations with a buffer reflectivity of 0.2, 0.4 (default) and 0.8 and a buffer polish of 0.05, 0.1 (default) and 0.2. Half to twice of the default (measured) values should cover a wide enough range in which the parameters could vary. Since these three polish values do not generate obviously different structures in the corrected time distributions, only those with default polish and different buffer reflectivities are compared with data in Fig. 8.56. The MC default parameters (buffer reflectivity = 0.4, buffer polish = 0.1) describe the buffer reflection well. Figure 8.57 tells us that using the default reflectivity, no obvious difference is observed when the buffer polish takes any value below 0.2. Distinct differences

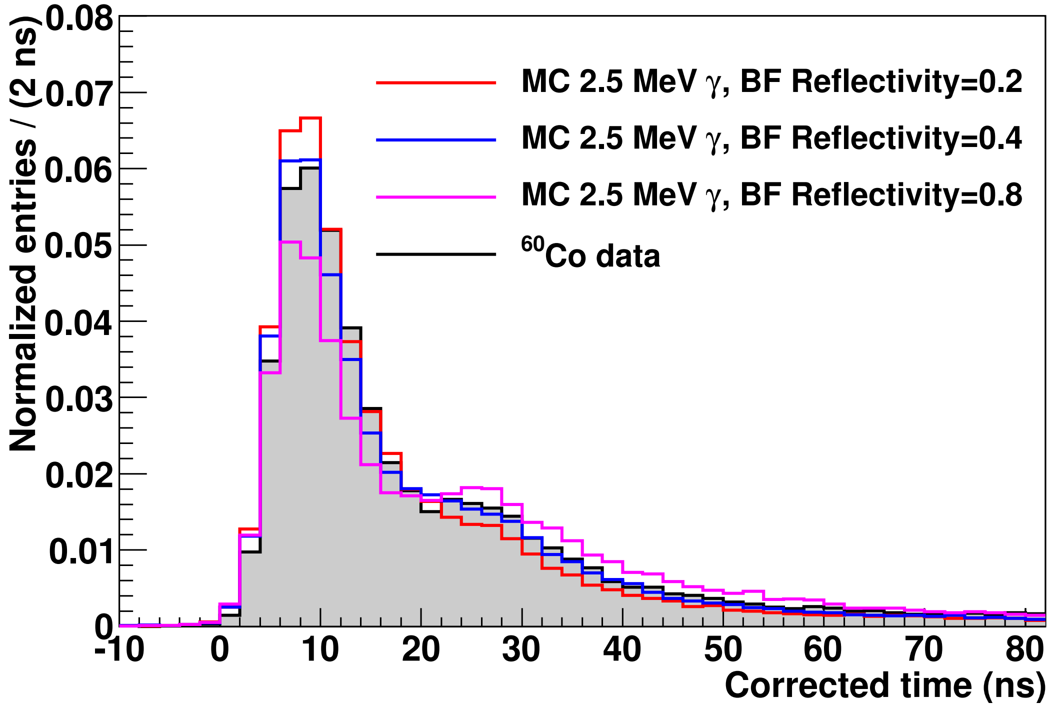

Figure 8.56: Corrected time comparisons of ring 1 for 2.5 MeV γ with different reflectivities and ^{60}Co data at (0, 0, -1120 mm).

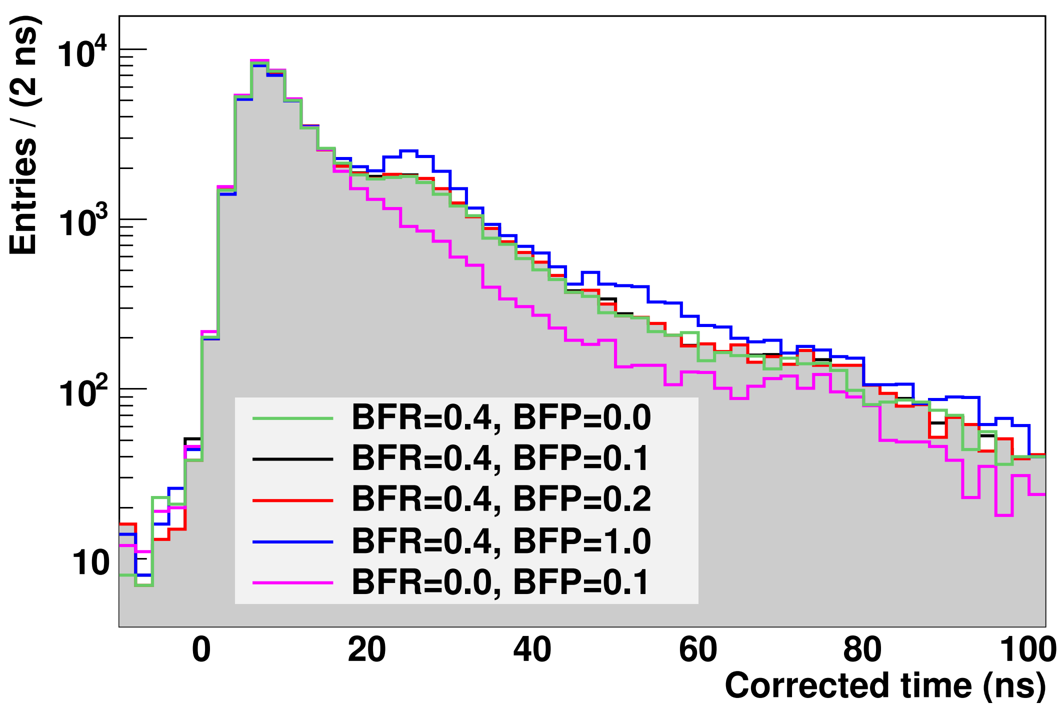

Figure 8.57: Corrected time comparisons of ring 1 for 2.5 MeV γ generated at (0, 0, -1120 mm) with different polishes.

show up when the buffer polish approaches to 1. The second peak is really generated by reflections, and it disappears as the buffer reflectivity is turned off.

With the help of MC track files, I was able to plot the photon tracks to visualize where reflections happen. Figures 8.58 and 8.59 show 200 photons hitting PMT 0 from vertex at $z = -1120$ mm in side and top perspectives. We confirmed that both direct and reflected light contribute to the PMT charge. However, the reflections do not appear to come from one particular place: they are all over the buffer wall, which means that the diffuse reflection dominates the MC simulation. Figure 8.57 also tells us that a polish = 0.1 does not make significant difference to a polish = 0.0 in the corrected time distribution, which means that the reflection off the buffer can be treated as pure diffuse reflection to a good approximation.

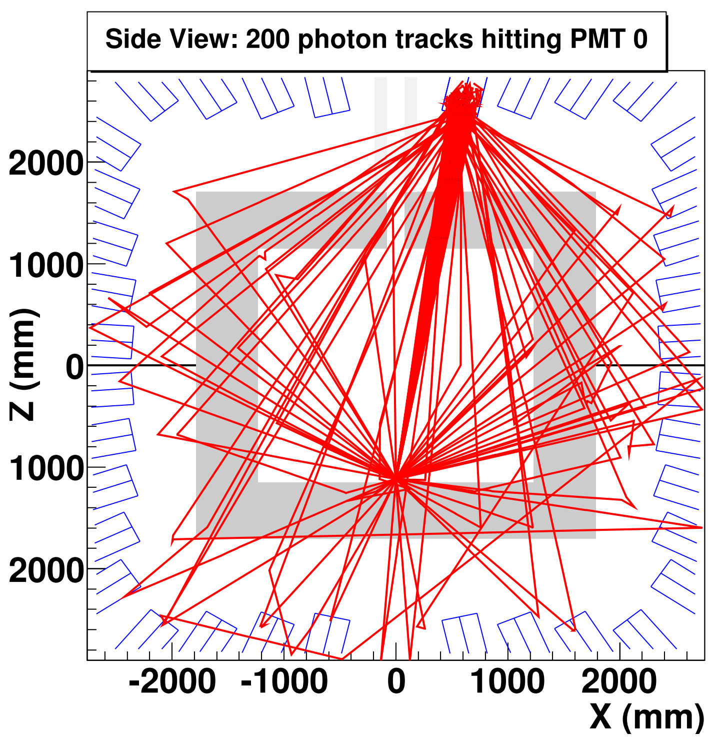

Figure 8.58: Side view of 200 isotropic photon tracks hitting PMT 0.

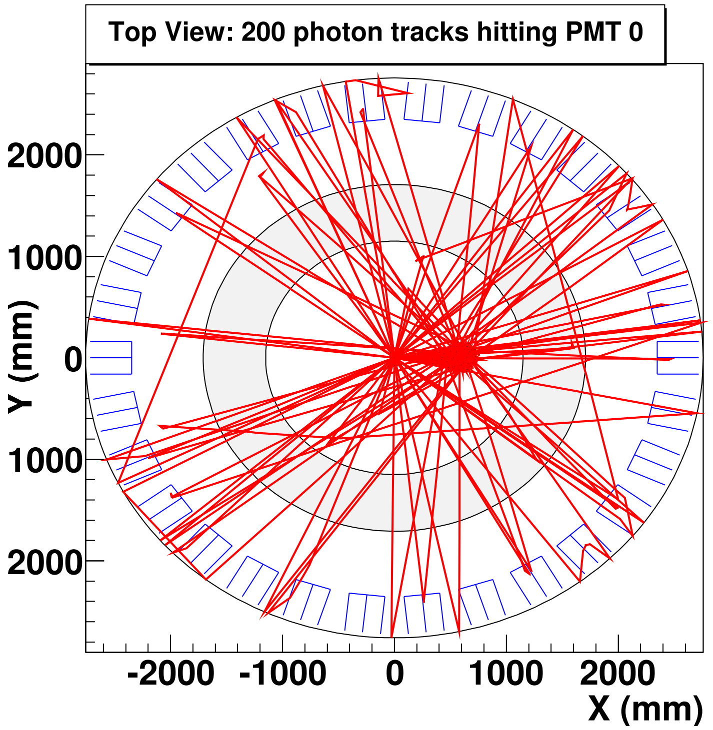

Figure 8.59: Top view of 200 isotropic photon tracks hitting PMT 0.

8.5.3.2 Modelling Reflection

Since the reflections in the MC are dominated by diffuse reflections, the PMT charge caused by reflections can be calculated to first order as the integration over the entire buffer surface. For simplicity, assuming no light attenuation and a linear response in the cosine of the incident angle for the PMTs, the predicted charge for the direct light can be expressed as:

$$\mu_d = \frac{\Phi \cos\theta_d}{r_d^2},$$

and the predicted charge for reflected light can be written as,

$$\mu_r = \frac{0.4\,\Phi}{2\pi} \int dA_{BF} \frac{\cos\theta_1}{r_1^2} \frac{\cos\theta_2}{r_2^2},$$

where r_d is the distance from the vertex to the PMT, θ_d is the incident angle of direct light, r_1 is the distance from the vertex to where the reflection happens, θ_1 is the incident angle to the buffer wall, r_2 is the distance from where the reflection happens to the hit PMT, θ_2 is the reflected light incident angle to the hit PMT, 0.4 is the reflectivity and $1/2\pi$ is the normalization factor of reflected light. The ratio of the reflected light with respect to the direct light in this model is,

$$R = \frac{\mu_r}{\mu_d} = \frac{\cos\theta_d}{5\pi r_d^2} \int dA_{BF} \frac{cos\theta_1}{r_1^2} \frac{cos\theta_2}{r_2^2}.$$

The histograms in Fig. 8.60 are filled with charge weighted time differences between reflected light all over the buffer and direct light. The charge-weighted time reproduces the second peak structure, and also fits the relative second peak position pretty well. Since the integration has no analytical solution, the total reflected charge has to be calculated numerically. One simple choice is to change the integration to the sum. The size of the basic summing

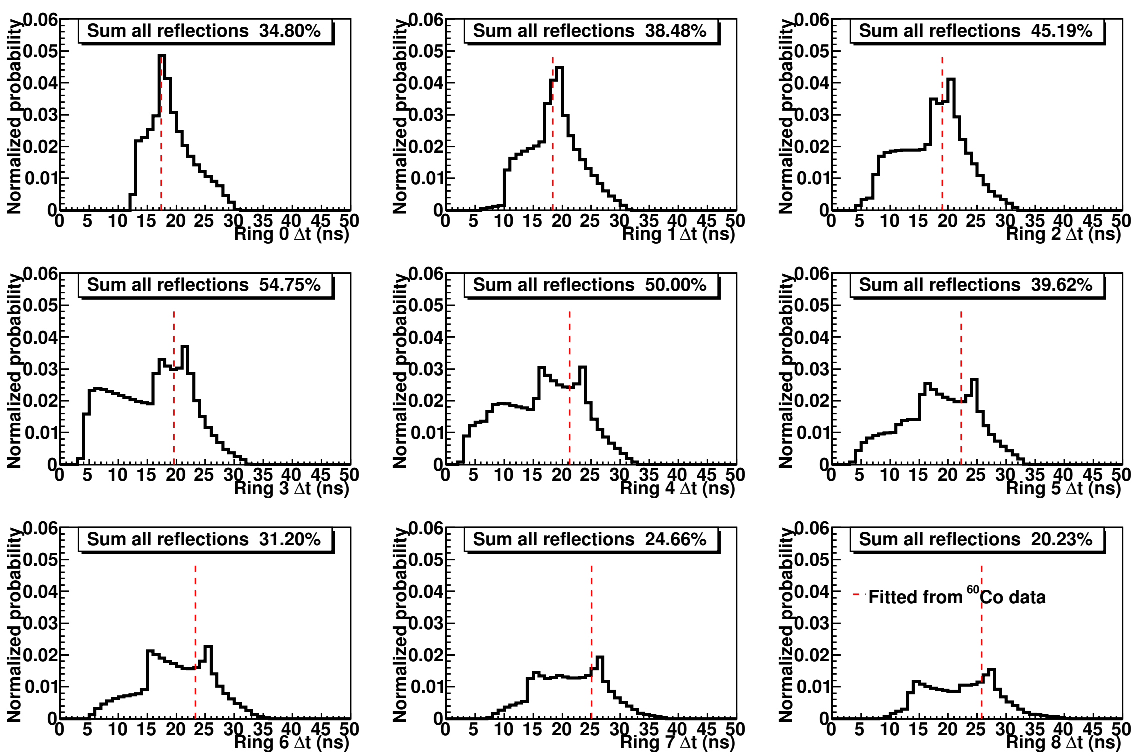

Figure 8.60: Calculated Δt (reflected PMT time - direct PMT time) distribution weighted by charge compares with Δt (2nd peak - 1st peak) fitted in ^{60}Co corrected time (red dashed lines) deployed at (0, 0, -1120 mm).

unit area decides the accuracy of the result. In other words, the smaller the basic unit, the more accurate the result will be but the longer time it will take. To balance the accuracy and running time, I examined the differences induced by various sizes of integration units at vertex (0, 0, -1120 mm) as shown in Fig. 8.61. The differences among mm^2, cm^2 and dm^2 are very small. Small deviations appear when it goes to 0.25 m^2, which was finally taken as the basic integration unit area.

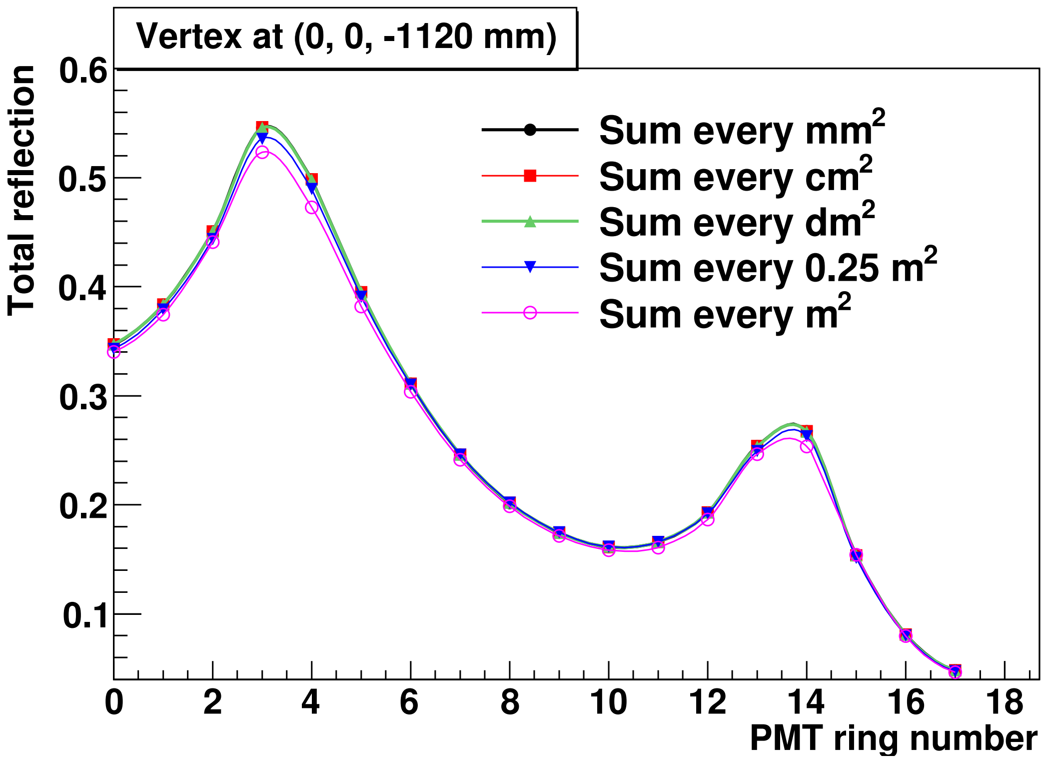

Figure 8.61: Summation of total reflected light with different basic unit area.

8.5.3.3 Monte Carlo Test of Optical Model with Diffuse Reflection

To test the diffuse reflection model, 100,000 1 MeV electron events uniformly distributed in the neutrino target were generated with and without reflections. The events without reflections were first used to determine the effective attenuation and effective area functions, $f(r)$ and $g(\cos\eta)$, respectively as shown in the top panel of Figs. 8.62 and 8.63.

The fit function to $f(r)$ is a constant plus an exponential, and the function for the angular response $g(\cos\eta)$ is a quadratic polynomial. From the fitted parameters shown in the plots,

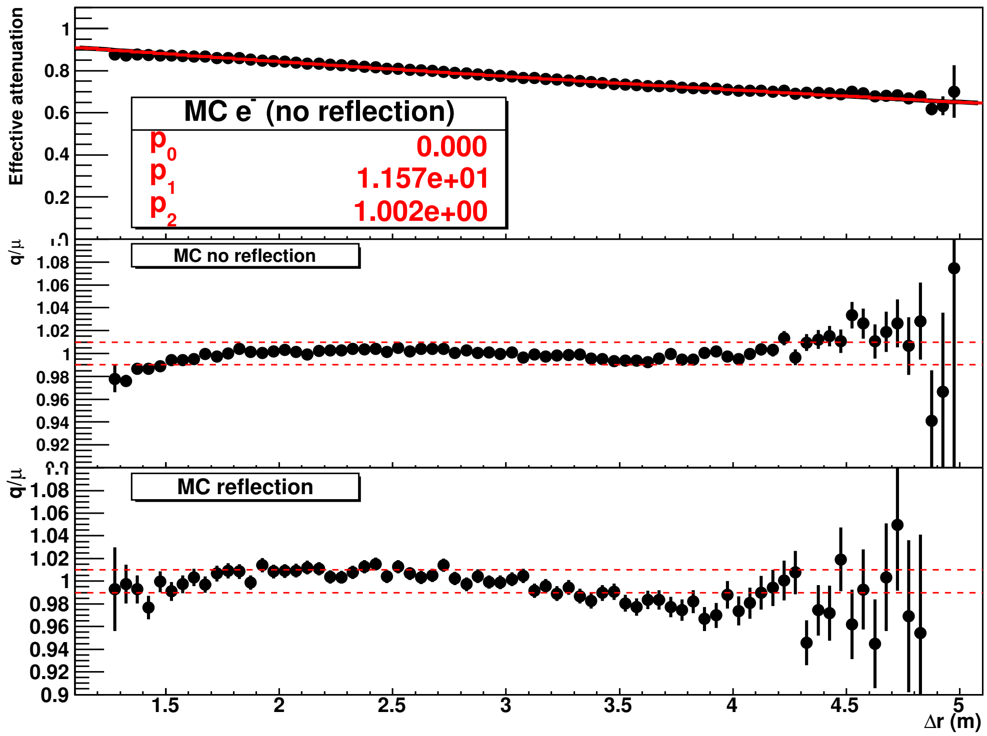

Figure 8.62: Effective attenuation, $f(r)$, fitted to $P_2\left[P_0 + (1-P_0)\exp(-r/P_1)\right]$ (top), and the corresponding q/μ ratio as a function of Δr for optical models with (bottom) and without (middle) reflections using MC data. The dashed lines indicate the $\pm 1\%$ deviations from unity.

$f(r)$ is a perfect exponential with a constant of 11.57 m, and $g(\cos\eta)$ drops to 0 at $\cos\eta \approx 0.5$ which is quite different from what we had in RecoBAMA. The q/μ ratios at most of the values of r and $\cos\eta$ are within 1%, as shown in the middle panel of Figs. 8.62 and 8.63. The q/μ ratio as a function of r, $\cos\eta$ and PMT number are compared for the optical models with and without reflection using the same functions $f(r)$ and $g(\cos\eta)$ obtained above, as shown in Figs. 8.62, 8.63 and 8.64. The charge in the middle panel in Figs. 8.62 and 8.63 and the top panel in Figs. 8.64 is from the MC events without reflection and μ is calculated by an optical model without reflection, while the charge in the bottom panels in these three figures is from MC events with reflection and μ is calculated by the an optical model with diffuse reflection. Since the reflection calculation requires significant amount of time, only 10,000 events were used. The optical model with reflection works reasonably well in predicting the charge.

Next, another set of MC electron events were generated at 15 positions in the (x, z)

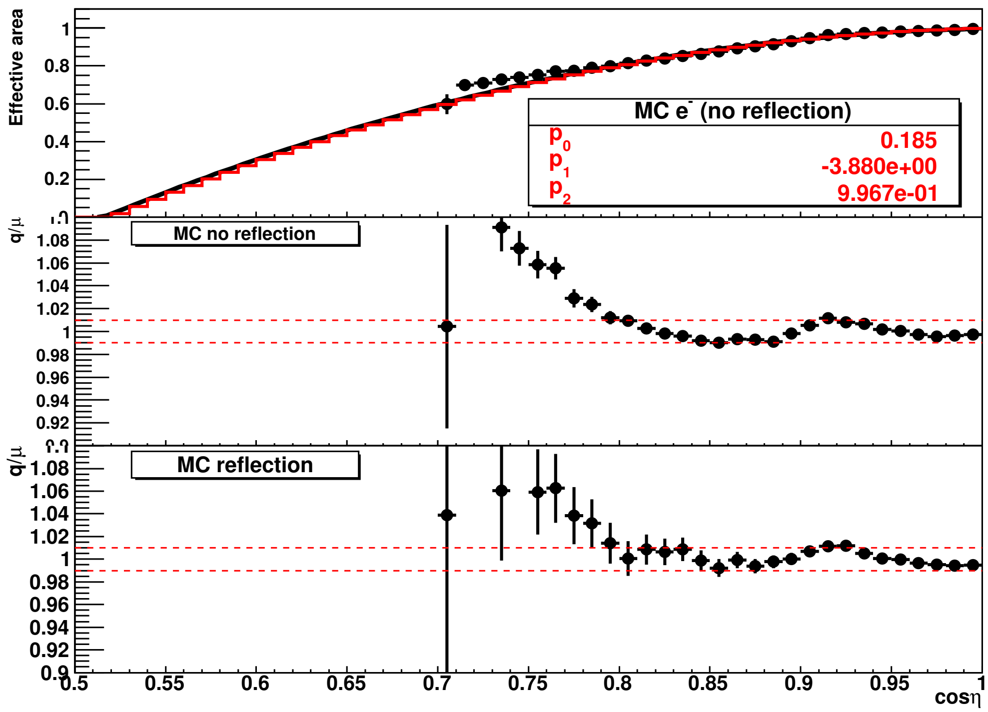

Figure 8.63: Effective area, $g(\cos\eta)$, fitted to $P_2(1 + P_0 \cos\eta + P_1 \cos^2\eta)$ (top), and the corresponding q/μ ratio as a function of $\cos\eta$ for optical models with (bottom) and without (middle) reflections using MC data. The dashed lines indicate the $\pm 1\%$ deviations from unity.

plane with and without reflection meant to test our reflection charge prediction at various certain positions. The vertices were at $x = 0$, 640, 1120 mm and $z = 0$, ± 640, ± 1120 mm. Since all of them generate similar consistent results, I picked only four extreme points for representations as illustrated in Fig. 8.65. The black histograms are the (reflections on/off) charge ratios for each PMT as obtained directly from the corresponding MC simulations and the red ones are our calculations. Comparing the total reflected light with the prediction for each vertex, the variations of 14 out of 15 vertices are very close or within 1%. Only the center one is 1.36% under-predicted.

8.5.3.4 Reflection in Position Reconstruction

Reconstruction biases have been observed in the z-axis calibration ^{68}Ge data, as reported in Ref. [197]. The bias increases as the deployment position goes away from the center.

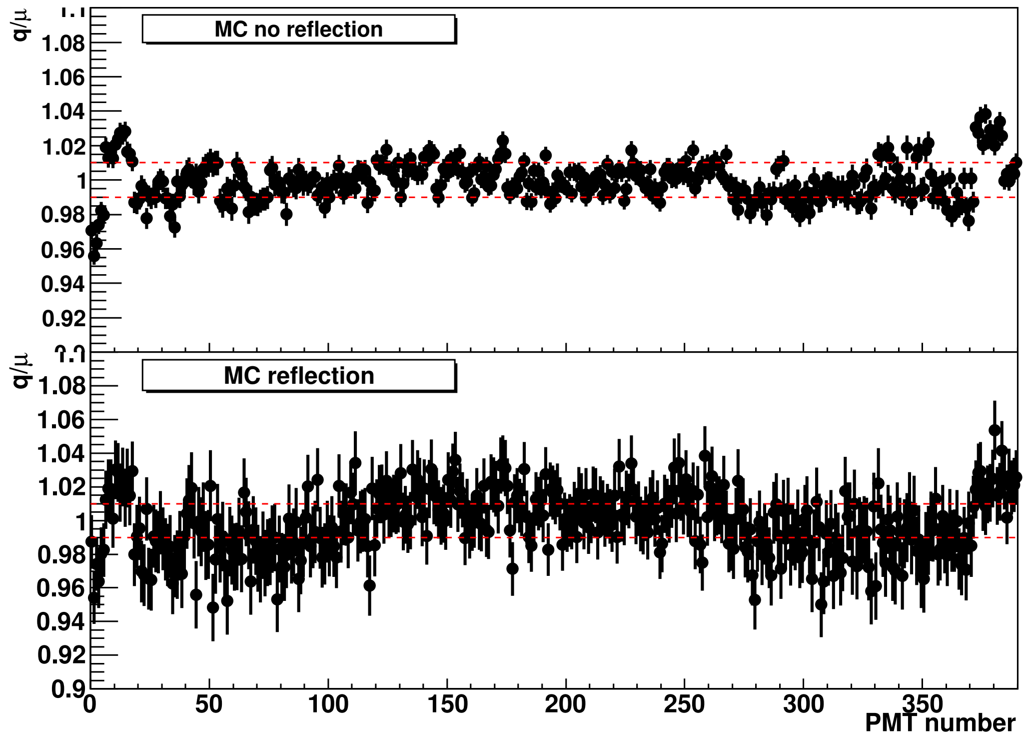

Figure 8.64: q/μ ratio as a function of PMT number for optical models with and without reflections.

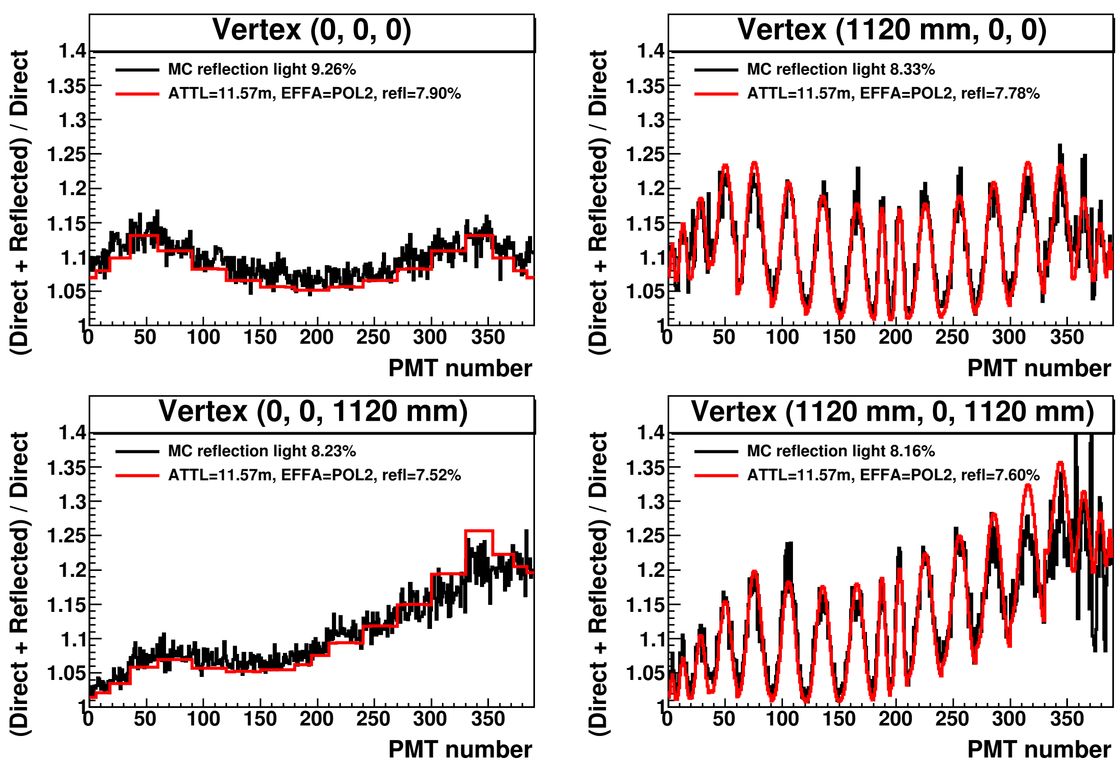

Figure 8.65: The calculated (total light/direct light) ratio from our optical model with reflection compares with actually ratio in MC electron events at vertices (0, 0, 0), (0, 0, 1120 mm), (1120 mm, 0, 0) and (1120 mm, 0, 1120 mm).

The reconstruction result of ^{60}Co by the T-only algorithm in which the TLLKs are directly obtained from the data is compared to that by QT algorithm with default input lookup tables. The only difference between TLLKs obtained from data and those obtained from the MC input is the second peak structure as shown in Fig. 8.66. Usually the result from the QT algorithm is better than that from the T-only algorithm, in both mean value and width. However, the result in Fig. 8.67 indicates that the bias in the z direction totally disappears when using TLLK lookup tables from data (as expected), while the RMS becomes comparable to that from QT algorithm. This means that if we can improve the TLLK lookup tables by introducing the second peak structure caused by reflection, we should be able to eliminate the position reconstruction bias (and probably improve the reconstruction resolution with the help of the QLLKs). However, this requires a good understanding of where to place the additional peak, its amplitude and width.

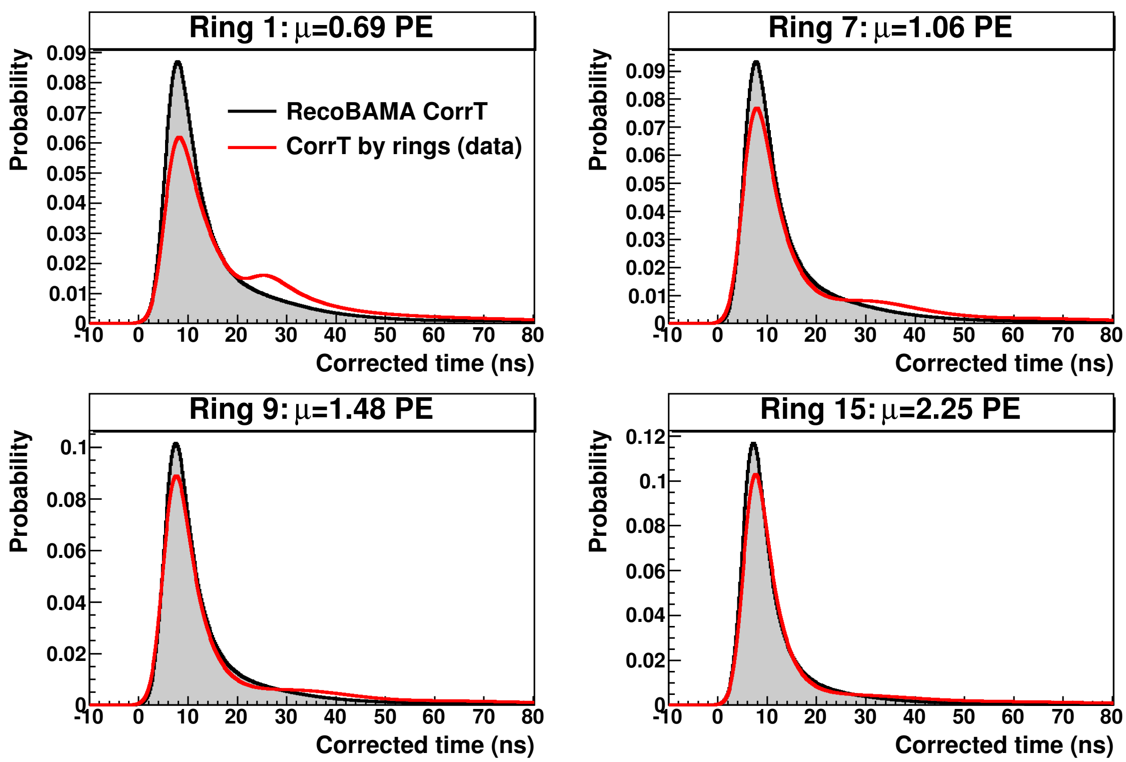

Figure 8.66: Comparison of input corrected time and those extracted from ^{60}Co data.

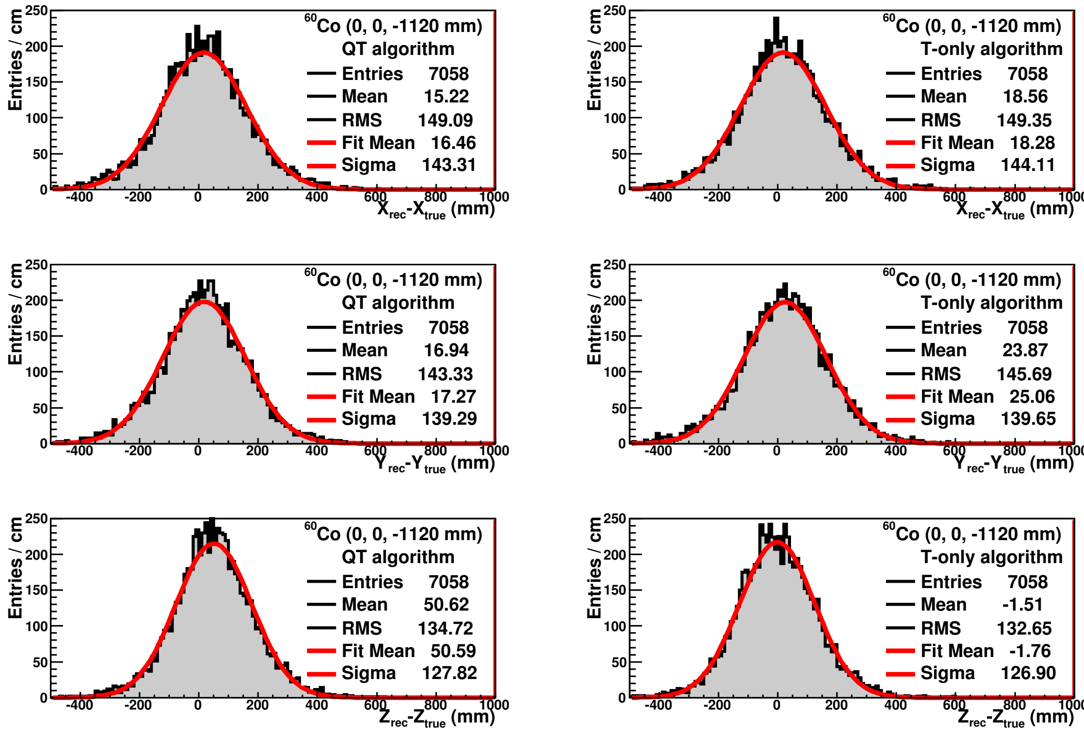

Figure 8.67: Comparsion of the reconstructed to the deployed position for default QT algorithm in RecoBAMA and T-only algorithm for the ^{60}Co data.

8.5.3.5 An Idea to Solve Energy Scale Problem

Our ultimate goal for the energy reconstruction is the variation of the flux within the neutrino target and gamma catcher to be within 1%. The current largest deviation using the total visible charge is about 7% in the neutrino target as shown in Fig. 8.47. Although one can empirically correct for positions, these corrections cannot be directly incorporated into the optical model, which in turn affects the reconstructed position. Thus, it is perhaps best to understand the optical model, which would directly generate the correct energy scale over the entire detector volume.

The idea is to try to keep our simple optical model as given by Eq. (8.1) and the extended version of it which includes diffuse reflections (as discussed in Section 8.5.3.2) and determine the effective attenuation and effective area functions, $f(r)$ and $g(\cos\eta)$, such that they minimize,

$$F = \sum_i \left(\frac{\Phi_i}{\Phi_0} - 1 \right)^2, \tag{8.3}$$

where Φ_0 is the flux in the center of the detector and Φ_i is the flux at different points. For each optical model, there are four combinations of data points selected. Figure 8.68 shows the flux after minimization for MC z-axis and guide tube ^{68}Ge events. The total number of deployed points along the z-axis is 17 and the guide tube is 11. It is obvious that there is a step in the guide tube where the last 3 points are at the boundary between the gamma catcher and the buffer. It tells us that the light yield in the buffer must be smaller. Therefore, in the other 3 combinations, only 8 guide tube points were used. The two plots in the second row of Fig. 8.68 have only 15 vertices from the z-axis where two points near the periphery of the neutrino target had been taken out. In the third row, the two outermost points on

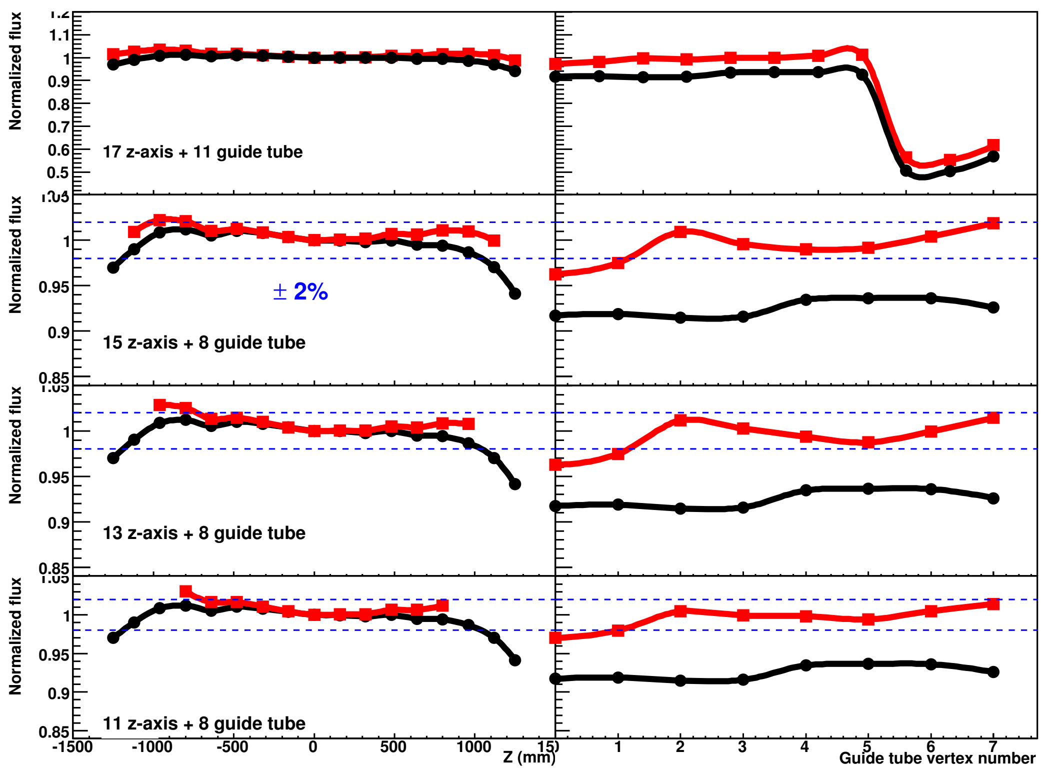

Figure 8.68: Result of flux for MC ^{68}Ge before (black) and after (red) minimization using optical model with reflection where 4 combinations of vertices are used 17 (z-axis) +11 (guide tube), 15 (z-axis) +8 (guide tube), 13 (z-axis) +8 (guide tube) and 11 (z-axis) +8 (guide tube).

the z-axis have been taken away and so on for the forth row. The fewer points are used, the smaller effect is introduced by light yield difference between the neutrino target and gamma catcher. Figure 8.69 is exactly the same plots for the ^{68}Ge data.

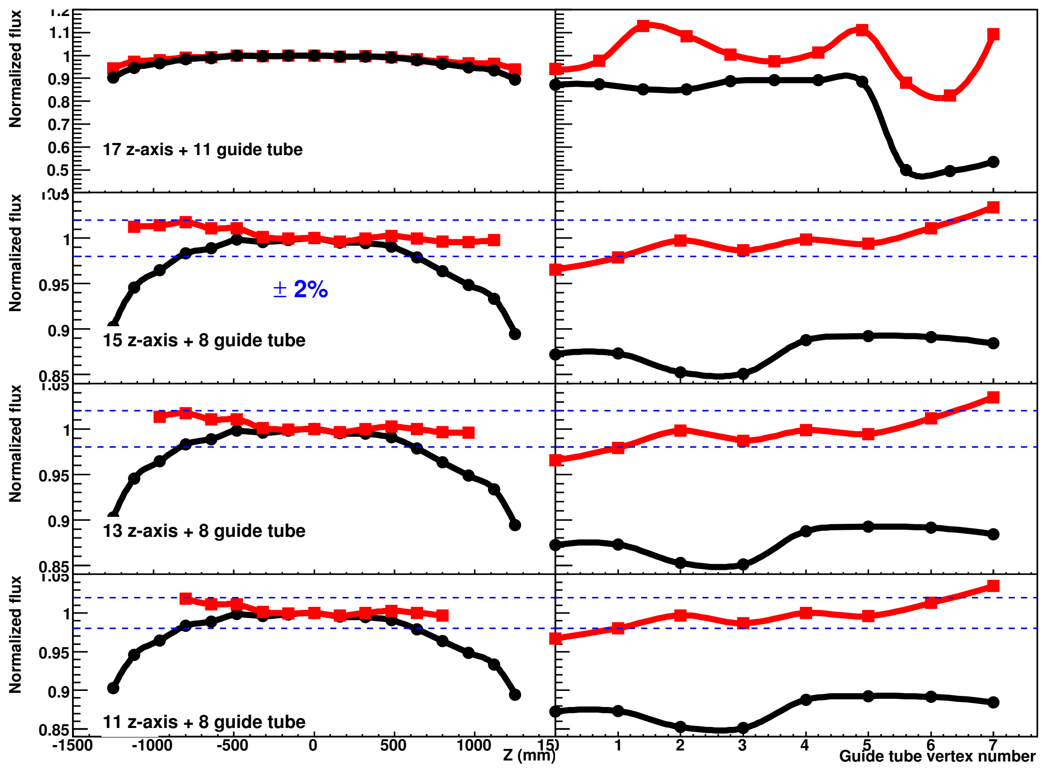

Figure 8.69: Result of flux for ^{68}Ge data before (black) and after (red) minimization by optical model with reflection where 4 combinations of vertices are used 17 (z-axis) +11 (guide tube), 15 (z-axis) +8 (guide tube), 13 (z-axis) +8 (guide tube) and 11 (z-axis) +8 (guide tube).

With these optimized functions $f(r)$ and $g(\cos\eta)$, the fluxes along the z-axis and the guide tube can be mostly confined into ±2%. Figures 8.70 and 8.71 are these optimized functions $f(r)$ and $g(\cos\eta)$ compared with the MC input for the MC and data for all the (z-axis and guide tube) combinations. Figures 8.72, 8.73, 8.74 and 8.75 are the same plots as Figs. 8.68, 8.69, 8.70 and 8.71 but with an optical model without reflections. Although the energy response can be largely improved, it is working for the wrong reason. Comparing the q/μ ratio as a function of PMT number before and after minimization, as shown in Figs. 8.76 and 8.77, the newly obtained $f(r)$ and $g(\cos\eta)$ functions improve the overall flux by sacrificing the flat distribution of the q/μ ratio for each PMT.

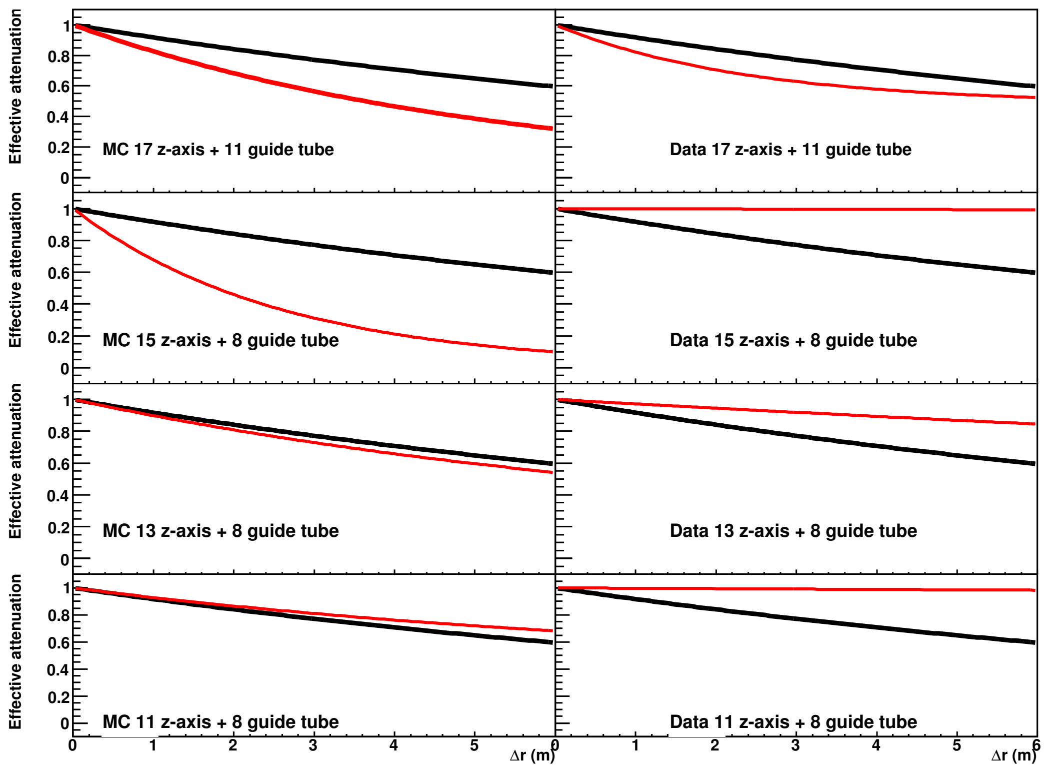

Figure 8.70: Effective attenuation function $f(r)$ before (black) and after (red) minimization of F in Eq. (8.3) (the optical model with reflection).

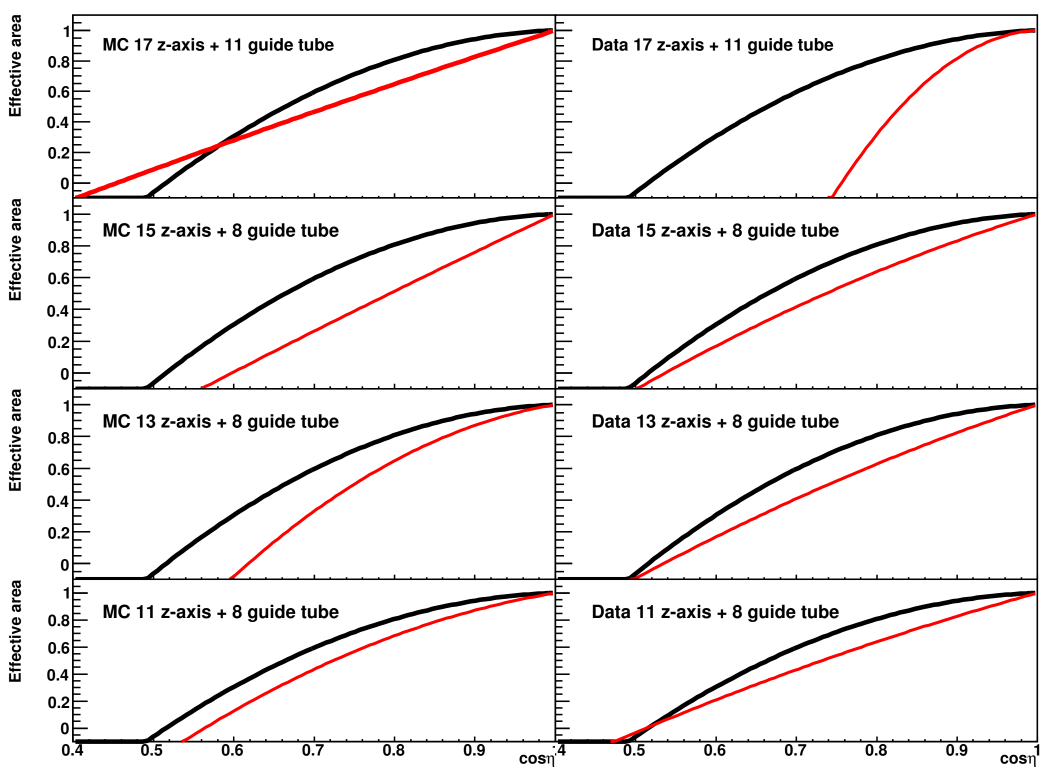

Figure 8.71: Effective area function $g(\cos\eta)$ before (black) and after (red) minimization of F in Eq. (8.3) (the optical model with reflection).

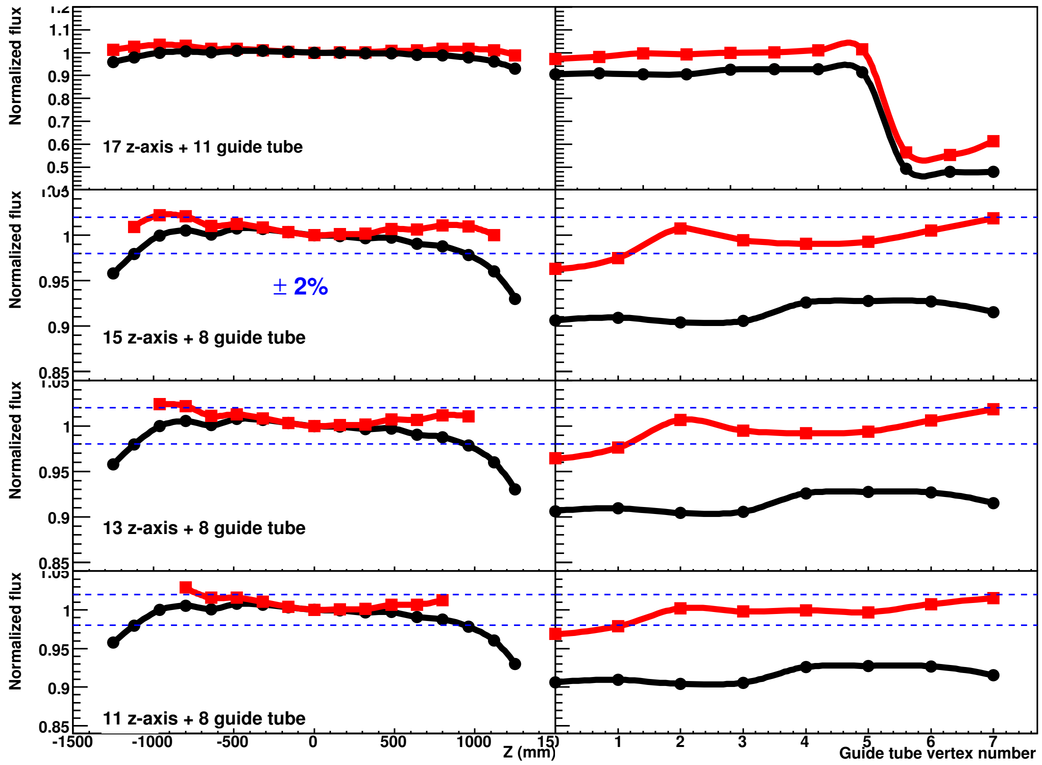

Figure 8.72: Result of flux for MC ^{68}Ge before (black) and after (red) minimization by optical model without reflection where 4 combinations of vertices are used 17 (z-axis) +11 (guide tube), 15 (z-axis) +8 (guide tube), 13 (z-axis) +8 (guide tube) and 11 (z-axis) +8 (guide tube).

Alternatively, the quantity to be minimized can be changed to,

$$F' = \sum_{j} \sum_{i=0}^{389} \left(\frac{q_i}{\mu_i} - 1 \right)^2 , \tag{8.4}$$

where i runs over all the PMTs and j represents the considered points. In principle, the minimized parameters should recover the input ones. This exercise can only be done in MC because we did not know the PMT gains (for the reason of non-linearity effect at that time) and quantum efficiencies in the data. Figures 8.78, 8.79, 8.80 and 8.81 show the results of 8 combinations of the z-axis and guide tube vertices namely 17 $(15, 13, 11) + 8$ and 17 $(15, 13, 11) + 0$ for the optical model with reflection. Zero means no guide tube vertices were used in the minimization. The flux can be flattened as before, and of course the q/μ for each PMT becomes better or as good as the starting functions of $f(r)$ and $g(\cos\eta)$, which

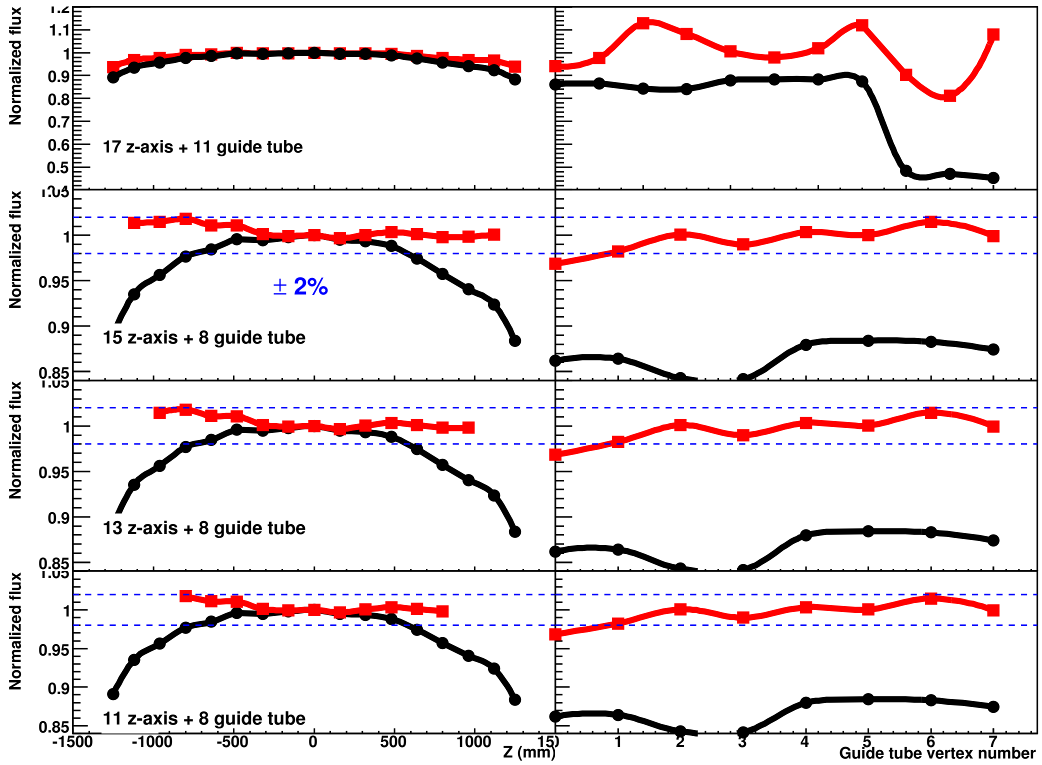

Figure 8.73: Result of flux for ^{68}Ge data before (black) and after (red) minimization by optical model without reflection where 4 combinations of vertices are used 17 (z-axis) +11 (guide tube), 15 (z-axis) +8 (guide tube), 13 (z-axis) +8 (guide tube) and 11 (z-axis) +8 (guide tube).

are those in RecoBAMA. The results recovered input parameters as we limited the z-axis vertices to only 13 or 11, which means this method is applicable in MC. Once we have the PMT gains and quantum efficiencies ready, this method can be applied to data.

8.5.3.6 Energy Response Studies Using the Hydrogen Capture Neutron Data

As soon as the charge likelihoods were obtained from the laser calibration data, we checked the energy resolution of the n-H peak in total charge, calculated flux and minimized flux by using both the charge likelihoods derived from MC and data. The RecoBAMA optical model was used to obtain the fluxes. All of the results are comparable as can be seen from Fig. 8.82.

The reason we do not see any improvement in the energy resolution when using the flux (calculated or minimized) can be attributed to the incapability of accurate prediction of the

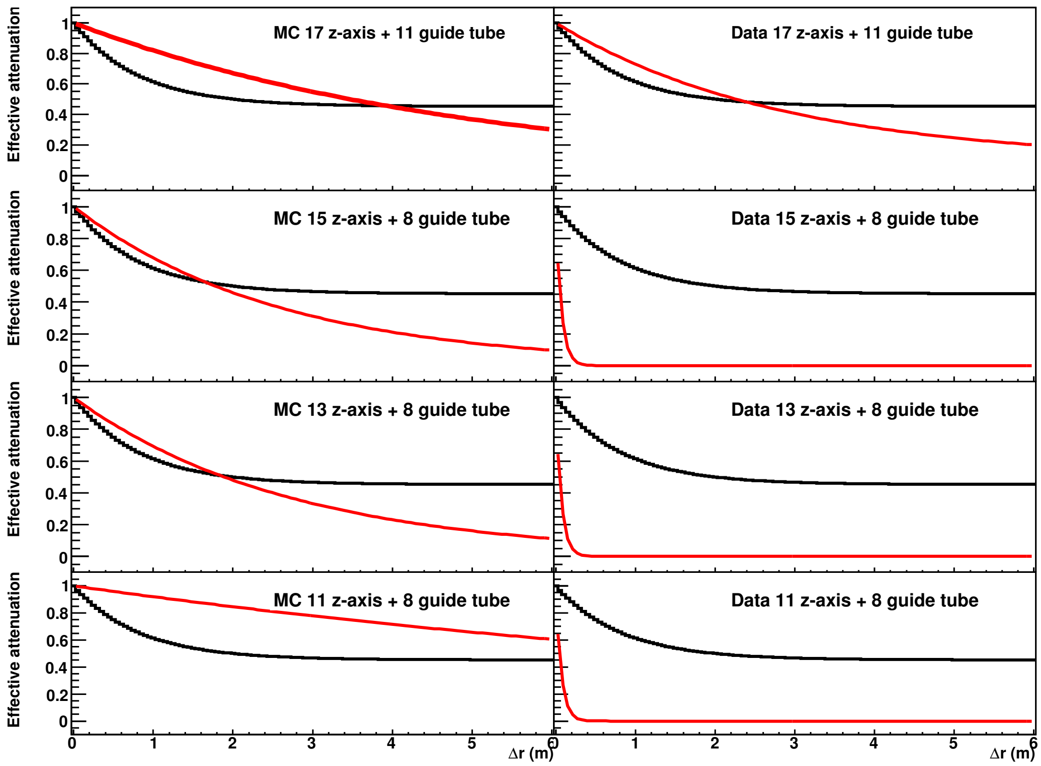

Figure 8.74: Effective attenuation function $f(r)$ before (black) and after (red) minimization of F in Eq. (8.3) (the optical model without reflection).

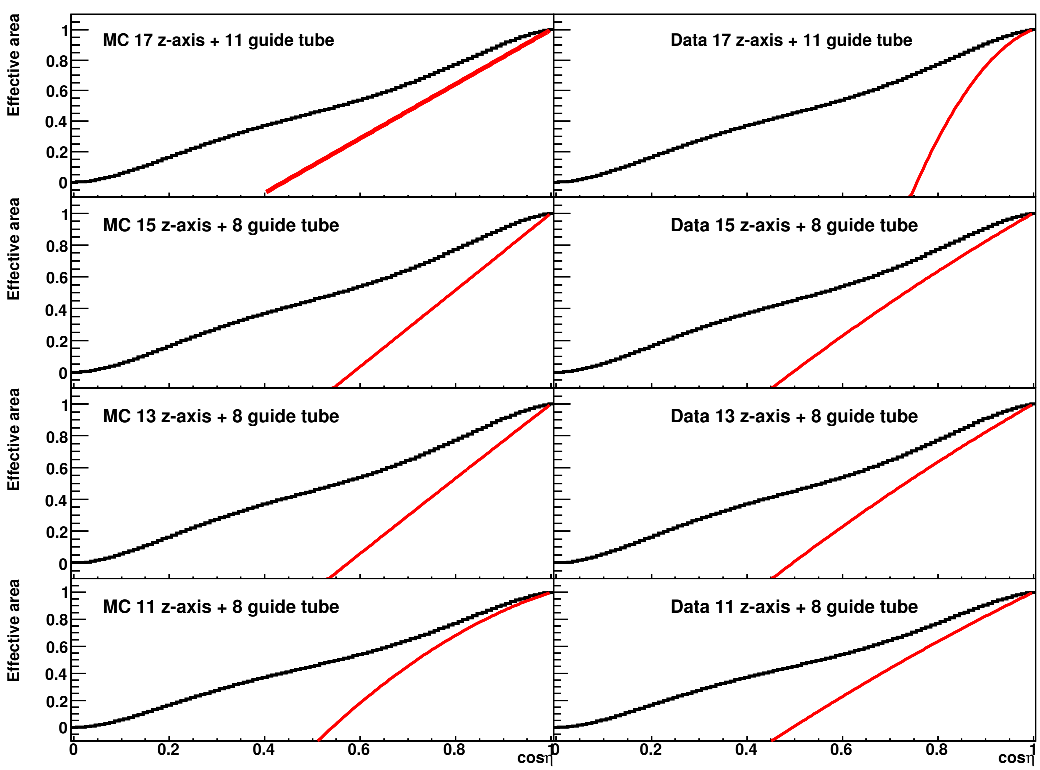

Figure 8.75: Effective area function $g(\cos\eta)$ before (black) and after (red) minimization of F in Eq. (8.3) (the optical model without reflection).

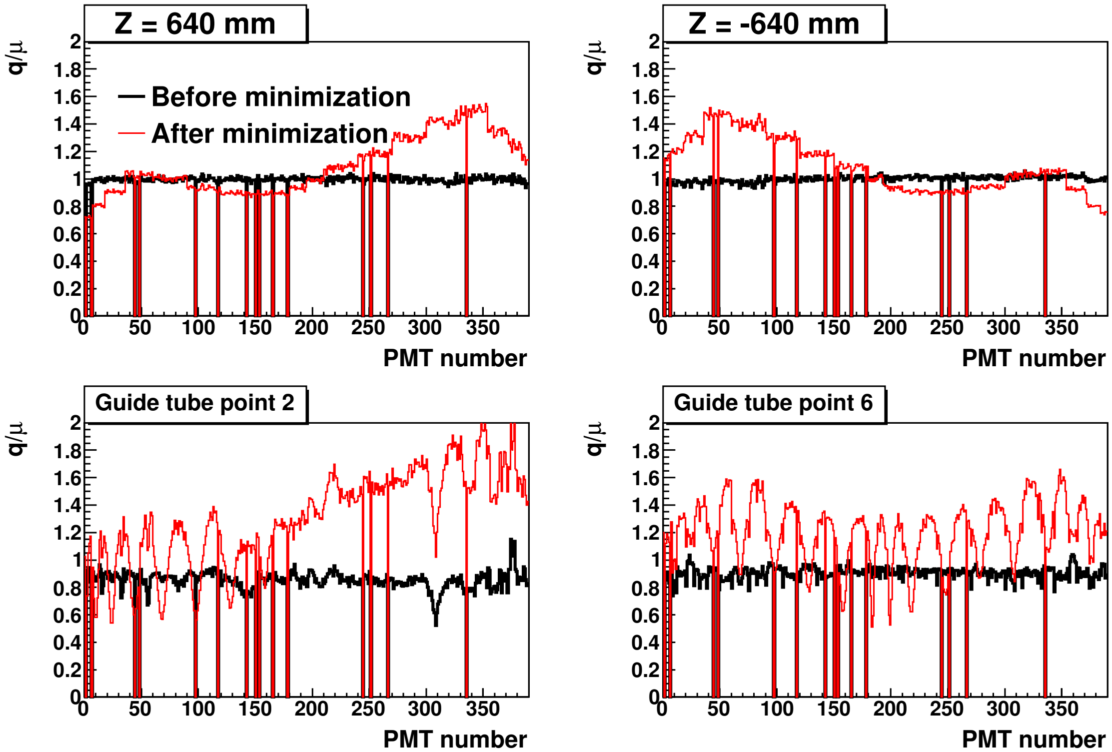

Figure 8.76: PMTs q/μ becomes worse after 15 (z-axis) +8 (guide tube) flux minimization in MC (the optical model with reflection).

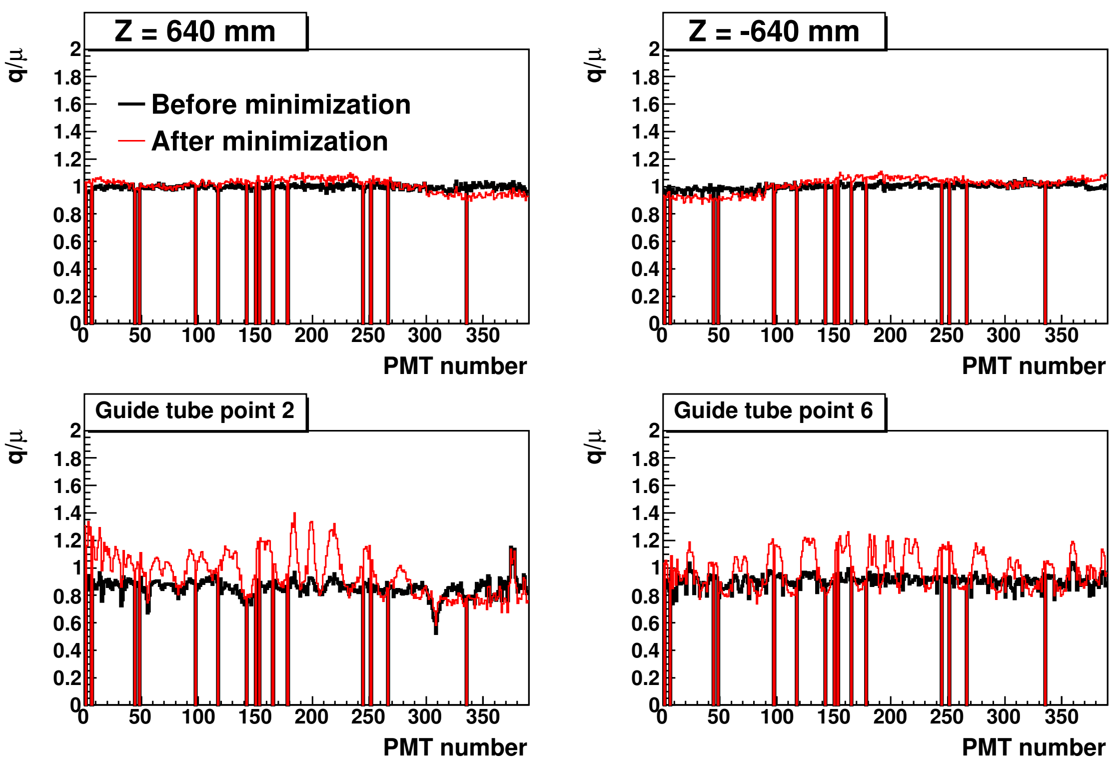

Figure 8.77: PMTs q/μ becomes worse after 15 (z-axis) +8 (guide tube) flux minimization in data (the optical model with reflection).

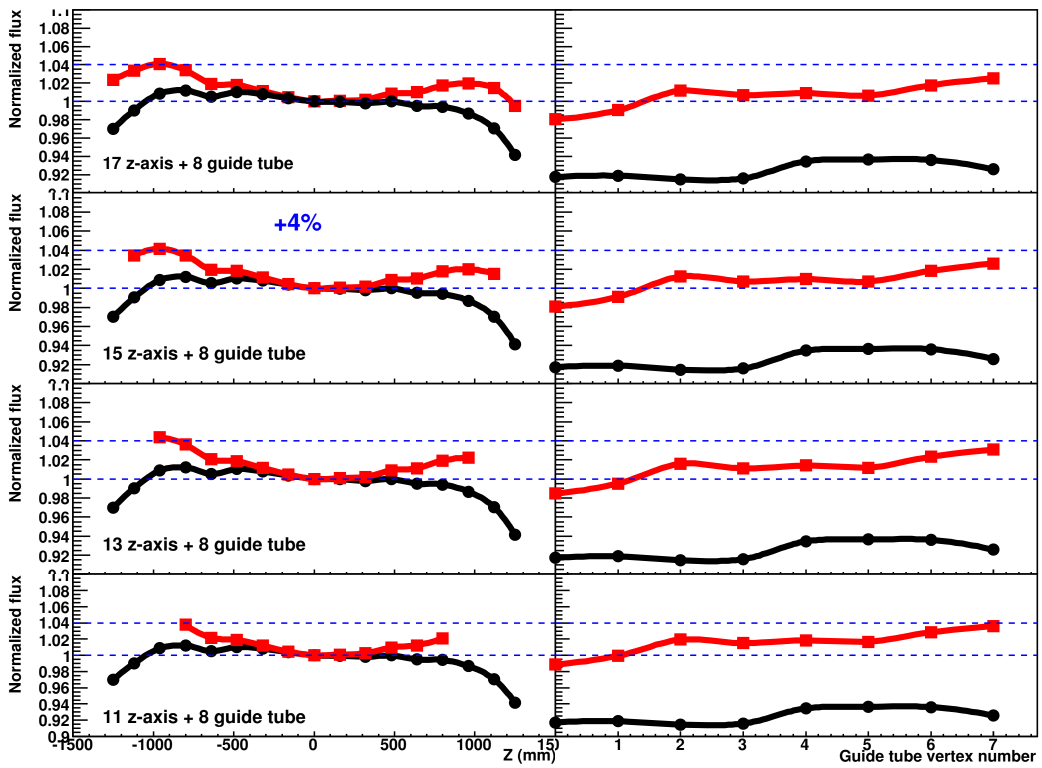

Figure 8.78: Result of flux for MC ^{68}Ge before (black) and after (red) F' minimization by the optical model with reflection where 4 combinations of vertices are used, 17 (z-axis) +8 (guide tube), 15 (z-axis) +8 (guide tube), 13 (z-axis) +8 (guide tube) and 11 (z-axis) +8 (guide tube).

charge on the PMTs, which may come from the PMT quantum efficiencies and an inaccurate optical model. We have tried using the PMTs q/μ ratios as the relative quantum efficiencies, which did not make any difference in the flux.

We checked how the RecoBAMA optical model works on the charge prediction for radioactive source ^{60}Co with known vertices. The result is shown in Fig. 8.83. Considering that the PMT quantum efficiencies are unknown, the charge predictions are good enough where most of the 9 deployed positions are within $\pm 10\%$.

The current parameters in the $f(r)$ and $g(\cos\eta)$ are from MC. We were prepared to update $f(r)$ and $g(\cos\eta)$ by using n-H data. The process has already been discussed in Section 8.3.2. With new $f(r)$ and $g(\cos\eta)$ from data, we wanted to check if the optical model can predict the charge-to-energy conversion map given by Ref. [203]. Compared to the MC RecoBAMA parametrizations, the new normalized flux gets closer to the n-H map by 1–2% in the neutrino

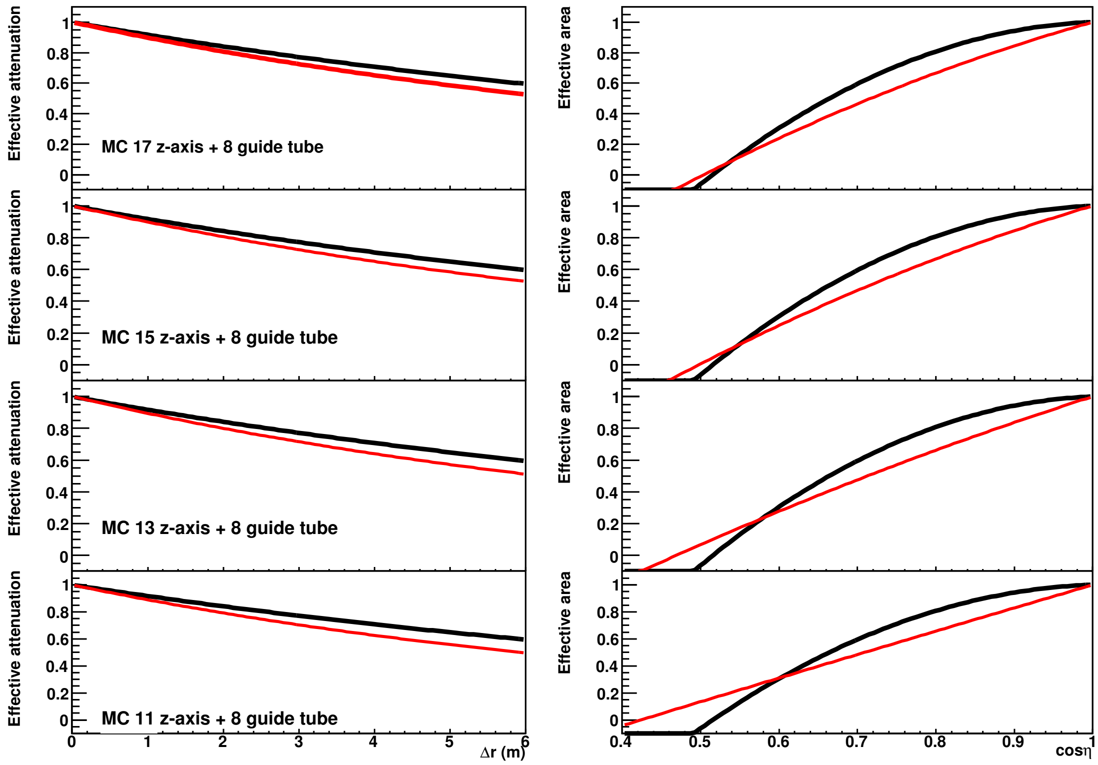

Figure 8.79: $f(r)$ and $g(\cos\eta)$ before (black) and after (red) minimization (the optical model with reflection).

target region, but there was still a long way to recover the map. Considering this, we wanted to see what kind of parameters can best reproduce the energy response map derived by the n-H data based on the same optical model. The minimization method was applied to not only points along z-axis but all over the neutrino target. Given the properly normalized trial functional forms of $f(r)$ and $g(\cos\eta)$,

$$f(r) = P_0 \exp(-P_1 r) + 1 - P_0, \tag{8.5}$$

$$g(\cos\eta) = 1 + P_2(1 - \cos\eta) + P_3(1 - \cos^2\eta), \tag{8.6}$$

the χ^2 of the difference between the predicted map and the energy map was minimized with

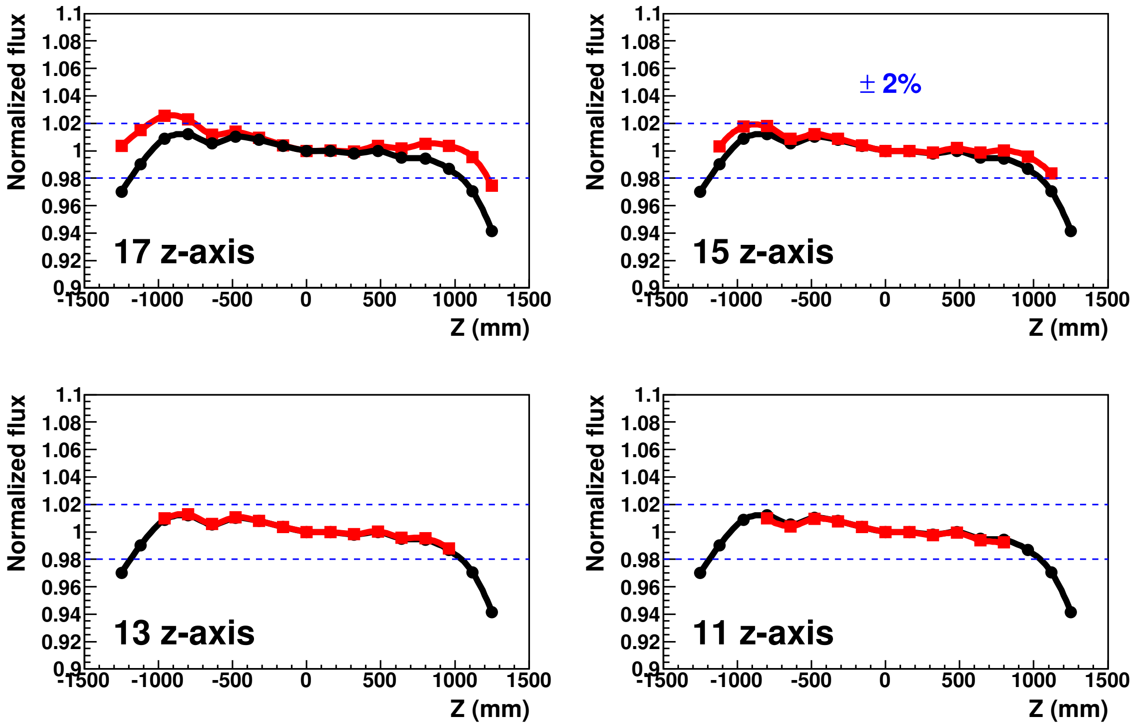

Figure 8.80: Result of flux for MC ^{68}Ge before (black) and after (red) F' minimization by the optical model with reflection where 4 combinations of vertices are used, 17 (z-axis) +0 (guide tube), 15 (z-axis) +0 (guide tube), 13 (z-axis) +0 (guide tube) and 11 (z-axis) +0 (guide tube).

respect to 108 original points for generating the energy map,

$$\chi^2 = \sum_{\rho,z} \left| \frac{E(\rho,z)}{E(0,0)} - \frac{\Omega(\rho,z)}{\Omega(0,0)} \right|^2, \tag{8.7}$$

where $E(0,0)$ is the total charge collected at the center of the detector, $E(\rho,z)$ represents the total charge collected at the vertex with coordinates ρ and z, $\Omega(0,0)$ is the total charge prediction at the center and $\Omega(\rho,z)$ represents the total charge prediction at the position with coordinates ρ and z. This method works towards the recovery of the n-H map, which does not guarantee precise charge prediction on each particular PMT, which turned out to be the case.

Recent analysis in Ref. [204] concluded that the PMT quantum efficiencies have $\cos\eta$ dependence [205]. It showed that the incorporation of the $\cos\eta$ effect into the RecoBAMA

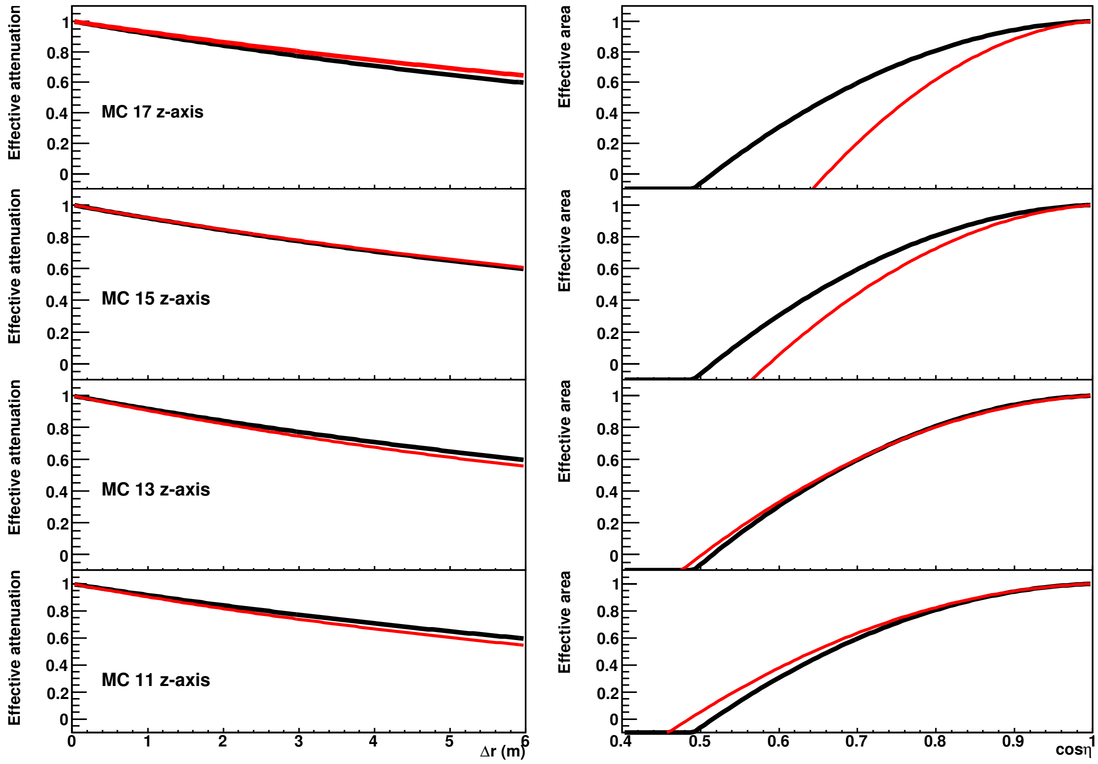

Figure 8.81: $f(r)$ and $g(\cos\eta)$ before (black) and after (red) minimization (the optical model with reflection).

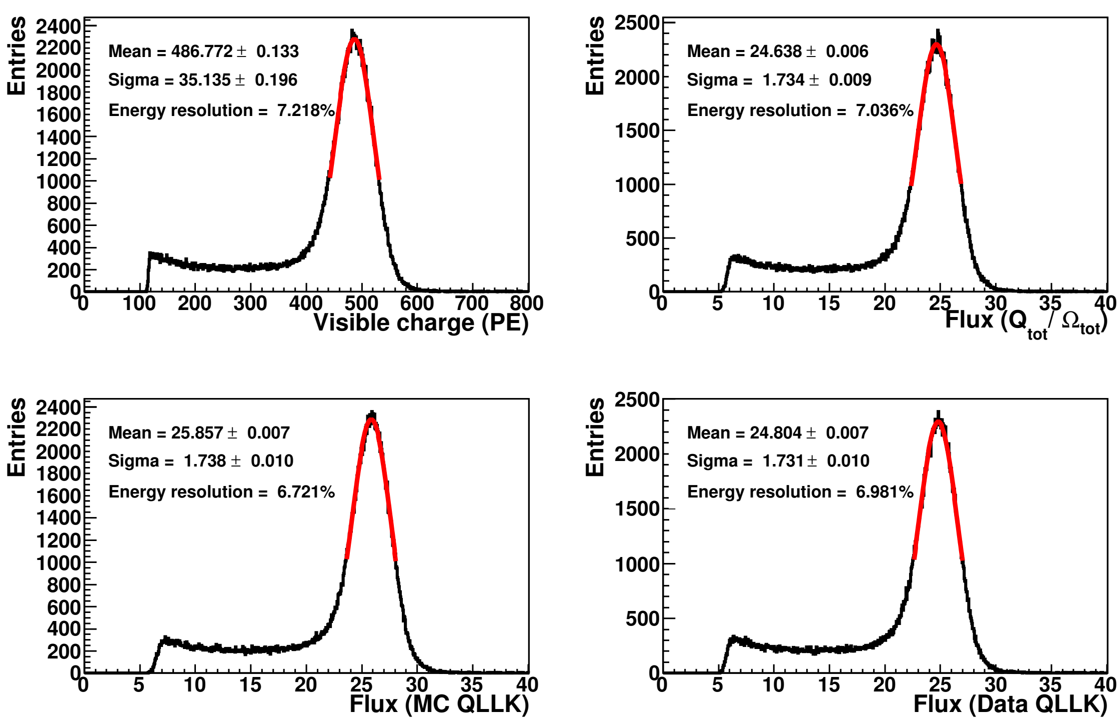

Figure 8.82: The 2.2 MeV n-H capture peak in total charge, calculated flux and minimized flux by using both the charge likelihoods derived from MC and data.

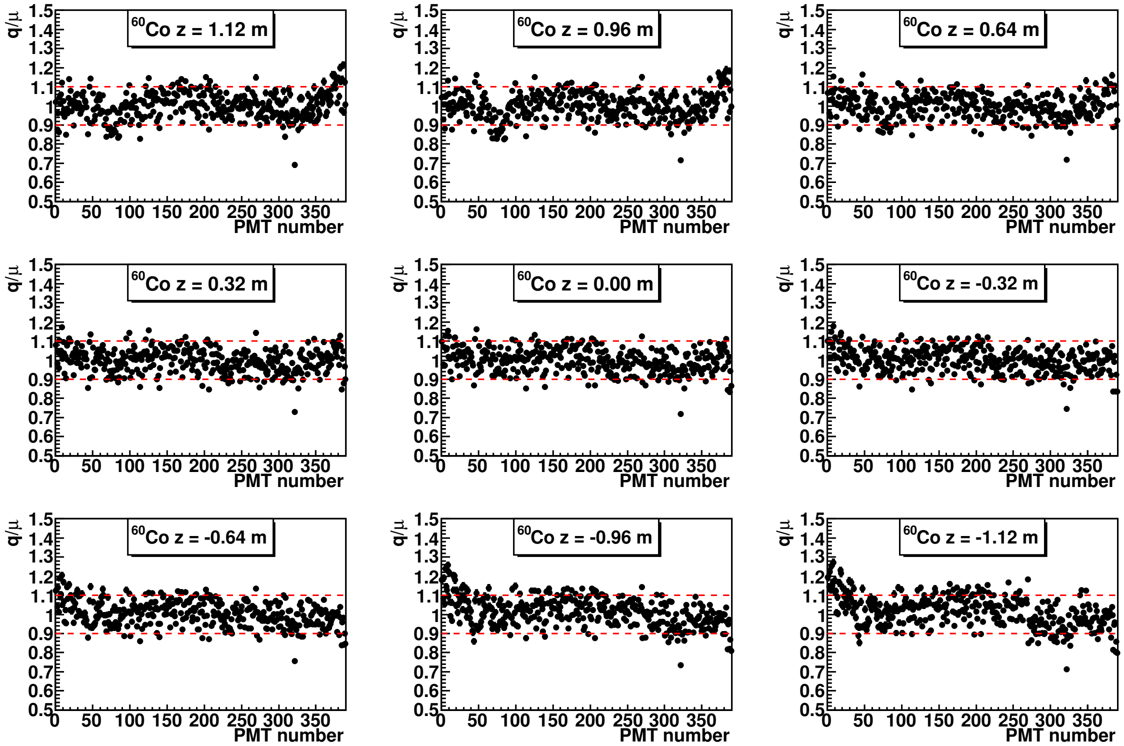

Figure 8.83: q/μ ratio of 390 PMTs for ^{60}Co deployed at 9 positions along z-axis. Red dashed lines are drawn as 10% labels in each plot.

optical model resulted in the similar pattern as n-H energy map. The incorporation can be realized by multiplying $\cos\eta$ to the effective area function $g(\cos\eta)$.

The ability of charge prediction on PMTs and the reproduction of the energy map of four sets of $f(r)$ and $g(\cos\eta)$ are compared. They are as follows:

- Model 1: effective attenuation and effective area from RecoBAMA optical model (MC parametrizations as in Section 8.3.1)

- Model 2: effective attenuation and effective area from RecoBAMA optical model (MC parametrizations as in Section 8.3.1) but with effective area corrected by $\cos\eta$ dependence, which becomes $g(\cos\eta) \times \cos\eta$

- Model 3: effective attenuation and effective area from the standard iteration method as in Section 8.3.2

- Model 4: effective attenuation and effective area from Eqs. (8.5) and (8.6) after χ^2 minimization in Eq. (8.7) using n-H data

The q/μ ratios for Model 1, Model 2, and Model 4 are shown in Figs. 8.84, 8.85 and 8.86. The q/μ ratios for Model 3 are shown in Figs. 8.7 and 8.8. Four sets of $f(r)$ and $g(\cos\eta)$ are compared in Fig. 8.87. The 2-dimensional q/μ ratio of four sets of $f(r)$ and $g(\cos\eta)$ are shown in Fig. 8.88. The predicted map and the differences between the predicted map and n-H energy map for four Models are shown in Fig. 8.89 and 8.90.

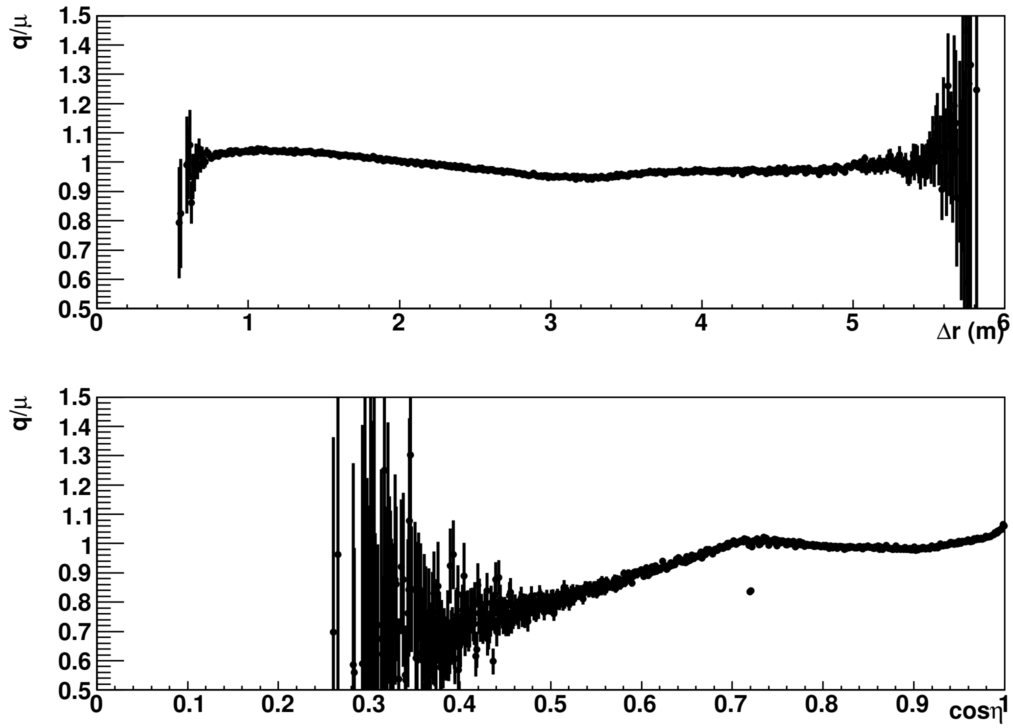

Figure 8.84: q/μ ratio as a function of r and $\cos\eta$ using Model 1.

Model 2 and Model 4 give similar patterns as the n-H energy map, and the comparison in Fig. 8.90 indicates the maximum deviations are only approximately 5% and 4% respectively. However, the 1-d and 2-d q/μ ratio with respect to r and $\cos\eta$ are not as good as those in Model 1 (although in the Model 1 the q/μ at $\cos\eta < 0.7$ is bad, most of the events especially in the neutrino target do not have $\cos\eta > 0.7$ entries) and Model 3 which can be seen from Figs. 8.7, 8.8, 8.84, 8.85 and 8.86. On the other hand, Model 1 and especially Model 3 have

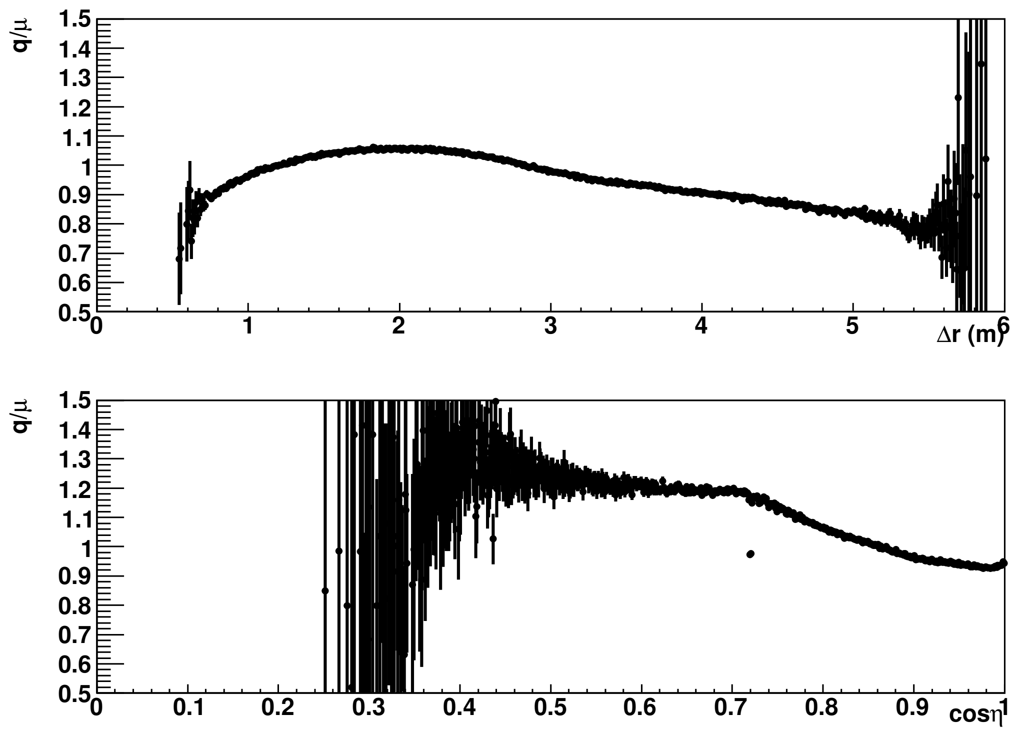

Figure 8.85: q/μ ratio as a function of r and $\cos\eta$ using Model 2.

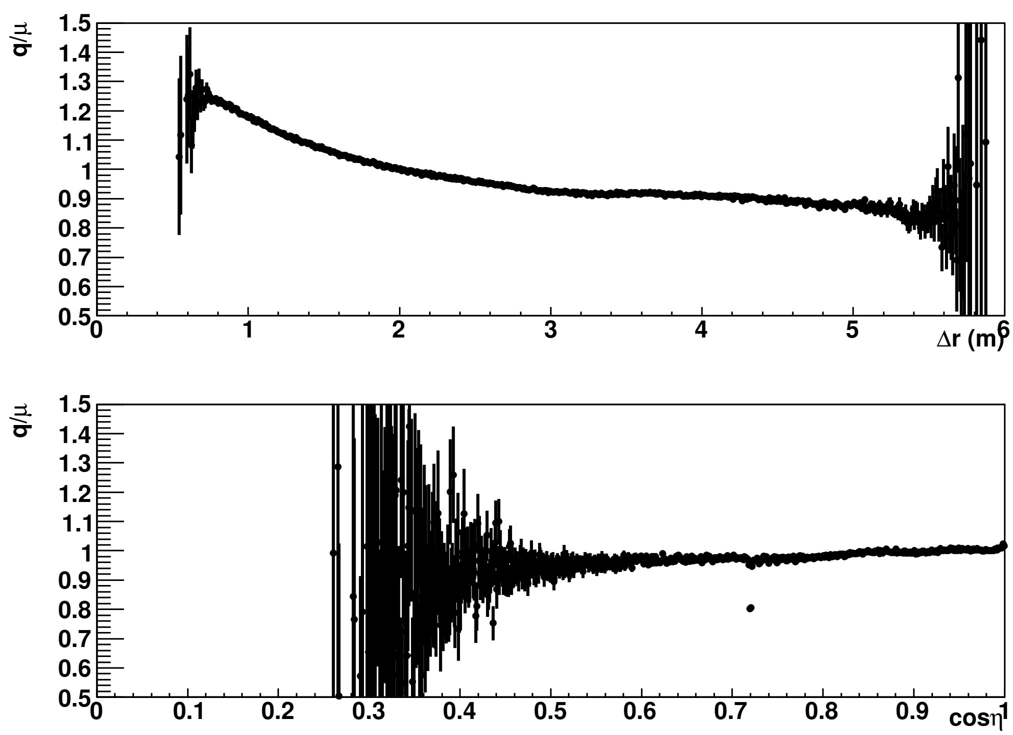

Figure 8.86: q/μ ratio as a function of r and $\cos\eta$ using Model 4.

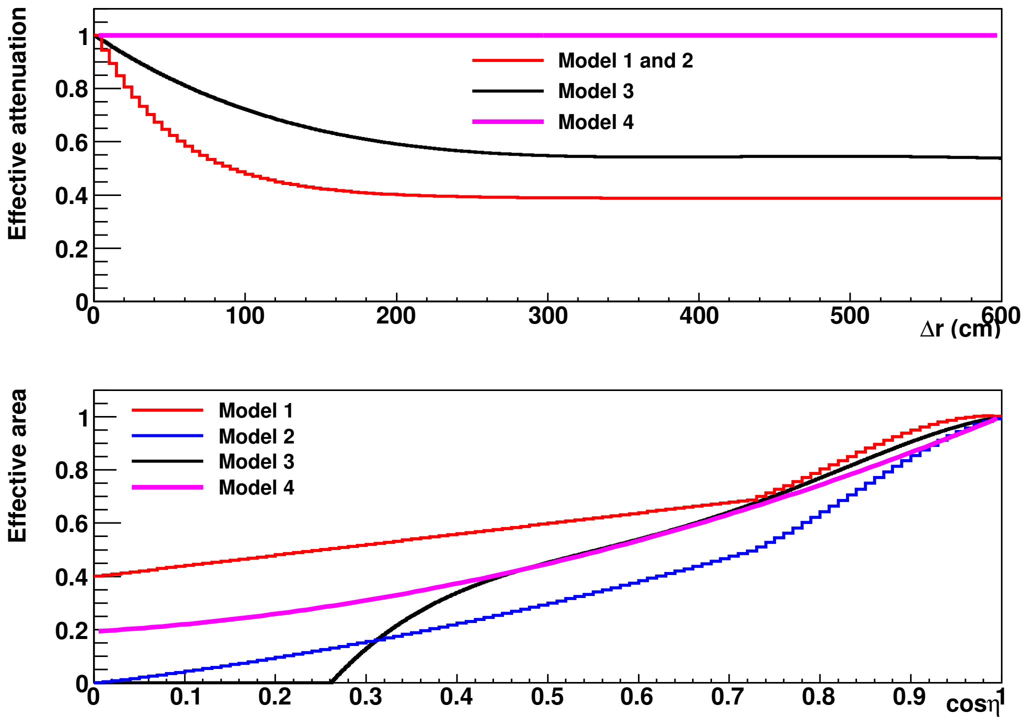

Figure 8.87: Comparison of $f(r)$ and $g(\cos\eta)$ four Models.

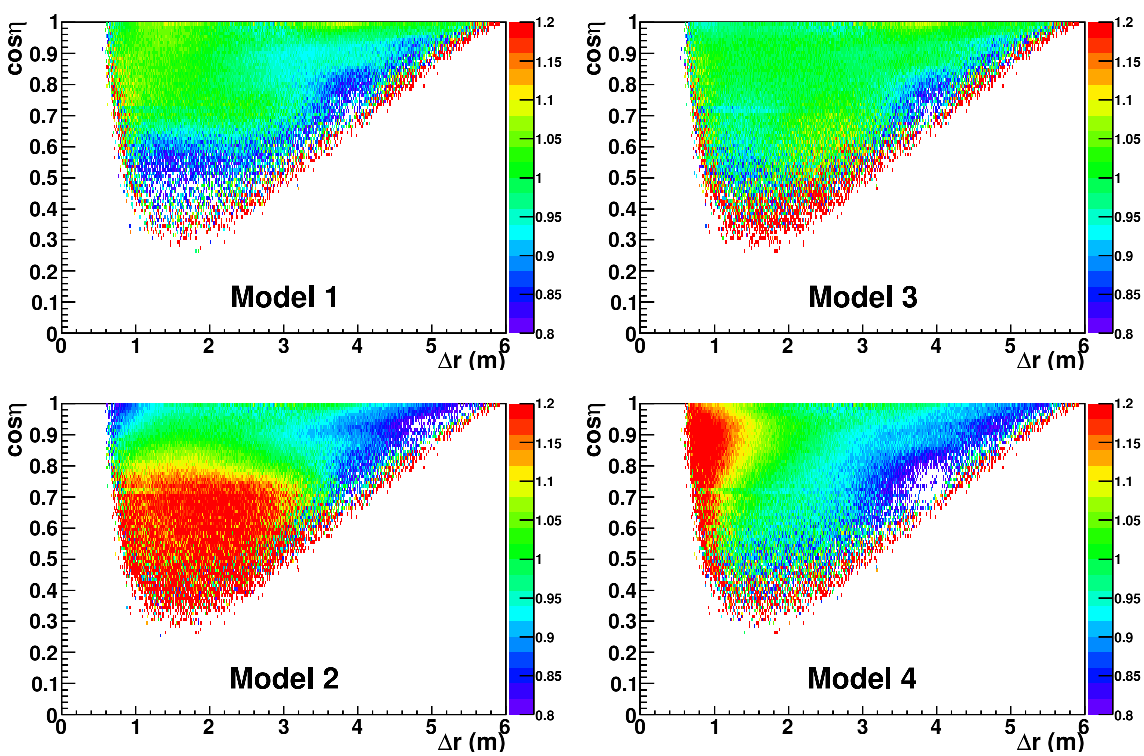

Figure 8.88: Two-dimensional q/μ ratio for four Models.

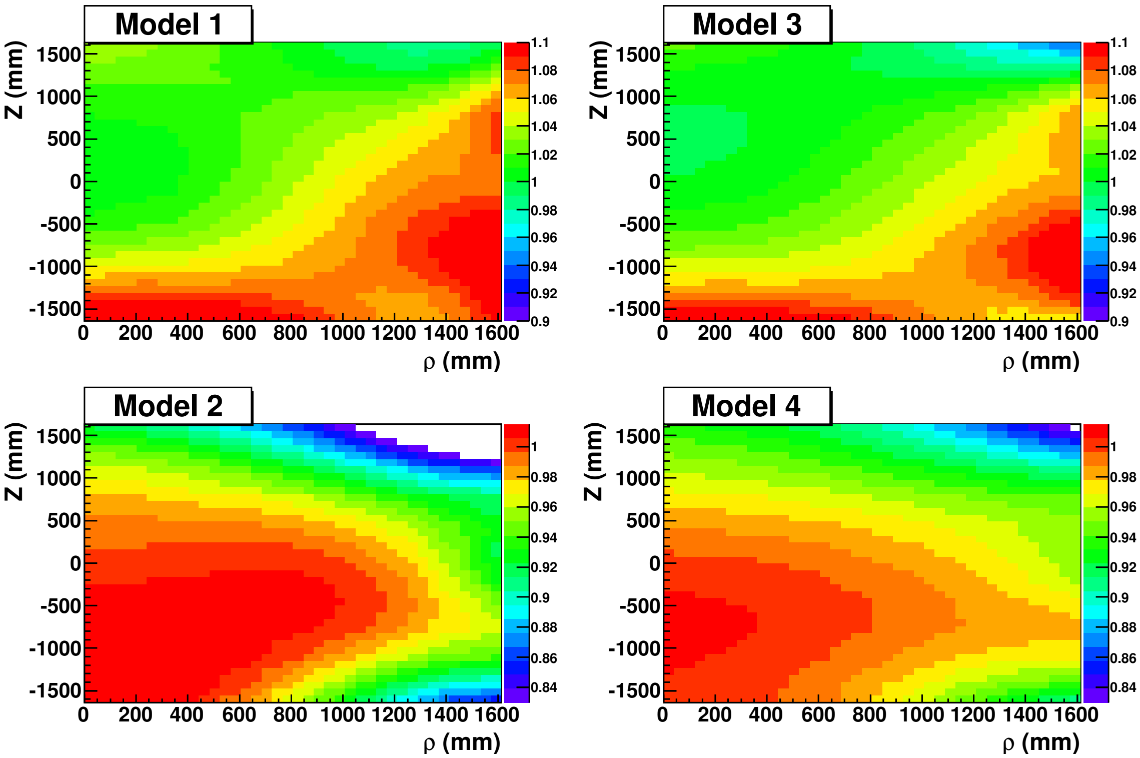

Figure 8.89: The predicted map for four Models.

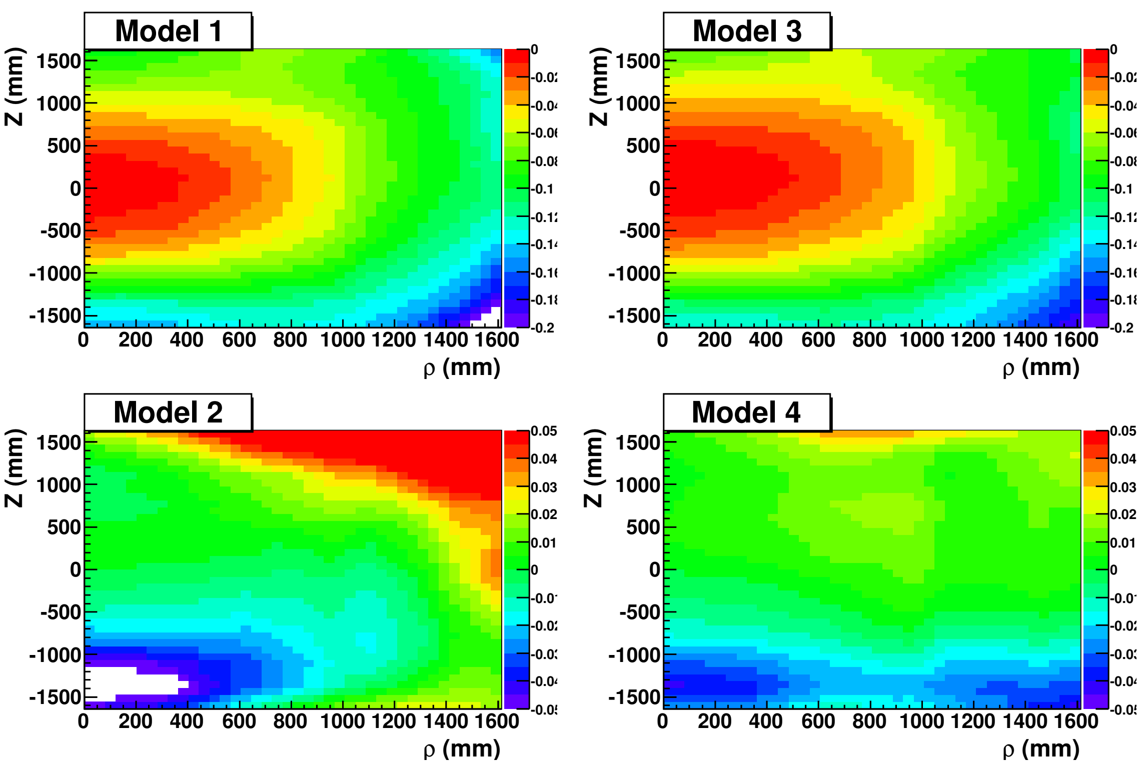

Figure 8.90: Comparison of the predicted map to the n-H map for four Models.

a better q/μ ratio but are incapable of reproducing the n-H energy map. From the Model 4, we also learned that the optical model prefers no attenuation length in recovering the n-H energy map.

It seems there is no perfect solution to this problem. Thus, we were going back to seek help from the MC, aiming to prove the feasibility of our standard iteration method. A set of approximately 300,000 2.2 MeV electron events were generated uniformly distributed in the neutrino target and gamma catcher. The reason for using electrons instead of neutrons is only because the electrons interact immediately after generated and it is easy to obtain the truth vertex in MC. Three configurations were simulated (the light yields in the MC were obtained from analyzing the calibration data):

1. No reflection, same light yield in the neutrino target and gamma catcher ($LY_{NT} = 9651$ photons/MeV, $LY_{GC} = 9651$ photons/MeV)

2. No reflection, default light yield in MC ($LY_{NT} = 9651$ photons/MeV, $LY_{GC} = 9185$ photons/MeV)

3. Default MC setting (with reflection and default light yield)

The standard iteration method was applied to all three configurations and three sets of corresponding $f(r)$ and $g(\cos\eta)$ were obtained. Figures 8.91, 8.92 and 8.93, Figs. 8.95, 8.96 and 8.97 and Figs. 8.100, 8.101 and 8.102 display the $f(r)$ and $g(\cos\eta)$ and the corresponding 1-dimensional and 2-dimensional q/μ ratio for configurations 1, 2 and 3. The $f(r)$ and $g(\cos\eta)$ for configurations 1, 2 and 3 can make the corresponding main part of 1-d q/μ ratio within $\pm 1\%$. The 2-d q/μ for three configurations shows great uniformity.

Figure 8.94 contains four plots for configuration 1, which are the MC energy map from 2.2 MeV electron events, the prediction by newly obtained $f(r)$ and $g(\cos\eta)$, the comparison between the MC energy map and the prediction and the comparison between the MC energy map and RecoBAMA prediction (MC parameterization). Figures 8.98 and 8.99 are the MC energy map and prediction as well as the comparison for configuration 2. The only difference between Fig. 8.98 and 8.99 is that in Fig. 8.99, the light yield in the gamma catcher has

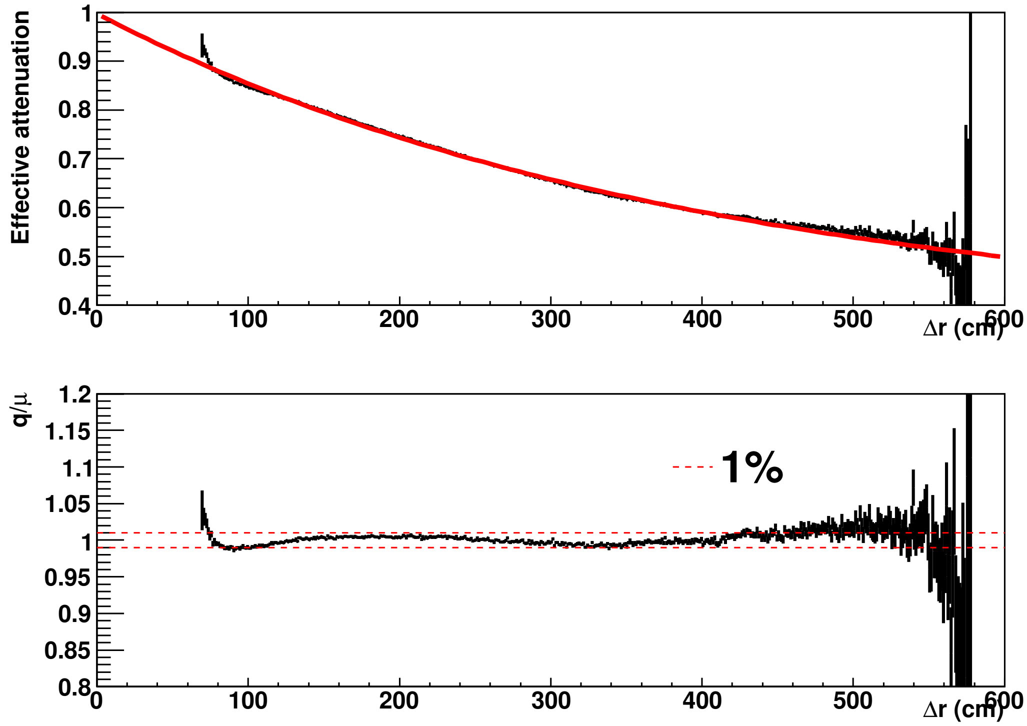

Figure 8.91: Effective attenuation $f(r)$ and the corresponding q/μ ratio for MC configuration 1.

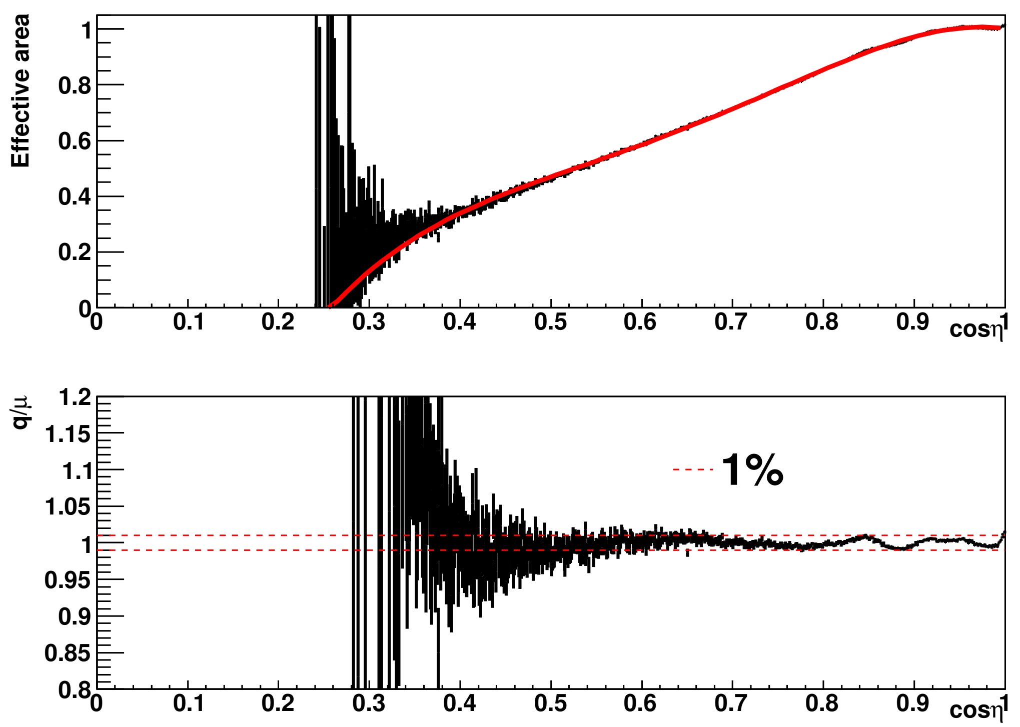

Figure 8.92: Effective area $g(\cos\eta)$ and the corresponding q/μ ratio for MC configuration 1.

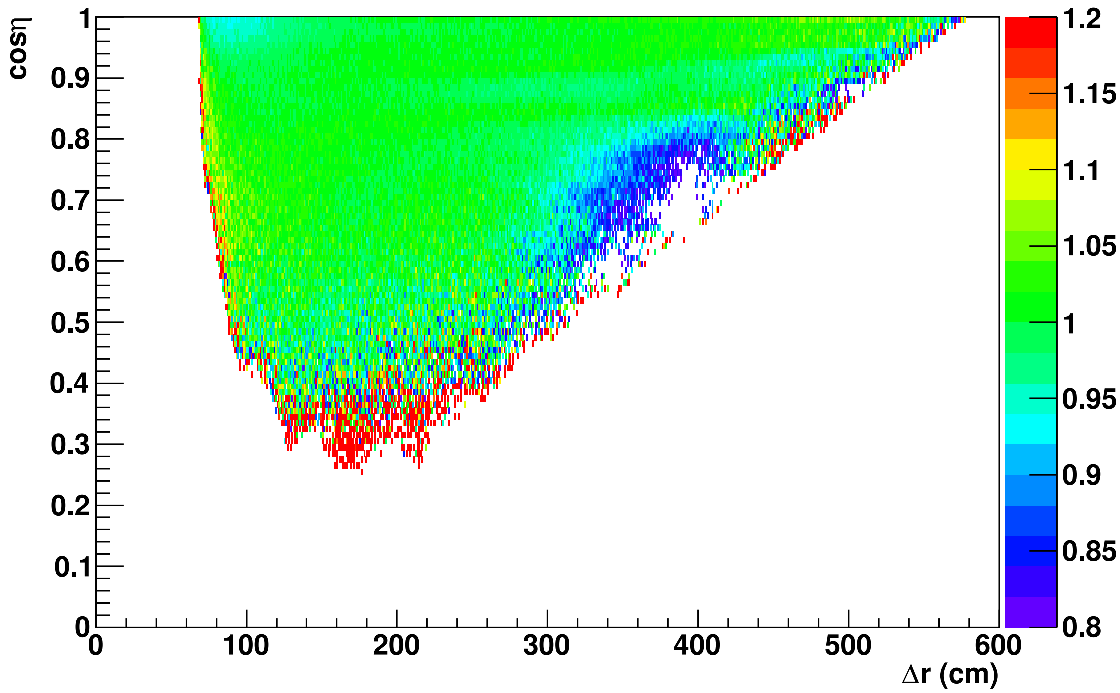

Figure 8.93: Two-dimensional q/μ ratio for MC configuration 1.

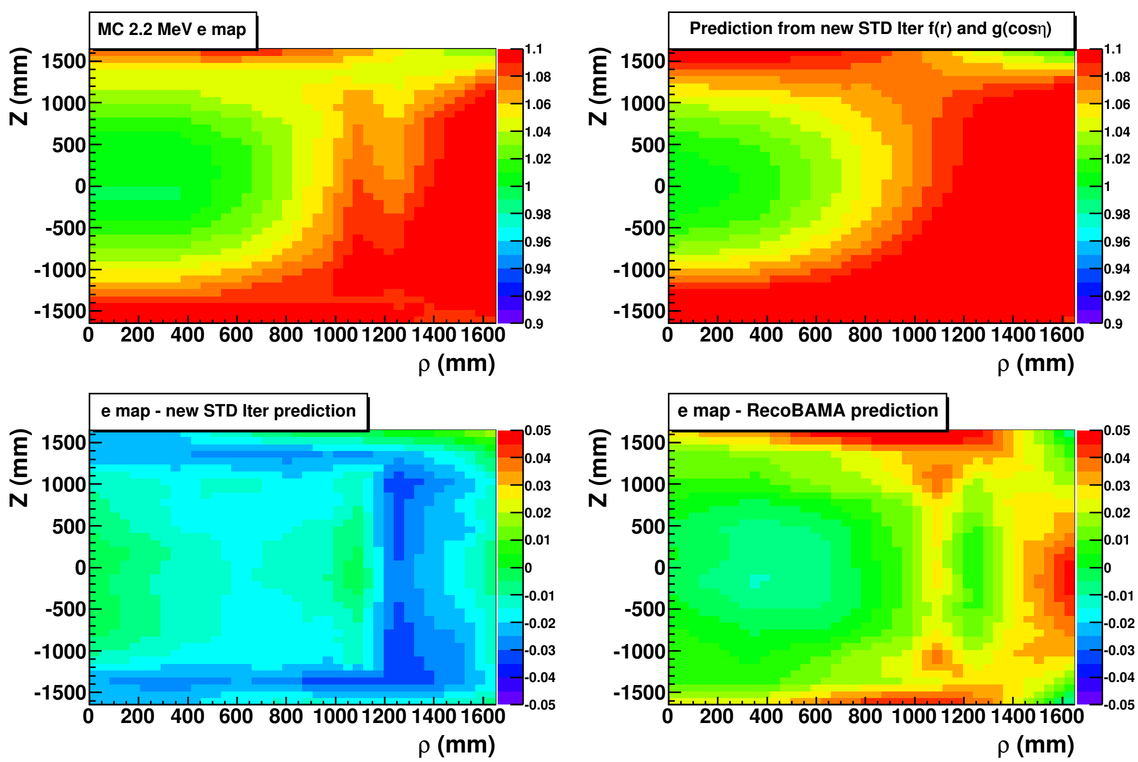

Figure 8.94: MC energy map, predicted map, their difference and the difference between MC energy map and RecoBAMA predicted map for MC configuration 1.

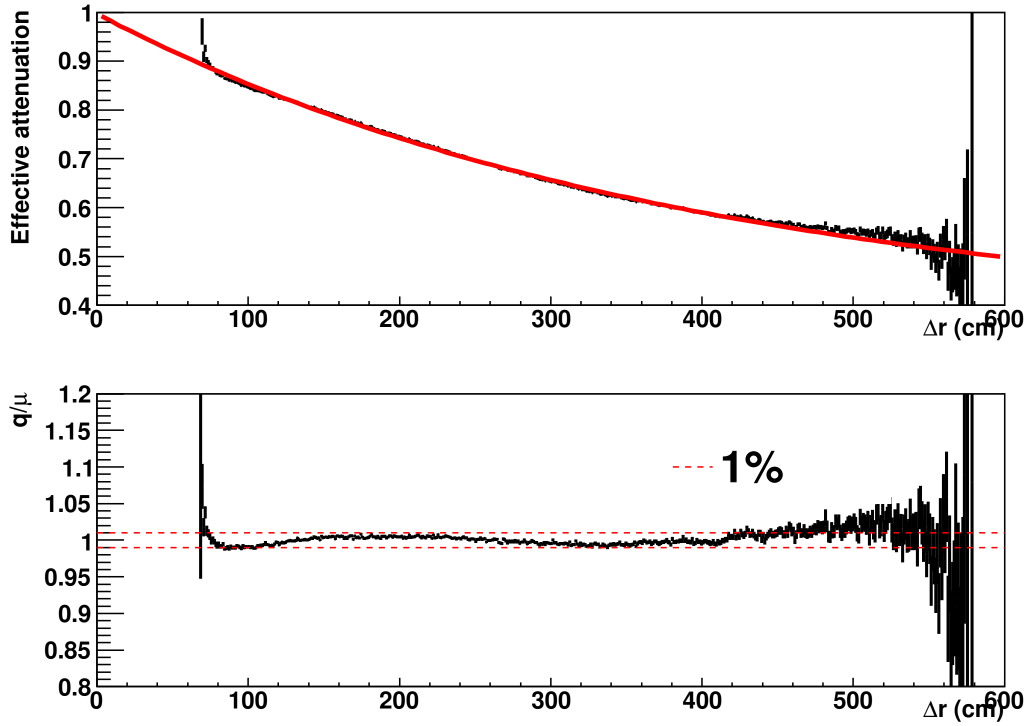

Figure 8.95: Effective attenuation $f(r)$ and the corresponding q/μ ratio for MC configuration 2.

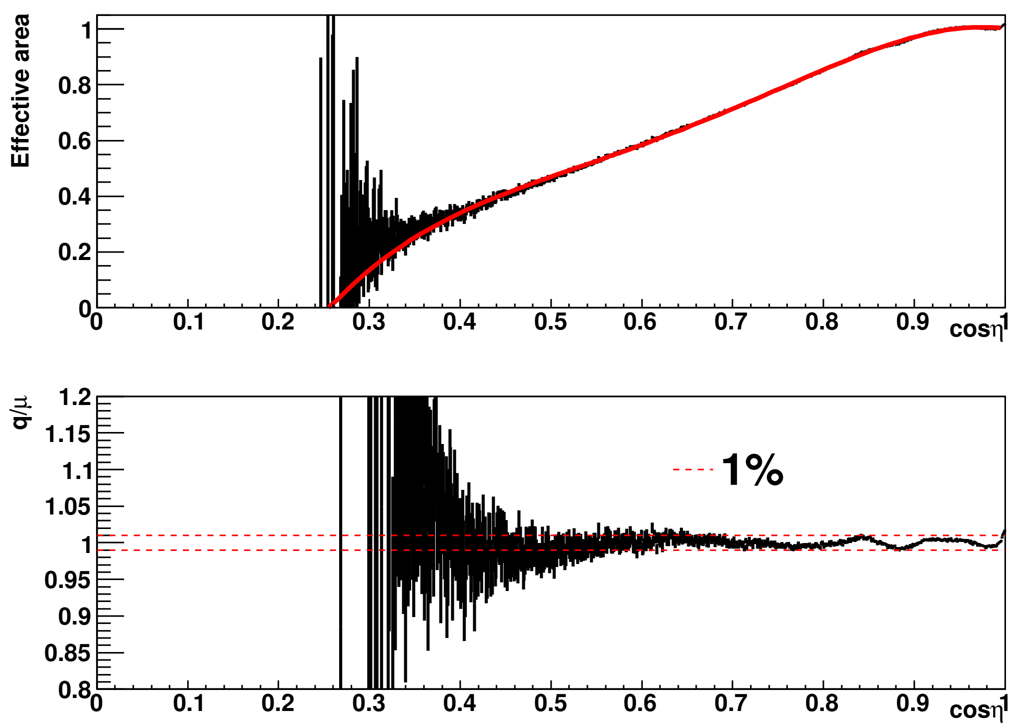

Figure 8.96: Effective area $g(\cos\eta)$ and the corresponding q/μ ratio for MC configuration 2.

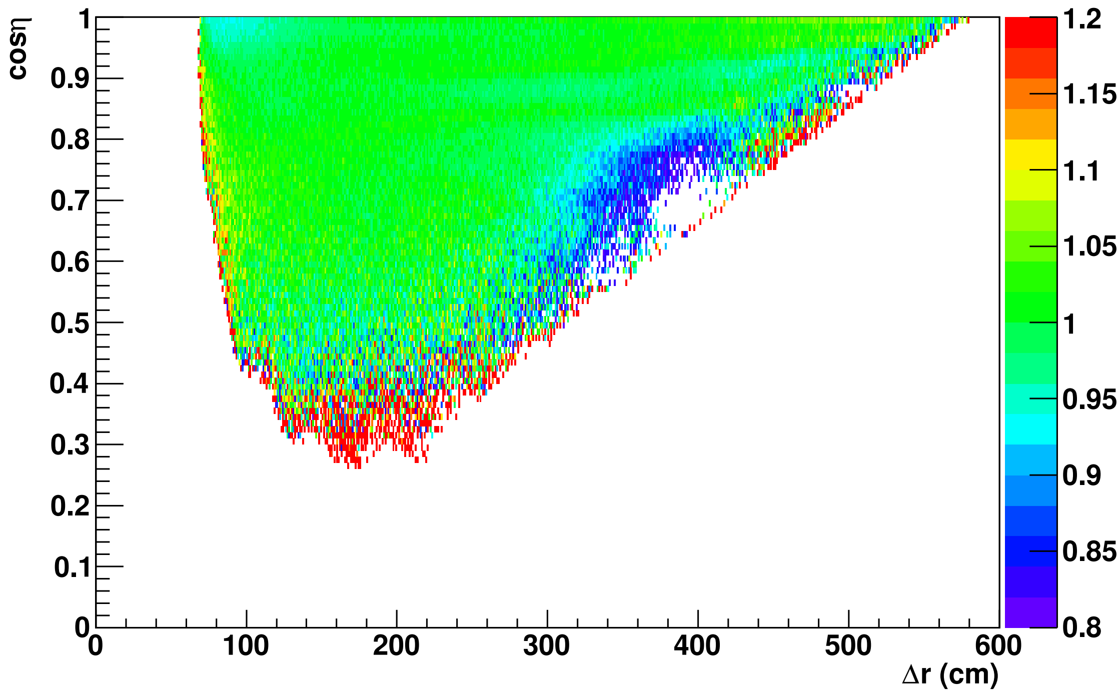

Figure 8.97: Two-dimensional q/μ ratio for MC configuration 2.

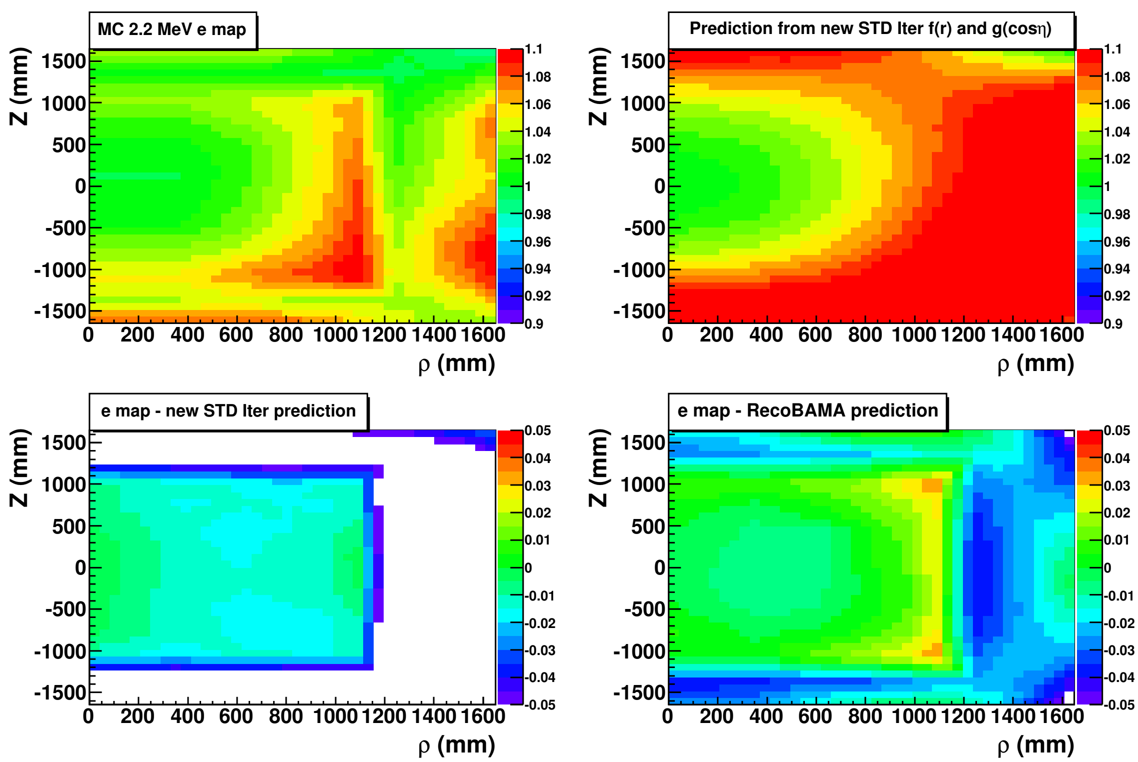

Figure 8.98: MC energy map, predicted map, their difference and the difference between MC energy map and RecoBAMA predicted map for MC configuration 2.

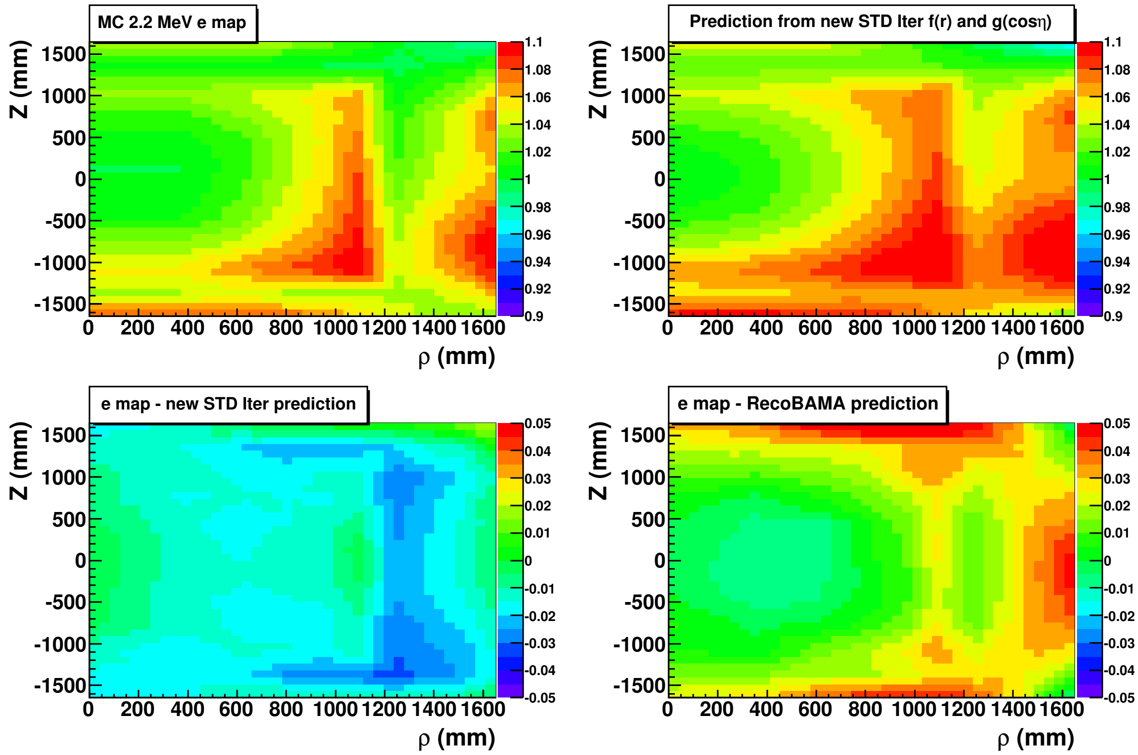

Figure 8.99: The same plots as Fig. 8.98 but considering light yield correction.

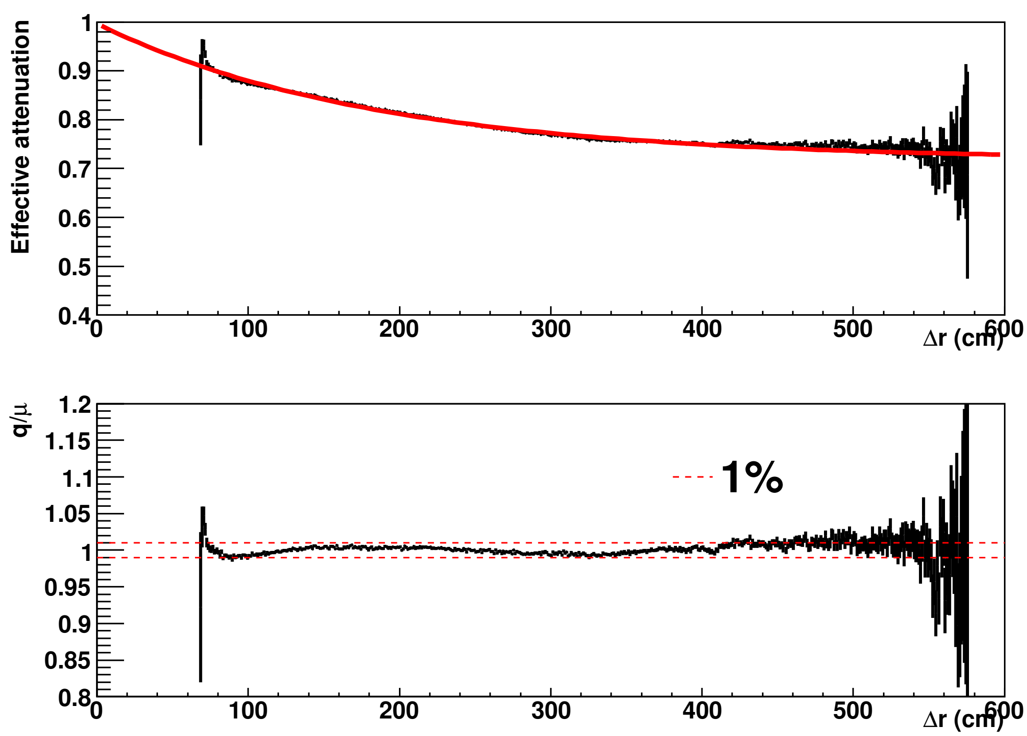

Figure 8.100: Effective attenuation $f(r)$ and the corresponding q/μ ratio for MC configuration 3.

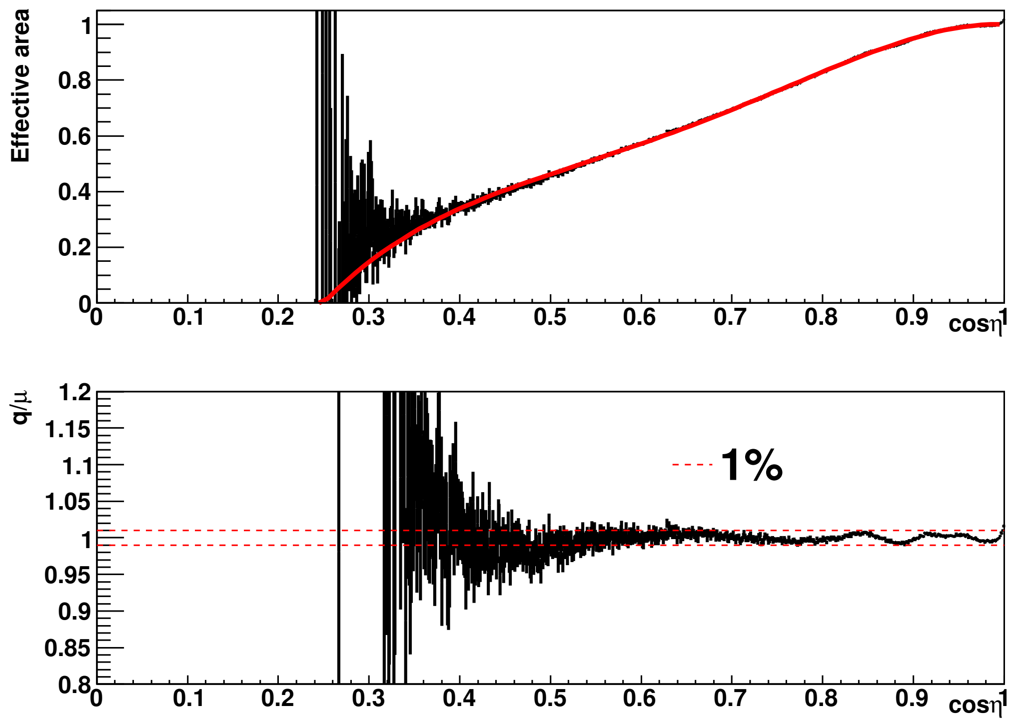

Figure 8.101: Effective area $g(\cos\eta)$ and the corresponding q/μ ratio for MC configuration 3.

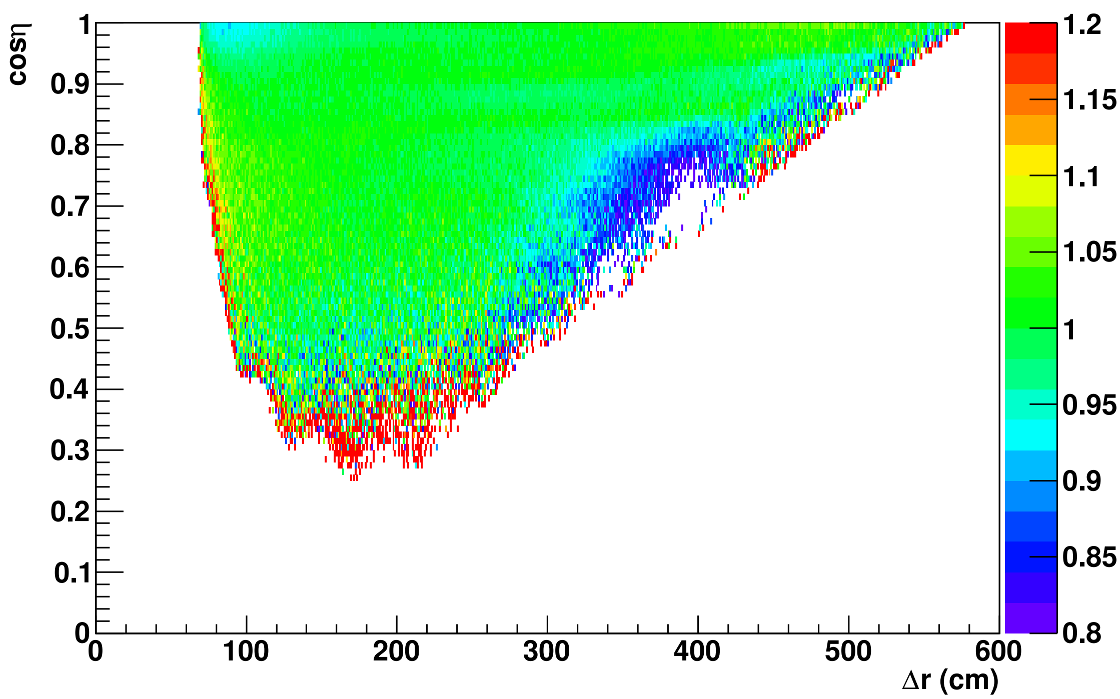

Figure 8.102: Two-dimensional q/μ ratio for MC configuration 3.

been corrected by multiplying the ratio of the light yield in the neutrino target to that in the gamma catcher. Fig. 8.103 and 8.104 display the MC energy map and prediction as well as the comparison for configuration 3, and the light yield correction has also been applied in Fig. 8.104. In general, the $f(r)$ and $g(\cos\eta)$ from the standard iteration method can recover the MC map within about 2% in the neutrino target and 5% in the gamma catcher for all configurations. If the light yield in the neutrino target and gamma catcher are different, such as configurations 2 and 3, we can clearly see it when we look at the comparison map. Once we put the light yield effect back in, the differences are also within several percent. Without reflection (configurations 1 and 2), the newly obtained $f(r)$ and $g(\cos\eta)$ from the standard iteration method predicts better than the RecoBAMA. When using default MC, the RecoBAMA predicts better only because of the linear extrapolation part of the RecoBAMA. If the same extrapolation is applied in the new $\cos\eta$ correction function from 0 to 0.7 as is done in RecoBAMA, the comparison will be as good.

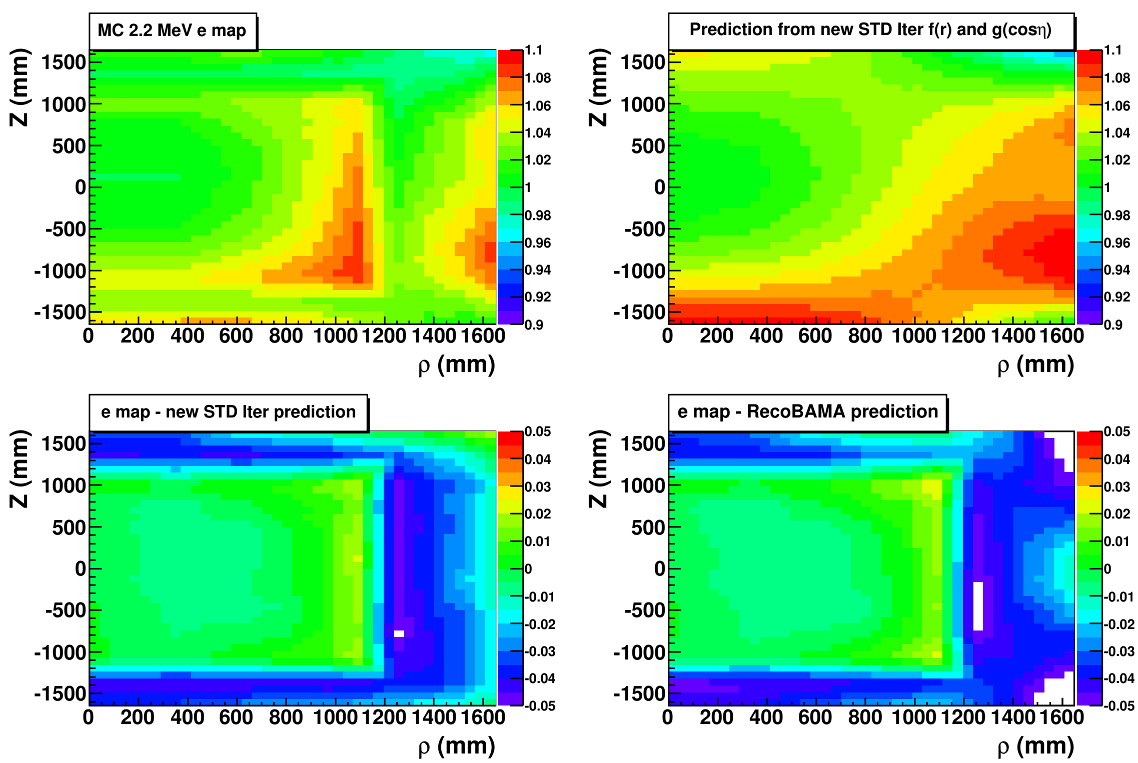

Figure 8.103: MC energy map, predicted map, their difference and the difference between MC energy map and RecoBAMA predicted map for MC configuration 3.

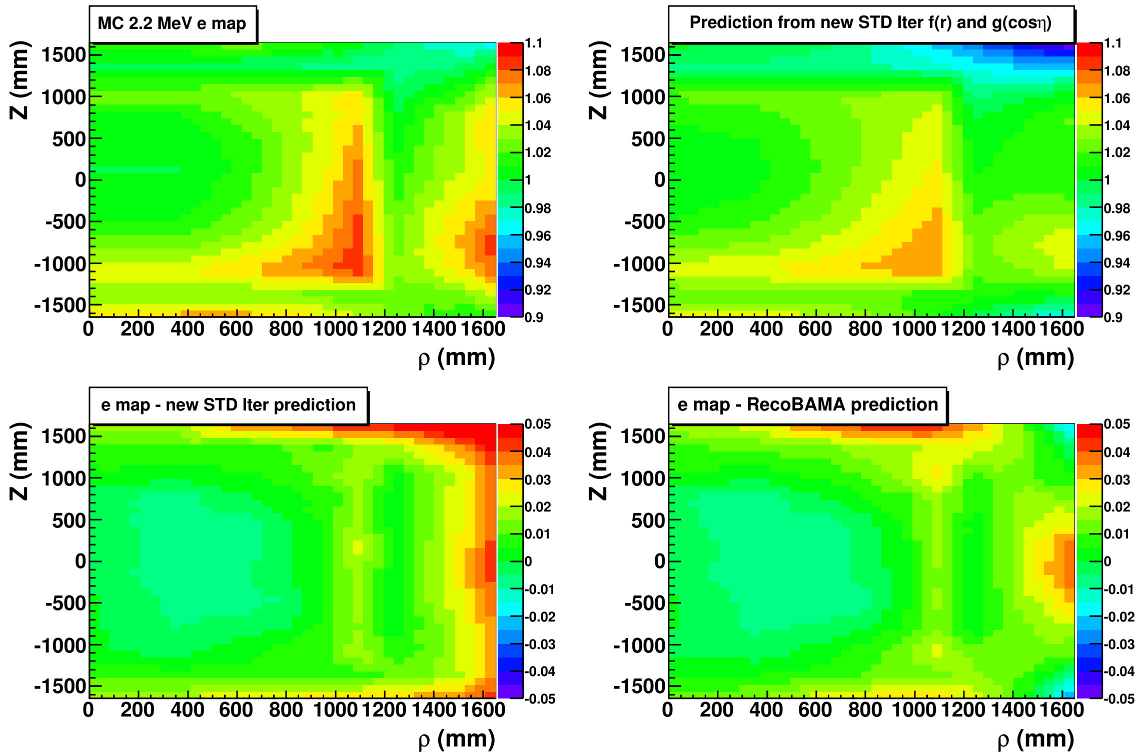

Figure 8.104: The same plots as Fig. 8.103 but considering light yield correction.

Figure 8.105 is the comparison of all the $f(r)$ and $g(\cos\eta)$ in the three configurations. The $f(r)$ and $g(\cos\eta)$ for 1 and 2 are almost the same which is as expected, since the only difference is the light yield which can be absorbed into the flux and therefore have no impact on the $f(r)$ and $g(\cos\eta)$. Interchange of these two sets of $f(r)$ and $g(\cos\eta)$ does not affect the result of the corresponding prediction map.

8.6 Summary

The behavior of reflections in MC has been understood and quantified very well. As it has been shown, the incorporation of reflection into TLLKs can improve vertex reconstruction in data. Since many issues are entangled in data, we have not fully understood the reflection and therefore have not yet applied it to data. The current solution to the energy scale is applying corrections for each position as derived from the 2.2 MeV γ from the hydrogen capture neutron data. From all the studies discussed in this chapter, the optical model will

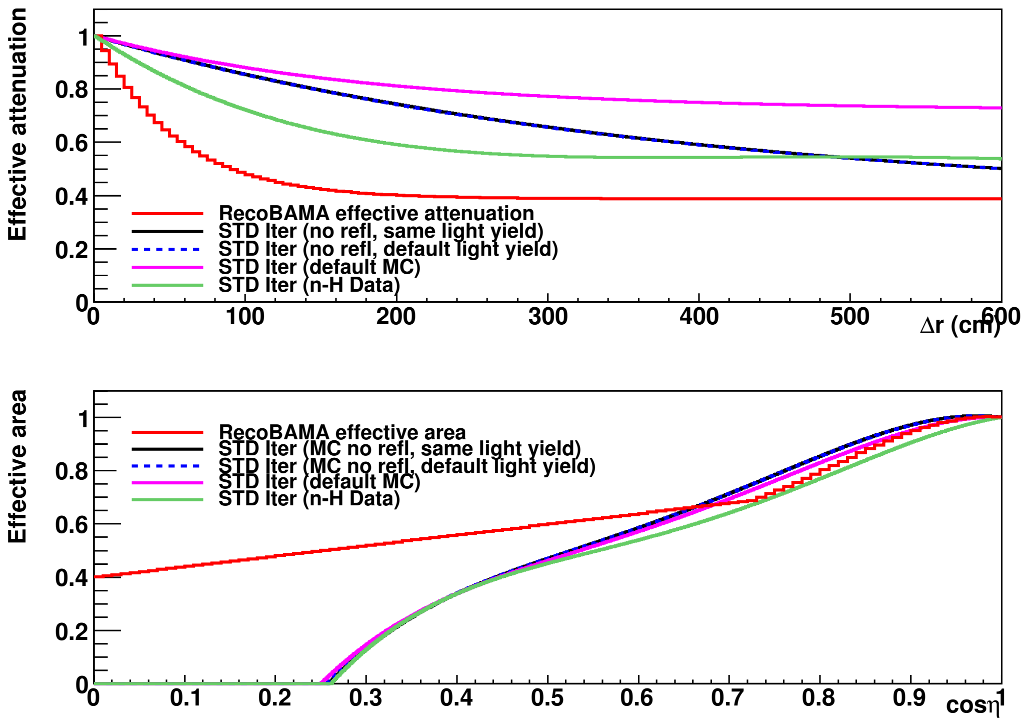

Figure 8.105: Comparison of $f(r)$ and $g(\cos\eta)$ for data and MC (configurations 1, 2 and 3).

most likely need to be modified to generate the proper energy response as obtained from the n-H data.

The parameterization of effective attenuation and effective area, $f(r)$ and $g(\cos\eta)$, were updated using n-H data. The corrections on r and $\cos\eta$ show great uniformity, but they cannot reproduce the energy map given by the n-H data. The difficulty is that the parameters in so called Model 1 and Model 3 can predict charge on PMTs very well but fail in reproducing the energy map, while the parameters in Model 2 and Model 4 can roughly recover the energy map but are incapable of charge prediction on PMTs. However, MC study shows that proper parameters in our optical model can complete both jobs. We still have a long way to go to fully understand the energy response in the data from simple principles.

Chapter 9

Conclusion

The Double Chooz experiment has been running with far detector only since April 2011. The first publication yielded $\sin^2 2\theta_{13} = 0.086 \pm 0.041\,(\text{stat.}) \pm 0.030\,(\text{syst.})$ based on an analysis using rate and energy spectrum information with an exposure of 96.8 live days. A second publication based on an exposure of 227.93 live days obtained $\sin^2 2\theta_{13} = 0.109 \pm 0.030\,(\text{stat.}) \pm 0.025\,(\text{syst.})$ and the no-oscillation hypothesis was excluded at 99.8% confidence level. A third analysis is currently underway. Double Chooz is continuous collecting data with more statistics and the near detector is being constructed; and it is expected to be completed in 2014, and will significantly reduce the systematic errors especially from the reactors.

The PMT constants including gains and time offsets, as well as charge likelihoods have been successfully extracted from the laser calibration data. The fact that PMT gains change with periodical power cycles requires frequent calibrations which prevent us from using our result. However, our PMT time offsets with only 0.15–0.20 ns uncertainty are stable with power cycles. The result has already been applied in all physics analyses. The reconstruction accuracy has been improved by our PMT time offsets. The charge likelihoods extracted from UV laser calibration data has also been put to use. The RecoBAMA using both time and charge information from inner detector PMTs is the default algorithm to generate the position information for all the Double Chooz analyses. The reconstructed flux which is the measure of the event energy based on our optical model recovers the MC map within about 2% in the neutrino target. With the better understanding of the buffer reflections, the detector energy response can be better understood, which could potentially decrease the detector related systematic errors and herewith improve the ultimate sensitivity of $\sin^2 2\theta_{13}$.

Bibliography

[1] A. H. Becquerel, Compt. Rend. Math. **122**, 420 (1896).

[2] P. Curie and M. Curie, Comptes rendus **127**, 175 (1898).

[3] E. Rutherford, Philosophical Magazine **ser. 5, xlvii**, 109 (1899).

[4] P. Villard, Comptes rendus **129**, 244 (1899).

[5] P. Villard, Comptes rendus **130**, 1010 (1900).
`http://gallica.bnf.fr/ark:/12148/bpt6k3086n.image.f1010`

[6] P. Villard, Comptes rendus **130**, 1178 (1900).

[7] P. Villard, Seances de la Societe francaise de physique, p.45–46 (1900).

[8] E. Rutherford and F. Soddy, Philosophical Magazine **4**, 370 (1902).

[9] C. D. Ellis, Proc. Roy. Soc. **A99**, 261 (1921).

[10] C. D. Ellis and H. Skinner, Proc. Roy. Soc. **A105**, 185 (1924).

[11] L. Meitner, Ergebnisse der Exakten Naturwissenschaften **3**, 160 (1924).

[12] K. Emeleus, Proc. Camb. Phil. Soc. **22**, 400 (1924).

[13] R. Gurney, Proc. Roy. Soc. **A109**, 540 (1925).

[14] C. D. Ellis and W. A. Wooster, Proc. Roy. Soc. **A117**, 109 (1927).

[15] W. Pauli, Phys. Today **31N9**, 27 (1978).

[16] J. Chadwick, Nature **129**, 312 (1932).

[17] F. Perrin, Comptes Rendus **197**, 1625 (1933).

[18] C. D. Anderson, Phys. Rev. **43**, 491 (1933).

[19] E. Fermi, Z. Phys. **88**, 161 (1934).

[20] H. Bethe and R. Peierls, Nature **133**, 532 (1934).

[21] F. Reines and C. L. Cowan, Phys. Rev. **92**, 830 (1953).

[22] C. L. Cowan, F. Reines, F. B. Harrison, E. C. Anderson, and F. N. Hayes, Phys. Rev. **90**, 493 (1953).

[23] C. L. Cowan, F. Reines, F. B. Harrison, H. W. Kruse, and A. D. McGuire, Science **124**, 103 (1956).

[24] F. Reines and C. L. Cowan, Phys. Rev. **113**, 273 (1959).

[25] B. Pontecorvo, J. Exptl. Theoret. Phys. **33**, 549 (1957).

[26] B. Pontecorvo, J. Exptl. Theoret. Phys. **34**, 247 (1958).

[27] M. Goldhaber, L. Grodzins and A. W. Sunyar, Phys. Rev. **109**, 1015 (1958).

[28] G. Danby *et al.*, Phys. Rev. Lett. **9**, 36 (1962).

[29] Z. Maki, M. Nakagava and S. Sakata, Prog. Theor. Phys. **28**, 870 (1962).

[30] J. N. Bahcall, Phys. Rev. Lett. **12**, 300 (1964).

[31] R. Davis, Phys. Rev. Lett. **12**, 303 (1964).

[32] R. Davis, D. S. Harmer, and K. C. Hoffman, Phys. Rev. Lett. **20**, 1205 (1968).

[33] P. Anselmann *et al.* (GALLEX Collaboration), Phys. Lett. **B342**, 440 (1995).

[34] J. N. Abdurashitov *et al.* (SAGE Collaboration), Phys. Rev. **C60**, 055801 (1999).

[35] Y. Fukuda *et al.* (Kamiokande Collaboration), Phys. Rev. Lett. **77**, 1683 (1998).

[36] Q. R. Ahmad *et al.* (SNO Collaboration), Phys. Rev. Lett. **87**, 071301 (2001).

[37] M. Gell-Mann, Phys. Lett. **8(3)**, 214 (1964).

[38] G. Zweig, CERN Report No. 8182/TH. 401 (1964).

[39] G. Zweig, CERN Report No. 8419/TH. 412 (1964).

[40] E. D. Bloom, *et al.*, Phys. Rev. Lett. **23(16)**, 930 (1969).

[41] M. Breidenbach, *et al.*, Phys. Rev. Lett. **23(16)**, 935 (1969).

[42] S. L. Glashow, J. Iliopoulos and L. Maiani, Phys. Rev. **D2**, 1285 (1970).

[43] J. E. Augustin *et al.*, Phys. Rev. Lett. **33**, 1406 (1974).

[44] M. Kobayashi, T. Maskawa, Prog. Theor. Phys. **49(2)**, 652 (1973).

[45] F. J. Hasert *et al.*, Phys. Lett. **46B**, 138 (1973).

[46] S. L. Glashow, Nucl. Phys. **22**, 579 (1961).

[47] A. Salam, Proc. of the 8th Nobel Symposium on "Elementary Particle Theory, Relativistic Groups and Analyticity", Stockholm, Sweden, edited by N. Svartholm, 367 (1968).

[48] S. Weinberg, Phys. Rev. Lett. **19**, 1264 (1967).

[49] M. L. Perl *et al.*, Phys. Rev. Lett. **35**, 1489 (1975).

[50] S. W. Herb *et al.*, Phys. Rev. Lett. **39**, 252 (1977).

[51] G. Arnison *et al.* (UA1 Collaboration), Phys. Lett. **B122**, 103 (1983).

[52] G. Arnison *et al.* (UA1 Collaboration), Phys. Lett. **B126**, 398 (1983).

[53] W. Gajewski (IMB Collaboration), In "Munich 1988, Proceedings, High energy physics" 1305 (1988).

[54] K. S. Hirata *et al.* (Kamiokande-II Collaboration), Phys. Lett. **B205**, 416 (1988).

[55] S. P. Mikheyev and A. Yu. Smirnov, Yad. Fiz. **42**, 1441 (1985). [Sov. J. Nucl. Phys. **42**, 913 (1985)]

[56] L. Wolfenstein, Phys. Rev. **D17**, 2369 (1978).

[57] L. Wolfenstein, Phys. Rev. **D20**, 2634 (1979).

[58] K. S. Hirata *et al.* (Kamiokande Collaboration), Phys. Rev. Lett. **58**, 1490 (1987).

[59] C. B. Bratton *et al.* (IMB Collaboration), Phys. Rev. Lett. **58**, 1494 (1987).

[60] K. S. Hirata *et al.* (Kamiokande Collaboration), Phys. Lett. **B205**, 416 (1988).

[61] Ch. Berger *et al.* (Frejus Collaboration), Phys. Lett. **B227**, 489 (1989).

[62] M. Aglietta *et al.* (NUSEX Collaboration), Europhys. Lett. **8**, 611 (1989).

[63] K. S. Hirata *et al.* (Kamiokande Collaboration), Phys. Rev. Lett. **63**, 16 (1989).

[64] L. Arnaudon *et al.* (Working Group on LEP Energy Collaboration), Phys. Lett. **B307**, 187 (1993).

[65] R. Akers *et al.* (OPAL Collaboration), Z. Phys. **C65**, 47 (1995).

[66] P. Abreu *et al.* (DELPHI Collaboration), Z. Phys. **C74**, 577 (1997).

[67] M. Acciarri *et al.* (L3 Collaboration), Phys. Lett. **B431**, 199 (1998).

[68] (ALEPH Collaboration), (DELPHI Collaboration), (L3 Collaboration), (OPAL Collaboration), (SLD Collaboration), (LEP Electroweak Working Group), (LEP Electroweak, Heavy Flavour Groups), Phys. Rept. **427**, 257 (2006).

[69] D. Casper *et al.* (IMB Collaboration), Phys. Rev. Lett. **66**, 2561 (1991).

[70] A. I. Abazov *et al.* (SAGE Collaboration), Nuclear Phys. **B19**, 84 (1991).

[71] P. Anselmann *et al.* (GALLEX Collaboration), Phys. Lett. **B285**, 376 (1992).

[72] P. Anselmann *et al.* (GALLEX Collaboration), Phys. Lett. **B342**, 440 (1995).

[73] J. N. Abdurashitov *et al.* (Sage Collaboration), Phys. Lett. **B328**, 234 (1994).

[74] Y. Fukuda *et al.* (Kamiokande Collaboration), Phys. Rev. Lett. **77**, 1683 (1996).

[75] B. T. Cleveland *et al.* (Homestake Collaboration), Nucl, Phys. Proc. Suppl. **B38**, 47 (1995).

[76] W. W. M. Allison *et al.* (Soudan-II Collaboration), Phys. Lett. **B449**, 137 (1999).

[77] Y. Fukuda *et al.* (Super-Kamiokande Collaboration), Phys. Lett. **B433**, 9 (1998).

[78] Y. Fukuda *et al.* (Super-Kamiokande Collaboration), Phys. Lett. **B436**, 33 (1998).

[79] K. Kodama *et al.* (DONUT Collaboration), Phys. Lett. **B504**, 218 (2001).

[80] S. Fukuda, *et al.* (Super-Kamiokande Collaboration), Phys. Rev. Lett. **85**, 3999 (2000).

[81] A. Aguilar *et al.* (LSND Collaboration), Phys. Rev. **D64**, 112007 (2001).

[82] Q. R. Ahmad *et al.* (SNO Collaboration), Phys. Rev. Lett. **89**, 011301 (2002).

[83] K. Eguchi *et al.* (KamLAND Collaboration), Phys. Rev. Lett. **90**, 021802 (2003).

[84] M. H. Ahn *et al.* (K2K Collaboration), Phys. Rev. Lett. **90**, 041801 (2003).

[85] Y. Ashie *et al.* (Super-Kamiokande Collaboration), Phys. Rev. Lett. **93**, 101801 (2004).

[86] K. Eguchi *et al.* (KamLAND Collaboration), Phys. Rev. Lett. **92**, 071301 (2004).

[87] S. L. Glashow, Nucl. Phys. **22(4)**, 579 (1961).

[88] S. Weinberg, Phys. Rev. Lett. **19**, 1264 (1967).

[89] A. Salam, "Weak and electromagnetic interactions", in Elementary particle theory: relativistic groups and analyticity, N. Svartholm, ed., p. 367. Almqvist and Wiksell. Proceedings of the eighth Nobel symposium. (1968).

[90] G. 't Hooft and M. Veltman, Nucl. Phys. **B44**, 189 (1972).

[91] C. Amsler *et al.*, (Particle Data Group), Phys. Lett. **B667**, 1 (2008).

[92] F. Englert and R. Brout, Phys. Rev. Lett. **13(9)**, 321 (1964).

[93] P .W. Higgs, Phys. Rev. Lett. **13(16)**, 508 (1964).

[94] G. S. Guralnik, C. R. Hagen and T. W. B. Kibble, Phys. Rev. Lett. **13(20)**, 585 (1964).

[95] G. S. Guralnik, Int. J. Mod. Phys. **A24(14)**, 2601 (2009).

[96] G. Aad *et al.* (ATLAS Collaboration), Phys. Lett. **B716(1)**, 1 (2012).

[97] S. Chatrchyan *et al.* (CMS Collaboration), Phys. Lett. **B716**, 30 (2012).

[98] R. G. Sachs *et al.*, Phys. Rev. Lett. **13**, 286 (1964).

[99] R. Wendell *et al.* (Super-Kamiokande Collaboration), Phys. Rev. **D81**, 092004 (2010).

[100] B. Aharmim *et al.* (SNO Collaboration), Phys. Rev. **C88**, 025501 (2011).

[101] A. Gando *et al.* (KamLAND Collaboration), Phys. Rev. **D83**, 052002 (2011).

[102] Y. Abe *et al.* (Double Chooz Collaboration), Phys. Rev. Lett. **108**, 131801 (2012).

[103] F. An *et al.* (DayaBay Collaboration), Chinese Phys. **C37**, 011001 (2013).

[104] J. Ahn *et al.* (RENO Collaboration), Phys. Rev. Lett. **108**, 191802 (2012).

[105] P. Adamson *et al.* (MINOS Collaboration), Phys. Rev. Lett. **106**, 181801 (2011).

[106] K. Scholberg (2003). [arXiv:hep-ex/0308011]

[107] Y. Fukuda *et al.* (Super-Kamiokande Collaboration), Phys. Rev. Lett. **81(8)**, 1562 (1998).

[108] V. M. Lobashev *et al.*, Nucl. Phys. Proc. Suppl. **91**, 280 (2001).

[109] C. Kraus *et al.*, Eur. Phys. J. **C40**, 447 (2005).

[110] V. N. Aseev *et al.*, Phys. Rev. **D84**:112003 (2011).

[111] K. Assamagan *et al.*, Phys. Rev. **D53**, 6065 (1996).

[112] CUPP, "Laboratory measurements and limits for neutrino properties" at `http://cupp.oulu.fi/neutrino/nd-mass.html` a web page maintained by the Center for Underground Physics in Pyhäsalmi.

[113] S. Hannestad *et al.*, JCAP08 **001** (2010).

[114] J. Wolf *et al.*, Nucl. Instrum. Meth. **A62** (2010).

[115] A. Nucciotti *et al.* (MARE Collaboration), Plenary Talk presented at the XXIV International Conference on Neutrino Physics and Astrophysics (2010). [arXiv:1012.2290]

[116] P. Minkowski, Phys. Lett. **B67**, 421 (1977).

[117] M. Gell-Mann, P. Ramond and R. Slansky, In "Supergravity", p. 315, edited by F. van Nieuwenhuizen and D. Freedman, North Holland, Amsterdam (1979).

[118] T. Yanagida, Workshop on the Baryon Number of the Universe and Unified Theories, Tsukuba, Japan, 13–14 (1979).

[119] R. N. Mohapatra and G. Senjanovic, Phys. Rev. Lett. **44**, 912 (1980).

[120] Z. Maki, M. Nakagawa and S. Sakata, Prog. Theor. Phys. **28**, 870 (1962).

[121] K. Abe *et al.* (T2K Collaboration), Phys. Rev. Lett. **107**, 041801 (2011).

[122] D. Ayres *et al.* (NOνA Collaboration), Fermilab-Proposal-0929 (2004). [arXiv:hep-ex/0503053]

[123] E. Majorana, Nuovo Cimento **5**, 171 (1937).

[124] J. Kotila and F. Iachello, Phys. Rev. **C85**, 034316 (2012).

[125] A. Gando *et al.*, Phys. Rev. **C85**, 045504 (2012).

[126] S. M. Bilenky *et al.*, Phys. Rep. **379**, 69 (2003).

[127] S. R. Elliott and P. Vogel, Ann. Rev. Nucl. Part. Sci. **52**, 115 (2002).

[128] S. R. Elliott and J. Engel, J. Phys. **G30**, R183 (2004).

[129] F. T. Avignone, S. R. Elliott and J. Engel, Rev. Mod. Phys. **80**, 481 (2008).

[130] S. M. Bilenky, Lect. Notes Phys. **817**, 139 (2010).

[131] W. Rodejohann, Int. J. Mod. Phys. **E20**, 1833 (2011).

[132] J. Gomez-Cadenas *et al.*, Riv. Nuovo Cim. **35**, 29 (2012).

[133] B. Schwingenheuer, prepared for TAUP (2011). [arXiv:1201.4916]

[134] M. Gianpiero *et al.*, Nucl. Phys. **B729**, 221 (2005).

[135] A. A. Aguilar-Arevalo *et al.* (MiniBooNE Collaboration), Phys. Rev. Lett. **98**, 231801 (2007).

[136] C. Giunti and M. Laveder, Phys. Rev. **C83**, 065504 (2011).

[137] G. Mention *et al.*, Phys. Rev. **D83**, 073006 (2011).

[138] The White Paper, "A New Nuclear Reactor Neutrino Experiment to Measure 13," is available at `http://www.hep.anl.gov/minos/reactor13/white.html` (2004). [arXiv:hep-ex/0402041]

[139] E. Tournu *et al.*, EDF TechnicalNote (2001).

[140] Standard AFNOR XP X 07-020, Palo Alto, CA. (1996).

[141] Y. Caffari and J. M. Favennec, EDF tech-note H-P1C-2011-02007-FR. (2011).

[142] T. A. Mueller *et al.*, Phys. Rev. Lett. **C83**, 054615 (2011).

[143] K. Schreckenbach, G. Colvin, and F. von Feilitzsch, Phys. Lett. **160B**, 325 (1985).

[144] F. von Feilitzsch and K. Schreckenbach, Phys. Lett. **118B**, 162 (1982).

[145] A. Hahn *et al.*, Phys. Lett. **B218**, 365 (1989).

[146] P. Huber, Phys. Rev. **C84**, 024617 (2011).

[147] G. Mention *et al.*, Phys. Rev. **D83**, 073006 (2011).

[148] A. Onillon, "Reactor plots UNDER REVIEW", Double Chooz internal document 3369 (2011).

[149] P. Vogel and J. F. Beacom, Phys. Rev. **D60**, 053003 (1999).

[150] A. Pichlmaier *et al.*, Phys. Lett. **B693**, 221 (2010).

[151] V. Kopeikin, L. Mikaelyan, and V. Sinev, Phys. At. Nucl. **67**, 1892 (2004).

[152] O. Meplan *et al.*, in ENC 2005: European Nuclear Conference; Nuclear power for the XXIst century: from basic research to high-tech industry (2005).

[153] NEA-1845/01, documentation for MURE (2009).

[154] G. Marleau *et al.*, Report IGE-157 (1994).

[155] C. Jones, "Prediction of the Reactor Antineutrino Flux for the Double Chooz Experiment", Ph.D. thesis, MIT (2012).

[156] Y. Declais *et al.*, Phys. Lett. **B338**, 383 (1994).

[157] T. Matsubara *et al.*, Nucl. Instrum. Meth. **A661**, 16 (2011).

[158] C. Bauer *et al.*, JINST **6**, P06008 (2011).

[159] E. Calvo *et al.*, Nucl. Instrum. Meth. **A621**, 222 (2010).

[160] C. Aberle *et al.*, JINST **7**, P06008 (2012).

[161] S. Abe *et al.* (KamLAND Collaboration), Phys. Rev. **C81**, 025807 (2010).

[162] Y. Abe *et al.* (Double Chooz Collaboration), Phys. Rev. **D86**, 052008 (2012).

[163] M. Appolonio *et al.* (CHOOZ Collaboration), Phys. Lett. **B466**, 415 (1999).

[164] F. Kaether and C. Langbrandtner, JINST **7**, P09002 (2012).

[165] D. Dietrich *et al.*, accepted for publication in JINST (2012). [arXiv:1207.1623]

[166] A. Franke, "OV General Documentation", Double Chooz internal document 1400 (2010).

[167] P. Barrillon *et al.*, MAROC: Multi-Anode ReadOut Chip for MAPMTs, proceedings of 2007 IEEE conference (2007), P. Barrillon *et al.*, 64-channel Front-End readout chip, MAROC2 datasheet, `http://omega.in2p3.fr/`. (2007).

[168] F. Beissel *et al.*, "The Trigger and Timing System of the Double Chooz Experiment" (2012). [arXiv:1209.5607]

[169] A. Cabrera, Nucl. Instrum. Meth. Phys. Res. **A617**, 473 (2010).

[170] T. Akiri, Ph.D. thesis, Universite Paris-Diderot. (2010).

[171] CAEN Corporation, `http://www.caen.it/`. The device was co-developed with APC.

[172] E. Caden, "Front End Electronics", Double Chooz internal document 2345 (2011).

[173] F. Ardellier *et al.*, "Double Chooz: A Search for the Neutrino Mixing Angle θ_{13}" (2006). [arXiv:hepex/0606025v4]

[174] B. Reinhold, "Development of a Level-1 Trigger and Timing System for the Double Chooz Neutrino Experiment", Ph.D. thesis, RWTH Aachen (2009).

[175] Z. Djurcic *et al.*, "Z-axis Deployment System IRR", Double Chooz internal document 2419 (2011).

[176] I. Ostrovskiy, "Guide tube IRR", Double Chooz internal document 887 (2009).

[177] P. Wahnon, "IDLI Test Bench Light Level Measurements", Double Chooz internal document 1652 (2010).

[178] J. Maricic and E. A. Damon, "Articulated Arm System Integration Readiness Review", Double Chooz internal document 2519 (2011).

[179] NIST, "Radionuclide Half-Life Measurements" (2011).

[180] J. Reichenbacher, "Update on work on untagged sources", Double Chooz internal document 2275 (2011).

[181] J. Reichenbacher, "Making New Calibration Sources at UA", Double Chooz internal document 4914 (2013).

[182] I. Stancu and Y. Sun, "Measuring the Time Offsets in the Empty Detector", Double Chooz internal document 2145 (2011).

[183] D. Kaplan, "Central LED Flasher Memo", Double Chooz internal document 1721 (2010).

[184] L. Camilleri, "Muon Rates at Chooz", Double Chooz internal document 1527 (2010).

[185] C. Thomas, "Radioactive Decay and Differentiating between Li-9 decay and IBD", Double Chooz internal document 1021 (2009).

[186] F. Ajzenberg-Selove, Nucl. Phys. **A506**, 1 (1990).

[187] V. Jampani, "B12 analysis", Double Chooz internal document 2899 (2011).

[188] P. Adamson *et al.* (MINOS Collaboration), Phys. Rev. Lett. **107**, 181802 (2011).

[189] G. J. Feldman and R. D. Cousins, Phys. Rev. **D57**, 3873 (1998).

[190] `http://akizukidenshi.com/download/ds/elandigital/usbpulse100ug.pdf`.

[191] Hamamatsu R2154-05 obtained from Bridgeport-Instruments.

[192] MCA base emorpho, `http://www.bridgeportinstruments.com/products/mcabases.html`.

[193] IGOR-PRO GUI, `http://www.wavemetrics.com/`.

[194] J. Goon, "laser system IRR version 3.1", Double Chooz internal document 2414 (2011).

[195] C. Buck, "Scintillator", Double Chooz internal document 292 (2008).

[196] McMaster-Carr acrylic, `http://www.mcmaster.com/$#$cast-acrylic/`.

[197] I. Stancu, "The Ge-68 Calibration Data and the SPE Inefficiency", Double Chooz internal document 3397 (2011).

[198] T. Matsubara, "Development of calibration method with LI system simulation", Double Chooz internal document 1058 (2009).

[199] I. Stancu, "Measurement of the Speed of Light in the Double Chooz Volumes Using the 470 nm Laser Data", Double Chooz internal document 4291 (2012).

[200] C. Aberle and B. Reinhold, "Position Dependency of Detector Response", Double Chooz internal document 2566 (2011).

[201] MINUIT, CERN Program Library entry D506. Available at `http://wwwasdoc.web.cern.ch/wwwasdoc/minuit/minmain.html`.

[202] I. Stancu, "Position Dependence of the Energy Function: Data vs MC", Double Chooz internal document 3499 (2011).

[203] C. Aberle and B. Reinhold, "Construction of Detector Response Maps", Double Chooz internal document 4066 (2012).

[204] K. Matsumoto, "Study on DATA/MC discrepancy in detector response map", Double Chooz internal document 4446 (2012).

[205] J. Reichenbacher, "Spatial Discrepancies Data/MC: Cos(Alpha) Dependence of QE compared to Maps", Double Chooz internal document 3905 (2012).